NIST Special Publication 988

# Technical Digest: Symposium on Optical Fiber Measurements, 2002

Sponsored by the National Institute of Standards and Technology
in cooperation with the IEEE Lasers and Electro-Optics Society
and the Optical Society of America

NIST National Institute of Standards and Technology • Technology Administration • U.S. Department of Commerce

The National Institute of Standards and Technology was established in 1988 by Congress to "assist industry in the development of technology . . . needed to improve product quality, to modernize manufacturing processes, to ensure product reliability . . . and to facilitate rapid commercialization . . . of products based on new scientific discoveries."

NIST, originally founded as the National Bureau of Standards in 1901, works to strengthen U.S. industry's competitiveness; advance science and engineering; and improve public health, safety, and the environment. One of the agency's basic functions is to develop, maintain, and retain custody of the national standards of measurement, and provide the means and methods for comparing standards used in science, engineering, manufacturing, commerce, industry, and education with the standards adopted or recognized by the Federal Government.

As an agency of the U.S. Commerce Department's Technology Administration, NIST conducts basic and applied research in the physical sciences and engineering, and develops measurement techniques, test methods, standards, and related services. The Institute does generic and precompetitive work on new and advanced technologies. NIST's research facilities are located at Gaithersburg, MD 20899, and at Boulder, CO 80303. Major technical operating units and their principal activities are listed below. For more information visit the NIST Website at http://www.nist.gov, or contact the Publications and Program Inquiries Desk, 301-975-3058.

## Office of the Director

- National Quality Program
- International and Academic Affairs

## Technology Services

- Standards Services
- Technology Partnerships
- Measurement Services
- Information Services
- Weights and Measures

## Advanced Technology Program

- Economic Assessment
- Information Technology and Applications
- Chemistry and Life Sciences
- Electronics and Photonics Technology

## Manufacturing Extension Partnership Program

- Regional Programs
- National Programs
- Program Development

## Electronics and Electrical Engineering Laboratory

- Microelectronics
- Law Enforcement Standards
- Electricity
- Semiconductor Electronics
- Radio-Frequency Technology[1]
- Electromagnetic Technology[1]
- Optoelectronics[1]
- Magnetic Technology[1]

## Materials Science and Engineering Laboratory

- Intelligent Processing of Materials
- Ceramics
- Materials Reliability[1]
- Polymers
- Metallurgy
- NIST Center for Neutron Research

## Chemical Science and Technology Laboratory

- Biotechnology
- Process Measurements
- Surface and Microanalysis Science
- Physical and Chemical Properties[2]
- Analytical Chemistry

## Physics Laboratory

- Electron and Optical Physics
- Atomic Physics
- Optical Technology
- Ionizing Radiation
- Time and Frequency[1]
- Quantum Physics[1]

## Manufacturing Engineering Laboratory

- Precision Engineering
- Manufacturing Metrology
- Intelligent Systems
- Fabrication Technology
- Manufacturing Systems Integration

## Building and Fire Research Laboratory

- Applied Economics
- Materials and Construction Research
- Building Environment
- Fire Research

## Information Technology Laboratory

- Mathematical and Computational Sciences[2]
- Advanced Network Technologies
- Computer Security
- Information Access
- Convergent Information Systems
- Information Services and Computing
- Software Diagnostics and Conformance Testing
- Statistical Engineering

---

[1] At Boulder, CO 80303.

[2] Some elements at Boulder, CO.

## NIST Special Publication 988

# Technical Digest: Symposium on Optical Fiber Measurements, 2002

Digest of a symposium sponsored by the
National Institute of Standards and Technology
in cooperation with the
IEEE Lasers and Electro-Optical Society
and the Optical Society of America

September 24-26, 2002
National Institute of Standards and Technology
Boulder, Colorado 80305

Edited by
P. A. Williams
G. W. Day

September 2002

**U.S. Department of Commerce**
*Donald L. Evans, Secretary*

**Technology Administration**
*Phillip J. Bond, Under Secretary for Technology*

**National Institute of Standards and Technology**
*Arden L. Bement, Jr., Director*

**National Institute of Standards and Technology Special Publication 988**
**Natl. Inst. Stand. Technol. Spec. Publ. 988, 232 pages (September 2002)**
**CODEN: NSPUE2**

U.S. GOVERNMENT PRINTING OFFICE
WASHINGTON: 2002

---

For sale by the Superintendent of Documents, U.S. Government Printing Office
Internet: bookstore.gpo.gov Phone: (202) 512-1800 Fax: (202) 512-2250
Mail: Stop SSOP, Washington, DC 20402–9325

# PREFACE

This year has been a challenging one for the optical fiber telecommunications industry. In spite of that, the 12th Symposium on Optical Fiber Measurements has seen a significant increase in the number of submitted papers. This year, we are bulging at the seams, having accepted 51 papers (9 invited and 42 contributed). The international participation in SOFM remains strong with a little more than half of the papers originating outside the United States.

Topically, the papers are more diverse than usual. Except for polarization-mode dispersion, which fills three sessions this year, there is a fairly even distribution across the measurement subjects of nonlinear behavior, fiber and waveguide geometry, group delay, dispersion, wavelength, polarization, multimode fiber, and systems modeling.

Happy reading,

Paul Williams
Gordon Day
Boulder, Colorado
September, 2002

# SYMPOSIUM COMMITTEE

G.W. Day, NIST, General Chair

P.A. Williams, NIST, Program Chair

A. Barlow, PerkinElmer

S.C. Fleming, Sydney University

D. Franzen, NIST

N. Gisin, University of Geneva

M. Hackert

T.A. Hanson, Corning

A. Inenaga, JDS Uniphase

J. Jackel, Telcordia

K. Okamoto, NEL

W. Reed, OFS Fitel

G. W. Schinn, EXFO

C. Shaar, NetTest

J. Taylor, NPL

K.K. Wong, Northstar Photonics

# CONTENTS

# The Unique Measurement Challenges of Raman Amplifiers

**Alan Evans, Stuart Gray, Mark Muktoyuk**
*Corning Inc., Science & Technology, SP-AR-01-4, Corning, NY 14831*

## I. Introduction

New technologies are required for the improved system performance of today's ultra long-haul 10 Gb/s and future 40 Gb/s transmission. Stimulated Raman scattering, discovered in 1925, and demonstrated as an amplifier in 1973, [1] has emerged as a key solution to greater transmission distance and bit rate by reducing cascaded amplified spontaneous emission build-up in the optical link. [2-5] The small gain coefficient of stimulated Raman scattering provides long interaction lengths thereby distributing gain (and spontaneous noise) over the transmission span. It is well known that distributed amplifiers have a signal-to-noise ratio in between that of post- and pre-amplifiers. [6] Given that fiber nonlinearities limit the launch power, today's long-haul systems operate in a pre-amplified mode. Distributed Raman amplification can reduce noise build-up by acting as a low-noise pre-amplifier to the subsequent in-line discrete amplifier.

As an amplifier, there are similarities between Raman and erbium; however, there are unique measurement challenges specific to using transmission fiber as the gain media. This paper reviews recent progress in Raman measurements and is broken into three parts: the first describes standard gain measurements highlighting details that improve accuracy and reliability; the second focuses on ASE and other noise sources and why optical noise can be a misleading indicator of performance; the third addresses field-deployment issues that need consideration for practical commercial systems.

## II. Raman Gain Measurements

Obtaining accurate Raman gain information is key to the design and deployment of distributed Raman amplifiers. Gain information includes: $g_R/A_{eff}$ (the ratio of the Raman gain coefficient divided by effective area of the fiber at the pump wavelength) and its spectral dependence; and the spectral attenuation, $\alpha_p$, of the Raman pump light in the 14xx nm wavelength band. The gain coefficient not only represents the wavelength-dependent strength of the pump-to-signal scattering-induced Raman amplification, but also the energy distribution of optical phonons. In a mechanical sense, the gain coefficient is the vibrational response to a pump impulse function. An independent measurement of the effective area could be used to obtain $g_R$, but this is not necessary for amplifier design in optical fiber. From the Raman gain coefficient and pump attenuation, a pump efficiency figure of merit, FOM, is derived which is the small signal pump on/off gain versus pump power in units of dB/W:

$$FOM = \frac{g_R}{A_{eff}\alpha_p} \approx \frac{g_R L_{eff}}{A_{eff}} = \frac{G_{R,On/Off}}{P_p} \text{ where } L_{eff} = \frac{(1-\exp(-\alpha_p L))}{\alpha_p L}$$ is the effective length, L is the fiber length and

$$G_{R,\ On/Off} = 10\log\left(\frac{P_{out}(Pump\ on, signal\ on) - P_{out}(Pump\ on, signal\ off)}{P_{signal\ out}(Pump\ off, signal\ on)}\right)$$

where the first term is the numerator is the signal power out of the fiber with the Raman pump(s) on, the second term in the numerator is the background amplified spontaneous emission and the denominator is the signal power out of the fiber with the Raman pump(s) off. The pump on/off gain is typically given at the spectral peak of the Raman gain coefficient so that multiplying the pump FOM by pump power gives the maximum small signal Raman on/off gain for a single pump wavelength.

An experimental setup for measuring Raman on/off gain is shown in Figure 1. A broadband light emitting diode signal source (ELED) provides unpolarized and low intensity signal light to the fiber under test. The low intensity avoids pump-depleted gain saturation and allows the use of analytic solutions to calculate the Raman gain coefficient of the fiber. The LED source also allows for continuous gain measurements across greater than a 25 THz wide gain bandwidth. For Phosphorous-doped fiber, a signal source greater than 40 THz is required as shown in Figure 2. For a 1450 nm pump, this implies an optical spectrum analyzer (OSA) scan beyond 1730 nm. A tunable laser could be used as the signal source but is slower since an individual measurement has to be made at each desired point verses a broadband, single scan capture of an OSA when using an ELED. The tunable also has a limited tuning range and several such sources may be required to cover the desired bandwidth. A bank of fixed wavelength DFB lasers could also be used but does not give a continuous gain spectrum.

One important issue related to the source is to ensure good optical signal-to-noise ratio: As a guideline, the signal output without pumps on should be 15 to 20 dB higher than the OSA noise floor; the measured gain should be greater than about 2 dB; and the signal output with pumps on should be 15 to 20 dB greater than the ASE power. While this sets limits on minimum and maximum fiber length and required pump power, the setup is robust against OSA power inaccuracy since the pump on/off gain is a relative (not absolute) measurement.

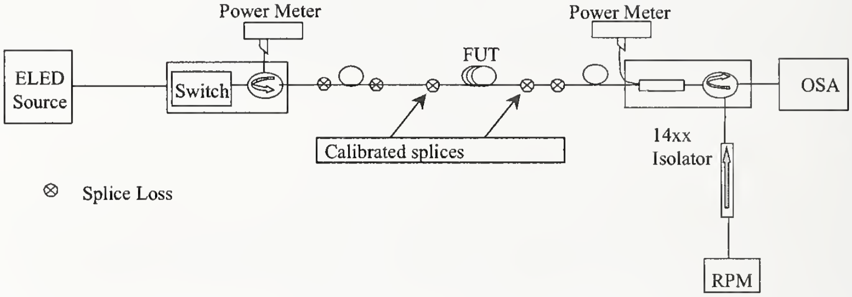

*Figure 1: Raman fiber gain experimental setup. RPM is the Raman pump module, FUT is fiber under test.*

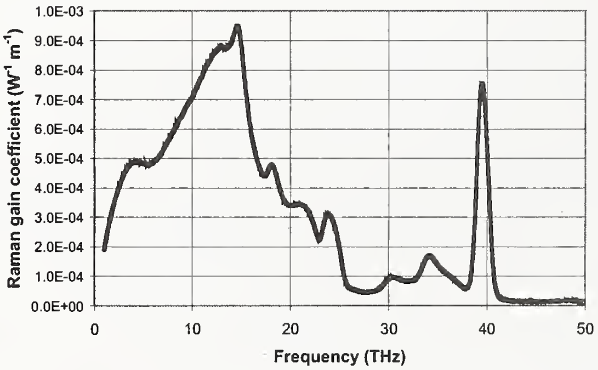

*Figure 2: Raman gain spectrum for a P-doped optical fiber. The gain peak near 13 THz is due to the silica glass matrix; the gain peak near 40 THz is due to the phosphorus dopant.*

Continuing with the experimental set up, the input switch is used to block the signal source so the amplified spontaneous emission spectrum can be measured and subtracted from the amplified signal spectrum with the pumps on. The input circulator removes unabsorbed pump while the output circulator injects the Raman pump counter-propagating with respect to the signal light. This is preferred over 14xx/1550 nm WDMs that are wavelength dependent and make it difficult to measure the Raman spectrum close to the pump wavelength. It is important that such information can be obtained to calculate levels of pump to pump interaction in Raman amplifiers. The power meter, with readings referenced to the power internal to the fiber under test (FUT), is used to measure pump attenuation and as a check to make sure pump depletion has not occurred. Finally, an unpolarized fiber laser or a set of two fiber grating stablized, 14xx nm, laser diodes orthogonally polarized are used as the Raman pumps. If the Raman pump is polarized, there can be polarization dependent gain and errors in the gain spectrum. This is illustrated in Figure 3 where the gain spectrum with one of the polarization-multiplexed pumps is turned off. Fortunately, polarization effects are easily avoided since signal and pump degree of polarization can be kept small;

in addition, fiber lengths can be large enough and the pump is counter-propagating so that polarization evolution is randomized. Finally, the set up can be enhanced by measuring the Raman gain at multiple wavelengths. This gives the of wavelength dependence of the Raman gain coefficient which, to a good approximation, is linear through the 14xx nm wavelength band.

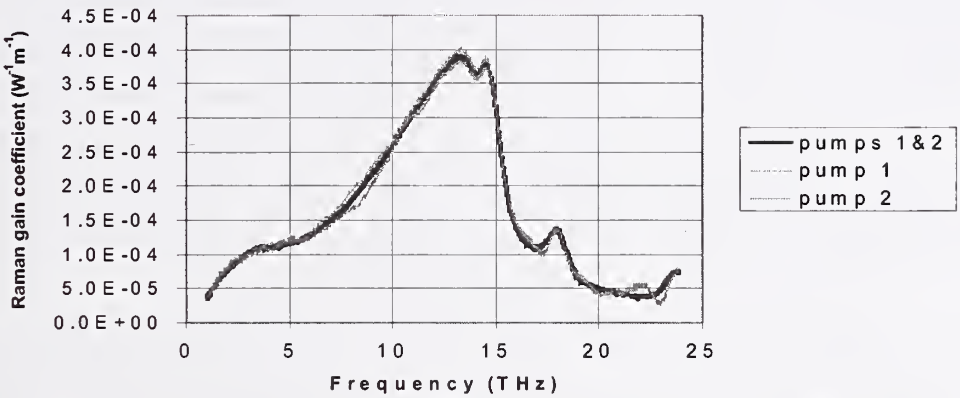

*Figure 3: Raman gain spectrum for 5 km of standard single-mode fiber with individual pumps on and both together (shown as the middle line).*

Any measurement procedure should have a number of automated steps that ensure the measurement is properly performed. First, there should be a check that the powers of the two pumps of the same wavelength are equal. Second, the power of the unabsorbed pump with and without the signals should be compared. If the difference is too great, either the input pump power is unstable (which can be checked with the other power meter channel) or pump-depleted gain saturation is occurring. Third, at any time, the user should be able to take a baseline pump spectrum and calculate a new power-averaged center wavelength. This is done to account for any wavelength drift, say at the beginning of the day or when the bench is idle for more than an hour. We recommend using power-averaged center wavelength in contrast to peak wavelength for a more stable and realistic characterization of the complex modal structure of grating-stabilized Fabry-Perot laser diodes. Finally, the pump attenuation should be measured and used in the effective length calculation.

The last issue addressed related to Raman gain measurements is the impact of launch conditions in few-moded fibers. For dispersion-compensating fibers (DCF), there can be additional design flexibility with selectively launching into the lowest order mode of a few-moded fiber. Launching into the lowest mode at both the signal and pump wavelength is required to get reliable gain spectrum data. For example, Figure 4 shows gain spectrum for two uncontrolled launches into a DCF. Note the difference in peak value and in high frequency secondary peaks. Measurements on unpackaged DCF need to account for this effect.

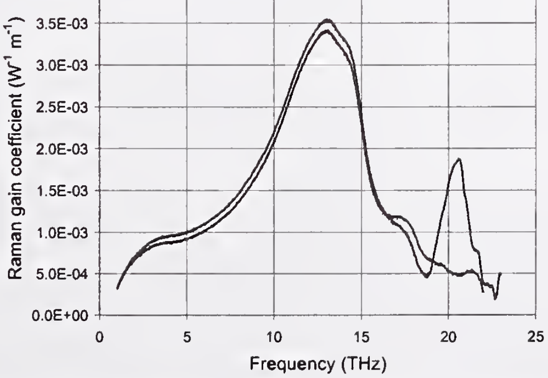

*Figure 4: Raman gain coefficient of a few-moded DCF under two different launch conditions*

## III. Noise Figure

Raman and EDFAs both generate amplified spontaneous emission resulting in signal-spontaneous and spontaneous-spontaneous beat noise. This noise source is captured in the standard optical noise measurement technique. However, the fast response time of Raman scattering and distributed Rayleigh scattering add terms only captured in electrical noise measurements. The fast response time allows pump power RIN (relative intensity noise) transfer to the signal [7] and pump-mediated signal cross-talk [8]. With the later, the pseudo-random signal depletes the pump, creating pump noise that transfers onto other WDM signals. Double Rayleigh backscattering (DRBS) of the signal creates distributed multi-path interference of random phase and intensity leading to Gaussian-like noise on the signal.[9, 10] The first two effects are mitigated by counter-propagating the pump with respect to the signal to average pump power fluctuations over the transit time of the amplifier; DRBS MPI is avoided in distributed amplifiers by keeping gain low and in discrete amplifiers by splitting gain between two, isolated stages. DRBS-induced MPI becomes a greater concern for high Raman gain in long span lengths. More recently discovered noise effects include broadening of the DRBS interference and enhanced ASE in properly phase-matched fibers, [11, 12] and an increase in DRBS for temporally-modulated Raman pumps. [13]

However, in a well-designed Raman amplifier, ASE-induced signal-spontaneous noise is the dominant noise mechanism. It is convenient to treat noise figure as a discrete, lumped quantity to cascade it through the optical link. Since distributed Raman amplification is added to the existing transmission fiber, a differential noise figure, known as the Raman effective noise figure is defined in terms of the amplified spontaneous noise, $\rho_{ASE}$, at the output of the transmission span: $\rho_{ASE} \equiv h\nu(G_{R,\, on/off}F_{eff} - 1)$. As an example of the dependence of the effective noise figure on Raman on/off gain, consider a 48 C-band signals from 1527.6 nm to 1565.1 nm with launch power per channel of 0 dBm propagating through 90 km of non-zero dispersion-shifted fiber. Two pumps at 1426 and 1455 nm are varied in power to sweep through a 0 to 22 dB range of Raman gain. The resulting effective noise figure for the bluest channel is shown in Figure 5, with the shortest wavelength channel having the worst noise figure of all the channels for a number of reasons: pump-to-pump Raman power transfer allows the lower frequency pump to penetrate deeper into the fiber so the lower frequency signals have more distributed gain than the higher frequency signals; phonon energy distribution means that the ground state is more populated for higher frequency signals; spectral attenuation of the pump and C-band signals are greater for shorter frequency; and signal-to-signal Raman gain means for spectrally flat gain, the gain of lower frequency occurs closer to the output end of the fiber where OSNR is lower.

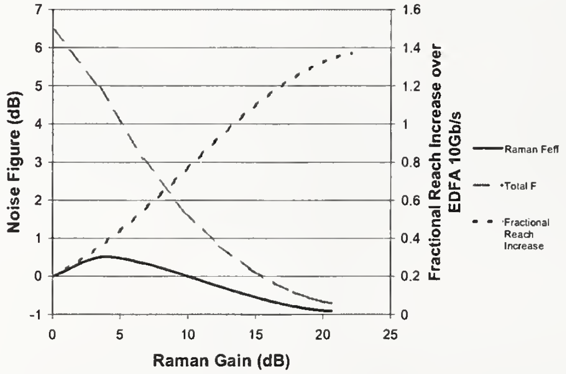

*Figure 5: Noise figure vs. Raman gain for a two pump wavelength C band example. Also shown is the total noise figure including a 6.5 dB EDFA and fractional reach increase assuming reach scales inversely with noise figure.*

With this definition of noise figure, cascaded noise build up through multiple spans can easily be considered by replacing the complicated, distance-dependent, distributed gain and noise functions with an equivalent lumped amplifier at the end of each span just before the next in-line amplifier. Tracking noise and signal power through a distributed Raman/EDFA hybrid amplifier gives the cascaded noise figure equation: $F_{total} = F_{eff} + F_{EDFA}/G_R$ where $F_{EDFA}$ is the noise figure of the EDFA, $G_{EDFA}$ is the gain of the EDFA, and $G = G_R G_{EDFA}$ is the total gain. Using the Raman noise figure of Figure 5 and assuming an EDFA noise figure of 6.5 dB independent of input power, gives the total noise figure shown as the dashed line also shown in Figure 5. The noise improvement can be converted to a fractional reach increase through the amplifier Q equation, as shown by the dotted line.

## IV. Field Deployment Issues

For EDFAs, the gain media is characterized and amplifier performance carefully measured prior to field deployment. In-service average gain changes are handled by total signal power taps at the input and output. By contrast, Raman amplifiers have well-characterized pump properties but the gain media and resulting amplifier performance is dependent on the transmission fiber and associated discrete losses - all of which can have significant variations in the field. In-service average gain changes may need to be handled by spectral signal power monitoring to account for the complexity of nonlinear power transfer.

While field-deployed Raman transmission has been demonstrated, universal commercial acceptance requires amplifier controls that ensure a known gain shape (average, ripple and tilt) over the full range of field conditions. Such conditions include variations between and within a given fiber type as well as variations in span length, signal input power, channel loading, cabled fiber attenuation, splice losses, insertion loss between the Raman module and the transmission fiber. Additionally, over the lifetime of the optical link there is the need to account for aging of the pumps and loss change in the components and cabled fiber. These conditions affect the launched signal and pump power, pump effective length, pump and signal power transfer, and pump-depleted gain saturation. In the end, the key field deployment issue is to obtain and maintain the desired composite gain spectrum by adjustment and feedback of the powers at all Raman pump wavelengths.

Given the difference between fiber types (e.g., standard single-mode fiber and various non-zero dispersion-shifted fibers) and manufacturing differences in dopant concentration, effective area and pump wavelength fiber attenuation, some approaches try to characterize the Raman gain at individual pump wavelengths as a first step. For example, a modified OTDR technique has been used to measure the pump effective length in the presence of pump-to-pump power transfer and pump depletion. [14] The wavelength dependence of the Raman gain is also determined. The multi-pump gain spectrum can be analytically calculated using a single gain measurement and the effective length information. Most techniques, this one included, rely on a direct measurement of gain spectrum. Typically this has meant the potential drawback of requiring control of remotely located launch signals to probe the gain. Sobe and Yano have proposed using the Raman ASE itself as the probe signal. [15] They have established a linear relationship between the normalized differential noise power and the Raman gain pump efficiency slope, $\Delta G_{Raman}/\Delta P_{pump}$. Normalized differential noise, measured at a single pump wavelength, is the difference in noise at two pump powers for a fixed optical bandwidth divided by the difference in pump powers, $\Delta \rho_{ASE}/\Delta P_{pump}$. Important to this approach is that the slope is strongly dependent on the optical bandwidth and also weakly dependent on temperature, so proper calibration is required. To illustrate, we modeled a 48 nm, 100 km of NZ-DSF case where three pump powers (50, 250 and 500 mW) at the pump wavelength of 1432 nm were used to calculate differential noise (no signals present) and Raman gain slope (one signal present at 1529.2 nm). Figure 6a shows a linear relationship using the ASE power only at the signal wavelength; Figure 6b shows a linear relationship with a different slope using the ASE power across the entire 48 nm signal band. Also shown is the dependence with temperature. For a 60 degree change, there is a ~5% change in slope.

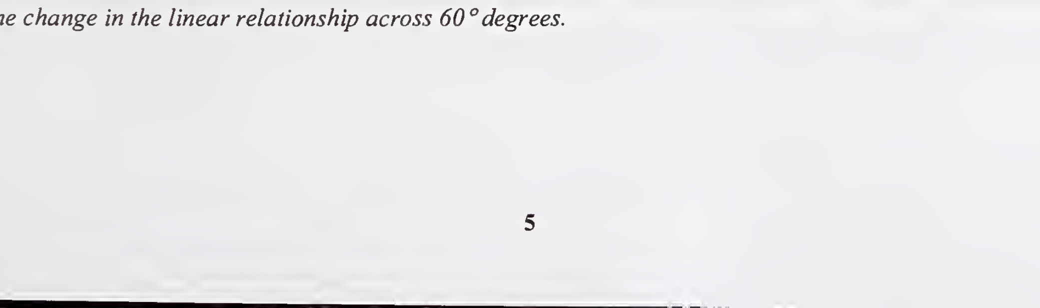

*Figure 6: (a) Dependence of the peak Raman gain on differential ASE noise measured under the gain peak; (b) Same relationship with the differential ASE noise measured across a 48 nm signal band. Two fiber temperatures shows the change in the linear relationship across 60° degrees.*

After a measurement of the fully-loaded channel spectrum, there are several approaches to pump control – trial-and-error feedback, use of a control algorithm or gain-to-pump look-up tables. We have developed a simple yet robust algorithm to find pump powers that maintain low gain ripple (i.e., maximum gain – minimum gain / minimum gain) over a wide range of average gain. As an example, consider a 54 signals from 1521.3 nm to 1607.7 nm spaced by 200 GHz propagating through 100 km of NZ-DSF pumped at the four wavelengths, 1421 nm, 1449 nm, 1471 nm, and 1509 nm. The ratio of individual pump power verses average gain is shown in Figure 7. Evident from the figure is the change in pump power ratio over the gain range due to pump-to-pump power transfer. As average gain increases, pump power at the edge wavelengths exhibit the greatest change in fractional pump power since the Raman gain monotonically increases for this range of pump frequency spacing. The dependence is nearly linear but has some saturation effects for gain greater than 12 dB.

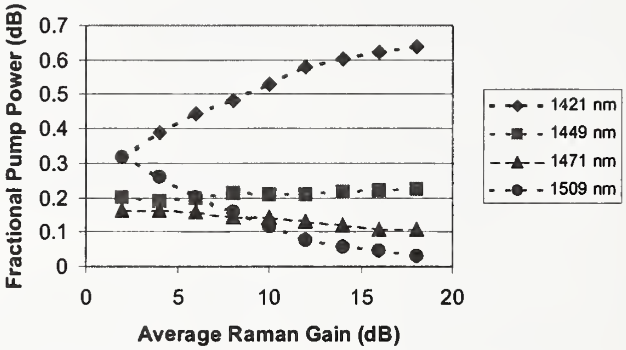

*Figure 7: A C+L band pump optimization example illustrating pump power transfer over a range of average Raman gain.*

## V. Conclusions

Raman amplification, particularly in transmission fiber, has rapidly become a critical tool in the design of high performance transmission pushing reach, capacity, amplifier spacing or spectral efficiency. While there are similarities in the measurement of gain and noise figure to EDFAs, there are also unique challenges particularly associated with a lack of apriori knowledge of the field-deployed gain media. Optimum design needs to consider additional noise sources, polarization (PDG and PMD) and fiber nonlinearities.

## VI. References

1. Stolen, R.H. and E.P. Ippen, "Raman gain in glass optical waveguides," *Applied Physics Letters*, **22**(6) p. 276-281.
2. Hansen, P.B., et al, "Capacity upgrades of transmission systems by Raman amplification," *IEEE Photonics Technology Letters*, **9**(2) p. 262.
3. Onhira, R., et al. "40 Gbits/s X 8-ch NRZ WDM transmission experiment over 80 km X 5-span using distributed Raman amplification in RDF," *European Conference on Optical Communications 1999,* p. 176.
4. Tanaka, T., et al. "2.1-Tbit/s WDM transmission over 7,221 km with 80-km repeater spacing," *European Conference on Optical Communications 2000,* p. 1.8.
5. Zhu, Y., et al. "1.28 Tbit/s (32X40 Gbits/s) transmission over 1000 km with only 6 spans," *European Conference on Optical Communications 2000,* p. 1.8.
6. Walker, G.R., *et al.*, "Noise performance of distributed fibre amplifiers," *Electronics Letters*, **27**(15) p. 1390-1391.
7. Fludger, C.R.S., V. Handerek, and R.J. Mears, "Pump to signal RIN transfer in Raman fiber amplifiers," *Journal of Lightwave Technology*, **19**(8) p. 1140-1148.
8. Forghieri, F., R.W. Tkach, and A.R. Chraplyvy. "Bandwidth of cross talk in Raman amplifiers," *Optical Fiber Communications 1994,* p. 294.
9. Lewis, S.A.E., S.V. Chernikov, and J.R. Taylor, "Characterization of double Rayleigh scatter noise in Raman amplifiers," *IEEE Photonic Technology Letters*, **12**(5) p. 528-530.
10. Burtsev, S., W. Pelouch, and P. Gavrilovic. "Multi-path interference nose in multi-span transmission links using lumped Raman amplifiers," *Optical Fiber Communication 2002,* TuR4, p. 120.
11. Gray, S., M. Vasilyev, and K. Jepsen. "Spectral broadening of double Rayleigh backscattering in a distributed Raman amplifier," *Optical Fiber Communication 2001,* MA2, p. 1-3.
12. Vasilyev, M., S. Gray, and M. Ricci. "Pump intensity noise and ASE spectrum of Raman amplification in non-zero dispersion-shifted fibers," *Optical Amplifiers and Applications 2001,* p. 57
13. Artamonov, A., *et al.* "Enhancement of double Rayleigh scattering by pump intensity noise in fiber Raman amplifiers," *Optical Fiber Conference 2002,* WB6, p. 186.
14. Kim, P., J. Park, and N. Park. "Performance optimization of distributed Raman amplifier using optical pump time domain reflectometry," *Optical Fiber Conference 2002,* ThB5, p. 387.
15. Sobe, M. and Y. Yano. "Automatic pump power adjustment for gain-flattened multi-wavelength pumped Raman amplifier," *Optical Fiber Conference 2002,* TuJ5, p. 63.

# Comparison of stimulated and spontaneous scattering measurements of the full wavelength dependence of the Raman gain spectrum

**N. R. Newbury and K. L. Corwin**
*National Institute of Standards and Technology, Optoelectronics Division, 325 Broadway, Boulder CO 80305*
*Tel: (303) 497-4227, Fax: (303) 497 -3387, E-Mail: nnewbury@boulder.nist.gov*

## Abstract

We present a direct comparison of the measured spontaneous Raman spectra and the measured stimulated Raman gain from a pump laser. We confirm that the spontaneous Raman spectrum is related to the stimulated Raman gain spectrum through a simple Bose-Einstein temperature factor. Given this simple relation, the full dependence of the Raman gain on both the signal *and pump* wavelength can be extracted directly from spontaneous Raman spectra, which are easily generated with a low-power (few milliwatts) diode laser and calibrated optical spectrum analyzer.

## Introduction

Since the early observations of Raman gain in optical fibers [1], Raman amplification has become increasingly important in optical-fiber communication because it can provide gain with a low effective noise figure over a very large bandwidth. Clearly, accurate measurements of the full wavelength dependence of the Raman gain are important in view of the growing use of Raman amplifiers. The gain will depend on both the signal and pump wavelength; however, since the gain depends most strongly on the wavelength difference between the pump and signal beams, the Raman gain is perhaps most usefully described in terms of its dependence on the pump wavelength and on the wavelength difference between the pump and signal beams. Historically, most measurements of Raman gain have used a pump-probe configuration with a fixed-wavelength pump beam to generate the Raman gain versus the pump-signal frequency offset [2]. In a recent letter, one of the authors showed that this same general pump-probe configuration can be used to determine not only the dependence of the Raman gain on the pump-signal frequency offset, but also its dependence on the pump wavelength, provided the probe light spans both the Stokes (gain) and anti-Stokes (loss) region of the Raman effect [3,4]. As a result, a single pump-probe measurement of the Raman gain can provide the full wavelength dependence of the Raman gain over the wavelength range of interest. An alternative method to the pump-probe configuration for measuring the Raman gain is to measure the spontaneous Raman spectrum from a pump laser, from which one can extract the stimulated Raman gain [5]. In this paper, we demonstrate measurements of the full wavelength dependence of the stimulated Raman gain using spontaneous Raman scattering. Using a single low-power pump laser we determine both the stimulated Raman gain curve dependence on the signal-pump wavelength offset and on the absolute pump wavelength.

The Raman gain spectrum and the spontaneous Raman spectrum will depend differently on temperature. Historically, the underlying vibrations responsible for the Raman gain were assumed to be those of a simple harmonic oscillator [6], in which case the temperature correction involves a Bose-Einstein factor. Although it has not been widely acknowledged in the literature, the presence of anharmonicities will, at some level, introduce errors into the simple temperature correction used in this model. Previous work comparing the noise figure from amplified spontaneous emission and the gain of Raman amplifiers indicates that this simple Bose-Einstein factor is at least accurate to a few tenths of a decibel [7,8,9]. One goal of this work is to demonstrate that this factor is accurate to better than 0.1 dB, the experimental limit on the measurement of the absolute spontaneous Raman spectrum.

Direct measurement of the stimulated Raman gain curve typically requires a strong pump of a few hundred milliwatts and a broad probe source. The advantage of measuring the gain from the spontaneous Raman spectrum, as described here, is that only a very low-power pump of a few milliwatts is needed along with a well-calibrated OSA. On the other hand, extracting the gain from the spontaneous Raman spectrum does require calibration of the fiber attenuation and absolute optical spectrum analyzer (OSA) power response at all wavelengths, while a direct measurements of the stimulated Raman gain requires these calibrations only at the pump wavelength. In practice, the choice of technique will be dictated by the available hardware.

## Theory

The standard equations governing the Raman effect in single mode fiber of length $L$ can be written in terms of the number of pump photons per mode, $n_p(z)$, and the number of counter-propagating signal photons per mode, $n_s$, at position $z$ down the fiber as [10]

$$\frac{dn_s}{dz} = -\alpha(\omega_s) n_s + \gamma(\omega_p, \Delta\omega) n_p(z)\left[n_s + C(T, \Delta\omega)\right] \tag{1}$$

where the fiber attenuation as a function of frequency is $\alpha(\omega)$, the frequency offset between the pump and signal beams is $\Delta\omega = \omega_p - \omega_s$, and the Raman gain coefficient $\gamma(\omega_p, \Delta\omega)$ is positive for the Stokes side ($\Delta\omega > 0$) and negative for the anti-Stokes side ($\Delta\omega < 0$). The factor C is responsible for the generation of spontaneous Raman photons and differs depending on whether the signal is on the Stokes side, in which case $C = 1 + \varphi(T, |\Delta\omega|)$, or on the anti-Stokes side of the pump, in which case $C = \varphi(T, |\Delta\omega|)$. The Bose-Einstein temperature-dependent correction factor $\varphi(T, \Delta\omega) = \left(\exp(\text{h}\Delta\omega/kT) - 1\right)^{-1}$ can be viewed equivalently as the phonon occupation number at the temperature $T$, or as the thermal average of the squared matrix element between adjoining states of the simple harmonic oscillator. This simple Bose-Einstein temperature correction results from the assumption of simple harmonic vibrations, for which the density of states is exactly the same regardless of the initial state (*i.e.,* the states are evenly spaced) and the matrix elements can be easily calculated. Experimentally, if this simple-harmonic assumption were incorrect, the measured and expected spontaneous Raman curves would deviate at frequency offsets $\text{h}\Delta\omega \le kT$, where $\varphi(T) \ge 1$.

In general, there is an equation similar to (1) that describes the pump evolution. For our parameters, the undepleted pump approximation is valid, so the pump decays exponentially in the $-z$ direction. At very low pump powers of a few milliwatts, the Raman gain is low and the spontaneously-generated Raman photons undergo negligible Raman gain. Equation (1) can then be solved in closed form as:

$$n_s(\omega_s) = \left[\frac{1 - e^{-\{\alpha(\omega_p) + \alpha(\omega_s)\}L}}{\alpha(\omega_p) + \alpha(\omega_s)}\right] \gamma n_p C = g_{RM}(\omega_p, \Delta\omega) P_p L_{eff,total} C \Delta f \tag{2}$$

where $L_{eff,total}$, the quantity in square brackets, is the total effective length, $\Delta f$ is the mode spacing so that $n_s/\Delta f$ is the number of photons per Hz bandwidth, $P_p$ is the initial pump power, and $g_{RM}(\omega_p, \Delta\omega)$ is the standard Raman gain. We will assume the pump is unpolarized so that $g_{RM}$ is the unpolarized gain (half the polarized gain) and $n_s/\Delta f$ is the number of photons per hertz *per polarization mode*. Solving Eq. (2) for $g_{RM}$ gives the Stokes Raman gain at a fixed pump wavelength or frequency. As discussed in detail in Ref. [3,4], the pump-wavelength dependence is contained in the asymmetry of the Raman gain spectrum; essentially, the anti-Stokes signal "pumps" the pump laser with a Raman gain corresponding to a pump wavelength equal to the anti-Stokes wavelength. If we assume the Stokes Raman gain varies as $\sim \omega_p^k$, then the exponent $k$ can be found from the solution to [3,4]

$$\frac{g_{RM}(\Delta\omega)+g_{RM}(-\Delta\omega)}{g_{RM}(\Delta\omega)-g_{RM}(-\Delta\omega)} = -\frac{k+1}{2\omega_p}\Delta\omega \tag{3}$$

**Experimental Measurements**

The experimental setup to measure the backward-generated Raman spontaneous spectrum is shown in Figure 1. As discussed earlier, the OSA calibration is critical to accurate measurements of the Raman spectrum. The OSA was calibrated for three factors: the wavelength scale was calibrated relative to the pump-laser wavelength, the power scale was calibrated relative to a calibrated optical power meter (OPM), and finally the effective resolution bandwidth was measured as a function of signal wavelength. We also separately measured the loss of the circulator and other components between the fiber end and the OSA. Finally, the attenuation over the full wavelength range of interest was measured with a broad source and adjusted by more accurate attenuation measurements taken over a smaller wavelength range with the cutback method. To avoid uncertainties from polarization-dependent loss the pump polarization was scrambled. The measured spectrum $S$ in dBm from the OSA was converted to the number of photons per Hz per polarization as $n_s/\Delta f = S\lambda_s^3/(2hc^2\Delta\lambda)$, where $\Delta\lambda$ is the calibrated OSA resolution bandwidth.

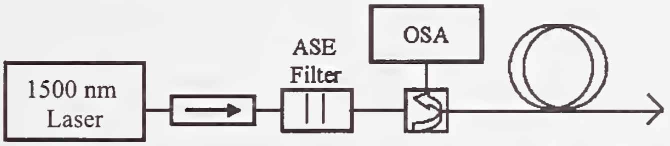

**Figure 1**: *Setup for measuring the spontaneous Raman spectrum. The laser power was ~4 mW, well below the stimulated Brillouin scattering threshold and low enough to provide negligible Raman gain.*

Figure 2a shows the spontaneous Raman spectrum, in units of $n_s/\Delta f$, measured directly for two different fiber types and calculated directly from Eq. (2) using the calibrated Raman gain curves measured for the same exact fibers, as reported in Ref. [3]. Figure 2b shows the same data set, but in this case in terms of the directly measured stimulated Raman gain and the indirectly measured stimulated Raman gain inferred from the spontaneous spectrum and Eq. (2). No free parameters were used in the comparison. The difference between the measured and predicted Raman spectra, shown in Figure 3, has an average offset of less than 0.1 dB and a standard deviation of ~0.1dB. We attribute these deviations to uncorrected wavelength dependence of the OSA power response or to fiber and component attenuation. No discrepancies attributable to anharmonicities, which would be evident at wavelengths offsets of ~ 45 nm or below, were observed, indicating the Bose-Einstein correction factor is valid to better than 0.1 dB.

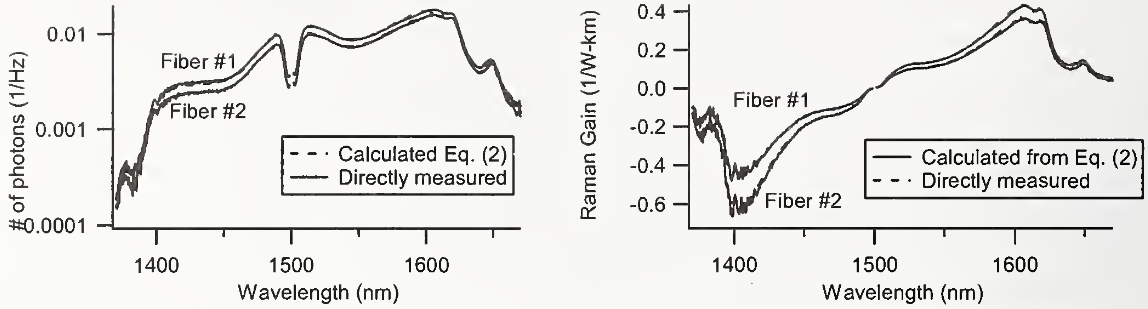

**Figure 2**: *a) Comparison of measured spontaneous Raman spectra with the calculated spontaneous Raman spectra for two typical communication fibers. b) Comparison of the same data in terms of the stimulated Raman gain spectrum.*

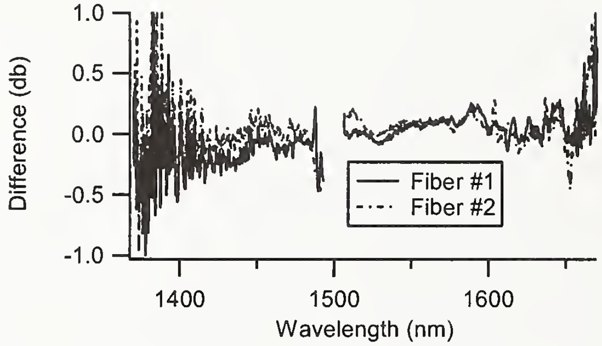

**Figure 3**: *The difference between the calculated and measured curves of 2(a) or 2(b).*

We have shown that the full wavelength dependence of the Raman gain can be obtained either directly from measurements of the gain or indirectly from measurements of the spontaneous Raman spectrum. In general, the uncertainty for the spontaneous-based measurement will be larger (~0.2 db) since this measurement requires absolute power measurements at each wavelength, whereas the direct measurement requires only relative power measurements at each wavelength. However, if this level of uncertainty is adequate and if only a low-power pump is available, measurement of the Raman gain through the spontaneous spectrum is an attractive choice.

---

1. R. H. Stolen and E. P. Ippen, Appl. Phys. Lett., **22**, 276 (1973).
2. R. H. Stolen in *Technical Digest: Symposium on Optical Fiber Measurements, 2000,* P.A. Williams and G. W. Day eds. (NIST Special Publication 953, Boulder CO, 2000) p.146; F. Coch, S.A.E. Lewis, S. V. Chernikov and J.R. Taylor, ibid., p. 143; D. Hamoir, N. Torabi, A. Bergonzo, S. Borne and D. Bayart, ibid., p.147; S. Gray, ibid., p.151.
3. N. R. Newbury, Opt. Lett., accepted for publication (2002).
4. N. R. Newbury, "Pump-Wavelength Dependence of Raman Gain", in *Optical Amplifiers and their Applications,* accepted for publication., July (2002).
5. F. Koch, S.A.E. Lewis, S.V. Chernikov, and J. R. Taylor, Electron. Lett., **37**, 1437 (2001).
6. W. D. Johnston Jr. and I. P. Kaminow, Phys. Rev., **168**, 1045 (1968).
7. C. R. J. Fludger, V. Handerek, R. J. Mears, "Fundamental Noise Limits in Broadband Raman Amplifiers", paper MA5-1 in *Optical Fiber Communication Conference (OFC)*, Vol 54 of OSA Trends in Optics and Photonics Series (OSA, Washington DC 2001).
8. S. A. E. Lewis, S. V. Chernikov and J. R. Taylor, Opt. Lett., **24**, 1823 (1999).
9. K. Rottwitt, J. Bromage, M. Du, and A. Stentz, "Design of Distributed Raman Amplifiers", paper 4.4.1, in ECOC 2000, Munich Germany, 2000.
10. J. Aeuyeung and A. Yariv, IEEE J. Quantum Electron., **QB-14**, 347 (1978).

# Fiber Nonlinear coefficient measurement scheme based on FWM method with externally modulated DFB laser source

**Bostjan Batagelj, Matjaz Vidmar**
*Laboratory of Optical Communications, Faculty of Electrical Engineering, University of Ljubljana,*
*Trzaska 25, 1000 Ljubljana, Slovenia*
*Tel: (386) 14768423, Fax: (386) 14768424, e-mail: bostjan.batagelj@fe.uni-lj.si*

## ABSTRACT

In this paper, we present measurement scheme for determining the optical fiber non-linear coefficient γ, using externally modulated continuous wave DFB laser source. The measurement technique is based on Four-Wave Mixing. The measurement source which uses one laser and one optical erbium-doped fiber amplifier only is described precisely. The proposed simple measurement scheme is polarization independent, enables high sensitivity and accuracy, and is applicable to all currently available types of fiber.

**Keywords**: Optical Fiber Communications, Fiber Measurements, Non-linear Coefficient, Four-Wave Mixing.

## 1. INTRODUCTION

Many schemes have been previously proposed to make measurement of non-linear coefficient (γ) [1]. Four-Wave mixing (FWM) is a reliable technique for determining the fiber γ. The well-known measuring setup [2]-[4] based on FWM is made up of two DFB lasers, where the wavelength spacing is adjusted by temperature tuning. It uses more than one optical erbium-doped fiber amplifier (EDFA) to raise the total optical power. One of the biggest disadvantages of this method is that the polarisation controllers must be adjusted all the measurement time in order to obtain maximum FWM efficiency. The determination of γ employing such FWM method has a limited measurement capability due to the polarization adjustment and insufficient amplification.

We have devised and demonstrated a measurement scheme based on FWM method [5]-[6], which uses one externally modulated DFB laser source only. The use of such source eliminates polarization dependence and making measurement scheme simple and highly sensitive, what leads to higher accuracy. The introduced measurement scheme is applicable to all currently available fiber types including Photonic Crystal Fibers.

## 2. THEORY OF THE FWM METHOD

The FWM is a non-linear process induced by Kerr effect in optical fiber. It occurs when two or more wavelengths of light propagate together through an optical fiber. Supposed the equal signal input power, the ratio between the power of new frequencies generated through FWM at the end of the fiber and the signal output power is written as [7]

$$\frac{P_{FWM}(L)}{P_s(L)} = \left(\gamma \cdot P_s(0) \cdot L_{eff}\right)^2 \cdot \frac{\alpha^2}{\alpha^2 + \Delta\beta^2}\left(1 + 4 \cdot \frac{e^{-\alpha L}}{\left(1 - e^{-\alpha L}\right)^2} \cdot \sin^2\left(\Delta\beta \cdot \frac{L}{2}\right)\right), \tag{1}$$

where $P_s(0)$ is the signal input power, $P_s(L)$ is the signal output power *and* $L_{eff}$ is the fiber effective interaction length. The phase-matching condition is given by

$$\Delta\beta = \frac{2\pi \cdot \lambda_p^2}{c} \cdot \Delta f^2 \cdot \left(D(\lambda) + \Delta f \frac{\lambda_p^2}{c} \cdot \frac{dD}{d\lambda}\right) - \gamma \cdot P_s(0) \cdot \left(\frac{1 - e^{-\alpha L_{eff}}}{\alpha L_{eff}}\right), \tag{2}$$

where $\Delta f$ is frequency spacing, $D(\lambda)$ is the fiber chromatic dispersion, $dD/d\lambda$ is the dispersion slope, and $\lambda_p$ is the wavelength corresponding to the pump frequency. The second part of equation (2) corresponds to the intensity dependence of the phase matching [8]. In our case, the measured fiber should be relatively short, in order to make measurements in the flat part of FWM characteristic and to achieve phase matching, so that sine term of equation (1) could be neglected. However, a numerical algorithm based on the above described FWM is usually used to relate the input and output fields and to determine the γ.

## 3. MEASUREMENT SOURCE WITH EXTERNALLY MODULATED DFB LESER

### 3.1 Mach-Zehnder intensity modulator

The key element of the measurement source, which is shown in the left side of Fig. 3, is the Mach-Zehnder $LiNbO_3$ guided-wave intensity modulator. The Mach-Zehnder modulator (MZM) transfer function shape is shown in Fig. 1. The output optical power of an ideal MZM is given by

$$P_{\text{out}} = 1/2 \cdot P_{\text{in}} \left(1 + \cos(\Delta\varphi)\right), \tag{3}$$

where $\Delta\varphi$ is the optical phase difference, $P_{\text{in}}$ and $P_{\text{out}}$ are the input and output optical power of MZM. The bias voltage changes the optical phase difference between the interfering waves at the output of the Mach-Zehnder interferometer and thus changes the output intensity. The MZM's halfwave voltage $U_\pi$ is defined as the change in bias voltage necessary to move between a peak and null on the transfer function curve. So, the optical phase difference can be written as

$$\Delta\varphi = \pi \cdot U(t)/U_\pi\,, \tag{4}$$

where $U(t)$ is the applied signal including DC bias, and $U_\pi$ is the modulator full-swing voltage.

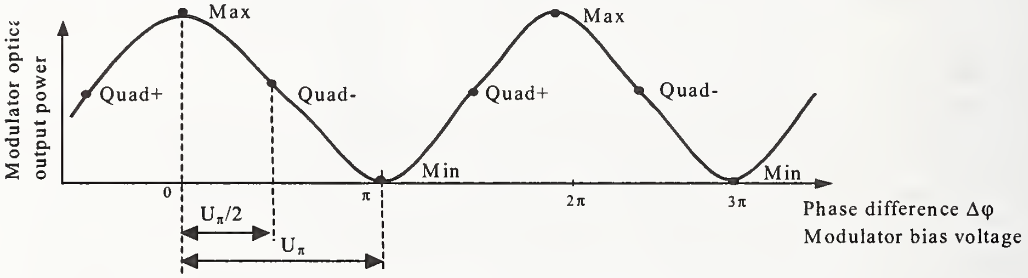

*Figure 1. Plot of the optical output power versus the applied voltage for MZM.*

There are basically two typical operation points on the MZM transfer function curve. In the first one MZM is biased at any voltage that is halfway between maximum and minimum transmission point on the transfer function curve. This point is called quadrature bias point. The second operation point is when the MZM is biased at either the maximum or minimum transmission point on the transfer function curve. At this bias point the odd-order products are minimized and even-order products are maximized as shown in Fig. 2.

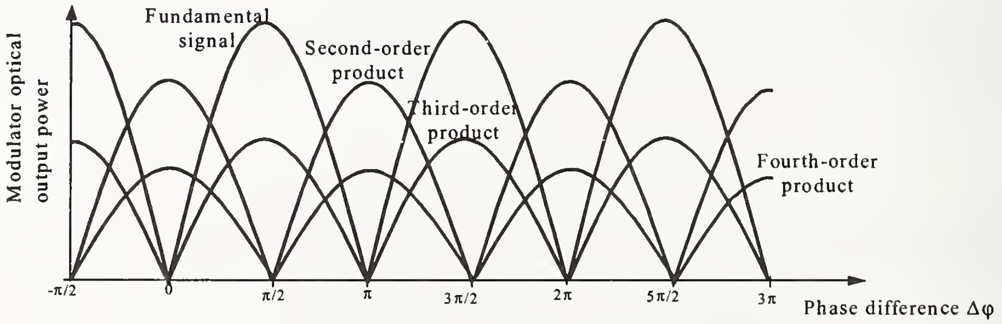

*Figure 2. MZ optical output power at the fundamental and high-order frequencies.*

### 3.2 Operation of measurement source

The experimental configuration for our method is shown in Fig. 3. The output from a single frequency laser is externally modulated in a $LiNbO_3$ Mach-Zehnder amplitude modulator (11GHz 3dB bandwidth, $U_\pi$=7V) preset to minimum transmission point. MZM is driven by pulsed RF signal of a fixed frequency 10GHz. The light source is single frequency DFB laser. In order to suppress stimulated Brillouin scattering, the continuous wave (CW) laser source is directly modulated with the signal of few MHz, which broadens the optical spectrum. Otherwise, the Brillouin scattering limits the optical power that can be launched in the fiber under test (FUT).

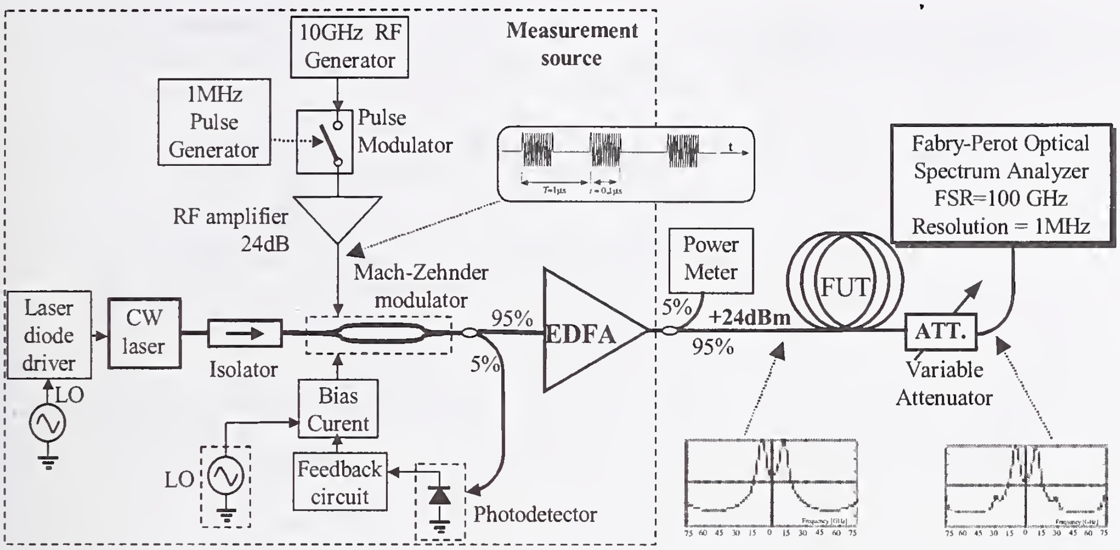

*Figure 3. Experimental setup for the measurement of fiber nonlinear coefficient.*

The electrical pulse modulator, switched by the 1MHz pulses, produces a train of 10GHz RF pulses as shown in Fig. 3. The train of pulses has width *t* and repetition time *T*. Pulse modulation is used to increase the optical peak power, while the RF modulation produces sidebands in the optical spectrum. The obtained optical spectrum is symmetrical around the incident lightwave frequency. Two sidebands are equally spaced in frequency by 20GHz. The bias of the MZM is set to the point where the carrier is maximally suppressed. Since there is an active bias control, the desired MZM bias point occurs at specific DC bias voltage that remains constant for all the time despite variations in environmental conditions. A typical modulated optical spectrum with suppressed carrier is shown in Fig. 3. The output spectrum mainly consists of two sidebands, separated by twice the RF modulation frequency. The sidebands have equal power and linear polarization parallel to each other. The frequency separation of 20GHz, however, is chosen since the Brillouin shift for silica fibers ranges from 10,5-11,5GHz [9]. Because of that the Brillouin scattering is unlikely to coincide with by FWM produced components needed for measurement.

Approximately 5% of the optical power is tapped off to an active bias controller for MZM. An external modulator bias controller uses tapped optical signal to maintain a desired bias point. The method of controlling is based on previously injected pilot tone from the local oscillator (LO) and feedback correction of bias voltage.

The remaining 95% of the optical power of modulated signal is amplified by an EDFA to the ~24dBm average power and propagated through the FUT. Thanks to the pulse modulation of the RF signal and suppressed optical carrier, the optical signal has a much higher peak power. To avoid pulse distortion due to gain dynamics, *T* was set much lower than the relaxation time of the EDFA, which thus react only to the average power ($T \approx 1\mu s$). High peak power is obtained by using low duty cycles. Higher peak power of the pulses is resulting in higher FWM products while travelling through the FUT. Due to the short length of the lumped amplifier, the fiber non-linearity effects such Stimulated Brillouin Scattering compared to the stimulated emission of $Er^{3+}$ ions are negligible.

## 4. MEASUREMENT PROCEDURE

While travelling through the FUT the optical signal experiences FWM, which leads to the generation of additional sidebands in the optical spectrum. The spectral analysis is performed by high dynamic and high resolution optical spectral analyzer. Fig. 4 shows a typical experimentally measured spectrum at the output of the FUT. By switching pulse modulation on and off, optical power at the input of FUT is changing. With power variations of the launched signal and measuring the strength of the spectral sidebands, it is possible to determine the magnitude of non-linear FWM product experienced by the signal and hence FUT $\gamma$.

The total signal input power is measured with an optical power meter. The partition of the power between the different spectral components is evaluated using optical spectral analyzer measurements. Finally, the power of sidebands is corrected for parameter $\alpha'$ and G'. Their determination is shown in Fig. 4, where $\alpha'$ is the decreased optical power due to the duty cycle of the pulse source and G' is the increase in gain due to higher amplification of the modulated signal.

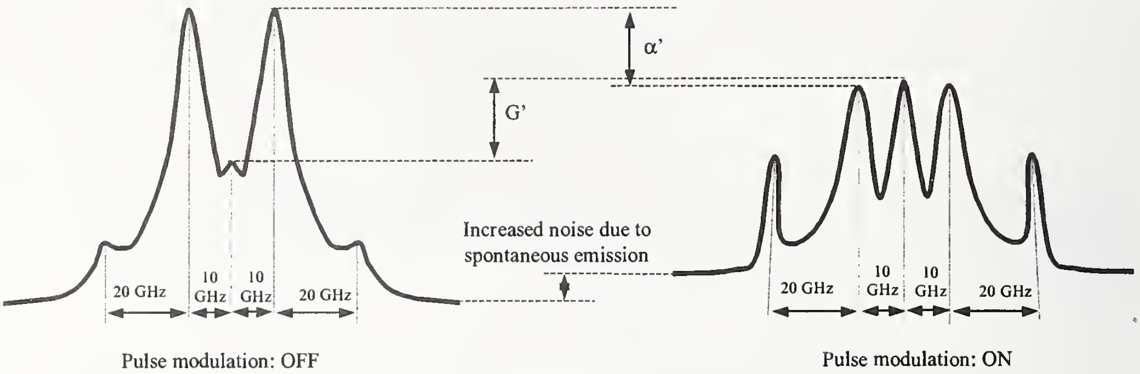

*Figure 4. Determination of α' and G' parameters.*

## 5. CONCLUSIONS

We introduce the measurement scheme of the fiber $\gamma$ using FWM technique. Simple measurement source uses one DFB laser only, eliminates polarization dependence and enables high sensitivity. With this measurement scheme it is easy to measure the $\gamma$ of all types of currently available fiber including Photonic Crystal Fibers.

In the further work we need to distinguish between the J4 Bessel component and the FWM components as they are coincident. The fourth order frequency component is a systematic error which is produced by external modulation in MZM. The consideration and determination of non-linear effect in EDFA is also needed. With additional elimination of these systematic errors the estimated error in our measurements of the fiber $\gamma$ is expected to be less than 5%. The higher accuracy depends on how accurately the launch and output power can be measured and also on how important the effect of electrostriction on the measurement is.

## REFERENCES

[1] B. Batagelj: Review of so far Proposed Fiber $n_2$ Measurement Schemes, *in Proc. ICTON 2002, Warsaw, Poland, April 2002.*

[2] L. Prigent, J. P. Hamaide: Measurement of Fiber Nonlinear Kerr Coefficient by Four-Wave Mixing, *IEEE Photonics Technology Letters, vol. 5, pp. 1092-1095, Sep. 1993.*

[3] M. Tadakuma, O. Aso, S. Namiki: Nonlinear coefficient measurement of reverse dispersion fiber using four-wave mixing, *in Proc. ECOC'99, Nice, France, September 1999, paper II-224.*

[4] J.-C. Antona, S. Bigo, S. Kosmalski: Nonlinear index measurements of various fibre types over C+L band using four-wave mixing, *in Proc. ECOC'01, Amsterdam, The Netherlands, Sept. 2001, paper We.L.1.2.*

[5] B. Batagelj: A simple non-linear coefficient measurement scheme based on Four-Wave Mixing, *in Proc. Optical Fiber Measurement Conference, United Kingdom, September 2001, pp. 73-76.*

[6] B. Batagelj and M. Vidmar: Patent application no. P-200200029, Slovenian Intellectual Property Office, *2002, pp. 1-7.*

[7] N. Shibata, *et al.*: Phase-mismatch dependence of efficiency of wave generation through FWM in a Single-Mode Optical Fiber, *IEEE JQE, vol. 23, pp. 1205-1210, July 1987.*

[8] S. Song, *et al.*, Intensity-dependent phase-matching effects on four-wave mixing in optical fibers, *J. Lightwave Technol., vol. 17, pp. 2285-2290, Nov. 1999.*

[9] Agrawal, G. P., *Nonlinear Fiber Optics, $2^{nd}$ ed.*, UK: Academic Press, 1995.

# A Comparison of Six Techniques for Nonlinear Coefficient Measurements of various Single Mode Optical Fibers

**Y. Namihira [#1], K. Miyagi [#1], K. Kaneshima [#1], M. Tadakuma [#2],**
**C. Vinegoni [#3], G. Pietra [#4] and K. Kawanami [#5]**

#2: The Furukawa Electric Co. Ltd., Japan, #3: University of Geneva, Switzerland
#4: Pirelli Labs Innovation, Italy, #5: Muroran Institute of Technology, Japan
#1: University of the Ryukyus, 1 Senbaru, Nishihara, Okinawa 903-0213, Japan
Phone/Fax: +81-98-895-8700, E-mail: namihira@eee.u-ryukyu.ac.jp

**Abstract** A comparison of six techniques for nonlinear coefficient (n2/A*eff*) measurements of various optical fibers using Pulsed-LD SPM, CW-LD SPM, sinusoidally modulated signal-SPM, XPM, self-aligned Interferometric, and FWM methods is first demonstrated. The (n2/A*eff*) obtained from the six different methods were in good interlaboratory agreement except for dispersion compensating fiber (DCF).

**Introduction:** Accurate determination of the nonlinear coefficient (n2/A*eff*){n2 is the nonlinear refractive index, A*eff* is the effective area} of optical fibers is required for the ultra-long amplified optical transmission systems. To date, the nonlinear coefficient of the optical fibers has been measured by using the self-phase modulation (SPM) method with a pulsed laser diode (LD) (P-SPM)[1], the SPM method with dual CW-LDs (CW-SPM) [2], the cross-phase modulation (XPM) method [3], self-aligned Interferometric (INT) method [4], sinusoidally modulated signal-SPM (S-SPM) method [5], and four wave mixing (FWM) method [6].

Heretofore, ITU-T (n2/A*eff*) round robin measurements for various optical fibers coordinated by Prof. Y. Namihira of University of the Ryukyus (formerly KDD) have been successfully performed [7-9].

This paper first presents the results of the interlaboratory fiber nonlinear coefficient (n2/A*eff*) measurements for various optical fibers such as standard single mode fiber (SMF), cut-off shifted fiber (CSF), dispersion shifted fiber (DSF), non-zero DSF (NZDSF) and large effective area DSF (LEDSF), and dispersion compensating fiber (DCF) using six different techniques such as the P-SPM [1] , CW-SPM [2], XPM [3], INT[4], S-SPM [5], and FWM [6] methods at 1550nm.

**Experiments:** The experimental set-up of the ($n_2/A_{eff}$) measurements for the various single mode optical fibers are shown in Fig.1. In Fig.1, (a), (b), (c), (d) and (e) are P-SPM method, CW-SPM method, XPM method, INT method, S-SPM, and FWM methods, respectively. Here, $n_2$ can be estimated by ($n_2/A_{eff}$) multiplying the $A_{eff}$. The $A_{eff}$ was measured by the far-field scan (FFS) technique [10]. The parameters of six kinds of single mode optical fibers are shown in Table 1. These fibers were circulated to the five Laboratories such as University of the Ryukyus (formerly KDD), Furukawa, University of Geneva, Pirelli Labs., Muroran Institute of Technology.

**P-SPM method:** In Fig.1(a), the transform limited (TL) Gaussian pulse-LD were used as a pulsed-LD [1]. The output optical pulse due to SPM was measured by the optical spectrum analyzer (OSA). As the input optical power increases, the maximum phase shift increases in proportion to the input peak power. The ($n_2/A_{eff}$) can be obtained from the numbers of peaks in the SPM broadened spectra [1].

**CW-SPM method:** In Fig.1(b), the optical beat signal was derived from dual CW-LDs operating at around 1550nm [2]. The beat signal was then amplified in a preamplifier (EDFA1) and transmitted through a optical band pass filter to suppress the amplified stimulated emission, and transmitted through a polarizer to a following high power EDFA2.

**XPM method:** In Fig.1(c), the probe signal power is set relatively weak so that ($n_2/A_{eff}$) in FUT is dominantly caused by amplified strong pump CW-LD through XPM and that the effect of SPM is negligible. When pump CW-LD or CW-SLD is modulated in its intensity, probe CW-LD is modulated in this phase through XPM [3].

**INT method:** In Fig.1(d), the Interferometric method is based on the detection of the Kerr phase shift by a self-aligned interferometer. Here, the distributed feedback laser (DFB), Erbium doped fiber amplifier (EDFA), polarization controller (PC), Farady mirror (FM), and fiber Bragg grating (FBG) were used [4].

**S-SPM method:** In Fig.1 (e), the S-SPM method is based on SPM effect estimation. This technique consists simply in propagating an optical signal sinusoidally modulated by means of an electro-optical $LiNbO_3$ modulator. The $\gamma$ -factor estimation is achieved using a simulation tool capable of reproducing the evolution of signal spectra along the fiber and doing a comparison between acquired experimental data and simulation result [5].

**FWM method:** In Fig.1(f), pump (DFB-LD1) and probe (DFB-LD2) sources are tunable with a temperature and current controller. The LD1 of pump source was amplified with a EDFA to compensate an insertion loss of polarization optics, and passed through a tunable band-pass filter (BPF) with $\Delta\lambda$=1nm to eliminate the ASE noise of EDFA. The $\lambda/2$ wave plate was used to rotate the input azimuth of linearly polarized light of LD1. In contrast, the output light of LD2 was depolarized with a depolarizer to examine the depolarization effect on FWM efficiency. Otherwise, the depolarizer was deleted in the setup so that the FWM efficiency was measured in linearly polarized states of LD1 and LD2 [6].

**Results and discussions:** The results of interlaboratory (n2/A*eff*) and n2 measurements at random polarization states (RP) using six different techniques of P-SPM, CW-SPM, XPM, INT, S-SPM, and FWM for a SMF, a CSF, two kinds of DSFs, two kinds of NZDSFs, a LEDSF and a DCF at 1550nm are summarized in Tables 2 and 3, respectively.

In Tables 2 and 3, n2(RP) = $\eta$ n2(LP), $\eta$ =1.0 for P-SPM, $\eta$ =8/9 for CW-SPM, S-SPM, and FWM, and the polarization factor $\eta$ =2/3 for XPM were used. Here, LP represents the linear polarization state.

Here, concerning the results of the self-aligned Interferometric (INT) method [4], the (n2/A*eff*) values were larger than that of the other methods. Then, a correction (scaling) factor of ~0.8 with respect to the mean values of the other methods were used. Such a scaling could easily arise from an erroneous estimation of the absolute peak power used for this measurements (underestimate of the power by a factor of just 0.8). Therefore, the special correction factor of k =0.8 {(*) in Tables 2 , 3, Figs.1,2} were used for the INT method because of the experimental error.

Meanwhile, in FWM method at Muroran Institute of Technology, only one (n2/A*eff*) measurement of 20 km long DSF was measured at present, however, they will measure (n2/A*eff*) of another fiber samples in the near future.

Fig. 2 show estimated values of n2 at random polarization states for various optical fibers as a function of six different measurement methods. Fig. 3 indicates the estimated values of n2 at random polarization states for six different measurement methods as a function of various optical fibers.

From Tables 2 and 3, it was found that the average values of $n_2$ at RP of SMF, CSF, DSF, NZDSF, LEDSF, and DCF were ~2.62, 2.43, 4.80, 4.16. 3.19 and 12.1 x $10^{-10}$ [1/W], respectively. Also, the average values of $n_2$ at RP for SMF, CSF, DSF, NZDSF, LEDSF and DCF were ~2.21, 2.14, 2.25, 2.31, 2.32, and 2.78 x $10^{-20}$ [$m^2$/W], respectively.

The average values of $n_2 \cong 2.25 \times 10^{-20}$ [$m^2$/W] of DSFs at random polarization states are in good agreement with that of 2.1 - 2.3 x $10^{-20}$ [$m^2$/W] range of published results, respectively.

**Conclusions:** From the interlaboratory nonlinear coefficient (n2/A*eff*) measurements for various optical fibers, the (n2/A*eff*) obtained from the six different techniques such as pulsed-LD SPM method, CW-SPM method, a XPM method, a self-aligned Interferometric (INT) method, a sinusoidally modulated signal SPM method, and FWM method were found to be a good agreement with each methods except for DCF.

It was confirmed that the average values of n2 at random polarization state obtained from these different methods were

2.1~2.3 x $10^{-20}$ [$m^2$/W] for SMF, CSF, DSF, NZDSF and LEDSF except for DCF of ~2.8 x $10^{-20}$ [$m^2$/W], respectively.

## References :

[1] Y. Namihira:"Higly accurated nonlinear coefficient measurements by SPM method for DSFs and large effective area fibers at 1.55 μm," SOFM 1988, NIST, Boulder, USA, pp.83-86, 1998.

[2] A. Boskovic,et al.,:"Direct continuous-wave measurement of $n_2$ in various types of telecommunication fiber at 1.55 μm", Optics Letters, vol. 21, no. 24, pp. 1966-1968, 1996.

[3] T. Kato et al.,: "Measurement of nonlinear refractive index in optical fibers by cross phase modulation method using depolarized pump light," Optics Lett.,20, p.988, 1995.

[4] C. Vinegoni et al.,:" Interlaboratory measurements of the nonlinear coefficient of standard SMF and DSF fibers using an interferometric method and an SPM based cw dual-frequency method", OFMC'01, pp.59-62, Canbridge, UK, 2001.

[5] G. Pietra: "Sinusoidally modulated SPM method", Private communications, May, 2002.

[6] K. Kawanami et al.,"Polarization effects on determination of nonlinear refractive index by four-wave mixing in a dispersion shifted fiber", OECC'02, Yokohama, Japan, 2002.

[7] Y. Namihira : "Nonlinear coefficient round robin measurements for various dispersion shifted fibers in Japan and UK", ECOC2000, 8.2.5, pp.97-98, 2000.

[8] Y. Namihira: "KDD nonlinear coefficient round robin measurements for various dispersion shifted fibers in Japan and UK", SOFM 2000, Boulder Co. USA, pp.49-52, 2000.

[9] Y. Namihira et al., "Interim report of ITU-T nonlinear coefficient (n2/A*eff*) round robin measurement results in Japan ", OFMC'01, pp.63-66, Canbridge, UK, 2001.

[10] Y. Namihira :"Relationship between nonlinear effective area and mode field diameter for dispersion shifted fibers", Electron. Lett., vol.30, no.3, pp.262-264, 1994.

Table 1 Fiber parameters for various single mode optical fibers.

| Fibers | SMF | CSF | DSF | NZDSF | LEDSF | DCF |
|---|---|---|---|---|---|---|
| D@1550nm [ps/ (nm- km)] | 16.3 | 19.4 | - 0.58 | - 2.19 | - 2.48 | - 109.1 |
| Aeff@1550nm [μ m$^2$] | 84.6 | 88.2 | 46.8 | 55.6 | 72.8 | 22.9 |

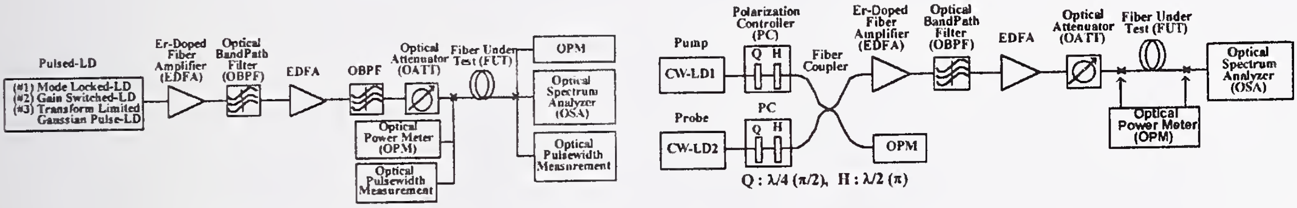

(a) Pulsed-LD SPM (P-SPM)

(b) CW-LD SPM (CW-SPM)

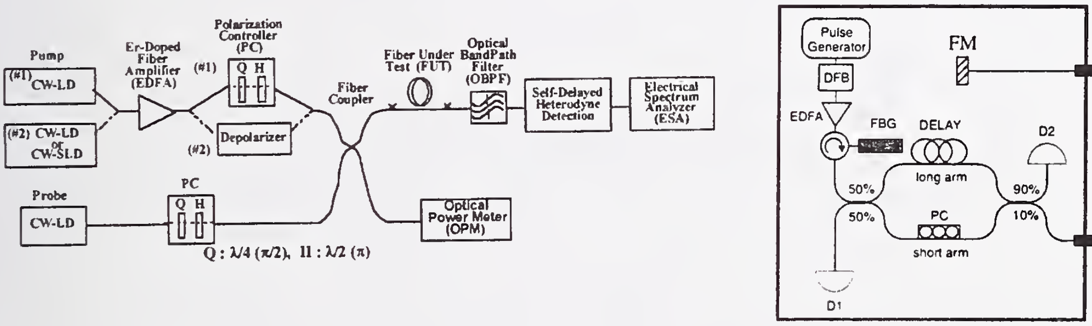

(c) XPM method

(d) Self-aligned Interferometric

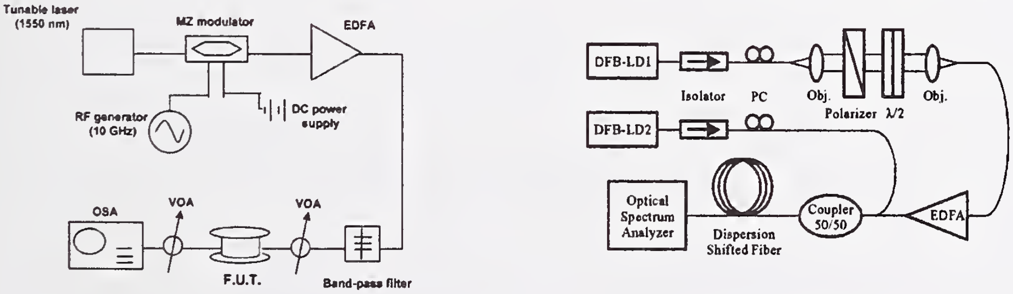

(e) Sinusoidally modulated signal SPM (S-SPM)

(f) Four wave mixing (FWM)

Fig.1 Experimental set up for six different (n2/Aeff) measurement methods.
(a) Pulsed LD SPM(P-SPM), (b) CW-LD SPM (CW-SPM), (c) XPM
(d) Self-aligned Interferometric (INT), (e) Sinusoidally modulated signal SPM (S-SPM),
(f) Four wave mixing (FWM)

Table 2 Measured values of (n2/Aeff) at random polarization states for various optical fibers using six different methods.

| Fibers | $(n2/Aeff)\times 10^{-10}$ [1/W] | | | | | | | |
|---|---|---|---|---|---|---|---|---|
| | P-SPM | CW-SPM | XPM | INT (*) | S-SPM | FWM | Ave | σ |
| SMF | 2.62 | 2.60 | 2.45 | 2.53 | 2.90 | - | 2.62 | 0.172 |
| CSF | 2.45 | 2.31 | 2.14 | 2.58 | 2.65 | - | 2.43 | 0.206 |
| DSF | 4.76 | 5.09 | 4.69 | 4.51 | 5.05 | 4.70 | 4.80 | 0.227 |
| NZDSF | 3.94 | 4.26 | 3.70 | 4.18 | 4.75 | - | 4.16 | 0.395 |
| LEDSF | 3.01 | 3.25 | 3.00 | 3.18 | 3.51 | - | 3.19 | 0.209 |
| DCF | 11.86 | 11.56 | 13.00 | 14.02 | 10.12 | - | 12.11 | 1.481 |

(*) : Using a correction factor of 0.8. (-) : Not Measured

Table 3 Estimated values of n2 at random polarization states for various optical fibers using six different methods.

| Fibers | $n2\times 10^{-20}$ [$m^2$/W] | | | | | | | |
|---|---|---|---|---|---|---|---|---|
| | P-SPM | CW-SPM | XPM | INT (*) | S-SPM | FWM | Ave | σ |
| SMF | 2.22 | 2.20 | 2.07 | 2.14 | 2.45 | - | 2.21 | 0.145 |
| CSF | 2.16 | 2.04 | 1.89 | 2.27 | 2.34 | - | 2.14 | 0.182 |
| DSF | 2.23 | 2.39 | 2.19 | 2.11 | 2.36 | 2.22 | 2.25 | 0.105 |
| NZDSF | 2.20 | 2.37 | 2.05 | 2.33 | 2.63 | - | 2.31 | 0.216 |
| LEDSF | 2.19 | 2.37 | 2.18 | 2.31 | 2.56 | - | 2.32 | 0.155 |
| DCF | 2.72 | 2.66 | 2.97 | 3.21 | 2.33 | - | 2.78 | 0.331 |

(*) : Using a correction factor of 0.8. (-) : Not Measured

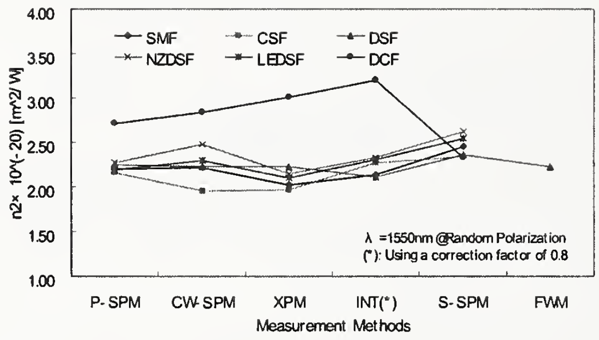

Fig.2 Estimated values of n2 at random polarization states for various optical fibers as a function of six different measurement methods.

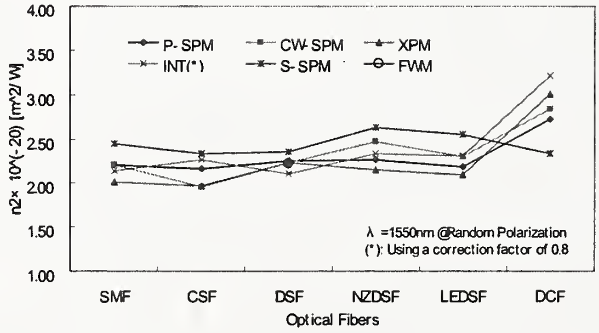

Fig.3 Estimated values of n2 at random polarization states for six different measurement methods as a function of various single mode optical fibers.

# Monitoring the Optical Network

Randy Giles
Advanced Photonics Research
Lucent Technologies
Holmdel, NJ 07733
randygiles@lucent.com

## Introduction

The sophistication and complexity of optical transport networks is apparent from their data capacity (Tb/s), transmission reach (1000's km), services functionality (voice, data, video) and global connectivity. As with any complex system, network operations are not fully deterministic, element specifications or testing may be flawed, databases may be erroneous or incomplete, software is not perfect, and things break. Yet through reliability analysis, redundant architectures, protection schemes, and ***performance monitoring***, optical networks can be engineered to give high availability and minimal service disruption. Examples include conventional SONET rings that have as part of their OAMP, overhead bytes that are set and monitored to generate critical alarms (loss-of-signal, loss-of-frame etc) and are detected in less than 10ms to activate line or path protection switching in less than 50ms. Similar cause (monitor condition) and effect (path restoration) protection schemes are used in mesh networks, often with lower costs relative to SONET rings through sharing of protection resources and sometimes at the expense of slower restoration times.

These conventional networks of both (inter)national and metropolitan extent are evolving from simple rings and point-to-point interconnections linked through end-terminals and electronic switches, to ones that are substantially transparent and perform more routing tasks in the DWDM optical layer than before. Figure 1 illustrates some features of modern transparent networks and begins to suggest the scope of monitoring needs. Transparent networks are economically feasible when the end-to-end demands between nodes are large enough to require the capacity of a WDM optical channel rather a lower subrate. End-to-end demands of OC-48 (2.5 Gb/s), OC-192 (10 Gb/s), and even OC-768 (40 Gb/s) are best routed using optical channel add/drop multiplexers and crossconnects. The trouble with this optical transparency is unavailability of the in-band monitor bytes of a data stream at intermediate points along the path, requiring instead alternate, dedicated ***optical*** monitoring methods. Furthermore, line engineering is more involved and faults are harder to find as links are transparently interconnected through the optical switch fabrics and accumulate optical impairments. Optical monitoring will be imperative for these networks to be practical.

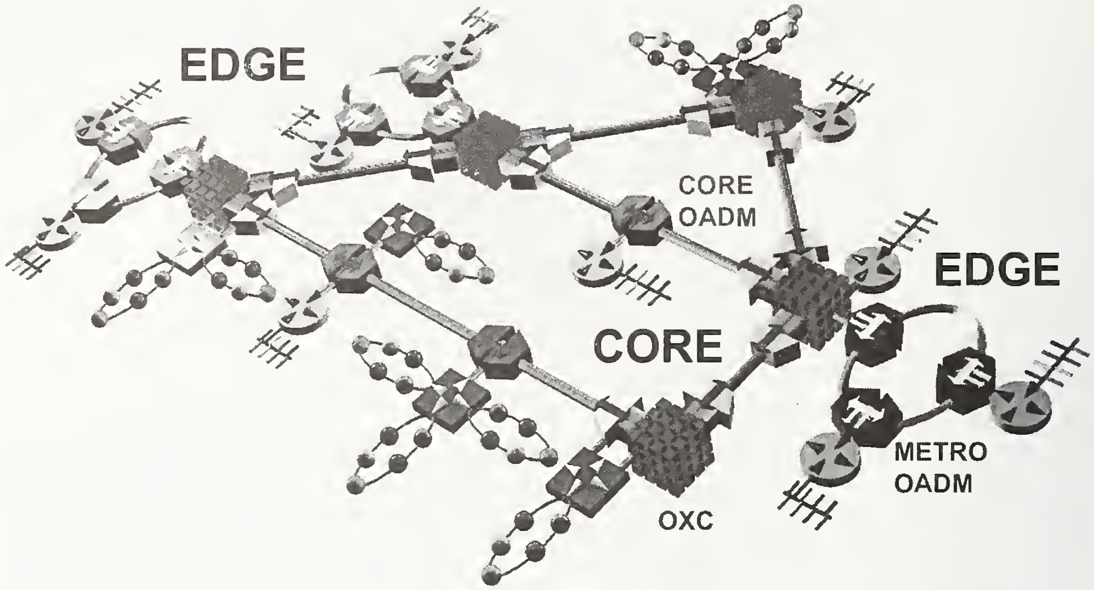

**Figure 1.** Wide-area (core) and regional (edge) networks transparently integrated through core- and metro- optical add/drop multiplexers, and optical crossconnects.

### Network Impairments

It is well known from point-to-point optical line systems that careful engineering is required in order to achieve the long reaches (1000's kms) and high capacities (several terabit per seconds) required for cost-effective transport. A guide to understanding a line system is given in figure 2 starting with the electrical input data stream $D_i(t)$ and ending in the output from the decision circuit . Omitting a rigorous formulation, noise $n_T(t)$ is present at the transmitter (eg shot noise) and the optical signal is propagated through the optical channel made of a series of fiber spans that contribute additive noise term, $n_s(t)$, and respond to the input optical field E(t) through $h_s(E;t)$. A common source of noise is the amplified spontaneous emission, ASE, produced in optical amplifiers and a crude estimate of the resulting optical signal-to-noise ratio measured in 0.1 nm bandwidth around a 1550nm and expressed in dB is $OSNR{\sim}58+P_{IN}-L_S-NF-10\log N_s$, where $P_{IN}$ is the transmitter power, $L_S$ is the span loss, NF is the amplifier noise figure (4-5 dB typically) and $N_s$ is the number of amplified spans. Typical requirements have OSNR at the destination to exceed 15-20dB, though forward error correction (FEC) technology relaxes these numbers.

The response function $h_s(E;t)$ may simply be a single constant attenuation coefficient, or it may incorporate chromatic and polarization dispersion and nonlinear optical phenomena including self-phase modulation, cross-phase modulation, four-wave mixing, Raman scattering and Brillioun scattering.

Fiber chromatic dispersion can cause signal distortion by temporally spreading the optical field's frequency components and lead to reduced transmission performance. The resultant optical field after chromatic dispersion is given by $E(z,t)=\int E(z,\omega)\exp(-i(\beta(\omega)z-\omega t))d\omega$. The frequency-dependent propagation coefficient can be expanded,

$$\beta(\omega)=\beta_0+\beta_1(\omega-\omega_0)+\frac{1}{2}\beta_2(\omega-\omega_0)^2+...$$

where the group velocity is $v_g=1/\beta_1$ and the dispersion coefficient is, $D=-2\pi c\beta_2/\lambda^2$. The nominal limit to the allowable chromatic dispersion for a channel data rate B is estimated from $B^2|D|L<10^5$ (Gb/s)$^2$ ps/nm. This corresponds to a residual group delay dispersion tolerance of approximately 1000ps/nm for 10 Gb/s data rates and 60 ps/nm for 40 Gb/s.

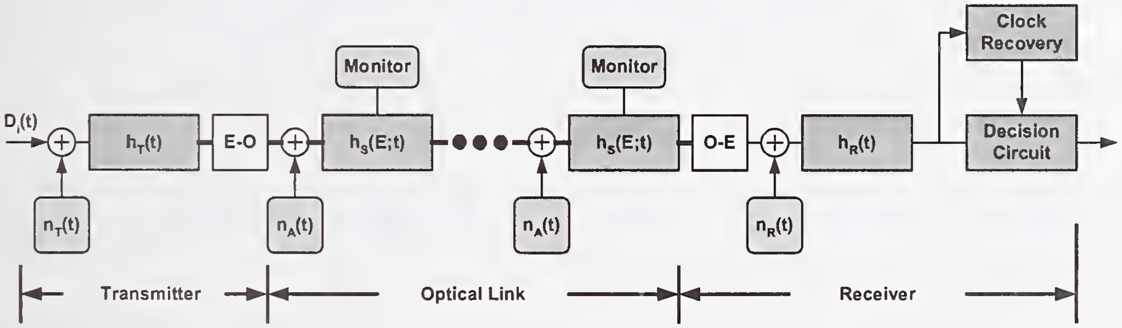

**Figure 2**. An optical communications line system comprised of a transmitter, optical link, and receiver.

Even after careful dispersion compensation of individual line systems, their concatenation through optically transparent switch nodes may compromise the end-to-end performance. Temperature effects are often neglected but the increases in data rates and system reach may alter this perspective. For example, where the temperature coefficient for the change of $\lambda_o$, the fiber's zero-dispersion wavelength, is $d\lambda_0/dT=0.03$nm/°C and the dispersion slope 0.05ps/nm$^2$/km, a 25°C change of temperature in a 1000km length optical path could disrupt 40Gb/s systems.

Polarization mode dispersion is an impairment arising from the residual birefringence present in optical fibers. Through PMD effects, the initial transmitter (single) polarization evolves into one that is randomly varying with the difference of mean power in orthogonal polarizaton states steadily decreasing as the light progresses down the line system. The differential group delay, DGD, induced by PMD is time-varying and the impairment, expressed as an outage probability, is a function of the fiber parameters, line length, and modulation format. The outage probability resulting from first-order PMD is approximately $P_{outage}=\exp[-P_{penalty}/K(\Delta T)^2B^2]$ where $\Delta T$ is the mean PMD-induced differential delay, $P_{penalty}$ is the threshold power penalty for an outage event, and the K value is a approximately 6 for RZ data and 14 for NRZ. Typical system limits have $\Delta TB<0.1$ to achieve outage probabilities below $10^{-7}$.

Optical nonlinearities in the fiber medium create additional boundary conditions to operating the optical line system. Very simply, with the inclusion of noise effects, they result in the establishment of optimum signal power requirements; if the power is low, noise is the predominant degradation, if the power is high, optical nonlinearities dominate. Only one class of nonlinearities will be discussed here for illustrative purposes, those originating from the Kerr effect. In the Kerr effect the refractive index of the transmission medium changes with the light intensity, $\Delta n=n_2P/A_{eff}$, where $n_2 \sim 2.6\times10^{-20}$ $m^2/W$ in silica fiber, P is the signal power, and $A_{eff}$ is the fiber effective area. The instantaneous self-phase modulation of a signal is $\Delta\phi_{spm}=N_s n_2 \omega_0 P L_{eff}/cA_{eff}$, where $L_{eff}=(1-\exp(-\alpha L))/\alpha$ is the fiber effective length for physical length L and attenuation coefficient $\alpha$. Impairments from Kerr-related nonlinearities (self-phase modulation, cross phase modulation, four-wave mixing) become important when $\Delta\phi_{spm}$ approaches $\pi$.

Finally, light traversing the line system is detected with a photodiode, additional noise is contributed from the receiver, and the signal is filtered before reaching the clock recovery and decision circuit.

### Optical Monitoring

The diversity of optical impairments and their dependence on device parameters and system design creates the need for accurate characterization of components and appropriate system performance monitoring and network element control. It is clear that in addition to the optical impairments, there are many other electrical, mechanical, and optical components that contribute to the end-to-end performance of a data flow. With many possible culprits it may not always be practical to identify the exact cause of deterioration or even failure of a line system, but finding its location may be. Fault location is currently the primary reason for measuring a line system's performance, particularly as the network becomes highly connected through transparent nodes, has large numbers of optical signal channels, or has very long reach. However, despite current limitations, optical monitoring needs are evolving in hand with optical networks and can be summarized as:

1. WDM channel presence, power, and wavelength. Used for link status verification.
2. WDM channel optical signal-to-noise ratio or Q-factor. Can sense non-alarm degradations and locate faults.
3. Feedback signal in gain equalizers, chromatic dispersion and PMD compensators.
4. Transparent network management. Channel performance verification after link concatenation.

5. In-situ link parameter extraction from detailed optical channel signatures. Used for preplanning and preprovisioning assessment.

Commerically available optical monitoring methods cannot perform all the tasks suggested by this list. Compact optical spectrum analyzers can report some optical attributes and in some instances give estimates of a channel's Q-factor, a measure of the error-rate margin in digital transmission. Specialized optical receivers can perform eye analysis and yield Q-factor numbers. However, these limited techniques are either not adequate or cost effective for the demands of fully transparent optical networks. Several new approaches to optical monitoring will now be described.

Recently, a number of RF signal analysis and optical sampling techniques have been reported, that suggest the possibility of not only indiscriminately sensing changes in signal parameters as a fault location method, but identifying the cause. For example, PMD is well known to cause RF signal fading through cancellation of frequency components that destructively interfere after a birefringence-induced relative delay. The normalized fading from first-order PMD effects measured at frequency f is $F=1-4r(1-r)\sin^2(\pi f\Delta T)$ where r is the power ratio in the two principal orthogonal states. If the monitor can derive PMD values from RF fading measurements, then a network operator could recognize PMD outage events, or in severe cases, identify out-of-spec fiber spans.

Optical sampling methods to obtain amplitude histograms or reconstructed eye diagrams are available to analyze signals at very high data rates (>100Gb/s). Figure 3 illustrates synchronous and asynchronous sampling of a data eye diagram and the corresponding distribution functions. Both approaches yield estimates of Q ( $Q=|\mu_1-\mu_0|/(\sigma_1+\sigma_0)$ ), trading off between requiring timing recovery at the monitor (synchronous), and reduced accuracy of the Q estimate (asynchronous). These sampling techniques offer better estimates of signal quality than OSNR as they are sensitive to time-domain features not observed in the optical spectrum. Optical sampling may also distinguish between chromatic dispersion-induced signal degradation and ASE noise penalties.

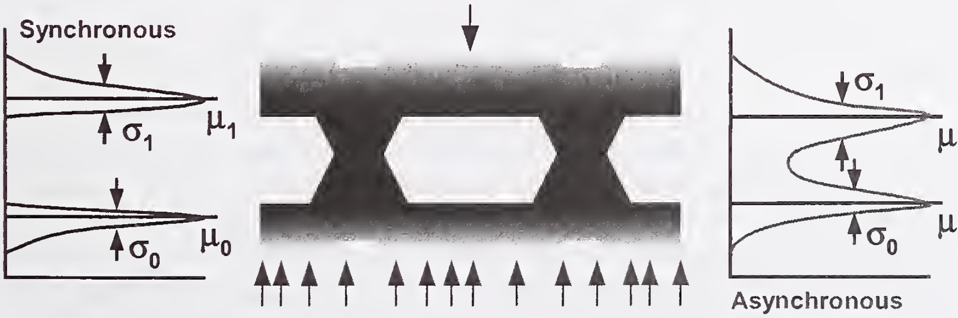

**Figure 3.** Data eye diagram and distribution functions for synchronous and asynchronous sampling.

Although conventional electrical sampling techniques can generate amplitude histograms, optical methods through either nonlinear or coherent homodyne detection are candidates for use at 40Gb/s and higher data rates. Figure 4 shows these sampling methods that involve mixing an incoming signal with a narrow-width sampling (gating) pulse such that recovered signal is the convolution of the signal and sampling pulse shapes,

$$\bar{V}out_{NONLINEAR}(t) \propto \eta \int P_{DATA}(\tau) P_{GATE}(\tau - t) d\tau$$

$$\bar{V}out_{HOMODYNE}(t) \propto \mathrm{Re} \int E_{DATA}(\tau) E^{*}{}_{GATE}(\tau - t) d\tau$$

where η is a conversion efficiency associated with the nonlinear interaction and generally is very small. In contrast, the coherent homodyne method can be very sensitive, but for eye diagram reconstruction requires two balanced receivers so that quadrature components of the homodyne signal can be added. Either sampling method enables detailed pulse characterization without high-speed (expensive) photodetectors, suggesting that practical implementations as monitors for transparent networks are possible.

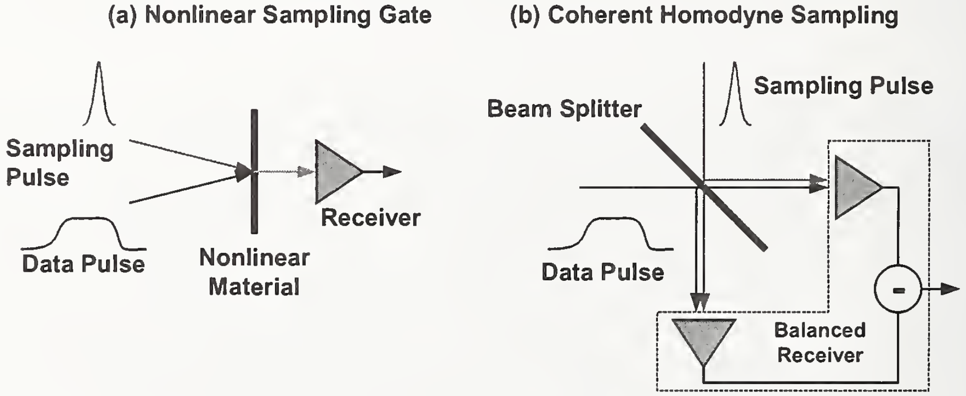

Figure 4. Nonlinear and coherent homodyne optical sampling techniques for Q-factor histograms and eye diagram reconstruction.

## Summary

Optical monitoring of optical networks is in its infancy. Channel monitoring in DWDM transmission systems and fault location in line systems are the first applications, but new requirements are arising as system architectures move to transparent ring and mesh networks. Identifying and quantifying optical impairments (noise, chromatic dispersion, PMD) during network operation will be needed and a variety of techniques based on RF and optical means are in development.

# Burial depth measurement for ion-exchanged glass waveguides with different widths

*Pratheepan Madasamy, Mike Morrell*[*],
*David Geraghty, Seppo Honkanen and Nasser Peyghambarian*
Optical Sciences Center, University of Arizona, Tucson, Arizona

[*]NP Photonics, Tucson, Arizona

## Introduction

Buried ion-exchanged glass waveguides are used extensively for making devices for communications because they have low loss, are mode matched with the fiber and can be polarization insensitive. It has been reported [1] that in an arrayed waveguide grating device having both slab waveguide regions and single mode channel waveguide regions, the two regions get buried to different depths. This would result in a significant loss at the intersection of these waveguide regions. In this paper we report a simple method to measure the burial depth and we investigate the difference in burial depths for different waveguide widths ranging from 2 to 10 μm. We show that the burial depth increases linearly for mask opening widths from 2 to 10 μm.

## Fabrication

BGG31 glass was used as the substrate material. Mask widths ranging from 2 to 10 μm were patterned on the sample. Buried ion-exchanged waveguides were prepared in two steps. The first step involved Ag/Na ion exchange at the surface. Two different samples were prepared using different first steps. In the first sample the first step involved thermal ion exchange performed in a 50:50 $AgNO_3$/Na $NO_3$ melt at T=553K for 75 mins. A 100 nm thick titanium film was used as the mask for the first step. The second step was an unmasked field assisted burial at T=523K, with a current density of 1.15 $Am^{-2}$ for 40mins. In the second sample, the first step involved field assisted ion exchange with a 100 nm thick Ag film as the ion source. Ion exchange was done at 90°C, 300 V for 3 hours. In the first step, photoresist itself was used as the mask [2, 3]. The second step was an unmasked field assisted burial at T=523K, with a current density of 1.79 $Am^{-2}$ for 26mins. Both processes have been commonly used to fabricate ion-exchanged devices.

## Measurement technique

We define the burial depth as the distance from the surface of the glass to the center of the waveguide mode. The experiment was set up using a Newport AutoAlign system. The data was taken with a resolution of 0.1μm. The setup used to find the center of the mode is given in Fig. 1a. The input fiber from a 1550nm SLD (superluminescent diode) source and the output fiber to the optical power meter are butt-coupled to the waveguide, and the throughput is maximized. Then the output fiber is scanned in the y direction to get the profile in y direction as shown in the inset in Fig. 1a. The center of the profile gives the center of the mode ($y_0$). To find the surface of the glass, the input fiber is moved about 1mm from the surface of the glass as shown in Fig. 1b. This forms a Lloyd's mirror interferometer like set-up, as shown in Fig 2, with interference fringes formed due to the direct light from the input fiber and the reflected light from the glass surface. The intensity in y direction in the observation plane is:

$I = 4I_0 \sin^2(\frac{\pi a y}{s\lambda})$ for y>0 where y=0 is the surface.

The interference fringe has a minimum at the surface of the glass and there are no fringes below the surface of the glass. In the setup in Fig 1b, scanning the output fiber in the y direction from the center of the mode gives the fringes and the first minimum gives the surface point. The difference between the surface point and the center of the mode gives the burial depth for the waveguide.

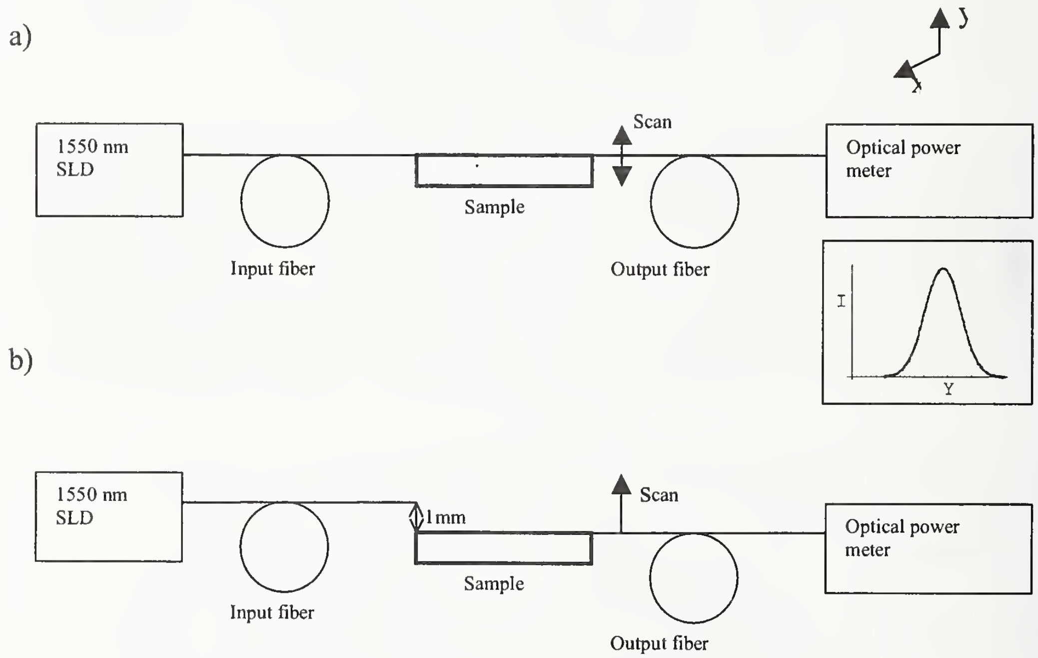

*Fig. 1 Set-up for measuring the burial depth; 1a shows the set-up to find the center of the mode and 1b shows the set-up to obtain the interference fringes to get the surface point.*

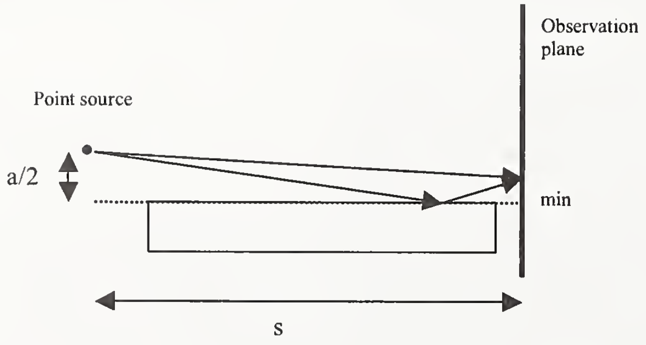

*Fig. 2 Lloyd's mirror interferometer.*

## Results

Using this technique, the burial depth is measured for all the waveguides on both samples. The burial depth increases linearly for mask opening widths from 2 to 10μm for both of the samples as shown in Fig. 3. This is in agreement with the observation made in [1] where larger burial depth for the slab waveguide region as compared to the single mode channel waveguide was obtained. The slope differs for the two samples because the burial parameters are not the same for the samples and the first step results in different $Ag^+$ concentration in the surface waveguides of the two samples.

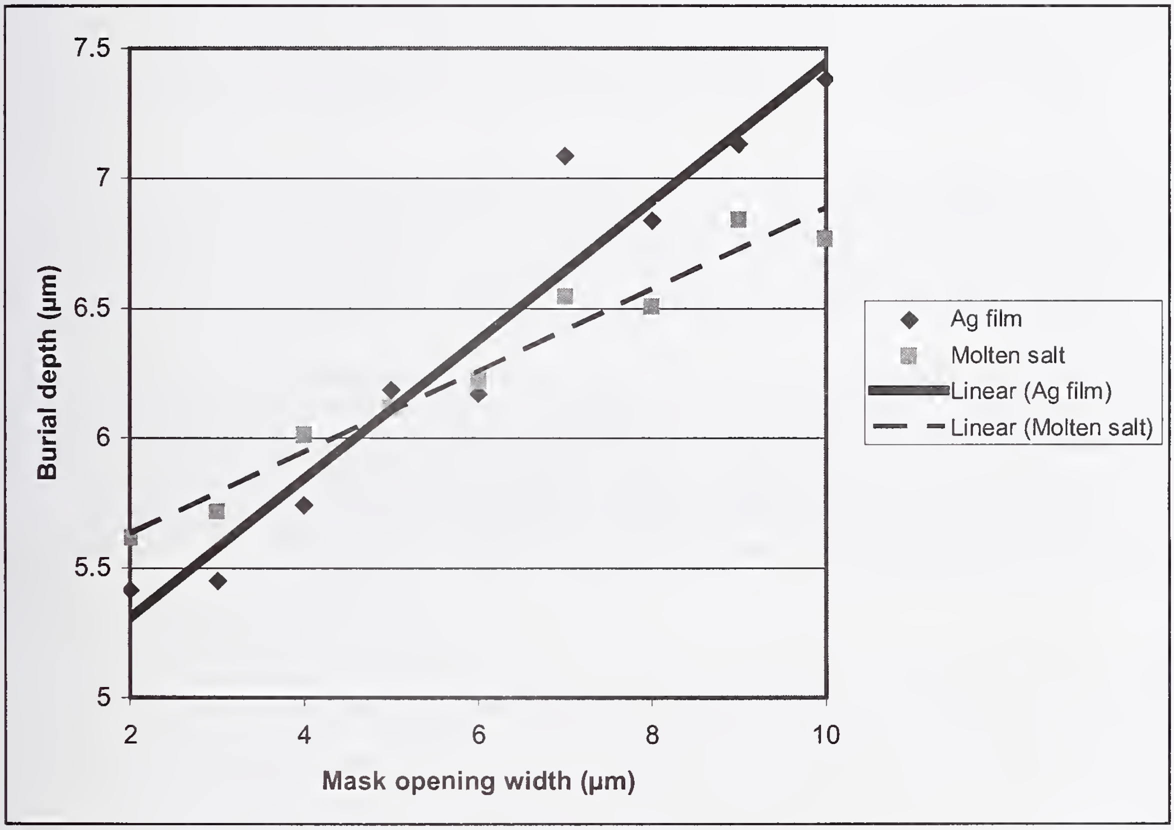

*Fig. 3 Burial depth as a function of mask opening width. The square data points are for sample 1 with molten salt ion exchange as the first step. The dashed line is a linear fit for this data. The diamond data points are for sample 2 with Ag film ion exchange as the first step. The continuous line is a linear fit for this data.*

## Discussion

We report a simple technique to measure the burial depth for buried ion exchange waveguides. We measured the burial depth as a function of waveguide width for two samples with two different but commonly used ion exchange processes. We found the burial depth to increase linearly for mask opening widths from 2 to 10 μm. The difference in burial depths for different waveguide widths can be explained by the effect of the conductivity change in the waveguide region on the field lines. For slab waveguides the field lines are not affected and the waveguide only results in a small change in the net conductivity of the glass. For a narrow channel waveguide the field lines are affected resulting in a smaller burial depth as opposed to when the field lines are perpendicular to the surface [4, 5]. Subsequently, in a wider waveguide the field lines are affected less in the center part of the waveguide and only affected near the edges of the waveguide which results in a larger burial depth for the wider waveguides compared to the narrower waveguides. By knowing the burial depths quantitatively as reported in this paper, the loss at the intersection of narrow and wide waveguides can be eliminated by adding a proper taper at the intersection of these waveguides.

## References

[1] B. Buchold and E. Voges, "Polarisation insensitive arrayed-waveguide grating multiplexers with ion-exchanged waveguides in glass," Electron. Lett. 32, pp. 2249-2250, 1996.

[2] P. Poyhonen, S. Honkanen, A. Tervonen, M. Tahkokorpi, J. Albert, "Planar 1/8 splitter by photoresist masked silver film ion exchange," Electron. Lett. 27, 1319-1320, 1991.

[3] P. Madasamy, G. Nunzi Conti, P. Poyhonen, Y. Hu, M. M. Morrell, D. F. Geraghty, S. Honkanen, N. Peyghambarian, "Waveguide distributed Bragg reflector laser arrays in erbium doped glass made by dry Ag film ion exchange," Opt. Eng. 41, pp. 1084-1086, May 2002.

[4] D. Cheng, J. Saarinen, H. Saarikoski and A. Tervonen, "Simulation of field assisted ion-exchange for glass channel waveguide fabrication: Effect of nonhomogenous time-dependent electric conductivity," Opt. Commun. 137, pp. 233-238, 1997.

[5] Jerome Hazart and V. Minier, "Concentration profile calculation for buried ion-exchanged channel waveguides in glss using explicit space charge analysis," IEEE Journal of Quantum Electronics, vol. 37, pp. 606-612, April 2001.

# Accuracy of MFD and $A_{eff}$ Measurements using Far-Field Scanning

Arthur J Barlow, Richard Castle, PerkinElmer Optoelectronics, Wokingham RG41 2GY UK
E-mail: arthur.barlow@perkinelmer.com
&
Andrew G Hallam, Halcyon Optical Services, Waltham Chase UK SO32 2LG
E mail: ahallam@halcyon-optical.co.uk

## Abstract:

This paper describes the implementation of a high-accuracy system for the measurement of Mode Field Diameter (MFD) and Effective Area ($A_{eff}$) in single mode fiber manufacturing environments. Certain engineering details are described, in particular the effect of the light collection angle subtended by the detector. This is examined both theoretically and experimentally.

## Introduction

The measurement of MFD by use of far-field scanning has long been the preferred route to high accuracy and more recently has been standardised by TIA [1], [2] and IEC as the reference test method (RTM). In this paper we describe some error sources and the engineering issues involved in designing an instrument to be both reliable and accurate, as well as being fast enough for production measurements. We describe some engineering details that were developed in order to implement a fast, accurate test instrument for use in fiber production environments.

In the far-field method, the test fiber is cleaved and the cleaved end placed at the centre of rotation of a detector placed on a rotating table. In addition the fiber must lie in the plane of rotation of the detector. These apparently easy fiber handling issues require surprisingly high tolerances of fiber positioning [1], [2]. Furthermore, additional issues such as light scattering can introduce a measurable experimental error [2].
To determine the MFD and $A_{eff}$, the detector is scanned around the fiber end to detect the far field radiation pattern. Prescriptive algorithms set out in FOTP-191 [3] and FOTP-132 [4] describe how to calculate the MFD and $A_{eff}$ respectively. These were updated in 2001 to cover the newer types of large $A_{eff}$ fiber being used in high-power, high bit-rate optical transmission systems, and throughout this paper we use these latest algorithm including side lobe reversal and noise-based integration limits.

A detailed analysis of the tolerances to fiber position [1], [2] reveals that the most critical parameter is the "in-out" (Z axis) position of the fiber end. In essence, the fiber must lie perfectly over the centre of rotation. Further substantive dependence upon the fiber height (Y axis) and tilt (the fiber must "aim" horizontally at the detector) are also evident. It is clear that in order to achieve a routine accuracy of MFD below a few percent, that a very precise fiber positioning system is required. We examine this issue later.

## Detector Design

A further parameter, so far not studied in detail in the literature, is that of the angle subtended by the detector at the fiber end (see Figure 1). The light "collection angle", d, is dependent on the radius R of the detector scan, and the detector size D. With modern fibers, the far-field scanning system must be capable of very high dynamic range (50dB), and so it is desirable to use a large collection angle, in order to collect more light and help speed up the measurement. Conversely, a small detector will exhibit less noise. This has to be balanced against the angular resolution requirement of $d<0.5$ degrees, set by the FOTP's [3], [4]. This requirement stems historically from the desire for high angular resolution [5]. Furthermore, the detector must be protected from any scattered light [2].

Before setting out on the design of a new instrument, we examine the collection angle dependence. It is important to understand the effects of deliberately increasing the collection angle in the search for higher dynamic range. We used some sample data from a standard dispersion-unshifted single mode fiber measured by NPL in London. They state that their collection angle is 0.4 degrees, and the data is taken at 0.4-degree intervals. To synthesise the effect of larger collection angles, we integrated the raw Intensity-angle data specially provided by NPL [6] over progressively wider angles, using a rectangular filter method.

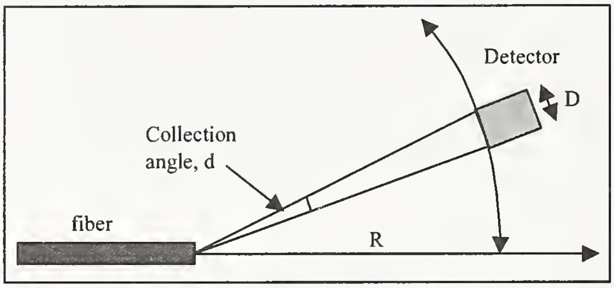

**Figure 1: detector subtends an angle, d, at the fiber**

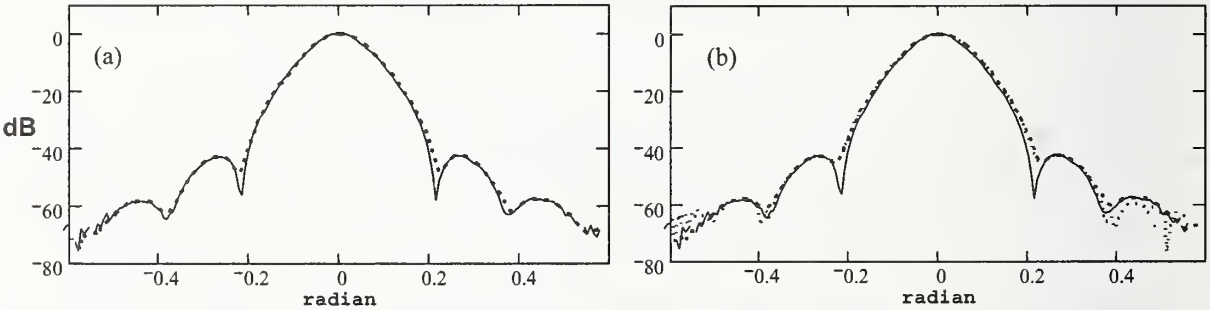

**Figure 2: a) Original NPL data (solid line) compared to an effective 2°collection angle (dashed line). b) Original NPL data (solid line) compared to an effective 3.2° collection angle (dashed line), obtained by filtering the data. Also shown is the same fiber measured on an instrument with a 3.2° collection angle (dotted line).**

Plots of far-field intensity versus angle for a matched-clad fiber at 1310nm with different amounts of filtering are shown in Figure 2. In Figure 2a), the "depth" of the minima between the main lobe and the first side lobes is reduced, as we would expect. However, a second effect, less obvious and somewhat unexpected, is the weighting of the data to higher angles. This becomes obvious in Figure 2b, where the collection angle has been deliberately increased to a large value. The smoothing effectively increases the width of the main lobe and thereby reduces the calculated MFD value accordingly. In addition, at the higher angles, and hence lower light levels, the smoothing can assist location of the second minima, in this case at ~ ±0.38 radians. A summary of the MFD and $A_{eff}$ values are given in Table 1.

| | **MFD, um** | **$A_{eff}$, $um^2$** |
|---|---|---|
| **NPL unsmoothed** | **9.16** | **65.6** |
| NPL 3.2 degree smoothing | 8.70 | 59.1 |
| Measured, 3.2 degree collection angle (Fig 2b) | 8.73 | 59.5 |
| Measured, <0.5 degree collection angle (Fig 5b) | 9.14 | 65.4 |

**Table 1. Summary of smoothing effect on MFD and $A_{eff}$**

In Figure 3, we show the effect of collection angle on the calculated MFD and $A_{eff}$ values for this fiber at three different wavelengths. In each case, the data calculated versus collection angle from 0.4 degrees to 6 degrees was fitted with a third-order polynomial and the intercept at zero inserted into the data set as a synthetic "zero collection angle" data point. This value was taken as the reference point for the percentage deviation shown in Figure 3c) and 3d). Because of the different shapes of Intensity-angle curve for differing fiber types, it is not possible to correct for large collection angles.

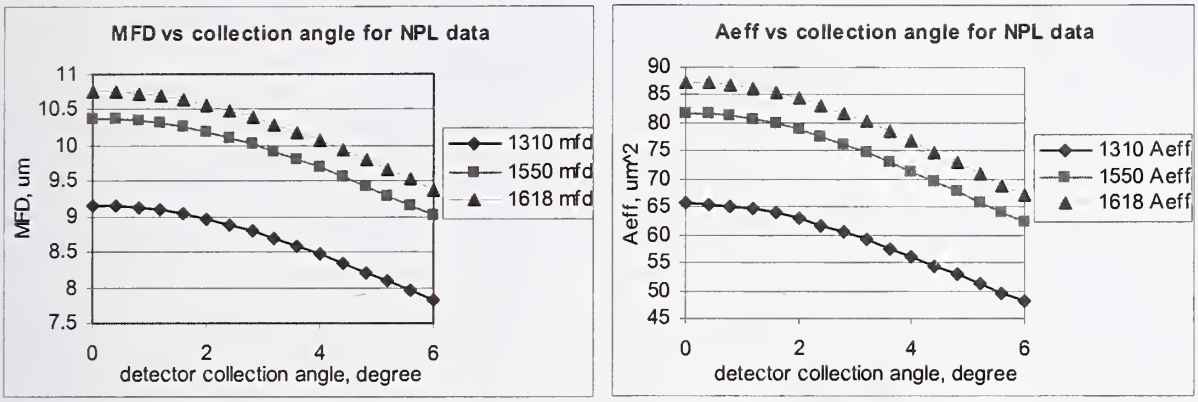

a) MFD versus collection angle

b) Aeff versus Collection angle

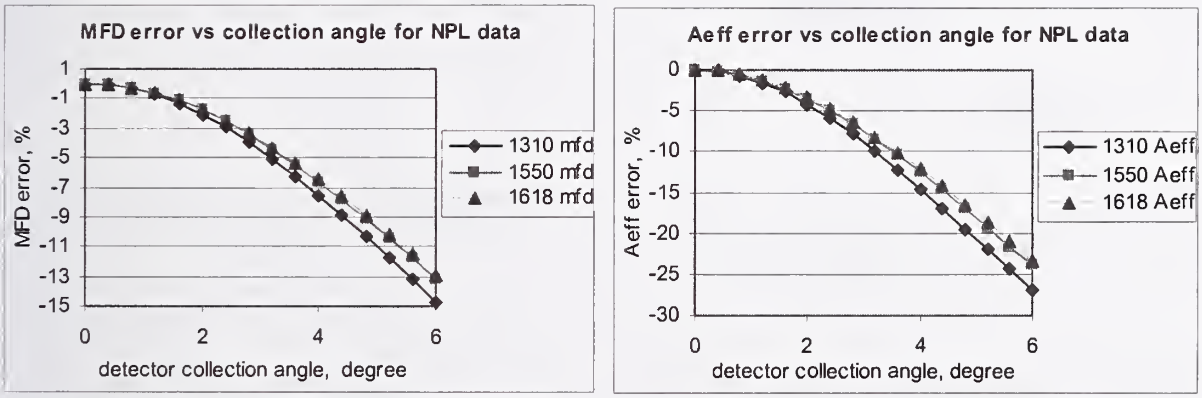

c) Percentage MFD change with collection angle

d) Percentage $A_{eff}$ change with collection angle

**Figure 3: the effect of light collection angle on MFD and $A_{eff}$**

These results confirm that to maintain a high accuracy, it is necessary to maintain a collection angle under 0.5 degrees, in accordance with the latest FOTP's. At 0.5 degrees collection angle, the error in MFD and $A_{eff}$ remains well under 1%.

Instrument Design

We now turn to the design of a production instrument. The light sources chosen were three high-power fiber-coupler LEDs, centred at 1310, 1550 and 1620 nm respectively, coupled via fiber couplers and a solid-state monochromator to allow the source wavelength to be tunable over the main fiber operating wavebands. To maximise dynamic range with these sources, the detector size was chosen as 350um to minimise the detector noise. The light sources were chopped and the signal measured using a digital lock-in amplifier. Data was collected by ADC and computer, which used variable averaging in accordance with the detector signal level.

The detector was placed on a heavy-duty rotation table capable of 0.01-degree steps and ±55 degrees of travel. The detector was encased in a special assembly designed to reduce the scattered light reaching the detector, consisting of a narrow-bore tube, specially lined to prevent reflections. This ensures only light coming directly from the fiber end gets to the detector, but careful attention must be paid to the internal surface in order not to artificially increase the light collection angle by virtue of the tube acting as a "light pipe".

The test fiber was placed in a fiber clip and the fiber cleaved using a specially adapted cleaver, whilst still held in the clip. The clip was then transferred to the instrument so that the protruding cleaved end fitted into in a long V-groove. The V-groove is pre-aligned to the detector in X- and Y-axis directions to allow precise and repeatable fiber location with very low tilt angles. Although the fiber clip itself is located against an end stop, this is not sufficient to ensure the fiber end is always in the correct Z-axis position, (i.e. directly over the centre of rotation). Instead, the entire V-groove assembly is mounted on a slide driven by stepper motor. A miniature video camera is positioned below the fiber on the axis of rotation so as to display a side-view image of the fiber on a PC monitor. The provision of digital cross hairs on the monitor then allows the fiber end to be precisely aligned over the centre of rotation using the Z-axis stepper motor. The image allows the fiber location and end cleave angle to be monitored. Figure 5a) shows the overall schematic of the detector area of the instrument with video image. Figure 5b) shows a typical result, obtained on the same fiber that was measured in Figure 2b), but this time with <0.5 degree collection angle, showing excellent agreement with the NPL value (Table 1). In this casc, at each step of the table, both 1310nm (red line) and 1550nm (blue line) sources were selected in turn, using an ultra-fast solid state monochromator, so both wavelengths could be measured in almost the same total measurement time as for one wavelength. This yields still more improvement in overall speed for production applications.

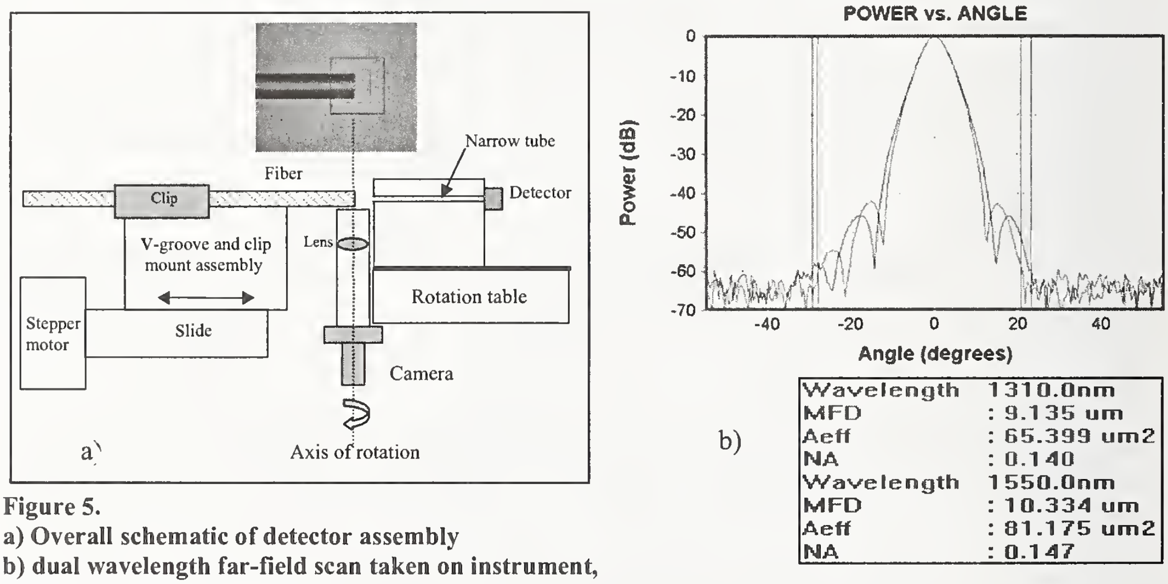

```
Wavelength  1310.0nm
MFD         : 9.135 um
Aeff        : 65.399 um2
NA          : 0.140
Wavelength  1550.0nm
MFD         : 10.334 um
Aeff        : 81.175 um2
NA          : 0.147
```

**Figure 5.**
**a) Overall schematic of detector assembly**
**b) dual wavelength far-field scan taken on instrument, 0.5 degree collection angle**
**1310 nm = red line, 1550 nm = blue line.**

## Conclusion

We have described the development of a fast and accurate tunable wavelength MFD and $A_{eff}$ measurement system (PerkinElmer MA400). It was found that the detector collection angle was a substantial source of error, and must be limited to less than 0.5 degrees to maintain <1% error. By careful optical design, with fiber location by a V-groove, and with a video camera to monitor the fiber position, it has been possible to design a production-compatible instrument which has an overall specified ~±2% accuracy on MFD and ~±4% accuracy on $A_{eff}$, with a typical measurement time below 1 minute. Moreover the unit has tunable light source wavelength and dynamic range ~65dB. Scattered light was held to a negligible level by using a narrow entrance tube for the detector.

We have shown for the first time that it is possible to implement the RTM (Far-Field Scanning) for MFD and $A_{eff}$ with variable wavelength and high dynamic range in a production environment.

## References

1. Roger Bighouse, Corning Inc., Private Communication.
2. M. Young., " Mode Field Diameter of Single Mode fiber by Far field scanning", Jnl. Appl. Optics-LP, vol.37, no..24, 1998, pp5605-5619.
3. TIA FOTP-191 "Measurement of Mode Field Diameter of Single-Mode Optical Fiber"
4. TIA FOTP-132 "Measurement of Effective Area of Single-Mode Optical Fiber"
5. W. T. Anderson at al, "Mode Field Diameter Measurements for Single Mode fibers with Non-Gaussian Field Profiles" Jnl. Lightwave Technology, LT-5, 1987, pp.211-217.
6. The authors are grateful to NPL for providing raw far-field scan data.

# Mode-Field Diameter and "Spot Size" Measurements of Lensed and Tapered Specialty Fibers

**Jeffrey L. Guttman**
*PHOTON, inc., 6860 Santa Teresa Blvd., San Jose, CA 95119*
*Phone: 408-226-1000, FAX: 408-226-1025, e-mail: jguttman@photon-inc.com*

**Abstract:** The Mode-Field Diameter (MFD) and "spot size" of an assortment of lensed and tapered specialty fibers were determined from far-field and near-field measurements. In the far field, measurements were made using a 3D-scanning goniometric radiometer that provides a complete hemispherical profile. Indirect measures of the near field derived from these data are reported, including the Petermann II MFD, the $1/e^2$ spot size using the far-field Gaussian approximation, and a measure obtained from 2D Fourier transform inversion of the far field using phase retrieval techniques. In the near field, direct profile measurements were made using an IR Vidicon camera and magnifying objective lenses, with the spot size reported as the $1/e^2$ diameter of the imaged profile.

## 1. Introduction

Lensed and Tapered specialty fibers are designed to optimize coupling between the fiber and various optical components such as edge-emitting laser diodes and AWGs. The light from these fibers forms a focus at some finite distance away from the fiber end. The MFD and corresponding spot size of these fibers is typically in the range of 5 microns or less. These small spot sizes and corresponding high divergence present challenges to near field and far field measurements. Typically the near-field measurements are limited by the optical performance, and the far-field measures must extend to very large angles. Results of measurements of 6 commercially available fibers are presented, including different type lensed/tapered fibers (4 axially symmetric and 1 elliptical) and a standard single-mode fiber for reference. Also, since the focused beams are in free space, there are some fundamental questions as to the applicability of the MFD, a measure originally formulated to describe the field distribution within a fiber.

## 2. Measurement Technique

The fibers were coupled to a stable narrow-linewidth diode laser source operating at a nominal wavelength of 1550 nm and output power of approximately 7dBm.

Far-field profiles were obtained using a 3D scanning goniometric radiometer, with optical dynamic range greater than 60 dB. This instrument provides NIST-traceable measures of MFD to the 0.5% level for single-mode fiber. The angular measurement range for each scan is ±90°, with sampling every 0.055°. By rotating the source about the scan plane, a full hemispherical measure of the far-field profile is obtained. The 3D profiles for each fiber in this study consist of 50 azimuthal scans at increments of 3.6° about the fiber axis.

Near-field profile measurements were made using an IR Vidicon camera and 2 different magnifying objective lenses: a 100X NA 0.9 microscope objective intended for use in the visible and a 40X NA 0.48 aspheric lens designed for the IR. The point-spread function of this lens at 1550 nm is approximately 2.6 μm. The characteristics of the 100X lens at 1550nm are not known. The fibers were positioned using a high precision 3-axis translation stage. Absorbing glass filters were used for optical attenuation. The RS-170 camera video images were acquired using a framegrabber with 8-bit resolution, i.e., 256 levels. Measurement accuracy depends on the camera noise, sensor response uniformity, the digitization, the number of pixels in the image, and on the optical properties of the lens used. With adequate pixel count and lens quality, the signal noise and sensor response provide accuracy to the ±3% level. Accuracy is also strongly dependent on the lens position because of the short depth of focus of both the lens and the fibers being measured.

## 3. Measurement Results

Complete hemispherical far-field profiles of the 6 fibers, (designated fibers # 1-6), and the corresponding 1D cross-sectional profiles through the principal axes of the distribution, are shown in figure 1. The background level of the measurements, seen in figure 1a for the profile of the standard single-mode fiber, is at the -60dB level relative to the peak. The profiles of the lensed/tapered fibers extend in all cases to ±90°. The profiles for fibers #1-5 have the appearance of a superposition of a main beam and a scatter background, probably due to surface modifications and defects introduced in the fabrication process. The angular extent of the main beam for these profiles ranges from approximately ±30° for the standard single-mode fiber to greater than ±70° for fiber #5. The profile for fiber #6, the elliptical fiber, consists of a main beam with a prominent diffraction structure. (Although not shown here, the scatter and diffraction structure extend to angles greater than ±90°, in the backward direction.)

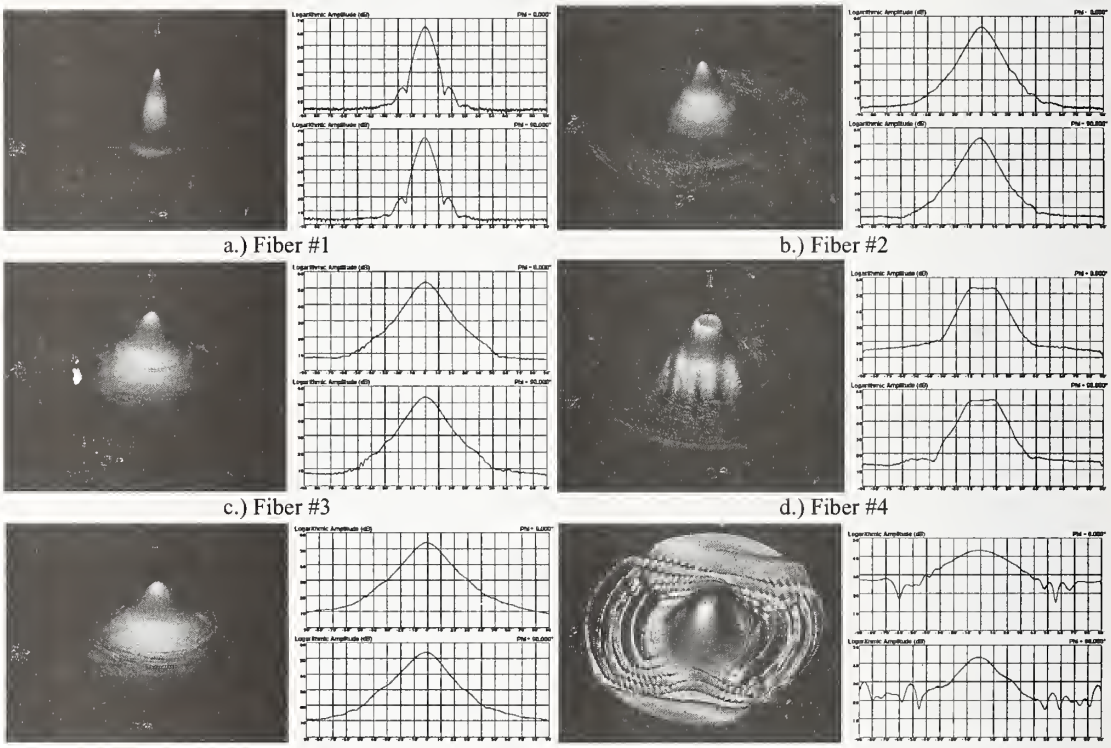
a.) Fiber #1
b.) Fiber #2
c.) Fiber #3
d.) Fiber #4
e.) Fiber #5
f.) Fiber #6

Figure 1. Complete hemispherical far field profiles of fibers # 1-6, and the corresponding 1D cross-sectional profiles through the principal axes of the distribution. The vertical scale is 10dB/division and the horizontal scale is 10°/division.

Example images obtained in the near field for fiber #6, the elliptical fiber with the smallest spot size of all the fibers measured here, are shown in figure 2. The profile in figure 2a obtained with the 40X lens is clearly seen to be broadened by the spread function of the lens, and is also near the limit of adequate pixel count.

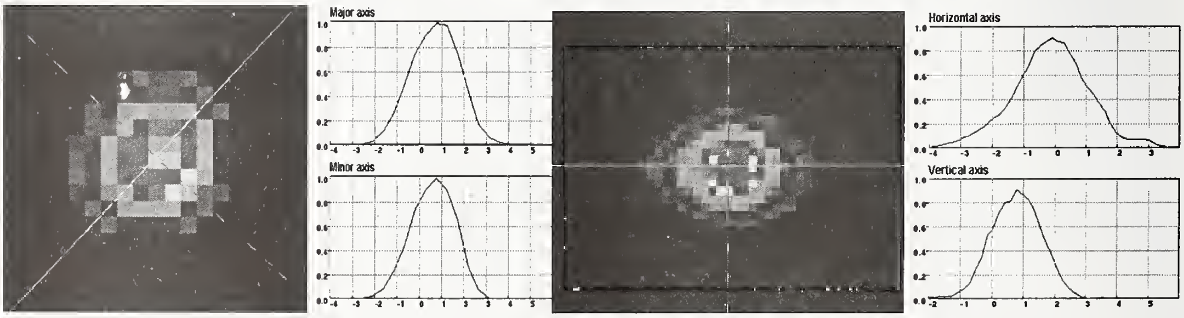

a.) 40X
b.) 100X

Figure 2. Near field profiles of fiber #6, the elliptical lensed/tapered fiber, obtained with a.) 40X lens and b.) 100X lens. The horizontal scale in the profile cross sections is 1 μm/division.

## 4. Analysis and Discussion

The far field data were analyzed to provide the Petermann II MFD [1], the $1/e^2$ diameter from a diffraction-limited Gaussian approximation using the ISO/DIS 13694 laser standard fit [2], and the $1/e^2$ diameter of the near field obtained from 2D Fourier analysis with phase retrieval [3-5]. The near field profile data were analyzed to provide the $1/e^2$ diameter, using the equivalent scanning slit method. The profile diameters obtained with the 40X lens were corrected for the spread function width.

The MFD for the lensed/tapered fibers depends significantly on the angular integration limit of the Petermann II integral, due to the wide angular extent of the far field. This is shown in the graph of MFD versus the Petermann II integral limit shown in figure 3. The MFD stabilizes for most of the fibers in the range from 40° to 60°. For the elliptical fiber #6 the integration needs to extend beyond 70°. However, the Petermann II formulation has radial symmetry as an underlying assumption. Therefore, strictly speaking, it is inappropriate to use this MFD measure for elliptical fibers. Table 1 summarizes the MFD results over the integral limit ranging from 40° to 60°. The fractional percent variation from the average value for fibers #1-5 is well within acceptable limits, and errors associated with the elliptical fiber are quite significant.

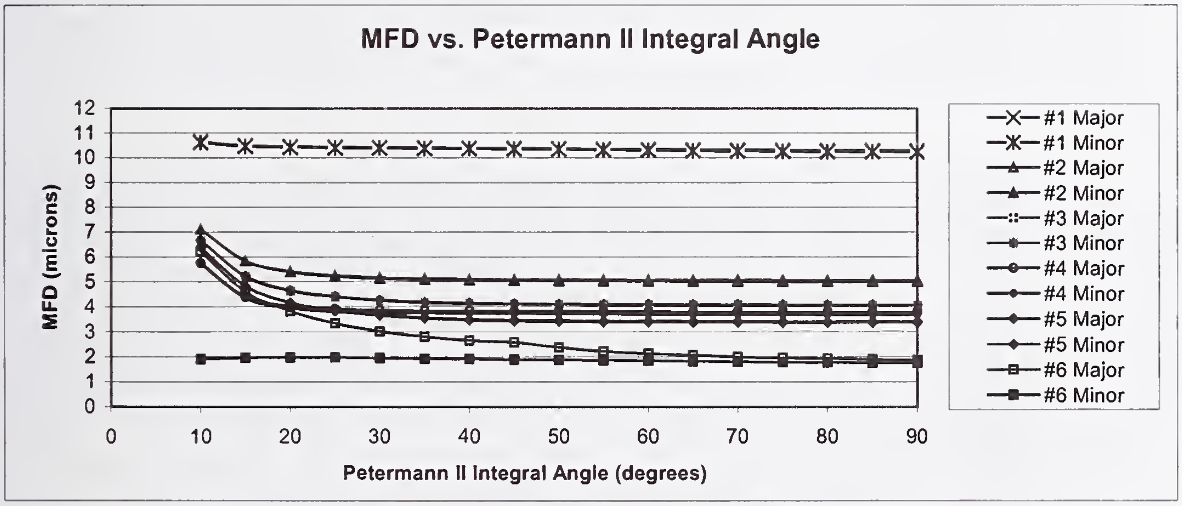

Figure 3. MFD vs. Petermann II integration limit for fibers #1-6.

Table 1. Mode-Field Diameter for Various Angular Limits of the Petermann II Integral

| | Mode-Field Diameter (µm) | | | | | | | | | | | |
|---|---|---|---|---|---|---|---|---|---|---|---|---|
| Fiber | 1 | | 2 | | 3 | | 4 | | 5 | | 6 | |
| Integral Limit | Major and Minor Axes | | | | | | | | | | | |
| 40 | 10.406 | 10.375 | 5.069 | 5.118 | 4.141 | 4.154 | 3.851 | 3.742 | 3.478 | 3.506 | 2.668 | 1.920 |
| 45 | 10.395 | 10.361 | 5.054 | 5.104 | 4.113 | 4.128 | 3.842 | 3.734 | 3.442 | 3.476 | 2.593 | 1.902 |
| 50 | 10.382 | 10.345 | 5.043 | 5.095 | 4.100 | 4.110 | 3.832 | 3.725 | 3.420 | 3.457 | 2.391 | 1.887 |
| 55 | 10.367 | 10.328 | 5.034 | 5.087 | 4.091 | 4.100 | 3.823 | 3.715 | 3.405 | 3.443 | 2.221 | 1.873 |
| 60 | 10.352 | 10.311 | 5.026 | 5.081 | 4.084 | 4.094 | 3.814 | 3.705 | 3.395 | 3.434 | 2.139 | 1.851 |
| Average | 10.380 | 10.344 | 5.045 | 5.097 | 4.106 | 4.117 | 3.832 | 3.724 | 3.428 | 3.463 | 2.402 | 1.887 |
| | Difference from Average MFD | | | | | | | | | | | |
| 40 | 0.2% | 0.3% | 0.5% | 0.4% | 0.9% | 0.9% | 0.5% | 0.5% | 1.5% | 1.2% | 11.1% | 1.8% |
| 45 | 0.1% | 0.2% | 0.2% | 0.1% | 0.2% | 0.3% | 0.3% | 0.3% | 0.4% | 0.4% | 7.9% | 0.8% |
| 50 | 0.0% | 0.0% | 0.0% | 0.0% | -0.1% | -0.2% | 0.0% | 0.0% | -0.2% | -0.2% | -0.5% | 0.0% |
| 55 | -0.1% | -0.2% | -0.2% | -0.2% | -0.4% | -0.4% | -0.2% | -0.2% | -0.7% | -0.6% | -7.6% | -0.7% |
| 60 | -0.3% | -0.3% | -0.4% | -0.3% | -0.5% | -0.6% | -0.5% | -0.5% | -1.0% | -0.8% | -11.0% | -1.9% |

The $1/e^2$ diameter spot sizes obtained from the far and near field analyses are summarized in Table 2. For any fiber, the diameter reported using the different methods varies significantly, on the order of ±15-20%. This result is not surprising for these sources. The extremely non-Gaussian shape of the far field makes the Gaussian approximation highly questionable. Similarly, the very small spot size of the lensed/tapered fibers is at or beyond the performance limits of the optical near-field imaging techniques, and the measured values must undergo significant corrections that increase uncertainty and error. The most accurate method here may be that of the 2D Fourier transform with phase retrieval. It is also observed that these values are overall the most consistent with the MFD values.

Table 2. Near Field $1/e^2$ Diameter Spot Size from Near Field and Far Field Data

| | $1/e^2$ Diameter (μm) | | | | | |
|---|---|---|---|---|---|---|
| Fiber | 1 | 2 | 3 | 4 | 5 | 6 |
| Method of Analysis | Major Axis × Minor Axis | | | | | |
| $1/e^2$ FF Gaussian | 11.77×11.77 | 6.20×6.16 | 5.07×5.11 | 3.64×3.51 | 4.23×4.25 | 3.62×2.07 |
| $1/e^2$ NF Profile 100X | 10.29×9.71 | 4.67×4.67 | 4.37×4.29 | 4.23×4.09 | 3.50×3.36 | 3.58×2.34 |
| $1/e^2$ NF Profile 40X | 9.24×9.03 | 4.85×4.73 | 4.24 ×4.15 | 3.79×3.55 | 4.03×3.79 | 3.55×2.77 |
| 2D FF Fourier Transform | 9.94×9.93 | 5.04×5.03 | 4.02×4.07 | 3.60×3.55 | 3.71×3.30 | 2.96×1.94 |

## 5. Conclusion

Lensed and tapered specialty fibers exhibit wide angular divergence and corresponding small spot sizes. These characteristics pose significant challenges to measurement of MFD and spot size. The results presented highlight the limitations of standard near-field optical techniques, and the necessity for far-field measurements to include very wide angles. Specifically, for some of the fibers measured here, far-field measurement instruments must acquire data at angles extending to ±60° or greater for accurate determination of the MFD. For near-field measurements using conventional optical techniques, the small spot sizes of these fibers push the limits of resolution and can lead to significant errors. Also, the typically non-Gaussian profiles of lensed and tapered fibers also lend doubts as to the accuracy of Gaussian approximations used to determine spot size. Estimation of spot size using these methods shows considerable variation. Due to this, and also to ease of measurement, far-field transform techniques are the preferred method of characterization.

For radially symmetric fibers, specification of the Petermann II MFD to characterize the focused beam yields consistent results and appears to be fine, but due to variation in the integral with angular limit and to avoid ambiguity, the actual limit used in the calculation should be specified as well as the MFD value. For non-radially symmetric fibers, use of the Petermann II MFD, although it does provide a measure, is problematic and highly questionable based on the underlying assumptions of radial symmetry in the Petermann II integral. For such non-radially symmetric fibers, the development of new metrics using 2D Fourier transform methods may provide more accurate and consistent specifications.

## 6. Acknowledgements

The author is grateful to David Pikey for his efforts in the implementation of the algorithm for the 2D Fourier transform with phase retrieval.

## 7. References

1. "Measurement of Mode-Field Diameter of Single-Mode Optical Fiber", Fiberoptic Test Procedure FOTP-191, Telecommunications Industry Association, Standards and Technology Department, 2500 Wilson Blvd., Suite 300, Arlington, VA, 22201 (1998).
2. ISO/DIS Standard 13694, "Test methods for laser beam power (energy) density distribution", International Organization for Standardization, September 1998.
3.J.R.Fienup, "Reconstruction of an Object from the modulus of its Fourier transform", Optics Letters, Vol. 3, No. 1, pp 27-29, July 1978.
4. J.R.Fienup, "Phase retrieval algorithms: a comparison", Applied Optics, Vol. 21, No. 15, pp. 2758-2769, August 1982.
5. J.R.Fienup and C.C.Wackermann, "Phase retrieval stagnation problems and solutions", J. Opt. Soc. Am. A, Vol. 3, No.11, pp. 1897-1907, November 1986.

# Anomalies in Online Fibre Measurements and Their Implications for Fibre Array Manufacture

Law, S. H., Phan, T. N., Barton, G. W.[1], Barton, M. J. and Elsey, J.
*Australian Photonics CRC*
*Optical Fibre Technology Centre, University of Sydney, NSW 2006, Australia*
[1]Department of Chemical Engineering, University of Sydney, NSW 2006, Australia

## ABSTRACT

V-groove fibre arrays are commonly used in the packaging of high port number devices. As alignment tolerances must be in the order of 0.1 micron for single-mode devices to ensure a consistent low insertion loss across all ports, any misalignments in the array can impact on device yields after packaging. In this paper the variation in cladding diameter along a single fibre is measured using both a laser shadowgraph technique and video greyscale analysis. It is found that there is significant variation over short length scales within a single fibre sample. This variation also has implications for the filtering of feedback control measurements of fibre diameter in the drawing process.

Keywords: photonics packaging, optical fibre manufacture, optical fibre arrays, optical fibre measurement.

## INTRODUCTION

Fibre metrology and consistency is becoming an area of increasing concern in photonic packaging. In particular, the packaging of high port number devices is dependent on the passive alignment of many fibres in large arrays. Although anomalies in fibre geometry can have a detrimental impact on device yields, this area has received little attention in the literature.

The most obvious time to measure fibre diameter variations is during the drawing process before the coating is applied. At this point, physical contact measurements are not possible, so optical techniques are typically used. Laser shadowgraphs are the most commonly used technique, whereby a laser beam is scanned over the moving fibre. The fibre edges are located as a function of the scanning position allowing the fibre diameter to be calculated. Unfortunately there is usually a significant amount of noise in these measurements.

Measurements are typically available from a shadowgraph at a rate of up to 1000 Hz, which is faster than can be utilised by the fibre draw tower's control system. Conventionally, the signal is averaged to smooth out any noise variations and give a stable indication of the mean fibre diameter. Therefore, although the control system only sees the filtered fibre measurements, the question arises as to what the true fibre diameter variation is.

The purpose of the present investigation is to study the accuracy of a laser shadowgraph and to compare its predictions with measurements obtained using the more accurate video greyscale analysis. By understanding the nature of the true fibre diameter variation, one can then be in a position to select the most appropriate filtering technique to remove noise while preserving the integrity of the true diameter measurement.

## ANALYSIS OF NOISE ON THE LASER GAUGE

### Static Fibre Measurements

The nature of the noise on the shadowgraph laser gauge was studied using a static length of stripped fibre mounted in the gauge's measurement area. The noise was measured over a range of different positions in the measurement area, and also using a variety of different data acquisition rates. A plot showing the signal as a function of time when the fibre is positioned at the centre of the measurement area is shown in Figure 1. The power spectrum, shown in Figure 3, is reasonably flat over the measured frequency range, indicating white noise, with a small peak at 50Hz corresponding to the mains power supply. Plotting the data against a normal $x$-axis results in a straight line, indicating that the noise is Gaussian with a correlation coefficient of

0.99. The standard deviation of the measurement is 0.13µm (Figure 2), and there are no outliers so that the entire signal lies within two standard deviations from the mean.

**On-line Fibre Measurements**

Figure 4 shows data collected from a fibre draw tower running at 20 m/min using a laser shadowgraph gauge. The dashed line shows the data collected at 62 Hz. It can be seen that there is rapid variation in the signal indicating measurement noise. The solid line shows the result of applying an advanced filter of window size 30 to the signal offline. A simple averaging filter is used online to massage the signal for the control system. Qualitatively, it can be seen that there are a larger number of outliers in the data compared to the static fibre measurements. This suggests that there might be additional noise introduced due to the movement of the fibre through the shadowgraph gauge (perhaps as a result of vibrations), or that there may be some significant variation in the fibre diameter over a short length scale.

**Video Greyscale Analysis**

Video greyscale analysis (VGA) is a destructive measurement technique that uses a magnified video image of the fibre end to measure the cladding diameter, core diameter, core eccentricity and ellipticity. The precision of the VGA equipment is 0.05µm, therefore it was used to ascertain the true variation in fibre diameter over short length scales. One end of a length of fibre to be measured was stripped, cleaved and placed into the source port of the VGA. The other end was prepared similarly and placed into the measurement port and the cladding diameter of this end was measured. This procedure was repeated by cutting back approximately 4 cm of the fibre each time. The results from these measurements are shown in Figure 5. It can be seen that there is appreciable variation in the fibre diameter even over these short lengths. While it is felt that procedural differences may account for some variation in the measurements, these results indicate that there is a real variation in fibre diameter over short length scales of sufficient magnitude to result in significant core offsets when the fibres are used for making V-groove arrays.

## IMPLICATIONS FOR V-GROOVE ARRAY MANUFACTURE

Fibre arrays have become a key component in the manufacture of high-channel-count devices. In most cases they are manufactured by passively aligning fibres from a single roll in undersized V-groove blocks. In most cases a lid of some sort (V-grooved or flat) is used to try and ensure that the fibres are sitting firmly in the bottom of the V-grooves. A simple study of the geometry will show that if one of the fibres is anomalously large (by as little as 0.2-0.3 µm) it will provide a pivot point for the lidding block (Figure6), and prevent many of the other fibres from being truly located. This will add significantly both to the average coupling between device and fibres, but also to the channel-to-channel variation [2].

An estimation of the increase in positional error of the end fibre can be obtained by simple triangulation. For an 8-fibre, 250 mm spaced array (as shown in Figure6), if we assume that the upper (clamping) block is resting on the first (normal) and fifth (anomalously large) fibre and that the large fibre is 0.2 µm larger than the normal, then the clamping block will be 1.75 x 0.2 = 0.35 µm above the top of the eighth fibre, and the potential error in the core position is correspondingly increased.

## CONCLUSIONS

In this preliminary study the question of fibre diameter measurement and consistency has been raised and investigated through experiments using a shadowgraph laser gauge and video greyscale analysis. Measurements using the shadowgraph appear to be laced with Gaussian white noise, and significant outliers. The observed rapid variation in fibre diameter over short lengths may at first glance be attributed to instrument noise or measurement errors. However, similar diameter variations are also observed when using the more accurate video greyscale analysis. While procedural errors may contribute to the observed fibre diameter variations, it appears that there is a significant variation in fibre diameters over short length scales. Such variations can have a significant impact on array precision for device assembly.

## REFERENCES

1. Anritsu Corporation, SLB DIA Measuring System Instruction Manual, 1988
2. Law, S. H. & Poladian, L., *Effect of Waveguide Optical Parameters on Alignment Tolerances for Fibre Attachment*, Session 38, Paper 2, 52nd Electronic Components and Technology Conference, San Diego (2002)

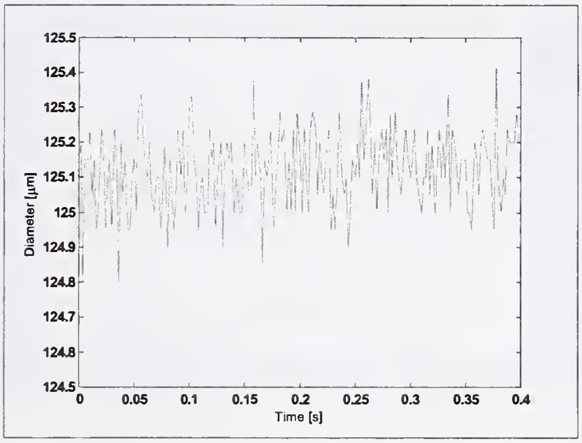

Figure 1: Static fibre readings from the laser gauge.

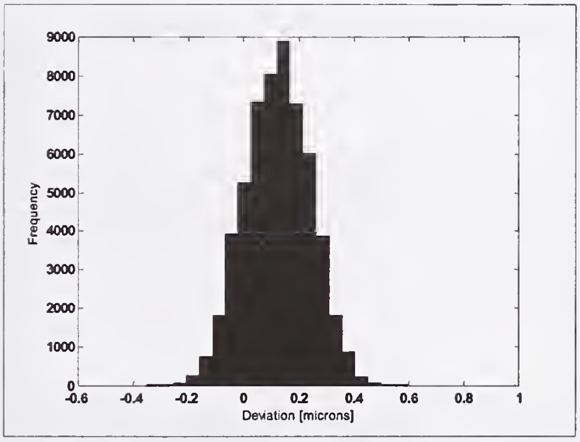

Figure 2: Distribution of diameter deviation readings for a stationary fibre.

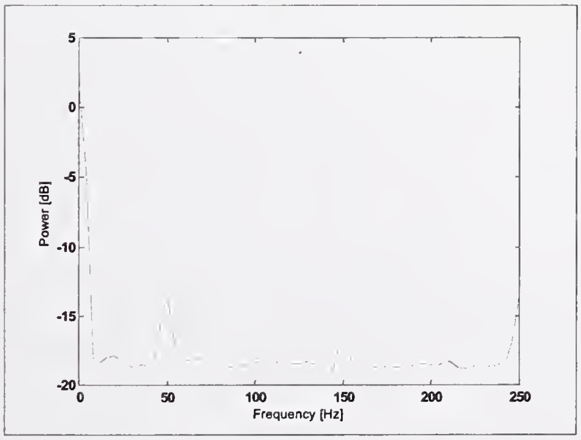

Figure 3: Power Spectral Density of the static readings.

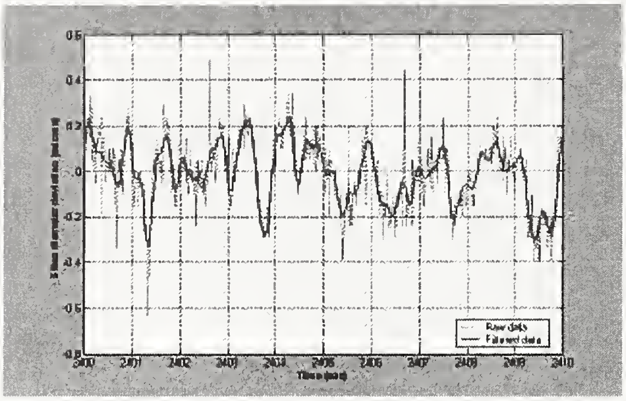

Figure 4: 10 seconds of fibre diameter deviation measurements sampled at 62 Hz (blue line) with filtering as typically applied for control purposes.

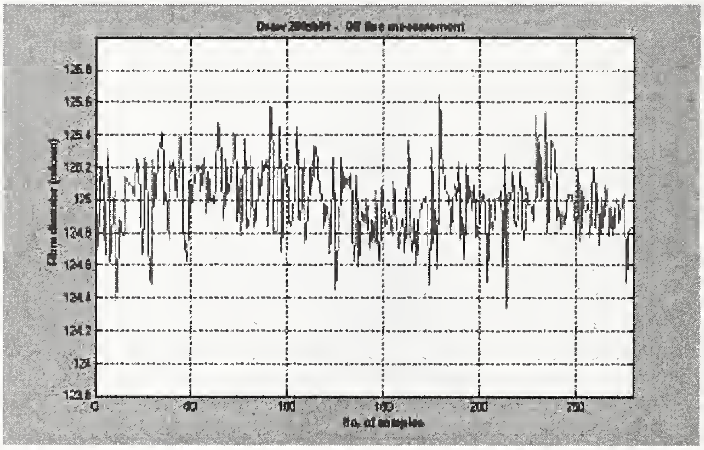

Figure 5: Diameter measurements taken at 4 cm intervals along a 12 m length of fibre with a VGA.

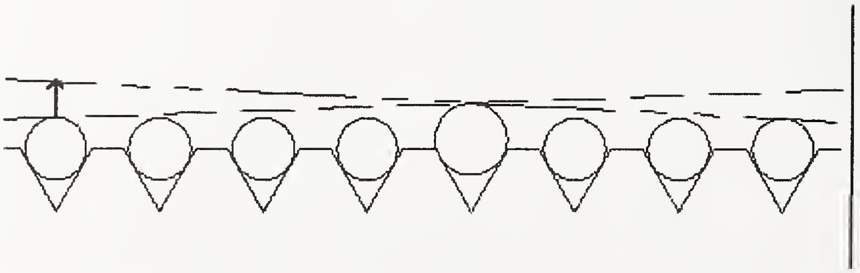

Figure 6: Potential alignment errors in a V-groove array due to a fibre diameter anomaly.

# Performance characterization of components with group delay fluctuations

Michael Eiselt, Carl Balslev Clausen, and Robert W. Tkach,
Celion Networks, Inc. One Sheila Drive, Ste 2. Tinton Falls, NJ 07724, USA

*Abstract*—A variety of components in optical communication systems exhibit group delay fluctuations, which degrade the quality of transmitted signals. In this paper, we present a method to derive two independent figure-of-merits, based on the measured group delay, which accurately determines the system performance degradation caused by any type of group delay fluctuations in a component.

## I. INTRODUCTION

Components in optical communication systems that are of a resonant or reflective nature, will often exhibit a transfer function with non-negligible ripples or fluctuations in both amplitude and phase. Some examples are fiber Bragg gratings, ring resonators, and etalons [1-5] which have found use as building blocks in dispersion compensation modules and add-drop modules, as circulators and interleavers, and more. It is evidently of interest to be able to determine, from a characterization of the component, the negative impact that the fluctuations have on system performance. Here, we will constrain ourselves to fluctuations in phase response (for amplitude fluctuations see e.g. [3]). The severity of phase fluctuations induced by a component is usually specified in terms of the group delay ripple, e.g. as a peak-to-peak value. However, the system performance degradation from a group delay ripple depends strongly on the period of the ripple [3,4]. A characteristic period may not exist or may not easily be identified from a measured group delay response. Indeed, it was shown in Ref. [5] that performance degradations caused by measured ripples of four particular fiber Bragg gratings were uncorrelated with the magnitude of single-period group delay ripples. Therefore, the peak-to-peak group delay ripple is not the most appropriate parameter to use when specifying component performance.

In this paper, we show with numerical simulations that performance degradations correlate with two independent parameters that are easily extracted from the measured group delay. The parameters may thus serve as figure-of-merits in specifications of the phase response of a component.

It is reasonable to expect that group delay fluctuations should have two separate and independent effects. Part of the fluctuations that are at the order of the signal bandwidth will affect the signal spectrum by imposing an average chromatic dispersion, whereas the remaining fluctuations, which contain higher order frequency variations, will distort the signal electrical field in a similar way as spectral phase noise does. The induced average dispersion is unsurprisingly found as a linear fit to the group delay within the signal bandwidth. A less trivial finding is that the remaining fluctuations cause a system penalty, which is proportional to the variance of the residual phase fluctuation within the signal bandwidth. We will show the validity of this statement later in the paper. First, we will describe how the figure-of-merits are extracted from an arbitrary group delay spectrum of a given component.

## II. CHARACTERIZATION RECIPE

We take as example a dispersion compensating module (DCM). We will assume that the group delay values, $\tau_{exp,i}$, have been measured in wavelength steps of $\Delta\lambda$, e.g., by the modulation phase shift method. The first step is to obtain the actual, undesired fluctuations, $\tau_{fluct,i}$, that are to be analyzed. This is found by subtracting the ideal group delay, $\tau_{ideal,i}$, for which the DCM was designed, from the measured group delay:

$$\tau_{fluct} = \tau_{\exp} - \tau_{ideal} - \tau_0.$$

The constant $\tau_o$ defines an arbitrary fixed group delay. The ideal group delay of the DCM is calculated as

$$\tau_{ideal}(\lambda) = D(\lambda_0)(\lambda - \lambda_0) + \frac{S}{2}(\lambda - \lambda_0)^2,$$

where $D(\lambda_0)$ is the target dispersion at a reference wavelength, $\lambda_0$, and $S$ is the (constant) target dispersion slope $(dD/d\lambda)$ of the DCM. For this particular example, we have generated $\tau_{exp,i}$ from a numerical model of a DCM with random group delay fluctuations added to the desired design target. The target dispersion at 1550 nm was –400 ps/nm, and the target dispersion slope was –8 ps/nm$^2$. A fixed group delay of -1250 ps and a random group delay of up to ±10 ps was added to the target group delay. Figure 1(left) shows both $\tau_{exp}$ and $\tau_{fluct}$ over a band of 1 nm. A sliding window, shown as an inset in Figure 1(left), centered at wavelength $\lambda_c$ and with the width $\lambda_{window}$ of the signal bandwidth, is applied to the group delay fluctuations, $\tau_{fluct}$. Here we choose a bandwidth of 0.2 nm, which is relevant for, e.g., a 12.5 Gbit/s RZ signal. At each position, the group delay fluctuations within this window are considered and we extract two numbers: the residual dispersion and the standard deviation of the residual phase.

First, the residual dispersion. A linear function is fit to $\tau_{fluct}$. The coefficients of the linear function represent a fixed group delay and the residual dispersion at $\lambda_c$. The dotted line in the inset of Figure 1(left) depicts the curve fit. If the curve fit can be written as $\tau_{fit} = a_1(\lambda - \lambda_0) + a_0$, then the residual dispersion at the considered wavelength is the linear fit parameter: $D_{res} = a_1$. In the example, the fit parameter $a_1$ yields a residual dispersion of 55.6 ps/nm.

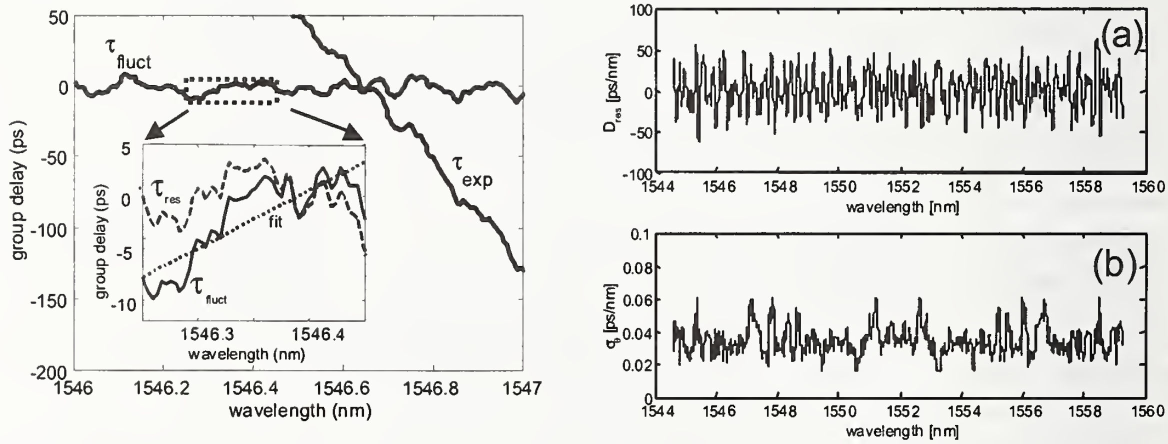

**Figure 1: Left figure: Measured ($\tau_{exp}$) group delay versus wavelength and the fluctuating part ($\tau_{fluct}$). Inset: Group delays in window of 0.2 nm. Dashed line is residual phase fluctuation. Right figure: (a) Residual dispersion in sliding window, and (b) standard deviation of residual phase fluctuation in sliding window over the full bandwidth of the DCM.**

Secondly, the standard deviation of the residual phase. The dashed line in the inset of Figure 1(left) is the residual group delay ripple, $\tau_{res}$, after the linear fit (the dispersion offset and the fixed group delay) has been subtracted. It represents the high frequency part of the DCM induced group delay fluctuations as opposed to the average dispersion. The phase fluctuation in the window is derived from the measured group delay by integrating within the window, the residual group delay over frequency,

$$\varphi_{res}(\lambda_i) = -2\pi \frac{c}{\lambda_0^2} \Delta\lambda \sum_{\lambda j = \lambda c - \lambda window/2}^{\lambda i} \tau_{res}(\lambda_j).$$

The term $(\lambda_0^2/c)$ equals 8 ps-nm around 1550 nm. A linear curve fit to the residual phase, representing a phase and delay offset, is then subtracted from the residual phase.

$$\theta_{res}(\lambda_i) = \varphi_{res}(\lambda_i) - \varphi_1(\lambda_i - \lambda_0) - \varphi_0,$$

yielding the pure, residual phase fluctuation, $\theta_{res}$. The constants, $\varphi_0$ and $\varphi_1$ are the linear fit parameters to

$\varphi_{res}$ within the window. Finally, we can then calculate the standard deviation, $\sigma_\theta$, of $\theta_{res}$. In the example of the window inset in Figure 1 we find $\sigma_\theta$ to be 28 mrad.

The procedure described above yields the two numbers $D_{res}$ and $\sigma_\theta$ for a given position of the window. These are the figure-of-merits that determine the impact on system performance resulting from group delay fluctuations. Figure 1(right) shows the values of $D_{res}$ and $\sigma_\theta$ as the window is moved across the usable bandwidth of the DCM. The maximum values of $D_{res}$ and $\sigma_\theta$ are seen to be about ±60 ps/nm and about 60 mrad, respectively. In order to obtain a statistical measure of $D_{res}$ and $\sigma_\theta$ we can calculate their average value and standard deviation. For the example, we find the average residual dispersion to be 0.1 ps/nm and the standard deviation of the residual dispersion to be 23 ps/nm. Likewise, the average value and the standard deviation of $\sigma_\theta$ is 34 mrad and 8 mrad, respectively.

## III. SYSTEM PENALTY

The figure-of-merits for the residual dispersion and the residual phase fluctuations in the DCM are based on their impact on the system performance.

When a component with residual dispersion is located inline it will disturb the dispersion map of the system. The performance penalty for disturbing the dispersion map is inherently system dependent. If the system is very nonlinear, the signals may be more tolerant to a residual dispersion, due to nonlinear self-trapping, than if the system is linear. On the other hand, if the system is linear, the accumulated residual dispersion can be compensated at the receiver. However, since each channel experiences a random residual dispersion offset, this requires per-channel dispersion compensation. In a specification of the residual dispersion it is reasonable to specify a maximum value just as a DCM is specified with a tolerance for an offset relative to the target dispersion. Therefore, we propose that the figure-of-merit characterizing the residual dispersion in the component should be based on the maximum value of the residual dispersion within the bandwidth of the component.

The impact of the residual phase fluctuation does not depend on the dispersion map or nonlinear propagation effects. We have performed numerical simulations of a system composed of 100 spans of NZDSF. A single RZ channel was propagated at a bitrate of 12.5 GHz. After each span a DCM provided chromatic dispersion compensation with 12 ps/nm under-compensation, and an erbium doped fiber amplifier compensated the fiber loss. The channel power was 1 dBm, which makes nonlinear propagation effects very visible after 100 spans. We added 100 phase fluctuations either inline at every DCM, or concatenated at the receiver. The phase fluctuations in the $j$'th DCM were based on the following group delay ripple:

$$GD_j(\Delta\lambda) = \tfrac{A_{pp}}{2}\cos\left(2\pi\tfrac{\Delta\lambda}{\lambda_p} + \vartheta_j\right),$$

where $A_{pp}$ is the peak to peak group delay amplitude ripple, $\Delta\lambda$ is the offset from some center wavelength, $\lambda_p$ is the period of the ripple, and $\vartheta_j$ is the phase of the ripple. In simulations we kept the amplitude and period the same in all 100 ripples, whereas the phases, $\vartheta_j$, were random. Also, an amount of dispersion was added to each fluctuation such that the residual dispersion was zero. The simulation results are shown in Figure 2(a). The dashed line shows the penalty versus group delay ripple period for the case when all ripples are concatenated at the receiver. The solid line shows the performance penalty when the group delay ripples are added inline at every DCM. Since they are approximately equal, the impact of residual phase fluctuations can be investigated by simulating a single instance of fluctuations at the receiver. The phase fluctuation distorts the signal electrical field and therefore depends on the particular shape of the pulses and the signal quality. We have found that it is generally valid that the impact is proportional to $\sigma_\theta^2$. In Figure 2(b) we show the performance penalty for various ripple periods together with the function: Penalty=$48\sigma_\theta^2$. The proportionality constant of 48 is specific to the particular pulse shapes and other signal distortions that have occurred in the particular system we simulated.

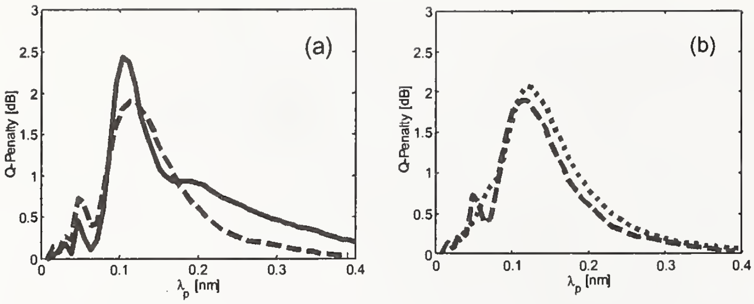

**Figure 2: Q-penalty for a system with perfectly periodic group delay fluctuations. Period of ripple is $\lambda_p$. Magnitude of group delay ripple, $A_{pp}$, is 42ps for all ripple periods. Solid line: Fluctuations added at every span. Dashed line: Fluctuations are added at the receiver. Dotted line: Estimate of penalty from the scaling: $\Delta Q = -48\sigma_\theta^2$.**

Most group delay fluctuations are not perfectly periodic. We have therefore made simulations with group delay fluctuations that are generated from random numbers. Figure 3(a) shows the results from simulations of the 100-span system. The random fluctuations are added at the receiver. The impact is seen to follow a scaling of $\Delta Q = -48\sigma_\theta^2$, which is indicated by the dashed curve. Figure 3(b) shows the induced dispersion (calculated as a change in optimum post-dispersion) versus the residual dispersion as calculated from the group delay fluctuations.

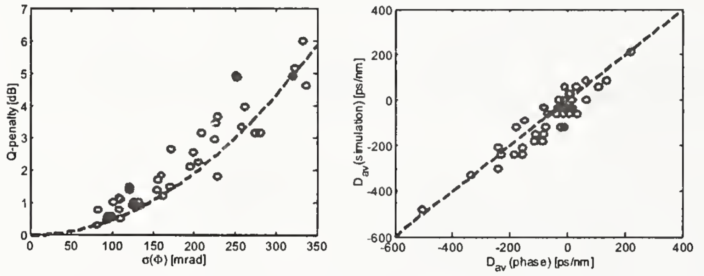

**Figure 3: Random group delay fluctuations. (a) Q-penalty versus standard deviation of residual phase fluctuation. (b) Change in optimum post-dispersion versus residual dispersion.**

When many instances of fluctuations are concatenated, they will accumulate in a random, linear way. We therefore propose that the figure-of-merit for the high-frequency phase fluctuations be based on the mean value of $\sigma_\theta$. In summary, we have proposed a method to characterize components with group delay fluctuations. We have shown that two numbers, the residual dispersion, $D_{res}$, and the standard deviation of the residual phase ripple, $\sigma_\theta$, determines the system impact.

## REFERENCES

[1] C. K. Madsen, G. Lenz, A.J. Bruce, M.A. Capuzzo, L.T. Gomez, and R.E. Scotti, *IEEE Photon. Techn. Lett.*, vol. 11, pp. 1623-1625, 1999.
[2] F. Oullette, *Opt. Lett.*, vol. 12, pp. 847-849, 1987.
[3] K. Ennser, M. Ibsen, M. Durkin, and M.N. Zervas, *IEEE Photon. Techn. Lett.*, vol. 10, pp. 1476-1478, 1998.
[4] B.J. Eggleton, A. Ahuja, P.S. Westbrook, J.A. Rogers, P. Kuo, T.N. Nielsen, and B. Mikkelsen, vol. 18, pp. 1418-1432, 2000.
[5] S. Jamal and J. C. Cartledge, *J. Lightwave Technol.*, vol. 20, pp. 28-35 (2002).

# High-resolution group delay measurements of a hydrogen cyanide gas cell using low-coherence interferometry

*Shellee D. Dyer, R. Joseph Espejo, and Paul A. Williams*
*National Institute of Standards and Technology*
*Optoelectronics Division*
*325 Broadway, Boulder, CO 80305 USA*
*sdyer@boulder.nist.gov*

**Abstract:** We demonstrate interferometric measurements of the relative group delay of a hydrogen cyanide gas cell with group-delay resolution of 0.3 ps at a wavelength resolution of 6 pm. We use simulations and measured data to illustrate the tradeoffs between group-delay resolution and wavelength resolution.

## 1. Introduction

Low-coherence interferometry is a fast and accurate method to measure the relative group delay (RGD) and spectral reflectance or transmittance of optical components. We have previously demonstrated repeatability better than 1 ps, and agreement with an independent measurement better than 1.5 ps [1].

In this paper we present high-resolution interferometric measurements of the RGD of a gas cell containing hydrogen cyanide ($H^{13}C^{14}N$) at a pressure of 13 kPa (100 Torr). Hydrogen cyanide has more than 50 strong absorption lines in the optical-communications C-band, making it very useful as a wavelength-reference artifact [2].

We chose to measure the relative group delay of a hydrogen cyanide cell for several reasons. First, the RGD of the cell can be predicted from a measurement of the cell's transmittance profile using the Kramers-Kronig relationship [3,4]. This predicted RGD is a valuable reference for estimating the uncertainty of our measurement. Also, the absorption lines of our hydrogen cyanide cell are very narrow (<100 pm), and therefore the group delay features are very narrow as well (<50 pm). The RGD of our hydrogen cyanide cell also includes weak hot-band lines, which are less than 2 ps deep. Therefore, an accurate measurement of the cell's RGD including the hot-band lines can be achieved only with a measurement system that has sub-picosecond RGD resolution and a wavelength resolution on the order of picometers. Thus, our hydrogen cyanide cell measurements will demonstrate the high-resolution capabilities of our interferometric measurement system. Additionally, the peak absorption wavelengths of the cell are well characterized; therefore, we can determine the absolute wavelength accuracy of our measurement system through a comparison with the NIST-certified absorption wavelengths of the cell. The final reason for measuring the cell's RGD is that the hydrogen cyanide cell might be applied in the future as an artifact for calibrating RGD measurement systems.

We have also created a simulation program to model the tradeoffs between wavelength resolution and RGD resolution. These tradeoffs are an important issue, regardless of the RGD measurement technique used, and wavelength and RGD resolution should always be specified together. Specifying an RGD resolution is meaningless unless the corresponding wavelength resolution of the measurement system is also specified.

## 2. Experiment

Our RGD measurement system is shown in Fig. 1. An erbium fiber superfluorescent source (BBS) provides our low-coherence signal. Our system consists of a fiber-optic Mach-Zehnder interferometer with the hydrogen cyanide cell (DUT) placed in one arm of the interferometer. We include a variable-length air path in the other arm of the interferometer, so that the total optical path difference (OPD) of the interferometer can be adjusted. At the output of the interferometer, two detectors (D1 and D2) receive two 1550 nm fringe signals that are 180° out of phase but have similar noise characteristics. By directing these two signals to a difference amplifier, we are able to reduce significantly the noise on our interference signal. We use a 1300 nm Nd:YAG laser (RL) to monitor the OPD as the translation stage moves. The interference signal created by the 1300 nm laser light is separated from the 1550 nm signal using a wavelength-division multiplexer, and the 1300 nm signal is sent to a zero-crossing detector circuit. This circuit triggers the A/D card sampling of the difference amplifier's output at every zero crossing of the 1300 nm interference signal. This gives a sampling rate of approximately 2.4 samples per 1550 nm fringe. This system is a significant improvement over our previous low-coherence interferometric system. The reference laser signal now travels in the same fiber as the broadband signal, virtually eliminating the large wavelength uncertainty that occurs when the two signals do not travel exactly the same path. Through improved electronics, we have also significantly increased the signal-to-noise ratio (SNR) of our system compared with our previous system (42.2 dB compared to 32 dB).

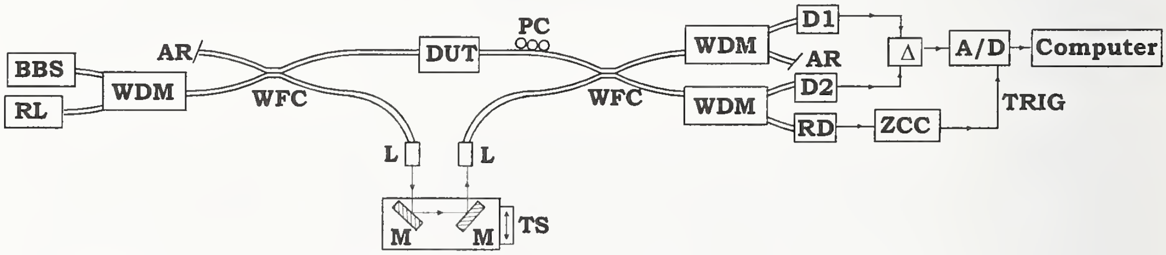

*Figure 1. Diagram of the low-coherence interferometer used to measure the RGD of optical components. A/D: analog-to-digital board, AR: antireflection endface, BBS: broadband source, D1,D2: 1550 nm signal detectors, DUT: device under test, L: lens, M: mirror, PC: polarization controller, RD: detector for 1300 nm reference signal, RL: 1300 nm reference laser, TS: translation stage, WDM: 1300/1550 nm wavelength-division multiplexer, WFC: wavelength-flattened coupler, ZCC: zero-crossing detector circuit, Δ: difference amplifier.*

To determine the RGD of our hydrogen cyanide cell, we first measure the 1550 nm interference signal as a function of OPD. We then calculate the Fourier transform of the interference signal, and separate the result into magnitude and phase. To calculate the RGD, we differentiate the phase of the Fourier transform with respect to wavenumber [1].

We determined the RGD of our hydrogen cyanide cell from the average of five independent measurements of the interferogram. Each measurement consists of 600,000 data points. The result is shown in Fig. 2, along with the RGD calculated directly from a measurement of the transmission of the gas cell using the Kramers-Kronig relations [4]. The standard deviation of the difference between our measured data and the Kramers-Kronig result is less than 0.3 ps, and the wavelength resolution is approximately 6 pm, as determined from the following formula:

$$\Delta\lambda = \frac{2\lambda_s^2}{N\lambda_r},$$

where $\Delta\lambda$ is the wavelength resolution, N is the total number of data points that are included in the interferogram, $\lambda_r$ is the reference laser wavelength, and $\lambda_s$ is the wavelength of the low-coherence signal. This formula is derived from the fact that the resolution of a discrete Fourier transform is inversely proportional to the product of the number of data points and the sampling interval [5].

## 3. Wavelength resolution and RGD resolution

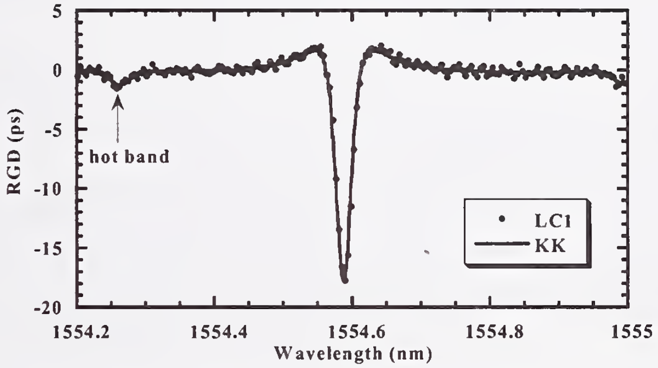

*Figure 2. Plot of relative group-delay results as a function of wavelength. LCI=Low-coherence interferometric measurement results (average of five measurements); KK=Kramers-Kronig calculation.*

We analyze the tradeoffs between wavelength and RGD resolution using a simulation program. Our simulation program starts from a measurement of the transmission of just one absorption line (P16) as a function of wavelength. Using the Kramers-Kronig relation, we calculate the complex refractive index of the gas cell [4]. Combining the complex refractive index with a measurement of our low-coherence source spectrum, we perform a Fourier transform to create a simulated interferogram. We add Gaussian random noise to the simulated interferogram to model the effects of noise in our experiment. The standard deviation of the Gaussian random noise was determined from the desired SNR. We quantize the result to simulate the discrete effects of our analog-to-digital (A/D) board, and truncate the interferogram to model the effects of interferogram length. We then calculate the group delay by taking a Fourier transform of our simulated, truncated interferogram and differentiating the phase. Comparing our simulation RGD results to the RGD predicted directly from the Kramers-Kronig calculation, we calculate the standard deviation of the difference between the two signals over a portion of the spectrum where the RGD is expected to be flat. The results are shown in Fig. 3, where the standard deviation between the two RGD results is shown as a function of wavelength resolution for three different values of SNR.

In Fig. 3, we also show our results for the standard deviation between measured RGD data and the Kramers-Kronig RGD for several different SNRs. We varied our experimental SNR by adjusting the polarization controller shown in Fig. 1 to reduce the total fringe visibility. We could not directly determine the time-domain SNR of our measured data because the interference signal created by a narrow absorption line extends to very large OPD. Therefore, we determined the frequency-domain SNR of our measured data from a Fourier transform of the interferogram [6]. Using our simulations, we derived a linear relationship between time-domain SNR and frequency-domain SNR, and we used that linear relationship to convert the frequency-domain SNRs of our measured data to equivalent time-domain SNRs.

The wavelength resolution of our measurement is inversely proportional to the total length of the truncated interferogram. Thus, longer interferograms give finer wavelength resolution, but they also include more noise, and that noise degrades the group-delay resolution. The limiting factor is the experimental SNR; with higher SNR, both the wavelength resolution and RGD resolution can be improved.

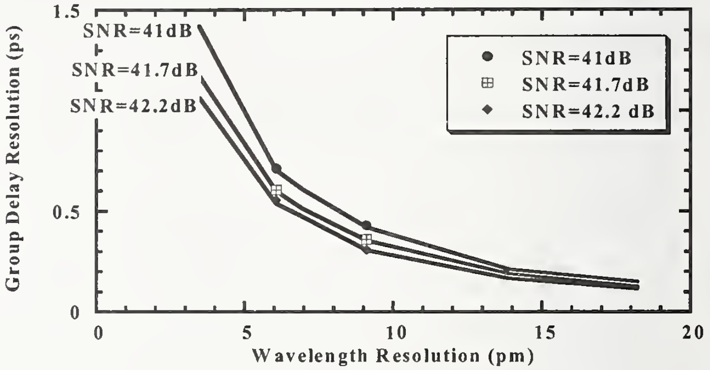

*Figure 3. Plot of group delay resolution as a function of wavelength resolution for three different SNRs with no averaging. The solid lines are simulation results, and the data points are experimental results. Averaging multiple measurements will improve the group delay resolution by approximately* $\sqrt{m}$*, where m is the number of measurements.*

## 4. Conclusions

We have demonstrated high-resolution interferometric measurements of the RGD of a hydrogen cyanide gas cell. When compared to a Kramers-Kronig prediction of RGD, our results have a 0.3 ps resolution at a wavelength resolution of 6 pm. We used simulations and measured data to illustrate the tradeoffs between group delay resolution and wavelength resolution.

**Acknowledgements:** The authors thank Tasshi Dennis of NIST for supplying the measured absorption data and Kramers-Kronig calculation routine.

**References**

[1] S.D. Dyer, and K.B. Rochford, "Low-coherence interferometric measurements of the dispersion of multiple fiber Bragg gratings," *IEEE Photon. Technol. Lett.*, vol. 13, pp. 230-232, 2001.

[2] S.L. Gilbert, W.C. Swann, and C.M. Wang, "Hydrogen cyanide $H^{13}C^{14}N$ absorption reference for 1530-1560 nm wavelength calibration – SRM 2519," Natl. Inst. Stnd. Technol. Spec. Publ. 260-137, 1998.

[3] A. Motamedi, B. Szafraniec, P. Robrish, and D. M. Baney, "Group delay reference artifact based on molecular gas absorption," in *Optical Fiber Communications Conference Technical Digest*, ThC8-1, 2001.

[4] T. Dennis and P.A. Williams, "Relative group delay measurements with 0.3 ps resolution: toward 40 Gbit/s component metrology," in *Optical Fiber Communications Conference Technical Digest*, pp. 255-256, 2002.

[5] E. O. Brigham, *The fast Fourier transform and its applications*, (Prentice Hall, Upper Saddle River, NJ, 1988), pp. 170-172.

[6] R.J. Bell, *Introduction to Fourier transform spectroscopy*, (Academic Press, Inc., San Diego, CA, 1972) pp. 7-9.

# Group delay and spectral response of free space optics Mux/Demux measurement using OLCR

X. Chapeleau(1,2), D. Leduc(1), C. Lupi(1), R. Le Ny(1) and C. Boisrobert(1)

(1)L.P.I.O., Université de Nantes, 2 rue de la Houssinière, 44300 Nantes, France.
(2)NetTest, 45 avenue Jean Jaurès, 78433 Les Clayes, France.

xavier.chapeleau@physique.univ-nantes.fr

## ABSTRACT

A complete characterization of the spectral response and group delay of a free space optics Mux/Demux is performed using Optical Low Coherence Reflectometry. OLCR allows for fast and accurate measurements and shows the similarity of the responses of the different channels.

## 1 INTRODUCTION

Recent advances in DWDM system designs have led to a significant increase of the number of wavelengths in a single fiber. As network architects start to apply DWDM to regional and metro networks, high performance characteristics for mux/demux (weak insertion and polarization-dependent loss, low group delay responses,...) are needed. Accurate measurements of these characteristics become also necessary [1, 2]. In this paper, we focus on the determination of the passband and group delay of a free space optic Mux/Demux and show that the optical low-coherence reflectometry is an efficient method for this kind of measurements.

## 2 EXPERIMENTAL SETUP

The optical system is a Michelson single mode fiber-interferometer lined up around a two by two coupler (fig. 1). The broadband infrared light source is 1.5 $\mu m$ amplified spontaneous emission fiber source. The sample under test is connected to the test arm fiber. The wave propagating along the reference arm is collimated at the output of reference arm fiber on a parabolic gold mirror, reflected and folded on an airborne sliding corner cube and reflected on a fixed plane mirror back to the coupler. The optical path length is known with a high accuracy using a frequency stabilized HeNe fringe counter.

When the corner-cube carriage slides along the rail, the infrared interferogrammes are detected by the InGaAs-PIN photoreceiver and sampled by the red fringe counter signal trigger. It can be shown [3] that they are the inverse Fourier transform of a function $\widehat{I(\sigma)}$ :

$$\widehat{I(\sigma)} = r(\sigma)\, S(\sigma)\, \exp\left[i\, \phi(\sigma)\right] \tag{1}$$

where $r(\sigma)$ is the reflection coefficient of the propagation defect, $S(\sigma)$ is the source optical

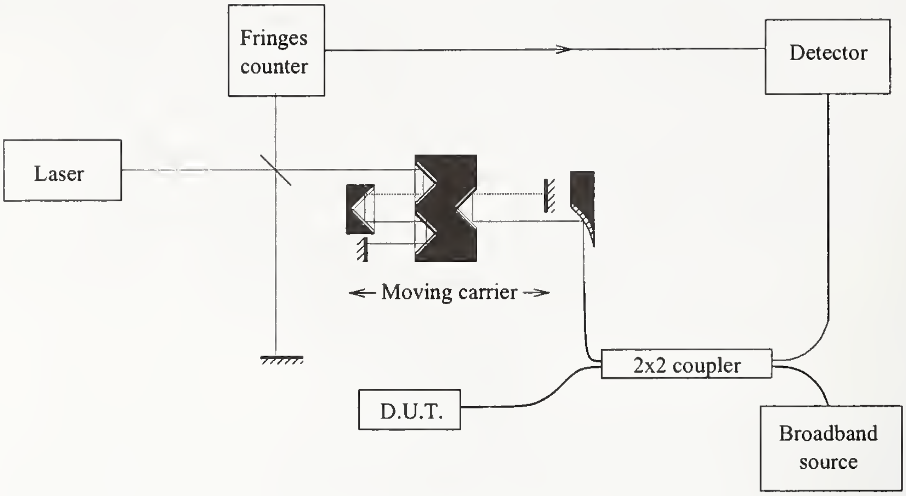

Figure 1: Experimental device

spectrum filtered by the system optical elements and $\phi(\sigma)$ is the phase difference between the two waves interfering on the photodetector. These quantities can be easily obtained from the interferogramme Fourier transforms. The phase $\Phi(\sigma)$ of this transform can then be used to calculate the group delay $\tau_g$ and the chromatic dispersion $D_\lambda$ of the component from the following relations :

$$\tau_g = -\frac{\lambda^2}{4\pi c}.\frac{d\Phi(\sigma)}{d\lambda} \qquad \text{and} \qquad D(\lambda) = \frac{d\tau_g}{d\lambda} = -\frac{1}{4\pi c}.\left[2\lambda\frac{d\Phi}{d\lambda} + \lambda^2\frac{d^2\Phi}{d\lambda^2}\right] \tag{2}$$

Thus, a single measurement gives the reflection coefficient and the group delay of the component vs wavelength inside the source bandwidth.

## 3 CHARACTERIZATION OF A FREE SPACE OPTICS MUX/DEMUX

The devices under test are NetTest commercial products using bulk gratings in a free space optics configuration to separate wavelengths [4]. The first sample is a 16 channels mux/demux. Figure 2a shows the measured normalized spectral responses of the first height channels. The peaks seem to be regularly spaced. This is confirmed by the "+" curve of the figure 2b, which represents the central wavelengths versus the channel number. The crosses are perfectly aligned and the linear fit gives a spacing equal to 800 pm between adjacent peaks. The difference between the measured central wavelengths and the constructor values is smaller than 10 pm for all channels except for 3 ones and remains always below 25 pm.

The similarity of the peaks shape can be observed on figure 2a. This appears clearly on figure 3a where the spectral responses of all the channels are plotted versus the wavelength detuning (ie the difference, for each channel, between the wavelength and the central wavelength of the channel). The different curves are hardly dinstinguishable and a non linear fit shows that all

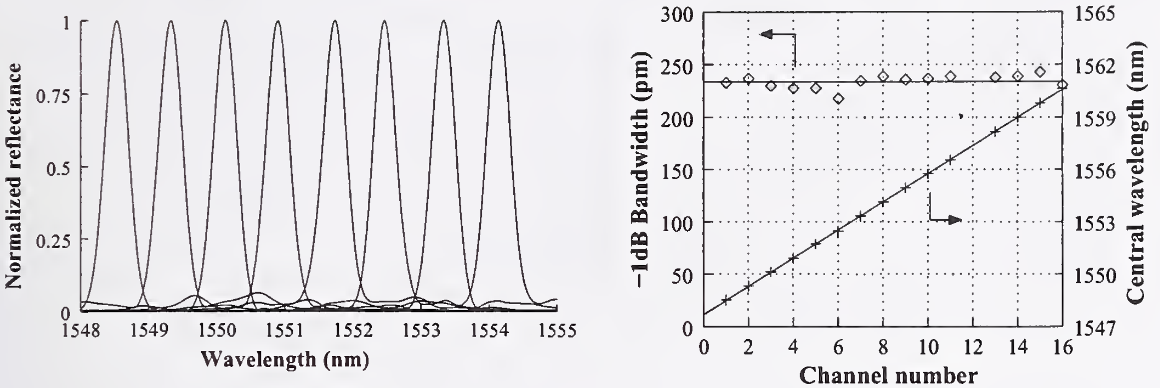

(a) (b)

Figure 2: Normalized response of the 16 channels multiplexer/demultiplexer and associated bandwidth and central wavelengths.

the peaks have the same gaussian shape. Their -1 *dB* bandwidths are almost the same (see the squares on figure 2b) and are close to 230 pm.

Figure 3b shows the relative group delays of all the channels versus wavelength detuning. The curves have almost the same shape. They are slightly decreasing inside the bandwidth, but the relative group delay variations remain small and lower than 0.2 ps.

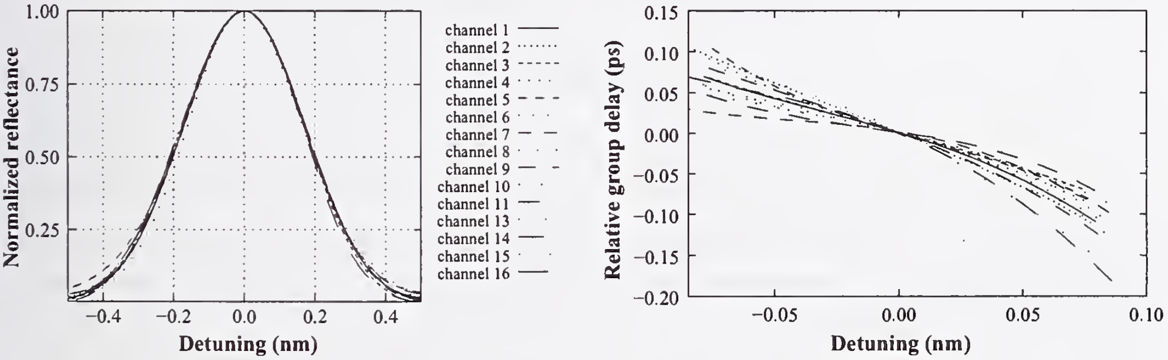

(a) (b)

Figure 3: Normalized responses and group delays of all the channels.

We also present on figure 4 the special cases of channels ♯1, ♯5, ♯10 and ♯15. The dotted curves correspond to the chromatic dispersion. As for spectral response and group delay, this characteristic is almost the same for all the channels. Its absolute value is less than 2 ps/nm inside the -1 *dB* bandwidth. This result remains valid for the other channels.

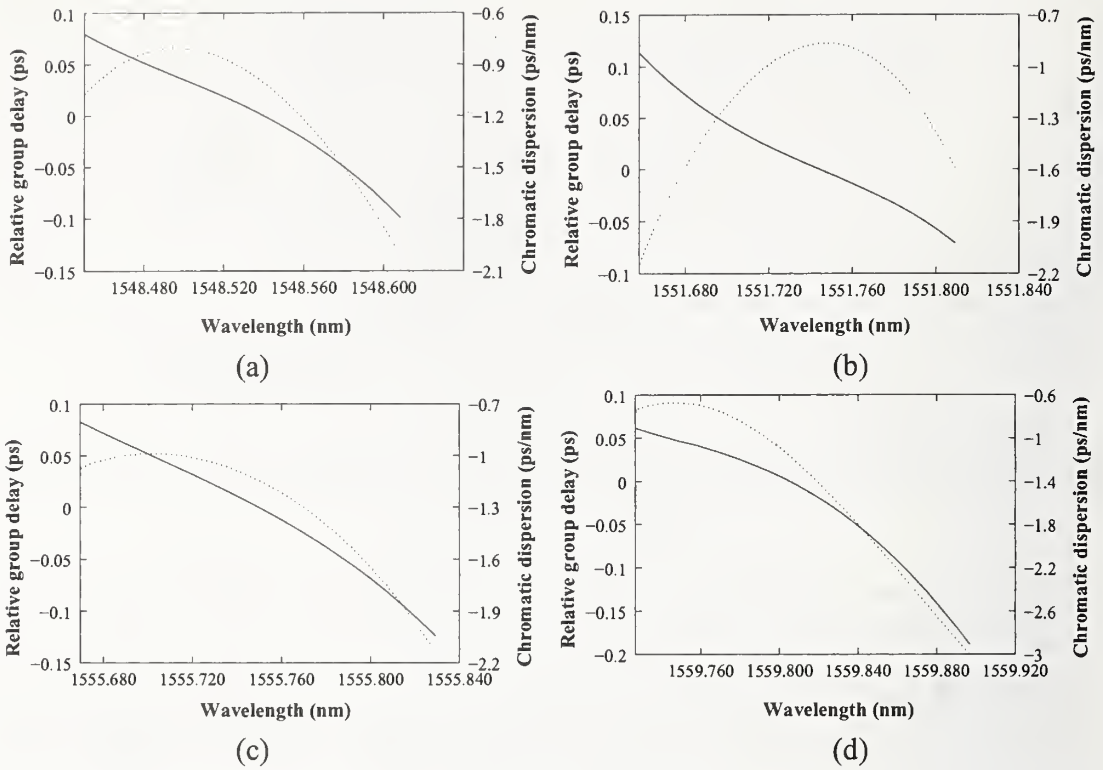

Figure 4: Group delay (straight lines) and chromatic dispersion (dotted lines) in the -1 dB bandwidth of (a) channel ♯1 (b) channel ♯5, (c) channel ♯10 and (d) channel ♯15.

## 4 CONCLUSION

OLCR is a very useful and fast method for characterizing optical Mux/Demux : one single measurement gives both spectral response and relative group delay of the component with high accuracy. In this paper we reported on the full characterization in terms of spectral response, group delay and chromatic dispersion of a 16 channels free space optics Mux/Demux and showed its homogeneity.

## References

[1] G.D. Maxwell M.E. Vieira Segatto and R. Kashyap. *Optics Communications 195*, pages 151–157, Aug. 2001.

[2] A.H. Rose, C. M. Wang, and S. D. Dyer. *J. Res.Natl. Inst. Stand. Technol.*, 105:839–866, 2000.

[3] C. Lupi. PhD thesis, University of Nantes, Sept 2001.

[4] B. Chassagne, K. Aubry, A. Rocher, B. Herbette, V. Dentan, S. Bourzeix, and P. Martin. *ECOC'01*, 2001.

# High accuracy relative group delay measurements of a chirped grating (NIST Telecom Round Robin)

X. Chapeleau(1), D. Leduc(1), M. Wicks(2), R. Le Ny(1) and C. Boisrobert(1)

(1)LPIO University of Nantes
2 rue de la Houssinière 44300 Nantes
Xavier.Chapeleau@physique.univ-nantes.fr
Tél: (33) 02 51 12 55 46 Fax: (33) 02 40 14 09 87
(2) National Physical Laboratory (NPL), UK

## Abstract

In this paper, we bring more results obtained on a chirped grating submitted to Round Robin tests. We confirm that the relative group delay can be accurately measured with optical low coherence reflectometry.

## Introduction

WDM telecommunications systems require more and more high-performance components like fiber gratings and mux/demux. The relative group delay (RGD) must be known with high accuracy. In June 1999, NIST launched the first round robin measurements of optical fiber Bragg gratings, called "telecom round robin". Its purpose was to compare different measurements methods of RGD. The NIST members A.H. Rose, C.M. Wang and S.D. Dyer analysed the results obtained by all participants and synthetized them in a report entitled "Round Robin for Optical Fiber Bragg Grating metrology" [1]. They considered optical low coherence reflectometry (OLCR) as one of the RGD measurements technique and showed results obtained by this method. In order to bring more results, we have analysed the chirped grating of NIST telecom round robin using our OLCR experimental set-up. In this paper, we present our results outline their precision.

## Experimental set-up

The experimental set-up [2] is a Michelson interferometer assembled around a "2×2" single mode fiber coupler and a broad spectrum C-band light source. The device under test (DUT) is connected to the test arm. In the reference arm, a moving reflector vary the optical path. The photodetector detects interferogramms which are representative of the DUT. These signals are sampled using a frequency stabilized laser He-Ne fringe counter to ensure accurate sample spacing.

We can demonstrate that the intensity received by the detector is a function of $\Delta x$ the distance of the reflector to the optical path balance and can be written as [3] [4] :

$$I(\Delta x) = I_o + \int_{-\infty}^{+\infty} r(\sigma)\, S(\sigma)\, e^{i\Phi(\sigma)}\, e^{-i\,4\pi\,\Delta x\, n_{air}\,\sigma}\, d\sigma \qquad (1)$$

where $S(\sigma)$ is the power spectral density of the source, $r(\sigma)$ is the amplitude reflection coefficient of the sample under test and $\Phi(\sigma)$ is the phase shift that it causes. This last relation means that the phase shift can be computed from the inverse Fourier transform of the interferogram. We can then calculate the group delay $\tau_g$ of the component with the help of the following relation :

$$\tau_g = -\frac{\lambda^2}{4\pi c}\frac{d\Phi(\sigma)}{d\lambda} \qquad (2)$$

The reflection coefficient and the group delay of the component vs wavelength can therefore be derived from a single measurement into the source spectrum.

## Characterization of a chirped grating

### Relative reflectance

The component under test has two ports, labelled #1 and #2, connected to either end of the grating. The figures 1(a) and 1(b) show the relative reflectance vs wavelength for the ports #1 and #2 respectively. Ten successive results have been plotted on the same graph. We can see a spectral "window" with a width of about 16 nm. The top of these two curves presents some ripples feature of a chirped grating.

The figures 2(a) and 2(b) show the relative reflectance vs wavelength into the -20 db bandwidth respectively for the ports #1 and #2. We clearly observe that the spectrum is different in accordance with the direction of the measurement. This demonstrates that a chirped grating is a non-reciprocal component.

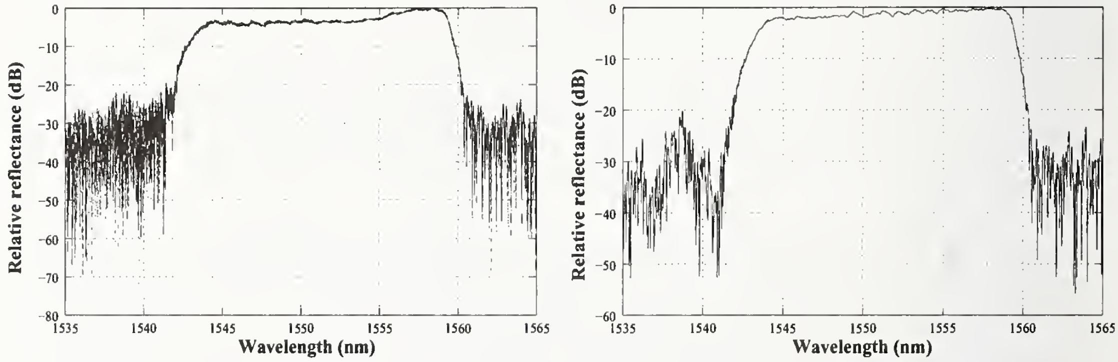

(a) *Port #1*

(b) *Port #2*

Figure 1: *Relative reflectance of the chirped grating*

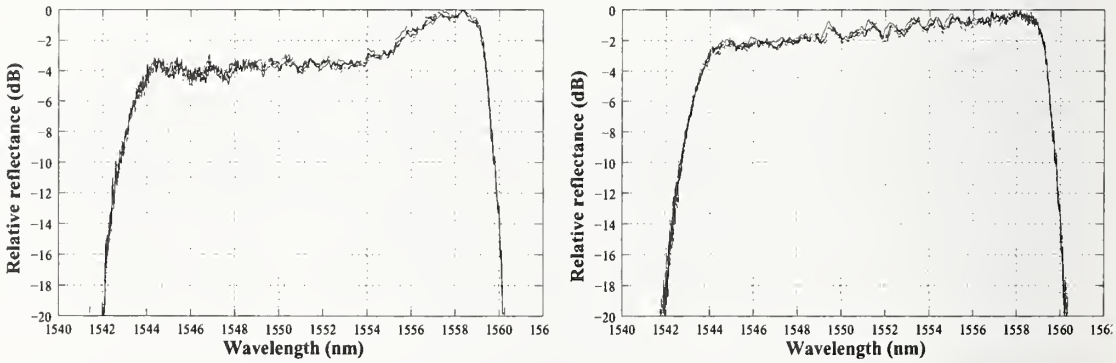

(a) *Port #1*

(b) *Port #2*

Figure 2: *Relative reflectance of the chirped grating into the -20 dB bandwidth*

### Relative group delay

The figures 3(a) and 3(b) show ten plots corresponding to successive measurements of the RGD respectively for the ports #1 and #2. We can see that the group delay varies linearly vs wavelength of about 100 ps between 1554 and 1558 nm. Moreover, ripples appear on the group delay curves. These results are in good agreement with those reported by NIST [1] [5]. We can also see on the figures 4(a) and 4(b), that the ten RGD measurements are very well superimposed on one another for the two ports. This demonstrates the high-precision of our measurements.

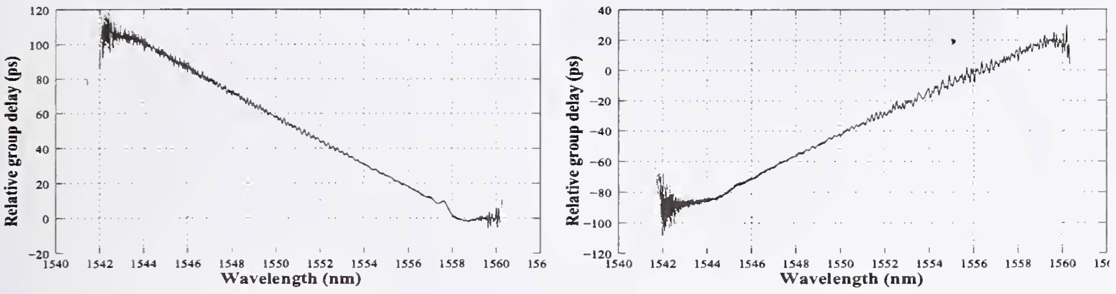

(a) *Port #1*

(b) *Port #2*

Figure 3: *Relative groupe delay of the chirped grating into the -20 dB bandwidth*

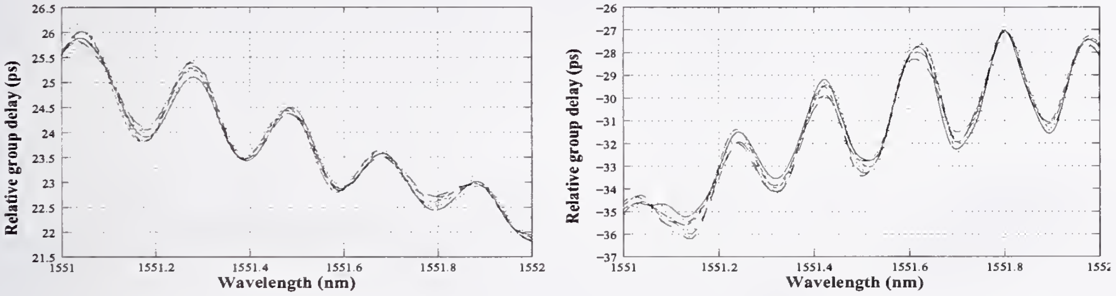

(a) *Port #1*

(b) *Port #2*

Figure 4: *Relative groupe delay of the chirped grating between 1551 and 1552 nm*

## Precision of the relative group delay

We have calculated the group delay deviation from the mean value for each measurement in order to estimate the precision of our results. The figures 5(a) and 6(a) show this deviation vs wavelength for the ports #1 and #2 respectively and the figures 5(b) and 6(b) their distribution. We can see on these last figures that the distribution follows the normal law and the precision of our measurements is about 0.5 ps for the two ports.

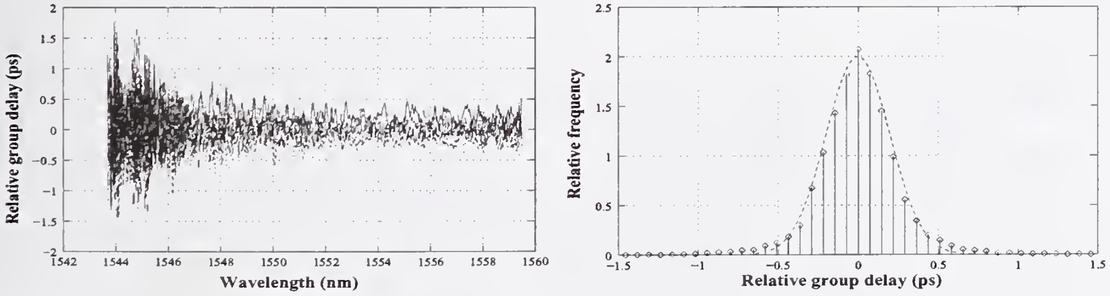

(a) *Deviation from the mean relative group delay*

(b) *Distribution of the deviation from the mean relative group delay*

Figure 5: *Precision of relative group delay for the port # 2 into the -5 dB bandwidth*

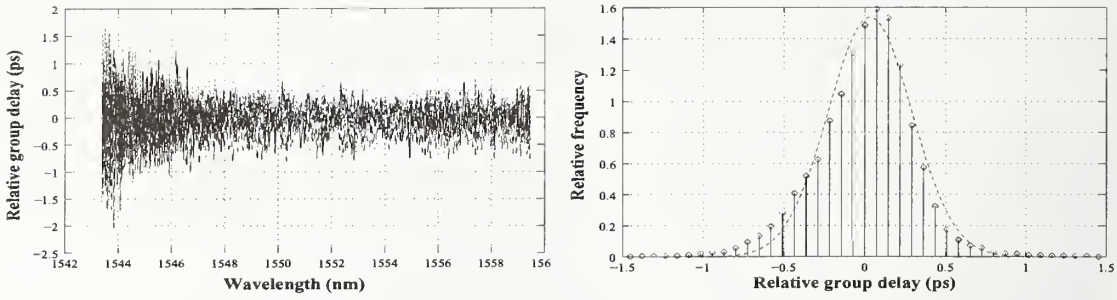

(a) *Deviation from the mean relative group delay*

(b) *Distribution of the deviation from the mean relative group delay*

Figure 6: *Precision of relative group delay for the port # 2 into the -5 dB bandwidth*

## Residual RGD linear fit

The significant parameters of the RGD are the linear slope across the operating bandwidth of the grating and the ripple magnitude. We have used a linear fit and found a mean slope of -6.63 ± 0.14 ps/nm (k=2) for the ten measurements. For each one, we have superimposed the residual RGD linear fit on the figure 7.

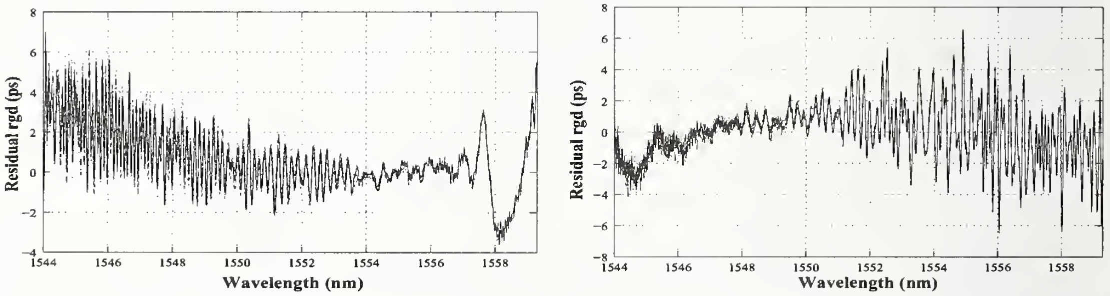

(a) *Port #1*

(b) *Port #2*

Figure 7: *Residual RGD linear fit of the chirped grating*

# Conclusion

In this paper, we have presented the relative reflectance and the relative group delay measurements for the ports #1 and #2. The results we obtained with our experimental system are reproducible and in good agreement with those reported by NIST. This study has been realized within the framework of the COST 265 action.

# References

[1] A.H. Rose, C. M. Wang, and S. D. Dyer. Round robin for optical fiber bragg grating metrology. *J. Res.Natl. Inst. Stand. Technol.*, 105:839–866, 2000.

[2] C. Lupi, D. Leduc, X. Chapeleau, R. Le Ny, J. L. Goudard, and C. Boisrobert. Measurements of resonant dispersion in short length $er^{3+}$ doped fibers. *ECOC'01, Amsterdam*, 2001.

[3] C. Lupi. *Réalisation et mise au point d'un banc de réflectométrie optique à faible cohérence: étude de fiabilité et caractérisation de fibres optiques passives et actives et de divers composants.* PhD thesis, University of Nantes, Sept 2001.

[4] S. Dyer and B. Rochford. A fast and accurate measurement of both transmission and reflection group delay in fiber bragg gratings. *Optical Fiber Communication Conf. (OFC'01)*, pages 169–172, Mar. 2001.

[5] M. Wicks, T. Niemi, M. Wegmüller, H. de Riedmatten, and N. Gisin. Preliminary results of a european intercomparaison of group delay measurements of fibre bragg gratings. *OFMC'01, Cambridge,* 2001.

# Direct Dispersion Slope Measurement by Mach-Zehnder Interferometer on Short Length Optical Fibre

Y. C. Zhao, S. Fleming
Australian Photonics CRC, Optical Fibre Technology Centre
University of Sydney, NSW, Australia
Tel: +61 02 9351 1939, Fax: +61 02 9351 1911
y.zhao@oftc.usyd.edu.au

**Abstract:** We propose and demonstrate a new direct method of second order dispersion measurement by determining the second symmetric interferometric fringe pattern. This measurement was performed with a Mach-Zehnder interferometer, a broadband LED and an optical spectrum analyser. We experimentally measured the dispersion and dispersion slope directly over an ultra-broad wavelength range of a short length of dispersion shifted fibre. Experimental results show close agreement with theoretical results.

## 1. Introduction

Application of new functional optical waveguide devices requires accurate knowledge of chromatic dispersion slope as well as dispersion. Many techniques have been developed for dispersion measurement. Conventional optical fibre dispersion measurements include the time of flight method and the phase shift method [1,2]. The time of flight technique injects different wavelengths into the test fibre where time delays through the test fibre are compared with a reference fibre. The phase shift technique measures phase delay as a function of wavelength. Both methods calculate chromatic dispersion curves from the derivative of the fitted polynomial time delay curves. Despite the importance of dispersion slope, it cannot be measured directly from these two techniques. It can only be derived by successive derivatives of the group delay spectrum. Shang first proposed the elegant white light interferometric method to measure optical fibre dispersion [3]. Stone and Marcuse first proposed a method based on white light interferometry to directly measure the dispersion coefficients by solving three simultaneous equations obtained from interferometric fringes [4]. Based on a Mach-Zehnder interferometer, we propose a new method to directly measure second order dispersion by determining the second symmetric interferometric fringe pattern position.

## 2. Theory

Based on a Mach-Zehnder interferometric scheme, the electric field of the two beams will superpose at the output point. Interference, which depends on the amplitude components and on the phase difference, will take place and maximize when the optical path lengths are equal. Due to chromatic dispersion, different wavelength components of the broadband light will propagate through the fibre with different time delay. The reference path time delay is varied to match the time delay of each wavelength of interest so that interference fringes can be observed in the optical spectrum. The output interference fringe pattern of the combined beams can be expressed following the general approach of Tateda [5] and Shang [3] *

$$I(\lambda)=2\sqrt{I_1(\lambda)\cdot I_2(\lambda)}[\gamma\cos(\Omega)]\cos\left\{\phi_0-\frac{2\pi c}{\lambda_\tau}\left(\tau(\lambda)-\frac{d}{c}\right)\left(\frac{\lambda-\lambda_\tau}{\lambda_\tau}\right)-\pi cLD(\lambda_\tau)\cdot\left(\frac{\lambda-\lambda_\tau}{\lambda_\tau}\right)^2\right.$$
$$\left.-\frac{\pi cL}{3}[\lambda_\tau D'(\lambda_\tau)-4D(\lambda_\tau)]\cdot\left(\frac{\lambda-\lambda_\tau}{\lambda_\tau}\right)^3+\cdots\right\} \qquad (1)$$

where $I_1(\lambda), I_2(\lambda)$ are the intensities of the two arms; $\gamma$ is visibility, $\Omega$ is the angle between the polarization directions of the two arms, L is the test fibre length, $D(\lambda_\tau)$ and $D'(\lambda_\tau)$ are dispersion and dispersion slope at

---

[*] Our analysis agrees with Shang to equation (3) in Ref. 3 for $I(\omega)$, however it diverges for $I(\lambda)$ where we believe that the correct form is as above which differs in a sign and a factor of 2.

$\lambda_\tau$ ,respectively. In the hypothetical case of constant dispersion, there will only be one wavelength at which the path lengths are matched. However, in the real case where dispersion itself is a function of wavelength, the path lengths may match at two (or more) wavelengths. Thus, typically over a broad enough observation wavelength range, two (or more) symmetric fringe patterns can be seen in the optical spectrum. As the air path is changed the positions of both these sets of fringes shift. The first order dispersion can be obtained by determining the shift of the first symmetric fringe pattern. The second order dispersion can be obtained by determining the second symmetric fringe pattern shift. As can be seen from Eq.1, the higher order terms have no influence on first symmetric fringe centre wavelength, but have some influence on symmetry. Both first and second order dispersion have influence on the position of the secondary symmetric fringes. Using the first order dispersion derived from the first symmetric fringe, the second order dispersion can be derived by determining the secondary symmetric fringe centre wavelength. Fig. 1 shows a simulation result in which second symmetric fringe appears on the left of the first symmetric fringe due to the influence of dispersion slope. In the calculation, the primary symmetric centre wavelength is $\lambda_1 = 1665.2nm$, dispersion $D = 8.4 ps/nm \cdot km$, dispersion slope $D' = 0.072 ps/nm^2 \cdot km$, and the secondary symmetric centre wavelength is $\lambda_2 = 1431.5nm$.

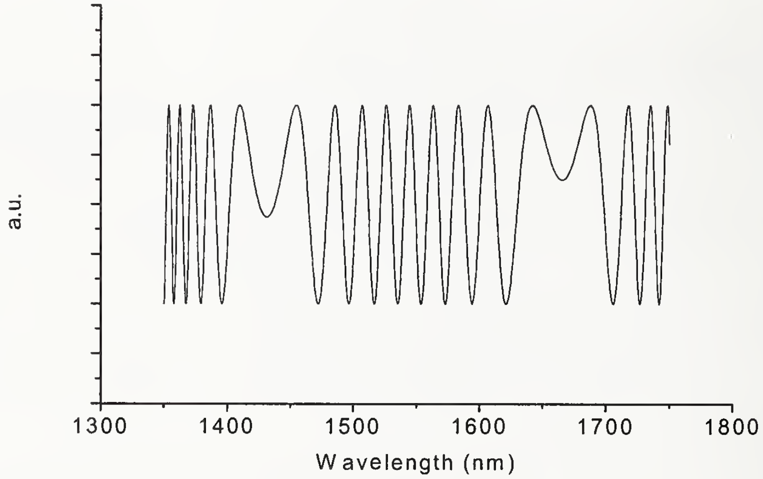

Fig. 1 Theoretical analysis of dispersion slope influence on interference fringe

## 3. Experiment

The experimental configuration based on a Mach-Zehnder interferometer (MZI) is schematically shown in Fig. 2. Light from the broadband LED is divided into two arms by a 3dB coupler, the test fibre is inserted into one arm and the other arm is built with a variable air path of negligible dispersion by attaching one lens

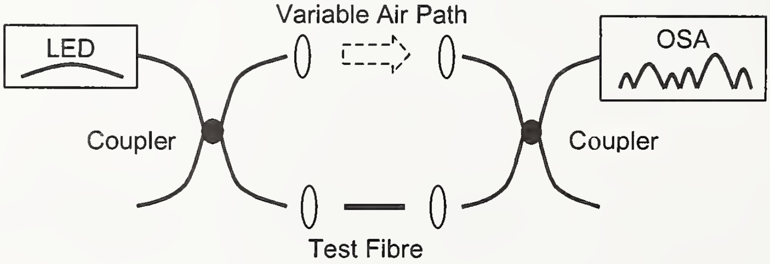

Fig.2 Experimental setup for first and second order dispersion measurement

to a translation stage. The test fibre is a short length of Corning SMF/DS CPC6 dispersion shifted fibre and its zero dispersion wavelength is near 1550nm. The test fibre length is 90cm. The two arms are combined through another 3dB coupler. The output of the interferometer is connected to an optical spectrum analyser. The length of the variable air path changes the relative time delay, $\tau_g(\lambda)$, between the MZI arms. When the optical path length of the reference air path is equal to the optical path length of the test fibre at a certain wavelength, the first symmetric fringe pattern will be easily observed in the optical domain. When the broadband source and observing wavelength range is broad enough, a second symmetric fringe can be observed either on the left or the right of the first symmetric fringe, depending on the relative sign of the first order dispersion to the second order dispersion. In this experiment, the first order and second order dispersion of test fibre are both positive in the observation wavelength range. The second symmetric fringe will be on the left of the first fringe. Fig. 3 shows two interferometer spectra corresponding to two different reference path lengths, showing the first symmetric fringes centred at wavelength $\lambda_{\tau 1}$ = 1656.64 nm (top right arrow) and $\lambda_{\tau 2} = 1634.81$ nm (bottom right arrow), and their corresponding second symmetric fringe centres are $\lambda'_{\tau 1} = 1435.53$ nm (top left arrow) and $\lambda'_{\tau 2} = 1464.06$ nm (bottom left arrow), respectively. The smaller the dispersion slope, the further apart the two symmetric fringes. Therefore, to measure small second order dispersion, a broader wavelength range light source is needed.

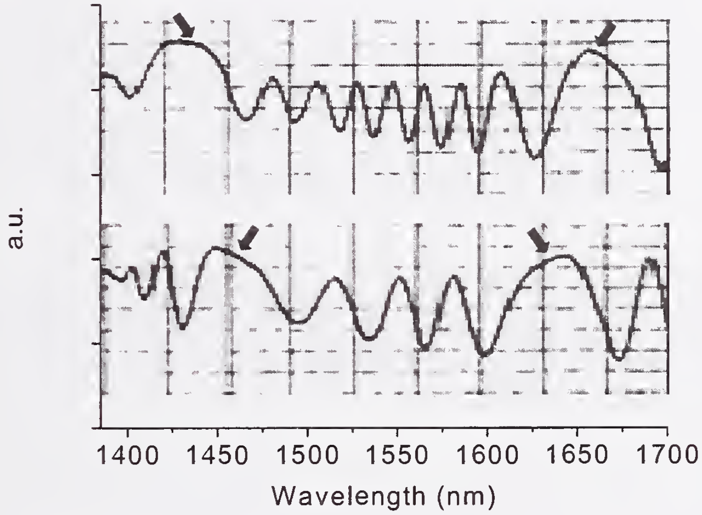

Fig. 3 Interferometer spectra obtained for $\lambda_{\tau 1}$ = 1656.64 nm (top trace)
and $\lambda_{\tau 2} = 1634.81$ nm (bottom trace)

### 4. Results and discussion

The first order dispersion can be obtained by the measured time delay curve of the first symmetric fringe shift. In the experiment, the first order term in Eq. 1 will be adjusted to be zero by the experimenter. The second order dispersion can be obtained by trial and error fitting Eq.1. Starting with an initial guess of the second order dispersion $D'(\lambda_\tau)$, the calculated second symmetric centre wavelength is compared with the test results to determine the second order dispersion. Measured first order and second order dispersion curves are shown in Fig.4. The solid line is the measured dispersion (left axis), the filled squares are the measured dispersion slope (right axis). The calculated dispersion (diamond) and dispersion slope (cross) are shown in Fig.4. A comparison of our results with calculated results show close agreement. Because the spectrum of LED source is not flat, the interference visibility varies across the test wavelength range. The interaction of dispersion and dispersion slope and the visibility variation makes the interference fringes asymmetric. The asymmetric interference fringe patterns affect the determination of the symmetric centre wavelength. In this work, we did not take the visibility influence into consideration in fitting the second order dispersion. These factors all lead to the discrepancy between the calculated results and experimental results. The maximum deviation between theory and experiment of the first order dispersion is less than 0.3 ps/nm.km, and of the dispersion slope is less than 0.01 ps/nm$^2$.km.

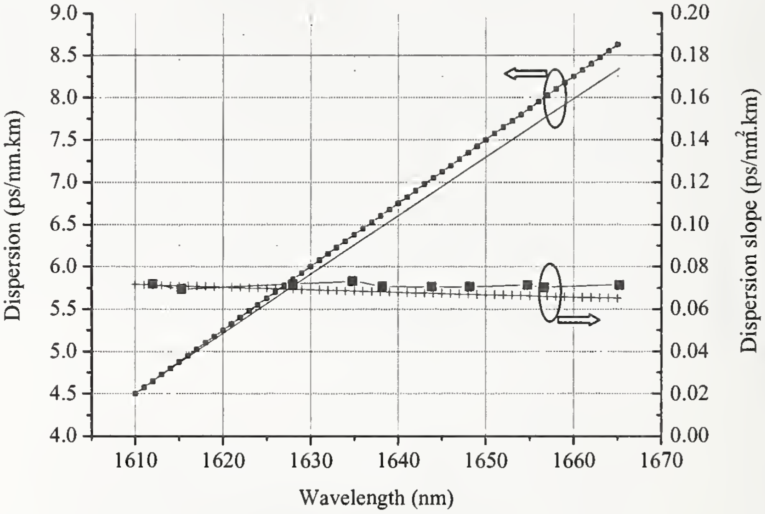

Fig.4. Measured first and second order dispersion

## 5. Conclusion

We have proposed and demonstrated a new direct method of dispersion and dispersion slope measurement based on an interferometric method. This method involves the observation of shifts in two sets of symmetric fringes. The first order dispersion was determined by calculating the first symmetric fringe position. The second order dispersion was determined by the shift of second symmetric fringe. Experimental results show close agreement with theoretical analysis.

**Acknowledgment:** We would like to thank Dr. Martijn van Eijkelenborg for helpful discussion.

## References

1. Cohen, Leonard G., 'Comparison of single-mode fiber dispersion measurement techniques' J. of Lightwave Technol. 1985, 3, pp.958-966
2. Chae Jung-Hye, Lee Yong-Tak, 'A novel chromatic dispersion measurement method in frequency domain using a multi-wavelength optical pulse train generated by Fabry-Perot laser diode', Optics Comm. 2002, 206, pp.1-6
3. Shang Hen-Tai, 'Chromatic dispersion measurement by white-light interferometry on metre-length single-mode optical fibres', Electron. Lett.1981, 17, pp.603-605
4. Stone, J., and Marcuse, D., 'Direct measurement of second-order dispersion in short optical fibres using white-light interferometry', Electron. Lett.,1984, 20 pp.751-752
5. Tateda, Mitsuhiro, Shibata Nori, Seikai Shigeyuki, 'Interferometric method for chromatic dispersion measurement in a single mode optical fibre', IEEE J. Quantum. Electron. 1981, 17, pp. 404-407

# Dispersion measurements on multiple kilometer-length few-mode fibers with an RF spectrum analyzer

J.W. Nicholson, S. Ramachandran, S. Ghalmi, and M.F. Yan
*OFS Laboratories*
*600-700 Mountain Avenue, Murray Hill, NJ 07974*

***Abstract:*** *We present a novel technique for measuring the chromatic dispersion of the higher order mode of an optical fiber. The measurement technique is simple, accurate, and capable of measuring the dispersion of kilometer lengths of fiber without the need for mode converters. The dispersion of the $LP_{02}$ mode is measured for 2, 5 and 10 km lengths of fiber, and accuracies of better than 4% are achieved.*

Recently, dispersion compensation using the $LP_{02}$ mode of few-moded fibers has gained a lot of attention because of the feasibility of achieving a variety of dispersion and dispersion slope values[1,2]. Higher-order-mode (HOM) dispersion-compensating modules (DCM) can achieve large dispersion and dispersion slope values while maintaining a large effective area for light propagation. This makes the device resistant to nonlinear distortions even at high input power levels, which can result in higher optical signal-to-noise ratios and thus longer transmission distances in optical communication systems[3].

A HOM-DCM typically comprises a few-moded fiber that is designed to provide the desired dispersion and dispersion-slope, and two mode-converters (such as long-period fiber-gratings[4]) at the input and output of the HOM fiber[2]. The mode-converters transform the incoming $LP_{01}$ mode into the dispersive $LP_{02}$ mode and vice-versa, at the input and output of the device respectively. The assembly of this device requires fabrication of the mode-converters and care in achieving adiabatic mode-transitions between the mode-converters and the HOM fibers. In order to effectively design new HOM fibers, one must be able to quickly and accurately characterize the dispersion of the higher order modes. Thus, ideally one would like to measure the dispersion on HOM fibers without using mode converters.

Typically, dispersion measurements of long (kilometer) lengths of fiber are done using the modulation phase-shift technique. A tunable laser is modulated at GHz frequencies and launched into the fiber under test. At the output end of the fiber, the RF phase is measured as a function of laser wavelength, giving the group delay, and ultimately the dispersion, of the fiber under test. While this technique works well for single mode fibers, the presence of multiple modes propagating in the fiber at once will cause the measurement to fail, unless strong mode-converters are employed at the input and output of the HOM fiber.

Recently, the group delay and dispersion of higher order modes in a HOM fiber was obtained by measuring the wavelength dependent spectral fringe spacings of a fiber-interferometer. The two arms of the interferometer were the distinct paths for light propagating in the $LP_{01}$ and the $LP_{02}$ modes of a HOM fiber, respectively[5]. This technique is attractive for quick measurements of the dispersion in higher-order-modes, because no mode-converters are needed. However, it is limited to measuring dispersion of a few meters of fiber because the fringe spacing of the interferometer must have a spacing larger than the wavelength resolution of the tunable laser.

We present here an alternate technique, based on RF measurements of an interferometer for obtaining the dispersion of higher order modes. This technique does not require the use of mode converters and works on kilometer lengths of fiber. Phase noise in coherent sources can be coupled to intensity noise in an interferometer. A photodetector placed at the output of the interferometer will have a photocurrent whose electrical spectrum shows a dependence on the relative delay, $\tau$, between the two arms of the interferometer. If the interferometer is in quadrature (i.e. the relative delay between the two arms is a multiple of $\pi$), the electrical spectrum will have the form[6]

$$P(f) \propto \frac{\Delta f}{f^2 + \Delta f^2}\left\{1 + e^{-4\pi\Delta f\tau} - 2e^{-2\pi\Delta f\tau}\cos(2\pi f\tau)\right\},$$

where $\Delta f$ is the source linewidth. In the case of a HOM fiber, the two arms of the interferometer are the two orthogonal co-propagating modes. Excitation of co-propagating modes in a HOM fiber can be easily achieved by butt-coupling (or splicing) a single-mode fiber to the HOM fiber, obviating the need for high quality mode converters since an interferometer with power ratios as small as 10% can yield sufficiently large modulation depths. The electrical spectrum of a coherent source at the output of the HOM fiber will show a cosine modulation whose frequency is the inverse of the relative group delay between the two co-propagating modes. Because of the high resolution of electrical spectrum analyzers, relative group delays from hundreds of picoseconds to hundreds of nanoseconds can easily be measured. To measure such long group delays with techniques based on the optical spectrum would require a wavelength resolution on the order of 100 femtometers. By measuring the beat frequency of the electrical spectrum as a function of source wavelength, the relative group delay as a function of wavelength can be obtained, and therefore the dispersion difference between the two modes can be calculated.

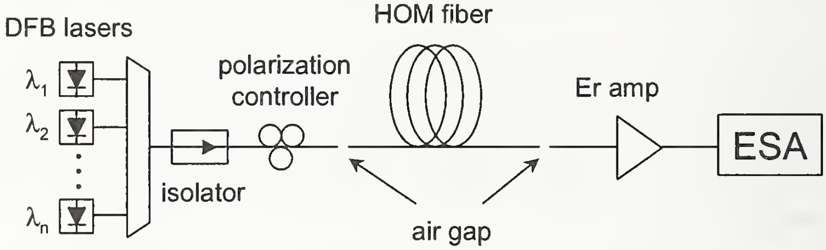

**Figure 1** Experimental setup for higher order mode dispersion measurement.

The experimental setup for the dispersion measurement is shown in Figure 1. A bank of multiplexed DFB lasers was used as a signal source. DFB lasers were chosen for their relatively broad (few MHz) linewidth, making measuring the beat note in the wings of the spectrum easier. An isolator was used to prevent feedback to the lasers, and a polarization controller was used to ensure parallel polarization at the detector by optimizing the beat note. The HOM fiber consisted of three lengths of 2.3 km, 5.25 km, and 10.32 km. This fiber had cutoff wavelengths greater than 2000 nm for the $LP_{02}$ and the $LP_{11}$ mode. An erbium amplifier was used to boost the signal after the HOM fiber and an electrical spectrum analyzer (ESA) was used to measure the RF power spectrum.

In order to ensure a simultaneous launch into the desired modes (in this case, the $LP_{01}$ and $LP_{02}$ modes), the SMF and HOM pigtails were cleaved and aligned with a small air-gap on the order of 100 μm between them at the input and output of the spools. The free spectral range of these air gaps was about 1.5 THz; therefore, any etalon effects from these gaps were well outside of the range of detection.

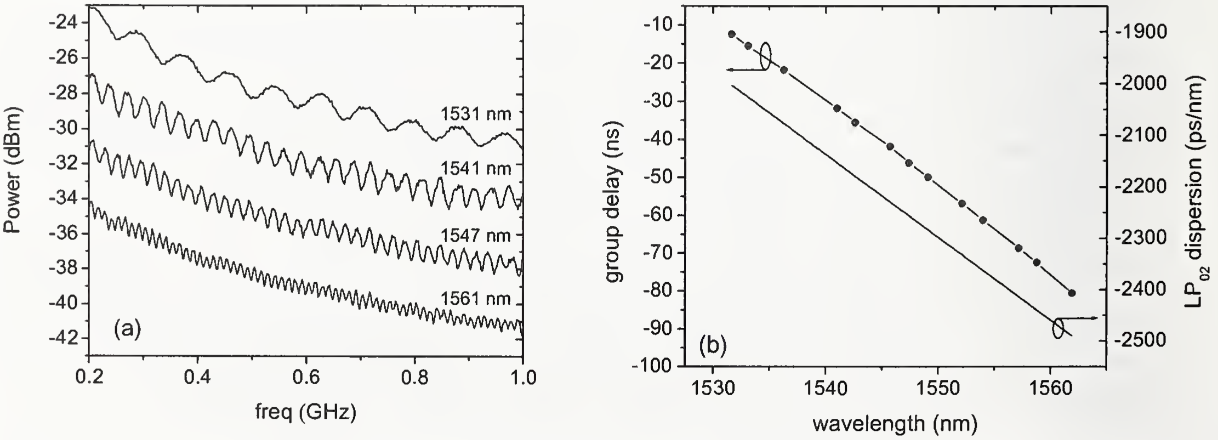

**Figure 2:** (a) Electrical power spectrum as a function of signal wavelength for the 10.32 km spool. The traces have been offset for clarity. (b) Measured relative group delay and calculated $LP_{02}$ dispersion for 10.32 km spool.

Although an interferometer in quadrature generates a strong cosine modulation, the electrical power spectrum from an out-of-quadrature interferometer is relatively smooth. Experimentally, we observed the power spectrum to oscillate between strong modulation and no modulation on a time scale of a second, meaning the interferometer was moving in and out of quadrature, and the polarization state of the interferometer was changing. The beat note could be optimized to a certain extent with the use of the input polarization controller; however, nothing could be done about the movement in and out of quadrature. We found that averaging the traces reduced the maximum observed amplitude of the beat note, but meant that the shift in quadrature was not a significant issue.

The electrical power spectrum for four different wavelengths for the 10.32 km spool is shown in Figure 2a. As the wavelength of the DFB laser increases, the frequency of the modulation increases, meaning the relative group delay between the $LP_{01}$ and $LP_{02}$ mode increases. The electrical power spectrum at each wavelength was Fourier transformed to obtain the peak of the modulation frequency, and therefore the relative group delay. The group delay, obtained from Figure 2a is shown in Figure 2b. This data was fit to a second order polynomial and the derivative taken to give the dispersion difference between $LP_{01}$ and $LP_{02}$. The $LP_{01}$ dispersion was measured with the modulation phase-shift technique (an Agilent 86037C Chromatic Dispersion Test Solution), and added to the dispersion difference measurement from the RF MPI technique to obtain the $LP_{02}$ dispersion, also plotted in Figure 2b.

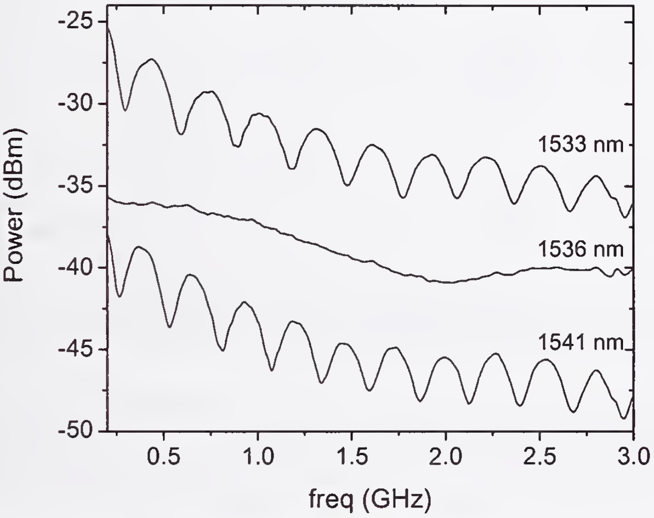

**Figure 3:** Electrical power spectrum as a function of signal wavelength for the 5.25 km spool. The low frequency of the beat note at 1536 nm indicates the spool has a turn-around point in this region, where the group delay of the $LP_{01}$ and $LP_{02}$ modes are equal.

It is worth noting that because the modulation frequency is obtained through the use of a Fourier transform, the presence of small amounts of unwanted higher order modes, such as the $LP_{11}$, do not show up as noise in the data. The $LP_{01}$ and $LP_{11}$ will have a different relative group delay, and thus a different beat frequency than the $LP_{01}$ and the $LP_{02}$. Fourier filtering during the data analysis will therefore effectively remove the $LP_{11}$ mode.

One potential difficulty in this measurement technique occurs at the wavelength where the group delays of the two modes are identical (this wavelength has also been called the turn-around point wavelength due to its significance for fabricating broadband long-period fiber-gratings[4]). At exactly this wavelength the frequency of the cosine modulation goes to infinity. This situation occurred in the 5.25 km spool around 1536 nm, and is illustrated in Figure 3. At 1536 nm the cosine modulation becomes very long, whereas at 1533 nm and 1541 nm, the modulation has nearly the same frequency, meaning the relative group delay has equal value but acquires a change in sign as the wavelength is swept through the turn-around point. Typically, we acquired the electrical spectrum out to frequencies of 3 GHz for the 2 and 10 km spools. However, we found that for the 5 km spool, where the turn-around point was within the measurement range, we had to increase the frequency range to 5 GHz to obtain repeatable results.

In order to test the accuracy of this measurement technique, complete HOM-DCMs were constructed (with mode converters at the input and output of the test fibers), and the $LP_{02}$ dispersion was measured directly with the modulation phase-shift technique. The results of the modulation phase-shift measurements and the RF MPI measurements are compared for the three different spools in figure 4a. The results of all three spools match very well for the two techniques. The percent deviation between the two measurements for the three different spools is plotted in figure 4b. Even for the 5.25 km spool, which was the most problematic due to the presence of the turn-around point within the measurement range, the maximum deviation is less than 4%. For the other two spools, the deviations are typically less than 1%. The oscillations in the percent deviation curves come from the modulation phase-shift measurement of the $LP_{01}$ mode, which showed increased noise due to small amounts of residual higher order modes.

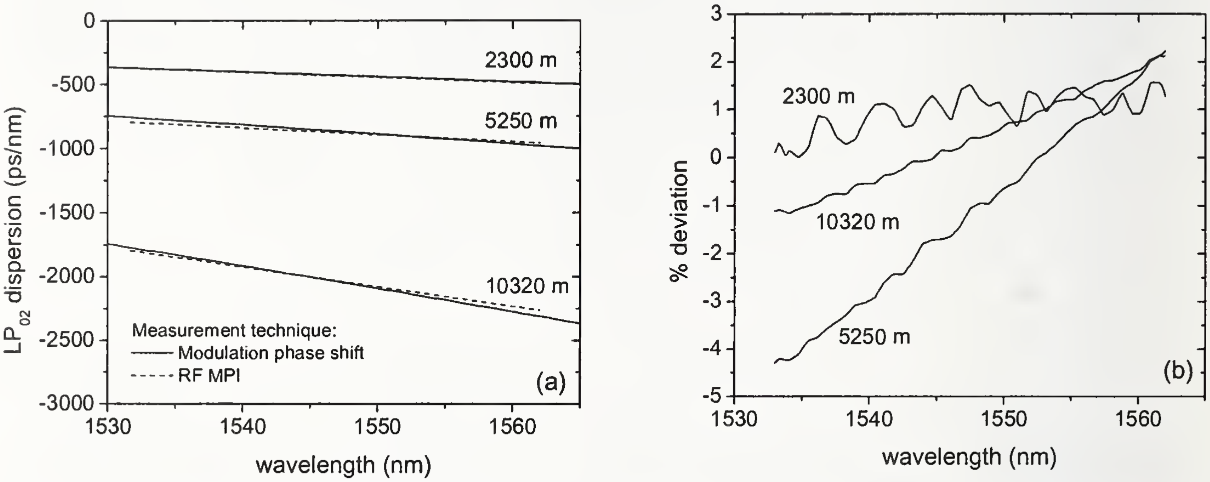

**Figure 4:** (a) Comparison between the modulation phase-shift measurement of the $LP_{02}$ dispersion and the RF MPI measurement for the three different spools. (b) Percent deviation between the two measurements for the three different of spools.

In conclusion, we have presented a simple measurement technique for obtaining the dispersion of higher order modes in an optical fiber. This measurement has the advantage, as compared to previous techniques, of not requiring the use of mode converters and being applicable to long lengths of fibers. The measurement is simple, accurate, and easy to implement.

---

## References

[1] A.H. Gnauck *et.* al, *Proc. Opt. Fiber Comm.*, PD-8, 2000.
[2] S. Ramachandran *et.* al, *IEEE Photon. Tech. Lett.*, vol. 13, pp. 632-634, 2001.
[3] S. Ramachandran *et* al, *Electron. Lett.*, vol.37, p 1352, October 2001.
[4] S. Ramachandran *et* al, *Optics Lett.*, vol. 27, p 698 (2002).
[5] D. Menashe *et* al, *Electron. Lett.*, vol. 37, p 1439 (2001).
[6] R. W. Tkach *et* al, *J. Lightwave Tech.*, **LT-4**, p 1711 (1986).

# Group-Delay Measurements with RF optical frequency scanning

**María C. Santos, Josep Prat and Marçal Soler**

*Universitat Politècnica de Catalunya, Signal Theory and Communications Dept.*

**Abstract:** We derive the analytical basis of a new group-delay measurement method at optical frequencies. By using a similar experimental setup to that required for the standard Modulating Phase Shift Method (MPSM) and computation of amplitude and phase measures, we show that it is possible to scan the optical frequency by frequency sweep of the rf modulating signal.

## 1. Introduction

Increasingly, the optical communications industry is demanding the characterization of optical components with respect to chromatic dispersion more accurately and more simply [1]-[4]. Standard to the matter is the modulation phase shift method (MPSM) [5], whose wavelength resolution is determined by the tunability of the laser which provides the optical signal to which sidebands are attached by external RF modulation prior to injection into the DUT. Group delay data are then obtained from determination of the phase difference acquired between sidebands [5]. We have shown recently that wavelength stability of the tunable laser employed constitutes a critical point determining to a great extent the accuracy of the measures [6].

Several modifications to the phase shift method have been proposed to ease the requirements of frequency stability of the laser source and improving its accuracy [1-4]. Some are based on the use of single sideband modulation [1] and other clever ways of combining the sidebands [2]-[4], the interest often being laid on benefiting from better frequency stability and resolution provided by radiofrequency signals.

Here we will outline the principles of a technique which by properly combining phase and amplitude measurements of all frequencies generated as a result of the modulation and optical detection process, namely, continuous wave, fundamental (modulating frequency) and its second harmonic, should allow for optical frequency scanning, and hence wavelength resolution control, in the electrical rather than the optical domain, through minimal modifications to the basic standard setup.

## 2. Measurement Technique

Figure 1 shows the experimental setup required. The use of phase instead of amplitude modulation of the optical carrier as usually encountered with MPSM, is not fundamental to the method that we derive here, because group delay data could in principle be extracted as well, but as it will be seen, the use of narrow band phase modulation helps to improve accuracy. Assuming a very small index of modulation, $m << 1$, the signal at the output of the phase modulator is given by

$$S_M = A_o \cos(\omega_o t + \theta_o) - \frac{mA_o A_m}{2}\left[\sin((\omega_o + \omega_m)t + \theta_o + \theta_m) + \sin((\omega_o - \omega_m)t + \theta_o - \theta_m)\right] \quad (1)$$

with the $A_o, A_m, \omega_o, \omega_m, \theta_o, \theta_m$ , respectively, the amplitudes, frequencies and phases of the optical and microwave (modulating) signals.

On reflecting from the DUT, each frequency component gets phase and amplitude variations here denoted $\gamma^o, \gamma^+, \gamma^-, \phi^o, \phi^+, \phi^-$ respectively, for the DUT's amplitude and phase response at the carrier frequency, the upper and lower sidebands. According to that, the signal reflected from the DUT is expressed

$$S_G = A_o \gamma_o \cos(\omega_o t + \theta_o + \phi^o) - \frac{mA_o A_m}{2}\begin{bmatrix}\gamma^+ sin((\omega_o + \omega_m)t + \theta_o + \theta_m + \phi^+) + \\ + \gamma^- sin((\omega_o - \omega_m)t + \theta_o - \theta_m + \phi^-)\end{bmatrix} \quad (2)$$

The detected signal includes terms at the modulating frequency as well as at its second harmonic provided they fall within the detector bandwidth, and a continuous power level. The power functions at each of these frequency components are given by

$$P_D(\omega=0)=\frac{A_o^2\gamma_o^2}{2}+\frac{(mA_oA_m)^2}{8}\left[(\gamma^+)^2+(\gamma^-)^2\right] \tag{3}$$

$$\begin{gathered}P_D(\omega=\omega_m)=-\frac{mA_o^2A_m\gamma^o}{2}\sqrt{(\gamma^+)^2+(\gamma^-)^2-2\gamma^-\gamma^+\cos(2\delta)}\\ sin\left(\alpha-\delta+\mathrm{tg}^{-1}\left(\frac{sin(2\delta)}{1+\gamma^-/\gamma^+\cos(2\delta)}\right)\right)\end{gathered} \tag{4}$$

$$P_D(\omega=2\omega_m)=\frac{(mA_oA_m)^2\gamma^+\gamma^-}{4}\cos(2\omega_m t+2\theta_m+\phi^+-\phi^-) \tag{5}$$

where $\alpha=\omega_m t+\theta_m+\frac{\phi^+-\phi^-}{2}$ and $\delta=\phi^o-\frac{\phi^++\phi^-}{2}$.

When using the standard MPSM, the group delay, $\tau_g$ is obtained from the phase difference between sidebands as

$$\tau_g=\frac{d\phi}{d\omega}\approx\frac{\Delta\phi}{\omega_m} \tag{6}$$

where the $\Delta\phi=\frac{\phi^+-\phi^-}{2}$ is the semi-difference between the phase acquired by each of the sidebands. The modulating frequency thus determines the frequency resolution when using the standard MPSM and therefore, it is usually set to be very small. That allows assumption of no significant fluctuations of the amplitude response that thus can be considered approximately constant over the bandwidth of interest. When an rf scanning is pursued, that could no longer be the case, and then the amplitude variations ought to be considered in the analysis.

In what follows we will outline the procedures which allow to perform optical frequency scanning through rf modulating frequency sweep using the setup in Figure 1, both for the simpler case when the DUT's amplitude response in reflection can be assumed constant over the range of frequencies of interest, and for the case when the amplitude reflections from the DUT are significantly different at each incident frequency.

## 3. Equal amplitudes

In the case when the amplitude response of the DUT can be assumed constant for all the frequency components contained in the incident signal, $S_M$, i. e. $\gamma^-\approx\gamma^o\approx\gamma^+=\gamma$, from (3)-(5), the expressions for the power at the three detected frequency components reduce to

$$P_D(\omega=0)=\frac{A_o^2\gamma^2}{2}\left(1+\frac{m^2A_m^2}{2}\right) \tag{7}$$

$$P_D(\omega=\omega_m)=-mA_o^2A_m\gamma^2\sin(\delta)\sin\left(\omega_m t+\theta_m+\frac{\phi^+-\phi^-}{2}\right) \tag{8}$$

$$P_D(\omega=2\omega_m)=\frac{(mA_oA_m\gamma)^2}{4}\cos(2\omega_m t+2\theta_m+\phi^+-\phi^-) \tag{9}$$

We use the measured phases (PH) and amplitude levels (L) at the three detected frequencies to obtain the $\delta$ and the $\Delta\phi=\frac{\phi^+-\phi^-}{2}$ values for each modulating frequency in the sweep. Directly, as with MPSM,

$$\Delta\phi=PH_\omega+m\pi \quad , \quad m\in\mathrm{Z} \tag{10}$$

Calculate the auxiliary value

$$LC_o = L_o - L_{2\omega} = \frac{A_o^2 \gamma^2}{2} \tag{11}$$

or alternatively, get it as the continuous power level measured when only the unmodulated carrier is launched into the system. And then get

$$\delta = sin^{-1}\left( \frac{L_\omega}{2\sqrt{2LC_o}\sqrt{L_{2\omega}}} \right) \tag{12}$$

A $\cos^{-1}$ instead of $sin^{-1}$ function is obtained for the calculation of $\delta$ when amplitude instead of phase modulation is used for the optical carrier and therefore narrow band phase modulation is preferred to improve resolution. From the values of $\delta_i$ and $\Delta\phi_i$ obtained for each modulating frequency $\omega_{mi}$ in the sweep, we get the phase differences at each side of the optical carrier, which is kept fixed (rf optical frequency scanning), as follows. First get the difference functions $\Delta S_i$ and $\Delta D_i$

$$\begin{aligned} \Delta S_i &= \delta_{i+1} - \delta_i = \frac{\phi_i^+ + \phi_i^- - \phi_{i+1}^+ - \phi_{i+1}^-}{2} \\ \Delta D_i &= \Delta\phi_{i+1} - \Delta\phi_i = \frac{\phi_{i+1}^+ - \phi_{i+1}^- - \phi_i^+ + \phi_i^-}{2} \end{aligned} \tag{13}$$

From those, addition and substraction gives the phase differences between the two lower and respectively, the two upper frequency sidebands (see Figure 2)

$$\Delta\phi_i^- = \phi_i^- - \phi_{i+1}^- = \Delta D_i + \Delta S_i \quad , \quad \Delta\phi_i^+ = \phi_{i+1}^+ - \phi_i^+ = \Delta D_i - \Delta S_i \tag{14}$$

and thus, the frequency resolution for group delay calculation is determined by the frequency difference between modulating frequencies in the rf scan

$$\tau_{gi}^+ = \frac{\Delta\phi_i^+}{\Delta\omega_m} \quad , \quad \tau_{gi}^- = \frac{\Delta\phi_i^-}{\Delta\omega_m} \tag{15}$$

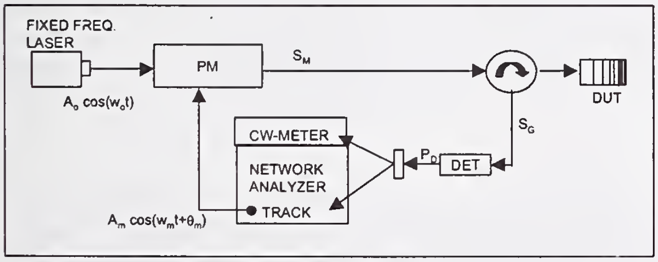

Figure 1. Experimental setup

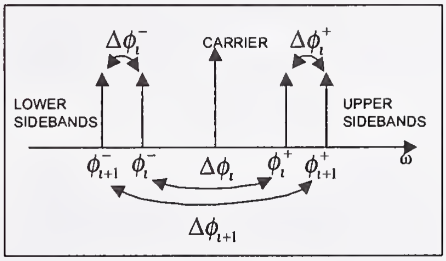

Figure 2. Schematic of phase differences between frequency components

### 4. Different amplitudes

When the amplitude differences among the reflected waves at each of the three detected frequencies need to be taken into account, one has to deal with the complete (3)-(5) expressions. It is important to note that even when using MPSM, a significant difference in the reflected amplitudes introduces an error in the detected phase difference, $\Delta\phi$ , between upper and lower sidebands. In such case the use of a Microwave Transition Analyser to measure the relative phase at the second harmonic frequency is advised, for direct obtaining of $\Delta\phi$ . On the other side, the auxiliary value $LC_o$ has to come necessarily from the cw power level detected when only the unmodulated carrier is launched into the system.

Using the definitions: $\Gamma^+ = A_o A_m m \gamma^+$, $\Gamma^- = A_o A_m m \gamma^-$, the measured power levels at the three detected frequencies are respectively,

$$L_o = LC_o + \frac{(\Gamma^+)^2 + (\Gamma^-)^2}{8} \tag{16}$$

$$L_\omega = \sqrt{2LC_o}\sqrt{(\Gamma^+)^2 + (\Gamma^-)^2 - 2\Gamma^+\Gamma^- \cos(2\delta)} \tag{17}$$

$$L_{2\omega} = \Gamma^+\Gamma^- / 4 \tag{18}$$

also, we measure the phase at the detected modulating frequency, and get

$$PH_\omega = 2PH_{2\omega} - \delta + \mathrm{tg}^{-1}\left(\frac{sin(2\delta)}{1 + \Gamma^- / \Gamma^+ \cos(2\delta)}\right) \tag{19}$$

The above four equations (15)-(19) provide the means to determine the $\delta, \Delta\phi, \Gamma^+\Gamma^-$, and $\Gamma^+ / \Gamma^-$ values. The $\delta$ and $\Delta\phi$ will be used to determine the group delay response following the procedure outlined in the previous section, while the other two, if one takes good care to keep the $A_o A_m m$ value unchanged through the sweep, will serve to characterize the amplitude response in reflection of the DUT at each side of the optical carrier, in a procedure that is explained next.
For each modulating frequency in the sweep, $\omega_{mi}$, let

$$\begin{aligned} \Delta\gamma_i(dB) &= 10\log(\Gamma_i^+ / \Gamma_i^-) = \gamma_i^+(dB) - \gamma_i^-(dB) \\ \Sigma\gamma_i(dB) &= 10\log(\Gamma_i^+\Gamma_i^-) = \gamma_i^+(dB) + \gamma_i^-(dB) + 20\log(A_o A_m m) \end{aligned} \tag{20}$$

Get the difference functions as follows

$$\begin{aligned} \Delta S_i &= \Sigma\gamma_{i+1} - \Sigma\gamma_i = \gamma_{i+1}^+ + \gamma_{i+1}^- - \gamma_i^+ - \gamma_i^- \\ \Delta D_i &= \Delta\gamma_{i+1} - \Delta\gamma_i = \gamma_{i+1}^+ - \gamma_{i+1}^- - \gamma_i^+ + \gamma_i^- \end{aligned} \tag{21}$$

and from here, the amplitude difference in dB at each side of the carrier follows

$$\Delta\gamma_i^- = \gamma_i^- - \gamma_{i+1}^- = \frac{\Delta D_i - \Delta S_i}{2} \quad , \quad \Delta\gamma_i^+ = \gamma_{i+1}^+ - \gamma_i^+ = \frac{\Delta D_i + \Delta S_i}{2} \tag{22}$$

## 5. Conclusion

We have established the theoretical basis of a new group delay measurement method that should provide, by appropriate combination of both phase and amplitude measurements, over the MPSM standard setup, frequency scanning in the electrical domain, enhancing wavelength resolution to the levels that can be accomplished in the RF part of the spectrum. Both the cases when the frequency amplitude response of the DUT can and cannot be considered constant have been analysed, providing in the latter a procedure to characterize the amplitude response of the DUT.

## 6. References

[1] J. E. Román et al., *Optics Letters*, vol. 23, pp. 939-941, 1998
[2] R. Fontenberry, *Technical Digest OFC'98*, pp. 363-364, 1998.
[3] C. K. Madsen. *Technical Digest OFC'01*, pp. MO6-1/-3, 2001.
[4] B. Christensen, J. Mark, G. Jacobsen and E. Bodtker, *Electron. Lett.*, vol. 29, pp. 132-134, 1993.
[5] Chapter 12, **Fiber Optic Test and Measurement**, Dennis Derickson, editor, Prentice Hall PTR, 1998.
[6] M. Soler, J. Prat, M. C. Santos, *IEEE Workshop on Fibre and Optical Passive Components*, Glasgow, June 2002.

# Optical waveform and Q-factor measurement using optical sampling for ultra-high speed TDM systems

Hidehiko Takara, Ippei Shake, and Satoki Kawanishi

NTT Network Innovation Laboratories, NTT Corporation
1-1 Hikari-no-oka, Yokosuka, Kanagawa, 239-0847 Japan

## Abstract

We report recent progress in optical sampling techniques for measuring optical signal waveforms. The principle of sum-frequency-generation optical sampling is explained, and our experimental results are presented. We also describe how it offers transparent and flexible monitoring of optical signal quality.

## 1. Introduction

With the development of ultrahigh-speed TDM systems (over 40 Gbit/s) [1], the need has arisen for a technique to measure optical waveforms with extremely high time resolution. The conventional approach is to combine a photodetector with electrical sampling. However, this combination limits the temporal resolution to 10 ps due to the bandwidth (up to 50 GHz) of the photodetector and the electrical sampling circuit. This is insufficient to measure optical signals at over 40-Gbit/s, where a timeslot is less than 25 ps. In contrast, optical sampling based on optical nonlinear effects is attractive because of the ultrashort response times possible. So far, several optical sampling methods have been demonstrated based on sum-frequency-generation (SFG) [2,3], cross-phase-modulation [4], and four-wave mixing [5].

We investigated an SFG optical sampling method in order to realize over 100 Gbit/s bandwidth optical waveform measurements [6,7]. We also recently assessed averaged Q-factor measurement based on optical sampling for optical signal quality monitoring in transparent optical networks. This paper describes the principle and features of this optical sampling method and demonstrates the waveform/Q-factor measurement of ultrahigh-speed TDM signals.

## 2. Principle of SFG optical sampling

The configuration of SFG optical sampling is shown in Fig. 1. Optical signal pulses and optical sampling pulses are combined and injected into a nonlinear optical material in order to generate the cross-correlation signals (sum-frequency light). The repetition rate of the sampling pulses is set to $f_0/N$ minus offset $\Delta f$ where $f_0$ is the repetition rate of the signal pulses. The sampled waveform is an expanded version of the signal pulse waveform and is displayed on a monitor.

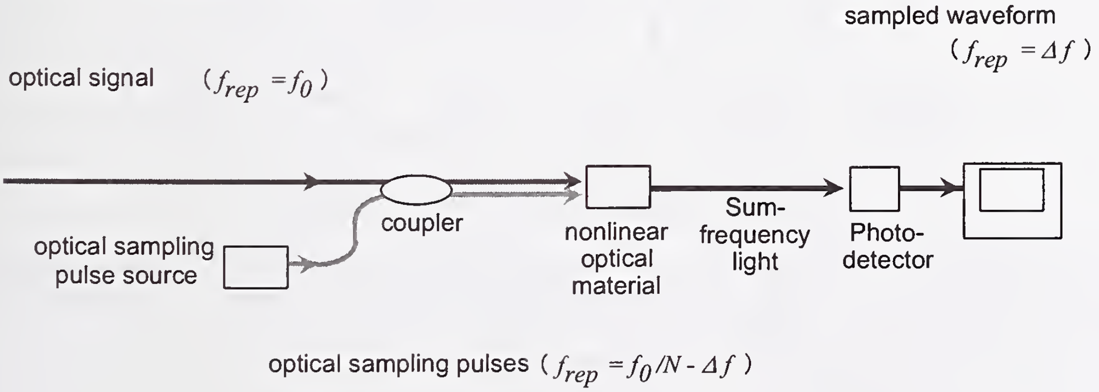

Fig. 1 Fundamental configuration of optical sampling

This optical sampling technique realizes waveform sampling all-optically by utilizing the ultrafast optical nonlinear effect and ultrashort sampling pulses. Therefore, it has high temporal resolution, subpicosecond order, and can be used to measure optical signals at over 100-Gbit/s.

## 3. Subpicosecond resolution waveform measurement

The temporal resolution of optical sampling depends on the optical sampling pulse duration, jitter, and SFG response time. A low jitter oscillator can hold the jitter under 0.3 ps, and the SFG response time is less than 0.1 ps. The main factor limiting the temporal resolution is the optical sampling pulse duration. We generate subpicosecond sampling pulses by utilizing a mode-locked Er-doped fiber laser and the supercontinuum (SC) technique [8].

Figures 2 (a) and (b) show the SC pulse generator and an autocorrelation trace of output pulses, respectively. The 3.0 ps optical pulses from the mode-locked Er-doped fiber ring laser (ML-FRL) are converted into SC pulses in an SC fiber. Subpicosecond sampling pulses are obtained by compensating the chirping and then filtering the pulses with an optical bandpass filter (OBF). The calibrated pulse duration of the SC pulse was 0.4 ps. These ultrashort pulses realize optical waveform measurements with subpicosecond resolution.

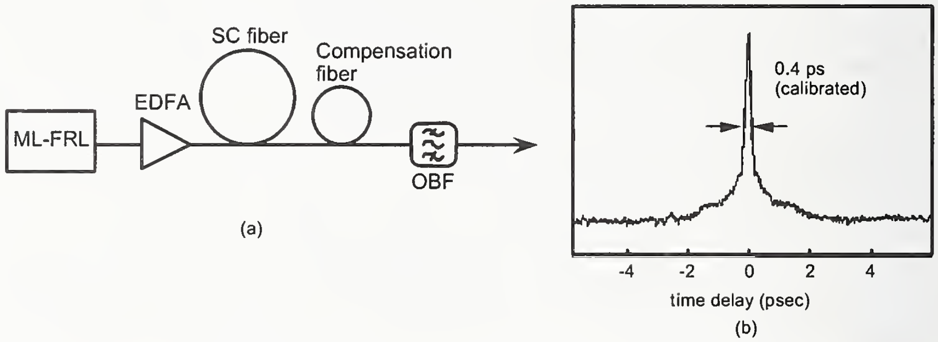

Fig. 2 Configuration of optical sampling pulse generator (a) and autocorrelation trace (b)

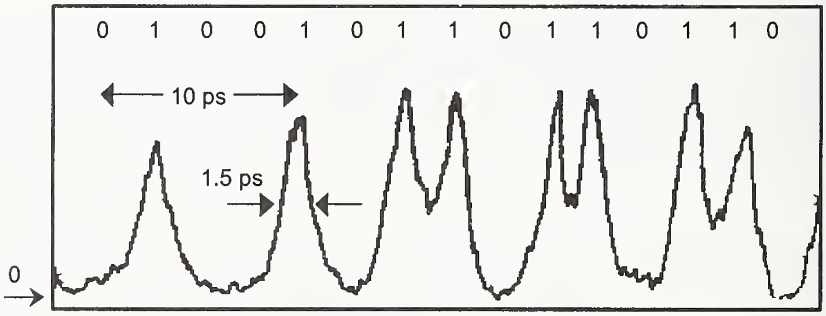

Fig.3 Measured waveform of 400 Gbit/s data pattern

Figure 3 shows the measured waveform of a 400 Gbit/s optical signal. The data pattern "010010110110110" with pulse duration of 1.5 ps was successfully measured. The temporal resolution of the measurement system is given by this equation

$$t_{res}=(t_{meas}^2 - t_{sig}^2 - j_{sig}^2)^{1/2} \qquad (1),$$

where $t_{meas}$ is the signal pulse duration as measured by optical sampling, $t_{sig}$ is the signal pulse duration as measured by an autocorrelator and $j_{sig}$ is the timing jitter of the signal pulses. From measured values ($t_{meas}$ =1.5 ps, $t_{sig}$ =1.4 ps, $j_{sig}$ =0.3 ps), the temporal resolution $t_{res}$ of this system is estimated to be 0.4 ps.

## 4. Eye-diagram measurement

Eye-diagrams that measure the waveforms of randomly-modulated optical short pulse signals are needed to evaluate the characteristics of ultra-high speed TDM systems. In order to measure the eye-diagram, each sampled signal must have a high signal-to-noise-ratio (SNR). We improved the SNR of the measured waveform by employing type II phase-matching SFG and an organic crystal (AANP) with high optical nonlinearity [9], and by amplifying sampling pulse peak power to 200 W.

The type II phase-matching condition is satisfied when the polarization states of the two input lights are orthogonal to each other, as shown in Figure 4. Therefore, this configuration is effective in eliminating the DC background light, the second harmonic light of the sampling or signal light, because each input light has only one polarization component [3,6].

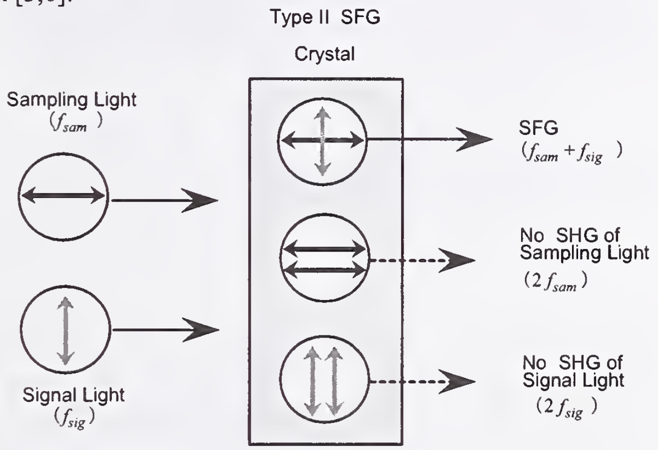

Fig. 4 Type II phase-matched SFG

The AANP crystal has femtosecond response time and high nonlinearity ( $d_{31}$= 80 pm/V). Figure 5 shows the wavelength dependency of SFG efficiency for both the AANP crystal and a KTP crystal, which is the conventional choice. The AANP crystal offers SFG efficiencies that are at least 10 times those of the KTP crystal for the wavelength range from 1535 nm to 1570 nm. The maximum efficiency value obtained is 3 x $10^{-4}$ $W^{-1}$. Broader wavelength range, 1530-1600 nm, was recently reported in ref. [10].

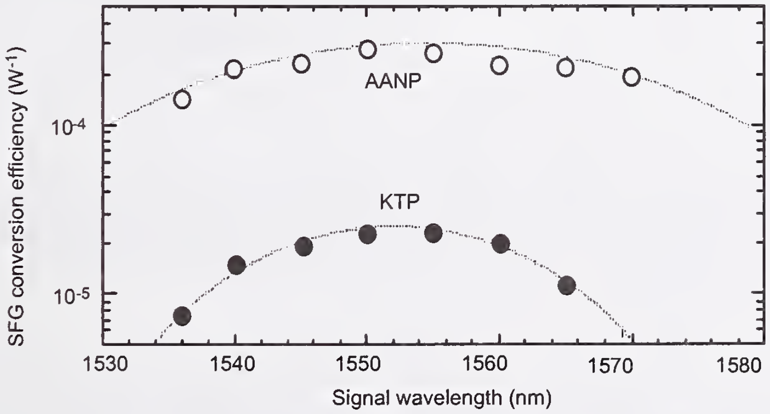

Fig. 5 SFG efficiencies of AANP crystal and KTP crystal

With these improvements, SNR values greater than 20 dB can be obtained, and the optical sampling system can produce high-speed TDM signal eye-diagrams.

Figures 6 (a)-(c) show the waveforms of the 100-Gbit/s optical signal as measured with electrical sampling (a 50-GHz bandwidth pin-photodiode + a 50-GHz bandwidth sampling oscilloscope), a streak camera, and optical sampling, respectively. With the electrical sampling method, the pulses of the 100-Gbit/s optical signal could not be resolved due to the system's limited temporal resolution (Fig. 6(a)). The streak camera could measure only averaged waveforms at 1.5 μm (Fig. 6(b)). In contrast, our optical sampling method accurately captured the 100-Gbit/s optical signal's eye-diagram (Fig. 6(c)).

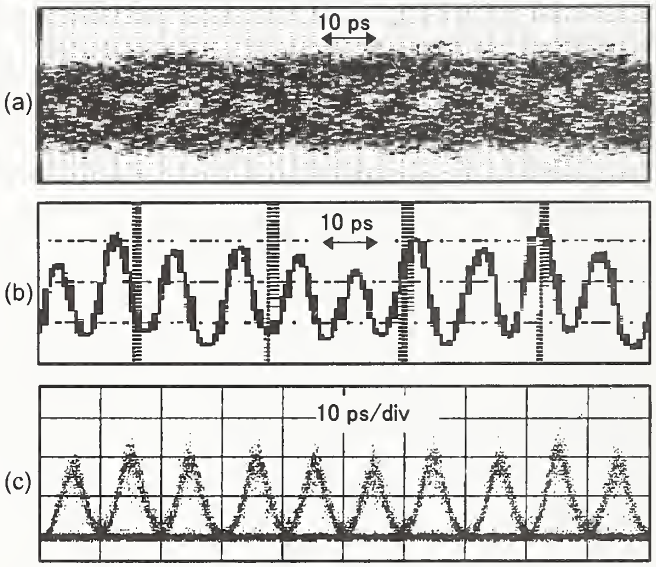

Fig.6 Measured 100 Gbit/s optical signal eye-diagram
(a) pin-photodiode + sampling oscilloscope
(b) streak camera
(c) optical sampling

## 5. Averaged Q-factor monitoring

The proposed optical sampling technique can also be used to monitor the optical signal quality in optical networks. We have investigated a simple, asynchronous sampling technique for averaged Q-factor measurement [11-13]. Its bit rate range is up to 160 Gbit/s, and asynchronous sampling allows bit-rate independent Q-factor monitoring [11, 14, 15].

A block diagram of the averaged Q-factor ($Q_{avg}$) measurement circuit using optical sampling is shown in Figure 7. The optical signal is received at the O/E converter after being sampled using a locally-configured short pulse generator. It is then launched into a signal processing circuit. The insets in Fig. 7 show a typical asynchronous eye-diagram and its amplitude histogram obtained by asynchronous optical sampling, which illustrates the principle of our method. Among the sampling points that constitute the histogram, we determined that the set of points whose level is higher than a predetermined threshold level, $\mu_{th1}$, belongs to level "MARK" (i.e., "1"), while the set of points whose level is lower than a predetermined threshold level, $\mu_{th0}$, belongs to level "SPACE" (i.e., "0"). We define $Q_{avg}$ by

$$Q_{avg} = | \mu_{1,avg} - \mu_{0,avg} | / (\sigma_{1,avg} + \sigma_{0,avg}) \qquad (2)$$

where $\mu_{i,avg}$ and $\sigma_{i,avg}$ are the mean and standard deviations of the MARK and SPACE levels distributions, respectively. The data obtained by asynchronous sampling includes unwanted cross-point data in the eye-diagram, which decreases the measured value of the averaged Q-factor. Thus, it is necessary to remove the cross point data. In this way, we set two threshold levels, $\mu_{th1} = \mu_1 - \alpha\mu$ and $\mu_{th0} = \mu_0 + \alpha\mu$; coefficient $\alpha$ is defined to lie between 0 and 0.5.

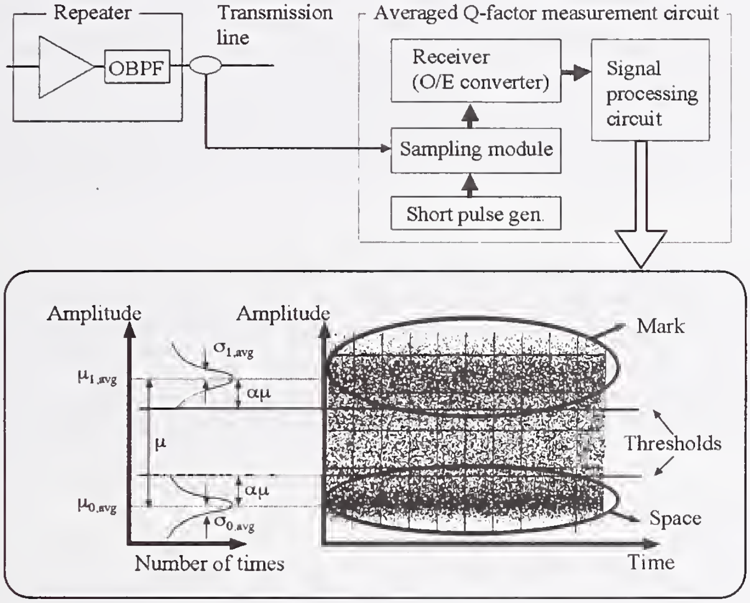

Fig. 7 Block diagram of averaged Q-factor measurement circuit, using optical sampling

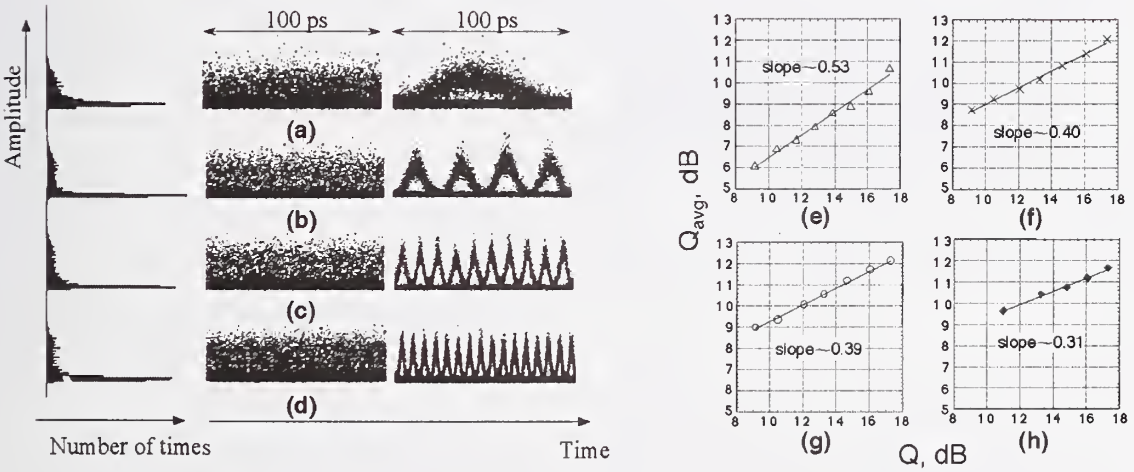

Fig. 8 Amplitude histograms (left), asynchronously measured eye-diagrams (middle) and synchronously measured eye-diagrams (right) ((a) 10-Gbit/s, (b) 40-Gbit/s, (c) 100-Gbit/s,(d) 160-Gbit/s RZ signal), Relationship between $Q_{avg}$ and $Q$ for (e) 10-Gbit/s, (f) 40-Gbit/s, (g) 100-Gbit/s, (h) 160-Gbit/s RZ signal.

Figures 8(a)-(d) show the eye-diagrams and amplitude histograms of the RZ optical signals where the BER equals $1 \times 10^{-10}$, as measured by optical sampling. The figures on the left show the amplitude histograms obtained from the asynchronous eye-diagrams. These eye-diagrams from (a) 10 Gbit/s to (d) 160 Gbit/s were measured by using the same averaged Q-factor monitoring circuit. The amplitude histograms show that high bit-rate signals, over 40 Gbit/s, can be easily processed by our method. Eye-diagrams recorded using conventional synchronous measurement are shown on the right for comparison. Figures 8(e)-(h) show the relationship between $Q_{avg}$ and $Q$ for the 10, 40, 100, and 160-Gbit/s RZ optical signals, respectively, when the signal SNR was changed. Coefficient $\alpha$ was set to 0.3. The figures show that the averaged Q-factor changes with $Q$ in each case. The maximum value of $Q$ in this experiment is 17.3 dB; therefore, we expect this method can be used for BERs better than $10^{-13}$. $Q_{avg}$ is strongly correlated to $Q$ at each bit rate, which shows that bit-rate flexible monitoring of the optical signal quality is achieved by this method. We can also obtain the BER by measuring the averaged Q-factor and by referring to Figs. 8(e)-(h). The reason why the slopes of the 40, 100, and 160 Gbit/s plots are lower than that of the 10 Gbit/s plot is probably due to the bit-by-bit pulse peak power fluctuation and to the differences in the bit-to-bit interference caused by waveform differences.

## 6. Summary

We have described an optical sampling technique for measuring optical waveforms with subpicosecond resolution. With this method, over 100 Gbit/s optical signals were successfully measured with 0.4 ps temporal resolution and more than 20 dB signal-to-noise ratio. We also introduced an optical signal quality monitoring method that uses asynchronous sampling. Bit-rate flexibility with 10 to 160 Gbit/s optical RZ signals was also demonstrated. This method is intrinsically flexible with respect to the signal format and modulation format. It is expected that this optical sampling technique will prove essential for future high-speed TDM systems.

## References

[1] S. Kawanishi et al., Tech. Dig. OFC'96, PD-24, 1996.
[2] T. Kanada et al., Opt. Lett., 11, pp. 4-6, 1986.
[3] H. Takara et al., Transactions of IEICE (B-1), J75-B-1, pp. 372-380 (in Japanese), 1992.
[4] B. P. Nelson et al., Electron. Lett., 27, pp. 204-205, 1991.
[5] P. A. Andrekson et al., Electron. Lett., 27, pp. 1440-1441, 1991.
[6] H. Takara et al., Electron. Lett., 30, pp. 1152-1153, 1994.
[7] H. Takara et al., Electron. Lett., 32, pp. 1399-1400, 1996.
[8] K. Mori et al., J. Opt. Soc. Am. B, 18, pp. 1780-1792, 2001.
[9] A. Yokoo et al, Journal of Crystal Growth, 156, pp. 279-284, 1995.
[10] A. Otani et al, OFC2001, WDD65, 2001.
[11] I. Shake et al., Electron. Lett., 22, pp. 2152-2154, 1998.
[12] I. Shake et al., Electron. Lett., 25, pp. 2087-2088, 2000.
[13] I. Shake et al., IEEE Photonics Tech. Lett., Vol. 13, No. 4, 2001.
[14] G. Bendelli, et al., ECOC2000, Vol. 4, pp. 113-116, 2000.
[15] C. M. Weinert, ECOC2000, Vol. 4, pp. 121-122.

# Frequency-controlled supercontinuum lightwave source applied to optical measurements with high frequency accuracy

Kunihiko Mori, Toshio Morioka, Atsushi Takada and Etsushi Yamazaki
NTT Network Innovation Laboratories, NTT Corporation
1-1 Hikari-no-oka, Yokosuka, Kanagawa, 239-0847 Japan
Phone: +81-468-59-4664, Fax: +81-468-59-3396, e-mail: morikuni@exa.onlab.ntt.co.jp

## Abstract

A frequency-controlled supercontinuum lightwave source with high frequency accuracy and stability is applied to optical measurements at a frequency spacing of 25 GHz, such as multi-carrier optical frequency sweep and calibration of linearity in optical spectrum analyzers.

## 1. Introduction

The recent progress of optical amplifiers such as S-band amplifiers [1] or fiber Raman amplifiers [2] has expanded the fronteer of optical transmission. Also, the progress of optical filtering devices such as arrayed-waveguide gratings has allowed dense WDM (wavelength-division-multiplexing) signals to be easily manipulated. For measurements and testing of these optical devices under development, multi-carrier optical sources with high accuracy and high stability are in increasing demand [3, 4, 5] which cover a wide range of wavelength and whose optical frequencies are well-aligned on the standardized optical frequency grid [6]. Using such multi-carrier optical sources, optical devices and equipments can easily be calibrated to be aligned to the optical frequency grid as a secondary optical multi-carrier standard.

Supercontinuum (SC) lightwave source is one of the promising solutions for such multi-carrier optical sources for measurements and testing which can emit a well-aligned optical frequency grid and can compactly be realized as is shown in Figure 1. The SC lightwave source has already been used to measure chromatic dispersions in optical fibers [10, 11]. For the demonstrations of high capacity dense WDM communication, the SC lightwave sources have been used to generate the well-aligned optical frequency grids with frequency spacings of 12.5 GHz [7], 25 GHz [8] and 50 GHz [9] by employing a mode-locked laser diode as a seed optical pulse source. These SC lightwave sources can also be used for optical frequency measurements by controlling wavelengths of their longitudinal modes. In this report, we present optical frequency domain measurements employing the SC lightwave source. Optical frequencies of longitudinal modes are manipulated by thermally controlling the optical frequency of the seed optical source. Two applications demonstrated are a multi-carrier optical frequency sweeper and calibration of linearity in optical spectrum analyzers.

Figure 1: The prototype of SC lightwave source with an optical frequency spacing of 25 GHz. Dimension: W43 x H13 x D48 (in centimeter)

## 2. Optical-frequency control of SC lightwave

A 25-GHz SC lightwave source consists of the following components: A mode-locked laser diode (ML-LD) with an average wavelength of 1538 nm (optical frequency: 194.9 THz) driven at frequency of 25 GHz was employed as a seed optical pulse source. A decreasing dispersion fiber with convex dispersion profile [12, 13] was employed as a SC generating fiber into which the amplified output of the ML-LD. An optical amplifier was employed for boosting the output of the ML-LD before the SC generating fiber. Figure 2 shows the output spectrum of the 25-GHz SC lightwave source. Optical signal-to-noise ratio defined as the visibility of longitudinal modes lay from 10 dB to 25 dB over the spectral range from 189 THz (1586 nm) to 199 THz (1507 nm).

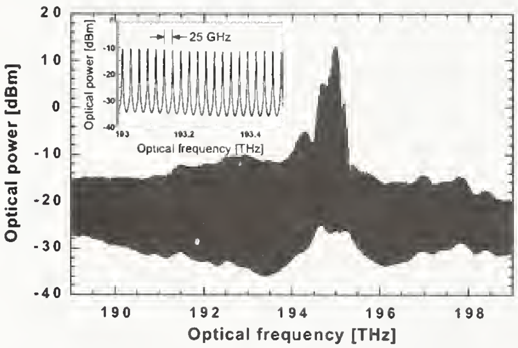

Figure 2: The spectrum of SC lightwave with an optical frequency spacing of 25 GHz. Frequency resolution is 2 GHz.

Figure 3 schematically illustrates the detection of frequency deviation of the SC frequency grid from the optical frequency standard. A beat signal is detected between the optical frequency standard $\nu_0$ and the nearest longitudinal mode in the SC lightwave. By controlling the beat frequency $f_B$, the whole longitudinal modes of the SC lightwave can be tuned that is realized by tuning optical frequencies of the longitudinal modes of the ML-LD output with its operation temperature. The frequency spacing of longitudinal modes can also be tuned within a detuning range of up to 100 MHz. As an anchor of optical frequency, an optical frequency standard source was employed which generates the optical frequency fixed at $\nu_0$ = 193.1000 THz (1552.524 nm) and guarantees a frequency accuracy of ±10 MHz and a frequency stability within 0.4 MHz. When optical frequency control was active, the temperature of ML-LD was adjusted so that the beat frequency $f_B$ matched the target frequency. Figure 4 shows the stabilization of optical frequency of the SC lightwave by thermal control of the ML-LD. With the optical frequency control, the fluctuation of the beat frequency $f_B$ was suppressed with a standard deviation of 5.0 MHz for 2 hours. Without optical frequency control, the beat frequency drifted more than 100 MHz away from the target frequency of 1 GHz. The relative frequency accuracy of longitudinal modes with respected to the optical frequency standard in the SC grid depends on that of the beat frequency $f_B$ and degrades proportional to the absolute value of mode number N.

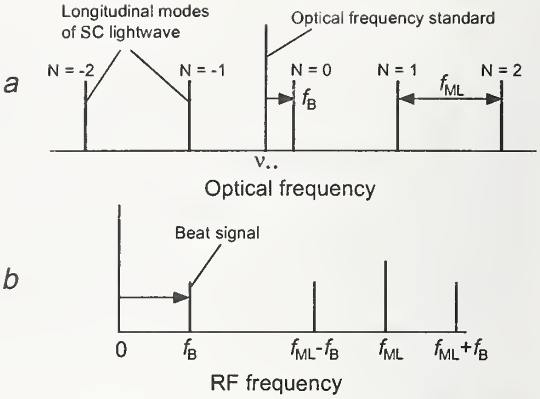

Figure 3: Schematic illustration of anchoring of longitudinal modes of SC lightwave. *a*: optical spectrum, *b*: RF spectrum. $\nu_0$: optical frequency standard, $f_{ML}$: frequency spacing of SC lightwave, $f_B$: beat frequency.

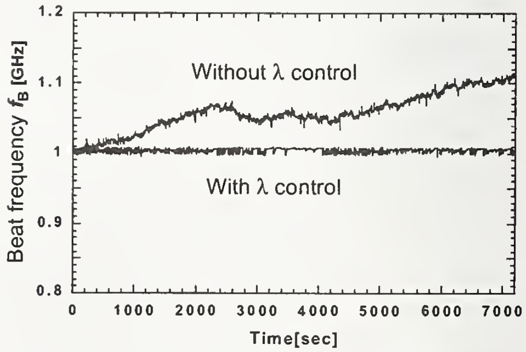

Figure 4: Frequency stabilization of SC lightwave.

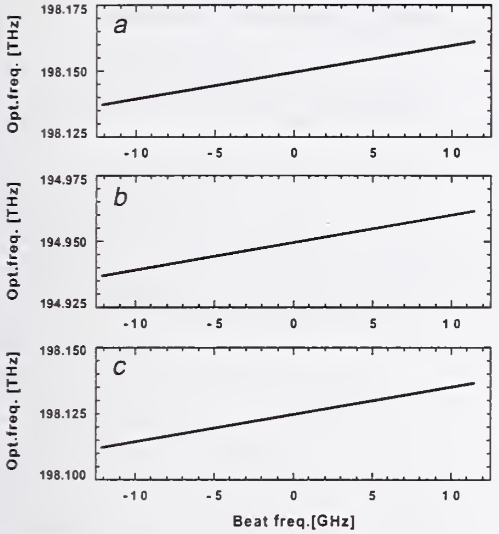

Figure 5: Measured optical frequencies in the SC lightwave when varing the beat frequency $f_B$. Mode numbers: *a*: N = 202, *b*: N = 74, *c*: N = -199.

## 3. Multi-carrier optical frequency sweep

There can be two modes of manipulating optical frequencies of SC lightwave: (1) by shifting optical frequencies via changing operation temperature of ML-LD or (2) by expanding or shrinking frequency spacing via changing driving frequency of the ML-LD. Figure 5 shows the measured optical frequencies when varing beat frequency $f_B$. Figure 6 shows the measured optical freqencies when varing the driving frequency $f_{ML}$ of ML-LD. The longitudinal mode nearest to $\nu_0$ was adjusted to be fixed at $\nu_0 + f_B$ as a mode number N = 0. The mode number of SC lightwave can be obtained by calculating the slope of the graph.

## 3. Frequency calibration of optical spectrum analysers

Using the optical frequency grid generated from the SC lightwave source, optical spectrum analyzer can easily be calibrated. Figure 7 shows characterization of optical frequency accuracy for two models of optical spectrum analyzers. Optical frequency deviations from the SC grid were measured over the spectral range from 186 THz (1611 nm) to 203 THz (1476 nm). Model *a* shows a uniform deviation within 5 GHz over the entire range measured, while model *b* shows a large deviation at optical frequencies of more than 198.8 THz (1508 nm).

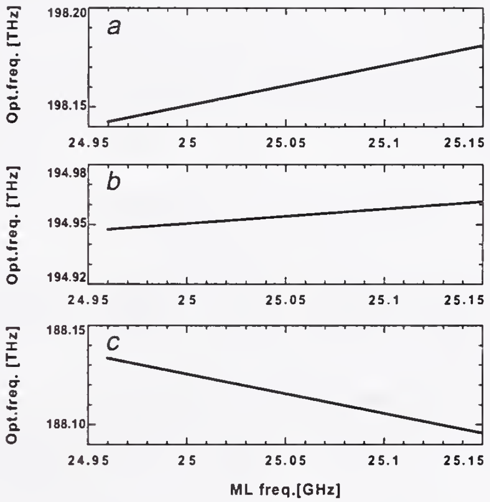

Figure 6: Measured optical frequencies in the SC lightwave when varing the driving frequency of ML-LD. Mode numbers: *a*: N = 202, *b*: N = 74, *c*: N = -199

## 4. Conclusion

Frequency-controlled supercontinuum lightwave source for optical measurements with high frequency accuracy and stability was presented. Stability of optical frequency of thermally stabilized SC lightwave with a frequency spacing of 25 GHz was achieved to be 5.0 MHz. Applications were demonstrated as multi-carrier optical frequency sweep and calibration of optical spectrum analyzers.

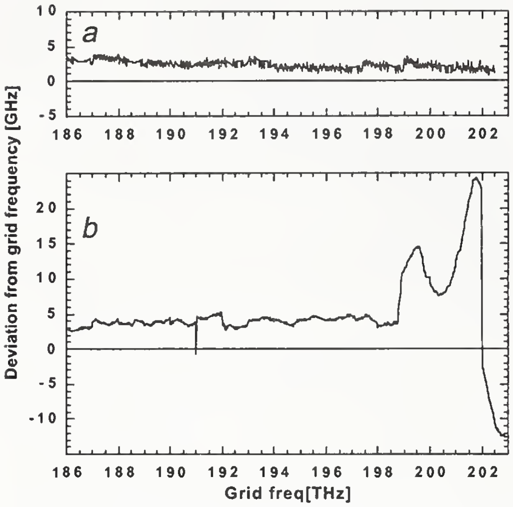

Figure 7: Characterization of linearity in optical frequency for two models of optical spectrum analyzers.

## References

[1] S. Aozasa, H. Masuda, H. Ono, T. Sakamoto, T. Kanamori, Y. Ohishi and M. Shimizu, "1480-1510 nm-band Tm doped fiber amplifier (TDFA) with a high power conversion efficiency of 42Proc OFC2001, PD1 (2001).

[2] M. Nissov, C. R. Davidson, K. Rottwitt, R. Menges, P. C. Corbett, D. Innis and M. S. Bergano, "100 Gb/s (10 × 10Gb/s) WDM transmission over 7200 km using distributed Raman amplification," Proc. ECOC'97, vol. 5, pp.74-76 (1997).

[3] L. Hollberg, C. W. Oates, E. A. Curtis, E. N. Ivanov, S. A. Diddams, Th. Udem, H. G. Robinson, J. C. Bergquist, R. J. Rafac, W. M. Itano, R. E. Drullinger and D. J. wineland, "Optical frequency standards and measurements," IEEE J.Quantum Electron., vol.37, pp.1502-1513 (2001).

[4] R. Holzwarth, Th. Udem, T. W. Hänsch, J. C. Knight, W. J. Wadsworth and P. St. J. Russel, "Optical frequency synthesizer for precision spectroscopy," Phys. Rev. Lett. vol.85, pp.2264-2267 (2000).

[5] S L. Gilbert, S. M. Etzel and W. C. Swann, "Wavelength accuracy in WDM: Techniques and standards for component characterization," Proc. OFC2002, THC2, pp.391-393 (2002).

[6] ITU-T Recommendation G.694.1, "Spectral grids for WDM application 1: DWDM frequency grid," Geneva, May, 2002.

[7] H. Takara, T. Ohara, K. Mori, K. Sato, E. Yamada, K. Jinguji, Y. Inoue, T. Shibata, T. Morioka and K-I. Sato, "More than 1000 channel optical frequency chain generation from a single supercontinuum source with 12.5 GHz channel spacing," Electron. Lett., vol.36, pp.2089-2090 (2000).

[8] E. Yamada, H. Takara, T. Ohara, K. Sato, T. Morioka, K. Jinguji, M. Itoh and M. Ishii, "150 channel supercontinuum CW optical source with high SNR and precise 25 GHz spacing for 10 Gbit/s DWDM systems," Electron. Lett., vol.37, pp. 304-306, (2001).

[9] H. Takara, H. Masuda, K. Mori, K. Sato, Y. Inoue, T. Ohara, A. Mori, M. Kohtoku, Y. Miyamoto, T. Morioka and S. Kawanishi, "Ultra-wideband tellurite/silica fiber Raman amplifier and supercontinuum lightwave source for 124-nm seamless bandwidth DWDM transmission," Proc. OFC 2002, FB1 (2002).

[10] K. Mori, T. Morioka and M. Saruwatari, "Group velocity dispersion measurement using supercontinuum picosecond pulses generated in an optical fibre," Electron. Lett., vol.29, pp.987-988 (1993).

[11] K. Mori, T. Morioka and M. Saruwatari, "Ultrawide spectral range group-velocity dispersion measurement utilizing supercontinuum in an optical fiber pumped by a 1.5 $\mu m$ compact laser source," IEEE Trans. Instrumentation and Measurement, vol.44, no.3, pp.712-715 (1995).

[12] K. Mori, H. Takara, S. Kawanishi, M. Saruwatari and T. Morioka, "Flatly broadened supercontinuum spectrum generated in a dispersion decreasing fibre with convex dispersion profile," Electron. Lett., vol.33, pp.1806-1808 (1997).

[13] K. Mori, H. Takara and S. Kawanishi, "Analysis and design of supercontinuum pulse generation in a singlemode optical fiber," J. Opt. Soc. Am. B, vol.18, pp.1780-1792 (2001).

# Recent developments of excited-state optical frequency standards for telecommunications

**D A Humphreys, C Campbell, F Bernard and P Patel:** *National Physical Laboratory, Queens Road, Teddington, Middlesex, TW11 0LW, UK.*

## Abstract

Optogalvanic transitions in metal vapour falling close to the ITU grid in L-band are reported and a portable saturated optogalvanic reference standard based on the Krypton transition at 1582.441 nm is described. This work is part of the Certified Reference materials for wavelength standards (CREW) European Community project.

## Introduction

High accuracy optical frequency references are required to support the continuing development of dense wavelength division multiplex (DWDM) systems. For operation at spacings of 50 GHz or less, some form of active reference is essential. Local references such as etalons and filters are commonly used. However, in some designs it is possible to lock to an adjacent channel in error. Molecular absorptions or excited-state optogalvanic transitions can be used to provide a local absolute reference. Many of the available lines will be inconveniently placed for the ITU grid. It is possible to synthesise lines close to the ITU grid by four-wave mixing[1] but this adds additional complexity. If the reference material is correctly chosen, it should also be possible operate within the transmission system tolerances.

DWDM component manufacture also requires high measurement accuracy. This is often achieved using wavelength meters. Although these instruments are predominantly based on the Michelson Interferometer, and contain an internal reference, they still require calibration to correct for systematic errors, such as optical alignment and reference stability.

Molecular absorptions and excited-state transitions are being studied for this application as part of the Certified Reference materials for wavelength standards (CREW) project[2].

## Metal vapour lines

Noble gasses are normally used for excited-state transitions. These can be operated at low currents, extending the cell life to several years, and the transitions can be saturated at modest optical powers. However, by operating the cell at high currents, (5-15) mA, it should also be possible to access metal vapour lines by sputtering material from the electrodes. This approach increases the number of lines available but at the expense of the cell lifetime.

**Table 1 L-Band metal-vapour excited-state optogalvanic transitions**

| Element | Wavelength, nm | Frequency, GHz | Difference from ITU 50 GHz grid, GHz |
|---|---|---|---|
| Cd | 1571.6128 (2) | 190754.636 (24) | 4.636 (24) |
| Mg | 1577.0147 (2) | 190101.217 (21) | 1.217 (21) |
| Mg | 1575.3294 (2) | 190304.597 (24) | 4.597 (24) |

In a previous paper[3], a number of possible elements were proposed, based on their emission spectra. Experimental results using cells with magnesium and cadmium electrodes have shown encouraging results. Measurements have been made using a wavelength meter to measure the optogalvanic transitions and $^{13}C_2H_2$ lines as a reference. The results are given in Table 1.

## *Portable Kr saturated reference*

Saturated optogalvanic transitions have been reported by a number of authors[4, 5]. At NPL, we have achieved saturation of a number of L-band and C-band transitions[6], at powers of < 10 mW, which is within the powers achievable from a DFB laser. In these experiments the laser was frequency modulated (123 Hz) and a chopper (1.5 kHz) was used to distinguish between the unsaturated and saturated signals. The signal processing required two cascaded lock-in amplifiers and this placed restrictions on the laser modulation rate and the chopper speed so that the filtering of the first instrument's output stage had sufficient bandwidth to accommodate the optical signals. A new approach, using a complex interrogation waveform, has been adopted as it gives considerable design flexibility. The principle of operation is shown in Figure 1. The laser modulation frequency was 5 kHz, with a chopper frequency of 330 Hz.

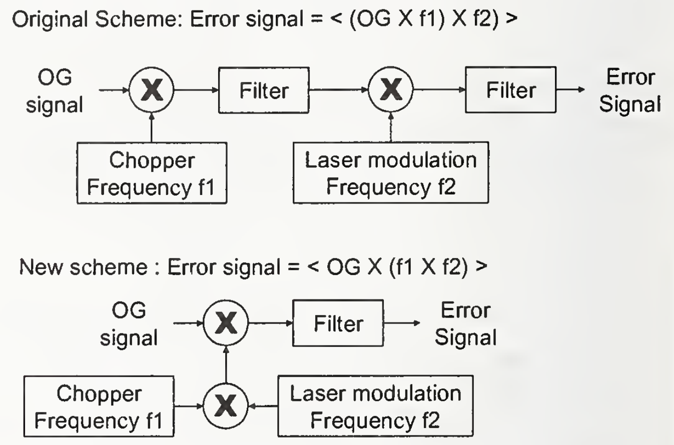

**Figure 1 Signal processing to recover the saturated signal**

A DFB laser can be tuned over (1-2) nm and modulated at much higher speeds, offering considerable design flexibility. The DFB lasers used in the experimental work can be tuned at approximately 10 GHz/C. However, this gives a separate problem because temperature stabilities in the milli-kelvin range are required to achieve accuracies of a few MHz. The width of the saturated dip at the turning points is about 220 MHz. Within this region the loop is stable and will close on the centre of the dip. However, outside this region, the error signal has the opposite slope and gives positive feedback, driving the system out of lock. Additional heat or cold input can throw the control loop out of lock and so to reduce the temperature sensitivity, the laser is thermally insulated and mounted on a metal block to increase the thermal mass.

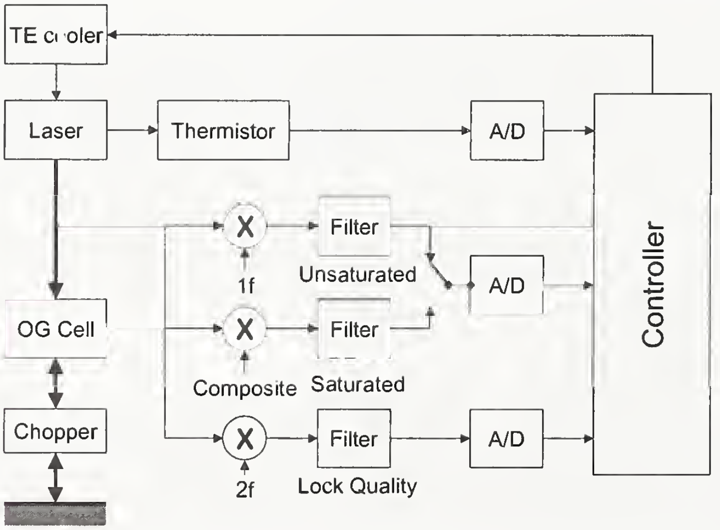

**Figure 2 Block diagram of portable optogalvanic reference**

The instrument is controlled by a microcomputer that stabilises the laser temperature and searches for the transition. Once the lock has been acquired under unsaturated conditions, the control loop is switched to the saturated path. If lock is lost, the control program reverts to the unsaturated lock as this has a wider capture range. If the lock has been lost irrecoverably, then the software will scan the laser across a range of wavelengths to reacquire the signal.

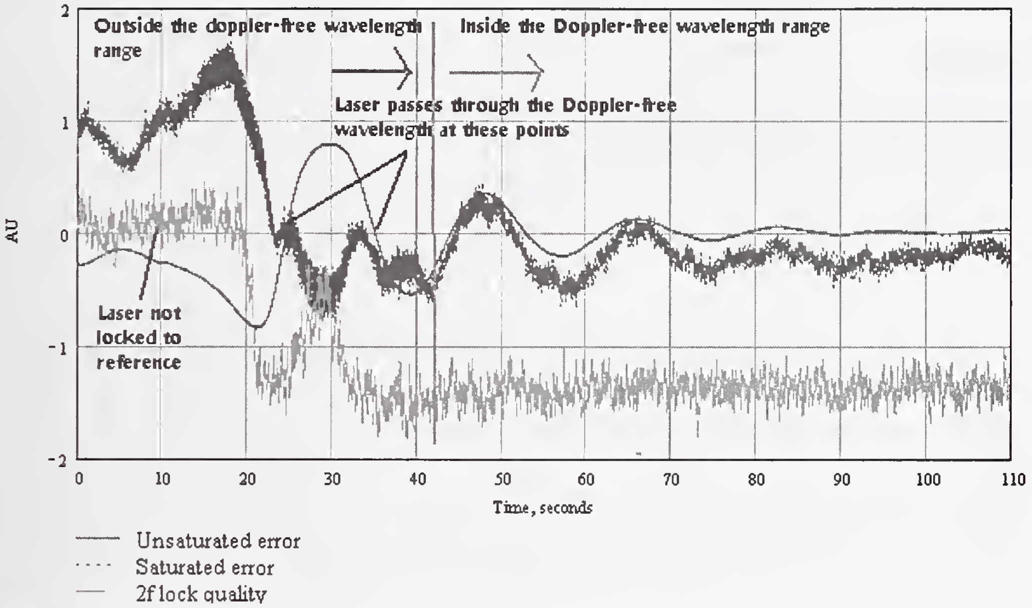

Figure 3 Evolution of error and lock quality signals during the locking process

The saturated signal and locking process can be seen in Figure 3. At the start of the trace, the laser wavelength oscillates through the transition and the slope of the Doppler broadened transition can be seen. As the loop closes, the oscillations fall within the Doppler free region and the slope of the error signal is opposite.

The electronics and optics have been designed so that the completed system can be housed in a compact unit (283 x 380 x 104) mm that is easily portable. By using the controller to search for and lock to the transition, the source is simple to use.

Figure 4 Portable locked saturated optogalvanic source and OSA

Measurements of the source wavelength have been made using two wavelength meters and an external cavity laser locked to $^{13}C_2H_2$ gas absorption lines as the reference. Eight acetylene lines were measured and the results give the frequency of the source as 189449.319 (26) GHz, this falls within the uncertainty bounds of the previous measurement. The dominant contribution to the uncertainty was the difference in the mean results for the two wavelength meters.

## Summary

A compact portable saturated optogalvanic source has been described. This system uses a novel signal processing approach to simplify the design. Preliminary measurement results for exited-state-metal vapour optogalvanic lines have also been presented.

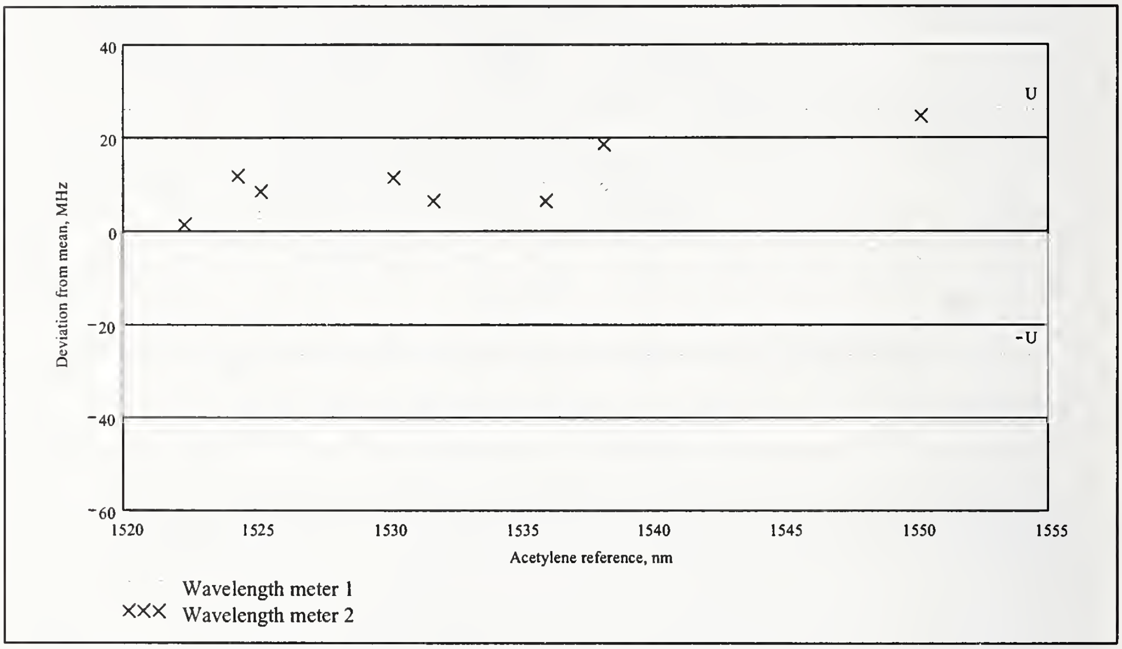

## Acknowledgements

The work is funded by the European Community within the 5th Framework GROWTH, generic activity "Measurement and Testing", dedicated call "Certified Reference Materials", under contract no. G6RD-CT-2001-00425 and by the UK Department of Trade and Industry National Measurements Programme.

## References

---

[1] D A Humphreys: ‘Synthesis of optical frequencies by four-wave mixing in optical fibre’, pp. 69-72, OFMC 2001, Cambridge, UK, September 2001.

[2] E.G. Grosche et al.: ‘Certified Reference Materials for Optical Telecommunication Wavelengths’, OFMC 2001.

[3] David A Humphreys, Colin Campbell: ‘Preliminary results of L-band exited-state optical frequency reference survey’, pp. 179-182, OFMC 2001, Cambridge, UK, September 2001.

[4] A. J. Lucero, Y. C. Chung, S. Reilly, and R. W. Tkach: ‘Saturation measurements of excited-state transitions in noble gases using the optogalvanic effect’, *Optics Lett.*, vol. 16, no. 11, pp. 849-852, 1991.

[5] U. H. P. Fischer and C. V. Helmolt: 'Saturation and Isotopic Shift of the Kr84 Excited-State Transition at 1547.825 nm',IEEE Photonics Technology Letters, **Vol. 7**,No. l, January 1995, p. 65.

[6] D A Humphreys :‘Saturated Optogalvanic transition in Krypton at 1564 nm’, pp. 25-28, SOFM 2000, Boulder, CO, USA, September 2000.

# FIBER BRAGG GRATINGS AS WAVELENGTH REFERENCES - DEVELOPMENT AND CHARACTERIZATION [λ]

**E.G. Grosche[1] and J. Meissner[2]**

[1] ***Physikalisch-Technische Bundesanstalt, Bundesallee 100, D-38116 Braunschweig, Germany***
***(gesine.grosche@ptb.de)***
[2] ***Advanced Optics Solutions, AOS GmbH, Ammonstraße 35, D-01067 Dresden, Germany***
***(meissner@aos-fiber.com)***

## ABSTRACT

Wavelength references for current and future DWDM systems require intermediate accuracy ($\Delta\lambda/\lambda \sim 10^{-6}$), wide wavelength coverage, flexibility, easy handling and strong contrast. We report on special fiber Bragg Gratings (FBGs), which show great potential as they can fulfill these requirements, and achieve adequate wavelength stability to complement fundamental references - especially outside the C-band. We present measurements of such FBGs, giving examples of SI-traceable characterization of both fundamental and artifact-based wavelength references, by using a custom-built large vacuum Fourier transform spectrometer.

## 1 INTRODUCTION

Fiber Bragg gratings have found wide-spread application in optical telecommunications. Due to the well-developed technology, their narrow spectral width, fiber compatibility and comparatively low cost, FBGs also show potential as cost-effective reference materials for optical wavelengths.

To increase the capacity of DWDM systems, in recent years the channel spacing has been decreased, and in addition the usable wavelength range is being extended from the C-band to other communication bands. Therefore, more stringent demands are now made on the wavelength accuracy of system components and measurement instrumentation, thus requiring accurate wavelength references, which also have to cover a larger wavelength interval.

For the C-band, well-established standardized reference materials based on molecular absorption are commercially available with wavelength uncertainty quoted to better than $10^{-6}$ [1]. Developments are underway to extend this to the L-band. Molecular references of similar accuracy are more difficult to realize for the L-band due to the small absorption strength of suitable molecules, such as carbon monoxide [2,3], and alternative fundamental references are also investigated [4].

Self-contained references e.g. for the calibration of optical spectrum analyzers should be compact, easy to handle (fiber-compatible) and feature a simple spectrum with good contrast, ideally displaying lines at ITU-T grid frequencies. For the $10^{-5}$-$10^{-6}$ accuracy class, FBGs may fulfill most of these requirements comparatively easily and allow reference wavelengths to be generated on the ITU-T grid, or indeed anywhere in any communication band, without reduced contrast.

## 2 FIBER BRAGG GRATING DESIGN

In their simplest form, the refractive index is modulated with period $\Lambda$ along the core of the fiber, resulting in a band stop in the spectrum, i.e. light around the wavelength $\lambda_{\text{Bragg}} = 2\, n\, \Lambda$, is reflected. Several FBGs with different Bragg wavelengths can be combined to produce a multi-wavelength reference. The main challenges for the use of FBGs as wavelength references are a) their sensitivity to environmental effects, such as mechanical strain and temperature and b) their comparatively large line-width. However, with special design and suitable packaging, one can overcome these difficulties.

---

[λ] This work is funded by the European Community as part of the project "CREW" (**C**ertified **Re**ference Materials for Optical Telecommunication **W**avelengths) under contract no. G6RD-CT-2001-00425 within the 5th Framework GROWTH, generic activity "Measurement and Testing", dedicated call "Certified Reference Materials".

### 2.1 Environmental effects

An unpackaged FBG typically shows a wavelength shift with ambient temperature of about 10 pm/K. We have achieved passive stabilization by mounting the FBG on a material of a suitable *negative* thermal expansion coefficient, so that the resulting stresses counteract the normal wavelength shift observed with temperature for a bare FBG. It was possible to reduce the net wavelength shift with temperature by one order of magnitude, from + 9pm/K to less than (-)1pm/K. Active stabilization on its own using a thermoelectric cooler (operative between about 5 and 50°C) has been found to achieve 0.1 K or better long-term stability. A combination of both techniques can thus be expected to keep wavelength drifts due to temperature changes below 0.1 pm long-term. This corresponds to a relative long-term stability of better than $7 \times 10^{-8}$.

### 2.2 Narrow line-width structures

The accuracy with which an FBG can represent a wavelength depends on the line-width or the filter *slope* of the spectral features generated by the Bragg grating structure. In contrast to molecular absorption lines with Doppler widths of only a few hundred MHz, commercial FBGs display typical line-widths larger 400 pm (50 GHz). For use as wavelength references we have obtained FBGs with a line-width of 200 pm (or 25 GHz, FWHM) and about 30% maximum reflectivity.

Even narrower spectral features can be obtained by introducing a phase shift of π into the FBG-structure. The resulting narrow transmission peak within the stop band can be extremely sharp: line-widths of less than 1pm (about 100 MHz) have been reported [5]. We believe that such FBGs have great potential as accurate wavelength references, and have produced narrow line-width FBGs in standard fiber featuring a narrow transmission peak within a wider stop-band by using the phase-shifting technique. Structure and theoretical spectrum are shown in figure 1.

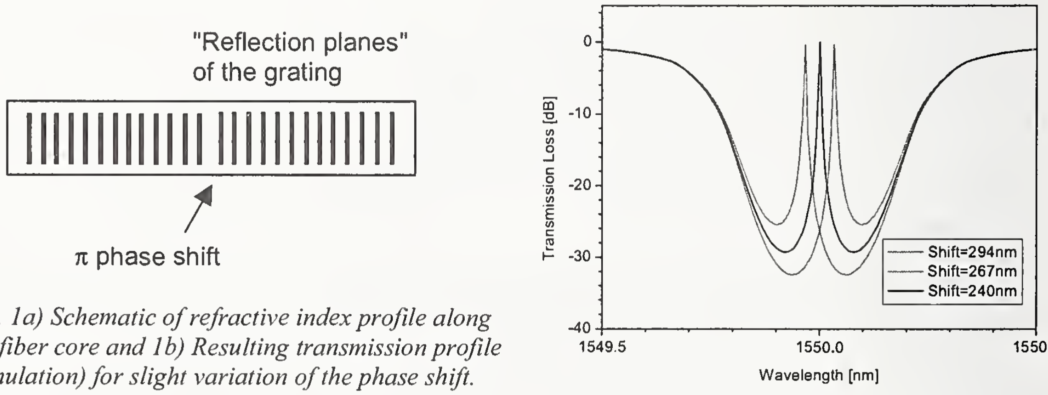

*Fig. 1a) Schematic of refractive index profile along the fiber core and 1b) Resulting transmission profile (simulation) for slight variation of the phase shift.*

## 3 CHARACTERIZATION AND TRACEABILITY

High-precision instrumentation providing traceability to the SI-unit of length is required to guarantee the wavelength accuracy of newly developed references. *Active* wavelength references, i.e. frequency stabilized lasers, are often characterized by performing beat measurements with established frequency standards. For visible wavelengths, where excellent frequency standards are available, such equipment can reach an accuracy better $10^{-9}$. With frequency doubling and the development of frequency combs, a wider wavelength range has also become accessible in the near-infrared.

To date, however, mainly *passive* wavelength references, in particular molecular absorption cells, have found widespread acceptance in the telecommunication community. In combination with broad band sources they allow simple multi-wavelength calibration of measuring equipment. Two possibilities for determining e.g. the transmission spectra of such wavelength references are a) using a tunable laser, detection system and high accuracy wavelength meter and b) an optical spectrum analyzers used with a broad band source.

We employ a custom-built vacuum wavelength meter based on a Michelson interferometer with maximum 1.8 m mirror movement and incorporating an iodine-referenced, stabilized HeNe laser as reference [6]. The instrument can give wavelength readings that are traceable to the SI-unit meter and for its operation as a wavelength meter we estimate an absolute accuracy of about $10^{-9}$, which is supported by measurements in the near infrared [7]. This instrumentation has recently been adapted to operate as a Fourier transform spectrometer. Thus directly SI-traceable measurements of new wavelength reference materials become possible across a wide wavelength range.

### 3.1 Spectral characterization of narrow line-width FBG

The FBG reflects light only in the narrow spectral region of interest. By using a broad-band source and measuring the reflected intensity of the FBG, we obtain an almost background free signal. From this, the transmission spectrum is calculated. Fig. 2 shows measurements of a FBG with phase-shift structure, obtained with a) a commercial tunable laser and wavelength meter and b) our system, consisting of a broadband ASE-source, optical isolator, fiber optic couplers, the device under test (FBG) and our Fourier transform spectrometer. We note the narrow transmission peak as predicted by theory and the excellent agreement of the spectral shape between the two measurements. We also point out the significant frequency off-set of about 7 GHz between the two results: this is attributed predominately to the device-under-test itself, being a bare FBG which was measured at ambient temperatures of 25°C and 20°C respectively.

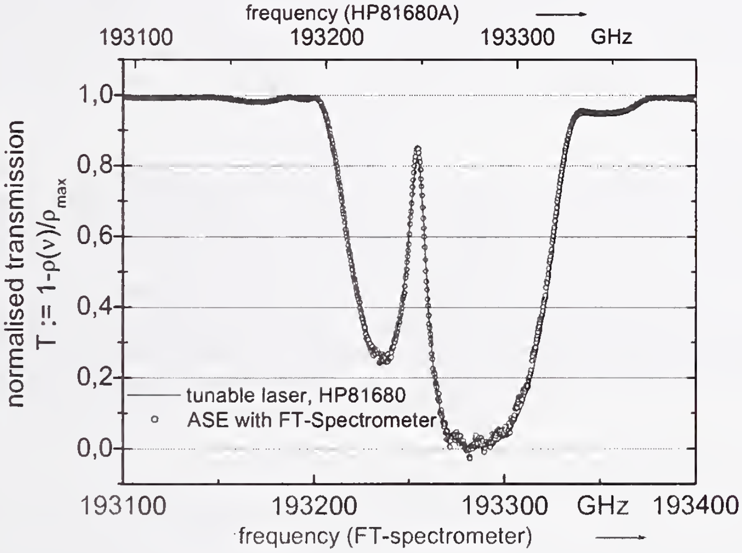

*Fig. 2. Transmission spectra obtained from measured reflectance ρ for a bare FBG incorporating a phase-shift to generate a narrow transmission peak (line-width < 10 GHz) within the band-stop. Measurements taken by a) commercial system with tunable laser (resolution 2 pm, FBG at a temperature of 25°C) and b) custom-built high resolution FT-spectrometer, using ASE broadband source (FBG at approx. 20°C).*

### 3.2 Absorption spectrum of acetylene

To verify our instrumentation we have tested it using the currently best-characterized multi-line reference available around 1.54 μm: we have measured absorption spectra arising from the rotational-vibrational combination transitions in $^{13}C_2H_2$ (acetylene). A large number of lines for the $\nu_1+\nu_3$ band have been analyzed by laser spectroscopy in the low pressure limit and are tabulated in [8] with an accuracy of $10^{-9}$. One limiting factor for absolute frequency references based on molecular absorbers is the pressure dependence, as collisional frequency shifts and broadening of absorption lines occur. We have used cells containing $^{13}C_2H_2$ at a pressure of 50 Torr (66mbar) and 200 Torr (266 mbar) respectively, so we also obtain information about these pressure effects.

A typical spectrum covering some 30 nm and obtained at a resolution of 300 MHz is shown in figure 3a. We note the overlapping bands. Figure 3b illustrates the effect of pressure broadening: We have obtained line center frequencies for a set of lines in the $\nu_1+\nu_3$ band of $^{13}C_2H_2$ at both 50 Torr and 200 Torr. Comparison to the published values in [8] gives very good agreement, indicating that our measurement uncertainty is better than $10^{-7}$ for the center wavelength, and is dominated by influences due to interfering nearby lines. We also deduce a significant dependence of the pressure shift on the rotational quantum number of the initial state, similar to findings by [2,3] and [9].

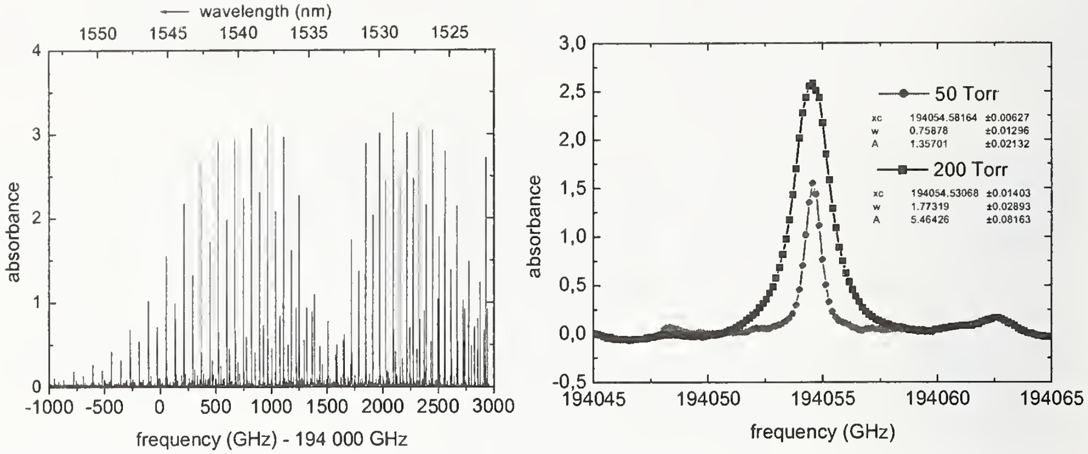

*Figure 3a, 3b: Absorption spectrum of* $^{13}C_2H_2$ *near 1,54µm obtained by Fourier transform spectroscopy: overview spectrum showing overlapping bands* ($\nu_1+\nu_3$ *and* $\nu_1+\nu_2+\nu_4+\nu_5$)*, and b) effect of pressure broadening, exemplified for line P(20) of the* $\nu_1+\nu_3$ *band.*

## 4 CONCLUSIONS

We have described the requirements, development and characterization of wavelength references for modern Dense Wavelength Division Multiplexing (DWDM) systems. Man-made artifacts, such as fiber Bragg gratings (FBGs) can be cost-effective, robust and easy to handle, while offering wide wavelength coverage and strong contrast. Special fiber grating structures make devices with a relative wavelength uncertainty in the part per million range feasible. For the development, characterization and eventual certification of narrow spectral filters we employ a self-built large vacuum Michelson interferometer, originally designed as a wavelength meter. This instrument has been adapted to also operate as a Fourier transform spectrometer and allows SI-traceable high resolution measurements of new wavelength reference prototypes.

## 5 ACKNOWLEDGEMENT

We thank Uwe Sterr and Peter Weßelhöft for generous technical support.

## 6 REFERENCES

1. S. L. Gilbert and W. C. Swann: "Acetylene $^{12}C_2H_2$ Absorption Reference for 1510-1540 nm Wavelength Calibration - SRM 2517", *NIST Spec. Publ.* 260-133 (1997); S. L. Gilbert, W. C. Swann and C.-M. Wang: "Hydrogen Cyanide $H^{13}C^{14}N$ Absorption Reference for 1530-1560 nm Wavelength Calibration - SRM 2519", *NIST Spec. Publ.* 260-137 (1998)
2. W.C. Swann and S.L.Gilbert: "Wavelength Calibration Standards for the WDM L-Band" *Conference Digest of 6th Optical Fibre Measurement Conference,* 26-28.09.2001 Cambridge (UK), 175-178.
3. J. Henningsen, H. Simonsen, T. Mogelberg and E. Trudso: "The 0->3 Overtone Band of CO: Precise Linestrengths and Broadening Parameters", J. of Mol. Spectr. **193**, 354-362 (1999)
4. E.G. Grosche et al.: "Certified Reference Materials for Optical Telecomm. Wavelengths", *Conference Digest of 6th Optical Fibre Measurement Conference*, 26-28.09.2001 Cambridge (UK), 289-192.
5. J. Canning and M.G. Sceats: "π-phase-shifted periodic distributed structures in optical fibres by UV post-processing", Electr. Lett. **30** (16), 1344-1345, (1994).
6. U. Sterr et al.: "A high accuracy Fourier transform wavelengthmeter", in preparation.
7. J. Stenger, C. Tamm, N. Haverkamp, S. Weyers and H.R. Telle: "Absolute frequency measurement of the 435.5 nm $^{171}Yb^+$-clock transition with a Kerr-lens mode-locked femtosecond laser", *Opt. Lett.* **26** (20), 1589 (2001)
8. K. Nakagawa, M. deLabachelerie, Y Awaji, M. Kourogi: "Accurate optical frequency atlas of the 1.5 µm bands of acetylene", *J. Opt. Soc. Am. B* **13** (12), 2708-2714, (1996)
9. M. Kusaba and J.Henningsen: "The $\nu_1+\nu_3$ and the $\nu_1+\nu_2+\nu_4+\nu_5$ combination bands of $^{13}C_2H_2$. Line strengths, broadening parameters and pressure shifts", J. Mol. Spec. (in press)

# SIMULTANEOUS MEASUREMENT OF TRANSVERSE STRAIN AND TEMPERATURE USING FBG WRITTEN IN HIBI FIBER

I. Abe[a,c], M. W. Schiller[c], R. Nogueira[a,b], P. Lopes[a], O. Frazão[d], J. L. Santos[d],
J. L. Pinto[a,b] and H. J. Kalinowski[c]

[a]Departamento de Física, Universidade de Aveiro and
[b]Instituto de Telecomunicações - Polo de Aveiro, 3810-193 Aveiro, Portugal
[c]Centro Federal de Educação Tecnológica do Paraná, 80230-901 Curitiba, Brasil.
[d]INESC Porto, Rua Campo Alegre, 687, 4169-007 Porto, Portugal

e-mail: ilda@fis.ua.pt

## Abstract

Fiber Bragg grating (FBG) written in high-birefringence (HiBi) fibers for the simultaneously determination of transversal strain and temperature have been studied. The sensor is based on the monitoring of a complex spectrum resulting from the transversal load applied to the fiber. This work describes the characterization of the sensor with the variation of the applied load and temperature. The results obtained enable the simultaneous characterization of these two variables.

## Introduction

Fiber Bragg grating sensors are generally based on a unique grating written in a standard fiber optic. The wavelength shift in the reflection spectrum peak of these sensors may be used to measure a single component of strain or temperature variation, but not both simultaneously [1].

Various sensors have been demonstrated for the simultaneous measure of longitudinal strain and temperature: by using two overlaid gratings in different wavelengths [2], with two different types of sensors (Bragg gratings and polarization-rocking filters) [3], using gratings written in fibers with different diameters [4] or using a Bragg grating based Fabry-Perot cavity [5].

FBGs written in high birefringence (HiBi) fibers are being studied as a means to determine strain along different axis, and temperature simultaneously [6,7]. In this work we analyze the complex spectral response of FBG written in HiBi fiber for determination of transversal strain and temperature. Many applications based on embedded sensors may benefit from a sensor capable of measuring temperature and transversal load components simultaneously.

## Sensor description

In HiBi fibers, regions with high thermal expansion coefficients induce mechanical stress in the core. Due to the birefringence induced by the intrinsic stress, the X and Y polarizations of the $LP_{01}$ mode are now split and have each one different effective index. These linear polarizations are the slow (axis Y) and fast (axis X) modes associated to the main axes of the fiber (Fig.1). The reflection spectrum of FBG written in HiBi fibers, with non-polarized light injected into the fiber, has a two-peak structure corresponding to the two orthogonal polarization modes of the fiber. Fig.1 shows a diagram of a FBG written in a HiBi fiber with Internal Elliptical Cladding (IEC). The axis X, Y and Z are the coordinate system of the fiber.

One of the characteristics of the fibers written in HiBi fibers is their spectral response to an applied transversal load. Due to the non-homogeneous structure of the fiber, the internal stress variations and, consequently, the deformation to each one of the main axes of the fiber will be different [8].

If a load is applied to one of the main axes X or Y, it should lead to a variation in the respective band in the reflection spectrum of the grating. However, the band associated to the other axis will have a lower variation [8]. With a transverse load, the peak separation will increase.

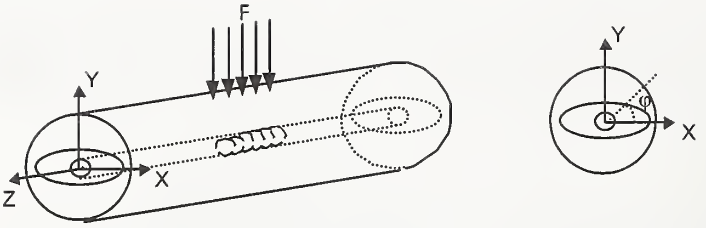

Figure 1 – FBG written in IEC HiBi fiber

The stress-strain relationship, for completely diametric load (applied force F during the length L of the grating) over a fiber with circular profile and considering a plane-stress, may be written as [9,10]

$$\varepsilon_Y = -2\frac{F}{Y\pi rL} \tag{1}$$

where r is the core radius (125 $\mu$m), and Y the Young's modulus (for glass Y= $69\text{x}10^9$ N/$m^2$).

The wavelength change, in the reflection spectrum of the sensor, due to a temperature variation $\Delta T$ and a strain $\Delta\varepsilon_Y$, is, for each axis,

$$\Delta\lambda_Y = \frac{\partial\lambda_Y}{\partial T}\Delta T + \frac{\partial\lambda_Y}{\partial\varepsilon}\Delta\varepsilon_Y \tag{2}$$

$$\Delta\lambda_X = \frac{\partial\lambda_X}{\partial T}\Delta T + \frac{\partial\lambda_X}{\partial\varepsilon}\Delta\varepsilon_Y \tag{3}$$

where $\partial\lambda_Y/\partial T$ and $\partial\lambda_X/\partial T$ are the temperature variation coefficients and $\partial\lambda_Y/\partial\varepsilon$ and $\partial\lambda_X/\partial\varepsilon$ are the deformation coefficients. The expressions (2) and (3) can be rearranged and written in matrix form in order to calculate the transverse strain and temperature, given the measured wavelength shifts:

$$\begin{bmatrix} \Delta T \\ \Delta\varepsilon_Y \end{bmatrix} = K^{-1}\begin{bmatrix} \Delta\lambda_x \\ \Delta\lambda y \end{bmatrix} \tag{4}$$

where K is a non-singular matrix given by,

$$K = \begin{bmatrix} \frac{\partial\lambda_x}{\partial T}, \frac{\partial\lambda_x}{\partial\varepsilon} \\ \frac{\partial\lambda_y}{\partial T}, \frac{\partial\lambda_y}{\partial\varepsilon} \end{bmatrix} \tag{5}$$

## Simultaneous measurement of transverse strain and temperature

The FBGs have been written in HiBi fibers using a phase mask illuminated by UV light (248 nm) [11]. The FBG has a length L=10 mm and a period of 535 nm. Fig.2(a) presents the reflection spectrum of a FBG written in an IEC fiber. The figure also displays the simulation spectrum based on the values of L and period [12]. The birefringence value obtained by simulation has been $6.7 \text{ x } 10^{-4}$.

The transversal load used for the sensor characterization has been performed by a micro-scratch mechanical system. The system uses an arm to apply a load with a precision of 0.1 N. The grating written in HiBi fiber has been placed between two plates having a length of 13mm. Two other fibers have been placed in parallel with the FBG to serve as a guide and then, the load has been applied by the arm to the upper plate.

The FBG has been previously characterized with several applied loads over different fiber angles $\varphi$. Fig.2(b) shows the reflection spectrum obtained with the pressure over the Y axis ($\varphi = 90^o$).

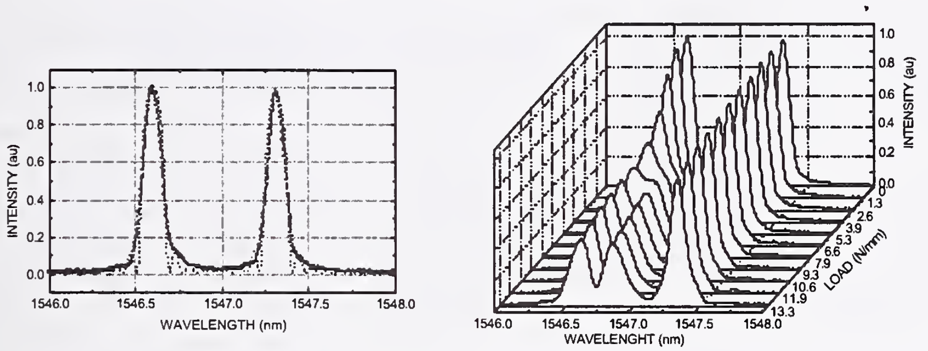

(a) (b)

Figure 2 – (a) Reflection spectrum of a FBG written in IEC fiber (solid line) and theoretical fitted bands (dotted lines)
(b) Spectral changes of the reflection spectrum for several applied loads. Applied angle $\varphi = 90^0$

The first band ($\lambda_Y$) has a strong spectral variation as the applied load increases, while the second band ($\lambda_X$) has only a slight change. This is due to the phase shift induced by the applied load. The phase shift effects are known to lead to spectral changes due to the corresponding change in the core refractive index [9]. The change occurs in the same spatial region where the grating is located (due to the position of the applied load), causing a phase shifting region superimposed to the Bragg gratings. The resulting complex structure is known to be responsible for spectral changes of Bragg gratings subject to mechanical stress.

The strain calibration line for the $\lambda_Y$ band has been obtained by identifying and measuring the several peaks (to a certain extent, then followed by depressions – Fig.2(b)) as a function of the applied load. Peaks have been observed from 0 to 3.9 N/mm, the turning point at 5.3 N/mm and depressions from 6.6 to 13.3 N/mm. Data has been acquired at a constant temperature of 21°C. The strain calibration lines are shown in Fig.3(a). The slopes for those lines have been evaluated as being equal to -0.00146 nm/ $\mu\varepsilon$ and -0.00021 nm/ $\mu\varepsilon$.

The cooling/heating system has been placed outside the holding plate of the fibers in order to avoid any influence from the applied strain. That system is composed of two thermoelectric coolers (TEC) controlled by a dedicated electronic circuit. The calibration lines for the temperature variation are shown in Fig.3(b). The obtained slopes have been 0.00676 nm/ °C and 0.00671 nm/ °C.

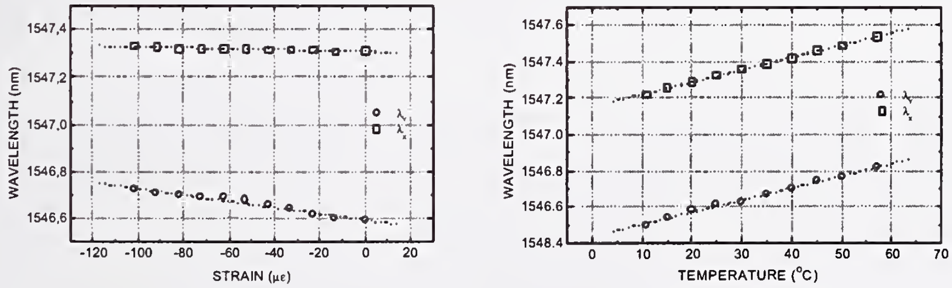

(a) (b)

Figure 3 – Variation of band peak with (a) strain and (b) temperature.

Measurements have been made with simultaneous variation of strain and temperature. The results have been obtained by spectral analysis and using the two slopes got from the separate experimental evaluation of peak wavelength dependence on strain and temperature. On Table 1, some of those measurements are shown.

Table 1 – Obtained results with simultaneous variation of strain and temperature

| T<br>$\varepsilon_Y$ | 12 °C | 23 °C | 31 °C | 46 °C |
|---|---|---|---|---|
| **-61 με** | 11.8 °C | 24.6 °C | 31.6 °C | 45.5 °C |
| | -65 με | -71 με | -70 με | -75 με |
| **-76 με** | 12.0 °C | 25.4 °C | 32.6 °C | 46.3 °C |
| | -69 με | -79 με | -73 με | -81 με |
| **-91 με** | 12.7 °C | 26.8 °C | 34.0 °C | 48.0 °C |
| | -76 με | -83 με | -78 με | -79 με |

The strain values have been evaluated with an error of ± 15 με for the interval between -61 and -91 με, while the temperature error has been estimated to be ± 4 °C for values from 12 to 46 °C.

## Conclusion

Simultaneous measurements of strain and temperature have been made possible and actually obtained in HiBi IEC fibers, by knowing in advance the calibration lines for the peak wavelength shift of the reflection spectrum, for strain and temperature, separately. The associated errors have been found to be ± 15 με and ± 4 °C, respectively.

## Acknowledgments

This work has been supported by CNPq, Fundação Araucária, CAPES (Brasil) and ICCTI (Portugal).

## References

[1] R. Kashyap, "Fiber Bragg Grating", San Diego, Academic Press, 1999.

[2] M. G. Xu, et. al., "Discrimination between strain and temperature effects using dual-wavelength fiber grating sensors", *Electronics Letters*, vol. 30, p. 1085, 1994.

[3] S. E. Kanellopoulos, et. al., "Simultaneous strain and temperature sensing with photogenerated in-fiber gratings", *Optics Letters*, vol. 20, nº.3, pp. 333-335, 1995.

[4] S. W. James, M. L. Dockney and R. P. Tatam, "Simultaneous independent temperature na strain measurement using in-fibre Bragg grating sensors", *Elec. Letters*, vol. 32, nº. 12, pp.1133-1134, 1996.

[5] W. C. Du, X. M. Tao and H. Y. Tam, "Fiber Bragg grating cavity sensor for simultaneous measurement of strain and temperature", *IEEE Photonics Technology Letters*, vol. 11, nº. 1, pp. 105-107, 1999.

[6] M. Sudo, et. al., "Simultaneous Measurement of Temperature and Strain using PANDA Fiber Grating", *12 th Int. Conf. on Optical Fiber Sensors, Technical Digest Series*, v. 16, pp. 170-173, 1997.

[7] C. M. Lawrence, D. V. Nelson and E. Udd, "Measurements of transverse strain with fiber Bragg gratings". *Proc. SPIE 3042*, pp. 218-228, 1997.

[8] I. Abe, R. Nogueira, B. W. Diesel, A. S. Ehlke, J. Tosin, P. S. André, J. L. Pinto and Hypolito J. Kalinowski, "Analysis of Bragg grating written in high birefringence fibre optics", Proc. 4th *International Conference on Photonics, Devices and Systems*, Prague, 2002.

[9] P.I. Torres, "Análise Teórica e Experimental de Aplicações de Redes de Bragg em Fibra Óptica", *Ph.D. Thesis*, Physics Department, Pontifical Catholic University of Rio de Janeiro, Brasil, 2002.

[10] R. Gafsi and M. A. El-Sherif, "Analysis of Induced-Birefringence Effects on Fiber Bragg Gratings". *Optical Fiber Technology 6*, pp. 299-323, 2000.

[11] F. M. M. Araújo, "Redes de Bragg em Fibra Óptica", *Ph.D. Thesis*, Department of Physics, University of Porto, Portugal, 1999.

[12] I. Abe, M. C. Fugihara, B. W. Diesel, R. C. Kamikawachi, J. L. Fabris, H. J. Kalinowski, C. L. Barbosa. "Modeling and Production of High Birefringence FOBG Sensors", *Proc. SPIE*, v.4419. pp.371-374, 2001.

# A Simple and Direct Method to Estimate Long Period Grating Parameters

K. Thyagarajan*, Mini Das and M. N. Satyanarayan
Department of Physics, Indian Institute of Technology, New Delhi-110016, India.

## Abstract

*We demonstrate a novel and simple technique to estimate the parameters of long period gratings (LPGs). It is shown that by measuring the diffraction pattern obtained by the side illumination of the fiber grating, we can estimate the grating period as well as the duty cycle. This technique can be used to characterize the LPGs fabricated by any method.*

## 1. Introduction

Long period fiber gratings (LPG) which have periodicity typically above 100μm find applications as wavelength filters, gain flattening components and sensors [1-3]. While the grating parameters of a fiber Bragg grating can be estimated from the reflectivity profile [4], the estimation of grating parameters from transmission spectra of LPG is not straight forward. Moreover the measurement of reflection or transmission spectra of these gratings requires sophisticated and expensive equipments. Estimation of Bragg grating parameters with sinusoidal refractive index modulation was done by Krug et.al,[5] where Bragg reflection of the probe beam at a suitable incidence angle was used to study the grating properties. In this paper we extend the method of Ref. [5] for the evaluation of the parameters of a long period grating.

## 2. Theory

Since fiber gratings are periodic modulations of refractive index along the length of the fiber, they behave as phase gratings when side illuminated by a light beam. Since LPGs have periods of 100 μm or above they behave as thin phase gratings. The refractive index modulation of the grating induces a transverse phase modulation on an incident light wave which then undergoes diffraction after emerging from the fiber. The Fourier Transform of the phase modulated wave emerging from the LPG gives an estimation of the diffraction pattern of the LPG.

As a specific example we consider a rectangular modulation of the refractive index such that each period $\Lambda$ comprises of two regions $l_1$ and $l_2 = \Lambda - l_1$. Thus the refractive index modulation may be described by:

$$\begin{aligned} n(z) &= n_0 + \Delta n & 0 < z < l_1 \\ &= n_0 & l_1 < z < \Lambda \end{aligned} \tag{1}$$

where Δn is the peak change in refractive index and $n(z+\Lambda) = n(z)$.In order to obtain the diffraction pattern we first make a Fourier expansion of Eq.1 and obtain

$$\delta n(z) = \Delta n\left[(l_1/\Lambda) + \left(\sum_{n=1}^{\infty}(2\Delta n/n\pi)(\sin(2n\pi\, l_1/2\Lambda)\cos(2n\pi\, z/\Lambda)\right)\right] \tag{2}$$

The phase of the plane wave incident normally on the fiber, $E_{in}(x=0) = E_0 \exp(i\omega t)$ gets periodically modulated and the wave emerging is given by

$$E_{out}(x=d) = E_0 \exp[i(\omega t - k_0 n(z) d)] = E_0 \exp[i(\omega t - k_0 n_0 d - k_o \delta n(z)\, d)] \tag{3}$$

where d is the fiber diameter and $\delta n(z)$ is given by Eq. 2.

The Discrete Fourier Transform (DFT) of Eq. 3 is found using the Fast Fourier Transform (FFT) algorithm to estimate the diffraction pattern.

Fig. 1(a)

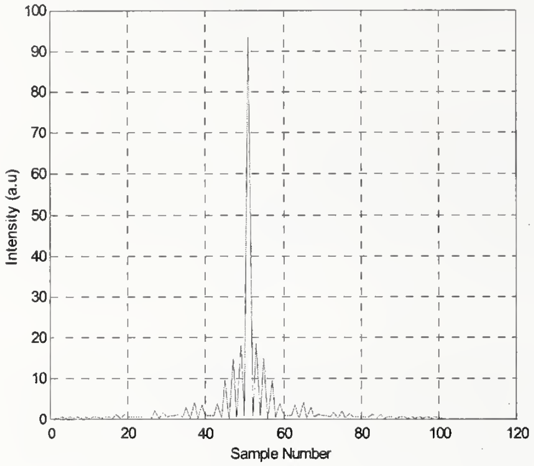

Fig. 1(b)

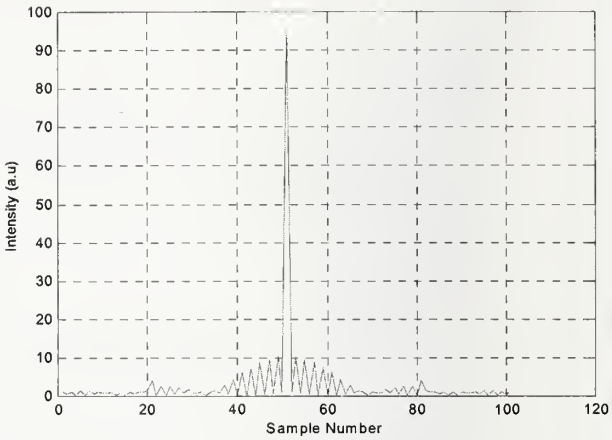

Figure 1(a) shows the numerically evaluated intensity distribution in the diffraction pattern of a grating with a rectangular refractive index modulation with Λ=50μm, $l_1$=10μm and $l_2$=40μm, and Fig. 1(b) corresponds to that for $l_1$=5μm, $l_2$=45μm, again with Λ=50μm. It can be seen that the fringe width (β) depends on Λ, while the position of the first zero of the envelope depends on the smaller of $l_1$ and $l_2$. The number of fringes separating the principle maxima and the first zero of the envelope is just the ratio of the grating period Λ to the length of the shorter region of the grating. Thus from measurement of the diffraction pattern, we can estimate the period Λ as well as the duty cycle $(l_1/\Lambda)$ of the index modulation.

## 3. Experiment

LPGs were fabricated by arcing an optical fiber (Corning SMF-28) periodically along its length using a commercially available splice machine. The electric arcing results in a perturbed region whose width would depend on the spatial extent of the electric arc between the electrodes of the splice machine. This results in a refractive index modulation. For any period of the fabricated grating the width of this region would remain almost the same if the same arc current and exposure time has been used on the same fiber type for grating fabrication. Upon viewing the fabricated grating under high-resolution microscope, it was seen that no physical deformation of the fiber had resulted by arcing which was expected since there was no tension applied on the fiber.

A laser beam (the probe beam used in our experiment was He-Ne laser beam of wavelength 0.633μm) illuminated normal to the fiber axis containing the grating resulted in a clear diffraction pattern. Figure 2 shows the experimental setup used showing the axes.

Fig. 2

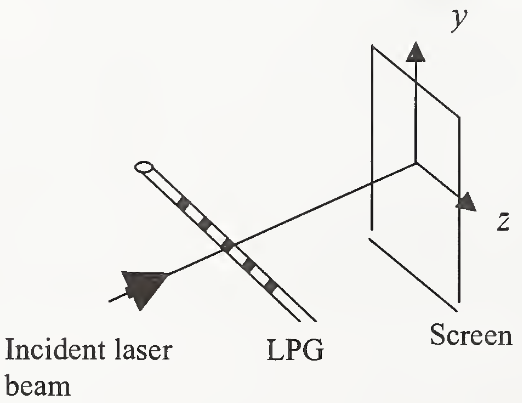

Figure 3(a) shows the diffraction pattern on the screen as produced by a fiber region without the grating and Fig. 3(b) shows the corresponding pattern produced by the fiber portion containing a typical LPG with a period of 450μm. These patterns were obtained using a high resolution CCD camera.

Fig. 3(a)

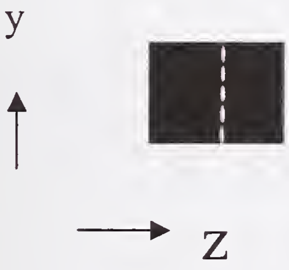

Fig. 3(b)

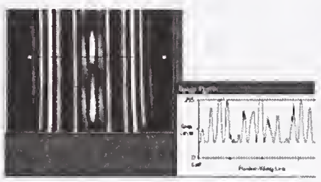

The presence of LPG clearly produces a diffraction pattern parallel to the fiber axis. The other artifacts are due to the cylindrical nature of the optical fiber. The inset of Fig. 4(b) shows the intensity distribution obtained at a selected plane.

Gratings used in the experiment had different periods and were fabricated on Corning SMF-28 with the same arc current and exposure time to ensure uniform refractive index modulation and dopant diffusion width. By scanning a photodetector along the diffraction pattern of the LPG the intensity pattern at any plane can be measured. We can measure the average distance $\beta$ between the diffraction peaks, from which the grating periodicity $\Lambda=\lambda D/\beta$ can be estimated assuming normal incidence of light on the grating. The average distance between the central maximum and the first principal minima, $\gamma$ is measured experimentally. From this we could find $l_1=\lambda D/\gamma$. The same experiment was repeated for gratings with periodicity 450 μm, 680μm and 830μm. Table 1 gives the grating parameters as estimated from the diffraction pattern.

Table I Comparison of the estimated grating period with the fabricated values.

| Fabricated Period of the grating | Estimated grating period from the diffraction pattern. | $l_1$ (smaller width in the rectangular grating) | $l_2$ (larger width in the rectangular grating) |
|---|---|---|---|
| 450μm | 458μm | 152μm | 306μm |
| 680μm | 685μm | 314μm | 364μm |
| 830μm | 832μm | 316μm | 516μm |

It can be seen from Table I that the grating period estimated from the diffraction pattern match very well with the values used for fabrication. In all these gratings, we find regions of widths 306μm, 314μm and 316μm which are very close to each other in spite of the very different periodicities in the grating. We saw earlier in Sec.2 that the first principal minimum of the diffraction envelope is determined by the smaller of the widths

$l_1$ and $l_2$. From this we can conclude that the width of the region that gets modified due to the arc must be about 312μm. Hence apart from the grating period, the proposed technique clearly gives us the width of the modified region as well in the LPG. This is not easy to estimate from the transmission spectrum.

It is estimated from experiment that the width of the perturbation due to arcing is 312 micrometers. A very interesting observation during the grating fabrication is that the grating formation almost vanished when the period of grating was brought as low as 315 micrometers point out that the perturbation due to arcing was about that width.

## 4. Conclusion

In conclusion we have proposed and demonstrated a simple and direct experimental technique to estimate the period and the duty cycle of a long period grating by measurements on the diffraction pattern obtained by a transverse illumination. Apart from the grating period, the method also gives us an estimate of the width of the perturbed region. The experimental results have been shown to match fairly well with actual parameters. The proposed method does not require any sophisticated equipments and can be used to estimate the parameters of long period fiber gratings fabricated using different techniques.

## Acknowledgements

The authors thank Dr. Joby Joseph (Physics Dept., IIT Delhi) for help in imaging the fringe pattern and for fruitful discussions. One of the authors (Mini Das) would like to thank G. Unnikrishnan (Physics Dept., IIT Delhi) for technical discussions and the Council of Scientific and Industrial Research, Govt. of India for providing with a Senior Research Fellowship. This work was partially supported by a research project sponsered by the Department of Electronics, Govt. of India.

## References

1. A. M. Vengsarkar, P. J. Lamaire, J. B. Judkins, V. Bhatia, T. Erdogan, J. E. Sipe, J. Lightwave. Technol. **14**, 58 (1996).
2. A. M. Vengsarkar, J. B. Judkins, P. J. Lamaire, Opt. Lett. **21**, 336 (1996).
3. V. Bhatia and A. M. Vengsarkar, Opt. Lett. **21**, 692 (1996).
4. E. Brinkmeyer, Opt. Lett. **20**, 810 (1995).
5. P. A. Krug, R. Stolte and R. Ulrich, Optics Lett. **20**,1767 (1995)

# A Simplified Model of Modal Dispersion in Multimode Fiber

(Invited)

A. John Ritger
*OFS Fiber Optics Division*
*2000 Northeast Expressway*
*Norcross GA 30044*
*ritger@ofsoptics.com*

Steven E. Golowich
*Bell Laboratories, Lucent Technologies*
*700 Mountain Avenue*
*Murray Hill, NJ 07974*
*golowich@research.bell-labs.com*

## Abstract

*We develop a simplified model of modal dispersion, where the fiber is described by the delay properties of the principal mode groups. We demonstrate how this model explains the modal structure seen in Differential Mode Delay measurements. We compare model predictions to correlations observed between 850 and 1300 nm overfilled launch bandwidth for collections of multimode fiber. We use the model to show how one can calculate overfilled launch bandwidth from DMD data.*

## Introduction

The growth of data network applications and data rates has led to increased interest in the use of multimode fiber over the last several years. While the data rates that can be realized over multimode fiber are much lower than those that can be realized over single mode fiber, multimode fiber lends itself well to the use of low cost laser devices, such as 850 nm VCSEL's, which would be unsuitable for use over single mode fiber. Also, the large core of a multimode fiber allows use of reduced tolerance in aligning the laser source to the fiber, again reducing the cost of a practical laser transmitter. Applications of interest require transmission of up to 10 Gbs, and include local and storage area networks, as well as equipment interconnects.

The primary limitation of multimode fiber is its modal dispersion, which is caused by the various modes having different group velocities. It is possible to solve for the modal dispersion directly from Maxwell's equations with knowledge of the physical characteristics of the fiber, primarily the refractive index profile. However, much greater insight can be gained from the use of an approximate model that holds in the situations of interest.

We are concerned with propagation over distances of <~1000 m, at wavelengths near 850 and 1300 nm, in Germanosilicate glass fibers with nearly parabolic index profiles with index contrasts Δ of 1 or 2%. Such fibers support hundreds of guided modes, but the modes divide naturally into principal mode groups, indexed by an integer M=1,2,..., where the modes within a group have approximately equal wavenumber. The importance of principal mode groups is that the modes within such a group freely share power with one another over length scales of tens of meters, while modes in different mode groups remain almost completely uncoupled out to distances well over a kilometer. The effect of intra-group coupling is that when the constituent modes of a mode group are excited, the pulses in the various modes of the group coalesce into a single pulse, the width of which grows as the square root of the length of the fiber[1 ,2].Each of these mode group pulses travels at its own group velocity, so the separation between the pulses associated with different mode groups grows linearly in the length of the fiber. Since we are interested in short length applications, we can ignore mixing among the mode

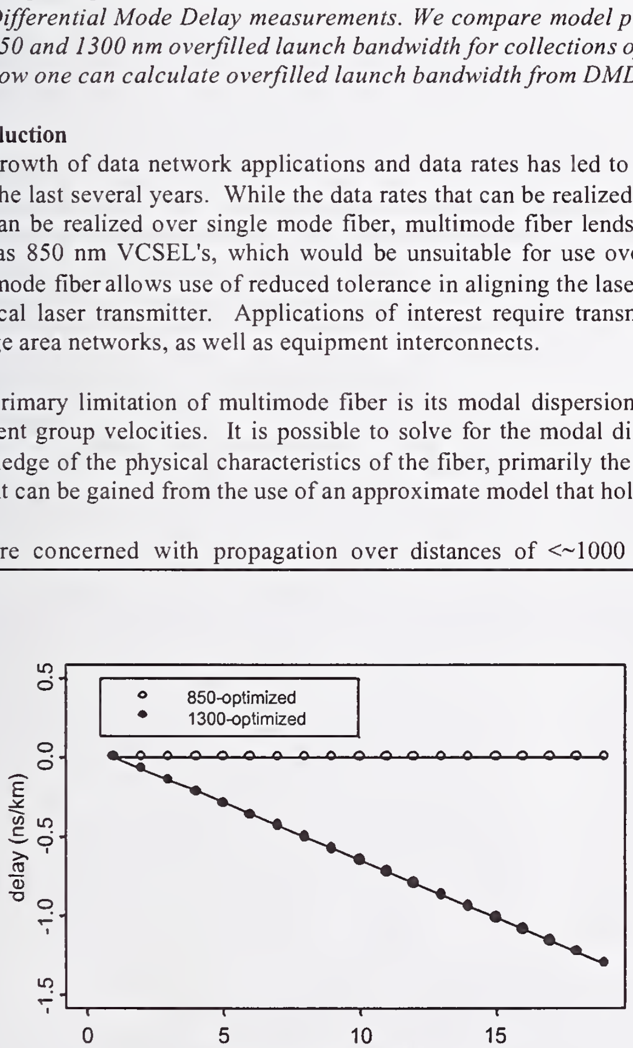

Figure 1: Relative modal delays

groups. We also assume that the index profile of the fiber, and therefore its modal structure, does not vary with position. Currently, the fiber design of most interest has core diameter of 50 µm and Δ = 1%. At 850 nm, such fibers support about 19 mode groups, M=1 to 19, each with M modes (2 M including polarization). So, such a fiber can be represented as a set of 19 mode group delays, conventionally as delays relative to the delay of the fundamental mode.

Figure 1 shows the representation of 2 such fibers, one optimized at 850 nm, and one optimized at 1300 nm. The linear change of delay with mode number for a fiber optimized at one wavelength when excited at a different wavelength will be discussed below. A convenient feature of this model is that if the mode group delays and the mode power distribution are known, it is straightforward to calculate the shape of the temporal impulse response. This allows detailed modeling of laser/fiber links, both from the standpoint of bandwidth and of inter-symbol interference. [3, 4]

**Differential Mode Delay**

The modal structure of a multimode fiber can be directly probed using Differential Mode Delay (DMD). [5, 6, 7]. A probe fiber, single mode at the measurement wavelength, is scanned radially across the face of the multimode fiber under test. At each radial offset position, a short-duration, spectrally-narrow pulse is injected into the multimode fiber and the output pulse is recorded.

Figure 2 shows 850-nm DMD data obtained from 0.75-km, 50-µm, 1%-Δ fiber that exhibits near-optimum performance at 1300 nm (OFL Bandwidth > 5 GHz-km), and compares it to simulated DMD data calculated using the delays from Figure 1. The data were obtained by exciting the SM probe fiber with pulses from a mode locked Titanium-Sapphire laser which produces pulses of FWHM ~ 4 ps. Injecting the probe pulse directly into our detector results in near Gaussian waveforms with FWHM ~ 45 ps.

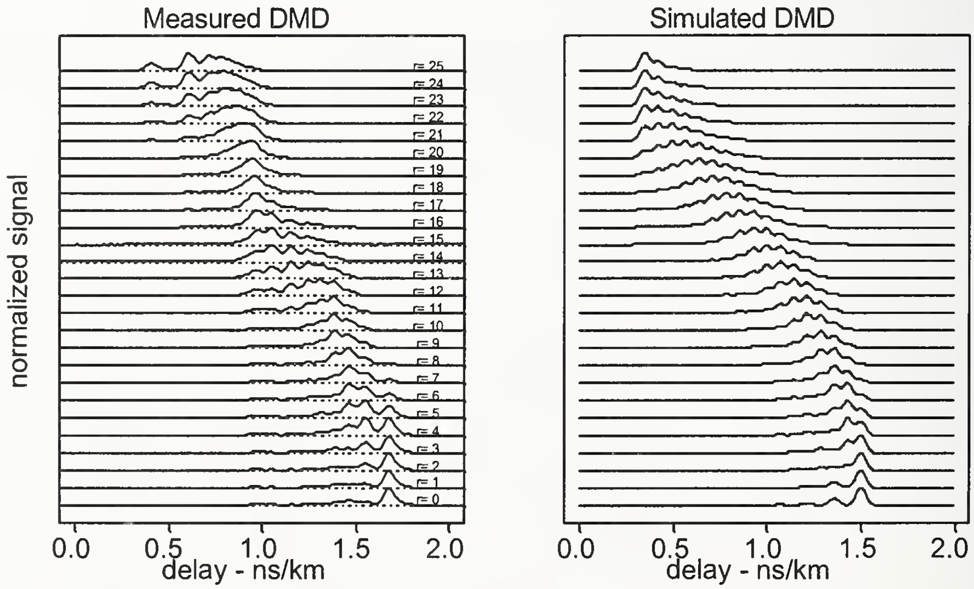

Figure 2: 850 nm DMD data for a fiber nearly optimized at 1300 nm, for SM probe fiber offsets from 0 um to 25 um.

To calculate simulated DMD data from a known set of delays, we need to know how much light from the probe SM fiber is coupled into each of the mode groups of the multimode fiber. Here we must make use of a full modal treatment, calculating the overlap integrals between the electric field of the output beam from the SM probe fiber and each of the mode fields of the multimode fiber. The energy coupled into each of the modes in a mode group is summed, resulting in a set of 19 coupling coefficients for each offset position. Each trace in the simulated DMD is the sum of 19 Gaussians, each with FWHM 45 ps, with temporal spacing given by the delays and fiber length, and with amplitudes given by the coupling coefficients for that offset.

Comparing the data and the simulation, we can see several interesting features. Except for several mode groups excited for offsets near 18 µm, we can see relative arrival times of the individual mode groups. Those mode groups that are well separated show the same temporal width, and are not appreciably broadened by intra-mode group dispersion. We can see that the magnitude of the M=1 mode, i.e. the fundamental mode, drops off radially as expected from the simulation. The M=2 mode is not seen for on-axis excitation, but increases and then decreases in magnitude, starting at r ~ 2 µm. The M=3 mode is present for on axis excitation, but then drops off before rising again. All these features are well captured by the calculated coupling coefficients. Finally, we note that the highest order modes are much smaller than expected from the attenuation free calculation. The highest order mode group, presumably M=19, is only weakly seen, even for excitation at the core-clad boundary. We know that the mode fields of M=19, and to a lesser extent M=18, extend well into the cladding, and that energy coupled into these modes is quickly attenuated, even over distances as short as a few 100 m.

**Spectral dependence of modal delays**

We will now discuss the linear change of delay with mode number for a fiber optimized at one wavelength when excited at a different wavelength. All communications grade multimode fibers are manufactured using $GeO_2$ doped $Si0_2$ to achieve a nearly parabolic index profile. A 50-µm, 0.20-NA fiber has a maximum index difference $\Delta$ = 1.0%, while a 62.5-µm 0.265-NA fiber has $\Delta$ = 2%. Since the index changes linearly with $GeO_2$ concentration over the range of interest, the $GeO_2$ concentration profile is also nearly parabolic, rising to about 10% for a 1%-$\Delta$ fiber. From the individual mode fields of a 50-µm, 1%-$\Delta$ fiber we first calculated the Near Field Intensity (i.e. $/E/^2$) for an incoherent superposition of the modes within each mode group. Using the resulting $NFI_M(r)$ we find the effective $GeO_2$ concentration of the mode group M as:

$$Eff.Conc.(M) = 2\pi \int_0^\infty NFI_M(r) C(r)\, r dr$$

$$C(r) = C_0\left(1-(r/a)^2\right) \quad for \quad r<a, \quad C(r)=0 \quad for \quad r \geq a,$$

where the maximum concentration $C_0$ is just $10\Delta$ for $GeO_2$ doped fibers.

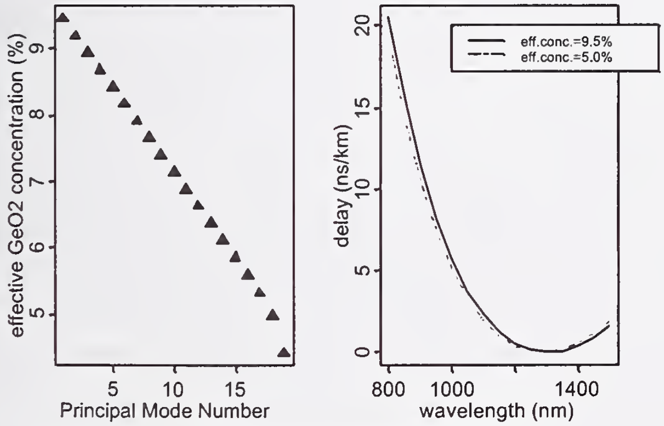

Figure 3: (a) Effective GeO2 concentration by mode group
(b) Delay vs. wavelength for PMN=1 and PMN=18

The results of this calculation are shown in Figure 3 (a). The effective $GeO_2$ concentration of each mode group changes nearly linearly with mode number, except for the M=19 mode group. This shows markedly lower effective concentration, reflecting the fact that modes in this group extend deeply into the undoped (and lossy) cladding.

Several studies have been published [8, 9] on the variation of chromatic dispersion with $GeO_2$ concentration. The spectral dependance of delay times was measured for graded index fibers with a wide range of $\Delta$, and the studies showed consistent behavior. Using the values from [8], and using 10% $GeO_2$ concentration for $\Delta$ = 1% we find values of zero dispersion wavelength, $\lambda_0(M)$, and dispersion slope, $S_0(M)$, to calculate the delay as a function of wavelength for the effective $GeO_2$ concentration of each mode group,

$$delay_M(\lambda) = (S_0(M)/8)\,\lambda^2\left(1+(\lambda_0(M)/\lambda)^4\right).$$

The result of this calculation is shown in Figure 3(b) for the M=1 mode and for the M=18 mode. The M=1 mode sees a higher $GeO_2$ concentration, and so has larger $\lambda_0(M)$ than do the M=18 modes. (Some fibers are co-doped with small admixture of $B_2O_5$. The impact of this on chromatic dispersion can be neglected in the current discussion. [8])

Now we consider the response of a 1300 nm optimized fiber when excited at 850 nm. The index profile of such a fiber has been adjusted to achieve the same delay for each mode group at 1300 nm. At 850 nm, the shifts with effective concentration of $\lambda_0(M)$ and $S_0(M)$ result in a chromatic delay that changes linearly with mode number (at least up to M=18). The difference in chromatic delay increases linearly with M, and between M=1 and M=18 we find a maximum chromatic delay difference of –1.31 ns/km going from 1300 to 850 nm. This is in good agreement with the observed delay difference in Figure 2, and is the value used to generate the delays in Figure 1. The value of maximum chromatic delay difference scales linearly with $GeO_2$ concentration, so a 2%-Δ fiber will be characterized by a value of about –2.6 ns/km.

While the number of mode groups for a given fiber varies with wavelength, at any given wavelength, the effective $GeO_2$ concentration varies linearly over the same range as in Figure 3(a). Mode groups at the same value of $M/M_{MAX}$ see the same effective GeO2 concetration. The value of maximum chromatic delay difference varies approximately linearly with the difference between excitation and optimization wavelengths for fiber optimized at any wavelength in the 800 to 1500 nm range. Figure 4 shows OFL bandwidth values obtained at 850 and 1300 nm for a random sample of 1000 50-µm, 1.25%-Δ fibers. (The values of 850 nm bandwidth were limited to less than about 1500 MHz-km by the chromatic dispersion associated with the laser used to make the measurements.) The solid line was calculated using a maximum chromatic delay difference of –1.65 ns/km, scaled for the non-standard Δ value. Each point on the line represents a fiber optimized at some wavelength but measured at either 850 nm or 1300 nm. At either wavelength, the delays vary linearly with mode group number. The overfilled launch is designed to put equal power into each of the modes of the fiber, so the power in each mode group also increases linearly with the mode group number. Pulses were calculated as a superposition of Gaussians, leading to approximately triangular pulse shapes. The distribution of 850 vs. 1300 nm bandwidth values is quite typical for large collections of multimode fiber, and is associated with typical (in the mid 1980's) manufacturing variations on the index profiles. The solid line shows the behavior of a collection of "perfect" fibers, and maps out the boundary for what is allowed by chromatic dispersion for real fibers. Similar plots can be made for 1%-Δ fibers using –1.3 ns/km, or 2%-Δ fibers using –2.6 ns/km. In all cases the limiting behavior of real fibers is accurately shown by the idealized calculation.

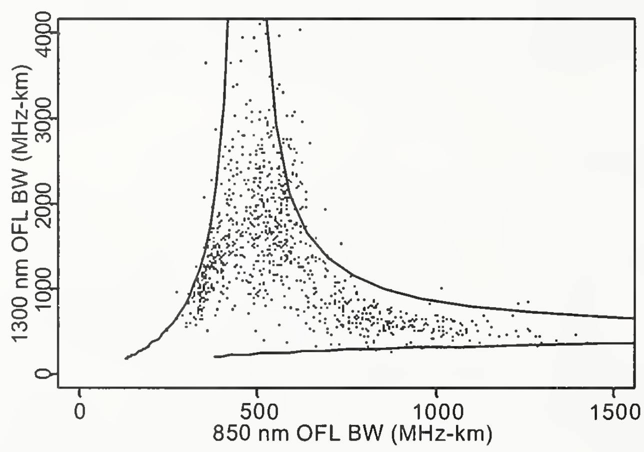

Figure 4: OFL BW for 1000 1.25% Delta, 50 um core fibers

**Calculating OFL Bandwidth from DMD data**

Given the modal delay values and the mode power weights, it is straightforward to calculate the temporal impulse response of a fiber. While it is possible to extract the actual modal delay values from a complete set of DMD data, it is much more convenient to work directly with the DMD data. It is particularly convenient to consider the case of the OFL measurement since in this case the mode power weight of each mode group is proportional to the mode group number. An excellent approximation for the mode power weight can be obtained by using the fact that an SM probe beam at radius $r$ launches a mode power distribution in a relatively narrow range of mode groups centered on mode number $M_{max}(r/a)^2$, where $M_{max}$ is the maximum principle mode number for that fiber. So, to obtain the OFL impulse response, we weight the DMD trace at radius $r$ by the factor $M_{max}(r/a)^2$ and compute a weighted sum of DMD traces.

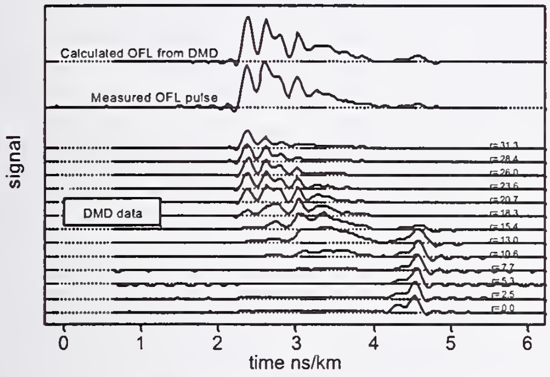

Figure 5: DMD data, OFL waveform, and OFL calculated from DMD, for a 450-MHz-km 62.5 um fiber

The results are illustrated in Figure 5. This was a 9 km, 2%-Δ, 62.5 μm fiber with OFL bandwidth 450 MHz-km. The data in this figure were obtained using a probe pulse from a diode laser, which had 1.8 ns FWMH when connected directly to the detector. The DMD data shows the low order modes arriving much later than the high order modes, but contributing little to the overall OFL output because in an overfilled launch most power is coupled into high order modes. The multi-peak character of the OFL pulse is typical of non-optimized fiber. The impulse response constructed from the DMD data shows is in excellent agreement with the pulse shape actually measured with OFL excitation.

**Discussion:**

Representing the modal dispersion of a multimode fiber by the delay values associated with the principle mode groups results in considerable simplification and insight into its behavior. We can explain the variation of modal structure with wavelength. In the special case of the known OFL distribution, we can explain observed limits on the bandwidth correlation between 850 nm and 1300 nm values. A straightforward approximation to the discrete mode delay picture allows us to predict the observed OFL temporal response of a fiber from DMD data.

**References**

[1] D. Marcuse, *Theory of Dielectric Waveguides*, Academic Press, New York, 1974

[2] S. Kawakami and H. Tanji, Electron. Lett., Vol. 19, no 3, pp 100-102

[3] S. E. Golowich, P. F. Kolesar, A. J. Ritger, and P. Pepeljugoski, "Modeling and Simulations for 10 Gb Multimode Optical Fiber Link Component Specifications", OFC 2001, paper WDD57

[4] P. Pepeljugoski, S. E. Golowich, "Measurements and simulations of intersymbol interference penalty in new high speed 50 μm multimode fiber links operating at 10 Gb/s", OFC 2001, paper WDD40

[5] D. Marcuse, *Optical Fiber Measurements*, Academic Press, New York, 1981, p288.

[6] C.M.Miller, S.C.Mettler, and I.A.White, *Optical Fiber Splices and Connectors*, Marcel Dekker, New York, 1986, p177.

[7] FOTP-220 (TIA-455-220), "Differential Mode Delay Measurement of Multimode Fiber in the Time Domain "

[8] J.J.Refi and H.T.Shang, "Determining the Zero Dispersion Wavelength and Dispersion Slope of Fibers used for the Fiber Distributed Data Interface", SPIE Vol. 841, p66 (1987)

[9] M.J.Hackert, "The impact of multimode fiber chromatic dispersion on data communications", SPIE Vol. 1178, p188 (1989)

# DMD Measurement and Simulation on Short-Length, 850-nm Laser-Optimised, 50 μm Core Diameter, GIMM Optical Fibres

F.J. Achten[1], M. Bingle[2,3], B.P. de Hon[2], M.J.N. van Stralen[1]

[1]Draka Fibre Technology, P.O. Box 1442, 5602 BK Eindhoven, The Netherlands
[2]Eindhoven University of Technology, Faculty of Electrical Engineering,
P.O. Box 513, 5600 MB Eindhoven, The Netherlands
[3]presently at EM Software & Systems, P.O. Box 1354, Stellenbosch 7599, South Africa

## Abstract

A new Differential Mode Delay (DMD) measurement set-up has been developed as standardised by the IEC [1]. This set-up will be used in an optical glass fibre production environment for characterising 850-nm laser-optimised, 50 μm core diameter, graded-index multimode (GIMM) optical fibres for 10 Gb/s applications. Additionally, the set-up has been used together with a new, full-wave numerical model for multimode fibres, to investigate the effect of profile deviations.

## Introduction

The demand for high bandwidth in data- and telecommunication systems has led to the development of 10 Gb/s Ethernet networks. The laser and detector characteristics, as well as the fibre characteristics determine the system bandwidth. In the IEEE standard for 10 Gb/s Ethernet networks, a new GIMM fibre with a 50 μm core diameter is considered as a feasible solution at 850 nm for fibre lengths up to 300 metres. The bandwidth of a multimode fibre is predominantly determined by intermodal dispersion. The observed intermodal dispersion depends on the specific source conditions. Therefore, in addition to the traditional bandwidth measurement (for an overfilled launch), the quality of the multimode fibre is tested by performing a differential mode delay (DMD) measurement, according to the IEC standard [1].

A DMD measurement provides a means to characterise the modal structure of a multimode fibre in detail. The multimode fibre is connected to a short, 850nm single-mode fibre probe. This single-mode probe is excited by a pulsed 850nm laser with a very narrow spectral width. The probe is moved gradually from the centre of the core towards the cladding of the multimode fibre and the output pulses are detected after propagating through a specified fibre length. The output pulses form the DMD pattern of the fibre. It exhibits the travel-time drift between the different mode ensembles excited for different probe positions, and the pulse broadening due to intermodal dispersion between mode groups. The DMD pattern provides a means to assess the quality of the fibre.

At Draka Fibre Technology, a DMD measurement set-up is developed to conform with the IEC 60793-1-49 standard [1], yet with the specific objective to perform DMD measurements in a PCVD (Plasma-activated Chemical Vapour Deposition) fibre production setting as a means of quality control. A commercial set-up to perform a standardised DMD measurement on short length fibres (hundreds of metres, up to two kilometres) does not yet exist to our knowledge. In order to support the DMD characterisation of multimode fibres, a full-wave numerical model was developed at the Eindhoven University of Technology. In this paper, we present the DMD results for a graded-index multimode fibre, with a typical deviation from the graded-index profile in the region around the fibre axis.

## The DMD measurement standard

The DMD measurement standard, as defined by [1] specifies the optical source, launch system and detection system. The end face of the fibre under test is irradiated by pulsed laser light at a specified wavelength (850 ± 5 nm). One option is to image the output spot of the probe fibre with a modefield diameter (MFD) of 5 ± 0.5 μm onto the end face of the fibre under test. The beam is moved across the end face of the fibre from the optical centre of the core towards the cladding. The spectral width of the laser and the duration of the pulses are specified, and dependent on the length of the fibre to be measured.

The propagating pulses are detected to form a DMD pattern from which the DMD values are calculated. The pattern is considered within two masks: an inner mask, including the pulses from radius 5 to18 μm, and an outer mask including all pulses from the core centre to a 23 μm radial offset. The DMD value is the time difference (at 25% of the maximum) between the leading edge of the fastest pulse and the trailing edge of the slowest pulse within the mask [1, 2, 5]. A set of standardised templates determines the quality of the fibre.

### The DMD measurement set-up

The objective was to develop a DMD set-up for production environment while it still complies with the DMD measurement standard [1]. The main challenge was to develop a low power laser, instead of the commonly used high power, mode-locked Titanium Sapphire laser. The safety regulations are less stringent for the pertaining low power laser. This laser generates pulses with a full width, half maximum (FWHM) duration of 90 ps, a centre wavelength of 849.9 nm and a line width smaller than 0.2 nm. The small line width is necessary to prevent the effect of chromatic dispersion in the fibre from influencing the DMD [1] [4]. The pulse is coupled into a single-mode probe fibre (launch fibre) with a core size of 5 μm. The other end of the probe fibre is scanned across the core of the multimode fibre, with the aid of a closed-loop piezo-electric system with nanometre resolution. The end face of the probe fibre is positioned at a distance closer than 10 μm from the cleaved multimode fibre end, as prescribed by the standard. The pulses are detected by an optical-to-electrical converter with a bandwidth of 8 GHz. The DMD value is calculated, and compared with the specifications of the two masks. These values are two of the parameters which determine acceptance of the 850 nm laser-optimised multimode fibre according to [5].

### The full-wave numerical model for DMD computations

The multimode fibres under consideration are assumed circularly symmetric, isotropic and translationally invariant along the longitudinal direction. A fibre consists of a radially inhomogeneous core, and a homogeneous cladding of infinite radial extent. The permittivity of the fibre material is characterised by the Sellmeier coefficients for a three-term harmonic oscillator model of doped, bulk, fibre glass [7]. In the relevant wavelength band, the losses are negligible. We employ a vectorial field model to compute the properties of the $HE_{mn}$ and $EH_{mn}$ modes, where $m$ and $n$ are the azimuthal and radial modal indices, respectively. In particular, we consider a vectorial transverse resonance method in the radial directions, involving numerical integration of a system of ordinary differential equations [3][7].

The determination of the modal field distribution excited in the multimode fibre at the splice with the single-mode fibre probe comprises a scattering problem. However, the actual splice is not specified, other than that the distance between the fibres should not exceed 10 μm. Further, the permittivity contrast between the fibres is small. Hence, it suffices to project the probe field onto the modal fields in the multimode fibre with the aid of overlap integrals [8]. The modal power distribution will also be affected by the differential mode attenuation, primarily due to bending losses. Differential mode attenuation has not been incorporated in the model. At the receiver end of the fibre, the transmitted signals are detected by a power sensor, which measures the moving time average of the total instantaneous power flowing through a cross-section. The instantaneous power corresponds to a convolution in the frequency domain. In general, modes at different frequencies cease to be orthogonal, inducing instantaneous-power coupling between modes. Further, for off-centred excitation the rotational symmetry with respect to the probe polarisation is broken. However, for the multimode fibre setting under consideration, these effects on the DMD are insignificant [3].

For DMD experiments conducted according to the DMD standard with a laser source that generates a single lasing mode, the pulse-width and the fibre length are such that the chromatic dispersion may safely be neglected. The modal group delays are of importance. Assuming an optimal resolution of the time window of observation of a few picoseconds, the group delays must be computed to within six significant digits. For the accurate computation of a group delay, we evaluate the total derivative of the characteristic equation and invoke the implicit function theorem [7]. Regarding the sum of the modal amplitudes, two significant digits suffice.

### Example: A graded-index fibre with a distortion near the centre

The DMD pattern for a good fibre in terms of 10 Gb/s standards shows minimal travel-time drift between the various offset pulses (i.e. they are aligned in time) and the pulse distortion is similar for all the pulses. It is well-known that there exists an optimal alpha-parameter in a graded-index profile for which the bandwidth of the fibre will be optimised at a specific wavelength. This is supported by numerical experiments, some of them reported in [3]. We found that the numerical optimal alpha-parameter (relating to the fibre refractive index profile) is slightly higher than the one used in practice (relating to the preform refractive index profile). This is mainly due to a change in the effective profile of the drawn fibre.

In order to demonstrate the worth of DMD measurements, we present a graded-index fibre with a distortion near the centre. The refractive index of the preform and its alpha-fit is plotted in Figure 1.

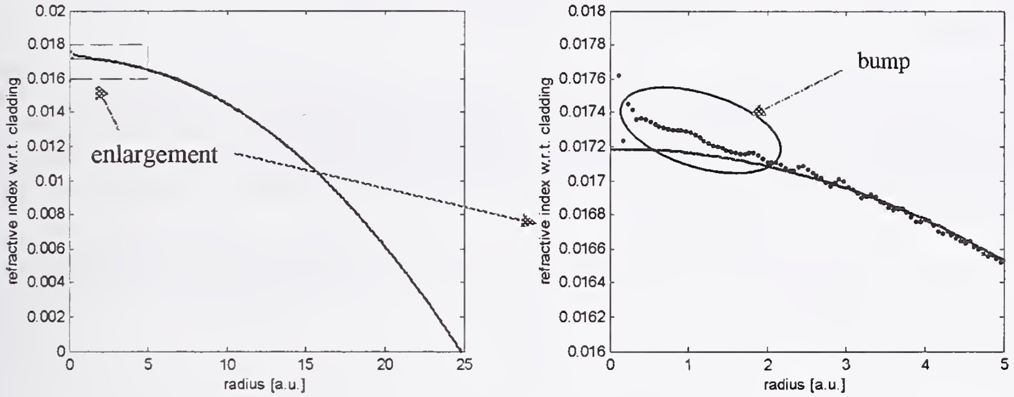

Figure 1: Refractive index profile of the preform from which the fibre under investigation is drawn. The right figure is an enlargement to show the "bump". The dots are the measured values; the solid curve is an alpha-profile.

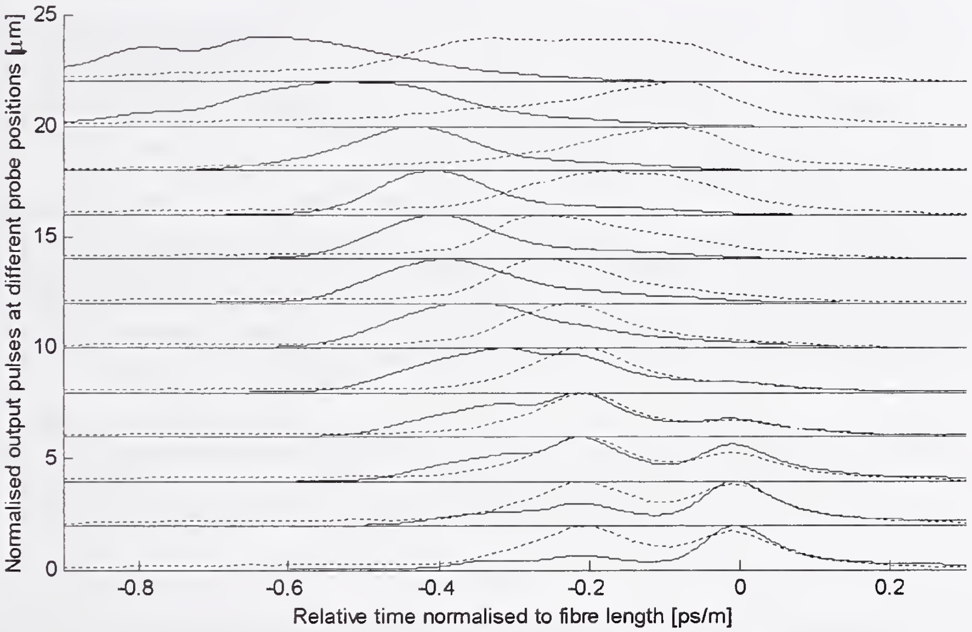

Figure 2: Measured (dotted line) and computed (solid line) DMD pattern of the fibre under consideration.

The inset shows a "bump" deviation from the graded index profile fit which results in pulse distortion in the DMD pattern for probe positions close to the centre. The measured and computed DMD patterns are shown in Figure 2. The result shows the combined effect of a non-optimal alpha-parameter and a deviation from the ideal graded-index profile. The appearance of a second peak in the DMD pulses is an indication of the non-ideal refractive index profile close to the fibre axis. It is important to recognise that the profile model for the computation is based on preform data and therefore it does not include the effect of the drawing process on the specific sample under test. A better agreement with the measured DMD pattern is obtained for a numerical profile model with a slightly higher value for the alpha-parameter. This supports the idea that the drawing process influences the refractive index. Further differences between the numerical model and practice might be a non-ideal intensity distribution for the light emanating from the probe (non-ideal cleaving) and the small offset between the probe and the fibre under test. In addition, differential mode attenuation is not included in the model. Nevertheless, computation and measurement show similar trends in the DMD patterns. A fibre with a DMD pattern shown in Figure 2 will be rejected according to the fibre specifications indicated in [5].

## Conclusions and future work

A new Differential Mode Delay (DMD) measurement set-up has been developed according to IEC [1] for short-length, 850-nm laser-optimised, 50 μm core diameter, GIMM optical fibres. The set-up is employed to investigate the influence of profile deviations on the fibre performance. The latter is supported by computations with a full-wave numerical model. Deviations in the refractive index profile of the preform are reflected in the measured and computed DMD patterns.

More measurements and computations will be performed in the future to obtain a better understanding of the relationship between DMD and the related refractive index profile, as well as the mapping from the preform to the drawn fibre profile.

## References

[1] *IEC 60793-1-49 Ed. 1 - Optical fibre - Part 1-49: Measurement methods and test procedures - Differential Mode Delay.*

[2] *TIA, FOTP-220 Differential mode delay measurement of multimode fiber in the time domain, TIA-455-220, PN3-0008, 2001.*

[3] M. Bingle, B.P. de Hon, *"Differential mode delay - Full wave modeling and various levels of approximations", paper 2060, URSI General Assembly, Maastricht, The Netherlands, 2002.*

[4] M.J.N. van Stralen, B.P. de Hon, M. Bingle, F.J. Achten, *"Short pulse, small spot size, central launch in multimode fibres: comparison between measurement and computation", SOFM 2000.*

[5] *TIA Standard, TIA-492AAAC, Detail Specification for 850-nm Laser-Optimized, 50-μm Core Diameter/125 μm Cladding Diameter Class of Graded-Index Multimode Optical Fibres.*

[6] W. Hermann and D. U. Wiechert, *"Refractive index of doped and undoped PCVD bulk silica," Mat. Res. Bull., vol. 24, p. 1083, 1989.*

[7] M. Bingle, B. P. de Hon, and M. J. N. van Stralen, *"Electromagnetic modelling and optimisation for the design of single mode optical fibres", Proc. 2001 URSI Int. Symposium on Electromagnetic Theory, Victoria, Canada, pp. 515-517, 2001.*

[8] E.-G. Neumann, *Single-Mode Fibers, Fundamentals. Berlin: Springer, 1988.*

# Determination of Skew in Multimode Ribbon Fibers[*]

Arthur J Barlow, PerkinElmer Optoelectronics, Wokingham RG41 2GY UK
E-mail: arthur.barlow@perkinelmer.com
Michael J Hackert, Corning Inc, Corning NY USA
Email: mHackert@stny.rr.com

## Abstract:

This paper discusses issues of how multimode (MM) fiber ribbon skew at 850 nm may be estimated from 1310 nm measurement with high accuracy using single-mode fiber test sets. Modern high-speed applications such as the 10 Gigabit Ethernet standard and high-speed parallel interconnects are driving measurement requirements. It is shown that less than 5 ps/m fiber-to-fiber skew should be achievable with careful fiber selection and cable design.

## Introduction

Modern multimode fibers have been developed to operate at 1 Gb/s, using the Gigabit Ethernet (GbE) standard. Considerable effort has been expended to ensure these fibers have sufficient modal bandwidth. This is typically achieved by careful differential mode delay (DMD) control via special attention to the index profile. In addition, by limiting the number of modes and/or mode groups that are launched, the required bandwidth for data transmission can be achieved. For the new 50 µm fiber designed for 10 GbE, such as Corning® InfiniCor® SX+ fiber, the fiber DMD characteristics are measured using the pulse delay method [1], and the results compared to a DMD mask.

In this paper, we discuss the prediction and measurement of skew in GbE optimized fiber ribbon cables, designed to operate at 850 nm. However, everything we present applies equally well to all types of MM fiber, including both 50 µm and 62.5 µm core diameter types. The key focus is on the fiber properties rather than cabling factors.

## Background

In digital parallel transmission, the term "skew" is used to denote the time difference between the different parallel-transmitted bits of data. In high-speed operation, there are strict standards for the permissible amount of skew [2]. Typical criteria range from ≤17-23 ps/m to ≤5 ps/m at typical lengths of a few hundred meters. The former is relatively easily achievable with careful cable construction; the latter challenges the intrinsic limits on the fiber properties and current measurement technology. Within such a system, the fiber transmission medium (most frequently in ribbon fiber form) is a strong potential contributor to the data skew.

Skew in a ribbon fiber is the relative delay time across the ribbon, so one fiber (typically one of the fibers at the edge, e.g., fiber #1), is chosen as the reference delay time for the other fibers [3]. The different relative delays $\tau_i - \tau_1 = \Delta\tau_i$ are the individual differential times of flight. The ribbon fiber skew is defined as the magnitude of the difference of the maximum relative time delay and the minimum relative time delay:

$$\text{SKEW} = |\max(\Delta\tau_i) - \min(\Delta\tau_i)| \qquad -(1)$$

Optical time delay differences will result from variation of group index N, called ΔN, across the different fibers within the ribbon. This variation originates from the effect induced by cabling, from the fiber itself, or the transmitter interacting with the fiber through its wavelength or launch. Once formed into a cable, changes will be photoelastically induced in N by stresses "frozen-in" to the ribbon package incorporated during the ribbonizing processes. The set of fibers used in the ribbon will have a range of indices due to the natural production tolerances on the group index. This range can be characterized by a skew measurement, time of flight or OTDR measurement, or measurement of chromatic dispersion if the intrinsic delay is captured. Delay differences also originate from the differential modal delay difference as measured by the DMD. Since restricted launch sources typical of lasers for high-speed application can selectively excite different modes, different launches can create skew in fibers that otherwise have no other source of skew. Likewise, the set of transmitters used with the ribbon may have a range of wavelengths. Skew can also be created since the index is wavelength dependent.

This work has two prime motivations – 1) to determine if a fiber can be adequately characterized for skew using a single-mode launch, and 2) to determine if measurements at 1310 nm can adequately characterize skew at 850 nm, which is the wavelength of most typical GbE short-length applications. This motivation arises from a practical consideration that single-mode fiber based strain/skew measurement equipment using 1310 nm sources is currently commonly available within a cable factory [4].

Skew Contributions

**CABLING INDUCED DIFFERENCE:** We consider first the cable fiber contributions to skew in turn. From the known theory of strain [5, equation 8] in fibers, the ΔN at the frozen-in stress within a ribbon is proportional to:

$$\Delta N = \left(-\frac{N^2}{2} . \{p_{12} - \sigma(p_{11} + p_{12})\}\right) \qquad \text{-(2)}$$

where p the strain tensor components and $\sigma$ is the Poisson's ratio. For fused silica, the values are $p_{11}=0.121$, $p_{12}=0.27$, $\sigma=0.17$, and $N=1.468$. Examination of equation (2) shows that the variation in skew across wavelength is due entirely to the dispersion of N. Since the variation of N from 1310 nm to 850 nm is less than 1% [6], we can make the assumption that the stress within a ribbon induces a similar "stress" skew value at 1310 nm as it does at 850 nm – in each case proportional to the stress differences across the fibers. Extending this argument further, we can expect the contribution to total skew due to stresses to be wavelength independent.

**FIBER INDEX DIFFERENCE:** Next, we consider the skew contribution due to the fibers having differing N values across the ribbon. Conceivably, the cabler could deliberately tension each fiber to counteract the natural index difference. Unfortunately, keeping track of specific fibers and adjusting the stresses is hardly a practical proposition for a modern cable factory. Realistically, the cabler can only reduce this source of skew by selecting closely matching fibers, such as using fibers drawn from the same preform.

**FIBER CHROMATIC DISPERSION DIFFERENCE:** In order to evaluate the variation in skew with wavelength starting with a comparison between 1310 nm to 850 nm, we consider the impact of the variation in chromatic dispersion between each fiber [7]. The chromatic dispersion is effectively a measure of the index as a function of wavelength. We expect the dispersion of each fiber to fall within a tolerance band defined by the fiber specification. From this allowed range, we can estimate the delay difference. In a standard unshifted fiber, the group delay curve follows a Sellmeier equation:

$$\tau(\lambda_i) = \left| A + \frac{1}{8} S_0 * \lambda_i^2 \left[ 1 - \left( \frac{\lambda_0}{\lambda_i} \right)^4 \right] \right| \text{ ps/m} \qquad \text{-(3)}$$

where

| | |
|---|---|
| A | a constant corresponding to the time of flight for a given length of fiber |
| $\lambda_0$ | the zero dispersion wavelength |
| $S_0$ | slope at the zero-dispersion wavelength |
| $\lambda_i$ | wavelength at which the delay is being calculated |

To evaluate this dispersive skew, we take the edge fiber in the ribbon as a reference for the other fibers. Because we have different fibers, the $S_0$ and $\lambda_0$ become unique to each fiber – $S_{01}$ and $\lambda_{01}$ for fiber 1 and $S_{0i}$ and $\lambda_{0i}$ for fiber i. By defining a reference wavelength $\lambda_1$, we can evaluate the skew at another wavelength $\lambda_2$. The dispersive skew at wavelength $\lambda_2$ is given by:

$$\Delta ti_{\lambda} = \left| \left[ (\tau_i(\lambda_1) - \tau_i(\lambda_2)) - (\tau_1(\lambda_1) - \tau_1(\lambda_2)) \right] \right| \text{ ps/m} \qquad \text{-(4)}$$

Substituting equation (3) in equation (4), we get:

$$\Delta ti_{\lambda} = \left| \frac{(\lambda_2^2-\lambda_1^2)}{8} \left\{ S_{01}\left[1+\frac{\lambda_{01}^4}{\lambda_2^2\lambda_1^2}\right] - S_{0i}\left[1+\frac{\lambda_{0i}^4}{\lambda_2^2\lambda_1^2}\right]\right\} + A_i - A_1 \right| \text{ ps/m} \qquad \text{-(5)}$$

Equation (5) allows the dispersive skew term to be evaluated across a ribbon fiber. Since we are focusing on the issue of skew difference across wavelength, we take 1310 nm as our reference wavelength (where the dispersion term in (5) reduces to a constant $\{A_i - A_1\}$ ). In fact, at this wavelength, a skew measurement would give the sum of the stress skew, the intrinsic fiber index difference (i.e., range of $A_i$), and the dispersive skew. If we now evaluate the dispersion skew difference between 850 nm and 1310 nm, this would be the only major difference in the total skew between 1310 nm and 850 nm. Evaluating equation (5) at 850 nm ignoring the constant $\{A_i - A_1\}$, the typical fiber "box spec" values for 50 µm fiber ($S_{01}$=0.093 ps/nm$^2$-km, $\lambda_{01}$ =1305 nm, and $S_{0i}$=0.095 ps/nm$^2$-km, $\lambda_{0i}$ =1315 nm) results in 1.69 ps/m of skew. For 62.5 µm fiber ($S_{01}$=0.090 ps/nm$^2$-km, $\lambda_{01}$ =1335 nm, and $S_{0i}$=0.093 ps/nm$^2$-km, $\lambda_{0i}$ =1345 nm), the result is 2.19 ps/m of skew. Therefore, over the ribbon, at 850 nm, we would expect a maximum skew difference of less than 2 ps/m due to this dispersive skew.

**TRANSMITTER WAVELENGTH IMPACT:** An additional concern with chromatic dispersion mismatch is that over the typical ±10 nm width of the 850 nm waveband there will be a finite difference in chromatic delay. Equation (5) reduces to equation (6) if the chromatic dispersion is assumed to be the same for all fibers. The half wavelength tolerance (e.g., ±x nm) is plotted for typical characteristics at 850 nm in Figure 1.

$$\Delta ti_{\lambda} = \left| \frac{S_0}{8} \left\{ \left[\lambda_2^2+\frac{\lambda_0^4}{\lambda_2^2}\right] - \left[\lambda_1^2+\frac{\lambda_0^4}{\lambda_1^2}\right] \right\} + A_i - A_1 \right| \text{ ps/m} \qquad \text{-(6)}$$

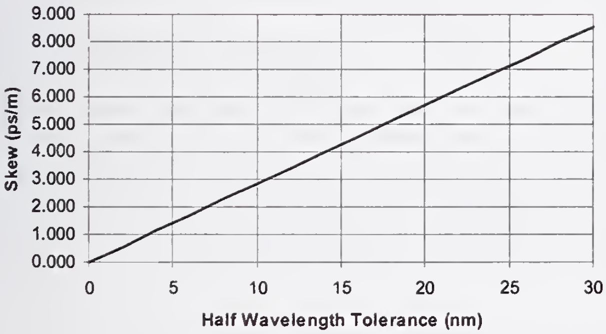

Figure 1 - Interaction of Wavelength and Fiber Index at 850 nm ($\lambda_0$ = 1310 nm, $S_0$ = 0.101 ps/nm^2-km)

Thus, even the simple wavelength tolerances across the parallel laser transmitters will invoke a "wavelength skew" term as well, amounting to approximately 3 ps/m of ribbon for the typical 10 nm wavelength variation. Moreover, this is outside the control of a ribbon cable or fiber manufacturer.

We can evaluate the dispersive skew if the dispersion characteristics of each fiber in the ribbon were known. Fortunately, test equipment typically used for skew testing in ribbons can also perform chromatic dispersion measurements at the same time [8]. These measurements enable the possibility of using a "correction factor" for skew at 850 nm versus 1310 nm. This is especially useful in the case where a multimode fiber might be used at either wavelength.

**DMD DELAY RANGE:** So far we have neglected the modal delay differences within the MM fiber. The fiber DMD can give rise to apparent skew [3]. The case of the most recently developed fiber, a 50 µm fiber designed for 10 GbE application, is the easiest to handle. This fiber, Corning® InfiniCor® SX+ fiber, is specified to have a restricted range of DMD. The maximum allowable delay difference is 0.7 ps/m. This results in 1.4 ps/m of skew between two fibers. This is well below the 5 ps/m typical tighter skew requirement. All other fiber types require approximation since it is only this new 50 µm fiber for which there is a DMD range requirement. During the course of 1 GbE development, 62.5 µm fiber was shown to have up to 2 ps/m delay difference [9]. The maximum DMD range can be approximated using simple Gaussian assumptions. In this case, the DMD range can be estimated by the following formula [10]:

$$DMD\ range\ (in\ ps/m) = \frac{440}{Bandwidth\ (in\ MHz-km)} \qquad \text{-(7)}$$

In the case of 500 MHz-km fiber, the DMD range is 0.88 ps/m, resulting in a potential 1.76 ps/m skew between two fibers. Although this approximation provides an estimation of the skew resulting from DMD, there can be a large difference between this prediction and the actual performance on fiber specified in terms of the standard overfilled bandwidth. This is evident by the difference between the 0.88 ps/m predicted and 2 ps/m previously shown. Thus, since the maximum fiber-to-fiber estimated DMD-induced skew is 4 ps/m, it is possible to use skew tests on only the lowest order mode, using single-mode optics to reveal the cable-related skew effects.

## Conclusion

This paper has focused on the issue of skew testing in multimode fibers, in particular fibers designed for high-speed applications operating at 850 nm operation. We have shown that:

- Better than 5 ps/m skew performance should be deliverable on new 50 µm fiber designed for high-speed application at 850 nm (i.e., meeting a DMD requirement) by testing at 1310 nm using a single-mode launch to confirm that the cable induced skew is negligible.
- The difference in skew resulting in measuring at 1310 nm to determine 850 nm performance and the mismatch in index between two fibers is estimated to be less than 2 ps/m for typical 50 µm and 62.5 µm fibers. This can be quantified from the measured chromatic dispersion.
- The ribbon fiber skew due purely to the wavelength tolerance of the set of transmitters used on a link can be significant compared to a 5 ps/m allowance. The effect using 850 nm sources with a 20 nm range is estimated to be less than 2 ps/m for typical 50 µm and 62.5 µm fiber.
- The impact of intermodal dispersion on skew should be less than 1.4 ps/m on new 50 µm fiber designed for 10 GbE application. It could be as high as 4 ps/m on installed base fiber.
- A few ps/m is close to the state-of-the-art skew accuracy that may be obtained for ribbon fibers. This makes delivery to a ≤5 ps/m requirement problematic, but a 15-20 ps/m specification more realistic.

Utilizing this understanding of the various factors affecting multimode fiber skew, delivery of ribbon cable meeting 5 ps/m skew should be achievable. Current measurement equipment can be utilized to improve the estimation of skew. For example, equipment designed for testing of single-mode fiber at 1310 nm can provide insight into the most significant factors affecting skew, specifically cabling induced stress. Therefore, the difficulty of obtaining costly single-mode optics at 850 nm, or indeed using 850 nm multimode optics with the corresponding requirements on launch control within the test instrument, can be avoided. Careful selection of the fiber, such as selection of fiber from the same preform, or by utilizing the measurement equipment to estimate any index differences should control the fiber related skew. By utilization of this measurement equipment in conjunction with careful selection of the fiber, this requirement should be achievable.

## Acknowledgement

The authors are grateful to Chris DiMinico of CDT Corporation for detailed and helpful discussions.

## References

1. TIA FOTP-220 "Differential Mode Delay Measurement of Multimode Fiber in the Time Domain".
2. IEEE HPPI-640-OPT standard in draft, Project number 1249-D.
3. A .Barlow et al, "Measurement of Ultra-low Skew in Ribbon Fibers". OFMC, 1997, London.
4. G. Brown, "Chromatic Dispersion Measurement in Graded-Index Multimode Optical Fibers", Jnl. Lightwave Technology. 12, 11, pp.1907-1909, 1994
5. M. Brininstool, Optical Engineering, 26, 1987, pp. 1112-1119.
6. M.J. Adams, "An Introduction to Optical Waveguides", Wiley, p.246
7. M. Hackert, "The Importance and Application of Dispersion of Multimode Fiber in LANs and Its Relation to NA", International Wire and Cable Symposium, 1988, pp.237-242.
8. PerkinElmer CD400 Series Measurement Systems.
9. M. Hackert, "Characterizing Multimode Fiber Bandwidth for Gigabit Ethernet Applications", SOFM 98.
10. Corning Cable Systems Application Note 20, "Bandwidth / Dispersion Equation Derivation".

# Phase imaging methods for optical fiber characterization

**A. Roberts[*], G. Baxter[†], N. Dragomir[†], S.T. Huntington[◊],**
**E. Ampem-Lassen[*], M.L. Michna[*] and K.A. Nugent[*]**

[*]School of Physics, University of Melbourne, Victoria, 3010, Australia
[†]School of Communications and Informatics, Victoria University, PO Box 14428, Melbourne, Victoria, 8001, Australia
[◊]Particulate Fluids Processing Centre, School of Chemistry, University of Melbourne, Victoria, 3010, Australia

## Abstract

In this paper we demonstrate the application of two phase imaging techniques, Differential Interference Contrast (DIC) and Quantitative Phase Microscopy (QPM), to the determination of the microscopic physical structure of optical fibers and fiber gratings. We also show that birefringence images can also be obtained using QPM with polarized light. As well as being able to image fibers, these methods can provide quantitative information on refractive index and axial stress profiles within axially symmetric fibers.

## Introduction

The development of a wide range of optical fibers with complex structures means that the ability to accurately determine the physical properties of the fiber is essential. Two quantities of central importance are knowledge of the refractive index profile of a fiber and stress introduced into the fiber during the fabrication process or through bending. In this paper we demonstrate the application of two phase imaging methods, DIC and QPM, to the determination of the physical structure of the fiber. In addition to enabling the determination of the physical properties of the fiber, we also present images of an in-fiber Bragg grating which display the artifacts introduced into the fiber by the grating writing process.

A knowledge of the refractive index profile is invaluable since from it fiber properties such as the mode profile, dispersion and cutoff wavelength can be calculated. The commonly used industry standard method, the Refracted Near Field (RNF) technique, cannot be used to study fibers where the refractive index varies along the axis of the fiber, has difficulty analyzing fibers with complex structure and it is destructive since the fiber must be cleaved. The calibration of any instrument based on the refracted near field technique is also critical if precise numerical values for the index change $\Delta n$ are required.[1] A range of other methods have also been considered and are summarized in Reference 2. Here we present two phase imaging methods, DIC and QPM, that can be used to quantitatively determine the phase shift in light as it traverses an optical fiber and from this information determine the refractive index profile.

There is also a great deal of interest at present in further understanding stress within fibers and its role in the index change of fibers on irradiation with ultraviolet light [3]. An understanding of the role that changes in stress play in the change in refractive index of a fiber on thermal annealing is also important if index change mechanisms are to properly understood. Commonly used methods for determining stress within fibers generally involve variations on polarimetry [3, 4] and tend to suffer from poor signal-to-noise and/or spatial resolution. Here we also demonstrate that QPM can be used to accurately measure birefringence and we are currently in the process of extending this research into the determination of intrinsic stress within fibers.

The optical microscopic methods discussed here are simple to implement, accurate, relatively inexpensive and non-destructive. Their spatial resolution is diffraction-limited. They can be used to study fibers where the refractive index profile and stress vary along the axis of the fiber (for example tapered fiber sensors and fibers containing gratings), and can be extended to the study of non-axisymmetric fibers by employing tomographic techniques.

**Phase Imaging**

Differential Interference Contrast (DIC) microscopy [5] has achieved widespread popularity amonst the biological community for its ability to very simply elucidate the structure of transparent specimens. DIC involves the inclusion of a Wollaston prism into the microscope beam path which splits the incoming light into two spatially separated, orthogonally polarized beams of light. These two beams are recombined after they have traversed the specimen and their interference provides information about phase gradients within the object. Using certain a-priori assumptions, this method can also be used to determine the refractive index profile of an axially symmetric fiber.

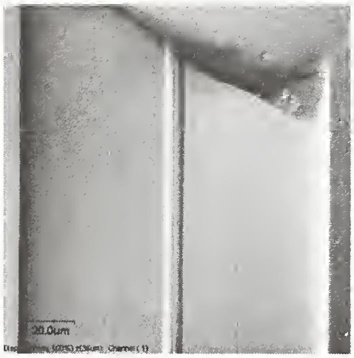

**Figure 1:** Typical DIC image of an optical fiber.

Quantitative Phase Microscopy (QPM) [6] is a new non-interferometric technique that can be used to quantitatively determine the phase of a transparent specimen. QPM is based on the transport of intensity equation where variations within the phase introduced into the lightfield by a specimen are manifested as variations in the transmitted intensity as the distance is varied. A recently developed algorithm [7] can be used to retrieve the phase of the field from three (or in the case of uniform intensity, two) intensity images. Two key advantages of this technique is that the phase determined in this manner does not been to be ‘unwrapped’ and the method can be used with partially coherent light. This algorithm has also been shown to be robust and has been applied to phase imaging with light, x-rays, electrons, atoms and neutrons. [8] We present below the application of this method to the determination of the refractive index profiles of axially symmetric optical fibers. In the case of non-axially symmetric fibers, a series of phase images can be obtained as the specimen is rotated about its axis and tomographic methods used to determine the index profile. [9] In addition, QPM can be used with polarized light to quantitatively determine the birefringence of a specimen and we have applied this to the determination of the axial stress induced when a fiber is bent through a known radius of curvature [10].

**Differential interference contrast imaging**

DIC images were obtained using an inverted Olympus IX FL infinity corrected optical system equipped with high resolution Nomarski optics. An argon ion laser operating on a single line at a wavelength 488 nm was used as the light source. In addition, the system used a computer to control the fine focus of the microscope via a stepper motor, translating the objective of the microscope in 0.1 μm increments along the optical axis of the microscope. The laser beam was raster scanned over an area of the specimen using galvo mirrors. Fibers under study had their plastic coating removed and placed in a cell and surrounded by index matching oil.

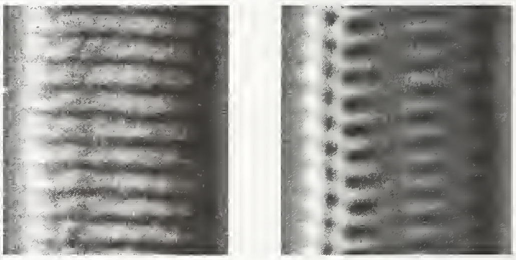

**Figure 2:** DIC images of a Bragg grating. The fiber was rotated about its axis by 90° to obtain the second image. Image sizes 9.7 × 10.4 μm.

A typical DIC image of a $Er^{3+}$-doped fiber is shown in Figure 1. The core, along with the well-known depression in index at its center, are clearly visible as is the boundary of the depressed cladding region. In order to demonstrate the high spatial resolution and the application of DIC to the study of fibers and devices possessing variation along the axis of the fiber we investigated a Bragg grating. This grating was fabricated at Victoria University using our own facilities by the familiar phase mask technique with standard communications fiber. The samples were hydrogen loaded prior to being irradiated with an UV laser source (244 nm CW). An interference pattern was formed at the core of the fiber using a 1.06 μm pitch phase mask. The spectral response of the fiber was measured and a transmission minimum found at approximately 1534 nm. Two DIC images of the Bragg grating are shown in Figure 2. The second image was taken after the fibre was rotated about its axis by 90° with respect to its initial orientation. The structure of the grating is apparent from these images. Particularly striking is the asymmetry of the grating and the appearance of artifacts resulting from the grating fabrication process.

**Quantitative Phase Microscopy**

QPM was performed using transverse images obtained with a standard bright-field microscope (Olympus BX-60 microscope, 0.95 40× UplanApo microscope objective). The condenser numerical aperture was set to 0.2 and a bandpass filter with a central wavelength of 521nm and a passband of 10nm was included in the light path. A dilute solution (~85%) was used as the index matching fluid. Fibers under investigation have their plastic coating removed.

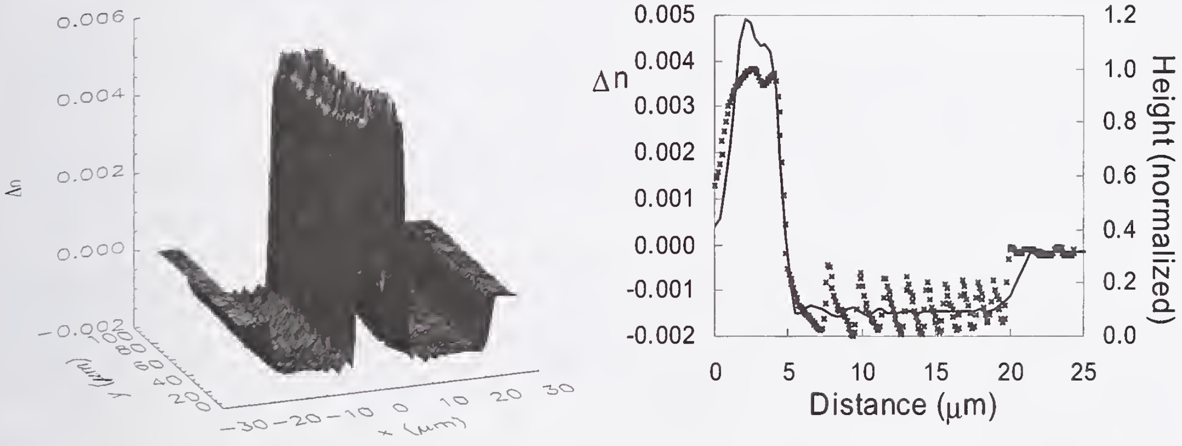

(a) (b)

**Figure 3:** Refractive index of an optical fiber determined using QPM. (a) shows a surface plot of the index as a function of radial and axial position within the fiber and (b) shows the average radial profile (solid line) compared with the topography measured with an AFM (dots) of the fiber after etching.

Three bright-field images of GF1 (Optical Fibre Technology Centre, Sydney, Australia) were obtained. These consisted of an in-focus image and two defocused images at ± 2.6 μm. The in-focus image displayed virtually no structural information about the fiber. These three images were then processed using an algorithm based on the transport of intensity equation [6] to produce a phase image of the fiber. The inverse Abel transform [11] was then applied to this phase image to determine the refractive index profile shown in Figure 3(a). The average profile over the 100 μm length of fiber displayed in Figure 3(a) is shown in Figure 3(b). Note that the core and the various deposition layers are clearly resolved. The maximum refractive index change measured using this technique was found to be 0.0064 ± 0.0003 (standard deviation), which is in good agreement with that found using a conventional profiling instrument of 0.0056. It should be noted, however, that the profiler did not resolve the feature near the index maximum at a radius of ~ 3μm and its resolution of the deposition rings in the depressed cladding was noticeably poorer than that obtained using QPM. In Figure 3(a) a shaded surface plot demonstrates the ability of this method to determine axial variations in refractive index, while in Figure 3(b) the refractive index determined using QPM is compared with the vertical structure of the endface of the fiber after it has been cleaved and etched in a saturated solution of buffered hydrofluoric acid for 3 minutes.

The topography was measured with an Atomic Force Microscope (AFM) operated in contact mode. [12] Given the complexity of the etch rate due to the presence of multiple dopants, the AFM profile is not expected to be proportional to the index profile, but structures seen in the topography measured in this way clearly match the features seen in the QPM profile.

### Polarized light QPM

We have also demonstrated that QPM can be used with polarised light [10] to determine the birefringence of specimens. This is performed by acquiring a phase image of the specimen when the light is polarised along one principal axis of the specimen (for example, along the axis of an optical fiber) and a second with the light polarized in the orthogonal direction. Simply subtracting these two images produces a quantitative birefringence image of the specimen. In particular, we obtained birefringence images of an optical fiber bent through known radii of curvature ranging from 1cm to 8cm and obtained excellent agreement between the birefringence determined and that calculated using a simple model which assumes that the fiber behaves as a homogeneous cylindrical cylinder. Figure 4 shows the birefringence image obtained when the fiber is bent through a radius of curvature of 1cm. The center of curvature is to the left of the image and the regions of compressive (dark) and tensile (light) stress are clearly visible.

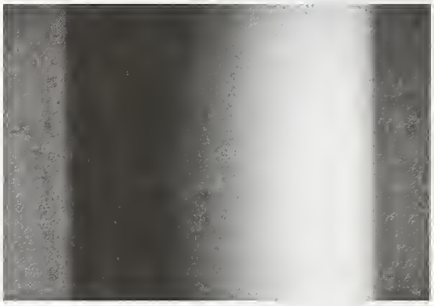

**Figure 4:** Birefringence image of an optical fiber bent through a radius of curvature of 1cm. The center of curvature is to the left. Image size 176 × 121 μm.

### Conclusion

We have demonstrated the applicability of phase imaging methods to the characterization of the physical properties of optical fiber and other photonic devices. In addition to the fact that these methods enable the visualization of the fiber or device structure with diffraction-limited resolution, they can also be used to determine the refractive index profiles of optical fibers. These techniques are straight-forward, relatively inexpensive and accurate compared with other techniques.

### Acknowledgements

The authors would like to acknowledge useful conversations with Peter Farrell and John Canning. The authors would also like to thank Tom Ryan of the Optical Fiber Technology Centre (OFTC), Australia, for obtaining independent refractive index profiles of samples, and the OFTC and the Laboratoire de Physique de la Matière Condensée, Université de Nice for the provision of the fiber specimens.

### References

1. D. Marcuse and H. M. Presby, Proc. IEEE, **68**, 666-688, 1980.
2. KW Raine, JGN Baines and DE Putland, J. Lightwave Tech., 1162-1169, 1989.
3. N.H. Ky, G.G. Limberger, R.P. Salathé, F. Cochet and L. Dong, Appl. Phys. Lett., **74**, 516-518, 1999.
4. K.W. Raine, R. Feced, S.E. Kanellopoulos and V.A. Handerek, Appl. Opt., **38**, 1086-1095, 1999.
5. T.R. Corle and G.S. Kino, Confocal scanning microscopy and related imaging systems, (Academic San Diego, California, 1996), p. 247.
6. D. Paganin and K.A. Nugent, Phys. Rev. Lett. **80**, 2586-2589, 1998.
7. A. Barty, K.A. Nugent, D. Paganin, and A. Roberts, Opt. Lett. **23**, 817-819, 1998
8. K.A. Nugent, D. Paganin and T.E. Gureyev, Physics Today, **54**, 27-32, 2001.
9. A. Barty, K.A. Nugent, A. Roberts and D. Paganin, Opt. Comm., **17**, pp. 329-336, 2000.
10. A. Roberts, K. Thorn, M.L. Michna, N. Dragomir, P. Farrell and G. Baxter, Opt. Lett., **27**, 86-88, 2002.
11. M Kalal and KA Nugent, Appl. Opt., **27**, 1956 – 1959, 1988.
12. S.T.Huntington, P.Mulvaney, A .Roberts and KA Nugent, J. Appl. Phys., **82**, 2730, 1997.

# Measurement of fiber birefringence using Lyot-Sagnac interferometer

**Chang-Seok Kim, Young-Geun Han*, Raymond M. Sova and Jin U. Kang**
*Department of Electrical and Computer Engineering,*
*Johns Hopkins University, Baltimore, MD 21218*
*Phone: 410-516-8186, Fax: 410-516-5566, E-mail: jkang@jhu.edu*

**Un-Chul Paek and Youngjoo Chung**
*Department of Information and Communications,*
*Kwangju Institute of Science and Technology, Kwangju, Korea*

* *Permanent Address: Department of Information and Communications, K-JIST, Kwangju, Korea*

**Abstract:** We propose and demonstrate a simple and accurate optical fiber modal birefringence measurement technique. The technique is based on discrete tuning of the periodic spectrum produced by the dual-segmented Lyot-Sagnac fiber interferometer.

The modal birefringence of optical fiber is an important parameter for both the polarization-dependent optical devices using high birefringence fibers [1] and the optical fiber telecommunication systems using low birefringence fibers [2]. Various techniques have been proposed to measure the birefringence of optical fibers [2][3][4]. A polarization-sensitive analysis of the backscattered signal was proposed for measurement of low-birefringence fibers [3], which requires a length of fiber too long to be practical for some applications. For the measurement of fibers with less than one beat length, fiber twist adjustment in the fiber-optic loop mirror was suggested [2]. The fiber Sagnac loop interferometer can be also used to determine the birefringence of fiber, where the birefringence, or beat length, of optical fiber could be determined from the periodic transmission spectrum of the standard fiber Sagnac loop interferometer [4]. However, this measurement technique has not been practical for a short section of a low-birefringence fiber because its periodic transmission function is very broad. In this paper, we suggest a novel technique based on a Lyot-Sagnac fiber interferometer to measure a birefringence of low-birefringence fiber by decreasing the width of the periodic transmission function without using a very long fiber length.

A conventional fiber Sagnac loop interferometer has been demonstrated for applications in wavelength-division multiplexing (WDM) filters and in sensors because of its several advantages, such as temperature insensitivity, high extinction ratio, and independence of input polarization [4]. This device consists of a directional coupler with two output ports connected by a birefringence fiber loop. A phase difference between two counter-propagating beams results in transmission dependence on wavelength or fiber birefringence. The wavelength period, $\Delta\lambda$, is a function of the $\Delta n \cdot L$ product value, which is the intrinsic properties of the fiber. This is shown in Eq. (1), where $\lambda$ is the operation wavelength, $\Delta n$ is the fiber modal birefringence, $L$ is the effective length of the fiber.

$$\Delta\lambda = \frac{\lambda^2}{\Delta n \cdot L} \qquad (1)$$

Since the wavelength period depends on the $\Delta n \cdot L$ product of the fiber, $\Delta\lambda$ is a large value for the short length of a low-birefringence fiber. This requires an additional curve fitting process to deduce the value accurately. [4]. In order to reduce the width of the transmission function significantly, one can use a very long length of a low-birefringence fiber, but a long fiber length is a cumbersome to deal with and there is an additional uncertainties due to a possible tension and strain in the spool.

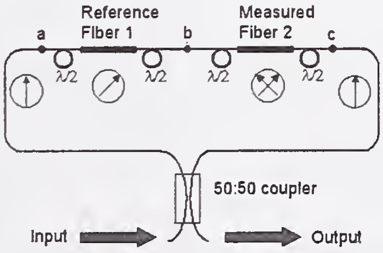

Fig. 1. Fiber Lyot-Sagnac interferometer setup.

Recently, we demonstrated a novel Lyot-Sagnac filter capable of discretely tuning the wavelength period, $\Delta\lambda$, by varying the effective value of the $\Delta n \cdot L$ product [5]. The fiber Lyot-Sagnac loop interferometer is composed with a 50:50 fiber coupler, two sections of fiber with a length L1 and L2, and all-fiber polarization controllers acting as half-wave plates, $\lambda/2$. This is schematically shown in Fig. 1. The arrows inside circle represent the relative angle directions of the fast axis of high birefringence fiber and the plane of Sagnac loop. By changing the fast axis direction angles of two fiber, such as each fast axis is either +45 ° or -45 ° relative to the plane of Sagnac loop, we can discretely vary the effective value of $\Delta n \cdot L$ and, thus, the wavelength period of the filter is discretely tuned. For the fixed angle polarization angles, 45 °, 0 °, -45 ° at the position of a, b, and c in Fig. 1, respectively, the effective value of $\Delta n \cdot L$ for the device becomes $\Delta n_1 \cdot L_1 + \Delta n_2 \cdot L_2$. In the other combination of relative angles, $\theta(a) = 45°$, $\theta(b) = -90°$, and $\theta(c) = 45°$, the effective value of $\Delta n \cdot L$ product becomes $\Delta n_1 \cdot L_1 - \Delta n_2 \cdot L_2$. Therefore, the distinct values of $\Delta n \cdot L$ product result in two different wavelength periods, $\Delta\lambda_S$ and $\Delta\lambda_L$ as shown in Eq (2), where S denotes the summing case and the L denotes the difference in that length;

$$\Delta\lambda_{\substack{S\\L}} = \frac{\lambda^2}{\Delta n_1 \cdot L_1 \pm \Delta n_2 \cdot L_2} \qquad (2)$$

In the fiber Lyot-Sagnac loop configuration of the Fig. 1, the section 1 is used as a reference section with a known high birefringence fiber and the section 2 becomes a measurement section having a low birefringence fiber to be measured. As compared with the conventional Sagnac loop, we could decrease the bandwidth of periodic transmission function of low-birefringence fiber easily and precisely since the denominator of Eq. (2) is increased as the larger value of $\Delta n_1 \cdot L_1$ is applied. Here, the small value of $\Delta n_2 \cdot L_2$ controls the discretely tuned two bandwidths of periodic transmission spectrum, $\Delta\lambda_S$ and $\Delta\lambda_L$, as represented in the Eq. (2). Therefore, from measuring the two distinct wavelength periods $\Delta\lambda_S$ and $\Delta\lambda_L$, and the length of $L_2$, we could precisely determine the birefringence, $\Delta n_2$, of optical fiber. From the Eq (2), the equation for the birefringence value of fiber 2 can be shown in Eq. (3);

$$\Delta n_2 = \frac{\lambda^2}{2L_2}\left(\frac{1}{\Delta\lambda_S} - \frac{1}{\Delta\lambda_L}\right) \qquad (3)$$

Note that the values of $\Delta n_1$ and $L_1$ of the reference fiber 1 are not required in calculating the birefringence value of fiber 2. For the experimental demonstration of measuring the small value of the $\Delta n_2 \cdot L_2$ in the fiber Lyot-Sagnac loop configuration, we used a commercial high-birefringence fiber 1 (FS-PM-7811) with $\Delta n_1$ of $7.47 \times 10^{-4}$ and a low-birefringence fiber 2 with $\Delta n_2$, of $2.6 \times 10^{-5}$. The birefringence value of fiber 2, which is 30 times smaller than that of fiber 1, was designed to set up the fiber Lyot-Sagnac loop with a similar length for each fiber section. Fig 2 shows the calculated transmission spectrum of the conventional fiber Sagnac loop interferometer having the fiber 2 with the length, $L_2$, of 1.8m. It is impossible to measure the wavelength period value, $\Delta\lambda$, of 51.3 nm using the conventional C-band light source of 1530~1565 nm wavelength range because the wavelength period value is larger than wavelength width of light source. Though we could measure the wavelength period value using a broadband white light source, it is hard to couple into a single mode fiber for the measurement and is a low power per bandwidth. This also requires a following curve fitting process to estimate the birefringence of fiber from the measured value of $\Delta\lambda$ and the Eq. (1) as explained earlier.

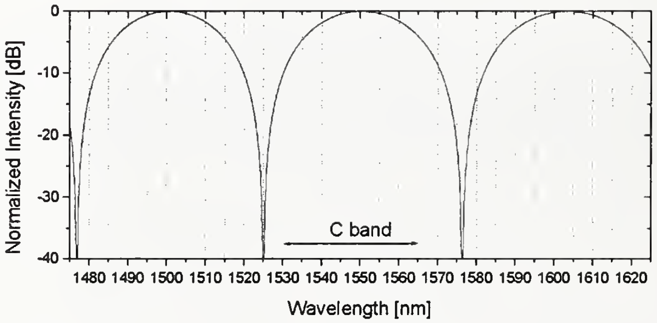

Fig. 2. Typical calculated transmission spectra of the conventional fiber Sagnac loop interferometer with low birefringence fiber 2 only.

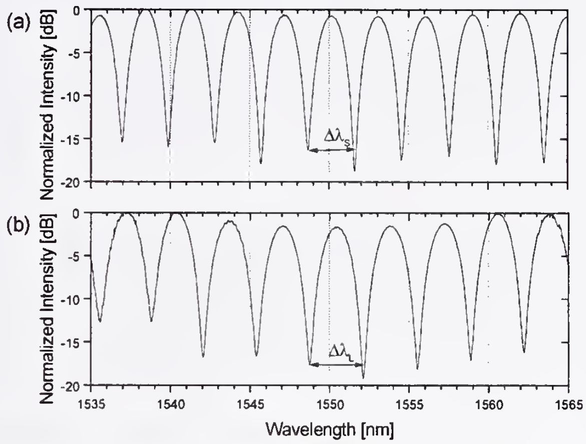

Fig. 3. Experimental measurement of two distinct bandwidths of periodic transmission of the fiber Lyot-Sagnac loop interferometer.

In the proposed fiber Lyot-Sagnac interferometer configuration, we could decrease the width of periodic transmission function using the reference section with 1.02 m of the fiber 1 (FS-PM-7811), which has a shorter length and a significantly higher birefringence than fiber 2. Fig. 3 (a) and (b) show the corresponding experimental result, respectively. The measured two different wavelength period values, $\Delta\lambda_S$ of 2.97 nm and $\Delta\lambda_L$ of 3.36 nm, can be directly obtained from the graph and the Eq. (3) can be used to determine the birefringence value as $2.61\times10^{-5}$. This method does not require the curve fitting because the wavelength period only vary insignificant amount within the spectral range needed to extract the period values. In general, $\Delta n_1 \cdot L_1$, of a reference fiber should be between 10 to 50 times the $\Delta n_2 \cdot L_2$, of a low birefringence fiber in question. In this experiment, the transmission spectra are measured using an Erbium-doped fiber laser source at the center wavelength of 1550 nm and an optical spectrum analyzer (Ando, AQ-6315) with a resolution of 0.05 nm.

In conclusion, we have proposed and demonstrated a simple and precise low-birefringence measurement technique for based on a Lyot-Sagnac interferometer configuration. Using the novel scheme, we discretely tuned the bandwidths of periodic transmission spectrum to induce the value of the $\Delta n \cdot L$ product.

## References

[1] Raymond M. Sova, Chang-Seok Kim, and Jin U. Kang, "Tunable dual wavelength All-PM fiber ring laser" IEEE Photon. Tech. Lett., 14, 287 (2002)

[2] E.A.Kuzin, J.M. Estudillo Ayala, and B. Ibarra Escamilla, "Measurements of beat length in short low-birefringence fibers", Opt. Lett. 26, 1134 (2001)

[3] A. Galtarossa, L. Palmery, M. Schiano, and T. Tambosso, "Measurements of beat length and perturbation length in long single-mode fiber", Opt. Lett. 25, 384 (2000)

[4] Xiaojun Fang and Richard O. Claus, "Polarization-independent all-fiber wavelength-division multiplexer based on a Sagnac interferometer", Opt. Lett., 20, 2146 (1995)

[5] Chang-Seok Kim, Raymond M. Sova, Jin U. Kang, and Jacob B. Khurgin, "Novel multi-wavelength cascaded-Raman source based on tunable fiber Sagnac loop filter", in the Technical Digest of Optical Fiber Communication Conference 2002, WJ1, Anaheim, CA (2002).

# Determination of the degree of polarization based on a coherent quantum measurement

*Matthieu Legré, Mark Wegmüller, Nicolas Gisin*

*Group of Applied Physics, University of Geneva,*
*20 rue de l'Ecole-de- Medecine, CH-1205 Genève, Switzerland.*

*Abstract: A novel method for the measurement of the degree of polarization is described. It is one of the first practical implementations of a coherent quantum measurement, the projection on the singlet state. Our first results demonstrate the successful operation of the method. However, due to the nonlinear crystals used presently, its application is limited to light beams with spectral widths larger than ~8nm.*

## I. INTRODUCTION

PMD (polarization mode dispersion) is one of the limiting factors in optical fiber data transmission. The degree of polarization (DOP) is routinely used in PMD compensators as a feed-back parameter to control the dynamic adjustment of the compensator [1,2]. For such applications, it is interesting to have a compact, fast, and cheap measurement apparatus to determine the DOP.

## II. BASIC IDEA AND PRINCIPLE OF OPERATION

The DOP of photons propagating at the same time, in the same spatial mode, and at the same wavelength equals 1. Depolarization appears when at least one of these conditions is no longer satisfied. A DOP<1 consequently means that there are temporal fluctuations of the polarization, or that the beam is composed by several spatial modes, or that the light is not monochromatic (or a combination of the above). In our case, we are interested in the depolarisation due to the action of the PMD on a telecom laser with a spectral bandwidth of ~0.3nm.

For this case, one of the authors has demonstrated in [3] the possibility to do a direct determination of the DOP with a coherent quantum measurement, the projection on the singlet state $\psi^{(-)} = \left(|H_1,V_2\rangle - |V_1,H_2\rangle\right)/\sqrt{2}$. $\psi^{(-)}$ is one of the four Bell states (which are the standard base of two photon polarization states). A fundamental property of the singlet state, exploited in your experiment, is its rotational invariance. This means that the result of the projection on $\psi^{(-)}$ is independent of the arbitrary frame chosen (or in other words, that only the relative, but not the absolute, polarization of the two photons determines the result). In [3], it is demonstrated that the result of the projection is proportional to (1-DOP$^2$).

Bell states are very common in quantum optics, so projection on the singlet state has already been done [4], however only for photons with a large wavelength difference (85nm). This value is very far from the <0.3nm desired here. $\psi^{(-)}$ is antisymmetric and photons are bosons, which makes it harder to realize the projection on the singlet state for photons with similar wavelengths.

The principle of the projection is described in figure 1. We use two identical crystal for SFG (Sum Frequency Generation, $(\lambda_1,\lambda_2)\rightarrow\lambda_3$) of type II (polarizations of $\lambda_1$ and of $\lambda_2$ are orthogonal). The second crystal is orthogonal to the first one (i.e. rotated by 90° around the light path). Using H for horizontal and V for vertical polarizations, we have, for exemple, in the first crystal $(H_1,V_2)\rightarrow V_3$ and $(V_1,H_2)\rightarrow H_3$ in the second one. The phase difference between the SFG waves created in the first and second crystal is adjusted to $\pi$ by tilting a birefringent plate. The two waves are then projected on a 45° polarizer. The intensity of the interference signal correspond to the (non-normalized) projection on the singlet state of the two input photons.

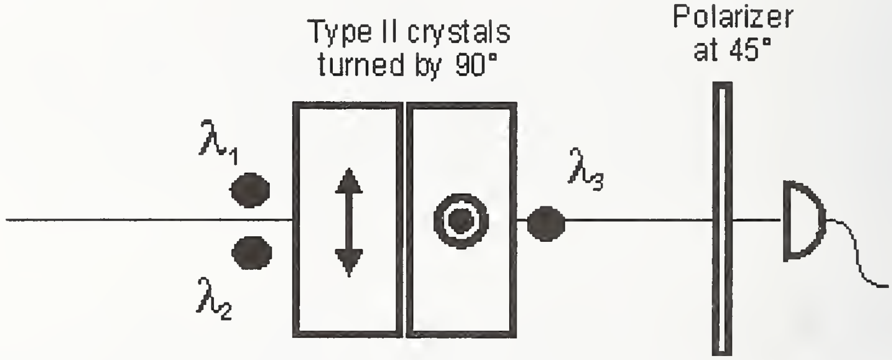

Figure 1 : Schematic of the principle of the projection on the singlet state of a photon pair $(\lambda_1,\lambda_2)$.

## III. EXPERIMENTAL SET-UP AND RESULTS

We chose KTP type II crystals (XZ plane) as they promise for a good SFG efficiency and are readily available. To avoid any problem with the spatial walk-off (3°) we opted for a short crystal. This however implies a low wavelength selectivity: for a KTP crystal of 3mm length, the phase-matching bandwidth equals 18nm -this means that for $|\lambda_1-\lambda_2|<18$nm, both $((H_1,V_2)\rightarrow V_3$ and $(V_1,H_2)\rightarrow V_3)$ SFG processes start to be phase-matched, perturbing the singlet projection as we will see later. The set-up used for the singlet projection

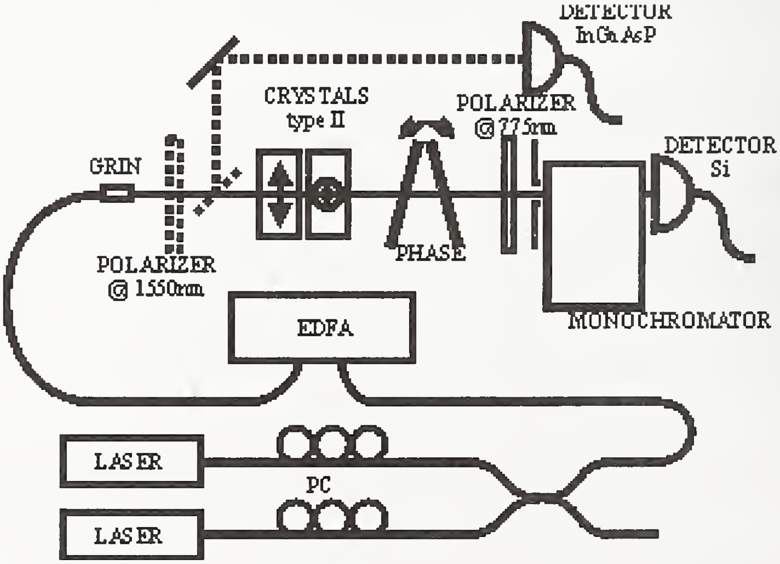

Figure 2:Diagram of the experimental setup.

is shown in figure 2. The source is composed of two tunable lasers around 1550nm, combined by a fiber coupler. Each polarization can be controlled independently. The total power after amplification is about 70mW. Before being projected on the singlet state, the light is collimated with a fiber GRIN lens. Further, to analyse the correct operation of the DOP meter, a polarization analyzer could be inserted in front of the crystals (dashed elements in Figure2). For simplicity of notation, we allow for linear polarizations only, and define the two polarizations with two angles $\theta$ and $\varphi$ in the plane (x,y), with x parallel to the X axis of the first crystal (figure 3). ). $\theta$ is the angle between the x axis and the polarization of $\lambda_1$, and $\varphi$ the angular difference between the two polarizations (i.e. $\lambda_2$ is polarized along $\theta+\varphi$). Note that for the elliptical polarizations we can use the same notation but $\varphi$ becomes the difference between $\chi_1$ and $\chi_2$ ($\tan\chi=E_y/E_x$) and $\theta$ equals $\chi_1$. The DOP of a source composed of two lasers with wavelengths $\lambda_1$ and $\lambda_2$ is $\sqrt{(I_1+I_2)^2-4I_1I_2\sin^2\varphi}\big/(I_1+I_2)$.

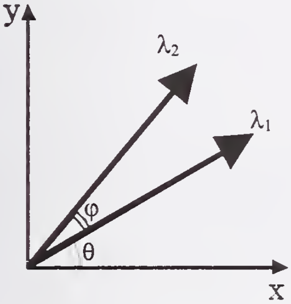

Figure 3: Definition of the angles $\theta$ and $\varphi$. The directions x and y are parallel to the optical axis of the first and second crystal, respectively.

The projection on the singlet state has been tested for several wavelength differences. For $\lambda_1$=1542nm and $\lambda_2$=1560nm (see figure 4), one sees that the closer $\varphi$ gets to 0, the smaller the number of counts. This is the expected behavior where the number of counts is proportional to (1-DOP$^2$). However, the (theoretically absent) $\theta$ dependence of the result reduces the accuracy of a single measurement, and one should therefore rather use the mean value from several measurements with different $\theta$s. As the figure demonstrates, this mean values follow the theoretical behavior very well.

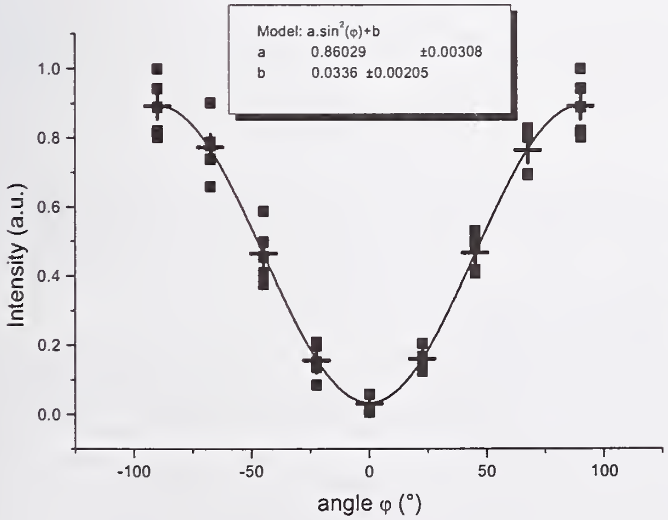

Figure4: Measured intensity of the singlet-state as a function of the relative polarization angle $\varphi$ for $\lambda_1$=1542nm and $\lambda_2$=1560nm. Square data points: results for different $\theta$s, crosses: mean values, solid line: fit with the function $a\sin^2(\varphi)+b$.

The results become qualitatively different for a wavelength separation as small as 4 nm (Figure 5). The noise 'fluctuations' are very large now, covering almost completely the dependence on φ, i.e. the DOP. Nevertheless, the experimental data are still found to be very reproducible. The mean values are not constant as one might expect at first view, but are found to vary as $a+b\sin^2(\varphi)+c\sin^2(\varphi+2d)$.

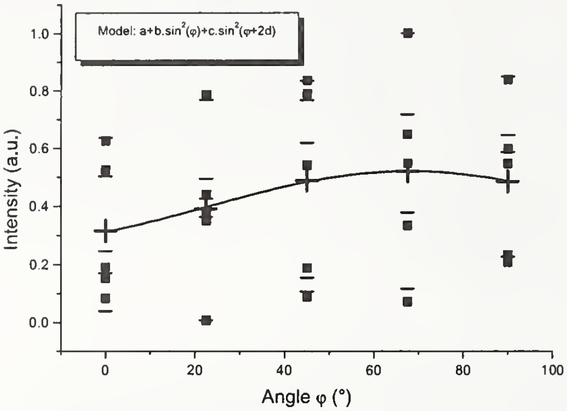

Figure 5: Measured intensity of the singlet-state as a function of the relative polarization angle φ for $\lambda_1$=1542nm and $\lambda_2$=1546nm. Square and bar data points: two different sets of measurements, solid line: fit with the function $a+b\sin^2(\varphi)+c\sin^2(\varphi+2d)$.

This is due to the earlier-mentioned co-existence of the two SFG processes for small wavelength separations. The relative weight of the second perturbing SFG interaction increases when the two wavelengths become closer. If we consider a signal to noise ratio (signal: contribution from first process, noise: from second process) of 1 as the limiting criteria for a proper singler projection, a minimal wavelength difference of ~5.5nm is find, this is in fairly good agreement with our experimental results.

## IV. CONCLUSION

A direct measurement of the DOP is possible with a coherent quantum measurement, the projection on the singlet state. This projection can be realized with nonlinear interactions. The minimal spectral bandwidth of the source we can measure is determined by the phase-matching bandwidth of the crystals. With crystals of GaSe or HgS of 1cm length, it should be possible to measure the DOP of a telecom laser working at 40Gbits.

***Acknowledgements:*** *Financial support from the Swiss OFES in the frame of the COST 265 project and EXFO Inc (Vanier, Canada) are acknowledged.*

## References

1- "A simple dynamic polarization mode dispersion compensator", F. Roy, C.Francia, F. Bruyère, D. Penninckx, Tech. Dig. OFC'99, San Diego (1999)
2- "Higher order polarization mode dispersion compensator with three degrees of freedom", M. Karlsson, C. Xie, H. Sunnerud, P.A. Andrekson, Tech. Dig. OFC'01, Anaheim (2001)
3- "Coherent quantum measurement for the direct determination of the degree of polarization and polarization mode dispersion compensation", N. Gisin, Journal of Modern Optics **48**, 1397(2001)
4- "Quantum teleportation of polarization state with a complete Bell state measurement", Y. Kim, S. P. Kulik, Y. Shih, Physical Review Letters **86**, 1370(2001)
5- "Experimental investigations of coherent quantum measurement of the degree of polarization of a single mode light beam", submitted to Journal of Modern Optics

# Visualizing the Limitations of Four-State Measurement of PDL and Results of a Six-State Alternative

R. M. Craig
Optoelectronics Division
Electronics and Electrical Engineering Laboratory
National Institute of Standards and Technology
Boulder, CO 80305

## Abstract

I present a method of visualizing polarization-dependent loss in single-mode optical fiber and components. This method uses generalized Poincaré spheroids wherein the power (though polarized) is no longer normalized to unity. The resulting graphical development permits a better understanding of the limitations of the four-state Mueller-Stokes measurement of this parameter in the presence of combined parasitic birefringence and external polarization-dependent losses. A six-state alternative that improves accuracy and repeatability is shown along with the results of preliminary comparative measurements. The alternative is also found to be more tolerant of non-orthogonal states while maintaining short measurement times.

## Introduction

The widespread use of wavelength multiplexing necessitates the rapid measurement of polarization-dependent loss (PDL) over wavelength, which I refer to as $\text{PDL}_\lambda$. Currently, $\text{PDL}_\lambda$ is typically measured with either a random all-states (A/S) technique [1] or the four-state technique of Nyman, et al.[2,3] which I refer to as Mueller-Stokes (M/S). The all-states technique is precise and simple to apply, but typically slow for wavelength-dependent measurements. However, the A/S method is only as accurate as the statistical sum of all internal system PDL's [4]. By contrast, the four-state M/S method is typically very fast and capable of subtracting the effect of internal system PDL, which makes it potentially much more accurate in a laboratory setting. However, in field or production situations, conditions can be far from ideal, with large parasitic birefringence and PDL sources in the optical circuit. In addition, the M/S technique assumes strict orthogonality of the polarized states wherein the four states are separated by equal quadrants on the Poincaré sphere [5]. When this condition is not met, the M/S method can show dramatic uncertainties that serve to negate much of the perceived benefits. Long, coiled and unrestrained patch cords can lead to large values of static and dynamic strain birefringence [6]. Poor connectors and open beams can lead to large parasitic PDL in the circuit, while misalignment or wavelength dependence in the polarization controller can lead to non-orthogonality of input states. Though not always present, the combination of these effects can be devastating to the accuracy of the M/S method. My goal has been to understand the nature of this limitation and to devise a suitable alternative that retains the speed benefit while reducing the impact of parasitic effects.

## Visualizing PDL

To visualize PDL and its interactions, it is useful to consider Poincaré spheroids: a unit intensity (radius) sphere representing the input polarization state, and an output spheroid of polarization-dependent intensity. A computer model produces the viewpoint seen in Fig. 1 for the example of a 3 dB PDL, where the distorted output spheroid (PDL) is coincident within the unit input sphere. Relative to the input reference frame, the output spheroid can appear "rotated" if the PDL is seen through a retarder (middle image). Adding two orthogonal 3 dB PDL's is equivalent to multiplying the equivalent spheroids, which overlap along the "PDL axis", to generate a half-unit Poincaré sphere, i.e., a 3 dB attenuator (right image).

With the aid of this device, it is now possible to better understand the limitations of the M/S method by allowing us to see the newly obvious symmetries or lack thereof.

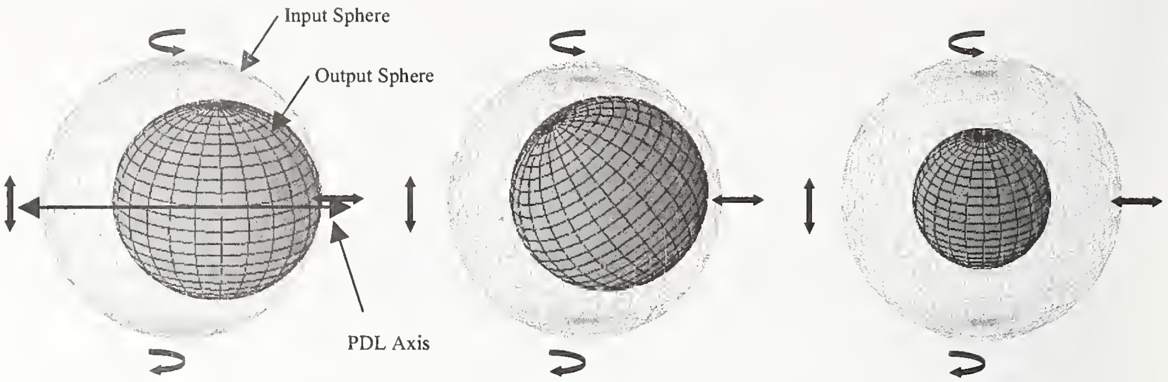

A 3dB PDL following an unpolarized source

A 3dB PDL as seen through a retarder

Result of crossing orthogonal 3dB PDL's

Figure 1: Visualizing a 3 dB PDL and certain interactions with the aid of Poincaré spheroids (inside the unit sphere) that depict the actual Stokes intensity.

### The Four-State Problem Viewed Geometrically

The ideal four states of the M/S method can be represented by partial, orthogonal great-circle trajectories, as in Fig. 2. In actual measurements, however, the relative positions of the four states may vary somewhat, particularly with wavelength $\lambda$. This variation will lead to non-orthogonal states and a further loss of symmetry. For the purposes of this example, we may take the unit sphere as representing the light as launched from the measurement system and the internal prolate spheroid as representing the light as it exits the device-under-test (DUT). Note that, as long as the axis of any retardance is coincident with the PDL axis, symmetry is maintained and ratios of relative radii between corresponding system and DUT trajectories (a – 1, b – 2, c – 3, d – 4) are maintained. Conversely, when the parasitic retardance axis is not coincident with the PDL axis, symmetry is broken and the 4-state approach loses information. A simplified M/S measurement system described by this and a later model is shown in Fig. 3.

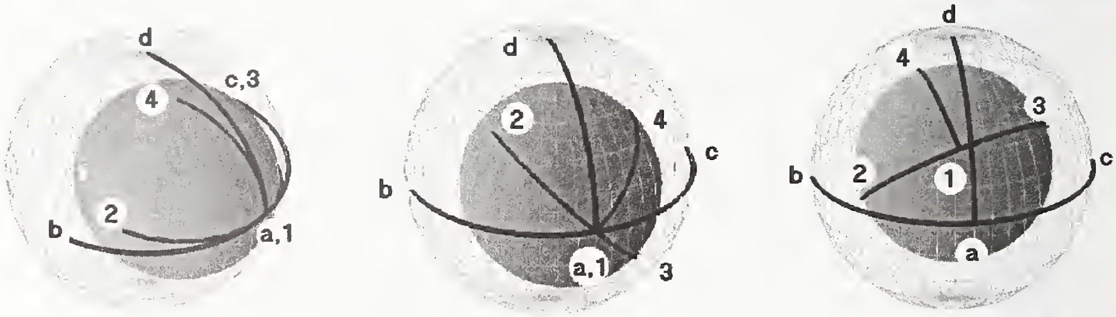

No Parasitic Birefringence

Lead Retardance Axis Coincident with PDL Axis

Lead Retardance Axis Not Coincident with PDL Axis

Figure 2: 4-State M/S trajectories superimposed on the input (system) and output (DUT) spheroids.

### The Six-State Generalization

Significant improvement is offered by the six-state approach of Fig. 3, which is characterized by the incorporation of additional geometrical information afforded by the greater symmetry available in Poincaré space. The fundamental idea is to require that 4-state measurements about the 1-2-3 plane must be equivalent, i.e., measurements at states 1,2,3,4 or 5,2,3,6. This equivalence is used to generate six equations in six unknown Mueller matrix elements. However four unknowns can be combined into two matrix elements ($m_{13}$ and $m_{14}$) by taking an average based on symmetry. The result is the comparison table shown below in Table 1, where $m_{11}(\lambda)\ldots m_{14}(\lambda)$ are the Mueller matrix elements relevant to PDL.

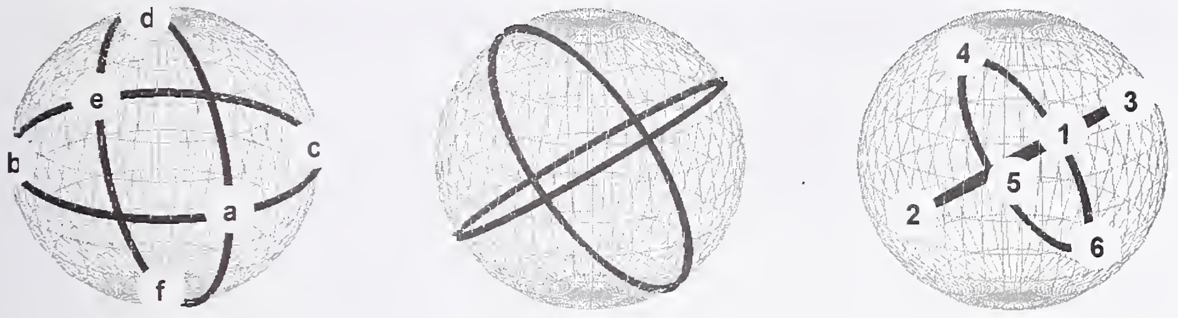

No PDL, No Birefringence

No PDL, Birefringence Present

PDL Present, Birefringence Present

Figure 3: Simplified representation of the polarization state trajectories associated with the 6-state generalization of the M/S technique for both the measurement system and DUT.

The $I_a(\lambda)\ldots I_f(\lambda)$ are measurement system baseline intensities at each input polarization state, while the $I_1(\lambda)\ldots I_6(\lambda)$ are the corresponding intensities when the DUT is in series with parasitic retardances.

Table 1

4-State Matrix Elements

$$\begin{bmatrix} m_{11}(\lambda) \\ m_{12}(\lambda) \\ m_{13}(\lambda) \\ m_{14}(\lambda) \end{bmatrix} = \begin{bmatrix} \frac{1}{2}\left[\frac{I_1(\lambda)I_b(\lambda)+I_2(\lambda)I_a(\lambda)}{I_a(\lambda)I_b(\lambda)}\right] \\ \frac{1}{2}\left[\frac{I_1(\lambda)I_b(\lambda)-I_2(\lambda)I_a(\lambda)}{I_a(\lambda)I_b(\lambda)}\right] \\ -\frac{1}{2}\left[\frac{I_1(\lambda)}{I_a(\lambda)}+\frac{I_2(\lambda)}{I_b(\lambda)}\right]+\frac{I_3(\lambda)}{I_c(\lambda)} \\ -\frac{1}{2}\left[\frac{I_1(\lambda)}{I_a(\lambda)}+\frac{I_2(\lambda)}{I_b(\lambda)}\right]+\frac{I_4(\lambda)}{I_d(\lambda)} \end{bmatrix}$$

6-State Matrix Elements

$$\begin{bmatrix} m_{11}(\lambda) \\ m_{12}(\lambda) \\ m_{13}(\lambda) \\ m_{14}(\lambda) \end{bmatrix} = \begin{bmatrix} \frac{1}{2}\left[\frac{I_1(\lambda)I_b(\lambda)+I_2(\lambda)I_a(\lambda)}{I_a(\lambda)I_b(\lambda)}\right] \\ \frac{1}{2}\left[\frac{I_1(\lambda)I_b(\lambda)-I_2(\lambda)I_a(\lambda)}{I_a(\lambda)I_b(\lambda)}\right] \\ \frac{1}{2}\left[\frac{I_3(\lambda)I_e(\lambda)-I_5(\lambda)I_c(\lambda)}{I_c(\lambda)I_e(\lambda)}\right] \\ \frac{1}{2}\left[\frac{I_4(\lambda)I_f(\lambda)-I_6(\lambda)I_d(\lambda)}{I_d(\lambda)I_f(\lambda)}\right] \end{bmatrix}$$

$$PDL_\lambda \equiv PDL(\lambda) = 10\log\left[\frac{m_{11}(\lambda)+\sqrt{m_{12}(\lambda)^2+m_{13}(\lambda)^2+m_{14}(\lambda)^2}}{m_{11}(\lambda)-\sqrt{m_{12}(\lambda)^2+m_{13}(\lambda)^2+m_{14}(\lambda)^2}}\right] \quad (dB)$$

## Results and Conclusion

From the figure and table above, it is clear that for the small additional "expense" of two additional measurements we are gaining considerable symmetrical information that will help to offset the uncertainties associated with parasitic birefringence and other PDL's in the system. The system of Fig. 4 was used to test this approach, and the results of a comparison measurement of a 0.395 dB PDL is presented in Fig. 5. A 0.1 dB PDL artifact was placed in series with the state randomizer (a separate polarization controller) that was stepped through 100 various states following the initial baseline measurement. The 0.1 dB artifact acted as a parasitic PDL in the optical circuit, and the polarization state

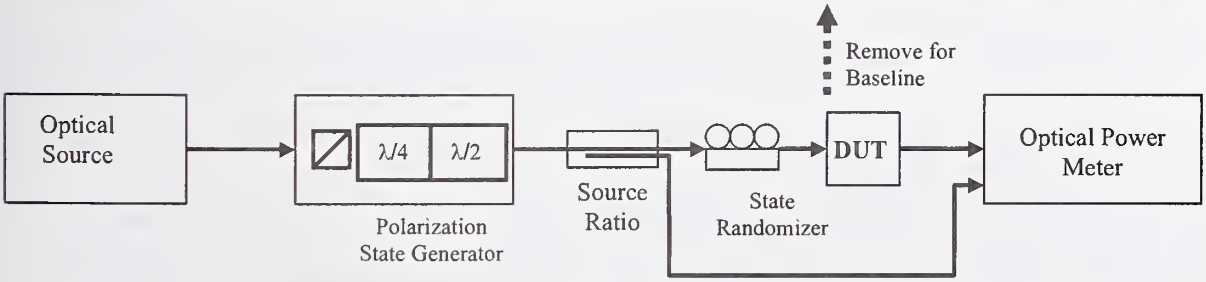

Figure 4: A typical configuration for 4 and 6-state PDL measurements. The randomizer allows for testing system repeatability under various conditions of parasitic birefringence.

randomizer allowed the method to be tested under various polarization conditions, simulating different orientations of parasitic birefringence within the measurement system. The result of these 100 measurements was a clear improvement in both mean and standard deviation for the 6-state method over the 4-state method. The 6-state result was 0.396 ± 0.009 dB while the 4-state result was 0.398 ± 0.021 dB. Though numerical models show that the 6-state method is essentially exact for perfectly orthogonal states, even under parasitic influence, the inclusion of slight non-orthogonality produces some uncertainty. However, for an equivalent deviation from orthogonality in both the 4-state and 6-state methods, the models readily reproduce the approximate factor of two improvement in standard deviation. This method and further generalizations are now being implemented at NIST with the goal of qualifying PDL artifacts to higher accuracy than before.

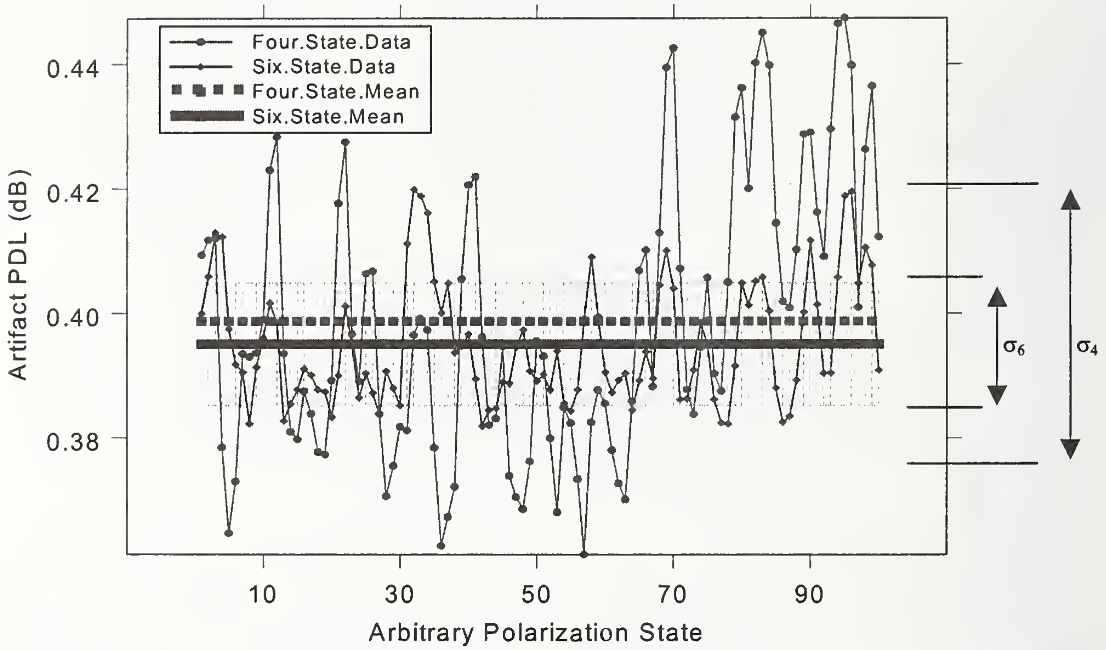

Figure 5: Comparison measurement of a 0.395 dB PDL at 1550 nm using the 4-state and 6-state M/S methods with the apparatus of Fig. 4. Standard deviations are shown at right.

## Bibliography

[1] Derickson, D., *Fiber Optic Test and Measurement* Upper Saddle River, NJ: Prentice Hall PTR, 1998.

[2] Craig, R. M., Gilbert, S. L., and Hale, P. D., "High-resolution, nonmechanical approach to polarization-dependent transmission measurements," *Journal of Lightwave Technology*, vol. 16, no. 7, pp. 1285-1294, July1998.

[3] Nyman, B. M. and Wolter, G., "High-Resolution Measurement of Polarization-Dependent Loss," *Ieee Photonics Technology Letters*, vol. 5, no. 7, pp. 817-818, July1993.

[4] Gisin, N., "Statistics of Polarization-Dependent Losses," *Optics Communications*, vol. 114, no. 5-6, pp. 399-405, Feb.1995.

[5] Collett, E., *Polarized Light, Fundamentals and Applications* New York, NY: Marcel Dekker, Inc., 1993.

[6] R.Ulrich, S.C.Rasleigh, and W.Eickoff, "Bending induced birefringence in single mode fibers," *Optics Letters*, vol. 5 pp. 273-275, 1980.

# Four-state measurement method for polarization dependent wavelength shift

W.C. Swann, S.D. Dyer and R.M. Craig
National Institute of Standards and Technology
325 Broadway, Boulder, CO 80305
swann@boulder.nist.gov

## ABSTRACT

We present a novel four-state method for measuring the polarization dependent wavelength shift (PDW) of a fiber Bragg grating. We show that measurement of the grating's wavelength for only four different polarization states is sufficient to completely determine the grating's PDW, and we show favorable comparison of four-states PDW measurement results with results obtained using the conventional "all states" technique.

## 1. Introduction

Use of Bragg gratings in wavelength division multiplexed (WDM) systems with ever decreasing channel spacing and in sensor systems with ever increasing accuracy requirements has placed stringent demands on the absolute accuracy and stability of a grating's wavelength. The two largest effects on a grating's wavelength: temperature and strain, are well understood and are often compensated by using active stabilization or athermal packaging. It is more difficult to control the grating's response to polarization, where the center wavelength of a grating can shift due to birefringence. In systems using unpolarized light, or where polarization is maintained using polarization maintaining (PM) fiber, this is not an issue. However, where polarized lasers are used or PM fiber is impractical, the grating's wavelength can wander with polarization. It is therefore important to know a grating's PDW if it is to be used in a system where wavelength accuracy is important. In this paper we define PDW as the maximum wavelength shift of the grating's spectrum that is induced by changes in polarization.

The most straightforward means of determining a grating's PDW is to monitor the wavelength shift of the grating's reflection (or transmission) spectrum while randomly varying the polarization of the light at the grating until the polarization state space has been reasonably well covered. A similar approach uses a large number of well-defined states uniformly distributed over the state space. Unfortunately, the large number of individual measurements these "all states" techniques require make them time consuming, and therefore impractical in a manufacturing environment. Furthermore these techniques can underestimate a grating's PDW; they will more closely represent the true PDW as the state space is more completely covered. The four-states technique described here allows a grating's PDW to be completely determined with only four measurements, and does not underestimate the PDW. This measurement technique can also be applied to the measurement of PDW for other types of wavelength-selective filters.

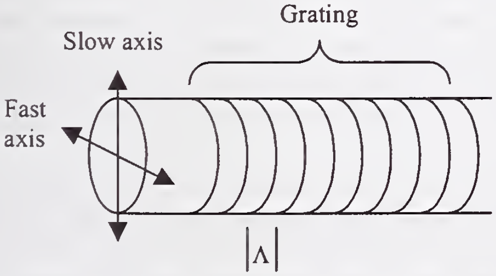

**Figure 1:** Birefringent fiber core in the region of the grating. Λ is the physical pitch of the grating.

## 2. Theory

The four-states technique assumes that PDW is caused by linear birefringence within the section of fiber containing the grating (Fig. 1). This birefringence may be caused by any combination of several mechanisms, most notable being fiber core geometry or strain asymmetry, asymmetry inherent in grating side writing techniques [1], or asymmetry due to the polarization of the writing light [2]. This birefringence results in polarization dependence of the Bragg grating's optical pitch, and thus the grating's center wavelength. Light polarized along the grating's fast axis sees a shorter optical pitch, and thus a shorter Bragg wavelength, than light polarized along the slow axis. For the purposes of this paper we define the fast and slow axes as the eigenaxes of the grating, and polarization states that lie on these axes as the grating's eigenstates. The difference between the grating's wavelengths for the two polarization eigenstates is the PDW of the grating. Arbitrarily polarized light has components along both the fast and slow axes, resulting in two spectral profiles shifted in wavelength with respect to each other. If the PDW is less than the grating's spectral width these two profiles overlap, resulting in a combined spectrum with a center wavelength somewhere between the fast axis and slow axis extremes. To determine the combined spectrum's wavelength shift verses polarization state, we modeled the grating's spectrum as a combination of two spectra shifted with respect to each other by the PDW shift, and weighed these spectra in proportion to the E field strength on the grating's eigenaxes for a given polarization state. We then observed the combined spectrum's wavelength shift as the model's polarization state was varied, and found that the shift varied sinusoidally as the polarization evolved from the grating's slow axis to its fast axis eigenstate [Fig. 2]. In theory a grating's PDW can be determined by finding the shift in the grating's center wavelength for the two polarization eigenstates. In practice determining the grating's eigenaxes is difficult, and furthermore any polarization state launched into the fiber may transform into some other, arbitrary state at the grating. With a suitable choice of four input polarization states, however, and assuming the unitary transformation between these input states and the states at the grating (i.e. the angular relationship between the states is preserved), in the absence of PDL and depolarization in the grating, we can determine the grating's PDW as follows.

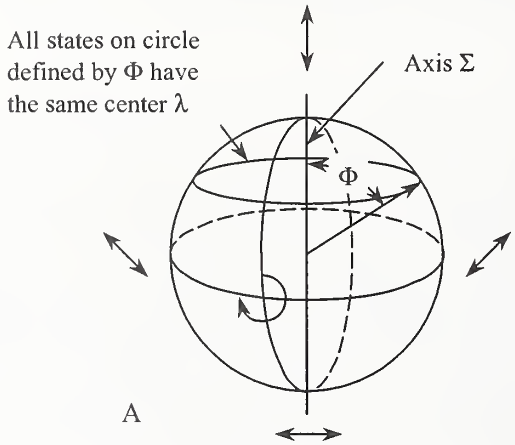

**Figure 2A:** Modified Poincaré sphere at the grating. The sphere is rotated with respect to conventional notation. The grating's mean wavelength is on the sphere's equator.

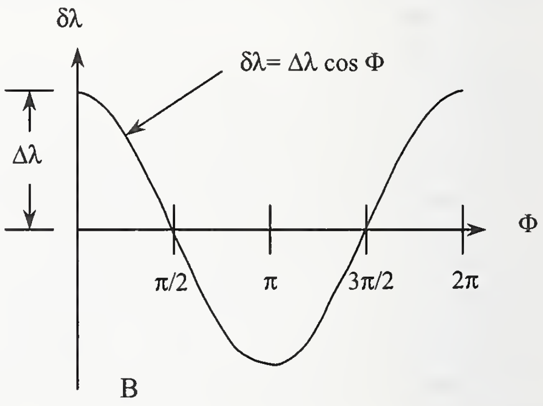

**Figure 2B:** Variation of wavelength shift δλ with angle Φ. Δλ is the maximum shift and occurs when the polarization is on either the grating's eigenaxes. The PDW for the grating is 2Δλ.

To discuss the theory behind the four-states technique we enlist the following conventions [Figs. 2 and 3]. We use modified Poincaré spheres S and S′, respectively to describe the polarization states $s_i$ and $s_i'$ at the input end of the fiber and at the grating. Our modified Poincaré sphere notation maps center wavelength rather than power onto the sphere's surface. $\Sigma'$ is an axis running through the grating's eigenstates on the sphere S′, and $\Phi_{si}'$ is the angle between $\Sigma'$ and polarization state $s_i'$ on S′. For the four input states we choose two orthogonal states (for example $s_1$ = linear horizontal and $s_2$ = linear vertical) and two states displaced by 90° on S from the first two states and from each other (for example $s_3$ = +45° linear and $s_4$ = right circular). An example showing this choice of four input states is shown in Fig. 3. Notice that the four states laid out on the sphere resemble three mutually perpendicular unit basis vectors together with a fourth vector directed opposite to one of the other three. These four input states $s_i$ will evolve to four other states $s_i'$ at the grating.

For each state $s_i$ launched into the fiber we measure the center wavelength $\lambda_{si}'$ of the grating's reflection peak. From the average of wavelengths $\lambda_{s1}'$ and $\lambda_{s2}'$ given by the two orthogonal polarization states, we determine a mean wavelength $\lambda_{mean} = (\lambda_{s1}'+\lambda_{s2}')/2$. From this we determine $\delta\lambda_{si}' = \lambda_{si}'-\lambda_{mean}$, where $\delta\lambda_{si}'$ is the shift from the mean wavelength for polarization state $s_i'$. Now, from Fig. 2 we see that $\delta\lambda_{si}'=\Delta\lambda\cos\Phi_{si}'$, where $\Delta\lambda$ is the difference between the maximum wavelength and $\lambda_{mean}$. Disregarding one of the two orthogonal states, and taking $\cos\Phi_{si'}$ as direction cosines [3] between $\Sigma'$ and $s_i'$, we use the relationship $\cos^2\Phi_{s2} + \cos^2\Phi_{s3} + \cos^2\Phi_{s4} = 1$ [4] to get $[(\delta\lambda'_{s2})^2 + (\delta\lambda'_{s3})^2 + (\delta\lambda'_{s4})^2]^{1/2} = \Delta\lambda$. (We could just as easily use $\cos\Phi_{s1}$ instead of $\cos\Phi_{s2}$, and $\delta\lambda_{s1}$ instead of $\delta\lambda_{s2}$.) The PDW for the grating is $2\Delta\lambda$.

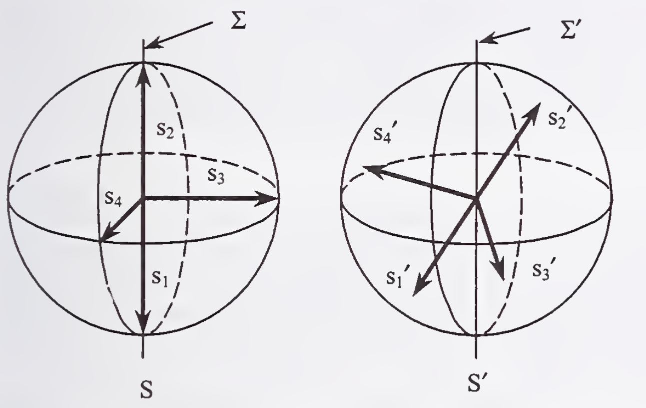

**Figure 3:** Poincaré spheres S at the input end of the fiber and S′ at the grating, showing evolution of input states $s_i$ to states $s_i'$.

### 3. Experimental Results

We measured three gratings with different amounts of PDW using the four-states technique, and compared the results to "all states" measurements of the same gratings. For the all states measurement we chose 26 states uniformly distributed about the sphere. Each state's measurement entailed setting a tunable diode laser's polarization to the desired state using a pair of waveplates and scanning the laser's wavelength across the grating's reflection spectrum while monitoring the wavelength with a wavelength meter. For each polarization state, we fitted the resulting plot of reflectance versus wavelength over the wavelength values ranging between the reflection spectrum's FWHM points using a fourth order polynomial fit. We found that the grating profiles were slightly asymmetric, leading to a slight difference between the profile's center and extremum wavelengths. Because the profile's extremum is better defined than its center, we used the shift in the extremum of the fit vs. polarization state to determine the grating's PDW.

For the all-states technique we took the difference between the maximum and minimum wavelength returned by the 26 scans as the PDW. This technique has the potential of under-determining the PDW by up to about 10 %, as dictated by how closely the launched states approach the fast and slow axes at the grating. In addition to this there is an uncertainty in the all-states PDW of $\sqrt{2}\sigma$, where $\sigma$ is the standard uncertainty in the extremum wavelength given by the polynomial fit. For the four-states technique we determined the PDW as described in the previous section, and we calculate the PDW uncertainty to be about $2.5\sigma$. Both of these uncertainties are given using standard propagation of errors formalism.

The results for the three gratings are shown in Table 1. We ran two trials on gratings 1 and 2, and four trials on grating 3 for both the four-states and all-states technique. Gratings 1 and 2 have a standard uncertainty σ in their extrema of about 0.25 pm, leading to an uncertainty of about ± 0.6 pm for the four-states PDW, and about 0.4 pm for the all-states PDW. Grating 3 has a standard uncertainty σ of about 0.14 pm, leading to a predicted uncertainty in the four-states PDW of about 0.4 pm and in the all-states PDW of about 0.3 pm. For gratings 1 and 2 the 26-states results are lower than the four-states results by up to 8%, as expected for reasons stated above, and the four-states and all-states results agree for grating 3. Also, the results for the two trials agree to within the expected uncertainties, indicating repeatability of the measurements.

Table 1: Comparison of 4-state and 26-state PDW results

| Grating | Trial | 26-states PDW (pm) | 4-states PDW (pm) |
|---|---|---|---|
| 1 | 1 | 30.7(4) | 32.3(6) |
| | 2 | 29.8(4) | 31.6(6) |
| 2 | 1 | 8.1(4) | 8.8(6) |
| | 2 | 7.9(4) | 8.5(6) |
| 3 | 1 | 1.0(3) | 0.9(4) |
| | 2 | 1.1(3) | 1.0(4) |
| | 3 | 1.1(3) | 0.9(4) |
| | 4 | 1.1(3) | 1.3(4) |

## 5. Conclusion

We have presented a four-states technique for measuring the polarization dependent wavelength shift of a fiber Bragg grating. Although we describe measurement of a relatively narrow grating, this technique should be applicable to measuring shifts in the band-edge of WDM channel filter or similar wide-bandwidth gratings. Furthermore, with suitable reference detectors, it could be generalized to include simultaneous measurement of polarization dependence in the reflectance, transmittance, or loss of the grating.

## References:

1. A.M. Vengsarker, Q. Zhong, D. Inniss, W.A. Reed, P.J. Lemarie and S.G. Kosinski, “Birefringence reduction in side-written photoinduced fiber devices by a dual-exposure method,” Opt. Lett. **19**, pp. 1260-1262 (1994).

2. T. Ergodan and V. Mizrahi, “Characterization of UV-induced birefringence in photosensitive Ge-doped silica optical fibers,” J. Opt. Soc. Am. B **11**, pp. 2100-2105 (1994).

3. G. Arfkin, *Mathematical Methods for Physicists*, third edition (Academic Press 1985), pp. 4, 191.

4. M.R. Spiegel, *Mathematical Handbook*, Shaum’s Outline Series (McGraw-Hill 1968), pp. 46.

# Measurement of Dispersion in Photonic Bandgap Fibers

**J. Jasapara**
*OFS Laboratories,*
*600 Mountain Ave.,*
*Murray Hill, NJ 07974.*
*Ph: 908-582-3234, email:jasapara@ofsoptics.com*

**Abstract:** Phase dispersion of light propagating in the fundamental mode in multiple bandgaps of a photonic bandgap fiber is measured using the technique of spectral interferometry. The dispersion data show a strong influence of the Bragg scattering crystal structure surrounding the core. A simple two dimensional model that includes the effects of a wavelength dependent angle of propagation, where the angle is determined by the Bragg scattering condition, and the effects of thin-film-like resonant scattering planes in the fiber is found to explain the observations qualitatively.

## 1 Introduction

Photonic bandgap structures consist of a crystal like periodic arrangement of materials of different refractive indices. Bragg reflections off structures having periodicity extending in greater than one dimension can result in the complete reflection of light at certain frequencies independent of the angle of incidence. The structure is said to possess a bandgap at these frequencies. If there is a defect in the periodicity of the structure then light frequencies lying in the bandgap would be confined to the defect by Bragg reflection from the surrounding crystal structure, thus making the defect a light guide. Photonic bandgap structures have been studied extensively over the past decade because of both their unique science as well as their potential applications in fields such as integrated light circuits, switches, etc.

Recently propagation of light in a hollow core fiber using photonic-bandgap-guidance (PBG) was demonstrated [1]. The PBG fiber consists of a periodic lattice of air holes embedded in a solid matrix that run uniformly along the fiber length. A break in the periodicity ("defect") serves as the core. PBG fibers are a new class of fibers in which light is confined to the core by Bragg reflections instead of total internal reflection (TIR) seen in standard fibers. They could prove to be disruptive to current technology trends since transmission down a hollow core would reduce pulse distortion due to effects such as nonlinearity, material dispersion and material losses.

So far only the amplitude response of bandgap fibers has been studied experimentally [4,5] while the phase dispersion has only been modeled theoretically [5–8]. Since PBG fibers are resonant structures propagation is strongly wavelength dependent. For example, the dispersion of 1-D [2] and 2-D [3] photonic bandgap devices were measured to vary strongly across the bandgap. The waveguide dispersion of a PBG fiber carries the signature of the mechanism of propagation. Its measurement is crucial to gain a physical insight into their working which would enable better fiber design for future applications.

Measuring the dispersion of PBG fibers is tricky. They have high losses (~ 5 dB/m). There might be variations along the fiber length arising due to imperfections during fiber draw. These factors make it desirable to use short fiber lengths of a few tens of centimeters for measurements. Hence conventional fiber dispersion measurement test beds cannot be used. In this paper we present the experimental measurement of chromatic dispersion of the fundamental mode across multiple bandgaps of a PBG fiber using the technique of spectral interferometry with a supercontinuum as a coherent white light source.

## 2 Experiment

The PBG-fiber used in our experiment consists of a triangular lattice of air holes in silica. The diameter of the air holes is 2.4 $\mu$m and their separation is 4.3 $\mu$m. The core is formed by removing the center most and its first surrounding ring of air holes (see inset of Fig. 1(a)). Ten rings of air holes surround the core. The air holes are filled with a high index liquid (index ranging from 1.8 at 600 nm to 1.76 at 850 nm) which raises the effective index of the cladding to above that of the silica core. This ensures that the bandgap effect is the only possible guidance mechanism. The unnormalized transmission spectrum of the fiber (cf. Fig. 1(a)) shows that light is guided only over discrete frequency bands.

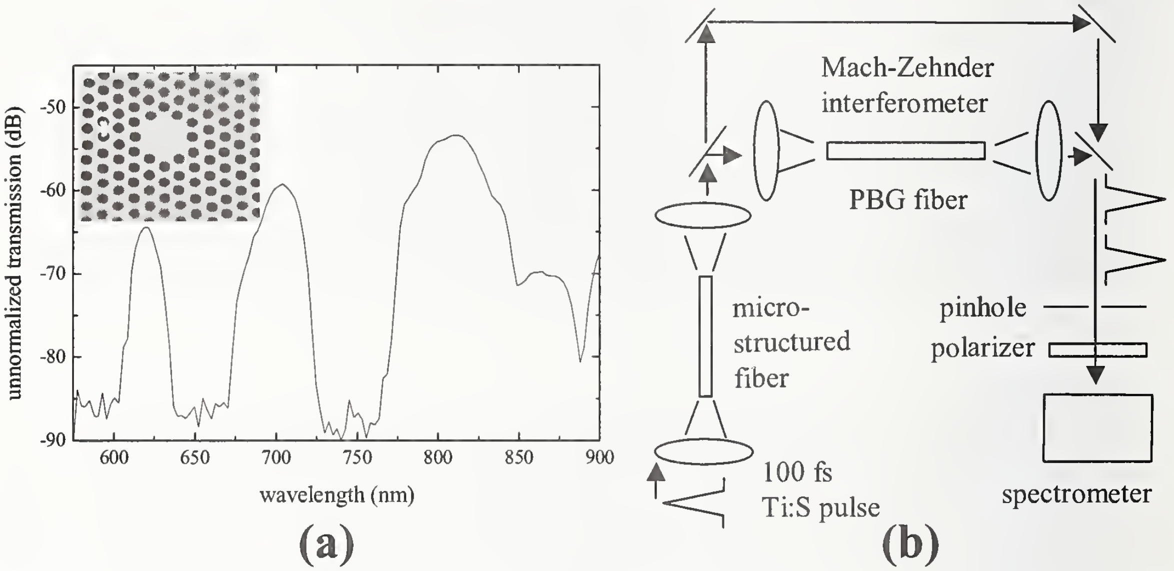

Fig. 1: (a) The unnormalized transmission spectrum of the PBG fiber over the wavelength range of interest. The inset is a cross section of the fiber – the dark regions are the liquid filled air holes. (b) Spectral interferometry setup.

Spectral interferometry [10, 11] is an extremely sensitive technique to measure the phase response of optical samples. In a spectral interferometry setup the sample to be characterized is placed in one arm of a Michelson or a Mach Zhender interferometer. Coherent broadband light is sent into the interferometer. The output from the interferometer is sent into a spectrometer. The dispersion of the sample gives rise to a wavelength dependent path length and phase difference between the arms of the interferometer. This gives a beating in the spectral domain with maxima and minima occurring at frequencies where the phase difference between the interferometer arms is an integral multiple of $2\pi$ and $2(m+1)\pi$ (m is an integer) respectively. By analyzing the spectral beat pattern one can recover the phase dispersion of the sample.

Figure 1(b) is a schematic of our spectral interferometer. It consists of a Mach Zehnder interferometer with the PBG fiber in one arm (referred to as the signal arm below). The other arm (called the reference arm) is left empty. In order to measure dispersion across multiple bandgaps of the fiber using spectral interferometry, we require a coherent broadband source of light that covers the spectral range. We used 100 fs pulses from a Ti:sapphire laser to generate a supercontinuum in an air-silica microstructure fiber [12] that stretched from $\sim 400$ nm to $\sim 1400$ nm. The collimated continuum is sent into the interferometer. The spectral response of the optics in our interferometer restricts our measurements to bandgaps lying between 600 nm and 850 nm. During the experiment the delay of the reference arm with respect to the signal arm is adjusted so that it is shorter than the signal arm at all wavelengths by $\geq 0.8$ ps.

The recombined light is sent through a pinhole and a polarizer into a spectrometer (resolution = 0.2 nm) with a CCD where interference is observed. The pinhole lets only the center-most part of the beam through and thereby transmits mainly the fundamental mode and discriminates against higher order modes of the PBG fiber. The polarizer defines the polarization of the detected light which increases the fringe contrast.

The air-silica microstructured fiber used for continuum generation is birefringent. If the signal arm is blocked, then light from just the reference arm itself gives rise to a beat pattern in the spectral domain due to the different propagation times along the two polarization axes of the fiber. Therefore the input polarization to the continuum generating fiber is matched with a $\lambda/2$ waveplate to the birefringence axis of the fiber which then defines the input polarization to our interferometer.

Similarly, the output from only the signal arm containing the PBG fiber, with the reference arm blocked, gives fringes in the spectral domain (see Fig. 2(a)). The fringe spacing increases linearly with a decrease in fiber length from which we conclude that the fringes arise due to multi-path interference (MPI) in the PBG fiber. From the contrast of the fringes the energy in the second mode is found to be about 2% of the fundamental mode. This MPI contributes to the noise in the spectral interference pattern between the reference and signal arms.

In order to obtain spectral fringes of good contrast it is essential that the wavefronts from both arms have the same curvature. To ensure this the recollimation of the light from the PBG-fiber is adjusted so that the spatial interference fringes between the reference and signal arms observed at zero delay with a slightly misaligned interferometer have no curvature. The interferometer is then realigned for optimal contrast. In addition, for good fringe contrast the intensity from the two arms are equalized using neutral density filters.

Besides the sample the interferometer is unbalanced by elements such as the focusing and recollimating lenses. Therefore the dispersion measurements are made at two different fiber lengths of 263 mm and 130 mm and the difference is taken to subtract out the dispersion of the unbalancing elements.

## 3 Analysis and results

Figure 2(a–f) shows an example of the recorded data and the retrieved phase dispersion over a small range of wavelengths. During the experiment the frequency ($\omega = 2\pi c/\lambda$, where $c$ and $\lambda$ are the velocity and wavelength of light in vacuum) dependent intensity of the interference pattern $I(\omega)$, the reference arm $I_r(\omega)$, and the signal arms $I_s(\omega)$, are recorded sequentially (Fig. 2(a–c)). The beating due to MPI is seen in the spectrum of the signal arm. The spectrum of the reference arm is noisy around the Ti:sapphire pump wavelength of $\sim$ 795 nm, probably due to modulational instability effects in the continuum generating fiber. The spectral

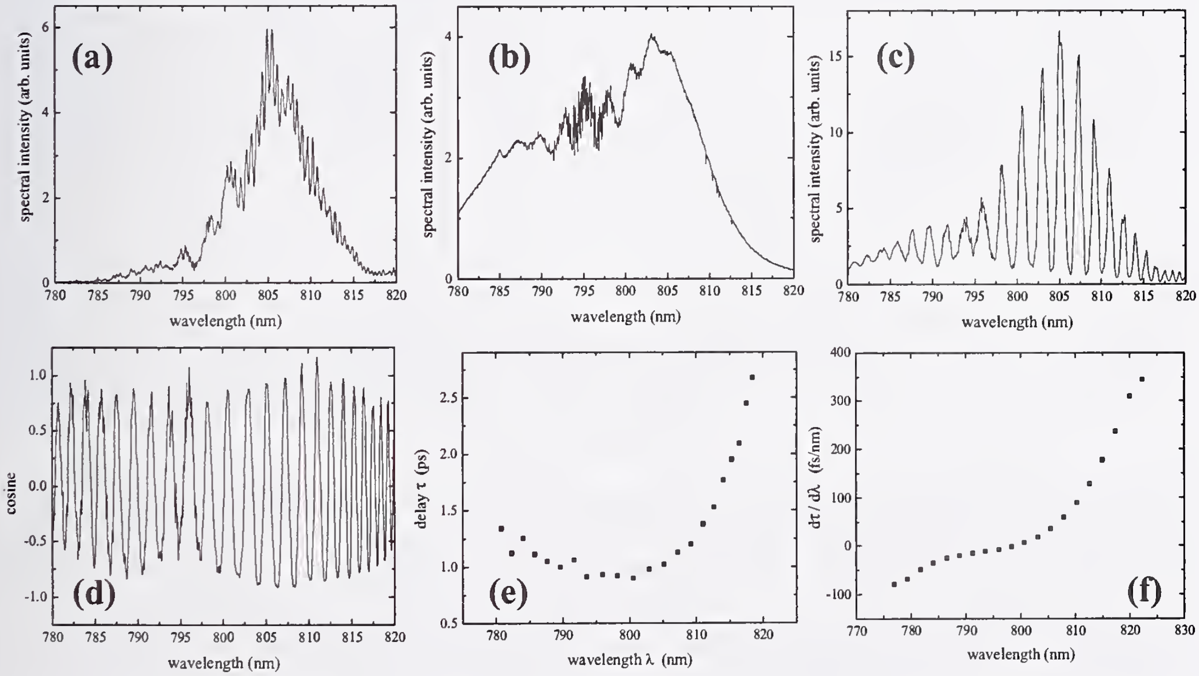

Fig. 2: (a) signal, (b) reference, (c) interference, (d) retrieved cosine modulation, (e) retrieved group delay, and (f) retrieved phase dispersion, over a small wavelength range.

intensity of the interference pattern is given by,

$$I(\omega) = I_r(\omega) + I_s(\omega) + 2\sqrt{I_r(\omega)I_s(\omega)}\cos(\Phi(\omega)), \tag{1}$$

where $\Phi(\omega)$ is the phase difference between the reference arm and the signal arm. From the recorded data the cosine modulation can be retrieved by inverting Eq. (1) and is shown in Fig. 2(d). Ideally the cosine should vary smoothly between $\pm 1$. However fluctuations in the continuum over the time taken to record all the data adds noise and misalignment of the interferometer reduces the fringe contrast. The cosine modulation can be smoothed to some extent to get rid of the noise so that the fringe peaks are sufficiently well defined. The peaks in the modulation occur at frequencies at which there is constructive interference between the reference and signal arms. The phase of the signal arm at frequencies at two consecutive peaks differs by $2\pi$. We find that the modulationis slower near the center compared to the edge. To retrieve the fiber dispersion, the group delay as a function of frequency is calculated as,

$$\tau(\omega') = \frac{d\Phi(\omega)}{d\omega} \approx \frac{\delta\Phi(\omega)}{\delta\omega} = \frac{2\pi}{\omega_i - \omega_{i+1}}, \tag{2}$$

where $\omega_i$ is the frequency of the $i^{th}$ peak in the cosine modulation and $\omega' = (\omega_i + \omega_{i+1})/2$. The retrieved group delay is shown in Fig. 2(e). As the wavelength increases the group delay goes through a minimum before it increases sharply near the long wavelength edge. This curve is to be compared against the linear group delay curve expected from a standard TIR guiding fiber. The delay is fitted with a polynomial curve. The derivative of the fit yields the dispersion $d\tau/d\lambda$ (Fig. 2(f)).

Figure 3 shows the dispersion from cutback measurements over three different bandgaps of the fiber overlaid with their transmission curves represented by $I_s(\omega)/I_r(\omega)$. The dispersion across all three bandgaps exhibit the same qualitative behavior: (i) $d\tau/d\lambda$ is strongly wavelength dependent, (ii) $d\tau/d\lambda$ has an inflection point as it goes from negative values at shorter wavelengths to positive values at longer wavelengths, (iii) the zero dispersion wavelength is shifted towards the shorter wavelength side of the transmission curve, and (iv) $d\tau/d\lambda$ increases very rapidly to greater than 5000 ps/nm-km near the peak of the transmission which is orders of magnitude greater than that of a standard fiber. The qualitative shape of the curve is in agreement with the theoretical calculations by West *et. al.* and Johnson *et. al.*. [5,8] These dispersion curves are unique and unlike those of any known fiber. The large group delay near the long wavelength edge of the bandgap suggests that the light propagates very slowly over that wavelength range.

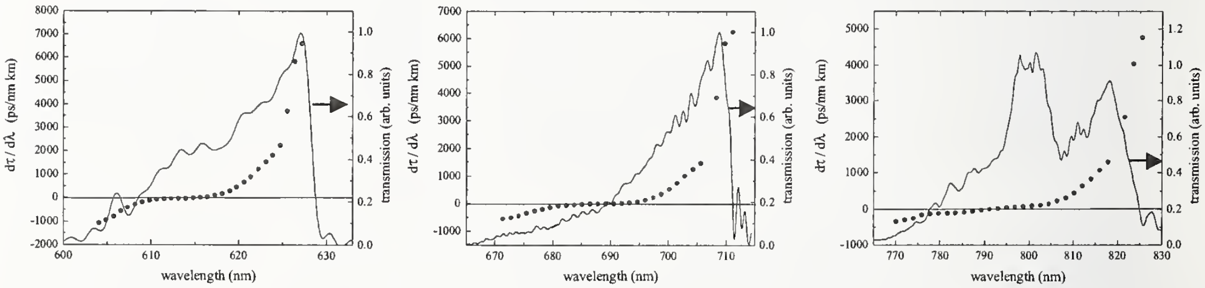

Fig. 3: Dots: Dispersion measured over three different bandgaps of the fiber. Solid curve: $I_s(\omega)/I_r(\omega)$.

The quantity $I_s(\omega)/I_r(\omega)$ (cf. Fig. 3), measured through the pinhole, represents the transmission spectrum of the fundamental mode of the PBG fiber convolved with effects such as the spectral response of the optics in the two arms of the interferometer, the efficiency of coupling into and the recollimation out of the fiber, etc. $I_s(\omega)/I_r(\omega)$ show a sharp cutoff at the long wavelength edge of the bandgaps. This cutoff arises due to the cutoff of the fundamental mode [3] and has been confirmed in another experiment where the spectrum of only the fundamental mode was measured. The short wavelength cutoff is governed by the loss characteristics of the bandgap structure.

## 4 Model

The PBG fiber dispersion curves are similar to the dispersion across the resonance peak of a resonant structure such as a Fabry-Perot cavity or a thin film. However the dispersion of such resonant structures is symmetrical about the peak of the resonance with the zero crossing occurring at the peak. To qualitatively explain the observed dispersion we propose a simple model of Bragg scattering from multiple planes of resonant structures. Consider the 2-D waveguide shown in Fig. 4(a) in which light propagates in the $z$ direction. The walls of the waveguide consist of Bragg scattering planes. These Bragg planes are depicted as thin films in order to represent the resonant nature of the actual crystal planes which contain liquid filled holes. They behave like resonant structures with internal multiple scattering determining the phase response. The phase change seen by the ray per reflection is given by,

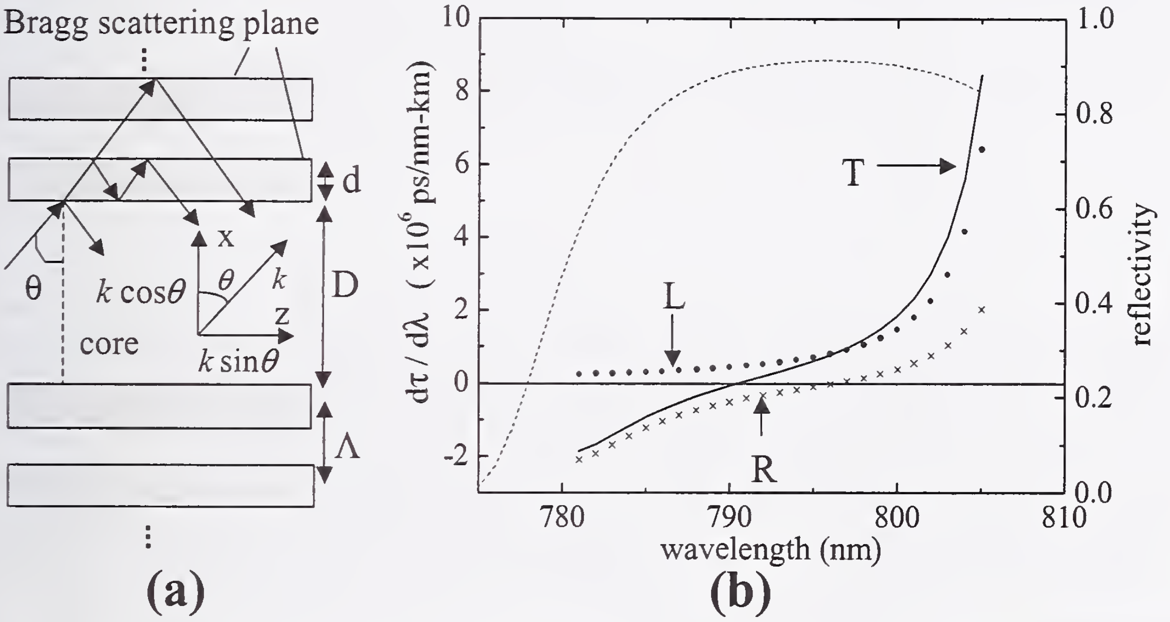

Fig. 4: (a) Geometry of propagation in a waveguide surrounded with a thin film Bragg crystal. (b) Dispersion under the condition that the transverse wave vector is a constant (equal to the total wave vector at 808 nm) for all wavelengths. The dashed line shows the reflectivity; R: dispersion on reflection off the film stack; L: dispersion of the longitudinal component; T: total dispersion.

$$\Psi(\omega) = k\sin[\theta(\omega)]L + k\cos[\theta(\omega)]D + \phi_r(\omega), \tag{3}$$

where $\theta(\omega)$ is the angle of incidence on the Bragg crystal as a function of frequency, $D$ is the width of the guide, $L$ is the length of propagation per bounce along the $z$ direction, and $\phi_r(\omega)$ is the phase change on reflection. Constructive interference between Bragg scattering from multiple crystal planes are a requirement for a defect mode to exist and is crucial for the high reflectivity needed for propagation over long fiber lengths. Hence the angle of propagation for wavelengths in the bandgap is defined by the Bragg condition $\Lambda k\cos[\theta(\omega)] = m\pi$, where $\Lambda$ is the spacing between the crystal planes, and $m$ is an integer. This implies that the transverse component of the wave vector, $k_x = k\cos\theta = m\pi/\Lambda$, is a constant across the bandgap and therefore its contribution to the phase dispersion is zero. The Bragg scattering condition also implies that the angle of propagation decreases with increase in wavelength resulting in a decrease in the forward propagating component of the wavevector $k_z = k\sin\theta$. Based on the long delays and sharp transmission cutoffs seen for the fundamental mode, we postulate that at the long wavelength edge of the bandgaps (frequency = $\omega_{edge}$), $\theta$ tends to the smallest angle $\theta_{min}$ that can support the fundamental mode. For our qualitative understanding we will assume that at the long wavelength edge of the band $\theta_{min} = 0$ and $k = m\pi/\Lambda$ so that no energy propagates in the $z$ direction. The propagation angle as a function of frequency in the band can now be defined as $\theta(\omega) = \cos^{-1}(\omega_{edge}/\omega)$. The phase dispersion of the fiber is hence given by,

$$\frac{d^2\Psi(\omega)}{d\omega^2} = L\frac{d^2}{d\omega^2}\left[k\sin(\theta(\omega))\right] + \frac{d^2\phi_r(\omega)}{d\omega^2}. \tag{4}$$

The dispersion of the waveguide in Fig. 4(a) is calculated assuming ten thin films of thickness $d = 2.4\,\mu$m and index 1.78, separated by silica regions of thickness $4.3\,\mu$m and index 1.45. The amplitude and phase change due to reflection ($\phi_r$) is calculated for p-polarized light using the stack-matrix formalism. [14] The transverse component of the wave vector is set equal to the wave vector at a point on the long wavelength edge of the resonance of the structure (chosen randomly here to illustrate the concept), which then defines the long wavelength edge of the bandgap and the wavelength dependent angle of propagation. Figure 4(b) shows the contribution to dispersion of each term from Eq. (4) as well as the total dispersion across a resonance. The dispersion due to reflection off the Bragg crystal (curve R) causes the inflection in the total dispersion curve. The dispersion of $k_z$ due to the wavelength dependent angle of propagation (curve L) gives rise to a rapid increase of dispersion at the long wavelength edge and also shifts the zero crossing of dispersion to the short wavelength side of the resonance peak. The three orders of magnitude difference between the observations and the calculations is due to the choice of setting $\theta_{min}$ to zero. Hence this simple model qualitatively explains the main features of our observed dispersion.

## 5 Summary

Spectral interferometry using a supercontinuum as a broadband light source was used to measure the phase dispersion of a photonic bandgap fiber across multiple bandgaps. Our experiments show that wave vector matching requirements between the propagating light and the surrounding Bragg crystal strongly influence propagation in PBG fibers resulting in a strong waveguide contribution to the dispersion. The wavelength dependent angle of propagation results in large positive dispersion at the long wavelength edge of the bandgap, while the reflections off the surrounding resonant structure results in an inflection point in the dispersion curve which resembles that of a Fabry-Perot structure. The former effect would be detrimental to the the use of PBG fibers for communication purposes. These studies provide a physical insight into the propagation mechanisms under PBG conditions and should aid in the design of new PBG fibers with desirable properties.

## References

1. R. F. Cregan, B. J. Mangan, J. Knight, T. A. Birks, P. S. J. Russell, P. J. Roberts, and D. C. Allan, "Single-Mode Photonic Band Gap Guidance of Light in Air," Science **285,** 1537–1539 (1999).
2. J. Tirapu, T. Lopetegi, M. A. G. Laso, M. J. Erro, F. Falcone, and M. Sorolla, "Study of the Delay Characteristics of 1-D Photonic Bandgap Microstrip Structures," Microwave and Optical Technology Letters **23,** 346–349 (1999).
3. M. Notomi, K. Yamata, A. Shinya, J. Takahashi, C. Takahashi, and I. Yokohama, "Extremely large group-velocity dispersion of line-defect waveguides in photonic crystal slabs," Physical Review Letters **87,** 253902(4) (2001).
4. J. A. West, J. C. Fajardo, M. T. Gallagher, K. W. Koch, N. F. Borrelli, and D. C. Allan, *European Conference on Optical Communication* (Munich, Germany, 2000), pp. 41–42.
5. J. A. West, N. Venkataraman, C. M. Smith, and M. T. Gallagher, *European Conference on Optical Communication* (Amsterdam, 2001), pp. 582–585.
6. S. E. Barkou, J. Broeng, and A. Bjarklev, *Optical Fiber Communication* (San Diego, CA., 1999), p. FG5.
7. J. Broeng, T. Sondergaard, S. E. Barkou, P. M. Barbeito, and A. Bjarklev, "Waveguidance by the Photonic Bandgap Effect in Optical Fibers," J. Opt. A: Pure Appl. Opt. **1,** 477–482 (1999).
8. S. G. Johnson, M. Ibanescu, M. Skorobogatiy, O. Weisberg, T. Engeness, M. Soljacic, S. Jacobs, J. D. Joannopoulos, and Y. Fink, "Low-loss asymptotically single-mode propagation in large-core OmniGuide fibers," Optics Express **9,** 748–779 (2001).
9. J. C. Knight, J. Broeng, T. A. Birks, and P. S. J. Russell, "Photonic Bandgap Guidance in Optical Fibers," Science **282,** 1476–1478 (1998).
10. C. Froehly, A. Lacourt, and J. C. Vienot, "Time Impulse Response and Time Frequency Response of Optical Pupils: Experimental Confirmations and Applications.," J. Opt. (Paris) **4,** 183–196 (1973).
11. J. Piasecki, B. Colombeau, M. Vampouille, C. Froehly,and J. Arnaud, Appl. Opt. **19,** 3749 (1980).
12. J. K. Ranka, R. S. Windeler, and A. J. Stentz, "Visible Continuum Generation in Air-Silica Microstructure Optical Fibers with Anomalous Dispersion at 800 nm," Optics Letters **25,** 25–27 (2000).
13. R. T. Bise, R. S. Windeler, K. S. Kranz, C. Kerbage, B. J. Eggleton, and D. J. Trevor, *Optical Fiber Communication* (Anaheim, CA, 2002), pp. 466–468.
14. M. V. Klein and T. E. Furtak, *Optics*, 2nd ed. (Wiley, New York, 1986).

# Counting Modes in Optical Fibres with Leaky Modes

**Alexander Argyros and Ian M. Bassett**

*Australian Photonics Cooperative Research Centre, Optical Fibre Technology Centre, University of Sydney, 206 National Innovation Centre, Australian Technology Park, Eveleigh, NSW 1430, Australia, and School of Physics, University of Sydney, NSW 2006, Australia.*

**Abstract:** The number of guided modes in optical fibres is an important aspect of their design and characterisation. Some optical fibres, such as microstructured fibres and Bragg fibres, have no strictly bound modes in the same sense as in conventional step and graded index fibres. All modes in these fibres are leaky so what exactly becomes regarded as a mode becomes important.. We propose a method for counting the number of modes in fibres that takes into account the leaky nature of some modes. The method is based on the loss of each mode and the length of the fibre. This leads to a definition of singlemodedness for fibres with no bound modes.

**1. Introduction:** The definition of singlemodedness, and indeed what constitutes a mode is fundamental to optical fibres and almost all aspects of their characterisation. In conventional step and graded index fibres there are strict definitions for bound and leaky modes: bound modes are radially evanescent in the depressed cladding layer whilst leaky modes have oscillatory fields in the cladding, allowing power to leak out of the fibre [1]. Equivalently, bound modes are described by real mode effective indices and leaky modes are described by complex mode effective indices, where the loss is proportional to the imaginary part of the effective index [1]. In the case of step and graded index fibres the number of modes unambiguously refers to the number of bound modes, and when this equals one, the fibre is unambiguously single-moded.

For other types of optical fibres such as W-fibres, holey fibres [2] – microstructured optical fibres (MOFs) or photonic crystal fibres (PCFs)), band-gap fibres [3] – and Bragg fibres [4] there are no bound modes in this strict sense. In holey fibres the guiding mechanism is effective index guidance [5]; the core is surrounded by an arrangement of air holes that effectively produce a depressed index annulus around the core. In band gap fibres and Bragg fibres guidance is achieved by surrounding the core with a 2- or 1-dimensional photonic crystal. In both cases the structure around the core that provides the guiding mechanism is finite in extent and therefore the fibre only supports leaky modes. Since all modes in these fibres are leaky, quoting the number of modes guided by each fibre design becomes ambiguous. Many such fibres have been claimed to be single-moded but no convention exists to clarify the statement. We propose a method for counting the number of modes in these fibres that takes into account the loss of each leaky mode and the length of fibre in question. This method also sets out the conditions required for singlemodedness and outlines the requirements through which some fibres may be effectively single-moded though some or all modes are leaky.

**2. Characterisation and Effective Singlemodedness**: We outline below a method for characterising and counting *modes* and for characterising *fibres*. Using this, we set out criteria by which fibres can be effectively single moded whilst having no bound modes.

**2.1 Characterising Modes:** If the power in a mode is attenuated to less than 1% of its original value (i.e. by more than 20 dB) the mode is no longer deemed useful. If the power in a mode is attenuated to less than 0.01% of its original value (i.e. by more than 40 dB) the mode is considered to not exist. Modes attenuated between 20 and 40 dB can be considered to display low guidance. Using this, we can characterise each mode with two length values: $L_{1\%}$ represents the length required for that mode to be attenuated by 20 dB and $L_{0.01\%} = 2L_{1\%}$ represents the length required for that mode to be attenuated by 40 dB.

The values of 20 and 40 dB have been chosen somewhat arbitrarily, with the justification that amplifiers are capable of recovering signals attenuated by 30 dB. Thus, an attenuation of 20 dB represents a useful signal, in that it can be recovered easily, and an attenuation of 40 dB represents a signal that cannot be recovered, is effectively lost, and may be treated as non-existent.

**2.2 Counting Modes in Fibres:** Any given fibre will have a set of leaky modes and may have some bound modes. For a fibre of a given length, the guided modes will be those whose $L_{0.01\%}$ value is greater than the length of fibre. A useful amount of power will be transmitted in those modes that have $L_{1\%}$ greater than the length of the fibre (useful guidance). The modes whose $L_{1\%}$ is less than the length of the fibre but their $L_{0.01\%}$ is greater than the length of the fibre cannot be said to be either extinct nor useful with certainty and so are said to exhibit low guidance but not useful guidance. We believe that this transition stage between "useful" and "non-existent" needs to be present to strengthen the definition of effective singlemodedness below. For example, a 3 m long fibre with three leaky modes characterised by $(L_{1\%}, L_{0.01\%}) = (4, 8), (2, 4)$ and $(1, 2)$ m will have two guided modes (the third mode will be lost) and will only have a useful amount of power in one mode (the first mode). The counting method is illustrated further in Fig. 1.

**2.3 Characterising Fibres and Effective Singlemodedness**: We can use the counting method outlined above to characterise a fibre as a whole using two length values, in a similar way to that of characterising the modes. The value $L_{max}$ denotes the maximum length of fibre over which a useful amount of power can be transmitted in any mode. The value $L_{max}$ is simply $L_{1\%}$ of the least leaky mode of that fibre. If the difference in the losses is sufficiently large and $L_{0.01\%}$ of the second least leaky mode is less than $L_{max}$ then there will be a length of fibre over which only the least leaky moded is guided and all other modes have been attenuated enough to deem them non-existent. In this case the fibre only guides one mode and can be classified as effectively single-moded (see Fig. 1). In the effectively single-moded regime we do not allow low guidance modes to be present, as we cannot say with certainty that they will be sufficiently extinguished to eliminate modal dispersion. A second length $L_{sm}$ denotes the length at which the fibre becomes effectively single-moded, and is equal to the $L_{0.01\%}$ value of the second least leaky mode. For a fibre to be effectively single-moded, the losses of the least and second least leaky modes must differ by a factor greater than 2 (when measured in dB/m) otherwise the value $L_{sm}$ will be greater than the value $L_{max}$ and no length of fibre will be effectively single-moded.

Matching the terminology used for standard fibres, we can allow the term "effectively single-moded" to include the case where there are actually two modes orthogonally polarised, with the same (or nearly the same) loss.

**3. Theoretical Calculations and Experimental Results:** We present below results from the literature as examples and to illustrate the applicability of the method outlined above. The first set of results reported in [6] are for a microstructured polymer optical fibre (MPOF) in which the core was surrounded with four hexagonal rings of holes – the four rings form the lower index region required for effective index guiding. The two least leaky modes of this structure as calculated in [6] are reproduced in Table 1(a). It can be seen that $L_{sm}$ for this fibre is 0.2 m and $L_{max}$ is $6.7\text{x}10^6$ m (material absorption was not accounted for in the modelling). Samples of this fibre of length 1 m were experimentally found to be single-moded [6], consistent with our definitions.

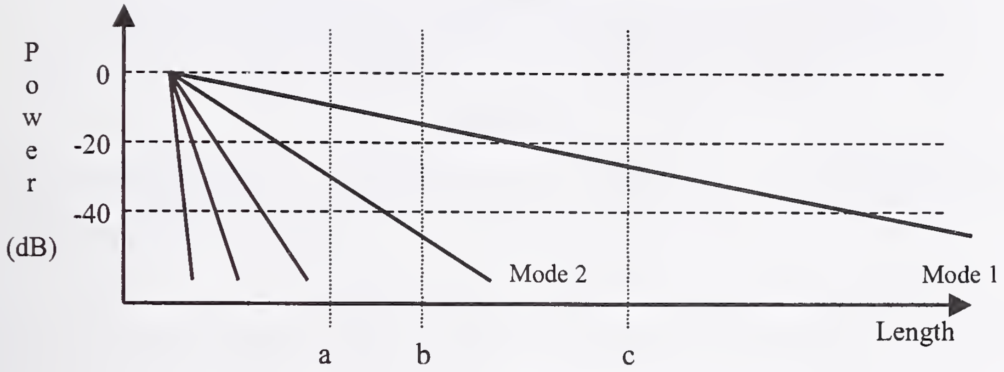

| Stage (a) Multimode 2 modes but 1 useful mode | Stage (b) Effectively Single-mode | Stage (c) 1 mode but 0 useful modes | | |
|---|---|---|---|---|
| X | X | | Guided | Useful Guidance Modes (< 20 dB attenuation) |
| X | | X | | Low Guidance Modes (> 20 dB but < 40 dB attenuation) |
| X X X... | X X X... | X X X ... | Lost | Negligible Guidance Modes (> 40 dB attenuation) |

**20 dB**
↓ Attenuation
**40 dB**

**Figure 1.** The graph above shows how the power in a set of modes would be attenuated along the fibre length. Three stages along the fibre are marked by the vertical lines and explained in the table to illustrate the mode counting method discussed. An "X" in each square indicates the presence of a mode that falls in the attenuation range indicated on the right column. In stage (a) there are 2 guided modes: 1 useful mode and 1 mode with low guidance. The number of lost modes is irrelevant. In stage (b) there is 1 useful mode and no low guidance modes so the number of guided modes is 1 and the fibre is effectively single-moded. Stage (c) has only one low guidance mode and the fibre is not considered to guide a useful amount of power.

The second set of results reported in [7] are for another MPOF, this time with three circular rings of holes surrounding the core. The calculations for the two least leaky modes are presented in Table 1(b). It can be seen that for this fibre $L_{sm} = 28$ m and $L_{max} = 1.1\times10^3$ m, once again material absorption was omitted. Experimentally, 20 cm lengths of this fibre were found to be single-moded whilst 5 cm lengths were found to be multimoded [7]. An explanation for the apparent inconsistency is given below.

These experimental results illustrate that our definitions, apart from forming a theoretical basis for describing fibres, also apply to experimental observations. These results show that single-modedness of fibres with no strictly bound modes, as treated in our definitions above, is a property that depends on the length of the fibre. The reason the experimental and theoretical results do not agree quantitatively is because of simplifications in the modelling – as with the

**Table 1(a)**

| Mode Label | Loss (dB/m) | $L_{1\%}$ (m) | $L_{0.01\%}$ (m) | |
|---|---|---|---|---|
| 1 | $3x10^{-6}$ | **$6.7x10^{6}$** | $1.3x10^{7}$ | **$L_{max}$** |
| 2 | 200 | 0.1 | **0.2** | **$L_{sm}$** |

**Table 1(b)**

| Mode Label | Loss (dB/m) | $L_{1\%}$ (m) | $L_{0.01\%}$ (m) | |
|---|---|---|---|---|
| 1 | $1.9x10^{-3}$ | **$1.1x10^{3}$** | $2.2x10^{3}$ | **$L_{max}$** |
| 2 | 1.48 | 14 | **28** | **$L_{sm}$** |

**Table 1.** (a) Calculations of the two least leaky modes of the fibre reported in [6]. (b) Calculations of the two least leaky modes of the fibre reported in [7]. The last two columns contain the two lengths that characterise each mode. The two lengths that characterise the fibres as a whole are in bold-face, with the corresponding label at the right of the table.

majority of fibre modelling, the fibre was assumed to be straight, with a perfect structure and a lossless material. We believe that quantitative agreement between theory and experimental observations can be reached with more accurate modelling, which includes material loss, scattering from hole surfaces, structural defects etc. Experimental observation of singlemodedness is independent of launch conditions since one of the tests for singlemodedness in [6,7] was to inspect the near field image of the mode and to observe that it remained unchanged as the launching conditions were changed.

**4. Conclusion**: We have presented a method for characterising leaky modes in fibres in terms of two lengths that represent the maximum length over which a mode is useful and the length required to extinguish the mode completely. This characterisation allows for the number of leaky modes guided in a fibre of given length to be counted unambiguously. This counting method in turn unambiguously defines effective singlemodedness for fibres with no bound modes. The fibre as a whole can be characterised in terms of a maximum useful length and, if applicable, a length required to attain singlemodedness.

## Acknowledgements

We wish to thank Maryanne Large, Simon Fleming and Martijn de Sterke for helpful discussions.

## References

[1] A.W. Snyder, J.D. Love. *Optical Waveguide Theory*. Chapman & Hall, London, 1983.

[2] J.C. Knight, T.A. Birks, P.St.J. Russell, D.M. Atkin. Endlessly single-mode optical fibre with photonic crystal cladding. Optics Letters **21**,(19) p. 1547 (1996).

[3] R.F. Cregan, B.J. Mangan, J.C. Knight, T.A. Birks, P.St.J. Russell, P.J. Roberts, D.C. Allan, Single-mode photonic band gap guidance of light in air. Science **285**, p.1537 (1999).

[4] P. Yeh, A. Yariv, E. Marom. Theory of Bragg fibre. Journal of the Optical Society of America **68**(9), p. 1196 (1978).

[5] T.A. Birks, J.C. Knight, P.St.J. Russell. Endlessly single-mode photonic crystal fibre. Optics Letters **22**(13), p. 961 (1997).

[6] M.A. van Eijkelenborg, M.C.J. Large, A. Argyros, J. Zagari, S. Manos, N.A. Issa, I. Bassett, S. Fleming, R.C. McPhedran, C.M. de Sterke, N.A.P. Nicorovici. Microstructured Polymer Optical Fibre. Optics Express **9**(7), p.319 (2001).

[7] A. Argyros, I.M. Bassett, M.A. van Eijkelenborg, M.C.J. Large, J. Zagari, N.A.P. Nicorovici, R.C. McPhedran, C.M. de Sterke. Ring structures in microstructured polymer optical fibres. Optics Express, **9**(13), p. 813 (2001).

# Measurement of multipath interference and resulting optical communication system penalty

D.L. Craig, M.G. Taylor, W. Zheng, J. Fowlkes, H. P. Sardesai
CIENA Corporation, 920 Elkridge Landing Road, Linthicum MD 21090, USA
dcraig@ciena.com

***Abstract:*** *Derivation and method for measuring multipath interference 'MPI' in broadband passive fiber devices is presented. Presented is an example of how these measurements can be applied, to determine the impact of MPI in an optical communication system*

## Introduction

Multipath interference 'MPI' from a discrete number of sources, e.g. dirty connectors, and from double Rayleigh backscatter have been presented in the literature. [1-3] A general measurement method for broadband optical devices and how the measured value relates to optical communication system performance has been lacking. MPI for these devices can be characterized as an amplitude noise from the generation of randomly polarized, delayed echoes of the signal. For optically amplified systems MPI can be defined as:

$$MPI = \frac{P_{fs}(L)}{P_s(L)} \,. \qquad (1)$$

*where* $P_{fs}(L)$ is the forward scattered power measured at a point L *and* $P_S(L)$ is the signal power measured at L. This definition is derived for an opticaly amplified system, where double Rayleigh backscatter is the dominant source of MPI. [4] Accurate MPI values depend upon knowledge of Rayleigh backscatter coefficients and attenuation. This knowledge is not necessary to measure MPI of passive fiber devices and more generally any passive optical component. Derivation of a definition, description of the measurement system and an example of applying the measured results to predict the system penalty to a 10Gbps optical system is presented.

## Derivation

Multipath Interference at the receiver can be defined as

$$MPI = \frac{\sum_{i=1}^{n} Pi}{Po} \qquad (2)$$

where Po is the optical power of the signal and Pi is the power of the ith multipath signal. The electric field at the receiver is the sum of the signal and the delayed multipath components. The resulting electric field at the receiver is expressed as

$$\vec{\mathbf{E}} = E_o e^{i(\beta_0 l-\omega t)}\widehat{\mathbf{s}_0} + \sum_{i=1}^{N} E_i e^{i(\beta_i l-\omega t)}\widehat{\mathbf{s}_{\mathrm{I}}} \,, \qquad (3)$$

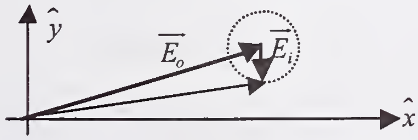

where $E_0$ is the amplitude of the signal and $E_i$ is the amplitude of the $I$th multipath component. $\beta_0$ is the propagation constant of the fiber, l is its length. $\beta_i$ is the effective propagation constant of the ith multipath component and accounts for differences in path length. The optical power seen at the receiver is

$$P = \overline{E} \cdot \overline{E^*} = E_0^{\,2} + 2\sum_{i=1}^{N} E_0 E_i \cos\phi_i \cos\theta_i + O\left(E_i E_j\right).$$

$$where, \qquad (4)$$

$$\phi_i = \left(\beta_0 - \beta_i\right) l - \omega t$$

$$\theta_i = \widehat{s_0} \cdot \widehat{s_i}$$

$$O\left(E_i E_j\right) istheremainingtermsof\ order\ E_i E_j$$

For path length much greater than wavelength (e.g. $\lambda << l$ or equivalently $2\pi \ll \phi$) and the interfering light is depolarized then $\cos\phi,\theta \approx 1/\sqrt{2}$ for time averages much longer than the bit period. The average power and standard deviation are

$$P_{av} = E_0^{\,2} = P_0 \quad and$$

$$\sigma^2 = P_0 \sum_{i=1}^{N} Pi \qquad (5)$$

Plugging into equation (2) MPI can be defined as

$$MPI = \frac{\sigma^2}{Pav^2} \qquad (6a)$$

or equivalently in decibels

$$MPI = 20\log\left(\sigma/_{Pav}\right) \qquad (6b)$$

where σ is the standard deviation of the insertion loss ripple in transmitted power and $P_{av}$ is the average transmitted power. Using the techique in the next section, MPI can be determined by a simple insertion loss measurement. No prior knowledge of the device is needed, except for the shortest and longest path length to be measured.

**Measurement**

A JDSU swept wavelength (i.e. SWS15100) with the PDL option was used to make the insertion loss measurements. The system consists of a SOM (Source Optics Module) a JDS tunable laser, a receiver that has a control module and a detector, and a PDL module. Features of the system are a 3pm step size and the ability of the tunable laser to sweep across the wavelength range, increasing the speed of the measurement. Insertion loss can be measured every 3pm at a sweep speed of up to 20nm/sec. Sample points in the measurement were every 3pm and the standard deviation was calculated on 1nm intervals. For fiber devices with multiple path lengths of 10cm to 8km a scan speed of 8nm/sec works best. The laser coherence length, and the path length of the interference must be taken into consideration when determining optimal scan and sampling speed. [5]

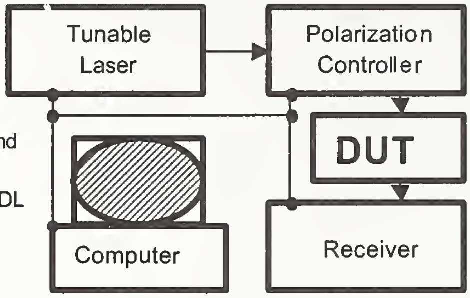

*Figure 2* Measurement Set-up

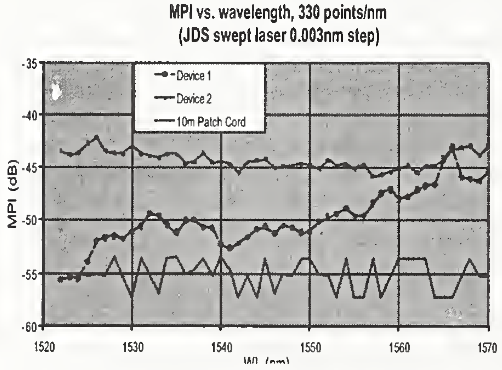

***Plot* 1** MPI vs. wavelength for fiber devices

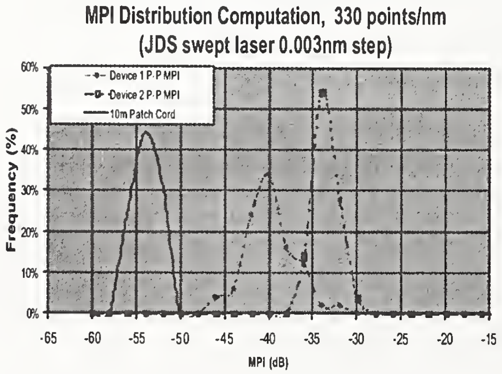

***Plot* 2** Distribution of MPI values per device

Plots 1 and 2 show typical results from measurement of some fiber-based devices. A 10 meter patch cord is plotted as well to show where the noise floor occurs. In both cases data was taken every 3pm, then 330 points (i.e. every 1nm) bins were used to calculate the MPI as a function of wavelength. Notice the wavelength dependence of the MPI in plot 1. Measuring a few discrete wavelengths using a RIN based measurement would not uncover this wavelength dependence. Next is shown how these measurements can be used to determine OSNR penalty for a 10 gigabit/second system.

**Experiment**

Multipath interference (MPI) is becoming a more significant impairment in long haul fiber optic transmission systems. The system penalty from MPI arising from multiple discrete reflections has been calculated as a result of phase noise to amplitude conversion [3]. The impact of distributed and discrete back reflections have been characterized as a power penalty [6-8] and the expressions obtained, although not explicitly stated in those papers, were equivalent to an optical signal to noise ratio (OSNR) contribution. This paper will show that forward scattering MPI can be treated as an OSNR contribution.

To observe the effects of MPI in isolation from other impairments, a single channel was propagated through three different system configurations, one of which was a special MPI loaded test bed. The three configurations used the same transmitter and receiver subsystems. The transmitter generated a conventional NRZ signal at 9.953Gb/s, and comprised an external cavity laser at 1545nm modulated by a lithium niobate Mach-Zehnder modulator. Its output was combined with three other wavelengths from c.w. DFB lasers, the closest 14nm away, whose purpose was to keep the EDFAs at a known saturation point. The receiver employed an 8GHz bandwidth pin-preamp detector going into a commercially available clock/data recovery unit. Prior to the receiver were an EDFA and variable optical attenuator, which were used to add controlled amounts of ASE noise to the signal under observation.

The three different system configurations were as follows.

*Case 1* Six spans of standard non dispersion shifted fiber (NDSF) of lengths 60, 40, 60, 60, 60 & 20km, roughly with each span followed by dispersion compensation modules (DCMs) having the same magnitude of chromatic dispersion as the NDSF span. The DCMs were of a low dispersion slope type, available on the market for several years. The spans were each preceded by a two-stage gain flattened EDFA, with the DCMs located between stages.

*Case 2* Instead of the DCMs of case 1, high slope DCMs were used which were of an old design known to have high MPI. These DCMs had a higher loss, and were placed both between the EDFA stages and following the NDSF spans. The end-to-end dispersion was the same as case 1.

*Case 3* No transmission fiber, DCMs or line amps. This configuration was used to make noise loaded measurements of the transmitter and receiver back-to-back.

Note that because it is a single channel experiment the difference in dispersion slopes of the two DCM types does not affect the result, and the MPI of the DCMs is the relevant parameter. The output power of the EDFAs (main output and mid-stage output) was -3dBm for the 1545nm channel. The experiment was designed so that most impairments which usually have to be considered in a WDM transmission system do not contribute to the *Q* factor: SPM, cross phase modulation, four wave mixing, PMD, etc; only the MPI and the OSNR were varied.

The multipath interference in the high slope DCMs is of the forward scatter type. It arises because some light is scattered into transverse modes other than the one carrying the signal, and then scattered back into the same transverse mode as the signal. The MPI was determined from the measured ripple in insertion loss vs. wavelength via equation (6) where $\sigma$ is the standard deviation of the ripple in transmitted power and $P_{av}$ is the average transmitted power. This is the correct equation assuming the multipath interfering light is depolarised. The spacing between points in the measurement was 3pm and the standard deviation was calculated on 1nm intervals. The time delay between the signal and the interfering light for this type of DCM is thought to be of the order 500ns.

The *Q* factor was repeatedly measured using the decision threshold technique as a function of OSNR for the three cases. The results are plotted in figures 1 & 2. Case 2, the high MPI case, shows a substantial penalty in *Q* at high OSNRs. There is more scatter in the data points for the high MPI case than the other two. This is probably because the linewidth of the signal laser is less than the reciprocal of the typical multipath delay, 500ns, and there is phase coherence in the multipath interference process, so it depends on the environmental conditions which varied over the 24h period that the measurements were made.

**Analysis of results**

The multipath interference is expected to appear as an additional noise contribution, behaving like extra ASE. Because the MPI is the sum of replicas of the signal after many random time delays, it has the same shape as the signal's optical spectrum, but the phase of each component is random. Thus it is similar to ASE, which has a flat optical spectrum and random phase. The equivalent OSNR of the multipath interference is

$$OSNR_{eq} = \frac{B_{sig}}{MPI.B_{res}} \qquad (7)$$

where $B_{sig}$ is the signal's optical bandwidth and $B_{res}$ is the resolution bandwidth associated with the OSNR.

The results of the experiment were used to test whether equation (7) applies. A curve, the solid line in figure 1, was drawn through the data points of case 3 with the equation

$$Q = f(OSNR) \qquad (8)$$

where

$$f(x) = 0.0130x^2 + 0.0395x + 1.41 \qquad (9)$$

is simply a polynomial fit to the back-to-back (case 3) data points.

The two curves drawn on figure 4 (reproduced as the dashed curves on figure 3 so that all three cases can be seen on the same graph) are mapped versions of the solid curve on figure 3 following the relationship

$$Q = C.f\left(\left[\frac{1}{OSNR} + \frac{MPI.B_{res}}{B_{sig}}\right]^{-1}\right) \qquad (5)$$

The contents of the brackets is the sum of the MPI equivalent OSNR from equation 7 and the actual OSNR. The multiplier *C* is there to account for the eye opening being slightly different in the three cases. This was attributed to the end-to-end dispersion being different, because of the granularity of the available DCMs. The values of *C* and *MPI* used are given in Table 1, and $B_{sig}$=16GHz, $B_{res}$=12.5GHz.

| | *C* | *MPI* (dB) |
|---|---|---|
| case 1 | 1.02 | -34.6 |
| case 2 | 0.98 | -25.4 |

***Table 1*** *Values used in equation 5.*

The *MPI* values are the sum of the measured MPIs of the individual fiber spans and DCMs at the signal wavelength. Factor *C* is fitted based on the *Q* values at the low OSNR region.

Clearly, the two mapped curves do indeed fit their respective experimental data points. In particular the curve through the high MPI DCM points predicts the deviation at high OSNRs correctly. We conclude that the multipath interference can be treated as a noise

If the variation of $\alpha_{RS}(r)$ is very small it may be excluded from the integration and the integrals left is the inverse of the effective area. Combining with (1) the following dependence of $\kappa$ is obtained:

$$\kappa \propto \frac{\alpha_{RS,SiO_2} + K_{Ge}\Delta n^{+} + K_{F}\Delta n^{-}}{\lambda^2 A_{eff}} \tag{6}$$

***Experimental setup:***

Previous measurements of Rayleigh backscattering [6,7,8] are based on an OTDR but lack the availability of scanning the signal wavelength. The setup presented here is based on a return loss module, a tuneable laser and a powermeter (schematic in Fig. 1), all commercially available instruments. A measurement with a reflection reference cable of known return loss is used to calibrate the return loss module and the recorded return loss and power through the reference cable is used as a reference for all the measurements.

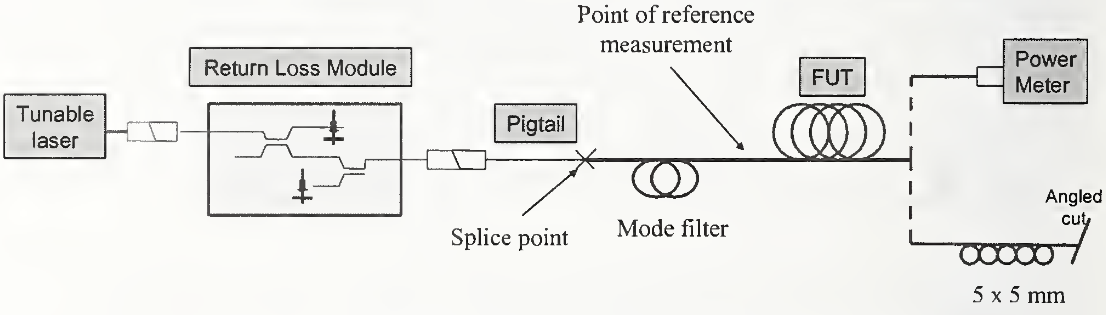

**Figure 1:** Schematic of the experimental setup used for measuring Rayleigh backscattering.

The fiber under test (FUT) is spliced to a pigtail fiber and the splice is kept fixed for stability. To exclude multimode effects a higher order mode filter is applied to the FUT right after the splice by two coils of a suitable diameter. One complete measurement consists of 4 cycles:

1. The end of the FUT is terminated by 5 to 10 coils of a diameter less than 5 mm and an angular cut to remove end reflections. The backreflected power of the FUT is recorded.
2. The end of the FUT is connected to the powermeter and the power throughput is recorded.
3. The FUT is cut approx. one meter after the splice and the mode filter and is again terminated by small coils and an angular cut, and a reference return loss is recorded.
4. The fiber end is connected to the powermeter and the reference power is recorded.

According to (3) the power returning to the input end due to Rayleigh backscattering in the FUT of length L is given by:

$$P_{RBS}(0) = \kappa P_{in}(0)\int_0^L e^{-2\alpha z}dz = P_{in}(0)\frac{\kappa}{2\alpha}\left(1 - e^{-2\alpha L}\right) \tag{7}$$

where $\alpha$ and L is the spectral attenuation and the length of the FUT respectively. Defining $R_{FUT}=P_{RBS}(0)/P_{in}(0)$ as the return power ratio due to the FUT we get for $\kappa$:

$$\kappa = \frac{2\alpha R_{FUT}}{1 - e^{-2\alpha L}} \tag{8}$$

The total return power ratio $R_{tot}$ seen by the return loss module is the sum of the return power ratio from the pigtail + splice and the FUT:

$$R_{tot} = R_{pigtail+splice} + \frac{P_{RBS}\alpha_{pigtail+splice}}{P_{in}/\alpha_{pigtail+splice}} = R_{pigtail+splice} + R_{FUT}\alpha^2_{pigtail+splice} \tag{9}$$

where $\alpha_{pigtail+splice}$ is the loss of the pigtail and the splice and is found from the calibration and reference measurements. This leads to

$$\kappa = \frac{2\alpha(R_{tot} - R_{pigtail+splice})}{\alpha^2_{pigtail+splice}\left(1 - e^{-2\alpha L}\right)} \tag{10}$$

The tunable laser makes it possible to measure $\kappa$ as a function of wavelength.

***Results:***

A vast amount of different fibers have been measured. The fibertypes are Standard single mode fiber (SSMF), Non-zero dispersion fiber (NZDF), Super large effective area fiber (SLA), Inverse dispersion fiber (IDF), Raman gain fiber and different kinds of dispersion compensating fiber (DCF) with varying relative dispersion slope for dispersion slope compensation of different types of transmission fibers. All fibers have been manufactured by OFS. The lengths of the fibers under test have varied from about 1 km up to 50 km and cutback measurements have shown no indication of any length dependence in the measurement.
The repeatability variation of the measurement is below 2% looking at actually measured values. Comparing results where a linear fit has been applied to the data the repeatability variation is below 1%.

In fig. 2 (to the right) measurements of the different fiber types are shown. The variation with wavelength is seen to be almost linear and linear fits have been applied to the measured $\kappa$ values. It is seen that not only the magnitude of $\kappa$ but also the slope of $\kappa$ changes for different fiber types. From (6) it is seen that the slope of $\kappa$ is proportional to $1/A_{eff} \times \lambda^{-3}$.

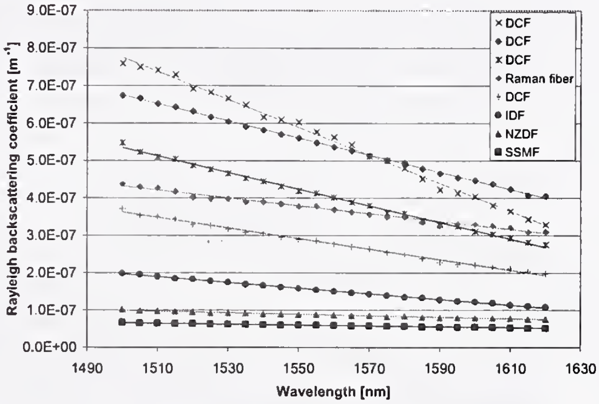

Using measured values for $\kappa$, $A_{eff}$, $C_R$ and fiber loss to predict [1] gain, noise figure and MPI of a Raman amplifier gives good agreement with measured values. An example is shown in fig. 3: A measurement of a dispersion compensating Raman amplifier consisting of 3.9 km Extra High Slope DCF (EHS DK) compensating the dispersion and dispersion slope of 90 km Truewave®RS from 1528.8 nm to 1567.2 nm [9]. The DCF has been backward pumped by pumps at three different wavelengths.

Fig. 4 shows $\kappa$ vs. spectral attenuation @1550 nm. A linear dependence can be sensed but the large spreading of the data indicates that the backscattering of a fiber cannot be predicted by just knowing the spectral attenuation. That is due to other loss factors different from fiber to fiber (e.g. bending losses, anomalous losses etc.).

Fig. 5 shows the expected $1/A_{eff}$ dependence of $\kappa$.

Fig. 6 shows the relation between $\kappa$ @1550 nm and the peak value of the Raman gain coefficient $C_R = g_R/A_{eff}$ measured with a pump wavelength of 1453 nm. A distinct linear correlation is seen. To a good approximation $g_R$ can be written as [10,11] $g_R = C_1 g_{SiO2} + C_2\Delta n^- + C_3\Delta n^+$ where $g_{SiO2}$ is the Raman gain coefficient of pure silica and $C_1$, $C_2$ and $C_3$ depend on the overlap between the pump and the signal. Comparing to (6) the observed linear correlation is expected.

***Conclusion:***

We have described a fast, simple and repeatable method to measure the Rayleigh backscattering coefficient of optical fibers as a function of wavelength, and measurement results from a broad range of fibertypes have been presented. In combination with measurements of $A_{eff}$ and $C_R$ we have shown that it is possible to calculate the behavior of the fiber in a Raman optical amplifier, especially predicting the MPI due to double Rayleigh backscattering which is a limiting factor in Raman amplification.

***References:***

[1] P.B. Hansen, L. Eskildsen, A. J. Stentz, T. A. Strasser, J. Judkins, J. J. DeMarco, R. Pedrazzani and D. J. DiGiovanni, *"Rayleigh scattering limitations in distributed Raman pre-amplifiers"* , IEEE Photonics Tech. Letters, vol. 10, No. 1, pp. 159-161, 1998
[2] E. Brinkmeyer, *"Analysis of the backscattering method for single-mode optical fibers"* , J. Opt. Soc. Am., Vol. 70, No. 8, pp. 1010-1012, 1980
[3] M. Nakazawa, *"Rayleigh backscattering theory for single-mode optical fibers"* , J. Opt. Soc. Am., Vol. 73, No. 9, pp. 1175-1180, 1983
[4] I. Garret and C. J. Todd, *"Components and systems for long-wavelength monomode fibre transmission"*, Optical and Quantum Electronics, vol. 14, pp. 95-143, 1982
[5] A. Hartog and M. Gold, *"On the Theory of Backscattering in Single-Mode Optical Fibers"* , J. Lightwave Tech., vol. LT-2, No. 2, pp. 76-82, 1984
[6] A. Hartog and M. Gold, *"Measurement of backscatter factor in single-mode fibers"* , Electr. Lett., vol. 17, No. 25, pp. 965-966, 1981
[7] A. F. Judy, *"An OTDR based combined end-reflection and backscatter measurement"* , SOFM, pp. 19-22, 1992
[8] M. E. Fermann, S. B. Poole, D. N. Payne and F Martinez, *"Comparative measurements of Rayleigh scattering in single-mode optical fibers based on OTDR technique"*, Journ. Ligthwave Tech., vol. 6, No. 4, pp. 545-551, 1988
[9] Y. Qian, C. G. Jørgensen, P. B. Gaarde, B. Pálsdóttir and B. Edvold, *"C-band discrete Raman amplification with simultaneous dispersion and dispersion-slope compensation for NZDF"* , Proceedings of OOA 2002
[10] Y. Qian, *"Optically Pumped Waveguide Lasers and Amplifiers"*, Ph.D. Thesis, 2000
[11] J. Bromage, K. Rottwitt and M.E. Lines, *"A method to predict the Raman gain spectra of germanosilicate fibers with arbitrary index profiles"*, IEEE, Phot. Tech. Lett., vol. 14, Issue 1, pp. 24-26, 2002

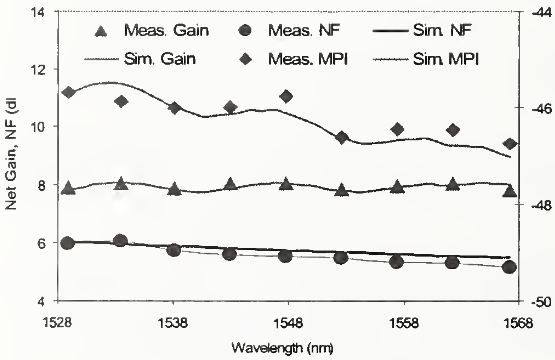

**Figure 3:** Measured and calculated netgain, noise figure and MPI of a C-band dispersion compensating Raman amplifier [9].

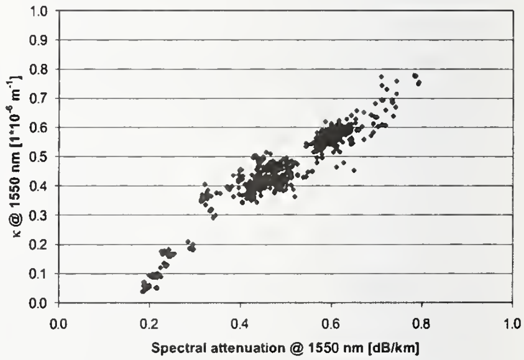

**Figure 4:** Measured Rayleigh backscattering coeff. vs. the fiber spectral att. @ 1550 nm for various types of fiber.

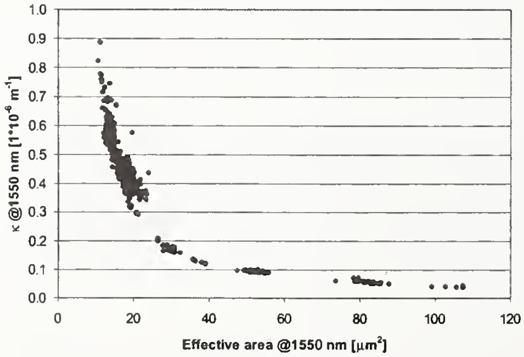

**Figure 5:** Measured Rayleigh bsc. coeff. @ 1550 nm vs. the effective area @ 1550 nm for various types of fiber.

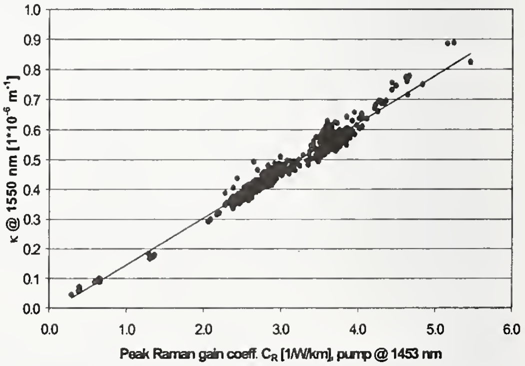

**Figure 6:** Measured Rayleigh backscattering coeff. @ 1550 nm vs. peak Raman gain coeff. @ 1551 nm (pump @ 1453 nm).

# Measurement of Multimode Resonances in Hexagonal Micro-Pillar Optical Cavities

Ma Ning and Andrew W. Poon
Department of Electrical and Electronic Engineering
Hong Kong University of Science and Technology, Hong Kong, China

## I. Introduction

Optical micro-pillar ( μ -pillar) resonators have attracted recent interests for potential applications in integrated photonics due to their compact size (of 10 - 100 μ m lateral dimensions and of ~ μ m height) and high-Q resonances. Ring and disk μ -pillar wavelength-division multiplexing (WDM) channel add/drop filters have been demonstrated [1]. Very large-scale integrated (VLSI) photonic chips using μ -pillar cavities are feasible [2]. High-Q optical resonances can be confined by nearly total internal reflection (TIR) at the μ -pillar resonator sidewall. The μ -pillar cavity can be evanescently side-coupled or vertically coupled [3] to input and output waveguides. The main drawback of the conventional side-coupled circular ring and disk cavities is the short interaction length between the curved cavity sidewall and the straight waveguide sidewall. Such short interaction length imposes a sub-micrometer gap distance for evanescent coupling.

Polygonal μ -pillar resonators provide an alternative means of increasing the evanescent side-coupled length for potential WDM add/drop filter applications [4]. The advantages of the polygonal cavities are twofold: (1) The entire flat polygonal sidewall allows a longer interaction length, and therefore a wider gap distance for evanescent coupling between the cavity and the straight waveguides; and (2) the optical path length is identical for rays having the same incident angle along the sidewall, and hence the same cavity mode can be coupled anywhere along the flat sidewall. Fabrication of polygonal μ -pillar cavities can be readily achieved with established microelectronic fabrication processes. Recently, multimode resonances in square-shaped μ -pillar cavities were demonstrated [4], and hexagonal microlasers have been reported [5].

In this paper, we report our recent measurement of multimode resonances in the elastic-scattering spectrum of hexagonal μ -pillar optical cavities, using Gaussian beam coupled along the cavity sidewall. The observed free spectral range (FSR) is consistent with the six-bounce closed-loop path length. By using the wavefront-matching concept [4], the observed multimode resonances can be attributed to round-trip trajectories that need not be closed after each round trip.

## II. Ray Optics in Hexagonal Cavities

Figure 1 (a) shows the six-bounce closed-loop trajectories with an incident angle $\theta = 60^\circ$. All hexagonal orbits with $\theta = 60^\circ$ (such as the solid and dashed lines) have the same path length of 3L (L is the distance between two parallel planes) and therefore have the same cavity modes. Trajectories with $\theta \neq 60^\circ$ do not close upon themselves in each round trip. Figure 1 (b) shows the six-bounce open-loop trajectory with incident angle $\theta \neq 60^\circ$, and a complementary incident angle $120^\circ - \theta$ at the adjacent sidewall. For the trajectory to be confined by TIR, θ needs to satisfy $\theta_c < \theta < 120^\circ - \theta_c$, where the critical angle $\theta_c = \sin^{-1}(1/n)$, and n is the refractive index of the dielectric cavity in air. In silica $n \approx 1.44$ ($\lambda \approx 1.5$ μ m), and

$\theta_c \approx 44°$, $44° < \theta < 76°$. In the cavity, the incident wavefront and the wavefront of the open-loop round trip ray can be spatially overlapped, as shown by the dashed line in Figure 1 (b). Following the discussion of multimode resonances in square μ-pillar cavities in [4], we believe such wavefront-matched open round trip can result in multimode resonances in hexagonal cavities.

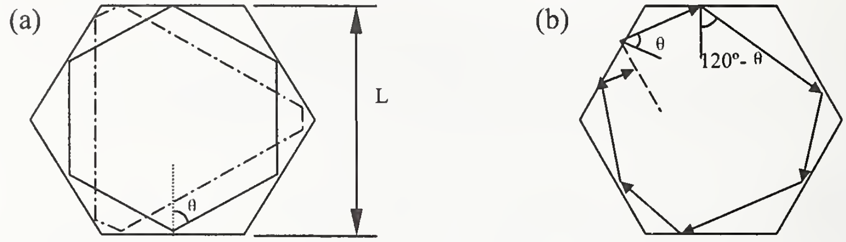

Figure 1 (a) Six-bounce closed-loop trajectories with incident angle $\theta = 60°$ . (b) Open-loop trajectory with incident angles $\theta$ and $120° - \theta$ .

## III. Experiment and Results

A commercially available hexagonal silica fiber was employed in the elastic-scattering experiment. The fiber was side-couple perpendicular by a Gaussian beam, and thus acted as an optical μ-pillar cavity. Two fiber sizes with L = 125 μm ± 2.5 μm and L = 200 μm ± 4 μm were used in the experiment. The fiber corners are slightly rounded. The fiber orientation was monitored with an uncertainty of ±2° by a top-view microscope. A Gaussian beam from a wavelength-tunable diode laser (1510 nm – 1580 nm-wavelength range) was weakly focused (by a f /20 ~ f /33 cylindrical lens) to the fiber and tangentially onto the fiber flat sidewall. The line beam was along the fiber axis. The estimated beam width was < 100 μm. The incident polarization was parallel to the fiber axis (TM mode). We tuned the separation between the line beam and the fiber sidewall in order to excite the cavity modes. The elastic-scattering spectrum was imaged (with an acceptance angle of 2.6°) from the fiber flat sidewall onto an InGaAs photodiode. An analyzer was placed in front of the photodiode to measure the TM spectrum. The laser linewidth is $\approx 2 \times 10^{-6}$ nm, and the spectral resolution was 0.003 nm. Figure 2 shows the schematic of the hexagonal fiber side-coupled with a Gaussian beam.

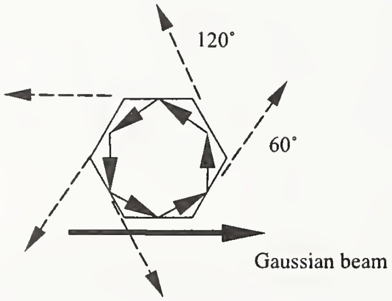

Figure 2 Schematic of the hexagonal fiber side-coupled with a Gaussian beam. The dashed arrows indicate the scattering tangential to the cavity sidewalls.

Figure 3 shows the measured TM polarized elastic-scattering spectrum of a L = 200 μm hexagonal fiber imaged at 60° from the Gaussian beam direction. The highest measured Q factor is > 2000. The spectrum is multimode. At least four orders of modes were observed (labeled as A, B, C, D) with a FSR ≈ 2.8 nm. The scattering spectra at other angles were also measured.

Assuming a six-bounce closed-loop trajectory, the FSR is calculated as follows:

$$FSR \approx \frac{\lambda^2}{3nL} \qquad (1)$$

where $\lambda \approx 1550$ nm, n = 1.44, L = 200 μm, and 3L is the closed-loop path length. The calculated FSR ≈ 2.78 nm is consistent with the measured FSR ≈ 2.8 nm.

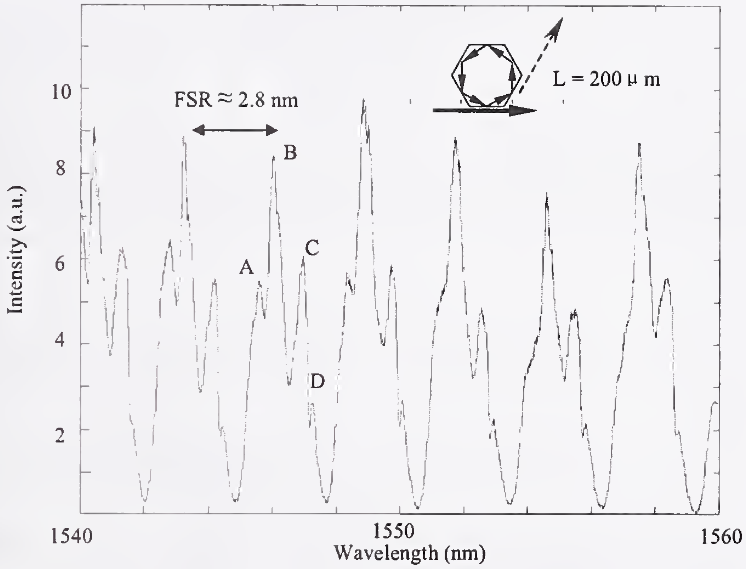

Figure 3 Measured multimode resonances (at 60° scattering angle) in a TM-polarized elastic-scattering spectrum of a hexagonal optical fiber (L=200 μ m). The FSR is ~ 2.8nm. The inset shows a schematic of the Gaussian beam (the thick arrow) grazing the hexagonal fiber sidewall and a six-bounce closed-loop trajectory.

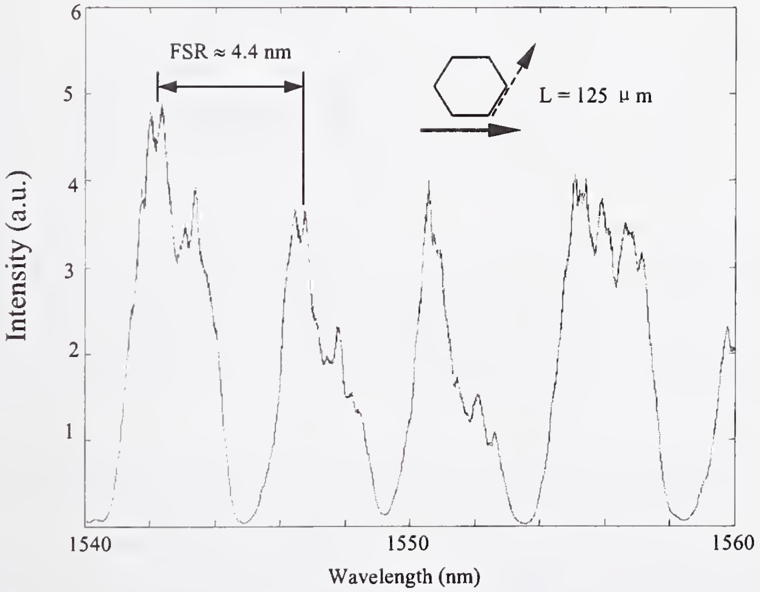

Figure 4 Measured multimode resonance in a TM-polarized elastic-scattering spectrum of a hexagonal optical fiber (L = 125 μ m) at 60° scattering angle. The FSR is ~ 4.4 nm.

Figure 4 shows the measured TM polarized scattering spectrum at 60° in a 125 μm hexagonal fiber. The observed FSR ≈ 4.4 nm is consistent with the calculated FSR ≈ 4.45 nm by means of equation (1). There are more than 4 orders of modes. By further reducing the cavity dimensions, larger FSR is expected, which is an essential requirement for WDM add/drop filter applications. In order to obtain a FSR > 30nm, which spans the 1.55 μm telecommunication window, a silica hexagonal μ-cavity with L < 20 μm is needed. Such small μ-pillar cavities can be readily fabricated by microelectronic technologies.

In summary, the elastic-scattering spectra of hexagonal μ-pillar resonators were measured. The multimode resonances can be attributed to the wavefront-matched open-loop trajectories. A smaller-sized hexagonal cavity coupled with waveguides has potential applications in WDM add/drop filters.

We gratefully acknowledge the support by the Hong Kong University Grant Council (HIA 01/02. EG05) and the Research Grant Council (DAG01/02. BG22). Andrew W. Poon's email address is eeawpoon@ust.hk.

## References

[1] B. E. Little, J. S. Foresi, G. Steinmeyer, E. R. Thoen, S. T. Chu, H. A. Haus, E. P. Ippen, L. C. Kimerling, and W. Greene, IEEE Photon. Technol. Lett. Vol. 10, no.4, pp.549-551, (April, 1998).

[2] B. E. Little and S. T. Chu, Optics & Photonics News, pp. 25-29 (Nov. 2000).

[3] P. P. Absil, J. V. Hryniewicz, B. E. Little, F. G. Johnson, K. J. Ritter, P. T. Ho, IEEE Photon. Tech. Lett. Vol. 13, no. 1, pp. 49-51 (Jan. 2001).

[4] A. W. Poon, F. Courvoisier, R. K. Chang, Optics Letters, vol. 26, no. 9, pp. 632-634 (May, 2001).

[5] S. Ando, N. Kobayshi and H. Ando, Jpn. J. Appl. Phys. Vol. 34(1995) pp. L4-L6.

# MEASUREMENT REQUIREMENTS FOR OPTICAL AND OPTOELECTRONIC MODEL VERIFICATION, VALIDATION, AND CALIBRATION
# (INVITED)

J. Morikuni, P. Mena, B. K. Whitlock, and R. Scarmozzino
RSoft Design Group, Inc.
200 Executive Blvd.
Ossining, NY 10562

## INTRODUCTION

As optical communication systems become more and more complex, an accurate modeling and simulation infrastructure becomes critical to their design. Even seemingly simple optical designs can become intractable when attempted by hand; this is particularly evident in the physical design of fiber-optic communication systems. Although any fiber-optic system can be described fundamentally as an optical source, a transmission medium, and a detector, its design involves hundreds, if not thousands, of choices, decisions, and trade-offs. For example, what is the optimum type of laser to use? Will the targeted link require optical amplification? If so, should Raman amplifiers or EDFAs be used? What is the impact of additional DWDM channels? These questions can all be answered through optical link simulation. Figure 1 depicts a typical simulation topology as seen from the graphical user interface of a physical-layer, link-level simulator [1].

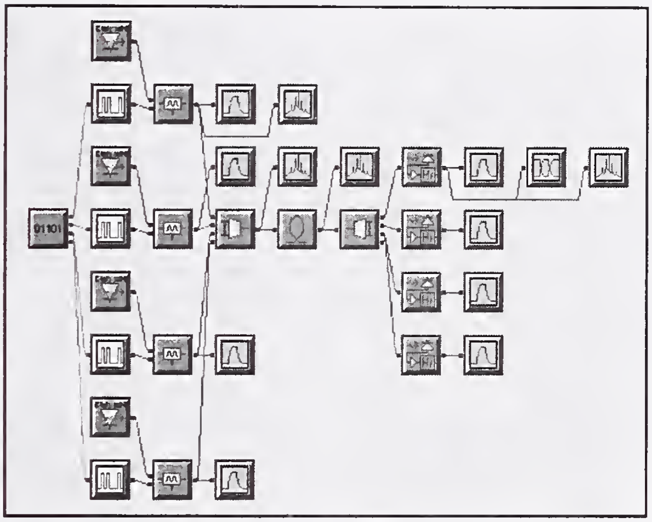

Figure 1: Topology of a link-level simulation as viewed from the graphical user interface.

In this figure, the simulation of a four-channel WDM system is depicted; each channel consists of a CW laser at a different wavelength connected to an external modulator driven by a PRBS pattern generator and an electrical signal generator. The four channels are combined with an optical multiplexer and transported through 40 km of single-mode fiber Finally, the four channels are separated with an optical demultiplexer and processed by individual photoreceivers. At any point along the link, the signal waveforms can be viewed in the time or frequency domain using "virtual" measurement instruments such as oscilloscopes, spectrum analyzers, BER testers, and the like.

The square icons in the topology of Figure 1 represent models describing the performance of each device in the system. The device models that comprise a link simulator are arguably the most critical aspect of the tool. Each model contains a very detailed physical description of the device's attributes using equations of quantum mechanics, semiconductor physics, electromagnetics and the like. Because these models are physical and general, each one can be used to simulate a wide range of device configurations. For example, the detector responsivity, the amplifier bandwidth, and the filter type are three of the many photoreceiver model parameters that can be individually tailored. In order to construct real-world systems, each of the models in the link must be properly calibrated to the device that it is intended to simulate. To this end, laboratory measurements are typically analyzed to extract all of the model parameters that are relevant to the system under study. In this paper, we will describe representative measurements required to validate and calibrate optical and optoelectronic models for the purposes of system simulation. We review methods for three critical aspects of the link: the laser, the fiber, and the photoreceiver.

## LASER DIODE

While there are many types of laser diodes, most of them can be described by the following rate equations [2]:

$$\frac{dN}{dt} = \frac{I}{q} - \frac{N}{\tau_n} - G_0(N-N_0)S \qquad \frac{dS}{dt} = \beta\frac{N}{\tau_n} + G_0(N-N_0)S - \frac{S}{\tau_s} \qquad P = kS \tag{1}$$

Here, $N$ and $S$ are the total electron and photon populations, respectively, in the laser cavity; $\tau_n$ and $\tau_s$ are the electron and photon lifetimes, respectively; $G_0$ is the gain coefficient; $N_0$ is the electron population at optical transparency; $\beta$ is the spontaneous emission coupling coefficient; $I$ is the injected current; $q$ is the electron charge; $t$ is time, and $k$ is the output power coupling coefficient. These parameters are clearly grounded very heavily in device physics. The rate equation model describes the time varying interchange of energy between the electrons and photons in the laser cavity; using these equations, it is possible to predict the amount of optical output power $P$ for a given amount of input current $I$. Although this model does a very good job of *qualitatively* describing laser operation, laboratory measurements are necessary to calibrate the model to an actual device.

The six physical model parameters in (1) are unfortunately not directly observable nor measurable with typical laboratory equipment. However, they can be determined through two commonly performed laboratory measurements: the light-current characteristic and the time-domain step response. The first measurement characterizes the amount of optical output power that results from a given amount of input current under steady-state conditions. The second measurement characterizes the transient response of the laser to a step current input of a fixed level. From these two measurements, we can determine the following laser attributes: the threshold current $I_{th}$, the slope efficiency $\eta_{qe}$, the turn-on delay $t_d$, the frequency of the laser relaxation oscillations $\Omega_R$, and the decay rate of the oscillations $\Gamma_R$ (Figure 2). One additional parameter is the magnitude of the input current $I_0$ used to produce the transient step response. Analysis of the rate equations over different regimes of operation (e.g., well below threshold and well above threshold) [3] combined with numerical parameter optimization can be used to map these physically observable parameters to the theoretical rate-equation ones. If they are available, the $S_{21}$ and $S_{11}$ responses of the laser can be used in place of the step response, though a different extraction procedure must be used.

For more complex device structures, the simple rate-equation description is insufficient. For example, the rate equations can be augmented by spatial and thermal ones to describe the attributes of a VCSEL (2)-(6):

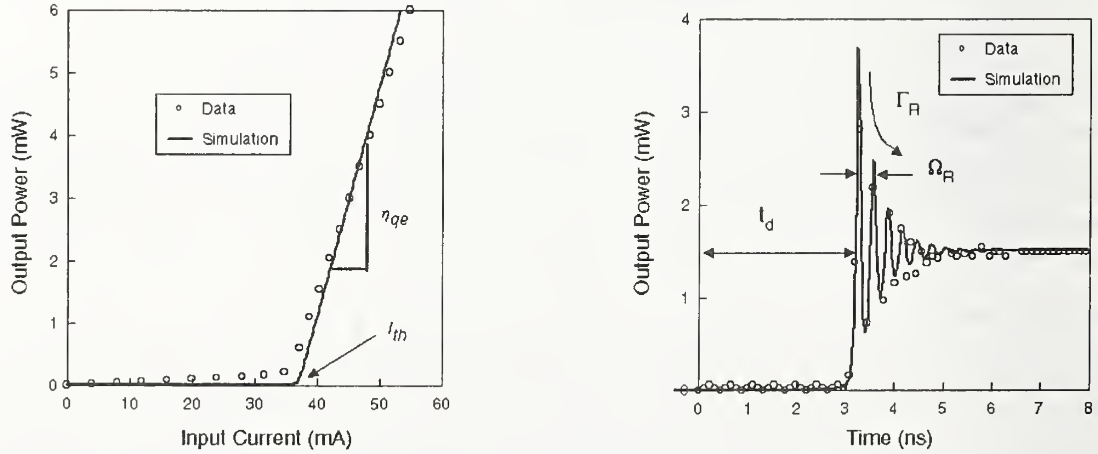

Figure 2: Representative laboratory measurements used to calibrate rate equation model.
Data taken from the datasheet for a Rohm RLD-83MF short-wavelength 830 nm edge-emitting laser diode.

$$\frac{dN_0}{dt} = \frac{\eta_i I}{q} - \frac{N_0}{\tau_n} - \frac{G(T)\{\gamma_{00}[N_0 - N_t(T)] - \gamma_{01}N_1\}}{1 + \varepsilon S}S - \frac{I_{leak}(N_0, T)}{q} \tag{2}$$

$$\frac{dN_1}{dt} = -\frac{N_1}{\tau_n}(1 + h_{diff}) + \frac{G(T)\{\phi_{100}[N_0 - N_t(T)] - \phi_{101}N_1\}}{1 + \varepsilon S}S \tag{3}$$

$$\frac{dS}{dt} = -\frac{S}{\tau_p} + \frac{\beta N_0}{\tau_n} + \frac{G(T)\{\gamma_{00}[N_0 - N_t(T)] - \gamma_{01}N_1\}}{1 + \varepsilon S}S \qquad T = T_{\mathrm{o}} + (I_{tot}V - P_{out})R_{th} - \tau_{th}\frac{dT}{dt} \tag{4}$$

$$I_{leak} = I_{lo}\exp\left(\frac{-a_0 + a_1N_0 + a_2N_0T - \dfrac{a_3}{a_4 + N_0}}{T}\right) \qquad G_{\mathrm{o}}(T) = G_{\mathrm{o}}\left(\frac{a_{g0} + a_{g1}T + a_{g2}T^2}{b_{g0} + b_{g1}T + b_{g2}T^2}\right) \tag{5}$$

$$G(N, T) = G_{\mathrm{o}}(T)[N - N_t(T)] \qquad N_t(T) = N_{tr}(c_{n0} + c_{n1}T + c_{n2}T^2) \tag{6}$$

We do not attempt to describe the model [4] here; the point of this discussion is to illustrate the level of complexity of a typical active device model. To properly calibrate the model to an actual device, the user can adjust over 40 parameters. While the first step in the analysis is to extract as many model parameters as possible from lab measurements (as in the previous example), the semi-empirical nature of this particular model necessitates a numerical optimization scheme such as least-squares fitting, the Levenberg-Marquardt method [5], or a genetic algorithm [6]. This process is generally referred to as parameter extraction and is used very commonly in the electronic design automation (EDA) industry. Figure 3 depicts the validated VCSEL model.

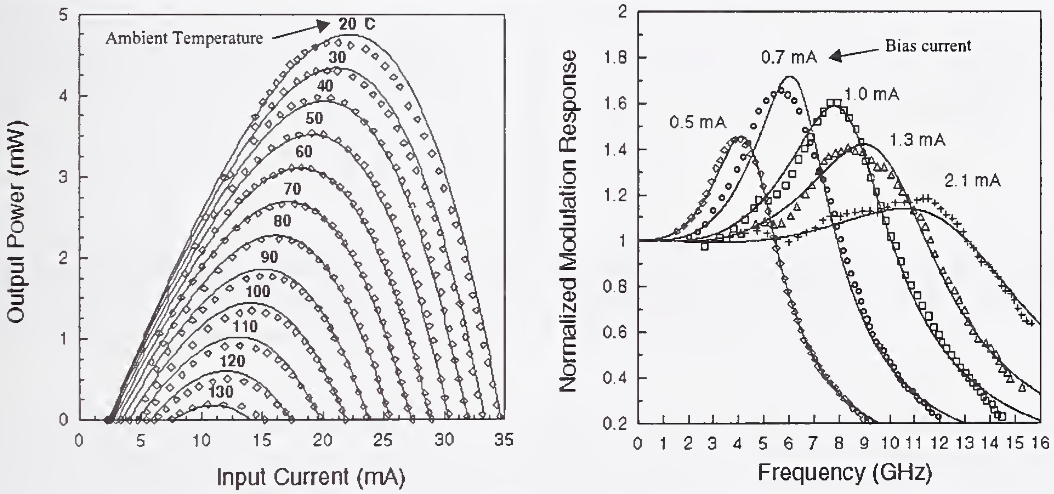

Figure 3: Validated VCSEL model. Markers represent data, curves represent simulation results. Light-current-temperature data (left) are from [7], $S_{21}$ data (right) are from [8].

## OPTICAL FIBER

System-level link analysis tools must also be able to model the optical transmission medium. The link simulator of [1] contains models for both single-mode and multimode fibers. One of the more interesting measurement-based examples is the multimode fiber. There are several ways to model multimode fibers; the most fundamental method is to analyze the fiber's refractive index profile and to extract information about the fiber's spatial modes and propagation constants [9]. This information can be used to predict fiber attributes such as modal dispersion, modal noise, and the like. The fiber propagation constants are extremely sensitive to minor perturbations in the index profile

[10]; consequently, for high-speed applications, the degree of accuracy required in the refractive index measurement often renders the index-based approach impractical. As a result, researchers have developed a measurement-based approach for characterizing multimode fiber bandwidth [11], [12]. This method is referred to as differential mode delay (DMD) [13] and involves injecting small, short spots of light at regularly spaced intervals of the multimode fiber input face and measuring the resulting signal that emerges from the fiber output (Figure 4). Since these pulses are scanned across the circularly symmetric fiber face, many of the fiber's relevant spatial properties can be captured. By interpreting the optical inputs as spatio-temporal delta functions, the corresponding outputs can be used to calculate the fiber's spatio-temporal impulse response.

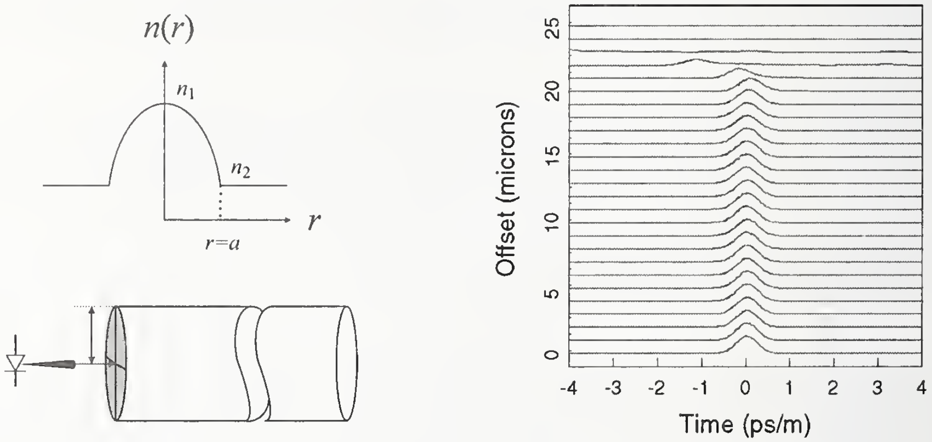

Figure 4: Refractive index profile of graded-index multimode fiber (upper left). Differential mode delay (DMD) measurement of multimode fiber (lower left). Simulated DMD impulse responses (right).

Multimode fiber performance can be estimated from the DMD measurements by combining them with encircled flux measurements. Encircled flux is a measure of the amount of optical power that is contained *inside the fiber* within a given radial distance from the fiber axis [14]:

$$EF(r) \propto \int_0^{2\pi} \int_0^r I(r, \theta) r dr d\theta \tag{7}$$

The encircled flux is clearly a function of the spatial attributes of the laser output, the laser/fiber positioning, and the fiber's spatial mode distributions. Since the DMD data contains considerable spatial information, the response of the fiber to an arbitrary optical input can be approximated as a weighted sum of these impulse responses. The weights applied to each DMD profile are functions of the spatial relationship between the optical input and the pulses used to generate each DMD response.

The interesting aspect of this approach is that it is almost entirely empirical. While the previous examples depicted models that were physical and semi-empirical in nature, the DMD approach to multimode fiber characterization relies almost completely on measured data. Consequently, the accurate measurement of these data is absolutely critical. The Telecommunications Industry Association has published several documents specifying the measurement procedures for high-speed multimode fiber systems [13] - [16].

## PHOTORECEIVERS

The photoreceiver is the final component in the optical link. As with the laser, a combination of optical and electrical measurements is necessary to accurately calibrate the photoreceiver. To facilitate use of a photoreceiver model, it should be designed with parameter extraction in mind. Using the system-level simulator of [1], the photoreceiver can be modeled a number of ways ranging from physical to semi-physical to empirical. To better illustrate the measurement-based aspects of the model, we focus here on the empirical approach. The photoreceiver's frequency response $H(f)$ and noise spectral density $S_i(f)$ are represented as (8) and (9):

$$H(f) = Z_T\left(\frac{f}{jf_z+f}\right)\left(\frac{f_p}{jf+f_p}\right) \qquad H(f)_{dB} = 20\cdot\log_{10}|H(f)| \tag{8}$$

$$S_i(f) = a_0 + a_2f^2 + a_4f^4 + a_6f^6 \tag{9}$$

Here, $Z_T$ is the DC transimpedance, $f$ is the baseband frequency, $f_z$ is the zero frequency of the photoreceiver, $f_p$ is the pole frequency, $j$ is the imaginary constant, and $a_0$-$a_6$ are empirical fitting parameters.

Often, the only information available is a few parameters from commercial data sheets or simple lab meaurements such as the 3-dB frequency and the receiver sensitivity at a given bit error rate. Using the above formulation, it is possible to calibrate the model with a few additional steps. Although most photoreceivers exhibit a single-pole response, (8) allows for both a pole and a zero. The photoreceiver's frequency-domain response can be calibrated by eliminating the zero frequency and setting the pole frequency to the measured 3-dB frequency.

The input-referred photoreceiver noise for a transimpedance-amplifier-based photoreceiver is defined to be [17]:

$$\langle i_n^2\rangle = \int_0^{\infty}\frac{|H(f)|^2}{|H(0)|^2}S_i(f)df \tag{10}$$

If we assume the noise to be white, then $a_2$-$a_6$ in (9) can be considered to be zero and (10) is easily determined from (8) and (9). The bit-error rate (BER) of a receiver is expressed as [18]:

$$BER = \frac{1}{2}erfc\left(\frac{Q}{\sqrt{2}}\right) \qquad Q = \frac{I_1 - I_0}{\sqrt{\langle i_{n1}^2\rangle} - \sqrt{\langle i_{n0}^2\rangle}} \tag{11}$$

Here, the complementary error function is represented as *erfc*; $I_1$ and $I_0$ are the photocurrents in the high and low states, respectively; and the standard deviation terms represent the noise in the high and low states. Thus, for a given BER, it is possible to determine what value of $Q$ is required. Although this cannot be performed analytically, it can be done either numerically or graphically. For example, from the BER vs. $Q$ relationship plotted in Figure 5, it is clear that to achieve a BER of $10^{-12}$ a $Q$ of roughly 7 is needed.

If we make the simplifying assumptions that the power in the low state is zero and that the noise is independent of signal level the average detected optical power $\eta\bar{P}$ (which is proportional to the sensitivity) can be approximated by (12) where $h$ is Planck's constant, $q$ is the electronic charge, and $\lambda$ is the wavelength. Thus, (9) - (12) can be used to calibrate the photoreceiver's noise attributes.

$$\eta\bar{P} \approx \frac{hc}{\lambda q}\cdot Q\langle i_n^2\rangle \tag{12}$$

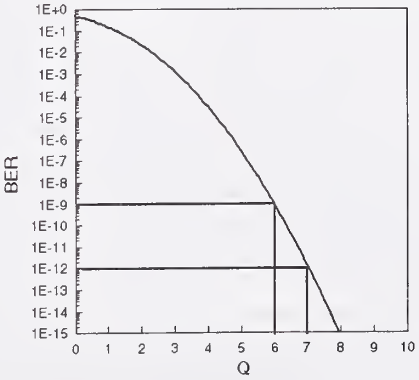

Figure 5: The relationship between BER and $Q$.

## SUMMARY

In this paper, we have described the model development and measurement challenges associated with the calibration, validation, and verification of optical and optoelectronic models for fiber-based communication system design. Integral to this approach is the identification of the necessary measurements as well as the development of the model with parameter extraction in mind from the start. We reviewed three basic examples (laser, fiber, receiver) that are key components of any optical communication system and demonstrated several methods for their verification.

This material is based upon work supported by the Naval Surface Warfare Center, Dahlgren Division under Contract No. N00178-01-C-3061. We would like to thank Gair Brown of the NSWC for his support.

## REFERENCES

[1] Z. Huang, B. K. Whitlock, and R. Scarmozzino, "CAD optimizes component design at many levels," *WDM Solutions*, pp. 41-48, August 2000.

[2] R. S. Tucker, "Large-signal circuit model for simulation of injection-laser modulation dynamics," *IEE Proceedings*, vol. 128, pt. I, no. 5, pp. 180-184, 1981.

[3] G. P. Agrawal and N. K. Dutta, *Long Wavelength Semiconductor Lasers*. New York, NY: Van Nostrand Reinhold, 1986.

[4] P. V. Mena, J. J. Morikuni, S.-M. Kang, A. V. Harton, and K. W. Wyatt, "A comprehensive circuit-level model of vertical-cavity surface-emitting lasers," *Journal of Lightwave Technology*, vol. 17, no. 12, pp. 2612-2632, 1999.

[5] W. H. Press, S. A. Teukolsky, W. T. Vetterling, B. P. Flannery, *Numerical Recipes in C*. Victoria, Australia: Cambridge University Press, 1992.

[6] D. E. Goldberg, *Genetic Algorithms: In Search, Optimization and Machine Learning*. Reading, MA: Addison Wesley Longman, 1989.

[7] Y. Ohiso, K. Tateno, Y. Kohama, A. Wakatsuki, H. Tsunetsugu, and T. Kurokawa, "Flip-chip bonded 0.85-μm bottom-emitting vertical-cavity laser array on an AlGaAs substrate," *IEEE Photonics Technology Letters*, vol. 8, no. 9, pp. 1115-1117, 1996.

[8] B. J. Thibeault, K. Bertilsson, E. R. Hegblom, E. Strzelecka, P. D. Floyd, R. Naone, and L. A. Coldren, "High-speed characteristics of low-optical loss oxide-apertured vertical-cavity lasers," *IEEE Photonics Technology Letters*, vol. 9, no. 1, p. 11-13, 1997.

[9] R. Scarmozzino, A. Gopinath, R. Pregla, and S. Helfert, "Numerical techniques for modeling guided-wave photonics devices," *IEEE Journal of Selected Topics in Quantum Electronics*, vol. 6, no. 1, pp. 150-162, 2000.

[10] M. J. Hackert, *NIST Symposium on Optical Fiber Measurements*, pp. 113-118, Sept. 1998.

[11] S. Golowich, P. Kolesar, J. Ritger, and P. Pepeljugoski, "Modeling and simulation for 10 Gb multimode optical fiber link component specifications," *Optical Fiber Communications Conference Technical Digest*, Paper #WDD57, 2001.

[12] J. E. George, S. Golowich, P. F. Kolesar, A. J. Ritger, and M. Yang, "Laser optimized multimode fibers for short reach 10 Gbps systems," *National Fiber-Optic Engineers Conference Technical Proceedings*, pp. 351-361, 2001.

[13] "FOTP-220: Differential Mode Delay Measurement of Multimode Fiber in the Time Domain," *TIA/EIA Standards Document*, TIA/EIA 455-220, November 6, 2001.

[14] "FOTP-203: Launched Power Distribution Measurement Procedure for Graded-Index Multimode Fiber Transmitters," *TIA/EIA Standards Document*, TIA/EIA 455-203, March 2000.

[15] "FOTP-191: Measurement of Mode Field Diameter of Single-Mode Optical Fiber," *TIA/EIA Standards Document*, TIA/EIA 455-191, September 1998.

[16] "FOTP-204: Measurement of Bandwidth on Multimode Fiber," *TIA/EIA Standards Document*, TIA/EIA 455-204, December 2000.

[17] R. G. Smith and S. D. Personick, "Receiver design for optical communication systems," in *Semiconductor Devices for Optical Communication*. New York: Springer Verlag, 1980.

[18] T. V. Muoi, "Receiver design of optical-fiber systems," in *Optical Fiber Transmission*. Indianapolis, IN: Howard W. Sams & Co., 1987.

# Photon-counting OTDR at telecom wavelength: high-resolution and long-distance measurements

F. Scholder, A. Fougères*, J.-D. Gautier, C. Barreiro, A. Haldimann, H. de Riedmatten,
M. Wegmüller, and N. Gisin

*GAP-Optique, University of Geneva, Rue de l'Ecole-de-Médecine 20, CH-1211 Genève 4*
*(*) GAP-Optique S.A., Rue de l'Ecole-de-Médecine 20, CH-1205 Genève*

***Abstract:*** *Photon-counting OTDR has a big advantage over conventional OTDR because of its higher detection sensitivity. This technique leads either to an improved spatial resolution or to an enlarged dynamic range. In this paper we experimentally demonstrate both modes of operation: a two-point spatial resolution of better than 10 cm and a 44-dB (one-way) dynamic range are obtained at a wavelength of 1550 nm.*

## Introduction

Optical time-domain reflectometry (OTDR) is the most widely used fiber-test technique. It can measure either fibers of lengths over 100 km with kilometric spatial resolution or shorter fibers with at best metric resolution. Further, state-of-the-art conventional OTDRs have a dynamic range of up to ~40 dB with spatial resolutions in the kilometer range [1]. On the other hand, an OTDR based on photon counting ($\nu$-OTDR) has spatial resolutions that can be as small as a few centimeters [2]. However, as for conventional OTDRs, the detection sensitivity is shown to depend on the spatial resolution [3]. Reducing this resolution from the centimeter range to the hectometer range can drastically increase the $\nu$-OTDR detection sensitivity and dynamic range.

## Photon counting and $\nu$-OTDR trace extraction

To detect single photons at a telecom wavelength of 1.55 µm, we are using an InGaAs avalanche photodiode (APD), cooled by Peltier elements down to –57 °C. This APD is used in the so-called "gated Geiger mode", with the detector being active only during a given time slot ("gate") [4,5]. During this period, a single photon falling on the APD can trigger an avalanche, which is then detected by discriminator electronics. This process is then repeated many times, and from the number of counts for a certain position (delay) of the gate, the reflectivity at the corresponding location in the fiber is obtained. Obviously, in order to extract the real signal, the detector has to be operated below saturation. In the present experiments, the probability for a count within one gate has to be smaller than 40% in order to remain in the linear regime. On the other hand, it has to be large enough to be distinguishable from the noise. In order to go beyond these two restrictions, one can use an appropriate data correction, which subtracts the noise and takes into account the non-linear response when being close to saturation. If $\eta$ is the detection efficiency, $p_n$ the noise count probability, and $p$ the overall detection probability (signal + noise), the mean number of photons per gate $\mu$ (i.e. the net signal) is given by the following equation, assuming a Poissonian photon distribution.

$$\mu = \frac{1}{\eta} \cdot \ln\left(\frac{1-p_n}{1-p}\right) \tag{1}$$

Hence—knowing the noise count probability $p_n$—this equation will be used to obtain the net signal power from the corresponding overall count probability $p$, and thus our ν-OTDR trace. This correction is especially useful when $p$ is either close to saturation or to the noise level.

## High resolution ν-OTDR measurement

Using the setup described in Fig. 1 we made a high-resolution measurement of an 11-cm-long standard singlemode optical patchcord connected with FC/PC connectors after a 2-km fiber. We used 500-ps-long laser pulses, detection gates of $\tau = 2$ ns, and a detection efficiency $\eta = 10\%$. We opened 100,000 detection gates for each of 200 different gate delays (by steps of 50 ps to have a 5-mm sampling resolution on a 1-m measurement range) at a repetition rate (gating frequency) $f = 50$ kHz allowing for only one laser pulse in the fiber. Hence the whole measurement took about 7 min. The corresponding ν-OTDR trace is shown in Fig. 2. The two reflection peaks are clearly distinguished and separated by slightly more than their FWHM (~10 cm), thus demonstrating a 2-point spatial resolution of about 10 cm. Therefore ν-OTDR is the reflectometry technique of choice if good spatial resolution at long distances is required. For instance optical frequency-domain reflectometry (OFDR) can have a better spatial resolutions of 2 cm (or even ~1 mm), but only for measurement lengths <200 m (<10 m, respectively).

## Dynamic range

To evaluate the dynamic range, we first calculate the noise equivalent power (NEP) of the detector. After having used Eq. 1 to correct the signal, the mean noise level goes to zero and thus towards minus infinity on the typically employed logarithmic dB-scale. Therefore we will use as NEP the noise mean fluctuation (i.e. the standard deviation of the noise). Due to the specifics of the gated photon-counting technique the number of noise counts for a given measurement time follows a binomial statistics. Hence the standard deviation of the noise goes as the square root of the mean number of noise counts given by the noise probability $p_n$ times the number of gates $N$ ($N = f \cdot \Delta t$, where $\Delta t$ is the measurement time for a given gate delay). Therefore the NEP level is equivalent to a mean number of photons per gate

$$\mu_{NEP} \approx \frac{1}{\eta} \cdot \sqrt{p_n/N} \qquad (\text{for small } p_n) \tag{2}$$

Note that theory and measurements both show that for small $p_n$ (i.e. $p_n < 10\%$) the noise probability is proportional to the gate duration $\tau$ (i.e. $p_n = \pi_n \cdot \tau$). The $\pi_n$ factor was measured to be 30 kHz for the APD used in the present experiments. Thus, using Eq. 2, the NEP is given by

$$\mathrm{NEP} = \mu_{NEP} \cdot \frac{hc/\lambda}{\tau} \approx \frac{hc}{\eta\lambda} \cdot \sqrt{\frac{\pi_n}{f \cdot \Delta t \cdot \tau}} \tag{3}$$

This simple model shows that the NEP is inversely proportional to the square root of the gate duration $\tau$ and the measurement time $\Delta t$ for each gate delay. Therefore measuring for a longer time or with larger gate duration (i.e. smaller spatial resolution) has the same effect on the sensitivity of the ν-OTDR. This behavior is illustrated in Fig. 3. The experimental data are seen to be in good agreement with the theory. Consequently, for a given measurement time, the ν-OTDR can be operated either in high-resolution or in high-sensitivity mode, but not both at the same time.

For classical OTDRs, the dynamic range is usually defined as the difference between the initial Rayleigh backscattering (i.e. at the beginning of the fiber)—for a laser source with a pulse length of 10 μs—and the noise level after a 3-min measurement time [1]. Let us now apply the same definition to our ν-OTDR. Since we are using a laser source with a peak power of +8 dBm and 10-μs-long pulses, the Rayleigh backscattering power at the input is –31 dBm for the Rayleigh backscattering coefficient of –72 dB/m of the fibers used in our experiment. From Eq. 3, a NEP of –121 dBm is obtained for 1-μs-long detection gates, a 3-min measurement time per gate delay, a detection efficiency of 10%, and a gating frequency of 400 Hz (allowing to measure distances up to 250 km). Thus the (one-way) dynamic range that could be obtained using our ν-OTDR can be estimated to 45 dB, whereas for the same conditions, classical state-of-the-art OTDRs reach 40 dB [1]. Note that for a laser peak power of +13 dBm, we could even increase the dynamic range up to 47.5 dB.

## High dynamic range ν-OTDR measurement

To illustrate the results found in the previous section, we performed a ν-OTDR measurement of three FC/PC-connected standard telecom fibers of 10.4-, 16.4-, and 25.3-km length, respectively. This measurement was done with the same scheme as previously described (Fig. 1), except that 10-μs-long laser pulses, detection gates of $\tau = 1$ μs, and a gating frequency $f = 1600$ Hz were used to reduce the measurement time. A 28-dB loss was added between the first two fibers using an optical attenuator (which simulates a ~140-km-long fiber). The ν-OTDR trace we obtained is shown in Fig. 4. The vertical scale is defined as the one-way loss with the initial Rayleigh backscattering level normalized to zero. Therefore the NEP level directly gives the dynamic range. We measured 44 dB, which is in excellent agreement with the theoretical value of 45 dB of above, even more so if considering that the extra 1-dB loss due to the optical circulator was neglected in the calculations. From the Rayleigh backscattering in Fig. 4, standard losses of 0.22, 0.30, and 0.25 dB/km are obtained for each fiber, respectively. Note that for the last fiber—for which the backscattered signal is close to the noise level—the correct loss is only obtained when the signal correction (Eq. 1) is applied. A loss of 0.047 dB/km is obtained otherwise. We also note that there are hardly any fluctuations in the ν-OTDR trace, except when we are close to the NEP. Of course these fluctuations can be reduced when integrating over a longer period of time, hence providing better statistics.

## Conclusions

An investigation of the spatial resolution and dynamic range of a ν-OTDR was presented. Calculations and measurements showed that the NEP scales as the inverse square root of gate duration and total measurement time. Therefore increasing the gate duration, and thus decreasing the spatial resolution, enhances the dynamic range. Our ν-OTDR can thus be operated in two different modes: high spatial resolution or high dynamic range. In the high-resolution mode, we reach a spatial resolution of 10 cm with ~30-dB dynamic range. On the other hand, setting the spatial resolution to 1 km—as typically used for OTDR characterization—we obtain a 44-dB dynamic range, which is better by 4 dB compared to state-of-the-art conventional OTDRs.

## Acknowledgment

We would like to thank EXFO and the Swiss Commission for Technology and Innovation (CTI) for financial support.

## References

1. EXFO Reference Guide 2001: dynamic range of ~40 dB with 10-μs pulses and a 3-min average at SNR = 1.
2. A. Lacaita, P. Francese, S. Cova, and G. Ripamonti, "Single-photon optical time-domain reflectometer at 1.3 μm with 5 cm resolution and high sensitivity", *Optics Lett.*, **18**, pp. 1110–1112 (1993).
3. F. Scholder, M. Wegmüller, and N. Gisin, "Long-distance OTDR using photon counting and large detection gates", *OFMC '01*, pp. 169–172 (2001).
4. G. Ribordy, J.-D. Gautier, H. Zbinden, and N. Gisin, "Performance of InGaAs/InP avalanche photodiodes as gated-mode photon counters", *Appl. Optics*, **37**, pp. 2272–2277 (1998).
5. D. Stucki, G. Ribordy, A. Stefanov, H. Zbinden, J. Rarity, and T. Wall, "Photon counting for quantum key distribution with Peltier cooled InGaAs/InP APDs", *J. Mod. Opt.*, **48**, pp. 1967–1981 (2001).

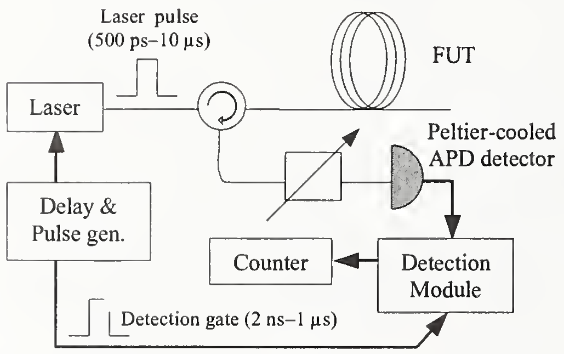

**Fig. 1** ν-OTDR experimental setup.

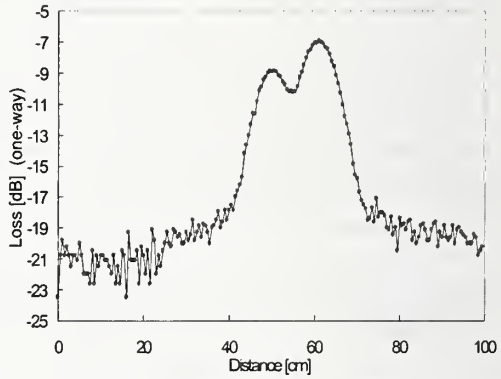

**Fig. 2** High-resolution ν-OTDR trace of two FC/PC connections separated by 11 cm and located after 2 km of optical fiber.

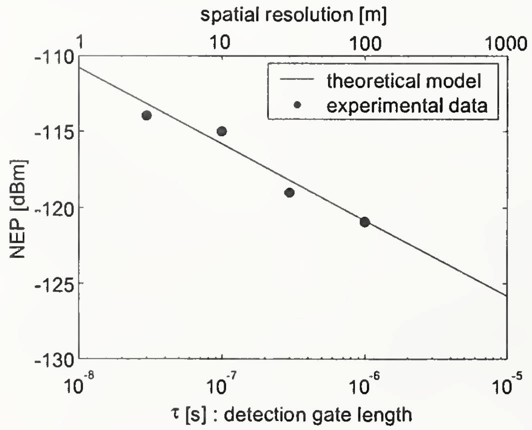

**Fig. 3** Theoretical and experimental behavior of the detection sensitivity (i.e. the noise equivalent power).

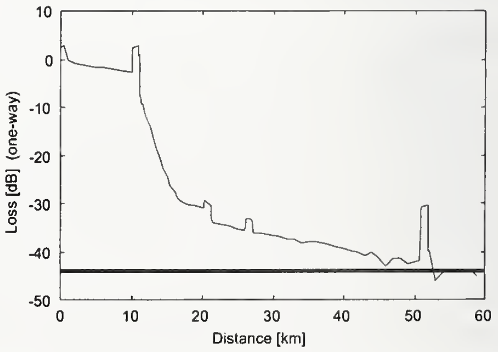

**Fig. 4** ν-OTDR trace of three FC/PC-connected standard telecom fibers with a 28-dB loss between the first two fibers. The bold line indicates the "NEP".

# Coherent speckle in direct-detection OTDR

S.G.Murdoch
*NetTest (UK) Ltd, York House, School Lane, Chandlers Ford, United Kingdom.*

Strong coherent speckle is seen in direct-detection optical time domain reflectometers whenever the coherence length of the source is of the same order of magnitude as the pulse width. Starting from the previously derived statistics for Rayleigh backscattering in single-mode optical fibers [1,2], we investigate the properties of coherent speckle in direct-detection OTDRs. We compare our predictions with the measured behaviour of the coherence speckle seen in a wavelength tunable direct-detection OTDR, and show that such a system can achieve at least the same level of speckle suppression as its standard fixed wavelength counterpart.

## 1. Introduction

Optical time domain reflectometry is a well-established technique for the measurement of distributed loss of optical fibers [3]. Though many variants of the technique exist [4], commercial long-haul OTDRs most commonly use a single pulse, direct-detection setup. Here the energy of the backscattered light of a single pulse travelling down the fiber is measured as a function of time, giving direct access to the distributed loss of the fiber. It is well known that when the coherence length of the optical source approaches the pulse width in such systems, the resultant OTDR signal takes on a jagged, noisy appearance [4]. This effect is called coherent speckle (or coherent fading) and is due to the random distribution of scatterers along the length of the fiber. Light returning from these scatterers interferes coherently at the receiver resulting in large fluctuations in the received signal power. Most commercial long-haul OTDRs use wide-band optical sources, with coherence lengths many orders of magnitude smaller than the pulse width so as to operate in an incoherent regime, where this coherent interference is much reduced. For other OTDR applications however, the use of wide-band optical sources is not possible, and these measurements often exhibit strong coherent speckle. For example, the distributed measurement of polarisation mode dispersion by polarisation OTDR [5], requires the use of a narrow-band source to avoid depolarisation. Other OTDR applications such as spectral modelling [6], distributed chromatic dispersion measurements [7], and the surveillance of passive optical networks [8], can also benefit from the use of tunable optical sources, which are themselves commonly narrow-band. In this paper we analyse the coherent speckle properties of just such a narrow-band tunable direct-detection OTDR.

## 2. Theory

Following the approach of references [1] and [2], we model the Rayleigh backscatter of a single-mode single-polarisation fiber as a series of point scatterers randomly distributed along its length. Assuming that the probability of multiple scattering is negligible, the backscatter signal seen at the receiver at time $t=T$ from a quasi-monochromatic pulse (pulse width $W$), is given by

$$E_R(T) = E_P(z,T) \otimes \sum_{i}^{M} h_i(z)\,, \tag{1}$$

where $E_P(z,t)$ is the pulse's electric field, $h_i(z)$ is the backscatter response of the ith scatterer, and the sum over $M$ is the sum over all scatterers lying between $z=L-W/2$ and $z=L$ ($L=v_g T/2$). Further, assuming that the scatterer amplitudes and positions are statistically independent, and the scatterer positions are uniformly distributed along the length of the fiber, it can be shown that $E_R(T)$ is Rayleigh distributed. This in turn implies the receiver power, $P_R(T)$, has a negative exponential distribution (just as with spatial speckle and the intensity statistics of thermal light) [9]:

$$\mathrm{P}(P_R(T)=p) = \begin{cases} \dfrac{1}{\langle P_R(T)\rangle}\exp\left(\dfrac{-p}{\langle P_R(T)\rangle}\right) & p \geq 0 \\ 0 & \text{otherwise} \end{cases} \tag{2}$$

The standard deviation of a negative exponential distribution is equal to its mean. Thus the contrast of $P_R(T)$ (defined as the standard deviation divided by the mean) is unity. This high contrast is what gives speckle patterns their pronounced granular appearance [10].

Equation (2) gives the probability distribution of the instantaneous receiver power at time $t=T$; however it makes no predictions as to what timescale $P_R(T)$ fluctuates over. To evaluate this, we calculate the normalised correlation between $P_R(T)$ and $P_R(T+\tau)$:

$$C_{P_R}(T,T+\tau)=\begin{cases}\left(\dfrac{W/v_g-|\tau|}{W/v_g}\right)^4 & |\tau|<W/v_g\\ 0 & \text{otherwise}\end{cases} \tag{3}$$

By analogy with the theory of spatial speckle, we define the speckle size as the half-width of this correlation function. This gives the timescale, $t_f$, over which $P_R(T)$ fluctuates as $t_f \sim 0.1W/v_g$ - a tenth of the pulse duration. In direct-detection OTDR the receiver integration time $T_R$ is usually much larger than this speckle size. In this limit, the distribution of the measured receiver power tends towards a normal distribution, with mean $<P_R(T)>$ and contrast proportional to $1/sqrt(T_R)$ [9,11]. Also in this limit, we find that the measured speckle size is proportional to $T_R$, rather than to the pulse width.

High speckle contrast makes it difficult to extract fiber parameters or identify events in an OTDR trace. In this sense, the small receiver bandwidth of a commercial long-haul OTDR is advantageous, as it results in a reduction of the speckle contrast. Another well known technique for reducing speckle contrast in OTDR is to use a source whose coherence length is much smaller than the pulse width [2,9,12]. For a source consisting of N discrete wavelengths (far enough apart in frequency that the speckle at each wavelength is uncorrelated), the contrast of the coherent speckle varies as *1/sqrt(N)*.

## 3. Results

Our experimental setup consists of a direct-detection OTDR (NetTest 8000) into which we have integrated a tunable external cavity laser. Pulses are produced by electronically pulsing the external cavity laser just as one would a standard OTDR source. This gives us a narrow linewidth tunable OTDR which is ideal for the study of coherent speckle.

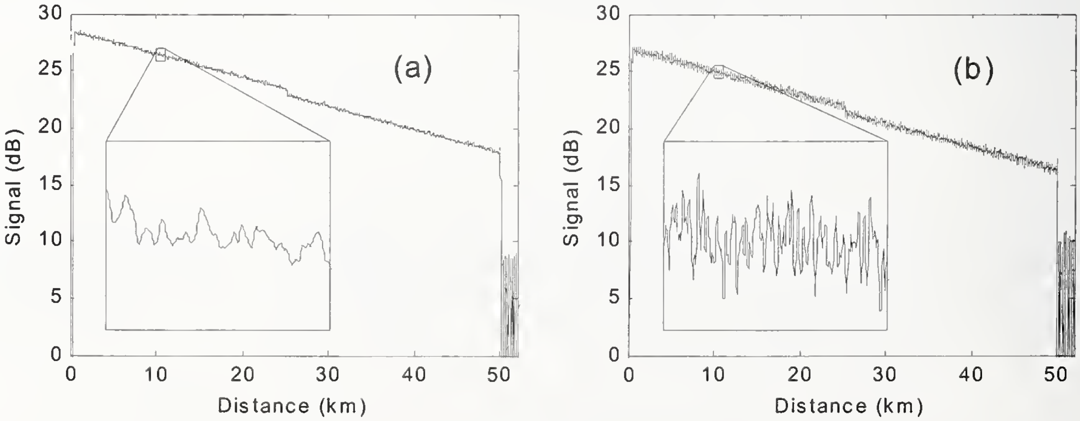

Figure 1

Figure 1 shows two typical traces measured using our tunable OTDR. The two traces were measured using different receiver bandwidths. In figure 1a the receiver bandwidth used was 1MHz, and in figure 1b, 3MHz. The pulse width was 100m, the averaging time 30s, and the laser wavelength 1549.90nm. The fiber under test (used throughout this paper) consists of two 25km lengths of standard single mode fiber. The speckle is clearly visible on the two traces. If the fiber under test is left undisturbed the speckle pattern remains stationary over a period of 5 to 10 minutes, until small changes in the environmental conditions perturb it. Monitoring the correlation of this speckle has previously been used to build distributed fiber sensors [13].

For a pulse width of 100m, $t_f$ is approximately 100ns - much smaller than the receiver integration time. Thus we expect the speckle amplitude to vary as $1/sqrt(T_R)$, and the speckle size to vary as $T_R$. The measured RMS speckle amplitudes of the two traces in figure 1 are 0.18dB, and 0.32dB respectively. The ratio of these two amplitudes is very close to $1/sqrt(3)$ which is in good agreement with the theory. The speckle sizes of the two traces are 47m and 14m respectively. The ratio of these sizes is close to 3, also in good agreement with the theory.

Next we investigate the correlation of the coherent speckle as a function of source wavelength and input polarisation. Figure 2a shows the correlation between the coherent speckle of an OTDR trace taken at 1549.90nm, and subsequent traces detuned by multiples of 17pm. The OTDR setup is the same as that used in figure 1a. A 17pm change in source wavelength results in complete decorrelation between the speckle of the two traces. This result is in agreement with the theory of the previous section, which requires $\Delta k \cdot W$ to be of the order of $2\pi$ or less for two traces to retain a degree of correlation. For 100m pulses this implies a decorrelation range of the order of several MHz.

Figure 2b shows the correlation of the coherent speckle as a function of input polarisation. The OTDR setup is again the same that used in figure 1a. The correlation is calculated between a trace taken at a reference linear input polarisation, and a trace taken with the input polarisation rotated by $d\theta$ degrees. A separate reference trace was taken for each point to avoid any decorrelation of the trace speckle due to changes in the environmental conditions over the duration of the experiment. We see little decorrelation in the trace speckle as the input polarisation is rotated 90 degrees. With a more complete exploration of the Poincaré sphere the lowest correlation we measure is 0.75. If the fiber were isotropic (non-birefringent) then we would expect no decorrelation. In real fiber with a randomly varying birefringence, the accumulated round-trip phase of the backscattered light from each scatterer becomes polarisation dependent. This results in a dephasing of the backscattered light as the input polarisation is varied, and hence the decorrelation we observe. In principle this allows a measure of the distributed birefringence of the fiber; however in practice this measurement may be difficult to interpret quantitatively.

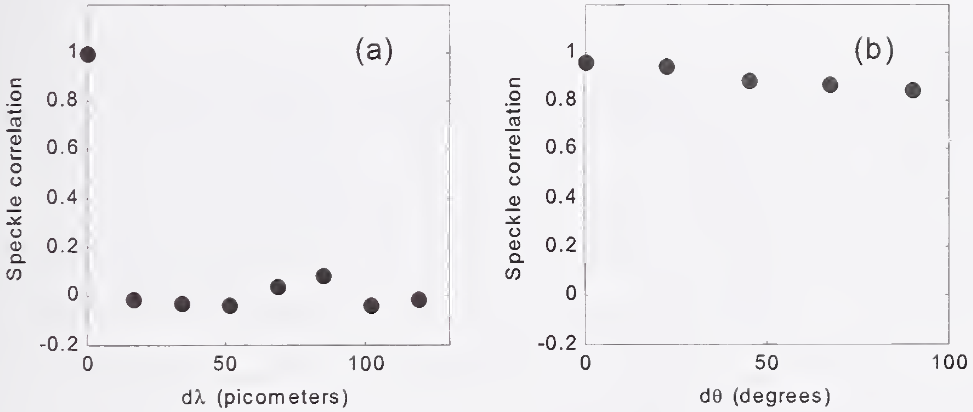

Figure 2

Finally, we wish to examine the effect of source linewidth on the amplitude and size of the trace speckle. We have no simple mechanism to change the linewidth of our source, but we can scan its wavelength during an acquisition thereby increasing its effective linewidth [12]. In figure 3a we plot the RMS speckle amplitude (solid dots) and speckle size (open squares) of an OTDR trace as a function of the number of discrete wavelengths stepped over during the acquisition. The start wavelength is 1549.90nm, the step size 17pm, the pulse width 40m, the receiver bandwidth 1MHz, and the total acquisition time 120s. The dotted line is the coherent speckle amplitude of a standard 1550nm Fabry-Perot OTDR laser (3dB spectral width ~10nm), measured under identical conditions. This shows that by scanning the wavelength of our tunable OTDR, we considerably reduce the contrast of the coherent speckle. Large enough scan ranges result in speckle contrasts below that of standard OTDR lasers. As expected we see no change in the speckle size as a function of the number of wavelengths scanned.

In Figure 2a we saw a complete decorrelation between the coherent speckle of two OTDR traces taken at wavelengths separated by 17pm. This implies that the speckle contrast plotted in figure 3a should decrease as *1/sqrt(N)*, where *N* is the number of wavelengths scanned. Figure 3b shows the same data as Figure 3a but plotted on a log-log scale. The solid line is a fit to *1/sqrt(N)*, showing that the coherent speckle does indeed obey this relationship.

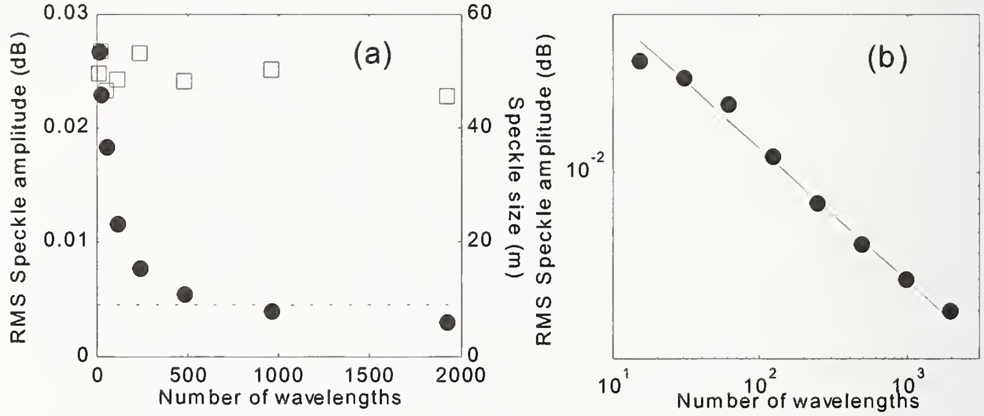

Figure 3

### 4. Conclusion

In conclusion, the measured characteristics of coherent speckle seen in our direct-detection OTDR are in good agreement with the theory presented. We find that coherent speckle may be suppressed by use of a small receiver bandwidth and a large effective source linewidth. Our results show that a narrow-band tunable direct-detection OTDR can achieve at least the same level of speckle suppression as its standard fixed wavelength counterpart.

### 5. References

[1] "Fading in heterodyne OTDR", P.Healey, Electron. Lett. **20** 30-32 (1984)
[2] "Statistics of Rayleigh backscatter from a single-mode optical fibre", P.Healey, Electron. Lett. **21** 226-228 (1985)
[3] "Fiber waveguides: a novel technique for investigating attenuation characteristics", M.K.Barnoski, S.M.Jensen, Appl. Optics **15** 2112-2115 (1976)
[4] "Fiber optic test and measurement", D.Derickson, Prentice-Hall (1998)
[5] "Polarization optical time domain reflectometry", A.Rogers, Electron. Lett. **16** 489-490 (1980)
[6] "Spectral attenuation modeling with matrix methods", T.A.Hanson, 8-11 Optical fiber measurement conference (1991)
[7] "Chromatic dispersion distribution measurement along a single-mode optical fiber", K.Nakashima, M.Ohashi, M.Tateda, J. Lightwave Tech. **15** 1095-1101 (1997)
[8] "Field trial of optical maintenance of PONs using a tunable OTDR", K.Ozawa, M.Shigehara, J.Hanai, A.Ban, T.Naitou, K.Shimoura, 65, ECOC (2000)
[9] "Statistical optics", J.W.Goodman, Wiley (1985)
[10] "Some fundamental properties of speckle", J.W.Goodman, J. Opt. Soc. Am. **66** 1145-1150 (1976)
[11] "Measurement of Rayleigh backscattering at 1.55µm with 32µm spatial resolution", W.Sorin, D.Baney, IEEE Photon. Tech. Lett. **4** 374-376 (1992)
[12] "Fading noise reduction in coherent OTDR", H.Izumita, S.Furukawa, Y.Koyamada, I.Sankawa, IEEE Photon. Tech. Lett. **4** 201-203 (1992)
[13] "Distributed interferometric fiber sensor system", R.Juskaitis, A.M.Mamedov, V.T.Potapov, S.V.Shatalin, Opt. Lett. **17** 1623-1625 (1992)

# Full Measurement of the Spatial Distribution of PMD Using Backscatter

A. J. Rogers and S. V. Shatalin
Department of Electronic Engineering,
University of Surrey, Guildford, Surrey, GU2 7XH, UK.
a.rogers@surrey.ac.uk

## Abstract

This paper describes a new technique for the determination of the full spatial distribution of the polarisation mode dispersion (PMD) in a monomode optical fibre. It operates from one end of the fibre, via backscatter.

## Background

The measurement of the spatial distribution of the polarisation properties of a monomode optical fibre, from one end of the fibre, has important application to polarisation mode dispersion (PMD) in high-bandwidth (>40 $\text{Gbs}^{-1}$) optical-fibre communications [1]. There is a requirement to analyse and to understand the sources of PMD along the fibre installation, so that anomalous sections can be replaced and other appropriate alleviative action taken, if required. Knowledge of the spatial distribution of the polarisation properties also is of considerable assistance in the design of PMD compensation schemes and in the fabrication of low-PMD fibre.

This paper describes a method for the accurate determination of the distribution of the full polarisation properties of a monomode fibre, from one of its ends, with significant implications for PMD diagnostics.

## POTDR

The new method is based on Polarisation Optical Time Domain Reflectometry (POTDR) [2] in which a polarised optical pulse is launched into a monomode fibre, and the Rayleigh-backscattered light is time-resolved and polarisation-analysed (via the Stokes parameters) as it re-emerges from the launch end. This, however, provides only incomplete information on the spatial distribution of the fibre's polarisation properties. To understand this, consider a section of fibre whose polarisation properties are reciprocal and uniform. These properties can, in general, be characterized by a linear retardance, $\delta$, and orientation, q, of that retardance's fast axis w. r. t. a reference direction 0x, and a circular retardance, $2\rho$. The polarisation transfer function can be represented by a Jones matrix, M. A go-and-return passage of the section is represented by the matrix M multiplied by its transpose:

$$M' = M^T M$$

which takes the form of a pure retarder. This is easily appreciated when the element M is modelled as a linear-retarder/rotator pair, because the rotation ($\rho$) will be cancelled in go-and-return passage, leaving only the retardation, $2\delta_e$, at orientation $q_e$. Hence the information represented by $\rho_e$ is lost in backscatter, and only two independent pieces of information ($\delta_e$ and $q_e$) are available for calculation of three unknowns: $\delta$, q, $\rho$. These latter, therefore, cannot be recovered.

## (iii) CPOTDR

Computational POTDR (CPOTDR) [3] is a development which overcomes the POTDR incompleteness problem.

In CPOTDR the polarisation element is divided into two equal halves, each half now assumed to be described by M. Firstly, the front half is interrogated in backscatter (i.e. go-and-return passage ($J_2$ in fig.1), followed by the two together ($J_3$ in fig.1). Each measurement provides two pieces of information, i.e. the retardance, and the axis orientation of the two equivalent retarders:

$$M' = M^T M \qquad M'' = M^{T^2} M^2$$

$M''$ provides two more equations for δ, q, ρ. Hence, we now possess four independent equations for these three unknowns, and the problem can be solved.

This stratagem can now be applied to successive elements of polarisation-uniform fibre (fig.1, upper diagram) in order to determine the complete spatial distribution of the fibre's polarisation properties.

However, in order to determine the relevant parameters for each element it is clearly necessary to know the input state and backscattered output state for a given element, and this requires an accurate knowledge of the properties of all elements which precede that element. Hence there inevitably will be an accumulation of measurement error with distance along the fibre, leading to a limitation on the total length of fibre which can be examined for any given accuracy.

### (iv) Avoidance of Error Accumulation

The error accumulation in CPOTDR can be avoided by using the averaged information in the length of fibre leading up to a given resolution element.

This 'lead' length again may be represented by a linear-retarder/rotator pair. Three backscatter measurements can now be made (see fig.1), i. e. $J_1$, $J_2$, $J_3$. The first of these determines $\delta_e$, $q_e$, the second and the third together provide four equations for the four unknowns $\rho_e$, δ, q, ρ. However, the physical effect of the element depends only on the relative orientation of the input polarisation state and the element's retardation axis, so that only $(q-\rho_e)$ can be recovered, not q, $\rho_e$ separately. Nevertheless, δ and ρ can be measured accurately throughout, without accumulation of error; q still suffers from some error accumulation in this case, but can be accurately determined (via CPOTDR) by using the backscatter information available at several wavelengths. This determination of q relies upon the fact that $\rho_e$ is dependent upon wavelength (λ), whilst q is not. The form of the dependence of $\rho_e$ is conditioned by the $1/\lambda$ dependence (to first order) of ρ and δ. This leads to $\rho_e$ being expressible as a power series in $1/\lambda$, thus allowing q to be determined by extrapolation, to infinite wavelength, of the measurable quantity $Q = (q-\rho_e)$. This process is illustrated in fig.2.

Hence this technique provides the spatial distribution of the linear retardance (δ), the linear birefringence's axis orientation (q), and the circular birefringence (ρ), all without any accumulation of error with distance along the fibre.

It, further, provides the wavelength dependence of these parameters. Consequently, all the information necessary for the derivation of the spatial distribution of PMD, of any order, becomes available for any given fibre, with this technique.

### (v) Results

Fig.2 shows the computed results for a sinusoidal variation of δ along the fibre length. A similar result is obtained for ρ: both are recovered with very good accuracy [4]. Fig.3 shows the results for a sinusoidal variation of q, recovered via wavelength diversity. Again, the accuracy is very good, and there is no accumulation of error.

Fig.5 shows the cumulative PMD distribution calculated from the experimentally-derived CPOTDR traces for a three-coil fibre arrangement.

### (vi) Conclusions

A new technique for the determination of the spatial distribution of polarisation properties of a monomode optical fibre has been developed. The method comprises a development of the

POTDR backscatter technique, and allows the determination of the spatial distribution of the full polarisation properties of the fibre, from one end, without accumulation of error with distance in two of the parameters.
This technique is applicable, with advantage, to PMD identification, analysis and compensation in optical communications fibres.

## (vii) References

(1) C. D. Poole, 'Statistical Treatment of Polarisation Dispersion in single-mode Fibre', Opt. Lett., Vol. 13, August 1988, pp 687-689.
(2) A. J. Rogers, 'Polarisation-Optical Time Domain Reflectometry : A Technique for Measurement of Field Distributions', Appl. Opt., Vol. 20, 1981, pp 1060-1074.
(3) Y. R. Zhou, V. A. Handerek and A. J. Rogers, 'CPOTDR for the Measurement of the Spatial Distribution of PMD in an Optical Fibre', Proc. of OFMC '97, NPL, Teddington, September 1997, pp 126-129.
(4) A. J Rogers, M. Wuilpart and M.Blondel, 'New Polarimetry for Fully-distributed Optical-fibre Strain and Temperature Sensing', SPIE Conference on 'Smart Structures and Materials 2000', Newport Beach, California, March 2000, paper 3986-42, pp 302-311.

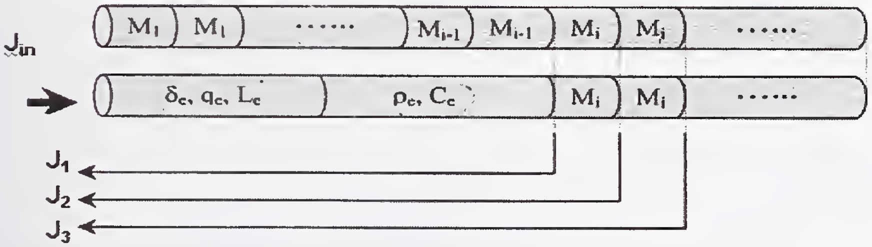

**Fig. 1 Concatenation of Resolution Elements**

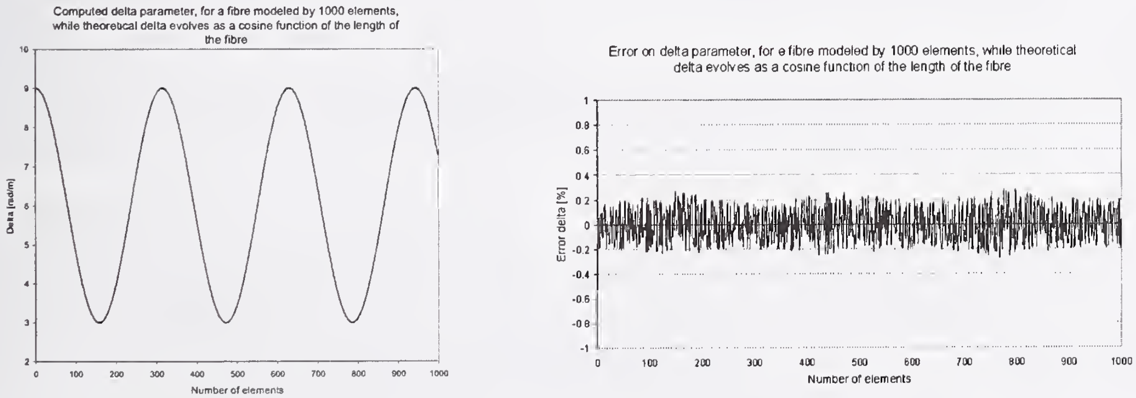
Computed delta parameter, for a fibre modeled by 1000 elements, while theoretical delta evolves as a cosine function of the length of the fibre

Error on delta parameter, for e fibre modeled by 1000 elements, while theoretical delta evolves as a cosine function of the length of the fibre

**Fig. 2 Determination of the Birefringence Distribution**

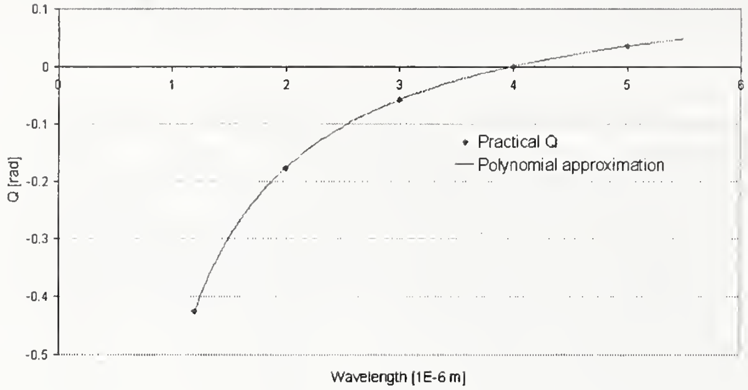

**Fig. 3 Extrapolation of Q**

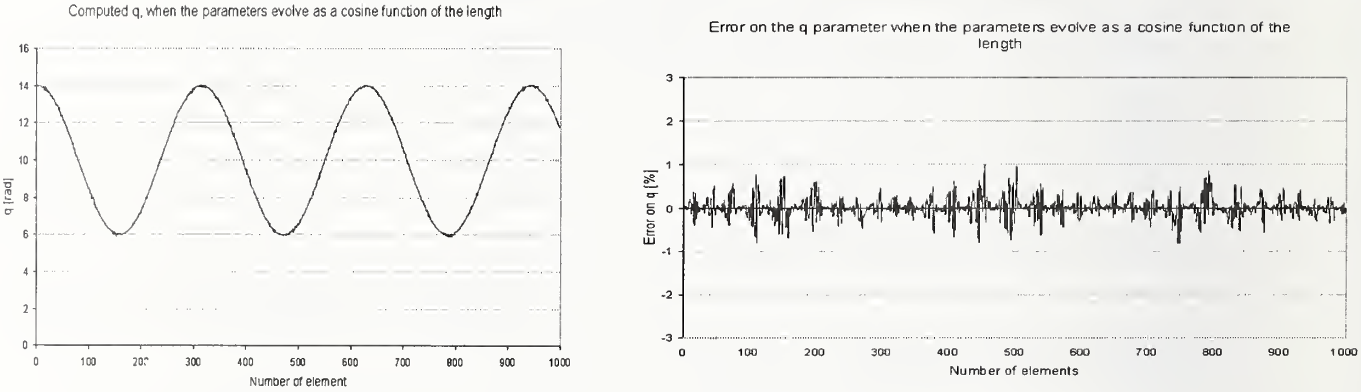

**Fig. 4 Determination of the Angle Distribution**

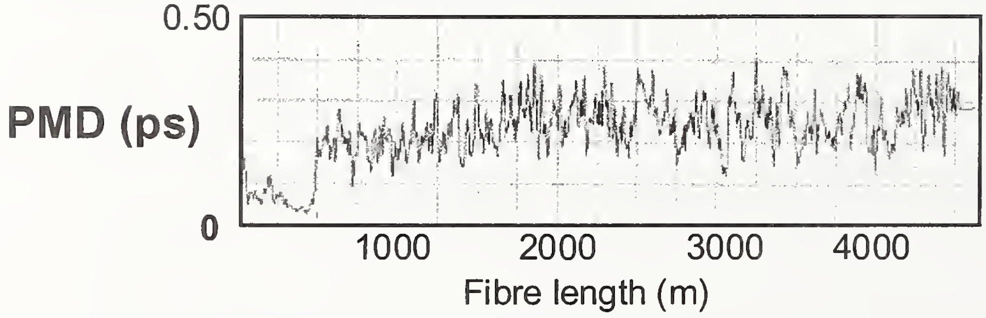

**Fig. 5 Experimental PMD Distribution for a Three-coil Arrangement**

# Polarisation Mode Dispersion in Restricted Optical Bandwidth: An Evaluation of Measurement Techniques

Subrena Harris and David Ives
National Physical Laboratory, Teddington, Middlesex, TW11 0LW, UK

## Abstract

An evaluation is made of the suitability of four techniques to measure Polarisation Mode Dispersion (PMD) in narrow optical bandwidth (a measurement condition that may arise when looking at low PMD in Dense Wavelength Division Multiplexing components). A figure of merit is assigned to the techniques, which reflect theoretical expectations. The interferometric technique has a figure of merit of 1, fixed analyser 1, stokes parameter evaluation 200, and phase shift 1800. The phase shift technique appears to be the most suitable for these measurements. Further experimental work is to be carried out for the phase shift technique, using the Stokes parameter evaluation technique for comparison.

## Introduction

Polarisation Mode Dispersion (PMD) is the dispersion of a signal in a fibre optic system due to birefringence in the optical fibre or components in the system, and is a limiting factor preventing higher rates of data transmission. As the PMD of single mode fibre has been reduced through improved technology, this has led to a reduction in the overall level of PMD in fibre systems. In order to reduce the PMD levels further, systems designers/manufacturers are now requiring that components have low values of PMD, so as not to add unnecessarily to the PMD budget of the system.

If PMD in components is to be measured using the same techniques as for fibre PMD, the suitability of the technique needs to be assessed. Components differ from fibre in that PMD can be low or high, depending on the device, and is likely to be deterministic due to fixed, low mode coupling. There may be more than one birefringent element, and reflections from any optical elements within the component (not necessarily PMD related). In addition, the level of PDL varies between components, and if the level is too high it may cause problems in correctly determining PMD. A component may also have a restricted operational bandwidth. [1]

This investigation is primarily concerned with the problem of measuring low PMD in restricted optical bandwidth. Our requirement for a measurement technique is that it is able to accurately measure PMDs as low as 0.1 ps, in an optical bandwidth as narrow as 0.2 nm at 1550 nm, also taking into consideration the other characteristics of components. A figure of merit (1) is defined for each technique.

$$\text{Figure of Merit} = \frac{1}{\text{DGD [s] x bandwidth [Hz]}} \tag{1}$$

where, 'bandwidth' is the spectral range needed to measure the associated Differential Group Delay, DGD.

An evaluation is made of the interferometric, fixed analyser, Stokes parameter evaluation and phase shift techniques, and a figure of merit is assigned to each.

## Evaluation of techniques

### *Interferometric technique*

The interferometric technique is capable of measuring PMD of components, but relies on using a broadband source without ripples, which severely limits the techniques effectiveness in restricted bandwidth. If a component has an operational bandwidth of just 0.2 nm then the coherence time of the source ${}_{source}t_c$, is such that the minimum PMD measurable is 40 ps (working under the condition that ${}_{source}t_c <$ PMD [2]). To reduce this PMD threshold the bandwidth would have to be larger. It is therefore very difficult to improve the figure of merit of this technique above 1.

An advantage of using the interferometric technique is that it clearly distinguishes between birefringent elements and so the dependence upon prior knowledge of the internal structure of a device is reduced. An additional advantage is its tolerance to movement of the optical test path during measurement.

### *Fixed Analyser technique*

It is possible to measure the PMD of components using the fixed analyser, or wavelength scanning technique. However, although able to operate in a limited spectral range, a large scan range is needed to measure small PMDs. For a bandwidth of 0.2 nm, the minimum PMD detectable is 40 ps. The technique has a figure of merit of 1.

An advantage of this technique is that, during processing of the data, polarisation insensitive contributions are removed or reduced from the device's PMD. Also, if processing is done using Fourier Transforms then the distinction is made between different birefringent elements if more than one is present

### *Stokes Parameter evaluation technique*

This technique is capable of measuring PMD in components. The polarimetric measurement system at NPL (figure 1) has been used to measure components such as chirped Bragg Gratings, isolators and circulators, although in these instances a large wavelength range was used to make the measurements [3]. However, measurements can be made in a restricted spectral range but at reduced accuracy. For a bandwidth of 0.2 nm, and using NPL's polarimeter that has a resolution of 1.7 degrees, the lower limit for PMD is 191 fs. This gives a figure of merit of 200.

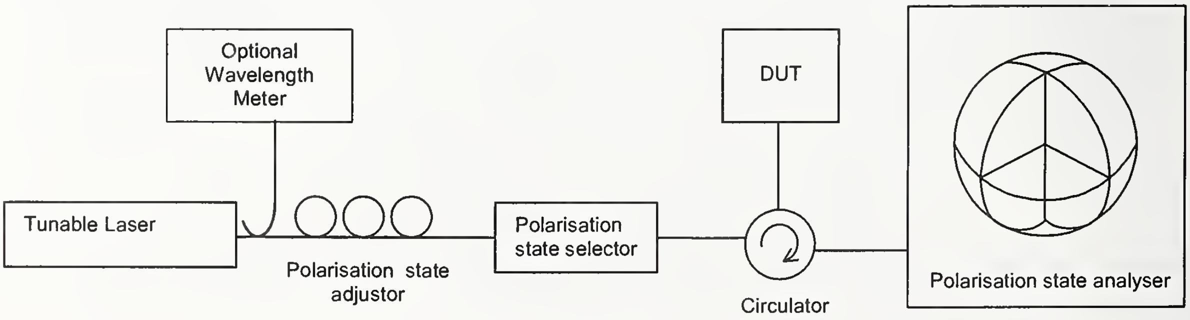

**Figure 1: PMD measurement system for Stokes Parameter Evaluation.**

(Set up shown for a reflective device.)

Stokes Parameter Evaluation methods determine DGD by measuring the polarisation state of light at the output of a DUT, and PMD from the distribution of these DGD values. It is possible to identify if there is more than one birefringent element in a device using this method, although it is of limited use without prior knowledge of the device structure. Also, as normalised Stokes Parameters are measured, the sensitivity to spectral shape is removed. A further advantage of this technique is its ability to remove erroneous contributions to the components PMD of polarisation-insensitive and polarisation-sensitive origins.

***Phase Shift technique***

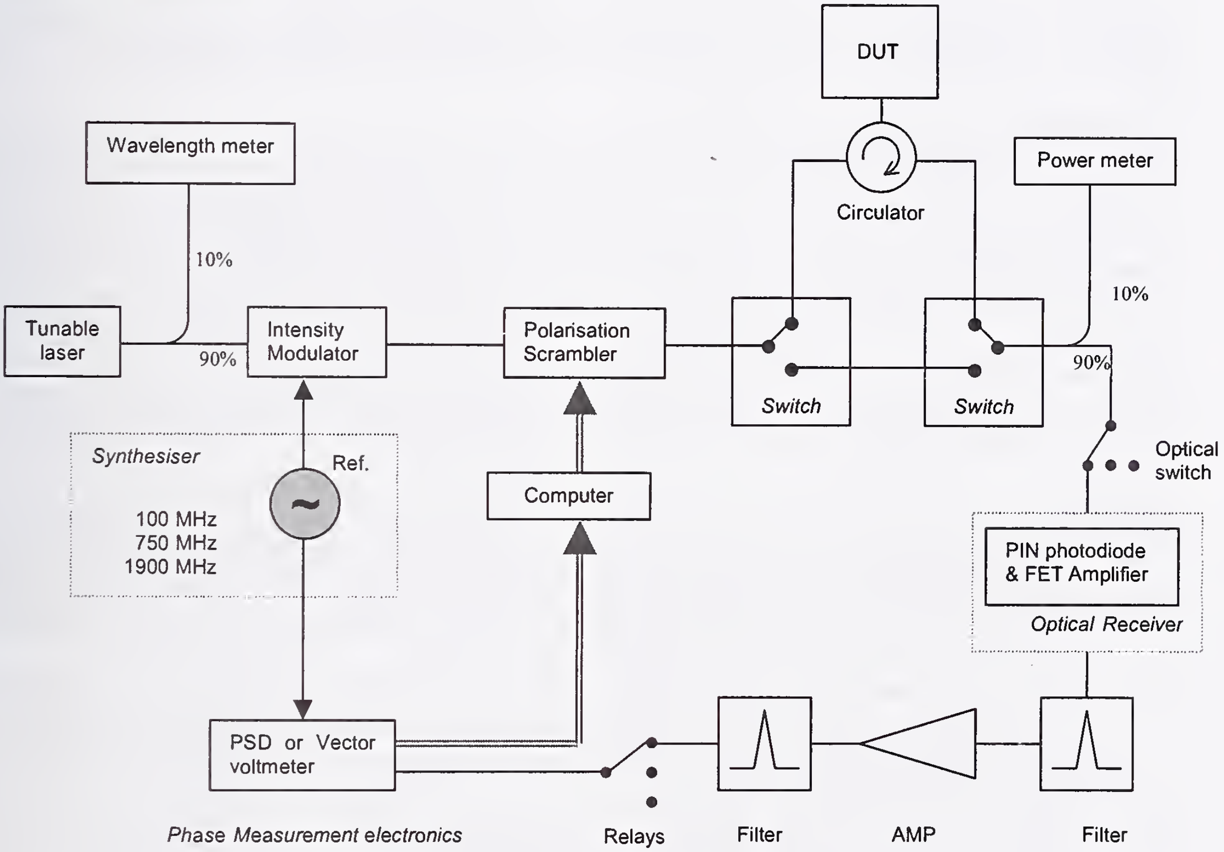

**Figure 2: Phase Shift system (used to measure PMD and other parameters of components).**

(Set up shown for a reflective device.)

The Phase shift method measures DGD by measuring the phase shift of light from one principal state of polarisation to the other. One implementation is to find the PSPs by sampling over the entire Poincaré sphere [4]. An alternative is to launch states that form a Muller Set, which eliminates the need to find the PSPs of the component to measure the DGD [5].

It is advantageous to use the Differential/Muller set method to measure the DGD of components with restricted bandwidths as DGD is found at a single wavelength point without the need to scan over a spectral range. A probable implementation will be to launch six polarisation states. NPL's Phase shift system (figure 2) has optional modulation frequencies of 1.9 GHz, 0.75 GHz and 0.1 GHz, and uses a vector voltmeter with a phase angle resolution of at least 0.1 degrees. This gives a theoretical lower limit of approximately 145 fs DGD and a figure of merit of 1800 (where the bandwidth is taken as twice the modulation frequency due to the sidebands that are created by modulation). The figure of merit is independent of modulation frequency.

Although the phase shift technique does not allow us to meet the target of measuring 100 fs PMD, it does offer detection of PMDs lower than the other 3 techniques discussed.

A further advantage of the phase shift technique is its removal of non-polarisation sensitive reflections. A disadvantage is that it does not remove polarisation sensitive reflections.

## Conclusions

The figure of merit of the interferometric technique is 1, fixed analyser is 1, Stokes parameter evaluation is 200 and the phase shift technique is 1800. After assessment the phase shift technique was selected as the most appropriate to measure PMD in components for our purposes. Further investigations will involve measurement of broadband and narrowband components using the phase shift system, and the Stokes parameter evaluation technique for comparison.

## Acknowledgement

The work reported here was funded by the National Measurement System Policy Unit of the UK's Department of Trade and Industry.

## References

[1] American Standard, TIA FOTP-196: to be published. Guideline for Polarization-Mode Dispersion Measurement in Single-Mode Fiber Optic Components and Devices.

[2] GISIN, N. and PELLAUX, J.P. Polarization mode dispersion: time versus frequency domains. *Opt. Commun.*, 1992, **89**, 316 – 323.

[3] IVES, D. Polarisation Mode Dispersion in Chirped Fibre Bragg Gratings. *Proceedings of the Symposium on Optical Fiber Measurements*, NIST, Boulder, Colorado, 1998, edited by G.W. Day, D.L. Franzen and P.A. Williams, Washington, DC, USA, U.S. Government Printing Office, 1998, 15 - 18.

[4] WILLIAMS, P.A., BARLOW, A.J., MACKECHNIE, C. and SCHLAGER, J.B. Narrowband measurements of polarization-mode dispersion using the modulation phase shift technique. *Proceedings of the Symposium on Optical Fiber Measurements*, NIST, Boulder, Colorado, 1998, edited by G.W. Day, D.L. Franzen and P.A. Williams, Washington, DC, USA, U.S. Government Printing Office, 1998, 23 – 26.

[5] WILLIAMS, P.A. Modulation phase-shift measurement of PMD using four launched polarization states: a new algorithm. *Electron. Lett.*, 1999, **35**, 18,1578 – 1579.

# Measurement and mitigation of multiple reflection effects on the Differential Group Delay spectrum of optical components

P.A. Williams and J.D. Kofler
*National Institute of Standards and Technology - Boulder, Colorado, USA*

***Abstract:*** *Ripple in the Differential Group Delay (DGD) spectrum due to multiple reflections is described theoretically and demonstrated experimentally. A technique of tilting the cavity element to reduce these multiple reflection effects is discussed and is demonstrated to remove the ripples in the DGD spectrum.*

## I. Introduction

In the field of optical fiber metrology, it seems that you can't measure anything without the result being affected by multiple reflections coming from a cavity somewhere in the optical path. Polarization-Mode Dispersion (PMD) or, more specifically, Differential Group Delay (DGD) is also affected by multiple reflections. The result is a ripple in the DGD spectrum with a surprisingly large amplitude [1].

In this paper, we derive the spectral DGD behavior in the presence of multiple reflections, and demonstrate how these effects can be significantly reduced by tilting the cavity component with respect to the optical path.

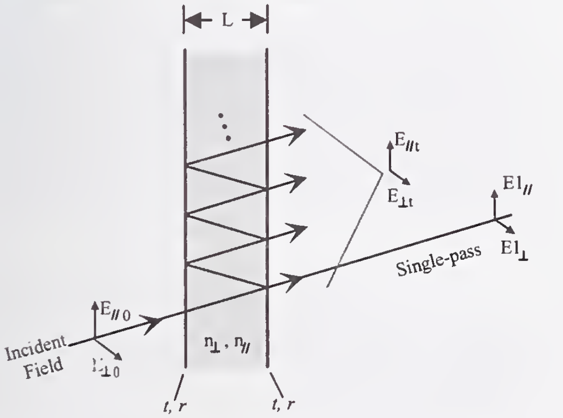

**Figure 1.** Schematic of Fabry-Perot cavity with transmission and reflection coefficients t and r, containing birefringent material with indices of refraction $n_{//}$ and $n_{\perp}$.

## II. Theory

We derive the DGD spectrum of a cavity composed of a simple birefringent material whose eigenaxes are independent of wavelength ("non-mode-coupled"). The physical length of the cavity is $L$, and its birefringence is $\Delta n=(n_{//} - n_{\perp})$. For simplicity, we assume the transmission and reflection coefficients ($t$ and $r$) at the input interface are equal to those at the output interface. Figure 1 illustrates the geometry. Note: this derivation assumes that the cavity is not tilted with respect to the light beam (ie. normal incidence). The tilted light beam in Figure 1 is only shown to schematically to illustrate the features.

We calculate the transmitted electric field for the two orthogonal polarization components aligned with the birefringence axes of the cavity. The electric field of the light that is transmitted through the cavity without experiencing any reflections ("single-pass") is given by

$$\begin{aligned} E1_{//} &= E_{//0} e^{i\delta_{//}} t^2, \\ E1_{\perp} &= E_{\perp 0} e^{i\delta_{\perp}} t^2. \end{aligned} \qquad (1)$$

$E_{//0}$ and $E_{\perp 0}$ are the input electric fields, and $\delta_{//}$ and $\delta_{\perp}$ are the phase delays accumulated by a single pass through the cavity for light polarized along each birefringent axis of the cavity. The phase delays are given as

$$\delta_a = \omega n_a L / c, \qquad (2)$$

where ω is the (radian) optical frequency, $c$ is the speed of light, $n$ is the index of refraction with the subscript $a$ denoting the corresponding polarization state (// or ⊥).

Group delay is given by the radian-frequency derivative of transmitted phase. So, we can find the DGD of the single-pass transmission as the difference in group delay for the two orthogonal components,

$$\frac{d(\delta_{//} - \delta_{\perp})}{d\omega} = \left( \Delta n + \omega \frac{d\Delta n}{d\omega} \right) \frac{L}{c} = \frac{\Delta n_g L}{c}, \qquad (3)$$

where $\Delta n$ is the phase birefringence and $\Delta n_g = n_{//,g} - n_{\perp,g}$ is the group birefringence, with

$$n_{a,g} = n_a + \omega \frac{dn_a}{d\omega}. \qquad (4)$$

So we find that the DGD seen by the single-pass light is

$$\Delta\tau_0 = \frac{\Delta n_g L}{c} = (n_{//,g} - n_{\perp,g})\frac{L}{c}. \quad (5)$$

This is the DGD that would be measured in this device if there were no reflections.

In order to find how the DGD is modified by multiple reflections, we use a standard Fabry-Perot approach [2] to write the vector components of the total electric fields transmitted through the cavity as

$$E_{//t} = E_{//0}\left[\frac{t^2}{1 - r^2 e^{-i2\delta_{//}}}\right], \quad (6)$$

and

$$E_{\perp t} = E_{\perp 0}\left[\frac{t^2}{1 - r^2 e^{-i2\delta_{\perp}}}\right], \quad (7)$$

where a term containing the time dependence is common to both and omitted. The phases of $E_{//t}$ and $E_{\perp t}$ do not include the phase accumulated by the first pass through the device. In other words, the phase in Equations (6) and (7) is the perturbation to the transmitted phase caused by multiple reflections.

Writing the expressions for $E_{//t}$ and $E_{\perp t}$ in phasor notation, we find the phases of each component:

$$\varphi_{//} = \tan^{-1}\left(\frac{-R\sin 2\delta_{//}}{1 - R\cos 2\delta_{//}}\right), \quad (8)$$

and

$$\varphi_{\perp} = \tan^{-1}\left(\frac{-R\sin 2\delta_{\perp}}{1 - R\cos 2\delta_{\perp}}\right), \quad (9)$$

where $R$, the intensity reflection coefficient, has been substituted for $r^2$.

We find the perturbation to the DGD caused by multiple reflections as

$$\Delta\tau_{FR} = \frac{d(\varphi_{//} - \varphi_{\perp})}{d\omega}, \quad (10)$$

or

$$\Delta\tau_{FR} = \frac{-2LR(\cos 2\delta_{//} - R)n_{//,g}}{(1 + R^2 - 2R\cos 2\delta_{//})c} + \frac{2LR(\cos 2\delta_{\perp} - R)n_{\perp,g}}{(1 + R^2 - 2R\cos 2\delta_{\perp})c}. \quad (11)$$

Since the complicated nature of Equation (11) clouds intuition about its behavior, we approximate $\Delta\tau_{FR}$ as

$$\Delta\tau_{FR} \approx 4R\tau_0 \sin\left(\frac{2\omega n L}{c}\right)\sin\left(\frac{\omega \Delta n L}{c}\right), \quad (12)$$

where

$$\tau_0 = n_g L / c \quad (13)$$

is the group delay for a single-pass through the cavity. Equation (12) requires the assumptions $R<0.1$, and $\Delta\tau_0/\tau_0<1$.

The total DGD measured for transmission through the Fabry-Perot cavity of Figure 1 is the sum of the single-pass DGD plus the perturbation DGD

$$\Delta\tau = \Delta\tau_0 + \Delta\tau_{FR}. \quad (14)$$

Equations (11) and (12) predict some important features of the perturbation to the DGD spectrum. Equation (11) has two obvious periodicities due to the $\cos(2\delta_{//})$ and $\cos(2\delta_{\perp})$ terms. Since $\delta_{//}$ and $\delta_{\perp}$ are functions of $\omega$, we expect the first term of Equation (11) to repeat over a frequency spacing or Free Spectral Range (FSR) of

$$\Delta\omega_{//} = \frac{\pi c}{L n_{//,g}}. \quad (15)$$

Likewise, the second term repeats over a FSR

$$\Delta\omega_{\perp} = \frac{\pi c}{L n_{\perp,g}}. \quad (16)$$

Note that the refractive indices in Equations (15) and (18) are group (rather than phase) due to the frequency dependence of $n$. When combined, these two ripple "periods" will result in a fast ripple on $\Delta\tau_{FR}$ that repeats over a frequency spacing of

$$\Delta\omega_0 = \left(\frac{1}{2\Delta\omega_{//}} + \frac{1}{2\Delta\omega_{\perp}}\right)^{-1} = \frac{\pi c}{L n_g}, \quad (17)$$

and in a "beat note" in the spectrum with a frequency spacing of

$$\Delta\omega_B = \left(\frac{1}{\Delta\omega_{//}} - \frac{1}{\Delta\omega_{\perp}}\right)^{-1} = \frac{\pi c}{L \Delta n_g}. \quad (18)$$

This behavior is more obvious in Equation (12) where the sine function at the left gives the fast ripples and the one at the right gives the envelope. Plots of the spectral behavior of Equation

(11) are shown Figures 2 and 3. The parameters used to generate these plots were: $L = 9.97$ mm, $R = 0.0014$, $n = 1.532$, $\Delta n = 0.00847$, $n_g = 1.554$, and $\Delta n_g = 0.0094$. These values were chosen to emulate the pigtailed quartz plate we measure in Section III.

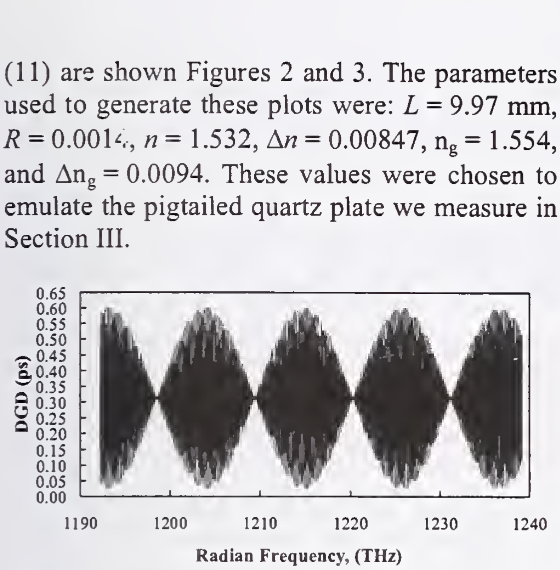

**Figure 2.** Simulated DGD spectrum showing Frequency beat notes due to multiple reflections in a birefringent cavity (from Equations (5), (11), and (14)).

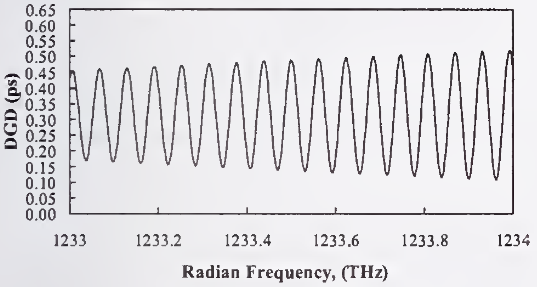

**Figure 3.** Close-up of DGD spectrum in Figure 2.

Equation (12) gives the amplitude of the ripple envelope as $4R\tau_0$. This result is somewhat surprising in that the ripple amplitude depends on the group delay of the cavity $\tau_0$ and not the DGD $\Delta\tau_0$. Since typical sources of birefringence in components have $\tau_0/\Delta\tau_0 >> 1$, the amplitude of the DGD spectral ripple can easily be larger than the DGD itself.

### III. Experimental Verification

These predictions are experimentally verified by measuring the DGD spectrum of a pigtailed quartz plate using a Modulation-Phase-Shift (MPS) technique [3] with a spectral resolution of $\Delta\omega$=4.92 GHz and a temporal resolution of 30 fs (yielding a bandwidth efficiency factor [4] of over 6700). The length and indices of refraction of the quartz plate are expected to be equal to those used in the above simulation. Both faces of the plate have a broadband anti-reflection coating expected to yield an $R$ of 0.01-0.02, but this was not measured directly.

Figures 4 and 5 show the measured DGD spectrum for this device. We see qualitative agreement with the theoretical predictions of Figures 2 and 3 when an $R$ of 0.0014 is used. This unexpectedly low $R$ value was estimated by using $R$ as a fitting parameter in Equation (12) to match the size of the ripple envelope in Figure 4. We attribute this low $R$ value to a possible tilt of the waveplate, preventing some of the forward reflected light from being captured.

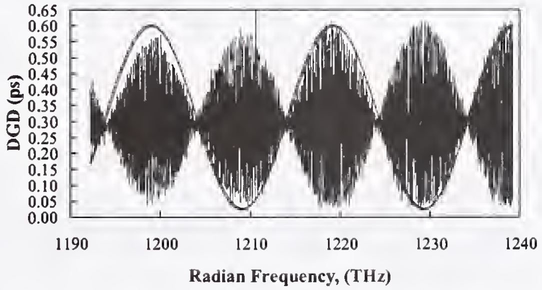

**Figure 4.** Measured DGD spectrum for pigtailed quartz plate with envelope portion of Equation (12) overlaid to estimate $R$.

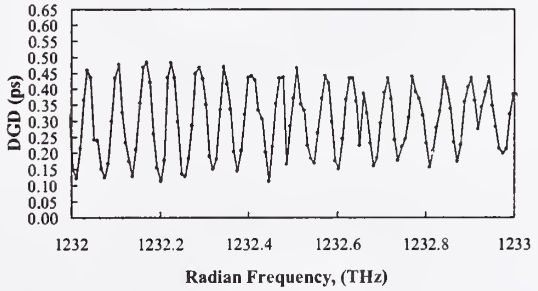

**Figure 5.** Close-up of DGD spectrum in Figure 4.

By counting cycles in Figures 4 and 5, we measured the frequency spacings $\Delta\omega_0$ and $\Delta\omega_B$ to be $6.16\times10^{10}s^{-1}$ and $1.00\times10^{13}s^{-1}$, respectively. Inserting $\Delta\omega_0$, $\Delta\omega_B$ and our estimate of the quartz plate thickness $L$=9.97 mm into Equations (17) and (18) yields estimates for $n_g$ and $\Delta n_g$ of 1.53 and 0.0094 respectively. These predicted values are in good agreement (1.5 %) with the expected values of 1.554 and 0.0094.

### IV. Mitigation

An efficient means for reducing multiple reflections in the backward direction (return loss) is to tilt the cavity element so that the backward-reflected beam reflects at an angle and misses the launch optics. However, in order to reduce the multiple reflection effect on DGD, we must suppress the multiple reflections that propagate in the forward direction. In general, this requires a larger tilt angle, since the forward-reflected beams experience only a transverse offset with tilt. Figure 6 illustrates how tilting the cavity lets the single-pass beam enter the collection optics, but causes a forward-reflected beam to miss.

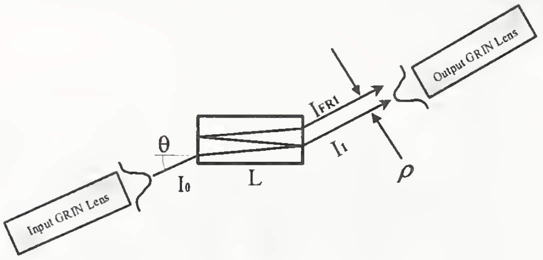

**Figure 6.** Schematic of launching light into tilted cavity element at angle θ to prevent the reflected beams from being captured.

From Figure 6, we see that the transverse offset $\rho$ between the single-pass and the first forward-reflected beams will be

$$\rho = \frac{2L\cos(\theta)\sin(\theta)}{\sqrt{n^2 - \sin^2(\theta)}}, \qquad (19)$$

where $L$ is the cavity thickness, θ is the tilt angle of the cavity, and $n$ is the mean refractive index in the cavity. With the collection lens and fiber arranged to efficiently collect the single-pass light (intensity $I_1$), the fractional power in the first reflected beam (intensity $I_{FR1}$) that will be collected is given by (assuming Gaussian beam profiles)

$$\frac{I_{FR1}}{I_1} = R^2 \exp\left(-\frac{2\rho^2}{w^2}\right), \qquad (20)$$

where $R$ is the intensity reflection coefficient and $w$ is the beam radius (defined by the $1/e^2$ point). Combining Equations (19) and (20) gives the fractional power ratio between the first reflected beam and the single-pass beam.

In order to minimize ripple in the DGD spectrum, the ratio of Equation (20) should be minimized. To demonstrate the effectiveness of tilting the cavity, we used the same pigtailed waveplate geometry measured in Figures 4 and 5 except with the quartz plate tilted by approximately 4-5° with respect to the incoming beam. For our collimating lenses, $w = 0.25$ mm, $L = 9.97$ mm, and $n = 1.532$, and we estimate $R \approx 0.02$. Equations (19) and (20) indicate that for the given parameters, the first reflected beam will be severely attenuated (~150 dB) from the single-pass beam. Therefore, we expect to see no spectral ripple on the DGD of this device. Figure 7 shows the measured spectrum for the tilted-plate device. Indeed, within the noise of the measurement, no spectral ripple can be seen.

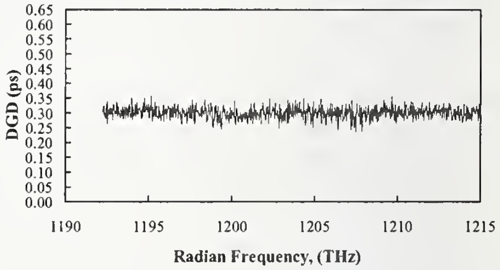

**Figure 7.** Measured DGD spectrum for pigtailed quartz plate with 4-5° tilt of plate with respect to beam path.

## V. Conclusion

We have characterized the effects on the DGD of a component with multiple reflections present. The resulting DGD spectral ripple has an amplitude proportional to the product of the intensity reflection coefficient and the single-pass group delay of the cavity. We have also shown that tilting a reflective cavity can successfully eliminate the multiple reflection effects on the measured DGD.

References:

[1] Normand Cyr, Michel Leclerc and Bernard Ruchet, "PMD measurements in multipath components: The single waveplate example", *Proceedings of Photonics North*, Quebec (2002).

[2] E. Hecht and A. Zajac, *Optics*, (Addison-Wesley, 1974), p. 305.

[3] P.A. Williams, "Modulation phase-shift measurement of PMD using only four launched polarization states: a new algorithm," *Elecron. Lett.* **35**, 1578-1579 (1999).

[4] P.A. Williams, "PMD Measurement Techniques – Avoiding Measurement Pitfalls," Presented at the Venice Summer School on PMD, Venice, (2002).

# π-shifted all-fibre Sagnac loop for characterization of femtosecond Polarization Mode Dispersion

**E. Simova and I. Golub,**
*Institute for Microstructural Sciences, National Research Council*
*Montreal Road, Build. M-23A, Ottawa, On, K1A 0R6*
eli.simova@nrc.ca; ilya.golub@nrc.ca;

**Abstract:** A novel configuration for measuring PMD consisting of an all-fibre π-shifted Sagnac interferometer is studied. Its advantages include insensitivity to the orientation of the device under test. This allows an extension of the dynamic range to few femtosecond PMD measurements and characterization of the device's principal states of polarization.

**key words:** Fiber optics and optical communications; Fiber characterization; Fiber measurements; Birefringence; Polarization Mode Dispersion (PMD).

## 1. Introduction

Polarization Mode Dispersion (PMD) in fiber and fiber devices is caused by the wavelength dependent birefringence and wavelength dependence of the birefringence axes orientation, or the associated principal states of polarization (PSP). The use of a Sagnac interferometer for characterization of PMD was proposed in [1] and it was compared to the fixed analyzer method [2], with the advantage of a better contrast between minima and maxima in the transmission spectrum. Since these methods rely on counting fringes, in order to measure femtosecond PMD, they require several hundred nanometers tunable laser/broadband source while measuring *wavelength averaged* PMD. Moreover, neither of these methods can determine PSP.

In this work, we present a novel π-shifted configuration of the Sagnac loop for PMD characterization. The main advantage of this configuration is that the half-wave plate (HWP) inserted in the loop makes it insensitive to the orientation of the birefringence axes of the device under test (DUT). As a result, one can characterize PMD values which correspond to a part of a fringe in the fixed analyzer method. This allows extending the dynamic range to femtosecond PMD values and measuring the *wavelength dependence* of PMD. Furthermore, the orientation of the birefringence axes of the DUT can be determined.

## 2. Theory of the Sagnac loop

The Sagnac interferometer has been studied theoretically using Jones calculus [3-5]. We include the HWP in the loop as shown in Fig.1 (the polarization controller, PC, is used for canceling the loop's residual birefringence). Effectively, here the HWP introduces a π-shift between the clockwise and counterclockwise propagating beams upon entry to the DUT. The polarization properties of the loop and the DUT can be described by the electrical field vectors into and out of the fiber coupler, $\vec{E}_{in}$ and $\vec{E}_{out}$, respectively, and the corresponding Jones matrix, $J(\omega)$. At the exit of the coupler, for arm 1 (the reflection arm), and for arm 2 (the transmission arm), the electric field vectors, $E_{1n}^{out}$ and $E_{2n}^{out}$ are:

$$\begin{aligned} E_{1n}^{out} &= K_n^{1/2}(1-K_n)^{1/2} J^a(\omega) E_{1n}^{in} + K_n^{1/2}(1-K_n)^{1/2} J^c(\omega) E_{1n}^{in} \\ E_{2n}^{out} &= K_n J^a(\omega) E_{1n}^{in} + (1-K_n) J^c(\omega) E_{1n}^{in} \end{aligned} \qquad (1)$$

where the coefficient $K_n$, represents the splitting ratio of the coupler with the index $n$ referring to the $x$- or $y$-component, $J^c(\omega)$ and $J^a(\omega)$ are the clockwise and counterclockwise Jones matrices, respectively, for the propagation of the light through the loop.

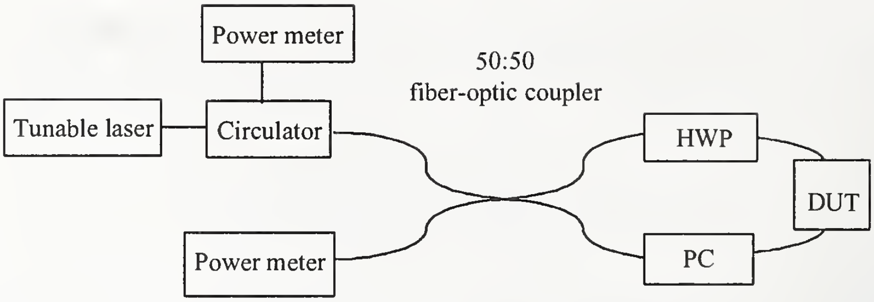

Fig. 1. Configuration of the π-shifted Sagnac interferometer.

As can be seen from Eq. (1), an uneven splitting ratio, $K_n$, of the fiber-optic coupler dependent on the wavelength results in a limited interference contrast, when the intensity distribution is recorded in the transmission arm 2, while for arm 1, $K_n \neq 0.5$ does not limit the attainable contrast. Indeed, the fact that the reflection arm 1 is more stable and gives better results was confirmed in the experiment. The following Jones matrices for the HWP and DUT were assumed in the calculations:

$$J^c_{HWP} = \begin{pmatrix} i\cos 2\rho & i\sin 2\rho \\ i\sin 2\rho & -i\cos 2\rho \end{pmatrix}; \quad J^a_{HWP} = \begin{pmatrix} i\cos 2\rho & -i\sin 2\rho \\ -i\sin 2\rho & -i\cos 2\rho \end{pmatrix} \qquad (2)$$

$$J^c_{DUT} = \begin{pmatrix} e^{i\frac{\delta}{2}}\cos^2\alpha + e^{-i\frac{\delta}{2}}\sin^2\alpha & 2i\sin 2\alpha \sin\frac{\delta}{2} \\ 2i\sin 2\alpha \sin\frac{\delta}{2} & e^{-i\frac{\delta}{2}}\cos^2\alpha + e^{i\frac{\delta}{2}}\sin^2\alpha \end{pmatrix}; J^a_{DUT} = \begin{pmatrix} e^{i\frac{\delta}{2}}\cos^2\alpha + e^{-i\frac{\delta}{2}}\sin^2\alpha & -2i\sin 2\alpha \sin\frac{\delta}{2} \\ -2i\sin 2\alpha \sin\frac{\delta}{2} & e^{-i\frac{\delta}{2}}\cos^2\alpha + e^{i\frac{\delta}{2}}\sin^2\alpha \end{pmatrix}$$

where $\rho$ and $\alpha$ are the orientation angles of the birefringence axes of the HWP and the DUT, respectively, relative to the coordinate system defined by the plane of the loop and the coupler, and δ is the birefringence of the DUT. Assuming $K_n = 0.5$ the transmission in arm 2, for example, is:

$$T(\lambda) = \cos^2\frac{\delta(\lambda)}{2}\sin^2 2\rho \qquad (3)$$

Eq. (3) shows that the transmission response of the π-shifted Sagnac loop is independent of the orientation angle, $\alpha$, of the DUT's birefringence axes and the polarization of the input light. It depends only on the DUT's birefringence provided that the HWP's orientation angle, $\rho$, is optimized at 45° relative to the coordinate system. The result in Eq. (3) is significant, because it allows us to recover the wavelength dependent phase and the associated PMD through intensity measurement. The Differential Group Delay (DGD or first order PMD) is calculated as $\mathrm{DGD} = d\delta/d\omega$, where ω is the optical frequency.

For comparison, a similar equation for the conventional Sagnac loop with only DUT can be derived:

$$T(\lambda) = \sin^2\frac{\delta(\lambda)}{2}\sin^2 2\alpha\,. \qquad (4)$$

The drawbacks of the conventional Sagnac loop become apparent from Eq. (4), namely the dependence on the DUT' s orientation angle, $\alpha$. Since the fiberoptic DUT's axes cannot be rotated, there are two unknowns in the equation. This problem is bypassed through the fringe-counting technique [1], but then the limiting factor towards measuring femtosecond PMD is the bandwidth of the source. Moreover, only the *wavelength averaged* PMD is measured.

In addition, using our scheme to determine the DUT's birefringence from Eq. (3), one can remove the HWP and determine the orientation of the birefringence axes of the DUT from Eq. (4).

## 3. Measurements

The measurements were carried out in the set-up according to Fig. 1. A tunable laser, a broadband 50:50 fiber-optic coupler and a broadband HWP were used to assure operation of the interferometer for a wide range of wavelengths. In order to verify the possibility of measuring femtosecond PMD, another coupler was tested as the DUT. The measurement system was calibrated to account for the losses in the loop, the HWP and in the DUT. The DGD calculated using Eq. (3) is presented in Fig. 2a for a wavelength step of 0.3 nm. For comparison, the DGD measured with the JME (Jones Matrix Eigenanalysis) based commercial instrument is shown in Fig. 2b. It can be seen that there is a good agreement between the two methods. Fig. 3 presents the angle of the DUT's birefringence axes calculated from Eqs. (3) and (4).

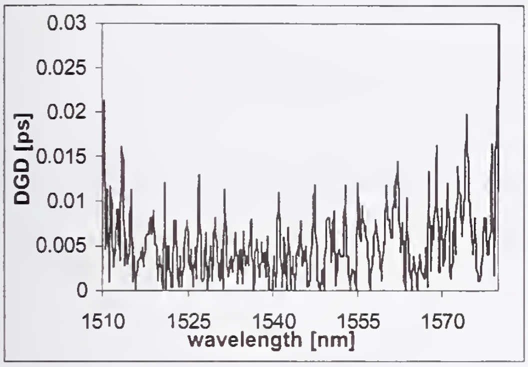

Fig.2a. DGD for the fiber-optic coupler calculated from the π-shifted Sagnac loop.

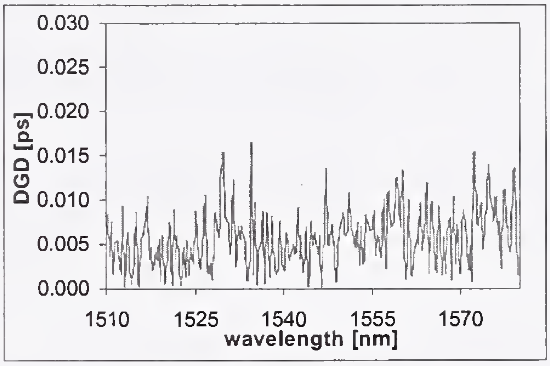

Fig.2b. DGD for the fiber-optic coupler calculated from the Jones Matrix Eigenanalysis.

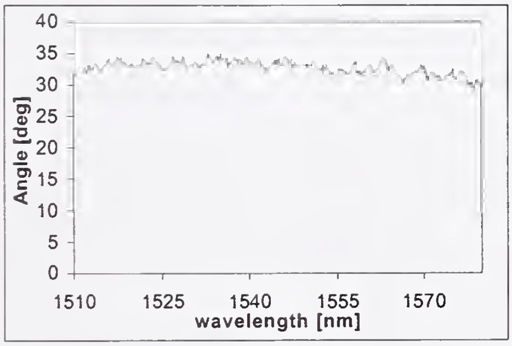

Fig.2. Orientation of the DUT's birefringence axes calculated using the π-shifted Sagnac loop in conjunction with a conventional one.

## 4. Conclusions

We have proposed and studied a novel π-shifted configuration of the Sagnac loop for characterization of PMD. The π-shift allows the recovery of the phase as a function of wavelength from the intensity scan. Thus the dynamic range is extended towards few femtosecond range without the need for a broadband source while measuring *wavelength dependent* PMD. A comparison with the more complex JME method showed a good agreement. Combining the proposed scheme with the conventional Sagnac loop allows determination of the DUT's birefringence axes.

## 5. References

1. B. Olson, M. Karlson and P. Andreson, "Polarization mode dispersion measurement using a Sagnac interferometer and a comparison with the fixed analyzer method, "IEEE Photonics Tech. Lett., 10, 997-999 (1998).
2. C.D. Poole and D. L. Favin, "Polarization mode dispersion measurements based on transmission spectra through a polarizer, "J. Lightw. Tech. 12, 917-934 (1994).
3. T. A. Birks and P. Morkel, "Jones calculus analysis of single-mode Sagnac reflector", Appl. Opt. 27, 3107-3113 (1988).
4. D. Mortimer, "Fiber Loop Reflectors, "J. Lightw. Tech. 6, 1217-121224 (1989).
5. X. Fang and R. O. Claus, "Polarization-independent all-fibre wavelength-division multiplexer based on a Sagnac interferometer, "Opt. Lett., 20, 2146-2148 (1995).

## Acknowledgments

The authors would like to express their gratitude to Prof. Xiaoyi Bao, Dr. Dongfeng Liu and David Waddy from the Physics Department of University of Ottawa, in Ottawa, Canada for their help with the JME measurements.

# Using Importance Sampling to Assess the Effects of PMD on System Performance

William L. Kath and Gino Biondini*

*Department of Engineering Sciences and Applied Mathematics, Northwestern University*
*2145 Sheridan Road, Evanston, Illinois 60208; E-mail: kath@northwestern.edu*

We describe the application of importance sampling to Monte-Carlo simulations of polarization-mode dispersion (PMD) in optical fibers. The algorithm significantly increases the frequency of rare PMD events, while at the same time keeping track of each event's original probability of occurrence, thus making it possible to assess the effect of PMD on power penalties at realistic outage probabilities. The numerical application of the algorithm is straightforward; we also describe its possible experimental implementation using a hardware-based PMD emulator.

## 1. Introduction

Polarization-mode dispersion (PMD) has been recognized as a potentially major impairment in both terrestrial and undersea transmission systems. To first order in frequency, PMD splits a pulse between the fast and slow axes of a fiber; at the same time, higher orders of PMD induce depolarization and polarization-dependent chromatic dispersion. At high bit rates, all of these effects lead to unacceptable transmission penalties.

A key difficulty with PMD is its stochastic nature. PMD is caused by random variations of an optical fiber's birefringence with distance. In addition, the penalties it produces change randomly over time as the ambient temperature and other environmental parameters vary. In system design, a maximum power penalty (typically 1 dB) is usually assigned to PMD, and one demands that the outage probability (that is, the probability of the PMD-induced penalty exceeding this allowed value) is very small (typically a minute per year, $10^{-6}$ or less). Because of this stringent requirement, it is very difficult to use either Monte-Carlo simulations or laboratory experiments to determine a system's outage probability, due to the extremely large number of system configurations that must be explored in order to obtain a reliable estimate.

A measure of PMD is provided by the PMD vector $\boldsymbol{\tau}$ (also known as the polarization dispersion vector) [1-3], the magnitude of which is the differential group delay (DGD). The rare events where the DGD is significantly larger than its mean are particularly important, since they are the ones most likely to result in system outages. Of course, the PMD vector is frequency-dependent, and therefore in general the DGD at any given frequency is not the sole determiner of system outages. In particular, second-order PMD, which includes both depolarization and polarization-dependent chromatic dispersion (PCD), is known to produce additional system penalties [4, 5].

In the absence of effective tools for determining outage probabilities, system designers must resort to stopgap techniques. One such technique is to produce artificially large DGD values, determine the penalties at these large DGDs, and then weight the results using the DGD's well-known Maxwellian probability distribution [1]. A fundamental problem with this method, however, is that there is no direct relationship between the DGD (and/or second-order PMD) and the power penalty. In addition, it is possible for different configurations to give both the same DGD and the same second-order PMD, but not contribute equally to the penalty (because of different higher-order PMD), and therefore they should be weighted differently in calculations of outage probability.

The technique of *importance sampling* (IS) [6-8], which is one member of a family of methods known as variance reduction techniques [9, 10], addresses these difficulties and provides a tool that can be used in numerical simulations — and, in principle, in experiments — to accurately estimate PMD-induced system penalties. The technique allows low probability events to be efficiently simulated by enabling one to concentrate Monte-Carlo simulations in the most significant regions of interest in sample space. In this case, the regions of interest in the sample space are the configurations that lead to large values of DGD and/or second-order PMD [11, 12]. This method has also been applied to numerically calculate PMD-induced transmission penalties [13, 14]. Here we give a description of the technique and its application.

## 2. The PMD concatenation equations

A standard technique for simulating PMD effects is the coarse-step method [15], which approximates the continuous birefringence variations present in real fibers by a concatenation of fixed length birefringent sections. Many experimental PMD generation techniques also employ a concatenation of birefringent elements, such as high-birefringence fibers [16] or birefringent waveplates [17],

---

*Department of Mathematics, Ohio State University, 231 West 18th Avenue, Columbus, Ohio 43210; E-mail: biondini@math.ohio-state.edu connected by either polarization scramblers (e.g., polarization controllers [16]) or rotatable connectors [17]. We will refer to the situation where there are no polarization controllers as the case of rotatable waveplates.

In the case of discrete birefringent sections, the total PMD vector after the $(n+1)$-st fiber section can be obtained from the PMD concatenation equation [3],

$$\boldsymbol{\tau}^{(n+1)} = \mathsf{R}_{n+1}\boldsymbol{\tau}^{(n)} + \Delta\boldsymbol{\tau}_{n+1}\,. \tag{1}$$

Here $\boldsymbol{\tau}^{(n)}$ is the PMD vector after $n$ sections and $\Delta\boldsymbol{\tau}_{n+1}$ is the differential contribution to the PMD vector of the $(n+1)$-st section. For fixed length sections, the magnitude of $\Delta\boldsymbol{\tau}_{n+1}$ is fixed, and only its direction varies. For linearly birefringent elements, $\Delta\boldsymbol{\tau}_{n+1}$ lies on the equatorial plane of the Poincaré sphere [18]. The Müller matrix $\mathsf{R}_{n+1} = \exp[\varphi_{n+1}(\hat{\mathbf{r}}_{n+1}\times)]$ represents a rotation through an angle $\varphi_{n+1}$ about the axis $\hat{\mathbf{r}}_{n+1}$. This rotation is frequency dependent; for linearly birefringent elements, $\hat{\mathbf{r}}_{n+1} = \Delta\boldsymbol{\tau}_{n+1}/|\Delta\boldsymbol{\tau}_{n+1}|$ and $\varphi_{n+1}(\omega) = 2b'\ell_{n+1}\omega = \varphi_{n+1}(\omega_0) + 2b'\ell_{n+1}(\omega-\omega_0)$, where $b'$ is the birefringence strength of each element and $\ell_{n+1}$ is its length [3]. A similar concatenation equation holds for the frequency derivative of the PMD vector, $\boldsymbol{\tau}_\omega$ [3]:

$$\boldsymbol{\tau}_\omega^{(n+1)} = \mathsf{R}_{n+1}\boldsymbol{\tau}_\omega^{(n)} + \Delta\boldsymbol{\tau}_{n+1}\times\boldsymbol{\tau}^{(n+1)}\,. \tag{2}$$

When polarization controllers are present, an additional rotation matrix $\mathsf{Q}_{n+1}$ appears between $\mathsf{R}_{n+1}$ and both $\boldsymbol{\tau}^{(n)}$ and $\boldsymbol{\tau}_\omega^{(n)}$ in Eqs. (1-2). The resulting equations are then formally equivalent to Eqs. (1-2) with a new rotation matrix $\mathsf{R}'_{n+1} = \mathsf{R}_{n+1}\mathsf{Q}_{n+1}$.

## 3. Importance sampling

In order to apply IS to the PMD concatenation Eqs. (1-2), the rare events in which the DGD and/or second-order PMD assume values much larger than their means must be targeted. We have found that to do so it is appropriate to control the orientation of the differential PMD vector of each section, $\Delta\boldsymbol{\tau}_{n+1}$, relative to the total first- and second-order PMD vectors up to that point, $\boldsymbol{\tau}^{(n)}$ and $\boldsymbol{\tau}_\omega^{(n+1)}$.

Suppose the orientations of the differential PMD vectors depends upon the set of angles $(\theta_1, \theta_2, \ldots \theta_N) \equiv \boldsymbol{\theta}$ where $N$ is the total number of sections (note, of course, there must be *two* angles for each differential PMD vector; we will see that the second angle does not need to be controlled and can be left uniformly distributed). Suppose further that we are interested in determining the probability $P$ that a random variable which depends upon these angles falls in a given range. Note that any random variable can be considered, such as the amount of pulse broadening, the power penalty, or any combination thereof. The probability $P$ can be represented as the expectation value of an indicator function $I(\boldsymbol{\theta})$, where $I = 1$ if the random variable of interest falls in the prescribed range and $I = 0$ otherwise. That is, $P$ is represented by the $N$-dimensional integral

$$P = \int_\Theta I(\boldsymbol{\theta})p(\boldsymbol{\theta})d\boldsymbol{\theta}, \tag{3}$$

where the $p(\boldsymbol{\theta})$ is the joint probability distribution function for the angles and $\Theta$ represents the configuration space. Importance sampling is performed by first rewriting the integrand in Eq. (3) as $I(\boldsymbol{\theta})p(\boldsymbol{\theta}) = I(\boldsymbol{\theta})L(\boldsymbol{\theta})p^*(\boldsymbol{\theta})$, where $p^*(\boldsymbol{\theta})$ is the biasing distribution, and where $L(\boldsymbol{\theta}) = p(\boldsymbol{\theta})/p^*(\boldsymbol{\theta})$ is the importance sampling likelihood ratio [6-8]. We then estimate the integral through Monte Carlo simulations; that is, we write an importance-sampled Monte-Carlo estimate of the above probability $P$ as [6-8]

$$\hat{P} = \frac{1}{M}\sum_{m=1}^{M} I(\boldsymbol{\theta}_m)L(\boldsymbol{\theta}_m)\,. \tag{4}$$

Here $M$ is the total number of trials, and the samples $\boldsymbol{\theta}_m$ are drawn according to the biased distribution $p^*(\boldsymbol{\theta})$. If $p^*(\boldsymbol{\theta}) \equiv p(\boldsymbol{\theta})$ (i.e., for unbiased Monte Carlo simulations), Eq. (4) is simply the relative frequency of trials falling in the range of interest. A problem with this choice is that, when simulating low probability events, an exceedingly large number of samples is necessary in order for the desired events to occur, and an even larger number is required in order to obtain an accurate estimate. Using a biased probability distribution causes the desired regions of sample space to be visited much more frequently, and the likelihood ratio $L(\boldsymbol{\theta})$ automatically adjusts the results so that all of the different realizations are correctly weighted, thus contributing properly to the final probability.

## 4. IS for first- and second-order PMD

As mentioned previously, the appropriate variables to control when applying importance sampling are the orientations of the individual PMD vectors of each section, $\Delta\boldsymbol{\tau}_{n+1}$. IS works by biasing these random vectors toward specific deterministic directions $\mathbf{b}^{(n)}$ which maximally increase the particular quantity of interest (e.g., the total DGD or the second-order PMD). In the following, we will concentrate on the case of polarization scramblers and will characterize the vector $\mathbf{b}^{(n)}$ relative to the orthonormal frame of reference $\mathcal{U}$ formed by the unit vectors $\{\mathbf{u}_1^{(n)}, \mathbf{u}_2^{(n)}, \mathbf{u}_3^{(n)}\}$, where

$$\mathbf{u}_1^{(n)} = \boldsymbol{\tau}^{(n)}/|\boldsymbol{\tau}^{(n)}|, \quad \mathbf{u}_2^{(n)} = \boldsymbol{\tau}_{\omega,\perp}^{(n)}/|\boldsymbol{\tau}_{\omega,\perp}^{(n)}|,$$
$$\mathbf{u}_3^{(n)} = \mathbf{u}_1^{(n)}\times\mathbf{u}_2^{(n)}\,. \tag{5}$$

Here $\boldsymbol{\tau}_{\omega,\perp}^{(n)}$ is the component of $\boldsymbol{\tau}_\omega^{(n)}$ perpendicular to $\boldsymbol{\tau}^{(n)}$, as illustrated in Fig. 1. The magnitudes of $\boldsymbol{\tau}_{\omega,\parallel}$ (the component of $\boldsymbol{\tau}_\omega^{(n)}$ parallel to $\boldsymbol{\tau}^{(n)}$) and $\boldsymbol{\tau}_{\omega,\perp}$ quantify the PCD and the depolarization.

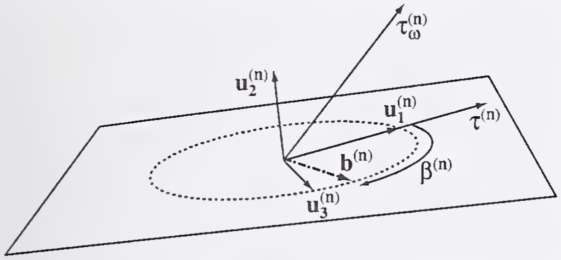

Figure 1: Diagram showing the preferential direction $\mathbf{b}$ for biasing the simulations in the plane identified by $\boldsymbol{\tau}^{(n)}$ and $\boldsymbol{\tau}^{(n)} \times \boldsymbol{\tau}_\omega^{(n)}$.

Biasing to increase the DGD is achieved by arranging for $\Delta\boldsymbol{\tau}_{n+1}$ to be preferentially aligned with the total PMD vector $\boldsymbol{\tau}^{(n)}$ up to that point, i.e., using $\mathbf{b}^{(n)} = \mathbf{u}_1^{(n)}$. Specifically, we set the polarization scramblers so that $\theta_n$ (the angle between the PMD vector at the output of the $n$-th scrambler and the $(n+1)$-st differential PMD vector) is biased towards zero. This choice does not uniquely determine the orientation of the PMD vector at the scrambler output, of course, because $\boldsymbol{\tau}_n$ can still be rotated by an arbitrary amount about $\Delta\boldsymbol{\tau}_{n+1}$ while keeping $\theta_n$ constant. We assume that this additional rotational angle is uniformly distributed.

In the unbiased case, the angles $\theta_n$ are independent random variables, with $\cos\theta_n$ uniformly distributed in $[-1,1]$. When applying importance sampling, we choose $\cos\theta_n = 2x^{1/\alpha} - 1$, where $x$ is a uniform random variable in $[0,1]$ and $\alpha \geq 1$ is a biasing parameter. Other choices are possible for the biased distribution used for the $\theta_n$; the effectiveness of the method is not very sensitive to the particular distribution used. The above choice yields the likelihood ratio as

$$L(\boldsymbol{\theta}) = \prod_{n=1}^{N} \frac{p_1(\cos\theta_n)}{p_\alpha(\cos\theta_n)}, \tag{6}$$

where $p_\alpha(\cos\theta) = (\alpha/2)[(1+\cos\theta)/2]^{\alpha-1}$ [19]. The value $\alpha = 1$ reproduces the unbiased case (i.e., $\cos\theta$ is uniformly distributed), while increasing values of $\alpha$ bias the configurations towards increasingly larger values of DGD. Thus, each biasing distribution allows us to sample a different range of DGDs, and simulations with different values of $\alpha$ can be combined in order to cover the whole range of DGD values. This produces region 1 in Fig. 2.

A technical detail is how to combine the results of the different biasing strengths. The simultaneous use of several biasing probability distributions is called *multiple importance sampling* [20, 21], and the proper way to combine the different results is to apply separate *weights* to the samples from each different distribution. The weights allow the biasing distributions that are expected to produce the best results in each given region to be favored. A particularly useful choice of weights is know as the *balance heuristic* [21].

We emphasize that different configurations with the same value of DGD (and/or second order PMD) can have quite different likelihood ratios, and thus their relative contribution to the final result can vary substantially. As a consequence, different configurations producing the same DGD and/or second-order PMD are expected to give very different contributions to the power penalty.

First-order biasing yields the largest values of DGD. It does not, however, produce very large values of $\boldsymbol{\tau}_\omega$, because when $\Delta\boldsymbol{\tau}_{n+1}$ is parallel to $\boldsymbol{\tau}_n$ the contribution from that section to $\boldsymbol{\tau}_\omega^{(n+1)}$ is zero. Thus, if all the $\Delta\boldsymbol{\tau}_{n+1}$ were parallel to $\boldsymbol{\tau}^{(n)}$, no second-order PMD would be produced. Random fluctuations add second-order PMD, but large values are not specifically targeted. Over a single section, one can easily show that the choice that maximizes the contribution to $\boldsymbol{\tau}_\omega^{(n+1)}$ is to align $\Delta\boldsymbol{\tau}_{n+1}$ with the direction of $\mathbf{u}_3^{(n)}$. The rate at which $\boldsymbol{\tau}_\omega^{(n+1)}$ increases, however, also depends on $\boldsymbol{\tau}^{(n)}$, and thus, when optimizing over many sections, the growth of $\boldsymbol{\tau}^{(n)}$ must also be considered.

When the number of sections in the emulator is large, we have found it useful to employ a continuum approximation to find the deterministic configuration that generates the maximum second-order PMD. Specifically, we let $\lim_{\Delta z \to 0} \Delta\boldsymbol{\tau}_{n+1}/\Delta z = \mathbf{b}(z)$. The magnitude of $\mathbf{b}(z)$ describes the relative rate at which PMD is added by the birefringent sections. For simplicity, we concentrate upon the case $|\mathbf{b}(z)| = b =$const. In the continuum limit, for the case of polarization scramblers one obtains

$$\frac{d\tau}{dz} = b_1, \tag{7}$$

$$\frac{d\tau_{\omega,\parallel}}{dz} = b_2 \frac{\tau_{\omega,\perp}}{\tau}, \tag{8}$$

$$\frac{d\tau_{\omega,\perp}}{dz} = b_3\tau - b_2 \frac{\tau_{\omega,\parallel}}{\tau}, \tag{9}$$

where $(b_1, b_2, b_3)$ are the components of $\mathbf{b}$ with respect to $\mathcal{U}$. This system of equations can be solved exactly for any $\mathbf{b}(z)$ (although the solution is not displayed here).

Note that $d[|\boldsymbol{\tau}_\omega|^2]/dz = 2b_3\tau_{\omega,\perp}\tau$. Thus, $b_2$ does not directly contribute toward increasing the magnitude of second-order PMD; rather, it induces a rotation of $\boldsymbol{\tau}_\omega$ about $\mathbf{u}_3$, as seen from Eqs. (8,9). Since the maximum $\tau_{\omega,\perp}$ under such a rotation occurs when $\tau_{\omega,\parallel} = 0$, we expect the maximum second-order PMD to be generated for $b_2 = 0$, i.e., when $\mathbf{b}$ lies in the $\mathbf{u}_1$-$\mathbf{u}_3$ plane. Calculus of variations can then be used to show that the maximum growth of second-order PMD is obtained when

$$\mathbf{b}(z) = b\,[\mathbf{u}_1 \cos\beta(z) + \mathbf{u}_3 \sin\beta(z)]\,, \tag{10}$$

where $\beta(z) = \beta_{\max}\, z/z_{\max}$ and $\beta_{\max} = \pi/2$. With multiple biasing strengths, this generates region 3 in Fig. 2. We

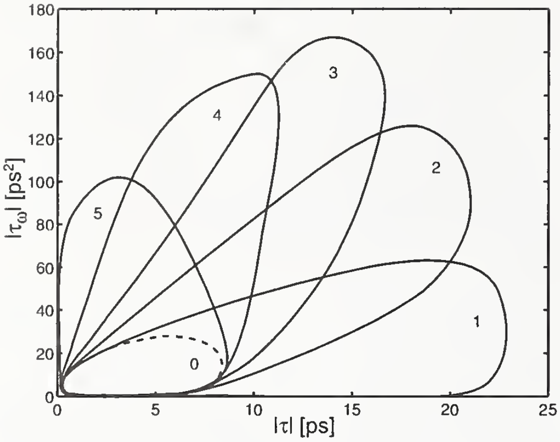

Figure 2: The regions of the $|\tau|$-$|\tau_\omega|$ plane targeted by the various biasing methods. Region 1 corresponds to first-order biasing ($\beta = 0$), region 3 to pure second-order biasing ($\beta_{\max} = \pi/2$), and regions 2, 4 and 5 to $\beta_{\max} = \pi/4$, $3\pi/4$ and $\pi$, respectively. The dashed line shows the much smaller region obtained with unbiased runs. 50 sections with 0.5 ps DGD each and polarization scramblers were used.

refer to this choice, which yields the largest values of $|\tau_\omega|$, as optimal second-order biasing.

Of course, a more complete coverage of the $|\tau|$-$|\tau_\omega|$ plane is often needed. In this case, intermediate biasing choices must also be used in addition to optimal first- and second-order biasing. These intermediate choices can be obtained by using calculus of variations to maximize a linear combination of $|\tau|$ and $|\tau_\omega|$. The resulting form of $\mathbf{b}(z)$ is the same as above, except that the value of the final angle $\beta_{\max}$ now varies between 0 and $\pi$, the particular value depending upon the specific linear combination of first- and second-order PMD being maximized. A selection of angles, together with the resulting regions in the $|\tau|$-$|\tau_\omega|$ plane, is shown in Fig. 2. The advantage of using multiple biasing — as opposed to just pure first- or second-order biasing or no biasing at all — is evident. When a range of biasing strengths are used, each value of $\beta_{\max}$ generates samples lying in a region that emanates in a roughly radial fashion from the location where the joint pdf is maximum. Together, a selection of angles $\beta_{\max}$ and biasing strengths $\alpha$ covers the entire $|\tau|$-$|\tau_\omega|$ plane.

When using rotatable waveplates, the relative orientations between birefringent sections are the primary variables determining the total DGD, and each differential PMD vector must lie in the equatorial plane of the Poincaré sphere. The biasing toward large DGD values is then done by choosing the next differential PMD vector, $\Delta\boldsymbol{\tau}_{n+1}$, to be preferentially aligned with the *projection* of the total PMD vector obtained thus far, $\boldsymbol{\tau}_n$, onto the equatorial plane. Specifically, we choose $\Delta\boldsymbol{\tau}_{n+1}$ so that the angle $\theta_n$ between it and the projection of $\boldsymbol{\tau}_n$ is biased toward zero (mod $2\pi$). This is done, for example, by taking $\theta = \pi\left[1 + \operatorname{sgn}(2x-1)|2x-1|^{1/\alpha}\right]$, where $x$ is again uniformly distributed between 0 and 1. Other choices for the probability distribution are possible, of course. Note that if $\alpha = 1$ (unbiased case), $\theta$ is uniformly distributed between 0 and $2\pi$, while for $\alpha > 1$, $\theta$ is concentrated near 0 and $2\pi$. Similarly, to increase the second-order PMD, or some combination of first- and second-order, the appropriate deterministic biasing directions are again obtained merely by projecting onto the equatorial plane the vectors $\mathbf{b}$ found as described previously.

If frequency dependence is desired, or in the case of rotatable waveplates, the differential phase retardations $\varphi_{n+1}(\omega)$ in the Müller matrix $\mathsf{R}_{n+1}$ must also be specified. Recall that each beat length of a birefringent section generates a $2\pi$ retardation. In practice, sections with significant DGDs will be many beat lengths long, and unless the section lengths are precise to within a small fraction of a beat length, these retardations will vary from section to section. We therefore choose the retardation angles $\varphi_{n+1}(\omega_0)$ to be uniformly distributed between 0 and $2\pi$. (Alternatively, one could assume a random distribution of lengths $\ell_{n+1}$; if the variance of the lengths is large compared with the beat length, however, an approximately uniform distribution of the angles $\varphi_{n+1}(\omega_0)$ results. If, of course, the lengths are very precise, then specific phase retardations should be used.) In the case of rotatable waveplates, different configurations are generated solely by rotating sections relative to one another. The results do not depend significantly upon the particular retardation angles used, except for certain clearly pathological cases such as identical angles with $\varphi_{n+1}$ equal to 0 or $\pi$. When including the frequency dependence, a simple strategy is to do the biasing at a single center frequency, but calculate the PMD vector over the required range of frequencies. Furthermore, when considering pulse evolution, it is also necessary to calculate the Jones' form of the input-output transfer matrix [3].

## 5. Experimental implementation

Experimental PMD emulators employing a concatenation of birefringent elements have been built [16, 17], and it is possible that an emulator could be constructed to use the importance-sampled algorithm described above. Essentially, in order for it to be possible to use the algorithm, it is necessary that the emulator be stable, repeatable and predictable. The biggest difficulty associated with a possible experimental implementation of the algorithm is the requirement that the orientation of the PMD vector and its frequency derivative be known after each birefringent section. One possible way of doing this would be to monitor the PMD vector after each birefringent section; obviously, such an implementation would be prohibitively cumbersome and expensive.

If the PMD vector is not monitored, then the next alternative is for each element of the emulator to be sufficiently well characterized that the PMD vector can be calculated if the orientations of the different birefringent elements is specified. Here the problem is that the differential phase retardations $\varphi_{n+1}$ in the Müller matrix $\mathsf{R}_{n+1}$ must then be well characterized. If they are not known relatively precisely, then the Müller matrix will rotate the PMD vector to an unknown location on the Poincaré sphere, and it will then be impossible to properly determine the preferential orientation of the next differential PMD vector. As mentioned earlier, each beat length of a birefringent section generates a $2\pi$ retardation. Because sections with significant DGDs will be many beat lengths long, this means that the section lengths must precise to within a small fraction of a beat length, and that these sections lengths must be stable with respect to temperature and other environmental fluctuations.

## 6. Examples

To demonstrate the ideas explained in the previous sections, we consider a concatenation of 50 birefringent sections with 0.5 ps of DGD per section (corresponding to a mean DGD of 3.26 ps), employing either polarization scramblers or rotatable waveplates. The average DGD is given by $\langle\tau\rangle = \sqrt{8\langle\tau^2\rangle/(3\pi)}$, where $\langle\tau^2\rangle = \sum_{n=1}^{N} a_n^2$, the $a_n$ are the individual DGDs of each section and $N$ is the number of sections. Figure 3 shows the pdf of the DGD, obtained with optimal first-order biasing, while Fig. 4 shows the pdf of second order PMD, obtained with the optimal second-order biasing technique. In both cases, the biasing parameters $\alpha = 1, 2, \ldots, 10$ were used, with 200,000 realizations each. The individual samples are combined by sorting the values of DGD and/or second-order PMD obtained from all of the simulations into bins and adjusting the contribution *of each individual sample* for the bias using its likelihood ratio, as explained earlier. The solid lines show the analytical pdfs for real fiber [22].

The emulator with rotatable sections yields better agreement with real fiber than the emulator with polarization scramblers. Note, however, that a concatenation of a small number of equal length, rotatable birefringent sections is not a good model for real fiber due to artificial periodicities of the PMD vector's autocorrelation function in the frequency domain [16, 25]. For both scramblers and waveplates, the pdfs deviate significantly from the real fiber distributions in the tails, since here the PMD is generated by an emulator with finite number of birefringent sections, which by necessity has finite maximums for both $|\boldsymbol{\tau}|$ and $|\boldsymbol{\tau}_\omega|$. As a result, large values may be inaccessible in the $|\boldsymbol{\tau}|$-$|\boldsymbol{\tau}_\omega|$ plane.

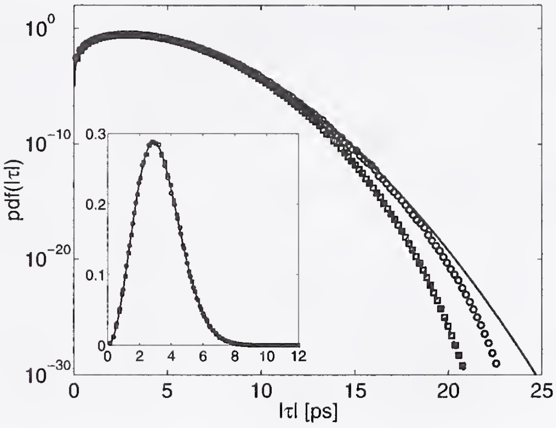

Figure 3: Importance-sampled pdf of the DGD for 50 sections with 0.5 ps DGD each and with polarization scramblers (squares) or birefringent waveplates (circles). Solid curve: Maxwellian distribution with mean DGD of 3.26 ps; dashed line: exact and asymptotic solutions from Ref. [23, 24]. Inset: the pdfs on a linear scale. A total of $2 \times 10^6$ Monte-Carlo realizations were used.

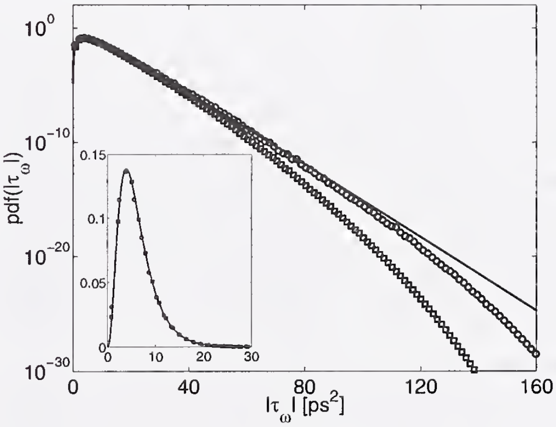

Figure 4: The pdf of second-order PMD for a concatenation of 50 sections with 0.5 ps DGD each, using scramblers (squares) or waveplates (circles). The solid lines show the pdf for real fiber, from Ref. [22]. Inset: the pdf on a linear scale. As in Fig. 3, $2 \times 10^6$ Monte-Carlo realizations were used.

Figure 5 shows the joint pdf of the magnitudes of first- and second-order PMD (a two-dimensional reduction of the full three-dimensional joint pdf of first- and second-order PMD [1]) for an emulator with polarization scramblers, as calculated with the multiple biasing technique. The results for the joint pdf confirm why the optimal first- and second-order biasing methods are the correct ones to use if one is only interested in first- or second-order PMD statistics, respectively. As seen from Fig. 5, for any fixed value of DGD (a vertical slice in Fig. 5), the maximum of the pdf occurs in a zone that falls within region 1 in Fig. 2. Similarly, for any given second-order PMD (a horizontal slice in Fig. 5), the maximum of the pdf occurs in a zone

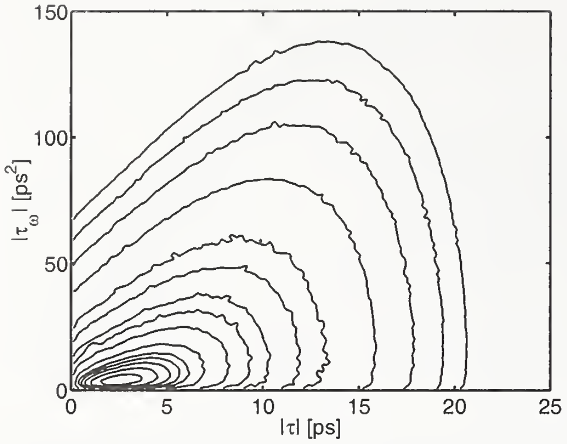

Figure 5: Contour plots of the joint pdf for a concatenation of 50 sections with 0.5 ps DGD each and polarization scramblers. The contours are at $10^{-n}$ with $n = 30, 25, 20, 15, 10, 8, 6, 5, 4, 3, 2.25, 2, 1.75$ and 1.5. A total of $10^6$ Monte-Carlo realizations were used.

falling within region 3 in Fig. 2.

The above applications of importance sampling focused on the probability distributions of first- and second-order PMD only as simple examples of the method. It is also possible, however, to directly apply the method to the calculation of PMD-induced power penalties and outage probabilities [14]. In particular, in a study of PMD compensation with a single fixed DGD element, it was demonstrated that for realistic power penalties of 1 dB the optimal value of the compensator's DGD is two to three times larger than $\langle\Delta\tau\rangle$. The results also show that it is not sufficient to determine the impact of a design upon the average penalty, because this is not directly related to the outage probability. It is therefore crucial to accurately model the tail of the probability density function of the power penalty, and importance sampling is a technique that makes such a study feasible.

## 7. Conclusions

We have described the application of importance sampling to Monte-Carlo simulations of the PMD generated by birefringent sections connected by either polarization scramblers or rotatable connectors. Importance sampling biases the random simulations so that configurations with large first- and/or second-order PMD occur more frequently than they would normally. As a result, the method allows rare PMD events to be simulated much more efficiently than with standard methods. Importance-sampled Monte-Carlo techniques therefore provide a natural and effective means to assess PMD-induced impairments in optical transmission systems at realistic bit-error rates.

## Acknowledgments

We thank J. N. Damask, A. Galtarossa, I. T. Lima and C. R. Menyuk for many interesting and valuable discussions. This work was supported in part by the National Science Foundation under grant numbers DMS-0101476 and DGE-9987577.

## References

1. G. J. Foschini and C. D. Poole, *IEEE J. Lightwave Tech.* **9**, 1439 (1991)
2. N. Gisin, R. Passy, J. C. Bishoff, and B. Perny, *IEEE Photon. Tech. Lett.* **5**, 819 (1993)
3. J. P. Gordon and H. Kogelnik, *Proc. Nat. Acad. Sci.* **97**, 4541 (2000)
4. P. Ciprut, B. Gisin, N. Gisin, R. Passy, J. P. Von der Weid, F. Prieto, C. W. Zimmer, *IEEE J. Lightwave Tech.* **16**, 757 (1998)
5. C. Francia, F. Bruyére, D. Penninckx, M. Chbat, *IEEE Photon. Tech. Lett.* **10**, 1739 (1998)
6. M. C. Jeruchim, *IEEE J. Select. Areas Commun.* **2**, 153 (1984)
7. J.-C. Chen, D. Lu, J. S. Sadowsky, and K. Yao, *IEEE J. Select. Areas Commun.* **11**, 289 (1993)
8. P. J. Smith, M. Shafi, and H. Gao, *IEEE J. Select. Areas Commun.* **15**, 597 (1997)
9. P. Bratley, B. L. Fox and L. E. Schrage, *A guide to simulation* (Springer-Verlag, New York, 1987)
10. G. S. Fishman, *Monte Carlo: concepts, algorithms and applications* (Springer-Verlag, New York, 1996)
11. G. Biondini, W. L. Kath and C. R. Menyuk, *IEEE Photon. Tech. Lett.* **14**, 310 (2002).
12. S. L. Fogal, G. Biondini and W. L. Kath, OFC2002, paper ThA1; *IEEE Photon. Tech. Lett.*, to appear (2002)
13. S. L. Fogal, G. Biondini and W. L. Kath, OFC2002, paper ThA2
14. I. T. Lima, G. Biondini, B. S. Marks, W. L. Kath and C. R. Menyuk, *Photon. Tech. Lett.* **14**, 627 (2002).
15. D. Marcuse, C. R. Menyuk, and P. K. A. Wai, *J. Lightwave Tech.* **15**, 1735 (1997)
16. R. Khosravani, I. T. Lima, P. Ebrahimi, E. Ibragimov, A.E. Willner, and C.R. Menyuk, *Phot. Tech. Lett.* **13**, 127 (2001)
17. J. N. Damask, OFC2000, paper ThB3
18. A. Galtarossa, L. Palmieri, M. Schiano, and T. Tambosso, *Opt. Lett.* **25**, 1322 (2000)
19. A. Papoulis, *Probability, Random Variables and Stochastic Processes* (McGraw-Hill, New York, 1965)
20. A. Owen and Y. Zhou, *J. Amer. Stat. Assoc.* **95**, 135 (2000).
21. E. Veach, *Robust Monte Carlo Methods For Light Transport Simulation*, Ph.D. thesis (Stanford University, 1997).
22. G. J. Foschini, L. E. Nelson, R. M. Jopson, H. Kogelnik, *IEEE Photon. Tech. Lett.* **12**, 293 (2000).
23. B. D. Hughes, *Random Walks and Random Environments* (Clarendon Press, Oxford, 1995).
24. M. Karlsson, *J. Lightwave Tech.* **19**, 324 (2001)
25. I. T. Lima, R. Khoshravani, P. Ebrahimi, E. Ibragimov, A. E. Willner, and C. R. Menyuk, OFC2000, paper ThB4

# Investigations on the relation between PMD coefficient and cable installation year in Deutsche Telekom fiber plant

H.-J. Tessmann, D. Breuer, H.M. Foisel, H. Reiner*, and H. Cremer*

T-Systems/Deutsche Telekom, Technology Center, Goslarer Ufer 35, D-10589 Berlin, Germany, email: d.breuer@t-systems.com
*T-Com/Deutsche Telekom, Am Kavalleriesand 3, D-64295 Darmstadt, Germany

**Abstract:** PMD data based on measurements of about 10'000 fiber sections within Deutsche Telekom fiber plant are analyzed. The relationship of the PMD coefficient and the installation year of the deployed fiber cables over a time period from 1985 till 2001 is investigated.

## 1 Introduction

Today network operators are facing the challenge of offering higher capacity to deal with the steadily growing demand of customers for transmission bandwidth at even reduced costs. In particular, during the last years a rapid capacity expansion of the core network with WDM links up to 600 km transporting up to 100 wavelength channels at 2.5 Gbit/s or 10 Gbit/s on a single fiber was necessary. To keep pace with this increasing capacity demand some carriers already performed field trials at 40 Gbit/s per wavelength [1]. For data rates per channel at and beyond 10 Gbit/s the assessment of the parameters of the installed fiber plant is a critical element for a carrier in the process of deploying these new terabit optical transport systems.

The impairments limiting the transmission performance generally include fiber loss, chromatic dispersion, polarization mode dispersion (PMD) and fiber non-linearities. From these limitations PMD is quite often considered as the most severe limiting effect, since it is complicated to compensate for. However, there is only rare data about PMD in a carriers installed fiber plant available. In this paper we present PMD measurements carried out in the installed fiber plant of Deutsche Telekom, which consists solely of G.652 fiber. The measurements were performed all over Germany during the last three years on nearly 10'000 fiber sections whereby these fiber cables were installed from 1985 till 2001. In this paper PMD measurement results are presented and a correlation of the PMD values with the initial operation and cable vintage (installation year) are shown. Moreover, based on published specifications the assessment of Deutsche Telekom fiber plant regarding 10 Gbit/s and 40 Gbit/s WDM transmission will be discusses.

## 2 Measurements and PMD specifications

The PMD measurements in the backbone network of Deutsche Telekom were performed with commercially available, interferometer based field measurement systems from EXFO (FTB 300/400 with the Polarization Mode Analyzer module FTB-5500). The broadband LED light source (module M2100 from EXFO) had a center wavelength of 1545 nm and a spectral width of 60 nm. To measure each individual cabled fiber receiver and transmitter are placed on opposite ends of the span, no loop-back was used. In each PMD measurement the cabled fiber section's mean DGD in picoseconds (ps) was measured. For characterization of the first order PMD coefficient in ps/√km, the fiber length of each investigated fiber section was also measured by OTDR measurements. Typically, in a selected cable all not-in-service fibers were measured.

Table 1 shows DGD's and PMD coefficients for 2.5, 10 and 40 Gbit/s based on the International Telecommunication Union (ITU-T) proposed guidelines for PMD limitation to maintain acceptable error rates [2]. The maximum DGD has to be lower than 1/10 of the bit duration. During the measurement process the fibers with the least PMD-values and attenuation were reserved for future high speed links.

| Bit rate (Gbit/s) | DGD (ps) | PMD-coefficient (ps/√km) |
|---|---|---|
| 2.5 | 40 | 2.0 |
| 10 | 10 | 0.5 |
| 40 | 2.5 | 0.125 |

**Table 1:** Relation ship between bit rate and proposed max. DGD and PMD coefficient for a 400 km link according to ITU-T recommendations [2].

It is noticeable to mention that for pre-1994 cables PMD was not yet specified by cable manufacturers. The fiber and cable manufacturers started to add the PMD value to their specifications around 1995. For today's G.652 cabled fibers a PMD coefficient of 0.5 ps/√km is guaranteed. However, the typical fiber PMD, without any cabling effects, can have PMD coefficients less than 0.1 ps/√km. Considering the PMD-limits in table1 and the above specifications from manufacturers there were considerable concerns about the suitability of the installed fiber plant regarding 40 Gbit/s and even 10 Gbit/s.

## 3 Results and Discussion

During the last three years 9'770 cabled G.652 fibers in the backbone network of Deutsche Telekom have been characterized with respect to PMD. The cable vintage of the measured fibers ranged from 1985 to 2001. Fig. 1 shows a histogram of the PMD coefficient of all measured fibers.

Please note that for showing the tail distribution in Fig.1 from 0.5 to 3.5 ps/√km the class width was increased from 0.02 ps/√km to 0.5 ps/√km. The mean measured PMD-coefficient of all fibers is 0.17 ps/√km and the maximum measured value is 4.79 ps/√km. Directly from this graph it is noticeable that the majority of the measured fibers will fulfill the ITU-T recommendation for 10 Gbit/s.

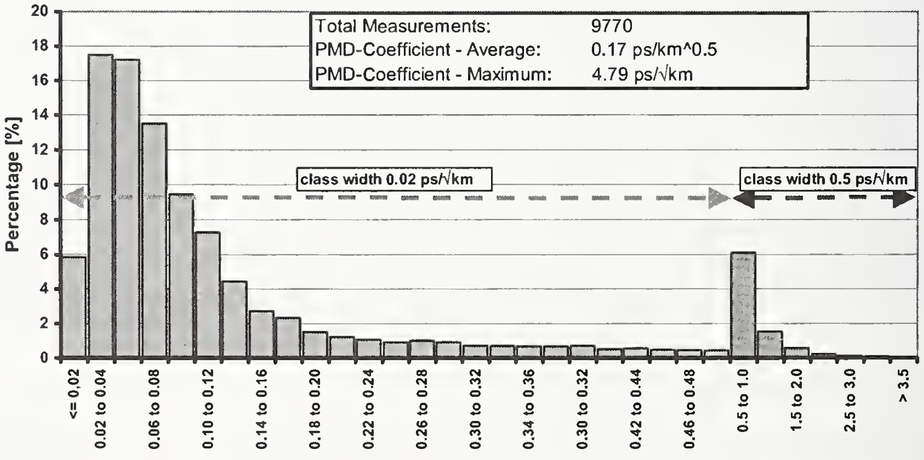

**Fig. 1:** Histogram of PMD coefficient (ps/√km) for all 9770 measured fibers

Based on all measured fibers Fig. 2 provides a summary of the assessment of the fiber plant for various link length according to the ITU-T recommendations in table1. Only fiber PMD was considered. For 2.5 Gbit/s transmission nearly all fibers (98,5%) are suitable up to the maximum considered link length of 1000km. For today's installed terrestrial 10 Gbit/s WDM-systems with typical link length up to 600 km nearly all fibers (89%) of the fiber plant are accessible and even for next generation systems with link length of about 1000 km still 86% of the cabled fibers support 10 Gbit/s operation. In particular, Fig.2

reveals that for future systems operating at 40 Gbit/s 63% of Deutsche Telekom fiber plant can be used for typical length up to 600km.

In a next step a possible correlation between cable vintage and mean PMD coefficient was analyzed (see Fig. 3). For each cable vintage the mean PMD value was determined from at least 200 to a about 1000 measured individual fiber sections of different cables from different manufacturers installed in the same year. In the early years usually cables from four different cable manufacturers were deployed.

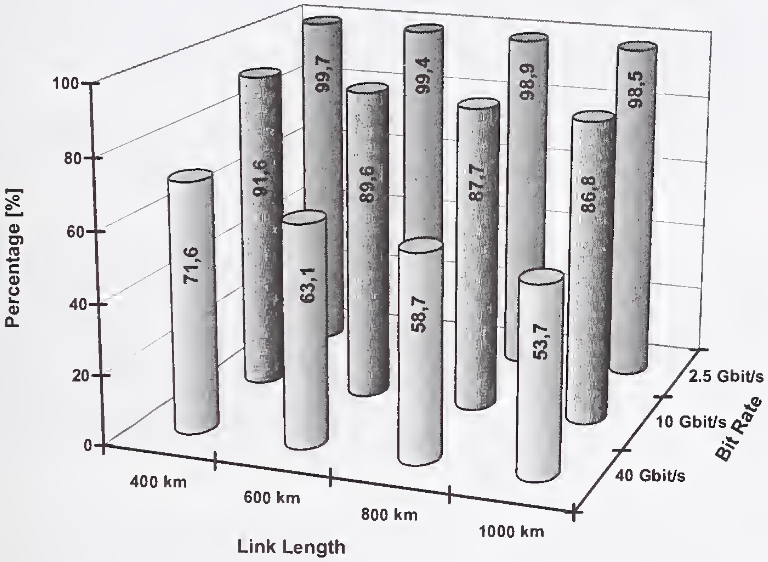

**Fig. 2:** Percentage of fibers suitable for 2.5 Gbit/s, 10 Gbit/s and 40 Gbit/s over various link length

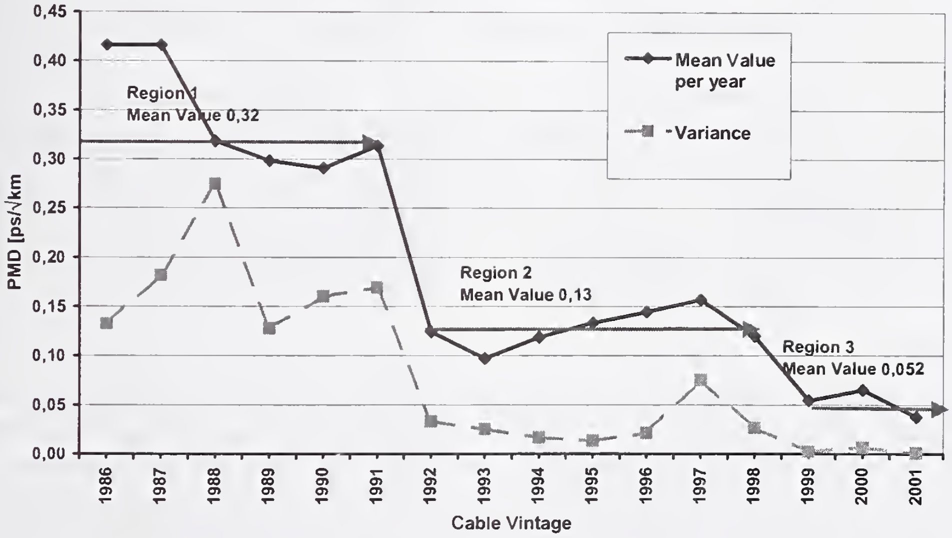

**Fig. 3:** Mean and variance of PMD coefficient as a function of cable vintage.

As depicted in Fig.3 there are 3 regions of almost constant PMD values. The first region with a high average PMD value of 0.32 ps /√km is for pre-1991 cables. The second one covers a time period from 1992 to 1998 with a typical PMD value of 0.13 ps/√km and the third region for post-1999 cables shows an even lower PMD coefficient of about 0.05 ps/√km which is attributed to improved manufacturing processes caused by more stringent carrier requirements on cabled fiber PMD. Also a significant drop of the PMD variance with cable vintage could be observed.

However, based on these results, particularly the improvement in PMD from 0.32 to 0.13 ps/√km for cable vintage of 1991 to 1992, could not be directly correlated to the introduction of the PMD specification from the manufacturers in 1995, but maybe correlated to an improvement in the fiber/cable manufacturing process. Anyway, the deployment specifications for fiber cables were not significantly modified during this time frame to explain the observed behavior.

A more thoroughly analysis of the three PMD regions is presented in Fig. 4 where the percentage of cabled fibers for the three regions with respect to different PMD coefficients is shown. Also the mean PMD value for each region is depicted. In region 1 the PMD classes from 0.3 ps/√km to 0.7 ps/√km occur with 1%. For region 2 (cable vintage 1992 till 1998) the percentage of the investigated fibers is about 0.1% for PMD-coefficients greater 0.46 ps/√km. The region 3 shows no value greater than 0.44 ps/√km and the classes over 0.18 ps/√km are less than 1%. But as obvious from Fig.4 even for "old" fibers (pre-1991) low PMD values (<0.125 ps/√km) suitable for 40 Gbit/s transmission can be found.

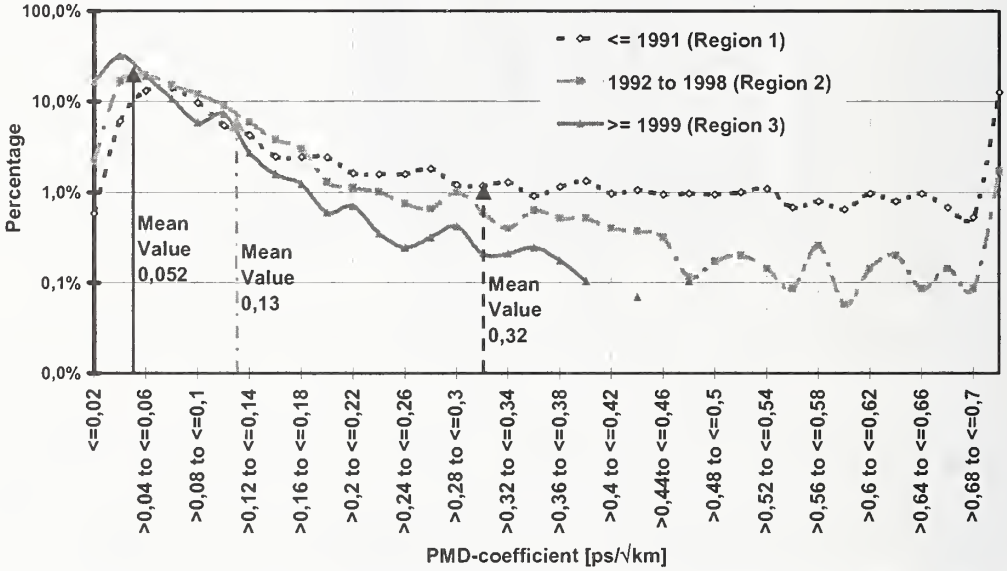

**Fig. 4:** Percentage of fibers in the different PMD classes for different cable vintages (installation years) according to Fig.3.

## 3 Conclusions

Deutsche Telekom has accomplished a thoroughly investigation of the installed fiber plant with respect to future transmission requirements. About 10'000 cabled fiber sections have been measured and the fibers with lowest PMD were identified and reserved for high capacity transmission. The data indicate that no direct correlation of the first-oder PMD coefficient value with the rollout of the PMD specification by the fiber and cable manufacturers is feasible. Even for cables which were installed during 1985 till 1991 a reasonable number of fibers is suitable for 40 Gbit/s transmission. For 10 Gbit/s selected fibers are used, thus PMD does not impose any limitations and therefore avoiding expensive exchange of fibers.

### References

[1] press release: http://www.lucent.com/press/0501/010523.nsa.html
[2] ITU-T G.650

# *Pulsed measurement of polarization mode dispersion in field-installed optical fibers*

Asbjørn O. Kleivstul, *asbjorn.kleivstul@telenor.com*,
Telenor R&D, Snarøyv. 30, 1331 Fornebu, Norway,
and Aasmund S. Sudbø, *sudbo@unik.no*,
University Graduate Center – UniK, P O Box 70, 2027 Kjeller, Norway.

*Abstract:* **Polarization mode dispersion (PMD) has been measured in optical fibers in field-installed cables. Two methods that allow simultaneous measurement of many fibers in parallel accessing one end of the cable have been investigated. Agreement with measurements based on Jones matrix eigenanalysis (JME) is observed for both methods.**

*Introduction:* The fixed analyser (FA) method [1] is well established for measuring polarization mode dispersion (PMD) in optical fibers. With this method, the transmission coefficient of the fiber is measured as a function of wavelength, for polarized input light and with an analyzer (polarizer) in front of the detector. The polarization analysed spectral response (PASR) curve thus obtained has oscillations, and the PMD is determined by the number of oscillations of the curve. Instead of the transmitted light, the light reflected back to the input end from the far end of the fiber may be measured [2], i.e., a two-way spectral response may be measured. Using pulsed illumination, several fibers in parallel may be measured simultaneously with one source and one detector, provided the fiber lengths are different, so that the pulses from different fibers arrive at different times at the detector. We have shown [3] that a two-way measurement on four fibers in parallel may be performed with a tuneable optical time-domain reflectometer (OTDR) with a polarizer and a power splitter. We show that a minor modification of the measurement setup in [3] also allows a one-way transmission measurement to be made. For a field-installed cable, the measurements may be performed by an operator only having access to one end of the cable. We demonstrate measurements on four fibers in parallel, performed on fibers in field-installed cable.

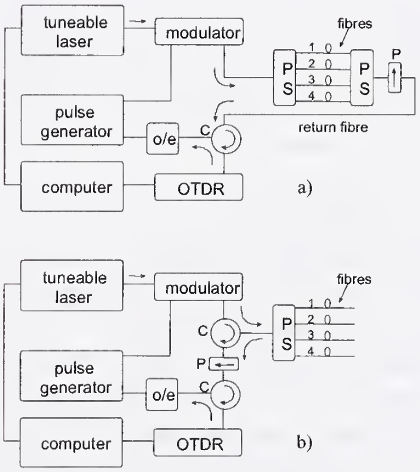

*Figure 1: Experimental setup for measuring polarization mode dispersion (PMD) in many optical fibers in parallel, using a tuneable optical time domain reflectometer (OTDR) with power splitter(s) and a polarizer (P). C: optical circulator, o/e: detector. (a) one-way. (b) two-way, as in [3].*

*Measurement setup:* The measurement setup described in [3] was used for making two-way measurements of PMD. In this setup, all the fibers to be measured are connected to a tuneable OTDR with a power splitter. To make one-way measurements, the far ends of the fibers were connected to a power splitter followed by a polarizer, as shown in Fig. 1(a), and the output power returned to the OTDR via a separate fiber in the cable. For comparison, the setup adapted from [3] is shown in Fig. 1(b).

A computer tuned the laser in wavelength steps of 0.25 nm from 1520 to 1580 nm, started the OTDR measurement for each step, and read the height of each pulse in the OTDR trace corresponding to a fiber. The OTDR pulse width used was 1 µs. For each pulse representing a fiber, the pulse height was recorded as a function of wavelength, yielding the polarization analysed spectral response (PASR) of the corresponding fiber. The number of extrema in the response curve for each fiber was counted manually. Both one-way- and two-way measurements were performed. With strong polarization mode coupling in the fiber, the PMD within a frequency interval $\Delta\nu$ (7.5 THz in our measurements) is

$$<\Delta\tau> = kN/\Delta\upsilon \ , \tag{1}$$

where $N$ is the number of extrema in the PASR, $k = 0.403$ for one-way, and $k = 0.247$ for two-way transmission [2]. (There is a misprint in Eq. (1) of [3], where 0.298 is written instead of 0.247, but the correct value was used in the data analysis in [3].) The relative rms uncertainty in the measured $<\Delta\tau>$ is

$$\sigma_{\Delta\tau}/\langle\Delta\tau\rangle = k'/\sqrt{N} \ , \tag{2}$$

where $k' = 0.72$ for one-way, and $k' = 0.88$ for two-way transmission [2].

For reference, we also measured PMD in the fibers with the one-way Jones-matrix-eigenanalysis (JME) method [4], using a commercially available polarimeter.

A total of 16 cabled standard (ITU type G.652) single-mode fibers were measured. The fibers were measured in groups of 4, as shown in Fig. 1, with each member of the group from a different cable or an uncabled fiber spool, to obtain a group of 4 fibers with different lengths. The fibers were selected from 9 different installed cables.

*Results:* Fig. 2 shows typical results from a measurement on 4 fibers with a one-way setup. An example of a PASR of a fiber with $N = 17$ extrema is shown in the bottom figure. Fig. 3 shows corresponding results for the two-way setup, with $N = 29$ extrema

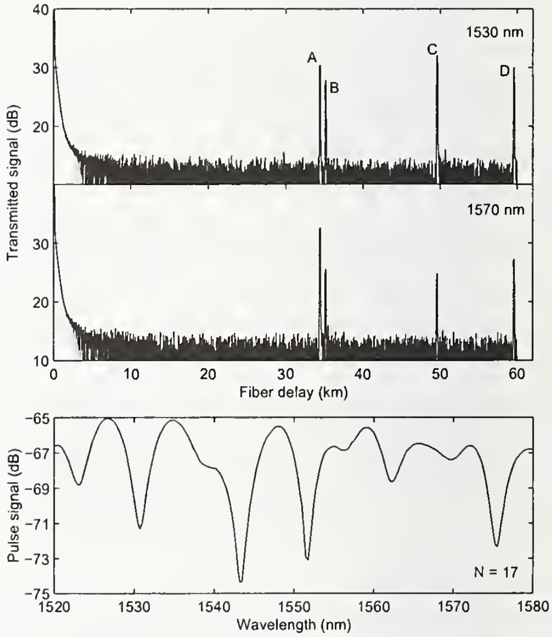

*Figure 2: Pulses observed in one-way measurement with four fibers (A, B, C, and D) at two wavelengths (top and middle), and sample polarization analysed spectral response of one fiber (bottom).*

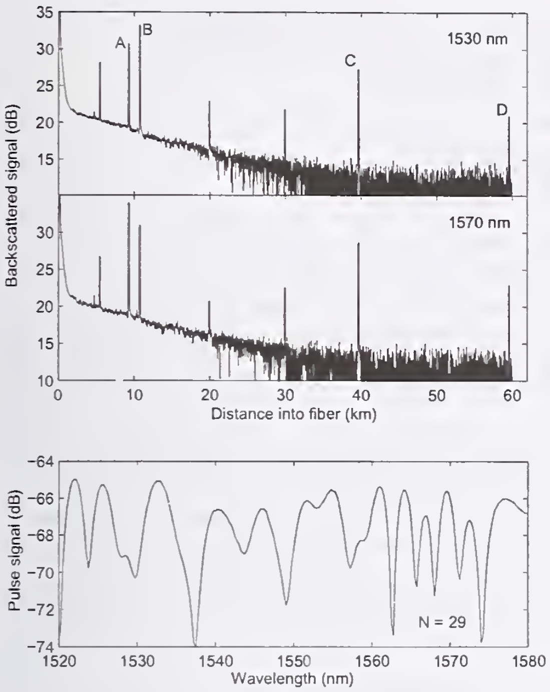

*Figure 3: Like figure 3, obtained with two-way measurements.*

in the PASR. Our results are compiled in Fig. 4. Each data point (ring) represents the average of two measurements made on a field-installed fiber, and the PMD value measured with the OTDR (one-way and two-way) is plotted against the PMD value measured with the JME method. We have included two error bars in the top figure (one-way measurements), $6\sigma_{\Delta\tau}/\sqrt{2}$ tall, with $\sigma_{\Delta\tau}$ computed from Eq. (2). (The $\sqrt{2}$ is introduced by an assumption of each data point representing two statistically independent measurements). For a given PMD value, corresponding error bars for the two-way measurements would be about 5% smaller than for the one-way [2]. Considering the error bars, accurate comparison between the two measurement methods cannot be made. The average ratio between the OTDR measurement results and the JME results is 1.012 ± 0.083 for the one-way measurements, and 0.957 ± 0.098 for the two-way. The '±' represents 3 standard deviations of the average (not of individual measurements).

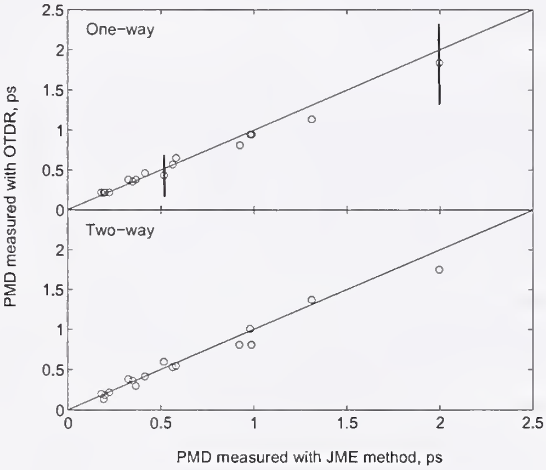

*Figure 4: Polarization mode dispersion (PMD) measured with the tuneable reflectometer (OTDR) plotted versus PMD measured with a polarimeter, using each of the setups in Fig. 1. The straight lines represent perfect agreement.*

*Discussion:* In [3] we estimated that it should be possible to measure tens of fibers in parallel with our setup, assuming shot noise limited detection and perfect Fresnel reflection from the fiber ends. Both assumptions may be difficult to meet in practice. An advantage of the setup shown in Fig. 1(a) compared to the one in Fig. 1(b) is that we do not have to rely on an unknown reflection from the far end. By using the far-end power splitter we obtain an OTDR signal that is more than 25 times larger than we can ever obtain with reflections from glass-air interfaces. (Somebody, however, has to go to the far end and mount a power splitter and a polarizer before the measurements can be performed.)

As discussed in [3], for large *N*, the time needed to perform a measurement on *N* fibers is proportional to $N^2$. An alternative then is to use a fiber switch instead of the power splitter, in which case the time needed to perform a measurement is proportional to *N*.

One purpose of our measurements was to find how well the two OTDR methods and the JME method for measuring PMD agreed on our field installed cables. Our measurements indicate agreement within a factor of 0.96, and are not nearly extensive enough for an accurate verification of any disagreement between the three methods. Most of the measurements shown in Fig. 2 yielded PMD values considerably less than 1 ps, corresponding to few oscillations in the PASR curve, with correspondingly large uncertainty in the measured PMD.

Eq. (2) seems to indicate that two-way measurements are more accurate than one-way, because they yield PASR curves with more extrema. Actually, the opposite may be true for long fibers, because of the reduced signal obtained in two-way measurements due to fiber attenuation.

*Conclusion:* We have demonstrated one-way and two-way measurements of polarization mode dispersion (PMD) on optical fibers in field installed cables, using a tuneable optical time domain reflectometer (OTDR). The measurements were performed on groups of four fibers in parallel, and access to both ends of the fiber was not required during the measurement. Within our measurement uncertainty, we have observed agreement between the two OTDR methods and the JME method. Even though individual measurements have limited accuracy, the measurement method is well suited for surveying the overall PMD status of an operator's network.

**References:**

1 POOLE, C. D., and FAVIN, D. L., 'Polarization-Mode Dispersion Measurements Based on Transmission Spectra Through a Polarizer,' *J. Lightwave Technol.*, 1994, 12, (6), pp. 917-929.

2 GALTAROSSA, A., PALMIERI, L., SCHIANO, M., and TAMBOSSO, T., 'Single-End Polarization Mode Dispersion Measurement Using Backreflected Spectra Through a Linear Polarizer,' *J. Lightwave Technol.*, 1999, 17, (10), pp. 1835-1842.

3 KLEIVSTUL, A. O. and SUDBØ, A. S., 'Simultaneous measurement of polarization mode dispersion in several optical fibers in parallel,' *Electronics Letters,* vol. 37, no. 10, pp. 621-623, 2001.

4 HEFFNER, B. L., 'Automated Measurement of Polarization Mode Dispersion Using Jones Matrix Eigenanalysis,' *IEEE Photonics Technol. Lett.*, 1992, 4, (9), 1066-1069.

# Analysis and comparison of measured DGD data on buried single-mode fibers

**Christopher Allen[1], Pradeep Kumar Kondamuri[1], Douglas L. Richards[2], and Douglas C. Hague[2]**
[1]Lightwave Communication Systems Laboratory
Information and Telecommunications Technology Center (ITTC)
The University of Kansas, Lawrence, Kansas 66045
[2]Sprint Corporation, Overland Park, Kansas

## Abstract

Temporal and spectral measurements were made on three different 95-km fibers within a slotted-core, direct buried, standard single-mode fiber-optic cable over many days to characterize DGD variability. From this data we observed that DGD varies slowly over time but rapidly over wavelength. This data showed good agreement with a Maxwellian distribution. The frequency-averaged mean DGD varied by about 10% or less during the periods that included significant temperature swings. Outage analysis showed that for system tolerances of three times the mean DGD, outages will occur typically every 3 to 8 years with mean outage durations ranging from about one to two hours. From this analysis we conclude that high-DGD episodes are spectrally localized and will be exceedingly rare and short lived.

## Introduction

Polarization-mode dispersion (PMD) may be a major impediment for network operators seeking to increase the per channel data rate on long-haul fiber-optic links. While the differential group delay (DGD, or $\Delta\tau$) in buried fiber had negligible impact at 2.5-Gb/s signaling rates, upgrades to 10 Gb/s, 40 Gb/s and beyond will require increasingly more attention. While there are PMD challenges facing carriers operating at 10 Gb/s, these challenges are not as severe as originally feared. Major carriers are successfully deploying 10-Gb/s dense-wavelength division multiplexed (DWDM) links across the core of their networks. A marked improvement in the DGD tolerance of 10 Gb/s long-reach receivers (to about 40 ps) will likely satisfy most length demands, obviating the need for PMD compensation (PMDC). Signaling rates of 40 Gb/s and beyond will most likely require some form of mitigation in long-haul applications, such as robust modulation schemes or PMDC.

To ensure signal quality on their fiber at higher bit rates, network engineers must anticipate the impact of PMD on the various fiber routes. An understanding of the variability of both the DGD and the principal states of polarization (PSPs) is required to specify appropriate transmission parameters. Factors such as the mean DGD, PMD correlation time and bandwidth, as well as second-order effects together with performance prediction models can provide this understanding.

The availability of measured PMD data on installed, buried fibers is limited. In this paper we present measured DGD data for buried, standard single-mode fiber to improve our understanding of the variability of PMD. While PMD is a vector quantity, with a magnitude (DGD) and a direction (PSP), we are only focusing on the DGD. The statistical distribution and behavior of PSPs has been extensively studied and is shown to be correlated to DGD behavior [1,2].

## Experimental setup

Experiments were conducted to measure the instantaneous DGD on three different 95-km fibers (1, 2, and 3) within a slotted-core, direct buried, standard single-mode fiber-optic cable made available by Sprint. A polarization analyzer employing the Jones-Matrix-Eigenanalysis (JME) method was used for measurements at wavelengths from 1510 nm to 1625 nm with a spectral resolution of 0.1 nm (about 12.5 GHz). Measurements on fiber span 1 were repeated approximately every 3 hrs and they were carried on for about 86 days whereas on fiber spans 2 and 3 they were repeated approximately every 1½ hours and carried out for about 14 and 9 days, respectively. Over the 86 days (from Nov. 9, 2001 through Feb. 2, 2002) 692 measurements were made on fiber span 1 across the 1150 discrete wavelengths representing 795,800 measured values. For fiber spans 2 and 3 the corresponding number of DGD measurements is about 271,600 and 181,700.

## Plots of DGD vs. wavelength and time

Figures 1, 2, and 3 show in a color-coded format normalized DGD data (i.e., DGD/mean DGD) measured on the three fiber spans, respectively. From the plots it is clear that for buried fibers DGD changes with time but not at a rapid rate. This variation is random and differs from fiber to fiber. It is also evident that the DGD varies significantly with wavelength and relatively high-DGD events are spectrally localized.

A histogram of the normalized DGD data on fiber span 1, shown in Figure 4, is seen to have shape consistent with a Maxwellian distribution, as expected. A curve representing a Maxwellian distribution for a 1-ps mean DGD is also plotted for comparison.

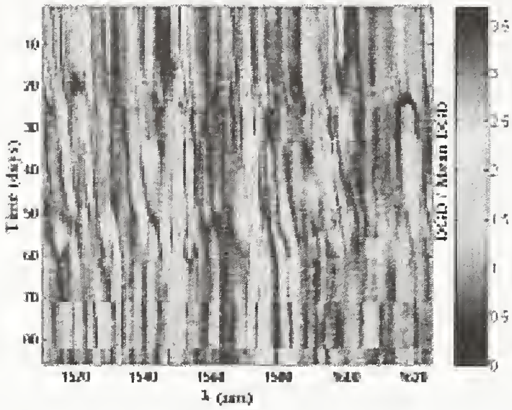

Figure 1. Measured, normalized DGD vs. wavelength and time for fiber span 1 (86 days of data).

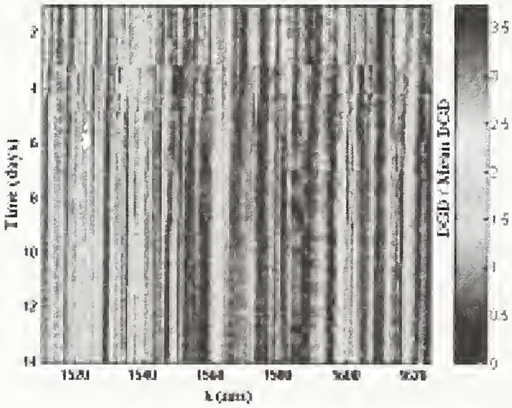

Figure 2. Measured, normalized DGD vs. wavelength and time for fiber span 2 (14 days of data).

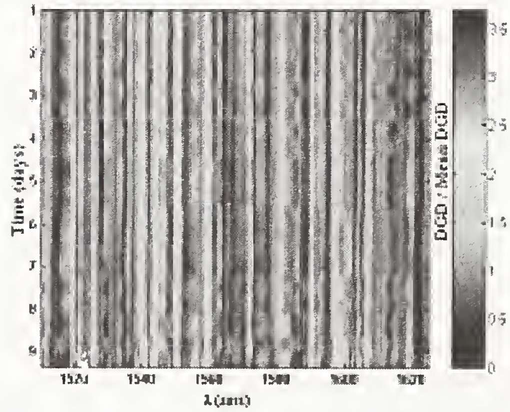

(c)

Figure 3. Measured, normalized DGD vs. wavelength and time for fiber span 3 (9 days of data).

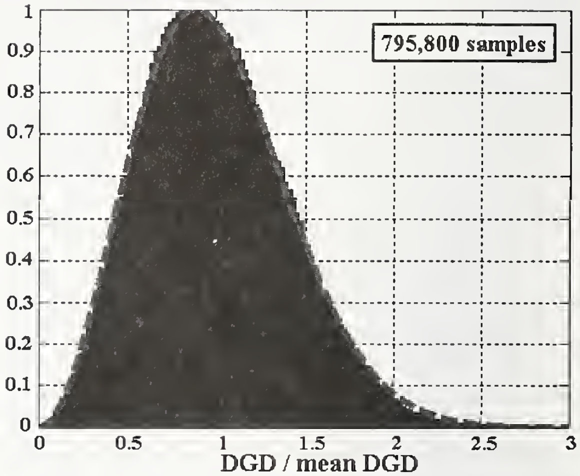

Figure 4. Histogram of measured, normalized DGD data on fiber span 1.

Similar histograms were obtained for the data on the other two fiber spans (plots not shown here) and they also showed good agreement with a Maxwellian distribution.

### Mean DGD variation with time

To observe the time-dependent nature of DGD more closely, 1150 DGD measurements over all wavelengths were averaged together to obtain frequency-averaged DGD data, denoted as $\langle DGD \rangle_{\lambda}$ normalized by the overall mean DGD (averaged over both time and frequency), denoted as $\langle\langle DGD \rangle_{\lambda} \rangle_{t}$. Since temperature is a known driver in changing DGD changes, hourly air temperature data for the region were collected as well. The variation of frequency-averaged DGD and temperature with time on the three fiber spans is shown in Figures 5, 6 and 7. From Figure 5 it can be observed that frequency-averaged DGD varies by only about ±10% over 86 days of observations that included significant temperature swings. Since the entire length of the fiber is buried, the diurnal temperature variations do not represent the fiber temperature. Statistical analyses reveal no significant correlation between long-term temperature variations and the frequency-averaged mean DGD.

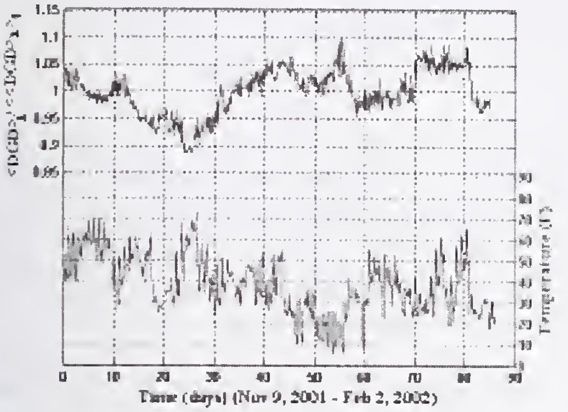

**Figure 5. Frequency-averaged DGD and temperature vs. time for fiber span 1.**

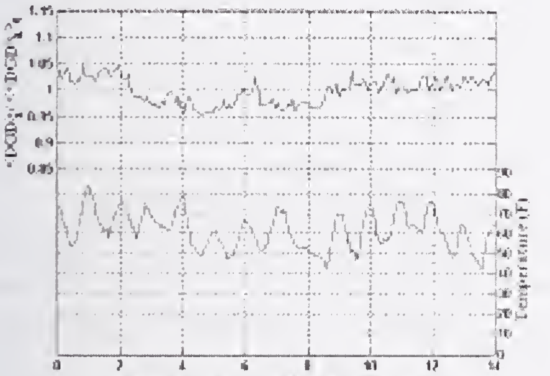

**Figure 6. Frequency-averaged DGD and temperature vs. time for fiber span 2.**

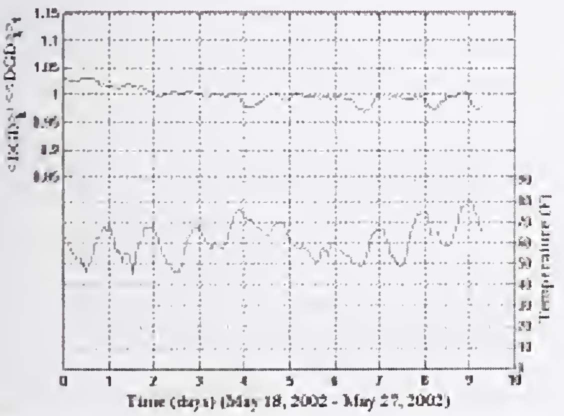

**Figure 7. Frequency-averaged DGD and temperature vs. time for fiber span 3.**

## System outage analysis

An outage event is one which exceeds the given threshold value of DGD, $\Delta\tau_{th}$. The outage probability $P_{out}$, expressed in minutes/year, can be calculated from the Maxwellian probability distribution function (pdf), $f_\tau(\cdot)$ as

$$P(\Delta\tau \geq \Delta\tau_{th}) = 1 - \int_0^{\Delta\tau_{th}} f_\tau(\Delta\tau)\, d\Delta\tau \qquad (2)$$

and then multiplying the number of minutes in a year. As $P_{out}$ is based on the Maxwellian pdf, it may be expressed as a function of one independent variable $M = \Delta\tau_{th}/(\text{mean DGD})$ as $P_{out}(M)$ and is clearly fiber independent and will be the same for all installations.

In cases where the probability of an outage is quite small, $P_{out}$ represents the annualized outage probability based on long time records, however no insight is provided regarding the outage rates and their durations. Accurate estimation of the impact of PMD on network availability requires statistical analysis of the DGD variability. Caponi et al. [3] showed how the mean time between PMD-related outages could be estimated from the temporal characteristics of DGD variations and the Maxwellian probability density function. The mean outage rate, $R_{out}$ (defined as the mean number of outage events per unit time with units of events/year), is found using [3]

$$R_{out} = \frac{1}{2} f_\tau(\text{threshold}) \int_{-\infty}^{\infty} f_{\tau'}(\Delta\tau')\,|\Delta\tau'|\, d\Delta\tau' \qquad (3)$$

where $\Delta\tau'$ is the time derivative of the DGD, and $f_{\tau'}(\cdot)$ is the pdf of $\Delta\tau'$. Caponi et al. observed $\Delta\tau$ and $\Delta\tau'$ to be statistically independent and also found that $R_{out}$ is cable and installation dependent.

Figure 8 shows the calculated outage probability, $P_{out}$, and the mean outage rate, $R_{out}$, for a given system threshold relative to the mean DGD on the three fiber spans.

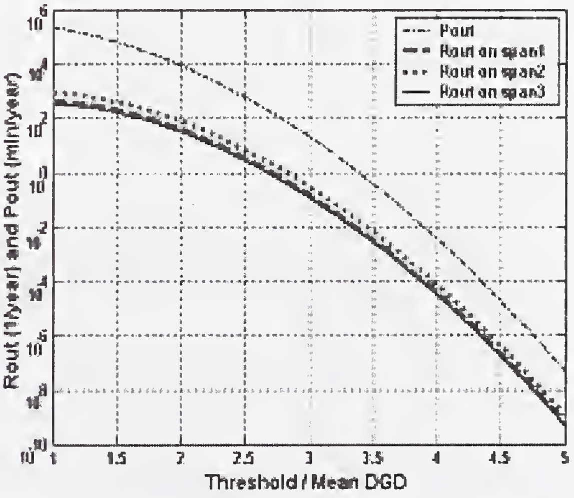

**Figure 8. Calculated outage probability, $P_{out}$, and mean outage rate, $R_{out}$, versus Threshold/Mean DGD.**

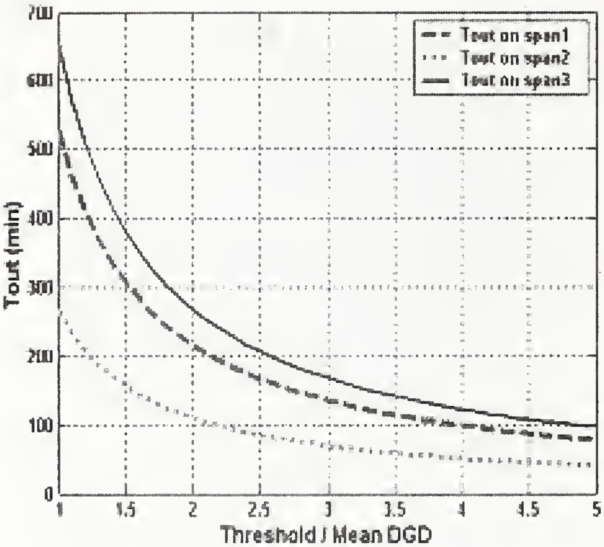

**Figure 9. Calculated mean outage duration, $T_{out}$, as a function of Threshold/mean DGD.**

**Table 1. Predicted mean time between outages (MTBOs) and mean outage durations for different DGD tolerances**

| | 3*<DGD> | 3.7*<DGD> |
|---|---|---|
| Span 1<br>MTBO<br>Outage duration | 6.39 years<br>136 min | 1648 years<br>108 min |
| Span 2<br>MTBO<br>Outage duration | 3.25 years<br>69 min | 833 years<br>55 min |
| Span 3<br>MTBO<br>Outage duration | 7.91 years<br>138 min | 2000 years<br>133 min |

The mean duration of DGD-induced outages can be determined using statistical analysis as well. Caponi et al. [3] showed that the mean outage duration, $T_{out}$, is

$$T_{out} = P_{out} / R_{out} \tag{4}$$

which has units of minutes.

Figure 9 shows the calculated mean outage duration, $T_{out}$, as a function of system threshold relative to the mean DGD. Since $T_{out}$ is found using $R_{out}$, which is cable and installation dependent, $T_{out}$ will also be cable and installation dependent.

From the above analysis, we can estimate the mean outage time between outages (MTBOs) and mean outage durations for various DGD tolerances for these fiber spans. Table 1 lists these values for system thresholds of three and 3.7 times the mean DGD.

For comparison, Nagel et al. [4] predicted that for the 114-km buried link they studied, the DGD will exceed three times its mean value once every 3.5 years and estimated a mean outage duration of between 10 and 20 minutes for their link. From data measured on 37-km of buried cable, Caponi [3] predicted the DGD will exceed three times the mean DGD once every 2.5 years with a mean outage duration of 56 minutes.

## Conclusions

We have measured DGD data on three different 95-km fibers within a slotted-core, direct buried, standard single-mode fiber-optic. From these measurements we observed that DGD varies slowly over time but rapidly over wavelength or frequency. Episodes of higher-that-average DGD were observed and seen to be spectrally localized and of limited duration.

To investigate the role of changing temperature on mean DGD variations, frequency-averaged DGD data were compared to temperature histories. The frequency-averaged DGD varied by only about ±10% over 86 days of observations that included significant temperature swings.

From this data predictions were made regarding the probability, and frequency of outage occurrence. While the statistics of Maxwellian processes adequately describe the annualized outage probability, further analysis of the DGD data revealed the mean time between outages and mean outage durations. For outages characterized by high DGD episodes (DGD more than three times the mean DGD), we found that the mean outage rates and durations for these three fibers to be similar. Our findings agree with reports by others that DGD excursions of three or more times the mean DGD are infrequent and relatively short lived. This finding is significant for network operators who must assess the impact of PMD on network reliability.

## Acknowledgment

This work was funded by Sprint Corporations Company, L. P. A special tribute is paid to Francis Yarkosky, for his leadership and support.

## References

[1] Karlsson, M. and J. Brentel, "Autocorrelation function of the polarization-mode dispersion vector," *Optics Letters*, 24(14), pp. 939-941, 1999.

[2] Karlsson, M., J. Brentel, and P. A. Andrekson, "Long-term measurement of PMD and polarization drift in installed fibers," *Journal of Lightwave Technology*, 18(7), pp. 941-951, 2000.

[3] Caponi, R., B. Riposati, A. Rossaro, and M. Schiano, "WDM design issues with highly correlated PMD spectra of buried optical fibers," *Proc. OFC 2002*, Anaheim, CA, ThI5, pp. 453-455, 2002.

[4] Nagel, J. A., M. W. Chbat, L. D. Garrett, J. P. Soigné, N. A. Weaver, B. M. Desthieux, H. Bülow, A. R. McCormick, and R. M. Derosier, "Long-term PMD mitigation at 10 Gb/s and time dynamics over high-PMD installed fiber," *Proc. ECOC 2000*, Munich, Germany Vol. II(4.2.1), pp. 31-32, 2000.

# Statistical evaluation of polarization-dependent losses and polarization-mode dispersion in an installed fiber network

C.J.K. Richardson[1], R. J. Runser[2], M. Goodman[2], L. Mercer[3]

[1]Laboratory for Physical Sciences, University of Maryland, College Park, MD
[2]Laooratory for Telecommunication Sciences & Telcordia Technologies, Adelphi, MD
[3]Naval Research Laboratory, Washington, D.C.

ABSTRACT: The statistical probability distributions of the differential group delay, the differential attenuative slope, and the polarization-dependent loss are determined from measurements of Jones matrices acquired as a function of time for several wavelengths within a single channel of several links on an installed metropolitan optical wavelength division multiplexed network. Analysis of the measured results forms a statistical picture that is not in conformity with theoretical descriptions that predict Maxwellian distributions.

The statistical behavior of pulse broadening in optical networks through the interaction of polarization-mode dispersion (PMD) and polarization-dependent loss (PDL) is needed by network operators and laboratory scientists in order to understand and predict real-world outage probabilities and to expand the limits of operation of installed networks to accommodate higher data rates and new modulation formats. It is known that the interaction between polarization mode dispersion and polarization dependent loss can combine to disperse an optical pulse by an amount that is greater than the contribution to dispersion made by birefringence alone.[1-3] Here we analyze the change in differential group delay (DGD), the differential attenuative slope (DAS), and the PDL of an installed fiber link on the Advanced Technology Demonstration Network (ATDNet) as a function of time. The measurements provide a means to compare the statistical transmission characteristics of a functional network link in a real-world environment with theoretical statistical models. To our knowledge, only one other measurement of PMD on an installed fiber span has been reported[4], but is the first to investigate a functional metropolitan area network and the first to consider PDL in addition to PMD.

Experiments were conducted on the ATDnet optical test bed, which is a transparent, 8 channel, wavelength division multiplexed network in the Washington, D.C. metropolitan area. Fig. 1 describes the experimental setup. The loop under test consisted of a round trip through a pair of 40 km SMF-28 fiber spans between two nodes, the LTS and DARPA/ISI, which have gain clamped Erbium-doped fiber amplifiers (EDFA) located at the midpoint. The test signal was passively multiplexed into the WDM fiber at the LTS. At the DARAP/ISI node, the WDM channel under test was separated from the network using a commercial 100 GHz wide wavelength division demultiplexer and patched directly into the output multiplexer for return to the LTS. EDFA's were located on both trunk sides of the optical add drop multiplexers at the loop-back location. Upon return to the LTS, the signal was split and filtered using a 200 GHz demux and sent to the measurement apparatus.

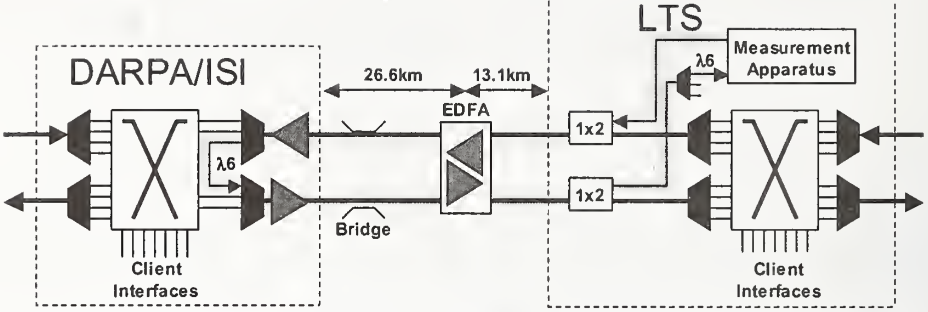

Fig. 1 Experimental test of a loop back between DARPA/ISI and LTS on ATDNet.

The CW optical signal was generated and detected in the same location using a tunable external cavity semiconductor laser. The output Stokes parameters from three input polarization states that were measured by an HP8509B polarization analyzer were used to calculate the Jones matrices of the fiber loop for twelve different wavelengths within a 100 GHz passband centered around ATDNet λ6. Measurements of the Jones matrix were obtained every 5 seconds for approximately 7 days. The DGD and the DAS are determined using the Pauli spin matrix equivalence[5] to examine the operator $T_\omega T^{-1}$ where T represents the frequency dependent Jones matrix of the network link under test, and the subscript ω denotes differentiation with respect to the angular optical frequency. In general, the operator $T_\omega T^{-1}$ calculated from measured data is not traceless. However, the Jones matrices can be represented as $T(\omega)=\exp[-A(\omega)-iB(\omega)]T_0(\omega)$ where $T_0(\omega)$ is the measured Jones matrix and $T(\omega)$ contains the polarization dependent information of interest here. The factors A and B are determined from the average values calculated from the Jones matrix at each wavelength under test. Satisfying the traceless condition allows the real (Ω) and imaginary (Λ) components of the PMD vector to be expressed in terms of the Pauli spin matrices, which can be determined from $T_\omega T^{-1}$ by inspection using

$$T_\omega T^{-1} = \frac{\left(T(\omega_o+\delta\omega)-T(\omega_o-\delta\omega)\right)}{2\delta\omega} T^{-1}(\omega_o) = -\frac{i}{2}\left[\vec{\Omega}+i\vec{\Lambda}\right]\cdot\vec{\sigma}. \tag{1}$$

The magnitude of $\vec{\Omega}$ is the DGD while the magnitude of is $\vec{\Lambda}$ the DAS. The derivative of the Jones matrix is completed using a center difference 2-point scheme, which is then averaged to obtain a single first-order value of the DGD and the DAS. This approach was selected to minimize the error associated with calculating the derivative and the influence of error resulting from time-dependent variations in the Jones matrix. The magnitude of the PDL vector is determined by converting the measured Jones matrix into a 4x4 Mueller matrix and calculating the maximum and minimum transmission components.

As shown in Fig. 2, measurements of the transmission characteristics indicated a dynamic behavior in the DGD, DAS, and PDL that evolved over time. Upon inspection of the fiber route for this link, it was discovered that there was a bridge crossing between the two nodes. To investigate the influence of possible environmental factors, the component of the average wind speed that is perpendicular to the bridge span was obtained for time duration of these measurements. It is apparent that there may be a causal relationship between this environmental variable and the transmission characteristics as suggested by the correlation. These observations are a departure from the formulation of conventional theoretical descriptions that use a fully stochastic model to describe the polarization dependent transmission characteristics for PMD and residual PDL.

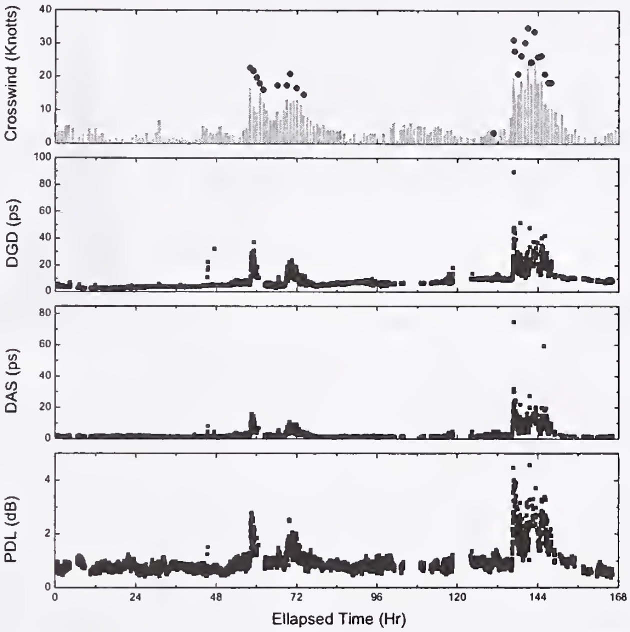

Figure 2. Temporal evolution of the DGD, DAS and PDL compared to one vector component of the average wind speed (gray bars) and gust speed (circles) measured from the National weather service. A causal relationship between wind speed and the transmission characteristics is suggested by the apparent correlation.

One would expect that the histograms of these measured components to vary from the expected Maxwellian distribution. Figures 3 and 4 show the normalized histograms of the DGD, the DAS, and the PDL compared with a normalized Maxwellian distribution that is calculated using the mean value of each quantity.

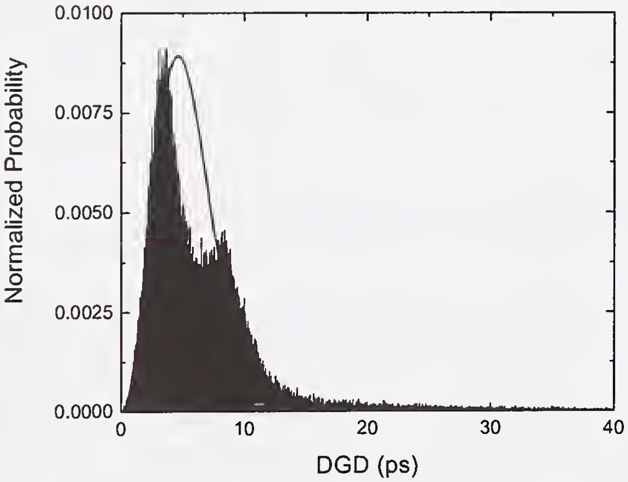

Figure 3 The normalized histogram of the DGD (filled distribution) and the normalized Maxwellian curve (solid line) that is calculated using the mean DGD.

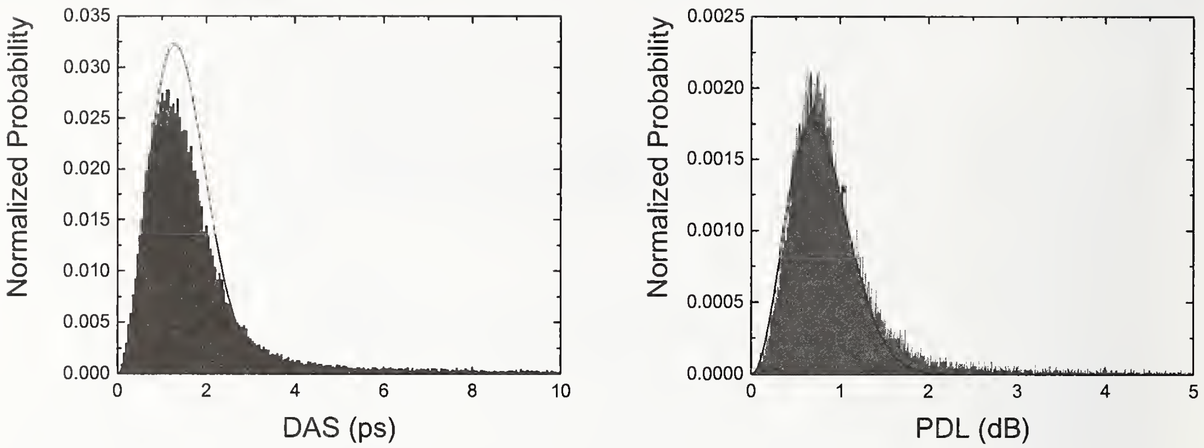

Figure 4 The normalized histogram of the DAS (left) the PDL (right) and the normalized Maxwellian curve (solid lines) that are calculated using the mean values.

Understanding the actual statistical behavior of links under the influence of dynamic real-world conditions is required to develop a complete model of the polarization evolution that is representative of an installed fiber plant. These measurements suggests that upgrading capacity and bit rate on fiber plant may depend upon the condition and placement of its installation. Given that a large portion of the installed fiber plant in metropolitan areas is older, SMF-28 fiber, designed to support low bit rate (<10 Gb/s), single wavelength channel applications, dynamic compensation and novel modulation techniques may be required along certain spans to enable capacity upgrades in the presence of these effects.

The results shown here will be presented and compared to measurements on other links of the ATDnet and as well as on BOSSNET, a long haul WDM testbed. Other statistical quantities relating to the DGD and the DAS such as magnitude and vector correlations will be explored.

**References:**

[1] B. Huttner, C. Geiser, and N. Gisin, "Polarization-induced distortions in optical fiber networks with polarization-mode dispersion and polarization-dependent loss," IEEE Journal of selected topics in quantum electronics, vol. 6, pp. 317-329, 2000.

[2] Y. Li and A. Yariv, "Solutions to the dynamical equations of polarization-mode dispersion and polarization-dependent losses," Journal of the Optical Society of America B, vol. 17, pp. 1821-1827, 2000.

[3] N. Gisin and B. Huttner, "Combined effects of polarization mode dispersion and polarization dependent losses in optical fibers," Optics Communications, vol. 142, pp. 119-125, 1997.

[4] M. Karlsson, J. Brentel, and P. Andrekson, "Long-term measurement of PMD and polarization drift in installed fibers," Journal of Lightwave Technology, vol. 18, pp. 941-951, 2000.

[5] J. P. Gordon and H. Kogelnik, "PMD fundamentals: Polarization mode dispersion in optical fibers," PNAS, vol. 97, pp. 4541-4550, 2000.

# Programmable Polarization-Mode-Dispersion Generation

J. N. Damask, P. R. Myers, T. R. Boschi
*YAFO Networks, 1340F Charwood Rd., Hanover, MD 21076, jdamask@yafonet.com*

**Abstract:** Combination of programmable polarization-mode-dispersion generation with numerically generated PMD statistics, field measurements of temporal PMD evolution profiles, and PMD measurement instrumentation rounds out a complete suite of tools that can provide reliable tests as to the long-term performance of an optical transmission system or any active subsystem such as a receiver or PMD compensator.

## 1. Introduction

It is an unfortunate misconception in much of the optical telecommunications industry that simply because fiber-generated polarization-mode-dispersion (PMD) is arbitrarily complex, testing a receiver for PMD tolerance needs to be arbitrary or complex [1-7]. The reality is that much detailed performance information can be derived from systematic measurements with a robust programmable PMD generator, numerically generated PMD statistics, and field measurements of temporal PMD evolution profiles. In particular, the total outage probability (TOP) of a receiver, transmitter / receiver pair, or entire system can be estimated by combining measurements of receiver sensitivity to first-, second-, and higher-orders of PMD with PMD probability statistics [8]. The mean-time-between failure (MTBF) and mean-duration of failure (MDoF) can also be estimated when the temporal PMD-evolution profile of a fiber link is measured [9-10]. The estimators TOP, MTBF, and MDoF form evaluation metrics necessary for apples-to-apples comparisons between system designs as well as for development of PMD mitigation techniques.

The paradigm followed in this paper requires direct measurements of receiver performance against PMD stress. PMD statistics are relegated to analysis rather than laboratory inputs. Direct measurements of receiver performance are essential due to the many factors that make numeric simulation of the receiver unreliable. Typical link receivers use square-law detectors, electrical band-limiting filters, and limiting amps. State-of-the-art receivers can also use active phase and threshold adjustments to tune performance. Moreover, a receiver in an optical link is sensitive to linear effects, including noise accumulation, chirp, chromatic dispersion, polarization-dependent loss, PMD, and jitter; and non-linear effects, including nonlinear pulse propagation, nonlinear polarization rotation, and forward-error correction. To date, the industry has developed actual or at least *de facto* standards on how to test for most of these impairments, isolated or combined. PMD testing, however, has remained an outlier.

The metrics to gauge a successful PMD generator implementation include: a) a complete addressable PMD space; b) stable PMD (and SOP) at any state; c) predictable PMD generation; d) repeatable PMD generation; e) access to 1st-order PMD, to 2nd-order PMD components depolarization and polarization-dependent chromatic dispersion (PDCD), and higher PMD orders; f) good optical performance such as insertion loss and PDL. Conspicuously absent is any requirement to match PMD statistics. A complete addressable PMD space means that any PMD state can be generated without regard to the likelihood that a fiber would arrive at that state.

## 2. Mapping a Transceiver for PMD Tolerance

The first step to qualifying a transmitter / receiver pair for PMD tolerance is to create a Tx/Rx map. Figure 1 illustrates a basic test setup to automatically generate a PMD tolerance map. A map is created by inserting a programmable PMD source between the transmitter and receiver. In order to cover all projections of the input state of polarization (SOP) onto the PMD vector, a polarization scrambler is added before the PMD source. In cases where the receiver is preceded by a polarization-tracking subsystem, such as a PMD compensator, a second polarization scrambler is required after the PMD source to scramble the output Principal State of Polarization (PSP) of the PMD source. An actual system link or a lumped model of one is located after the PMD source and scramblers. A typical lumped model is a noise source and low-PMD fiber spool to establish a known OSNR and level or chromatic dispersion. A BERT set is used to measure error rate, Q, or Q-penalty, depending on the application. Computer control is used to coordinate error measurements with the PMD state, OSNR setting, etc. One point to note is that the dwell time at any PMD state needs to be long enough for the first polarization scrambler to cover the Poincare sphere. In practice this can take about 5 minutes using a commercially available fiber-based scrambler. Haunstein has performed detailed analysis to show that polarization scrambling is about as pessimistic as launching known, worst-case polarization states [11].

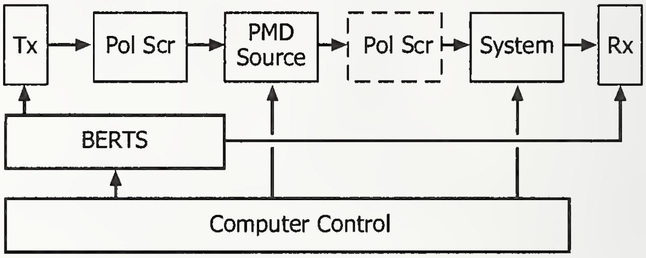

**Fig. 1:** Schematic diagram of an automated test set to create a PMD tolerance map of the Tx/Rx pair. A map may use 200 PMD states.

The number of PMD states addressed to create a map depends on the application. The first map of any receiver would likely cover 200 pre-determined, well separated states. It is reasonable to suppose that a program can be written to adaptively measure states to trace performance contours; however, no such program has been written to date. Once a receiver profile is known, spot sampling is typically performed to check for consistency. Figure 2 shows two Tx/Rx maps, each measured using 150 PMD addresses in DGD, SOPMD space. The SOPMD space was depolarization only. Regions of similar color indicate the same error-rate. Each map took about 13 hours to measure. The mapped receivers are clearly characteristically different. In the first case, the receiver is largely sensitive to both DGD and SOPMD. In the

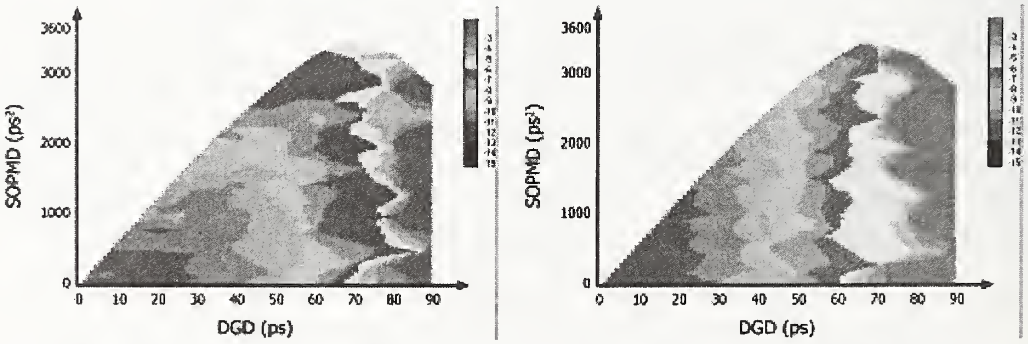

**Fig. 2:** Two receiver maps made with a programmable PMD source. Each map is generated with 150 states. The map on the left exhibits sensitivity to both DGD and SOPMD. The right map is much more tolerant to SOPMD.

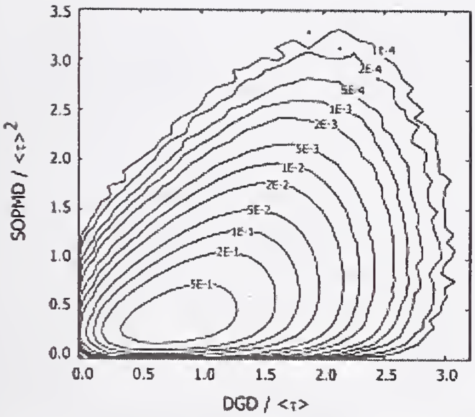

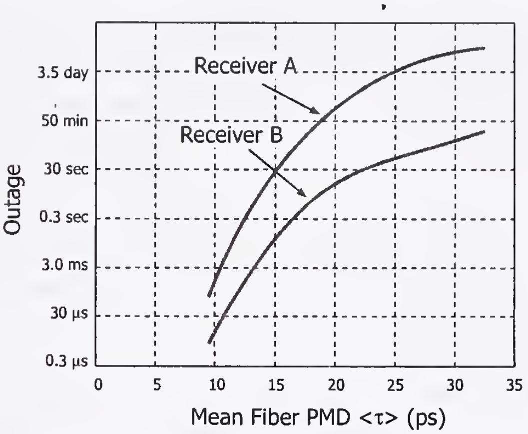

**Fig. 3a** Computer generated universal joint probability contours of 1st- and 2nd-order PMD statistics at one optical frequency for a fiber having 2000 sections. The labels indicate the area that remains outside of the associated contour. The DGD axis scales with <τ>, the fiber mean DGD, while the SOPMD axis scales with $<\tau>^2$.

**Fig. 3b** Estimates of TOP over measured PMD space. Since the JPDF scales with <τ>, TOP is calculated for any mean fiber PMD given a single BER map across PMD space.

second case, the receiver is quite insensitive to SOPMD but rolls off with DGD alone. Both receivers are of typical design and built using commercially available components. The PMD maps qualitatively reveal actual differences in the two receiver designs. Aided by a receiver map, a receiver designer can work to improve the PMD tolerance.

### 3. Measurement-Based Estimation of Total Outage Probability

Figure 2 showed the qualitative difference between two receivers. Quantitative metrics, such as the Total Outage Probability (TOP), can be estimated by combining receiver maps with a pre-calculated Joint Probability Distribution Function (JPDF) for DGD and SOPMD. Figure 3a shows a calculated JPDF. The function is universal because the DGD scales as the mean fiber PMD and the SOPMD scales as the square. This function was numerically calculated using 1 billion fiber instances where each fiber comprised 2000 sections [12]. The contours are of constant probability. Importance-sampling techniques have been developed by Kath [13] to calculate far more rare contours in DGD, SOPMD space. Such extensive JPDFs are definitely desirable for outage probability calculations.

TOP is calculated using the equation

$$\mathrm{TOP}(\langle\tau\rangle) = \sum_{\tau,\tau_\omega} \mathrm{I}(\mathrm{Penalty}_{\tau,\tau_\omega} > \mathrm{TOL})\ \Pr(\tau,\tau_\omega;\langle\tau\rangle) \tag{1}$$

where $\Pr(\tau, \tau_\omega; <\tau>)$ is the probability of address $\{\tau, \tau_\omega\}$ given a fiber mean PMD of <τ>. *I* is the indicator function, and *TOL* is some chosen tolerance for penalty. What is interesting with Eq. (1) is that TOP scales continuously with <τ>. Figure 3b shows TOP estimates for the two receiver maps of Fig. 2. The TOP estimates plot outage probability against the parameter axis <τ>. The plots cut off below DGD < 10 ps because the JPDF as used does not have enough visibility into events below 1E-4 and because the paucity of measured points at low PMD values. Work still needs to be done to evaluate the confidence bounds for the TOP values.

## 4. Measurement-Based Estimation of MTBF and MDoF

Total outage probability is a useful metric to estimate the expectation value how many severely errored seconds in a unit period of time, e.g. a year, one would encounter due to PMD. However, this metric doesn't really apply in a protected network. A protected network will typically switch to the backup line within 50 ms. After the switching event, the downed line can remain PMD-impaired for hours without affecting traffic (however, of course, the backup route now runs unprotected). The question then becomes how many switching events are likely (MTBF), and what is the average duration of an outage (MDoF), given a TOP estimate [9]. This question can be addressed combining a receiver map, which characterizes the receiver behavior, the JPDF, which provides the PMD statistics, and a fiber temporal evolution profile (TEP).

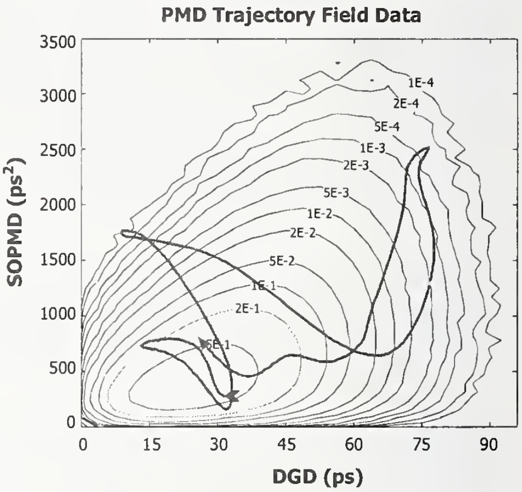

**Fig. 4:** Measured temporal trajectory of DGD, SOPMD at one frequency on an installed fiber, with the JPDF for <30>ps fiber

A TEP can be directly measured on a particular fiber route by taking a series of PMD vs. wavelength scans over a longer period of time. The work reported in [9] conjectured, and supported through experiment, that the temporal change of DGD was itself independent of the magnitude of DGD. From this observation they calculated a correlation time of DGD change and used to that to estimate MTBF and MDoF. Work done at Yafo and reported in [10] extends the conjecture to assert that temporal change in DGD and SOPMD are independent of any instantaneous DGD, SOPMD magnitudes. Long-term test data was measured by Yafo on a carrier network to determine the autocorrelation time of DGD, SOPMD change. The experiments supported the conjecture of separability. Figure 4 shows a particularly severe PMD evolution in time. Once the TEP is estimated, numerical calculations are

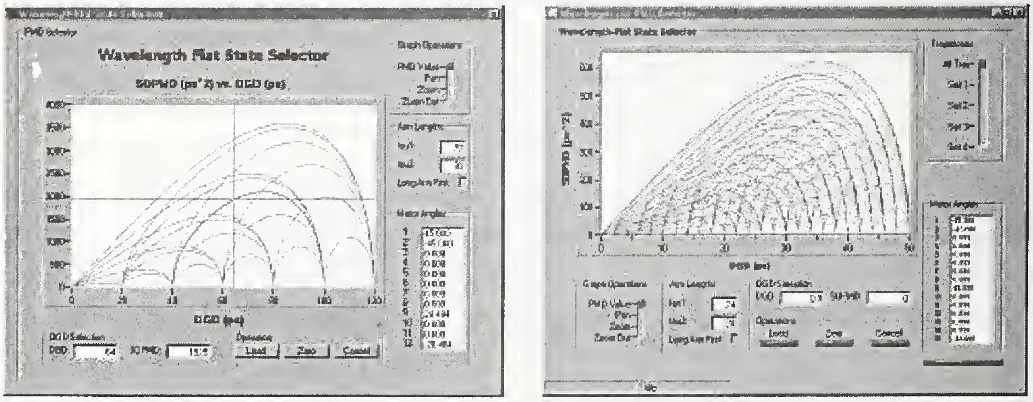

**Fig. 5:** GUI interfaces for 12-stage and 15-stage incoherent PMD emulators. Left, contours of wavelength-flat states for 12 equal-length stages over 10.0 ps per stage. Wavelength-flat states are those where the DGD and SOPMD are independent of frequency. The outer contour is governed by two groups of six stages. Right, contours of wavelength-flat states for a binary-weighted 15-stage emulator. The stages were 2x1 ps, 2x2 ps, and 11x4 ps. While the 15-stage state space is more complete than the twelve stage. Neither implementation offers continuous motion in PMD space.

used to find MTBF and MDoF distributions. While this work is fully reported in [10], the findings generally are that short durations at severe states are more common than long durations. Therefore, as TOP increases, the number of switching events expected in a network increases.

## 5. Incoherent PMD generation

Two types of incoherent programmable PMD sources have been built by the authors. The first type uses 12 equal length birefringent crystal stages, constructed to be passively athermal [14, 15]. The second type uses 15 stages, where the first stage pair is one-quarter the nominal length, the second pair is one-half the nominal length, and the remaining 11 stages are full length. Half-wave waveplates are inserted between each stage to programmatically induce polarization mode-mixing. Both source types are predictably operated in wavelength-flat states. A wavelength-flat state is one where neither the DGD nor SOPMD spectra vary with wavelength. This can only be achieved when the stages are arranged in two groups. Within a group the extraordinary crystal axes are aligned. The group lengths and the angle of the waveplate located at the interface of the two groups determines the DGD and SOPMD.

Figure 5 shows the GUI interface used to select the PMD states in DGD, SOPMD space. The interface on the left shows the 21 wavelength-flat trajectories available for a 12-stage PMD source. The interface on the right shows the ~134 wavelength-flat trajectories available for the particular 15-stage PMD source built at Yafo. The obvious purpose of the 15-stage design is to increase the coverage of wavelength-flat states within the outer envelope. Both sources have been used to generate receiver maps at both 10G and 40G. The maps shown in Fig. 2 were generated using a 12-stage source.

## 6. Coherent PMD generation

While the programmable sources of the last section have been used for years, there is need for advanced methods of PMD generation that provide predictable generation of PDCD. The preceding sources are called incoherent because the birefringent phase from one stage to the next is unknown at the time of construction. A new generation of PMD sources have been developed at Yafo where the three critical PMD parameters, the DGD of a stage, the mode mixing between stages, and the birefringent phase of each stage, are established during construction. An important way to construct a PMD source is where all the DGD stage values are an integral multiple of a unit value, e.g. equal, and where the birefringent phase of each section is the same. An instrument so constructed generates coherent PMD.

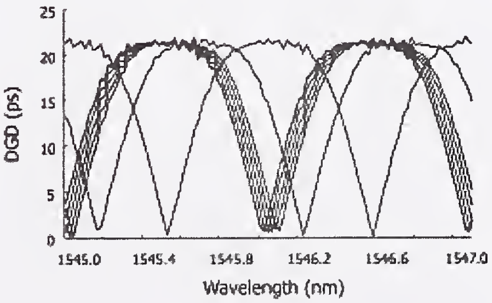

**Fig. 6:** Continuous frequency shift of a coherent DGD spectrum while the spectral shape remains intact. In a test, either the PMD source or the signal laser needs to sweep frequency. Here it is the source that sweeps.

A coherent multi-stage PMD source has been built by the authors where the birefringent phase is corrected using a classic ¼-½-¼ phase shifter as in [16, 17, 18]. During construction, the birefringent phase of a section is measured, then the phase shifter is engaged to correct for any error. Serial application of this procedure results in a fully coherent instrument. As the phase shifters in the instrument can be actuated, the frequency position of the PMD spectrum can be shifted without changing the shape of the spectrum. Figure 6 shows a DGD spectrum that has been frequency shifted over a free-spectral range. The ability to frequency shift the PMD spectrum is essential when the spectrum exhibits structure. Without this ability, the transmitter laser frequency would have to be swept in order to experience the structure of the spectrum.

Another feature of this coherent multi-stage source is that DGD and SOPMD can be independently controlled at the center frequency. Such independence allows the PMD state to be continuously addressed across DGD, SOPMD space, unlike the incoherent generators of the preceding section. Also, in combination with the frequency shift ability, the SOPMD magnitude can be resolved into depolarization and PDCD components. The user can then choose a fixed value of DGD and span the range of available depolarization and PDCD values. In this way, the coherent PMD generator can address three-dimensional PMD space: {DGD, depol, PDCD}. Figure 7 shows three generated spectra of DGD and SOPMD. The DGD value at center frequency is fixed at 35 ps while the SOPMD changes from maximum towards a narrow-band zero value.

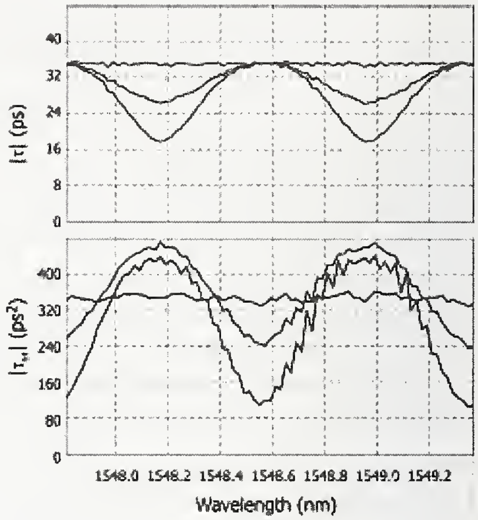

**Fig. 7:** Three measured PMD spectra from a coherent multi-stage PMD source. At center frequency DGD and SOPMD are independent. The PMD spectra exhibit structure. Combined with frequency shifting, a receiver can be inspected across a wide range of PMD states.

**Acknowledgement:** The authors wish to thank our colleagues G. Gray, P. Leo, D. Longbottom, K. Rochford, G. Simer, as well as the rest of the Yafo engineering staff.

**References**

[1] I. T. Lima Jr *et al*, “Polarization Mode Dispersion Emulator,” in *Proc. OFC 2000*, 2000, Paper ThB4.

[2] S. Lee *et al*, “A short recirculating fiber loop testbed with accurate reproduction of Maxwellian PMD statistics,” in *Proc. OFC 2001*, 2001, Paper WT2.

[3] I. T. Lima Jr. *et al*, “Comparison of Polarization Mode Dispersion Emulators,” *J. Lightwave Techno*., vol. 19, no. 12, pp. 1872, Dec. 2001.

[4] C. H. Prola Jr *et al*, “PMD emulators and signal distortion in 2.48 Gb/s IM-DD lightwave systems,” *IEEE Photon. Technol. Lett*., vol. 9, pp. 842, June 1997.

[5] S. Lanne *et al*, “Demonstration of adaptive PMD compensation for 40Gb/s,” in *Proc. OFC ’01*, Anaheim, CA 2001, Paper TuP3.

[6] Y. Xie *et al*, “Enhanced PMD mitigation using FEC coding and first-order compensator,” in *Proc. OFC ’01*, Anaheim, CA 2001, Paper WAA2.

[7] W. Shieh, “Accelerated Outage Probability Testing for PMD Induced Impairment,” *IEEE Photo. Technol. Lett*., vol. 12, pp. 1364, October 2000.

[8] A. Ayer *et al*, “Mapping PMD quantifies system performance,” *WDM Solutions,* April 2002.

[9] R. Caponi *et al*, “WDM design issues with highly correlated PMD spectra of buried optical cables,” in *Proc. OFC ’02*, Anaheim, CA 2002, Paper ThI5.

[10] P. J. Leo *et al*, “Estimation of system outage statistics due to polarization mode disperion,” submitted to Symposium on Optical Fiber Measurements, NIST, Boulder CO, Sept. 24-26, 2002.

[11] Haunstein, “Fast PMD penalty measurement using polarization scrambling,” in *Proc. OFC ’02,* Anaheim, CA 2002, Paper WQ6.

[12] P. J. Leo, internal communication.

[13] S. L. Fogal *et al*, “Multiple importance sampling for first- and second-order PMD”, in *Proc. OFC ’02,* Anaheim, CA 2002, Paper ThA1.

[14] J. N. Damask, “A Programmable Polarization-Mode Dispersion Emulator for Systematic Testing of 10 Gb/s PMD Compensators,” in *Proc. OFC ’00,* Baltimore, MD 2000, Paper ThB3.

[15] J. N. Damask, “Apparatus and method for controlled generation of polarization mode dispersion,” US Patent US6,377,719.

[16] J. Evans, “The Birefringent Filter,” *J. Opt. Soc. Amer.*, vol. 39, no. 3, pp. 229, 1949.

[17] C. Buhrer, *Applied Optics*, vol. 27, no. 15, pp. 3166, 1988, and vol. 33, no. 12, pp. 2249, 1994.

[18] J. N. Damask, “Methods and apparatus for frequency shifting polarization mode dispersion spectra”, US Patent Application US20020080467.

# Measurement of Differential Group Delay Profiles in Fibers and in $LiNbO_3$ Distributed PMD Compensator

S. Bhandare[1], D. Sandel[1], R. Noé[1], H. Hermann[2], H. Suche[2] and W. Sohler[2]

[1]Department of Optical Communication and High Frequency Engineering, [2]Department of Applied Physics, University of Paderborn, Warburger Str. 100, 33098 Paderborn, Germany

**Abstract:** Frequency-dependent reduced Müller matrix measurement enables to calculate the corresponding Jones matrix and hence the impulse response of the devices with polarization mode dispersion. From the later, the differential group delay profiles are determined by inverse scattering. These allow to identity, emulate and compensate the effects of higher-order PMD that persists after compensation of first-order PMD.

**Introduction:** Polarization mode dispersion (PMD) continues to impair high data rate in optical communication. It is conveniently modelled as a concatenation of differential group delay (DGD) sections connected by variable polarization transformers. Jones matrix measurement over optical frequency has allows to verify the structure having only 3 known DGD sections [1]. Möller has synthesized a 2x2 Jones matrix filter that has the inverse of a PMD fiber characteristic for broadband PMD compensation [2], by generalizing the basic work done by Harris [3]. Experimental validation of such a filter seems not to have been reported so far nor seems a PMD medium with complicated structure have been analysed. This method of determining the DGD profiles would be of particular help for identifying and emulating the effects of higher-order PMD and for the non-destructive characterization of distributed PMD compensators in $LiNbO_3$.

**Measurement Setup and Principle:** A measurement setup basically consists of tunable laser source, an electrooptic polarization transformer, and a polarimeter (see Fig. 1). Tunable laser source is connected to the input of polarization transformer. Fiber pigtailed and packaged electrooptic polarization transformer is based on X-Cut, Z-propagation $LiNbO_3$ [4] and is fabricated in house. It is used to generate 8 different polarization states, which are equally distributed onto the Poincaré sphere. These are given as input to the device under test (DUT). A polarimeter is connected to the DUT output. The laser is swept in the steps of 10 GHz between the 1525 nm and 1545 nm where it had no mode hops. The frequency-dependent 3x3 rotation matrix **R** of the device, i.e. rows and columns 2 to 4 of its Müller matrix are thereby determined. Each of the n (= 8 in our case) normalized input (in) Stokes vectors results in corresponding output (out) Stokes vectors. Both vector groups are arranged in form of a matrix

$$\mathbf{S}_{out} = \mathbf{R}\mathbf{S}_{in}.$$

The rotation matrix **R** is then obtained by

$$\mathbf{R} = \mathbf{S}_{out}\mathbf{S}_{in}^{T}(\mathbf{S}_{in}\mathbf{S}_{in}^{T})^{-1}.$$

Compared to a more compact method [5] with two launched polarizations this gives a better immunity against polarization measurement errors. Any existing nonorthogonality of **R** is removed by singular value decomposition of **R** according to

$$\mathbf{R} = \mathbf{u}\ \mathbf{s}\ \mathbf{v}^{+},$$

where **u**, **v** are orthogonal (or more generally: unitary) matrices and **s** is a diagonal matrix with the singular values. **R** is then redefined as an orthogonal matrix

$$\mathbf{R} = \mathbf{u}\,\mathbf{v}^{+}.$$

From this frequency-dependent rotation matrix, **R**, frequency-dependent Jones matrix, **J**, is obtained in the form

$$\mathbf{J} = \begin{bmatrix} A & B \\ -B^{*} & A^{*} \end{bmatrix}, \quad |A|^2 + |B|^2 = 1.$$

Inverse Fourier transform yields the time-dependent Jones matrix with impulse response as its elements. Its first column is the finite impulse response to a horizontally polarized pulse while last column is the finite impulse response to an orthogonally polarized pulse (vertical). It is sampled with a 785fs period. The structure is analysed on the basis of sections having DGDs equal to this value.

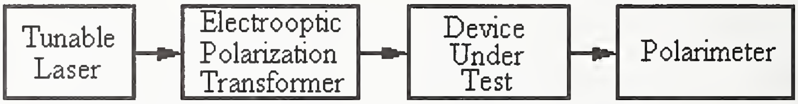

*Fig. 1: Experimental setup for DGD profile measurement*

The complex ratio between the field components of the first sample (and/or the last sample) allows to calculate retardation, φ, and orientation angle, ψ, of the mode converter present at the DUT output. Once it is known, the mode conversion effect can be easily removed from the overall impulse response by multiplication by a Jones matrix that is inverse to that which describes the mode conversion. The matrix that is used to describe this mode conversion effect is considered to be that of an elliptical retarder (**ER**).

$$\mathbf{ER} = \begin{bmatrix} \cos\varphi/2 + jV_1\sin\varphi/2 & j(V_2 + jV_3)\sin\varphi/2 \\ j(V_2 - jV_3)\sin\varphi/2 & \cos\varphi/2 - jV_1\sin\varphi/2 \end{bmatrix}$$

**V** simply equals to $\mathbf{V} = [0 \quad \cos\psi \quad \sin\psi]^T$ and its elements $V_1$, $V_2$, and $V_3$ represent the relative strengths of 0°, 45° and circular birefringence, respectively. Thereby the first sample is confined to one field component and the last sample is confined to an orthogonal one. Now a time shift of the samples in one field component is possible. It corresponds to a DGD section with principal states-of-polarization (PSPs) equal to these field components, preceding the already-known mode conversion. The pure time shift (without differential phase shift) means that the DGD section exhibits a retardation between the PSPs that is an integer multiple of 2π at the center frequency of the optical scanning range. It has been shown in [6] that this is not a restriction. The time shift results in a new impulse response which is shorter by one sample. It allows to determine an initial mode conversion which precedes the first DGD section. The impulse which generates the response and all local slow PSPs, are assumed to be horizontal ($\Omega_1$ direction, marked by an input arrow in Fig. 2). Experimentally, the inverse scattering range was chosen as 31.4ps. An inverse scattering algorithm will always display a full length DGD profile (40 sections).

The DGD or PMD profile of concatenated retarders is a concatenated sequence of input-referred PMD vectors $\tilde{\mathbf{\Omega}}_i$ with $\tilde{\mathbf{\Omega}}_i = \mathbf{R}_{<i}^{T}\mathbf{\Omega}_i$. Rotation matrix $\mathbf{R}_{<i}$ represents the

concatenated retarders preceding the retarder with PMD vector $\mathbf{\Omega}_i$. $\mathbf{\Omega}_i$ is the normalized Stokes vector of a PSP multiplied by the DGD. This holds also for the total PMD vector $\widetilde{\mathbf{\Omega}}_{\text{total}} = \sum \widetilde{\mathbf{\Omega}}_i$, $DGD_{\text{total}} = \left|\widetilde{\mathbf{\Omega}}_{\text{total}}\right|$. In order to allow a zero length of the last DGD section we mark its direction by an output arrow. It indicates the CW input polarization that would be necessary to hit the slow PSP of that section.

**DGD profiles in Fibers:** At first a back-to-back measurement without DUT was performed. In this case, all PMD vectors (= rods) should be cancelled by oppositely directed adjacent ones. This is indeed the case (see Fig. 2). The DGD profile travels 20 sections forth, then another 20 sections back on the same path, as if returning from a dead end. As a consequence, one has the impression to see only 20 sections, which in reality hide the other 20 sections. Input arrow tip and output arrow back end coincide within <100fs which is a measurement error since the true DGD was ~0fs. So the simplified back-to-back DGD profile is a frequency-independent polarization transformation specified by the arrows.

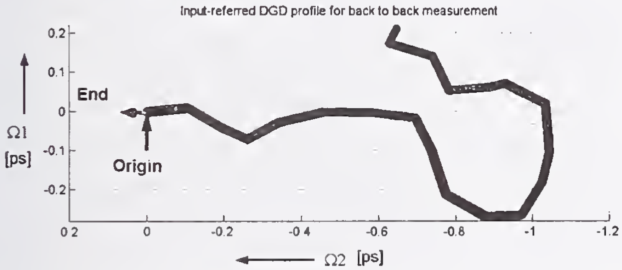

*Fig. 2: DGD profile back-to-back. DGD sections run forward and backward along the same path, ending at origin.*

Next DUT (Fig. 3) was a ~11 m long polarization-maintaining fiber (PMF) with ~25ps of DGD. It yielded a straight, 25.12ps long line (32 sections) followed by a short dead end (2×4 sections).

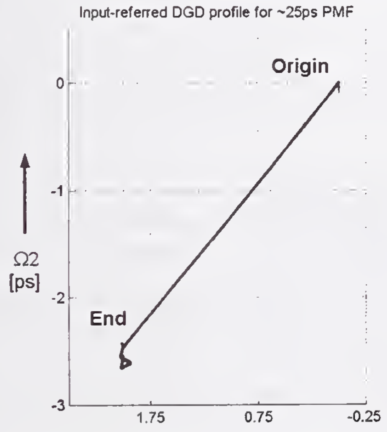

*Fig. 3: DGD profile of one ~25ps DGD section*

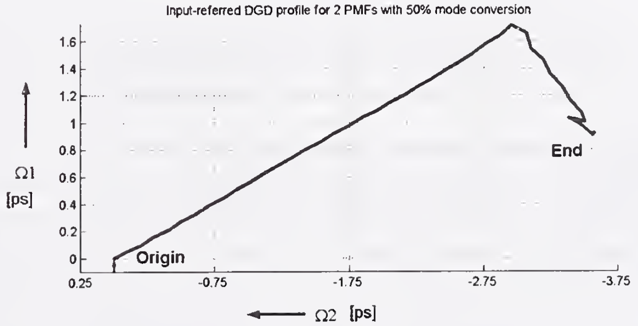

*Fig. 4: DGD profile of two DGD sections (22ps + 6ps) with 50% mode conversion. 90° angle is clearly seen.*

Figure 4 shows a DGD profile when two pieces of PMF with ~22ps and ~6ps of DGD are concatenated with 50% mode conversion (45° rotation) in between. The long section and the short section, which also contains a short dead end (2×1 section), are clearly seen. Angle between sections was ~90° as expected.

**DGD profiles of a distributed PMD compensator in $LiNbO_3$:** Fiber pigtailed X-cut, Y-propagation $LiNbO_3$ PMD compensator was fabricated in house, similar to those in [7]. 70 in-phase and quadrature TE-TM mode converters were distributed along a 94 mm long waveguide. Insertion loss was 4 dB and PDL was 1.1 dB. Required voltage times length product for full mode conversion in a single quadrature, with half of the length belonging to the other quadrature being unused, was 375V·mm. An average DGD was about 25ps. Without any voltages applied the DGD profile was similar to that of Fig. 3. Fig. 5(a) shows the DGD profile bent in a full circle when two full mode conversions distributed along the whole chip occur in one quadrature. A dead end with approximately 2×4 sections is also seen because the total DGD value of the chip is less than the inverse scattering range. In the pigtail-shaped profile of Fig. 5(b) only one and half mode conversions occur, but they are concentrated at about 3/4 of the total DGD. This demonstrates the versatility of the distributed PMD compensator with respect to emulation and compensation of higher-order PMD.

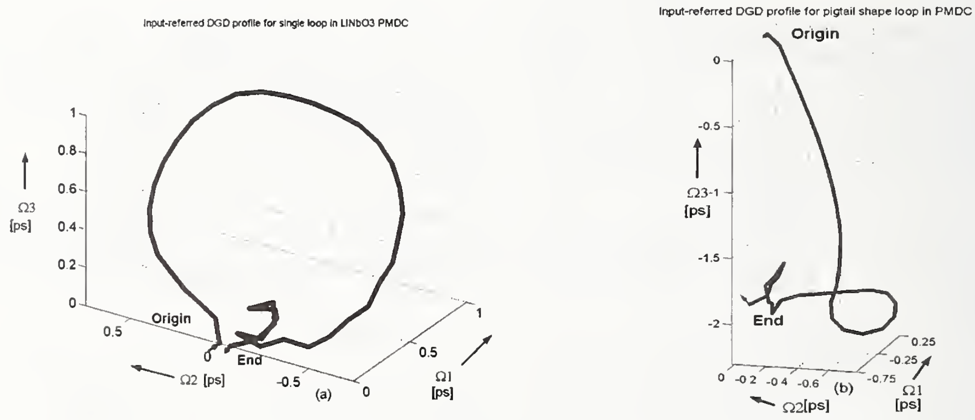

*Fig 5: DGD profile of the $LiNbO_3$ PMDC with (a) 2 full mode conversions (b) 1.5 mode conversions distributed over the whole length of the chip*

**Conclusion:** An inverse scattering algorithm for the characterization of devices with polarization mode dispersion has been implemented. This has allowed the non-destructive measurement of various DGD profiles in fibers and in distributed PMDC in $LiNbO_3$. It can be used as a base for the generation and compensation of higher-order PMD effects using the proposed PMDC based on the X-cut, Y-propagation $LiNbO_3$.

**Acknowledgement** is made to Deutsche Forschungsgemeinschaft for partial funding and Siemens AG or hardware support.

**References:**
[1] B.L.Heffner: IEEE PTL 5, 814 (1993)
[2] L. Möller: IEEE PTL **12**, 1258 (2000)
[3] S.E.Harris et al: JOSA **54**, 1267 (1964)
[4] R.Noé et al: IEEE JLT **6**, 1199 (1988)
[5] L.E.Nelson et al: Proc. ECOC **II**, 10 (1999)
[6] R.Noé et al: IEEE JLT **17**, 1602 (1999)
[7] R.Noé et al: Electron. Lett. **35**, 652 (1999)

# Estimation of system outage statistics due to polarization mode dispersion

Paul J. Leo[1], Daniel L. Peterson Jr.[2], and Kent B. Rochford[1]
[1]*YAFO Networks, 1340F Charwood Rd., Hanover, MD 21076*
[2]*Transmission Engineering, WorldCom, 2400 N. Glenville, Richardson, TX 75082*

**Abstract:** Measurements of fiber DGD and SOPMD over time and measurements of receiver tolerance to PMD are combined with a random-walk simulation model to estimate the rate and duration of PMD-induced system outages.

## 1. Motivation

Polarization mode dispersion (PMD) complicates the assessment of network performance because of its time-varying nature. Quantitatively, PMD is defined as the mean differential group delay (DGD) over wavelength and the statistics for DGD and second-order PMD (SOPMD) contributions are well known [1]. The joint probability distribution function (J-PDF) of DGD and SOPMD, calculated from a simulation of 1 billion fibers, is shown in Figure 1. The cumulative probability contours show the likelihood that an instantaneous pair (DGD, SOPMD) occurs. One can overlay boundaries demarcating high DGD & SOPMD combinations that cause transmission impairment, and calculate the probability that such impairment occurs. This process, however, gives no insight into the frequency and duration of events. For example, the instantaneous states at a given channel wavelength breach the 0.9999 contour 0.01% of the time. Does this occur as one 9 s event every day, one 53 minute event each year, or some combination of events? To answer this question we have combined numerical techniques with temporal measurements of DGD and SOPMD on an installed fiber to simulate the path that DGD and SOPMD values take as they evolve over time. We measured the receiver tolerance to DGD and SOPMD to determine the boundary on the J-PDF beyond which a system outage may occur. Performing a simulation of DGD/SOPMD evolution and monitoring crossings of the outage boundary allows us to gather statistics describing the occurrences and durations of PMD-induced outage events.

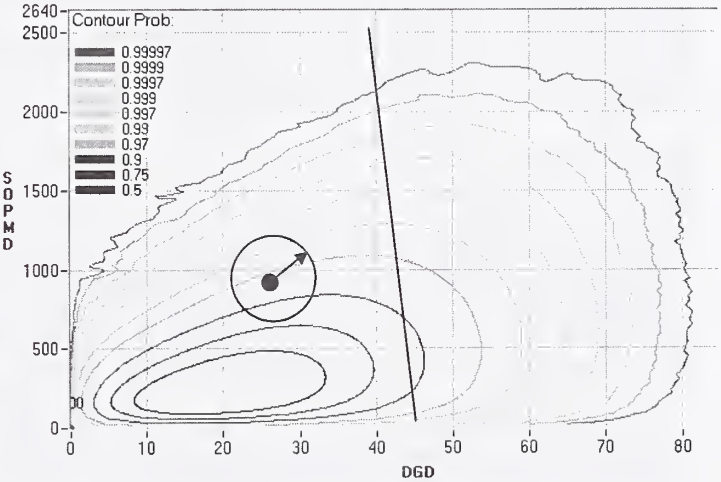

Figure 1. The joint probability density function (J-PDF) for DGD and SOPMD occurrences in a 25 ps PMD fiber. Also shown (and described in Section 2) is a starting value (DGD, SOPMD) and possible next values after obtaining a step size $R(t_i)$ from the distribution of measured rates of change. The sloped line demarcates the PMD values for which performance of a measured receiver is unacceptable.

## 2. Random-walk model

Recently Caponi used measured temporal DGD data to estimate the mean outage rate and the mean outage duration in a 9.4 ps embedded fiber [2]. The analysis was based on their observation that the Maxwellian probability distribution of the DGD and the probability distribution of the change in DGD (in units of ps/hr) were uncorrelated. This allowed the application of the analytic one-dimensional level crossing problem [3] to determine the mean outage rate.

We extend this method to a two-dimensional (2-D) random-walk model that includes the dependence of both DGD *and* SOPMD on outage occurrence and provides the statistics for outage events. Our method includes a powerful self-consistency check of the measured rate-of-change distribution of DGD/SOPMD (the accuracy of which is typically limited by the paucity of experimental data). The data that we collected on two 36ps underground fibers was properly filtered in frequency and time to exclude correlated measurements and to provide an effective 4.73yrs of data. These data verified the previous authors observation that the magnitude of change in the DGD was uncorrelated with the instantaneous value of DGD. Analogously, when considering both the DGD and SOPMD, we found that the step size taken on a normalized 2-D J-PDF in a given time interval was also independent of the instantaneous (DGD,SOPMD) value. However the experimental data indicated a strong correlation of the *direction* of the change on the J-PDF.

Our 2-D random-walk model consists of starting at an arbitrary position in the J-PDF. The instantaneous step size $R(t_i)$ is chosen from a random variable that is an analytic fit to the experimentally measured distribution of step sizes. To determine which direction to move, a circle of radius $R(t_i)$ (Figure 1) is then drawn about the current position ($DGD(t_i)$,$SOPMD(t_i)$) and the J-DPF evaluated on the perimeter of that circle. The step direction is determined by a random selection weighted by the J-PDF values on the circle of radius $R(t_i)$.

To improve computational efficiency the "weighted circle" that determines the direction was sampled at $11.25^{\circ}$ arc intervals and the J-PDF was discretized into a 400x500 grid. Sampling the weighed circle at smaller intervals or sampling the J-PDF on a courser grid provided similar results. By keeping a record of the (DGD,SOPMD) visited in a simulation, histograms of the simulated probability distribution of DGD and SOPMD can be constructed and compared to the expected distributions of the DGD and SOPMD [1].

We found that discrepancies between the simulated and expected distributions could be corrected by adjusting the tail of the analytic fit to the measured DGD/SOPMD data. The tails of these distributions correspond to the largest step sizes, and these rare steps are not well characterized by the limited amount of experimental data. To obtain accurate statistics of these very rare large DGD/SOPMD changes requires a prohibitively long measurement of the DGD and SOPMD on a given fiber. Thus we have employed a self-consistent feedback procedure, whereby the long-range tail of the stepsize distribution is adjusted so that the correct DGD /SOPMD statistics result from the simulation. We believe this provides some advantage over the integral technique where the stepsize distribution is assumed to be correct *a priori* over its entire range. Figure 2 shows the DGD and SOPMD results obtained from two step-size distribution fits and compares these to the expected probability distributions for DGD and SOPMD. The step size distribution "Fit 1" falls off as $\exp(x^{0.25})$ and using it for the simulation overestimates the probability of high DGD and SOPMD (Figure 2). Our simulations used a fit that decreases as $\exp(x^{0.15})$ (Fit 2).

As the simulation runs, the (DGD,SOPMD) states walk about the J-PDF. If an outage boundary is exceeded, i.e. the PMD state is one that produces penalties sufficient to cause a transmission system

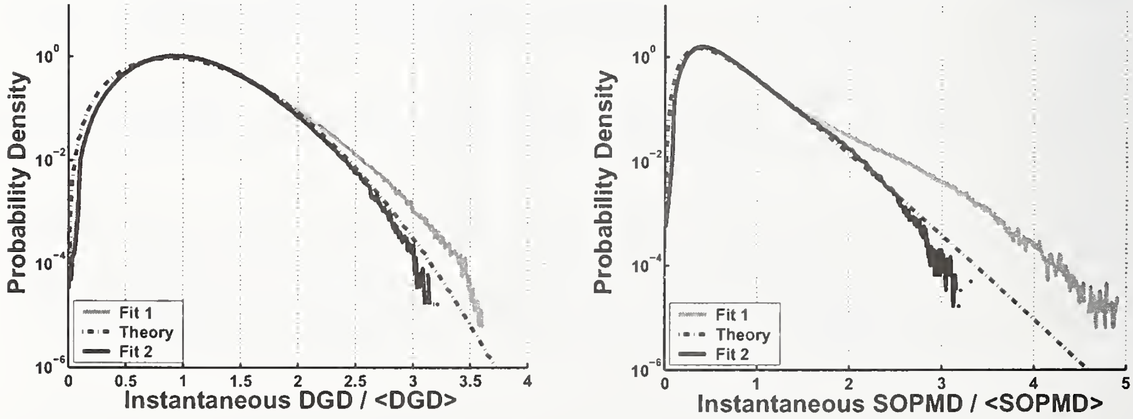

Figure 2. DGD and SOPMD probability densities obtained from random-walk simulations, plotted against the known probability distributions for two choices of rate-of-change fits. Fit 1 overestimates the step sizes for rare events.

outage, we record the outage time and, by monitoring when the PMD state again crossed the boundary, the duration of the outage event. We use this data to form histograms of outage occurrences and durations. As a final check a one-dimensional random walk (considering only DGD) was performed using this procedure, and the predictions for the mean outage rate and duration were found to be in excellent agreement with those obtained using the integral method [2].

## 3. Measurements of DGD/SOPMD evolution and system penalties.

Our random walk method requires a measurement of the first- and second-order PMD over time in a target fiber to obtain the PMD rate of change distribution. In addition, measurements of the effect of PMD on OC-192 system performance are needed to set an outage boundary. For our target fiber, we chose a 3-span, 110km route buried along railroad tracks in Texas. Two fibers from the first span were looped-back and connected to a tunable laser and commercial polarimeter to perform Jones Matrix Eigenanalysis (JME) measurements [4]. At each wavelength the Jones Matrix was measured, and appropriate numerical derivatives calculated over pairs of wavelengths to obtain DGD and SOPMD. A 20 nm wavelength range (using 20 pm steps) was measured every 1.6 hours for 174 hours on this 36 ps PMD fiber. (Sample spectra are shown in Figure 3). The measurement was repeated using a 36ps fiber pair on the third span with similar results. We estimate that the DGD and SOPMD values have better than 10% uncertainty, based on laboratory measurements of a stable programmable PMD generator [5]. These data sets were used to form the time-derivatives required for the simulation.

System penalties from PMD are measured using noise-loaded bit-error-rate (BER) measurements. The BER is measured at several optical signal-to-noise ratios (OSNRs) by attenuating the 10Gb/s NRZ transmitter signal just before an optical amplifier. First, we obtain the back-to-back characteristic of the transmitter/receiver pair with no impairments. Next a programmable PMD generator, located between polarization scramblers, is placed after the transmitter. The BER vs. OSNR curves are then measured for various combinations of DGD and SOPMD. The system penalty for each PMD is defined as the increase in OSNR (compared to the back-to-back curve) for which BER=$10^{-12}$. All receivers show increasing penalty with increasing DGD. The tolerance to SOPMD is less predictable and we have observed that a remarkable number of commercial receivers also show increasing penalty with increasing SOPMD (at a fixed DGD).

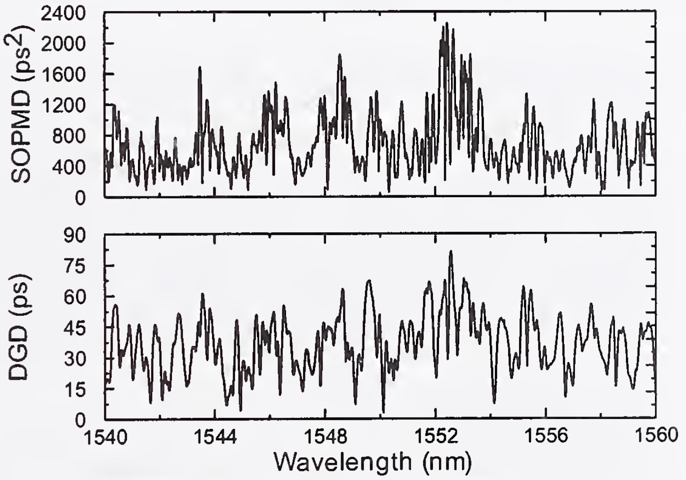

Figure 3. A sample of the DGD and SOPMD spectra for one measurement interval.

Each system has an OSNR margin that is allotted to various parameters that degrade performance (for example, chromatic dispersion, self-phase modulation, PMD, etc.). For our example, we allow 3 dB of OSNR penalty to be allotted to PMD; thus values of PMD that have > 3 dB penalty are unacceptable and considered an outage. An outage boundary based on mapping the PMD penalties on a commercial receiver is shown in Figure 1 as a nearly vertical line rising from 45 ps DGD; states to the right of this line show > 3 dB penalty.

## 4. Results

We used the outage boundary shown in Figure 1 that includes the additional receiver dependence on SOPMD; thus any (DGD, SOPMD) pairs to the right of this line are considered outages. Each simulation was run for an equivalent to 700yrs (≈ 6 million steps) and results scaled to a 20 year period. The resulting outage histograms for a fiber with 25 ps PMD are shown in Figure 4. Our random walk model

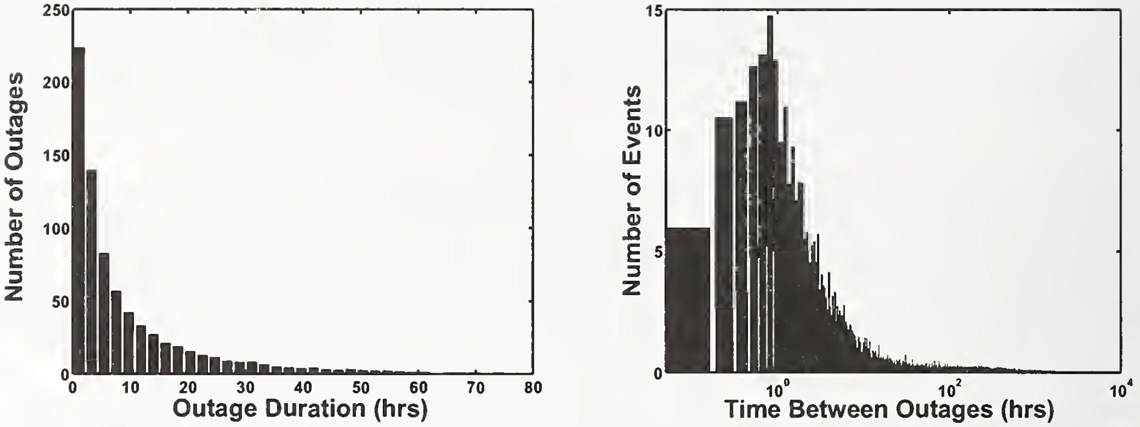

Figure 4. Histogram of outage events on a 25 ps PMD fiber scaled for a 20 year time period. The random-walk simulation provides statistics for the duration of outages and the time between outage events.

predicts that outages will occur an average of 38 times per year. The mean outage time is 10 hours, though the outage durations ranged from 4 mins to 6.7 days on this fiber.

We verified our random-walk model by comparing with the measured outage performance of the characterized receiver over the installed fiber we measured in the field. A 1+1 bi-directional OC-192 system was provisioned on the 110 km, 3-span route using fiber with a 25ps PMD. Chirped NRZ was transmitted through amplifiers at each span termination to a commercial receiver similar to the type mapped for PMD tolerance. No forward error correction was used during the tests. Bit error-rate (BER) performance was measured using the raw SONET data stream. Over a 25 day period, outage events occurred on three separate instances; day 2, day 12 and day 17, or roughly once every 8.3 days. As a comparison, our simulation of outages on a 25 ps fiber for this receiver suggests an outage would occur every 9.6 days.

## 5. Conclusions

A new random-walk model uses probability distributions derived from measured fiber data to provide new insight into the effects of PMD on system performance over time. This method includes a self-consistency test to judge the quality of measured data. Measured system degradation due to PMD, mapped by using a programmable PMD source, can be used to set thresholds defining outages. Running this random walk model with an outage threshold provides statistics that describe the quantity and duration of PMD-induced outages over time.

These methods are useful for evaluating the effect of rare outage events caused by PMD. This can be applied to the characterization of receivers and PMD compensators, and calculations of service availability in the presence of time-varying phenomena such as PMD.

## 6. References

1. G.J. Foschini, L.E. Nelson, R.M. Jopson, and H. Kogelnik, “Probability densities of second-order polarization mode dispersion including polarization dependent chromatic fiber dispersion,” *IEEE Photon. Technol. Lett.*, **12,** p.293 (2000).
2. R. Caponi, B. Riposati, A. Rossaro, M. Schiano, “WDM design issues with highly correlated PMD spectra of buried optical cables,” in *Proc. OFC '02*, Anaheim, CA, 2002, Paper ThI5.
3. A. Papoulous, *Probability, Random variables, and Stochastic Processes*, 3rd ed., McGraw-Hill, New York (1991).
4. B.L. Hefner, “Automated measurement of polarization mode dispersion using Jones matrix eigenanalysis,” *IEEE Photon. Technol. Lett.* **4**, p.1066 (1992).
5. J. Damask, “Apparatus and method for controlled generation of polarization mode dispersion,” US Patent US6,377,719.

# Low-coherence interferometric measurement of differential group delay and its dispersion to second-order in polarisation maintaining fibre

Dónal A. Flavin[1] Roy McBride[2] and Julian D.C. Jones[3]

*Department of Physical and Quantitative Sciences, Waterford Institute of Technology, Waterford. Ireland.*

*Department of Mechanical and Chemical Engineering, Heriot-Watt University, Riccarton, Edinburgh EH14 4AS. UK*

*Department of Physics, Heriot-Watt University, Riccarton, Edinburgh EH14 4AS. UK*

## *Abstract*

We present an interferometric technique for measurement of differential group delay (DGD) and its dispersion in polarisation maintaining fibres for a wavelength range of over 200 nm. The approach yields measurements from analysis of the phases of the Fourier transforms of a pair of interferograms, obtained in a tandem interferometer. The technique is demonstrated to measure DGD and its dispersion to second-order, with measurements immune to asymmetry in the interferogram being processed.

## Introduction

In recent publications, the incorporation of polarisation maintaining fibre (PMF) elements in active schemes for PMD mitigation has been widely reported [1]. There has also been realisation that pulse shape and distortion in such systems is governed not alone by the PMD vector but also by its higher-order dispersion [2,3]. This leads to a critical interest in characterisation of the dispersion of differential group delay (DGD) of PMF. Interferometric time domain techniques are often used to characterise fibre birefringence dispersion [4,5]. Typically two interferograms, corresponding to the individual propagation modes of the sample, are captured. Such approaches require a sequence of measurements at a range of wavelengths to determine birefringence over a broad wavelength range.

Here we propose and demonstrate an in-line interferometric scheme for measurement of DGD and DGD-dispersion to second-order on PMF sections over a broad wavelength range, based on only two OPD scans in a tandem interferometer. From the phases of the Fourier transforms of the interferograms, we determine the DGD parameters for a broad wavelength range, extending over 200 nm beyond the PMF's cut-off wavelength.

## Tandem interferometry for DGD and DGD-dispersion measurement in PMF

Representing the propagation constants of the fast and slow eigenmodes of polarisation-maintaining fibre as $\beta_f(\omega)$ and $\beta_s(\omega)$ respectively, we define the differential propagation constant $\beta_\delta(\omega)$ as $\beta_\delta(\omega)=\beta_f(\omega)-\beta_s(\omega)$; each term is explicitly dispersive. The corresponding differential phase accumulated over a length $L$ is then $\phi_\delta(\omega)=\beta_\delta(\omega)L$. The DGD and the $i$ th -order dispersion of DGD, represented as $\tau_\delta(\omega)$ and $\tau_\delta^{(i)}(\omega)$ respectively, can each be defined in terms of $\beta_\delta(\omega)$ and its derivatives relative to optical frequency:

$$\tau_\delta(\omega)\equiv\frac{d\beta_\delta(\omega)}{d\omega}=\frac{1}{L}\frac{d\phi_\delta(\omega)}{d\omega}, \qquad \tau_\delta^{(i)}(\omega)\equiv\frac{d\beta_\delta^{(i+1)}(\omega)}{d\omega^{(i+1)}}=\frac{1}{L}\frac{d\phi_\delta^{(i+1)}(\omega)}{d\omega} \qquad (1)$$

The experimental arrangement in Fig. 1 is designed for DGD and DGD-dispersion measurement on the length $L_{XY}$ of PMF element between points $X$ and $Y$. The technique is based on the capture of two interferograms; the first interferogram arises from mode-coupling induced at $X$, and the second for the case when the coupling point is transferred to $Y$.

Light from the low-coherence source is linearly polarised, and launched into the fibre to populate only one of its eigenmodes. A localised transverse stress is applied at test point X, thus causing partial coupling of light to the second eigenmode. The beam transmitted through the polariser A is then a linear combination of the eigenmodes propagating between X and the analyser, i.e. from the point at which the eigenmodes separate to the point of their recombination. This beam is made to illuminate a temporally-scanned Michelson interferometer, and the resulting low-coherence interferogram is detected at D1.

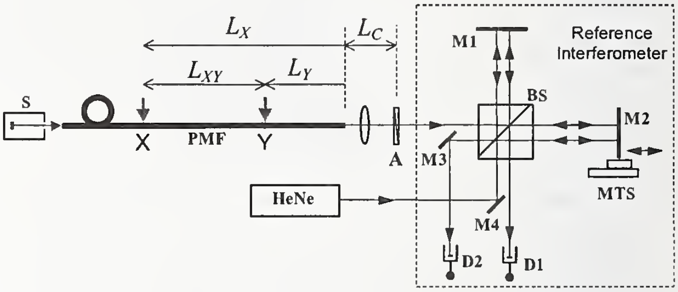

Fig.1 The optical configuration: S, low-coherence source, linearly polarised with polarisation adjusted to populate only eigenmode of the PMF; M1, M2, M3, M4, mirrors; A, polariser; D1, D2, photodetectors: MTS, translation stage.

This arrangement behaves as a tandem structure: the primary interferometer is formed by the section between X and the analyser, incorporating the PMF section of length $L_X$ and the air-lens section path of length $L_C$ ; the Michelson acts as the local reference interferometer. Scanning the OPD in the Michelson then produces a set of central and satellite interferograms associated with tandem interferometry [6], provided the DGD in the PMF section exceeds the coherence length of the source.

The captured satellite interferogram can be represented as [7]:

$$I_{Xsat}(\tau) \propto \mathrm{Re}\left[\tilde{\gamma}_{Xd}(\tau)\right] = \mathrm{Re}\left[\int_{-\infty}^{\infty} G(\omega)\exp\{-i\phi_{X\delta}(\omega)\}\exp\{-i\omega\tau\}d\omega\right] \qquad (2)$$

where $\tau$ is the group delay imbalance in the reference interferometer, $\tilde{\gamma}_{Xd}(\tau)$ is the dispersed mutual coherence function, $G(\omega)$ is the normalised source spectrum, and $\phi_{X\delta}(\omega)$ is the differential phase accumulated over the lengths $L_X$ and $L_C$.

From Eqn.2, we can derive $\phi_{X\delta}(\omega)$ from the phase of the inverse Fourier transform of the satellite interferogram. Similarly, repeating the experiment for the case where the mode coupling is induced at Y rather than X, gives a satellite interferogram $I_{Ysat}(\tau)$ , from which we can determine the differential phase $\phi_{Y\delta}(\omega)$ for transmission through the PMF section of length $L_Y$ and the air-lens section $L_C$.

The differential propagation constant $\beta_\delta(\omega)$ for the $L_{XY}$ section is then measurable in terms of $\phi_{X\delta}(\omega)$ and $\phi_{Y\delta}(\omega)$, and can be expanded in a Taylor expansion about a reference frequency $\omega_0$:

$$\beta_\delta(\omega) \equiv \frac{1}{L_{XY}}\{\phi_{X\delta}(\omega) - \phi_{Y\delta}(\omega)\} = \sum_i \beta_\delta^{(i)}(\omega_0)\ (\omega-\omega_0)/i! \qquad (3)$$

where $\beta_\delta^{(i)}(\omega_0)$ are the $i^{th}$ derivatives of $\beta_\delta(\omega)$ with respect to $\omega$ at $\omega = \omega_0$. The residual birefringence within the length $L_C$ is common-mode and does not enter Eqn. 3.

Thus, in principle, a single polynomial fit to the phase $\{\phi_{X\delta}(\omega) - \phi_{Y\delta}(\omega)\}$ yields measurements of the section's DGD, $\tau_\delta(\omega_0) = \beta_\delta^{(1)}(\omega_0)$, and $i^{th}$-order dispersion, $\tau_\delta^{(i)}(\omega_0) = \beta_\delta^{(i+1)}(\omega_0)$, for any optical frequency $\omega_0$ in the source spectral range. However, for both satellite interferograms, though digital signal processing will recover phase values for $\phi_{X\delta}(\omega)$ and $\phi_{Y\delta}(\omega)$ at a series of uniformly distributed frequencies across the source spectrum, the individual phase measurements are recovered modulo-$2\pi$ radian. Nevertheless, by sampling the interferograms within the Nyquist criterion, there is no ambiguity in the differences between the neighbouring phase measurements. Thus, though the measurement of $\beta_\delta^{(0)}(\omega_0)$ obtained from the polynomial fit is ambiguous, the required measurements of DGD and its dispersion at optical frequency $\omega = \omega_0$, obtained from the values $\beta_\delta^{(1)}(\omega_0)$ and higher derivatives of $\beta_\delta(\omega)$, are measured without ambiguity.

## Experiment and Signal Processing

The fibre under test was York HB 750, with a cut-off wavelength of 640 nm. The combination of a miniature tungsten-halogen lamp with Si photodetectors gave a detectable spectral range from 278 THz to 480 THz, (625 nm to 1075 nm), thus facilitating our study over a wavelength range well beyond the cut-off wavelength of the fibre. In the experiments reported here, the points X and Y were 10.491m and 3.601m from the end-facet; thus the section length $L_{XY}$ was 6.890 m. Precision calibration of the OPD scan was achieved by processing the complex-valued analytic signal of the high coherence interferogram derived from the HeNe laser and simultaneously captured during the scan [8].

The presence of high-order dispersion of DGD was immediately evident from the visibility profiles of the interferograms. Figs. 2 (a) and 2(b) respectively illustrate windowed central and satellite interferograms obtained for an OPD scan in the reference interferometer for mode coupling at the test point X; in each case the window is $\approx 1000$ femtoseconds ($\approx 300$ μm). The central interferogram is consistent with a source coherence time of $\approx 50$ fs (coherence length of $\approx 17$ μm). The corresponding satellite interferogram shows dramatic high-order dispersion-induced asymmetry and broadening, with an interferometric signal extending over a range exceeding 800 fs.

Fig. 3 (a) shows the sequence of phase values

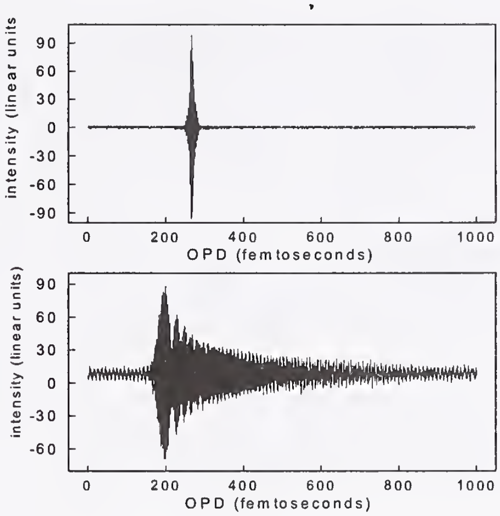

Fig. 2: Windowed sections of the central and satellite interferograms

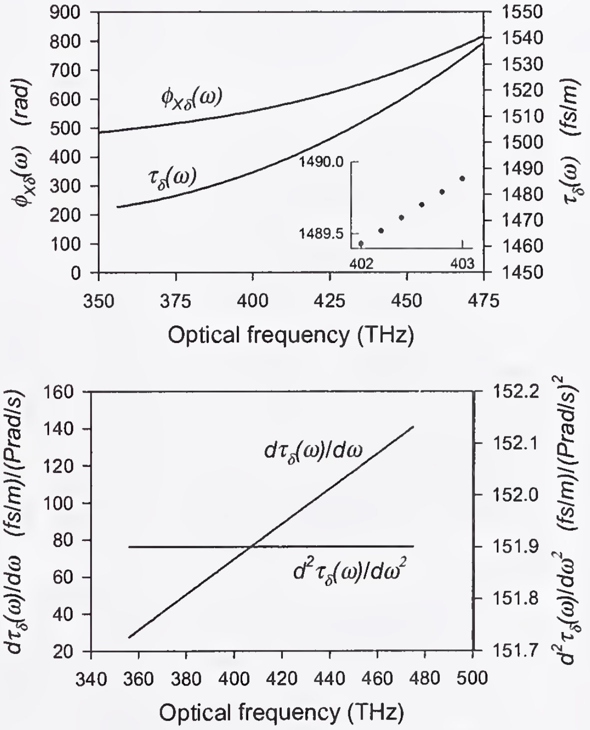

Fig . 3: **(a)** unwrapped differential phase, $\phi_{X\delta}$, over the range 353 THz to 475 THz (630 nm to 850 nm) recovered from the processing of the interferogram of Fig.2 (b), together with the DGD, $\tau_\delta(\omega)$, measurement at 0.2 THz intervals within the range; the inset shows the individual DGD measurements for the range from 402 THz to 403 THz.
**(b)** the first- and second-order DGD-dispersion measurements at 0.2 THz intervals over the full range

for $\phi_{X\delta}(\omega)$, recovered modulo-$2\pi$, from the unwrapped phase of the Fourier transform of the satellite interferogram of Fig. 2(b) over the frequency range 353 THz to 475 THz (630 nm to 850 nm). The phase can be readily corrected for the nonzero OPD by processing the HeNe interferogram in the interval between true zero, as identified by the central interferogram, and the window origin [9].

Corrected phase curves for the interferograms arising from coupling at X and Y were obtained and subtracted to yield the phase data for $\{\phi_{X\delta}(\omega) - \phi_{Y\delta}(\omega)\}$. From our earlier considerations, the DGD and DGD-dispersion at a specific frequency $\omega_0$ is measured unambiguously from the polynomial fit to this phase data. We performed third-order fits to the data for a sequence of reference frequencies at intervals of 0.2 THz over the range 353 THz to 475 THz. Thus we obtained measurements of DGD, $\tau_\delta(\omega)$, and DGD-dispersion to first and second order, $\tau_\delta^{(1)}(\omega)$ and $\tau_\delta^{(2)}(\omega)$ respectively, for the full frequency range. These measurements are represented on Fig. 3(a) and Fig. 3(b). The precision of the group delay measurement is better than 0.2 femtoseconds, corresponding to a precision of $\approx 0.08$ fs/m in the DGD measurement for the 6.89 m PMF section. .

## Discussion and Conclusion

The technique yields DGD and dispersion measurement over a broad wavelength range from the processing of the single pair of interferograms. In comparison with "centroid location" techniques, it obviates the need for a set of experiments using a narrow range of wavelengths at a series of different mean wavelengths. It also minimises the limitations associated with broad source bandwidth and consequent interferogram overlap of interferograms corresponding to the individual propagation eigenmodes [4]: in our case the critical separation is between the central and satellite interferogram; the former narrows with increased bandwidth and the latter broadens in a direction away from the central interferogram Further the technique benefits from increased bandwidth, which improves the accuracy of the polynomial fitting to the phase curve.

We have reported an interferometric technique for in-line measurement of DGD and DGD-dispersion to second-order over a broad wavelength range (630 nm to 850 nm) for sections of polarisation maintaining fibre. The measurements are obtained by tandem interferometry, from the processing of a single pair of interferograms, arising from induced mode coupling at the extremities of the section. The DGD and dispersion are determined from polynomial fits to the phase of the Fourier transforms of the interferograms arising from two OPD scans in the reference interferometer. The measurements are immune to the dispersion induced broadening and asymmetry of interferograms.

## References

1. D. Penninckx and S. Lanne, *Optical Fiber Communication Conference* 2001, OSA,Technical Digest), TuP, pp. 1.1 - 1.4.
2. H. Kogelnik, L. E. Nelson, J. P. Gordon, and R. M. Jopson, *Opt. Lett.,* 25, 1, pp. 19-21, 2000.
3. A. Eyal, Y. Li, W. K. Marsall and A. Yariv, *Opt. Lett.,* 25, 12, pp. 875-877, 2000.
4. P. L. Francois, M. Monerie, C. Vassallo, Y. Durteste, and F. R. Alard, *Journal of Lightwave Technology.,* 7, 3, pp 500 - 513, 1989.
5. L. Thevenaz, J-P Pellaux, N. Gisin, and J-P. VonDerWeid, *Journal of Lightwave Technology*, 7, 8, pp.1207- 1212, 1989.
6. Y. J. Rao and D. A. Jackson, Measurement Science & Technology, 7,7, pp.981-999,1996
7. D. A. Flavin, R. McBride and J.D.C. Jones, *Optical Communications*, 156, pp. 367 - 376, 1998.
8. D. A. Flavin, R. McBride, J. G. Burnett, A. H. Greenway and J. D. C. Jones, *Optics Lett.*, 19, 24, pp. 2167 - 2169, 1994.
9. D. F. Murphy and D. A. Flavin, *Applied Optics.* 39, 25, pp. 4607-4615, 2000.

# AUTHOR INDEX

# APPENDIX I - PROGRAM

## Tuesday, September 24, 2002

8:30 **Opening Remarks:** Gordon Day, NIST, Symposium General Chair

### Session I. Nonlinear Effects, Chair: William Reed, OFS Fitel

8:45 **INVITED:** The Unique Measurement Challenges of Raman Amplifiers, A. Evans, S. Gray, M. Muktoyuk, *Corning, Inc.*

9:15 Comparison of Stimulated and Spontaneous Scattering Measurements of the Full Wavelength Dependence of the Raman Gain Spectrum, N.R. Newbury, K.L. Corwin, *NIST*

9:30 Fiber Nonlinear Coefficient Measurement Scheme Based on FWM Method with Externally Modulate DFB Laser Source, B. Batagelj, M. Vidmar, *University of Ljubljana*

9:45 A Comparison of Six Techniques for Nonlinear Coefficient Measurements of Various Single Mode Optical Fibers, Y. Namihira, K. Miyagi, K. Kaneshima, *University of the Ryukyus,* M. Tadakuma, *Furukawa Electric,* C. Vinegoni, *University of Geneva,* G. Pietra, *Pirelli Labs Innovation,* K. Kawanami, *Muroran Institute of Technology*

10:00 **BREAK**

### Session II. Fiber Geometry, Chair: Ka Kha Wong, Northstar Photonics

10:30 **INVITED:** Monitoring the Optical Network, Randy Giles, *Lucent Technologies*

11:00 Burial Depth Measurement for Ion-Exchanged Glass Waveguides with Different Widths, P. Madasamy, *University of Arizona,* M. Morell, *NP Photonics,* D. Geraghty, S. Honkanen, N. Peyghambarian, *University of Arizona*

11:15 Accuracy of MFD and $A_{eff}$ Measurements Using Far-Field Scanning, A.J. Barlow, R. Castle, *PerkinElmer Optoelectronics,* A.G. Hallam, *Halcyon Optical Services*

11:30 Mode-Field Diameter and "Spot Size" Measurements of Lensed and Tapered Specialty Fibers, J.L. Guttman, *PHOTON, Inc*

11:45 Anomalies in Online Fibre Measurements and Their Implications for Fibre Array Manufacture, S.H. Law, T.N. Phan, *Australian Photonics CRC,* G.W. Barton, *University of Sydney*, M.J. Barton, J. Elsey, *Australian Photonics CRC*

12:00 **LUNCH**

### Session III. Group Delay and Dispersion, Chair: Andrew Inenaga, JDS Uniphase

1:30 Performance Characterization of Components with Group Delay Fluctuations, M. Eiselt, C.B. Clausen, R.W. Tkach, *Celion Networks*

1:45 High-Resolution Group Delay Measurements of a Hydrogen Cyanide Gas Cell Using Low-Coherence Interferometry, S.D. Dyer, R.J. Espejo, P.A. Williams, *NIST*

2:00 Group Delay and Spectral Response of Free Space Optics Mux/Demux Measurement Using OLCR, X. Chapeleau, *Université de Nantes, NetTest,* D. Leduc, C. Lupi, R. Le Ny, C. Boisrobert, *Université de Nantes*

2:15 High Accuracy Relative Group Delay Measurements of a Chirped Grating (NIST Telecom Round Robin), X. Chapeleau, D. Leduc, *Université de Nantes,* M. Wicks, *NPL,* R. Le Ny, C. Boisrobert, *Université de Nantes*

2:30 Direct Dispersion Slope Measurement by Mach-Zehnder Interferometer on Short Length Optical Fibre, Y.C. Zhao, S. Fleming, *Australian Photonics CRC*

2:45 Dispersion Measurements on Multiple Kilometer-Length Few-Mode Fibers with an RF Spectrum Analyzer, J.W. Nicholson, S. Ramachandran, S. Ghalmi, M.F. Yan, *OFS Laboratories*

3:00 Group-Delay Measurements with RF Optical Frequency Scanning, M.C. Santos, J. Prat, M. Solar, *Universitat Politècnica de Catalunya*

3:15 **BREAK**

### Session IV. Time and Frequency Measurements, Chair: Janet Jackel, Telcordia

3:45 **INVITED:** Optical Waveform and Q-Factor Measurement using Optical Sampling for Ultra-High Speed TDM Systems, H. Takara, I. Shake, S. Kawanishi, *NTT Network Innovation Laboratories*

4:15 Frequency-Controlled Supercontinuum Lightwave Source Applied to Optical Measurements with High Frequency Accuracy, K. Mori, T. Morioka, A. Takada, E. Yamazaki, *NTT Network Innovation Laboratories*

4:30 Recent Developments of Excited-state Optical Frequency Standards for Telecommunications, D.A. Humphreys, C. Campbell, F. Bernard, P. Patel, *NPL*

4:45 Fiber Bragg Gratings as Wavelength References – Development and Characterization, E.G. Grosche, *PTB,* J. Meissner, *Advanced Optics Solutions*

5:00 Simultaneous Measurement of Transverse Strain and Temperature Using FBG Written in HiBi Fiber, I. Abe[1,3], M.W. Schiller[3], R. Nogueira[1,2], P. Lopes[1], O. Frazão[4], J.L. Santos[4], J.L. Pinto[1,2], H.J. Kalinowski[3], *[1]Universidade de Aveiro, [2]Instituto de Telecomunicações, [3]Centro Federal de Educação Tecnológica do Paraná, [4]INESC Porto*

5:15 A Simple and Direct Method to Estimate Long Period Grating Parameters, K. Thyagarajan, M. Das, M.N. Satyanarayan, *Indian Institute of Technology*

5:30 **SESSION CLOSE**

7:00 **RECEPTION, REGAL HARVEST HOUSE**

## Wednesday, September 25, 2002

### Session V. Multimode Fiber and Fiber Characterization, Chair: Mike Hackert

8:30 **INVITED:** A Simplified Model of Modal Dispersion in Multimode Fiber, A.J. Ritger, *OFS Fiber Optics*, S.E. Golowich, *Bell Laboratories*

9:00 DMD Measurement and Simulation on Short Length, 850-nm Laser-Optimised, 50 µm Core Diameter, GIMM Optical Fibres, F.J. Achten[1], M. Bingle[2,3], B.P. de Hon[2], M.J.N. van Stralen[1], *[1]Draka Fibre Technology, [2]Eindhoven University of Technology, [3]EM Software and Systems*

9:15 Determination of Skew in Multimode Ribbon Fibers, A.J. Barlow, *PerkinElmer,* M.J. Hackert, *Corning, Inc.*

9:30 Phase Imaging Methods for Optical Fiber Characterization, A. Roberts, *University of Melbourne,* G. Baxter, N. Dragomir, *Victoria University,* S.T. Huntington, E. Ampem-Lassen, M.L. Michna, K.A. Nugent, *University of Melbourne*

9:45 Measurement of Fiber Birefringence Using Lyot-Sagnac Interferometer, C.S. Kim, Y.G. Han, R.M. Sova, J.U. Kang, *Johns Hopkins University,* U.C. Paek, Y. Chung, *Kwangu Institute of Science and Technology*

10:00 **BREAK**

### Session VI. Polarization and Engineered Fibers, Chair: Julie Taylor, NPL

10:30 Determination of the Degree of Polarization Based on a Coherent Quantum Measurement, M. Legré, M. Wegmüller, N. Gisin, *University of Geneva*

10:45 Visualizing the Limitations of Four-state Measurement of PDL and Results of a Six-State Alternative, R.M. Craig, *NIST*

11:00 Four-State Measurement Method for Polarization Dependent Wavelength Shift, W.C. Swann, S.D. Dyer, R.M. Craig, *NIST*

11:15 **INVITED:** Measurement of Dispersion in Photonic Bandgap Fibers, J. Jasapara, OFS Laboratories
11:45 Counting Modes in Optical Fibres with Leaky Modes, A. Argyros, I.M. Bassett, *Australian Photonics CRC*
12:00 **LUNCH:**

**Session VII. Cavities and Resonances, Chair: Simon Fleming, University of Sydney**
1:30 **INVITED:** Measurement of Multipath Interference and Resulting Optical Communication System Penalty, D.L. Craig, M.G. Taylor, W. Zheng, J. Fowlkes, H.P. Sardesai, *CIENA Corporation*
2:00 Predicting MPI in Raman Optical Amplifiers by Measuring the Rayleigh Backscattering Coefficient, P.B. Gaarde, Y Qian, S.N. Knudsen, B. Pálsdóttir, *OFS Fitel Denmark*
2:15 Measurement of Multimode Resonances in Hexagonal Optical Micro-Pillar Cavities, N. Ma, A.W. Poon, *Hong Kong University of Science and Technology*
2:30 **INVITED:** Measurement Requirements for Optical and Optoelectronic Model Verification, Validation, and Calibration, J. Morikuni, P. Mena, B.K. Whitlock, R. Scarmozzino, *RSoft Design Group, Inc.*
3:00 **BREAK**

**Session VIII. OTDR and Component PMD, Chair: Greg Schinn, EXFO**
3:30 Photon-Counting OTDR at Telecom Wavelength: High-Resolution and Long-Distance Measurements, F. Scholder, A. Fougères, J.D. Gautier, C. Barreiro, A. Haldimann, H. de Riedmatten, M. Wegmüller, N. Gisin, *University of Geneva*
3:45 Coherent Speckle in Direct-Detection OTDR, S.G. Murdoch, *NetTest*
4:00 Full Measurement of the Spatial Distribution of PMD Using Backscatter, A.J. Rogers, S.V. Shatalin, *University of Surrey*
4:15 Polarisation Mode Dispersion in Restricted Optical Bandwidth: An Evaluation of Measurement Techniques, S. Harris, D. Ives, *NPL*
4:30 Measurement and Mitigation of Multiple Reflection Effects on the Differential Group Delay Spectrum of Optical Components, P.A. Williams, J.D. Kofler, *NIST*
4:45 π-Shifted All-Fire Sagnac Loop for Characterization of Femtosecond Polarization Mode Dispersion, E. Simova, I. Golub, *Institute for Microstructural Sciences*
5:00 **SESSION CLOSE**

### Thursday, September 26, 2002

**Session IX. PMD – Field Measurements, Chair: Arthur Barlow, PerkinElmer**
8:30 **INVITED:** Using Importance Sampling to Assess the Effects of PMD on System Performance, W.L. Kath, G. Biondini, *Northwestern University*
9:00 Investigations on the Relation Between PMD Coefficient and Cable Installation Year in Deutsche Telekom Fiber Plant, H.-J. Tessmann, D. Breuer, H.M. Foisel, H. Reiner, H. Cremer, *Deutsche Telekom*
9:15 Pulsed Measurement of Polarization Mode Dispersion in Field-Installed Optical Fibers, A.O. Kleivstul, *Telenor R&D,* A.S. Sudbø, *University Graduate Center-UniK*
9:30 Analysis and Comparison of Measuree DGD Data on Buried Single-Mode Fibers, C. Allen, P.K. Kondamuri, *University of Kansas,* D.L. Richards, D.C. Hague, *Sprint Corporation*

9:45 Statistical Evaluation of Polarization-Dependent Losses and Polarization-Mode Dispersion in an Installed Fiber Network, C.J.K. Richardson, *University of Maryland,* R.J. Runser, M.Goodman, *Laboratory for Telecommunication Sciences and Telecordia Technologies,* L. Mercer, *NRL*

10:00 **BREAK**

**Session X. PMD – System Applications, Chair: Casey Shaar, NetTest**

10:30 **INVITED:** Programmable Polarization Mode Dispersion Generation, J.N. Damask, P.R. Myers, T.R. Boschi, *YAFO Networks*

11:00 Measurement of Differential Group Delay Profiles in Fibers and in $LiNbO_3$ Distributed PMD Compensator, S. Bhandare, D. Sandel, R. Noé, H. Hermann, H. Suche, W. Sohler, *University of Paderborn*

11:15 Estimation of System Outage Statistics Due to Polarization Mode Dispersion, P.J. Leo, *YAFO Networks,* D.L. Peterson Jr, *WorldCom*, K.B.Rochford· *YAFO Networks*

11:30 Low-Coherence Interferometric Measurement of Differential Group Delay and its Dispersion to Second-Order in Polarisation Maintaining Fibre, D.A. Flavin, *Waterford Institute of Technology*, R. McBride, J.D.C. Jones, *Heriot-Watt University*

11:45 **SYMPOSIUM CLOSE**

The Symposium is held in the auditorium of the Department of Commerce Laboratories, 325 Broadway, Boulder, Colorado. Attendees must register in advance and make accommodation arrangements. Details, can be obtained from Wendy Ortega, NIST, (303) 497-4500, FAX (303) 497-5208, ortegaw@boulder.nist.gov, or on the web at http://www.boulder.nist.gov/div815/current.htm.

**SYMPOSIUM COMMITTEE** (G.W. Day, NIST, General Chair, P.A. Williams, NIST, Program Chair)

A. Barlow, PerkinElmer
D. Franzen, NIST
M. Hackert
A. Inenaga, JDS Uniphase
K. Okamoto, NEL
G. W. Schinn, EXFO
J. Taylor, NPL
S.C. Fleming, U. of Sydney
N. Gisin, U. of Geneva
T.A. Hanson, Corning
J. Jackel, Telcordia
W. Reed, OFS Fitel
C. Shaar, NetTest
K.K. Wong, Northstar Photonics

# *NIST Technical Publications*

## *Periodical*

**Journal of Research of the National Institute of Standards and Technology**—Reports NIST research and development in metrology and related fields of physical science, engineering, applied mathematics, statistics, biotechnology, and information technology. Papers cover a broad range of subjects, with major emphasis on measurement methodology and the basic technology underlying standardization. Also included from time to time are survey articles on topics closely related to the Institute's technical and scientific programs. Issued six times a year.

## *Nonperiodicals*

**Monographs**—Major contributions to the technical literature on various subjects related to the Institute's scientific and technical activities.

**Handbooks**—Recommended codes of engineering and industrial practice (including safety codes) developed in cooperation with interested industries, professional organizations, and regulatory bodies.

**Special Publications**—Include proceedings of conferences sponsored by NIST, NIST annual reports, and other special publications appropriate to this grouping such as wall charts, pocket cards, and bibliographies.

**National Standard Reference Data Series**—Provides quantitative data on the physical and chemical properties of materials, compiled from the world's literature and critically evaluated. Developed under a worldwide program coordinated by NIST under the authority of the National Standard Data Act (Public Law 90-396). NOTE: The Journal of Physical and Chemical Reference Data (JPCRD) is published bimonthly for NIST by the American Institute of Physics (AIP). Subscription orders and renewals are available from AIP, P.O. Box 503284, St. Louis, MO 63150-3284.

**Building Science Series**—Disseminates technical information developed at the Institute on building materials, components, systems, and whole structures. The series presents research results, test methods, and performance criteria related to the structural and environmental functions and the durability and safety characteristics of building elements and systems.

**Technical Notes**—Studies or reports which are complete in themselves but restrictive in their treatment of a subject. Analogous to monographs but not so comprehensive in scope or definitive in treatment of the subject area. Often serve as a vehicle for final reports of work performed at NIST under the sponsorship of other government agencies.

**Voluntary Product Standards**—Developed under procedures published by the Department of Commerce in Part 10, Title 15, of the Code of Federal Regulations. The standards establish nationally recognized requirements for products, and provide all concerned interests with a basis for common understanding of the characteristics of the products. NIST administers this program in support of the efforts of private-sector standardizing organizations.

*Order the* **following** *NIST publications—FIPS and NISTIRs—from the National Technical Information Service, Springfield, VA 22161.*

**Federal Information Processing Standards Publications (FIPS PUB)**—Publications in this series collectively constitute the Federal Information Processing Standards Register. The Register serves as the official source of information in the Federal Government regarding standards issued by NIST pursuant to the Federal Property and Administrative Services Act of 1949 as amended, Public Law 89-306 (79 Stat. 1127), and as implemented by Executive Order 11717 (38 FR 12315, dated May 11, 1973) and Part 6 of Title 15 CFR (Code of Federal Regulations).

**NIST Interagency or Internal Reports (NISTIR)**—The series includes interim or final reports on work performed by NIST for outside sponsors (both government and nongovernment). In general, initial distribution is handled by the sponsor; public distribution is handled by sales through the National Technical Information Service, Springfield, VA 22161, in hard copy, electronic media, or microfiche form. NISTIR's may also report results of NIST projects of transitory or limited interest, including those that will be published subsequently in more comprehensive form.

**U.S. Department of Commerce**
National Institute of Standards and Technology
325 Broadway
Boulder, Colorado 80305-3328